

Utilisation and Reliability of High Power Proton Accelerators

Workshop Proceedings
Santa Fe, New Mexico, USA
12-16 May 2002



Nuclear Science

Utilisation and Reliability of High Power Proton Accelerators

**Workshop Proceedings
Santa Fe, New Mexico, USA
12-16 May 2002**

© OECD 2003

NUCLEAR ENERGY AGENCY
ORGANISATION FOR ECONOMIC CO-OPERATION AND DEVELOPMENT

ORGANISATION FOR ECONOMIC CO-OPERATION AND DEVELOPMENT

Pursuant to Article 1 of the Convention signed in Paris on 14th December 1960, and which came into force on 30th September 1961, the Organisation for Economic Co-operation and Development (OECD) shall promote policies designed:

- to achieve the highest sustainable economic growth and employment and a rising standard of living in Member countries, while maintaining financial stability, and thus to contribute to the development of the world economy;
- to contribute to sound economic expansion in Member as well as non-member countries in the process of economic development; and
- to contribute to the expansion of world trade on a multilateral, non-discriminatory basis in accordance with international obligations.

The original Member countries of the OECD are Austria, Belgium, Canada, Denmark, France, Germany, Greece, Iceland, Ireland, Italy, Luxembourg, the Netherlands, Norway, Portugal, Spain, Sweden, Switzerland, Turkey, the United Kingdom and the United States. The following countries became Members subsequently through accession at the dates indicated hereafter: Japan (28th April 1964), Finland (28th January 1969), Australia (7th June 1971), New Zealand (29th May 1973), Mexico (18th May 1994), the Czech Republic (21st December 1995), Hungary (7th May 1996), Poland (22nd November 1996), Korea (12th December 1996) and the Slovak Republic (14 December 2000). The Commission of the European Communities takes part in the work of the OECD (Article 13 of the OECD Convention).

NUCLEAR ENERGY AGENCY

The OECD Nuclear Energy Agency (NEA) was established on 1st February 1958 under the name of the OEEC European Nuclear Energy Agency. It received its present designation on 20th April 1972, when Japan became its first non-European full Member. NEA membership today consists of 28 OECD Member countries: Australia, Austria, Belgium, Canada, Czech Republic, Denmark, Finland, France, Germany, Greece, Hungary, Iceland, Ireland, Italy, Japan, Luxembourg, Mexico, the Netherlands, Norway, Portugal, Republic of Korea, Slovak Republic, Spain, Sweden, Switzerland, Turkey, the United Kingdom and the United States. The Commission of the European Communities also takes part in the work of the Agency.

The mission of the NEA is:

- to assist its Member countries in maintaining and further developing, through international co-operation, the scientific, technological and legal bases required for a safe, environmentally friendly and economical use of nuclear energy for peaceful purposes, as well as
- to provide authoritative assessments and to forge common understandings on key issues, as input to government decisions on nuclear energy policy and to broader OECD policy analyses in areas such as energy and sustainable development.

Specific areas of competence of the NEA include safety and regulation of nuclear activities, radioactive waste management, radiological protection, nuclear science, economic and technical analyses of the nuclear fuel cycle, nuclear law and liability, and public information. The NEA Data Bank provides nuclear data and computer program services for participating countries.

In these and related tasks, the NEA works in close collaboration with the International Atomic Energy Agency in Vienna, with which it has a Co-operation Agreement, as well as with other international organisations in the nuclear field.

© OECD 2003

Permission to reproduce a portion of this work for non-commercial purposes or classroom use should be obtained through the Centre français d'exploitation du droit de copie (CCF), 20, rue des Grands-Augustins, 75006 Paris, France, Tel. (33-1) 44 07 47 70, Fax (33-1) 46 34 67 19, for every country except the United States. In the United States permission should be obtained through the Copyright Clearance Center, Customer Service, (508)750-8400, 222 Rosewood Drive, Danvers, MA 01923, USA, or CCC Online: <http://www.copyright.com/>. All other applications for permission to reproduce or translate all or part of this book should be made to OECD Publications, 2, rue André-Pascal, 75775 Paris Cedex 16, France.

FOREWORD

These proceedings contain the papers presented at the Third Workshop on Utilisation and Reliability of High Power Proton Accelerators (HPPA), organised by the Nuclear Science Committee of the OECD Nuclear Energy Agency (NEA). The first meeting in this series was held in Mito, Japan on 13-15 October 1998 and the second meeting took place in Aix-en-Provence, France on 22-24 November 1999. The proceedings of both meetings have been published by the OECD/NEA (ISBN 92-64-17068-5 and ISBN 92-64-18749-9).

The third workshop focused on (1) the reliability of the accelerator and the impact of beam interruptions on the design and performance of the accelerator-driven system, (2) spallation target design characteristics and the impact on the multiplier design, including materials, radiation damage and embrittlement, enhanced corrosion, cooling issues with high-power density, and windowless design concepts, and (3) safety and operational characteristics of a multiplying system driven by a spallation source.

A fourth meeting in this series of workshops is planned to be held in spring 2004 in the Republic of Korea.

Acknowledgements

The OECD/NEA gratefully acknowledges the Los Alamos National Laboratory (LANL) for hosting the Third Workshop on Utilisation and Reliability of High Power Proton Accelerators. Special thanks are extended to Ms. Berylen Rogers (LANL) for having collected the workshop papers and to Ms. Hélène Déry (NEA) for having prepared the proceedings for publication.

TABLE OF CONTENTS

FOREWORD.....	3
EXECUTIVE SUMMARY	9
SESSION I: OPENING	
CHAIR: D. RUSTHOI	13
<i>B. Carlucci, H. Ait Abderahim, A.C. Mueller</i> The European programme	15
<i>W.S. Park, Y.S. Cho, B.H. Choi</i> Korean R&D programme for HPPA	33
<i>F. Goldner</i> The US advanced accelerator applications programme	45
<i>T.P. Wangler</i> Reliable linac design for accelerator-driven subcritical reactor systems	49
<i>Th. Stammbach, S. Adam, A. Mezger, P. Sigg, P.A. Schmelzbach</i> Reliable cyclotron design	59
<i>G.S. Bauer</i> Towards reliable high power spallation target designs	81
<i>M. Salvatores, A. D'Angelo, D. Naberejnev</i> The demonstration of the ADS concept	95
<i>S.A. Maloy, M.R. James, G. Willcutt, W.F. Sommer, M. Sokolov, L.L. Snead, M.L. Hamilton, F. Garner</i> The mechanical properties of 316L/304L stainless steels, Alloy 718 and Mod 9Cr-1Mo after irradiation in a spallation environment	105
SESSION II: ACCELERATOR, TARGET/WINDOW/MATERIALS AND MULTIPLIER	
CHAIR: R. SHEFFIELD	125
<i>R. Gobin, P.-Y. Beauvais, D. Bogard, R. Ferdinand, P. Mattéi</i> Reliability tests of the high-power proton source SILHI at CEA/Saclay.....	127

<i>E. Chiaveri, R. Losito, S. Calatroni, R. Ballantini, A. Chincarini, G. Gemme, R. Parodi D. Barni, A. Bosotti, C. Pagani, P. Pierini</i> Operational experience with a 352 MHz 5-cell accelerating structure for the high energy section of the TRASCO linac	135
<i>N.T. Callaway, R.D. Ryder</i> Beam reliability and equipment downtime tracking – How LANSCE closes the loop	145
<i>T. Matsumoto</i> Comments to accelerator-driven system	151
<i>N. Ouchi</i> R&D status of super-conducting proton linac and the KEK/JAERI high intensity proton accelerator project	157
<i>R. Valdiviez, D. Schrage, S. Shen, K. Kishiyama</i> The use of NEG vacuum pumps on the LEDA RFQ	167
<i>R.S. Lillard, G.T. Chandler, P.D. Ferguson, F.D. Gac, M.R. James, S.A. Maloy, M.A. Paciotti, L.S. Waters, G.J. Willcutt</i> Corrosion measurements on APT prototypic materials in the LANSCE high-power proton beam and applicability to other systems	175
<i>M.R. James, R.T. Klann, G.L. Morgan, E.J. Pitcher, M.A. Paciotti, J.M. Oostens</i> Preliminary measurements from a thick lead-bismuth target using 800 MeV protons	193
<i>R.C. Haight, M. Devlin</i> Gas production cross-section measurements at LANSCE	201
<i>X. Cheng, P.J. Finck, J. Roglans-Ribas, T. Schulenberg</i> Thermal-hydraulic design analysis of a 5 MW sodium-cooled tungsten target	209
SESSION III: TEST FACILITIES AND CONTROL/SAFETY/SHUTDOWN	
CHAIR: Ph. FINCK	225
<i>M. Eriksson, J. Wallenius, J.E. Cahalan, K. Tucek, W. Gudowski</i> Safety analysis of Na and Pb-Bi coolants in response to beam instabilities	227
<i>J.E. Cahalan, M. Eriksson</i> Active and passive safety control performance in subcritical, accelerator-driven nuclear reactors	237
<i>A. Negrini, G. Proto</i> Operating requirements for a proton beam accelerator to couple with a subcritical system	259
<i>B.E. Boyack, M.W. Cappiello, K.O. Pasamehmetoglu</i> Safe shutdown of accelerator-driven systems	289

<i>D. Barni, P. Michelato, D. Sertore, A. Bonucci, R. Giannantonio, P. Turrone, L. Cinotti</i> Theoretical and experimental evaluation of the windowless interface for the TRASCO-ADS project.....	299
<i>K. Van Tichelen, P. Kupschus, B. Arien, H. Ait Abderrahim</i> Design and verification experiments for the windowless spallation target of the ADS prototype MYRRHA	311
<i>L. Zanini, A. Ferrari, A. Herrera-Martínez, Y. Kadi, C. Rubbia, N. Burgio, M. Carta, A. Santagata, L. Cinotti</i> Radioprotection calculations for the TRADE experiment	327
<i>F.E. Dunn</i> Thermal response of the multiplier of an accelerator-driven system to beam interruptions.....	345
<i>M. Cappiello, K. Pasamehmetoglu, E. Pitcher, R. Guffee, W. Chaves, G. Willcutt</i> Accelerator-driven test facility: modular target and multiplier system concept design description	359
<i>Y. Gohar, P. Finck, A. Hanson, J. Herceg, M. Koploy, L. Krajtl, P. Mijatovic, W.D. Pointer, J. Saiveau, T. Sofu, M. Todosow</i> Lead-bismuth spallation target design of the accelerator-driven test facility (ADTF).....	373
<i>V. Tcharnotskaia, C. Ammerman, K. Woloshun</i> Results from the initial operation of the LANL DELTA loop	385
SUMMARY OF DISCUSSION SESSIONS.....	397
<i>Chair: M. Cappiello</i> Summary of working group discussion on design considerations, reliability performance and requirements for the accelerator	399
<i>Chairs: Carlo Pagani, P. Colestock</i> Summary of working group discussion on accelerators.....	401
<i>Chairs: E. Pitcher, E. Gonzalez</i> Summary of working group discussion on multiplier	405
<i>Chairs: K. Pasemehmetoglu, G. Laffont</i> Summary of working group discussion on target technology	409
<i>Chair: M. Cappiello</i> Summary of working group discussion on control/safety/shutdown	413
<i>Chair: K. Pasemehmetoglu</i> Summary of final working group discussion	417
List of participants.....	421

EXECUTIVE SUMMARY

Background

R&D activities and construction plans related to high power proton accelerators (HPPAs) are being considered in various countries to promote basic and applied sciences, including accelerator-driven nuclear energy systems (ADS). The performance of such hybrid nuclear systems depends to a large extent on the specification and reliability of the particle accelerator, as well as the integration of the accelerator with spallation targets and in some cases, subcritical assemblies.

The present meeting is a follow-up to the second workshop on “Utilisation and Reliability of High Power Proton Accelerators” that was hosted by CEA Cadarache and held in Aix-en-Provence, France in 1999. Many of the questions discussed during the Aix-en-Provence workshop were further developed at this meeting. In addition, there were specific presentations devoted to safety, regulatory and technological requirements for the commissioning, operation and restart of hybrid nuclear systems.

Topics covered by the workshop

The meeting consisted of plenary sessions with invited papers, contributed papers, working group discussions and general discussions. Topics of contributed papers included:

- accelerator technology;
- target, window and multiplier technology;
- control, safety and shutdown;
- test facilities.

Main findings, general conclusions and needed R&D

General

- **Safety vs. performance** – k_{eff} for an ADS needs to be established (lower is safer, higher provides more performance); however, fuel must first be determined before a specific k_{eff} can be implemented in a design.

- **Reference design** – A reference design is to be established to which one can assign a k_{eff} , define a fuel and a range of power. Much work has been done in the past two years, but there has been no progress on or application to a reference design.
- **Experimental validation** – Experimental evidence of the concept is needed. TRIGA/TRADE has great potential; the international scientific community should submit a proposal or define test plans for this experiment.
- **Safety** – Many accelerators and many reactors have been designed, but one may need to make changes in the designs to couple them together. A new safety envelope needs to be defined. Although the reactor and accelerator are separate concerns, and the accelerator beam can be tripped very reliably, one must be able to shutter or stop the beam in the reactor itself. Also, the accelerator designers should try to develop a list of shutdown concepts (passive vs. active) in each safety class.
- **Licensing** – One must consider engaging the licensing authority early. One should also implement a reference design or initiate a project with the involvement or under the scrutiny of a licensing authority. One idea would be to use existing reactor designs: MYRRHA and/or a US example could be considered as a test case on the design/licensing interactions.

Accelerator

- **Reliability requirement** – Consensus is that one can have an accelerator that will fulfil the reactor (reliability) requirements within the next four years.
- **Experimental programme** – An experimental programme (like LEDA and IPHI) is needed to gain the necessary confidence (in “beam continuity”, new electronics, over-design applications, etc.). This requires an R&D programme (with the estimated cost ranging between US\$30 and 300 million).
- **Focus** – One needs to focus on one application (multi-purpose is difficult).

Target/window

- **Focus on lead-bismuth eutectic (LBE)** – At the current pace of research worldwide, one could comfortably deliver the required LBE spallation target technology within about five years.
- **Window materials** – There are materials issues for the window, and there are no existing facilities to test the window at prototypic temperatures, fluence, etc.
- **Windowless technology** – R&D on windowless technology must continue to achieve this objective; there are many associated benefits. A test facility with a beam is an issue.

Multiplier

- Fast spectrum is the correct choice for multipliers.

- Liquid metal of 800-1 000 MWth is the desired system.
- LBE and a gas-cooled system are being pursued in Europe.
- Sodium is an option in the United States.
- The clad material choice is T-91 (9Cr-1Mo) as per MYRRHA X-ADS.
- Minimising reactivity swing is highly desirable.
- Fuel issues are among the most challenging in the development of ADS.
- Design improvements are possible for thermal fatigue (a focal issue for reference design studies).
- Multiplier designs should consider long beam trips (e.g. 1 hour, 1 day).
- Maintenance and scheduled shutdown should be considered for different components.

Next workshop

It is planned to hold a follow-up workshop in spring 2004 in the Republic of Korea.

SESSION I

Opening

Chair: D. Rusthoi

THE EUROPEAN PROGRAMME

Bernard Carluec

Framatome ANP

bernard.carluec@framatome-anp.com

10, rue Juliette-Récamier
F-69456 Lyon CEDEX 06

Hamid Aït Abderahim

SCK•CEN

haitabde@sckcen.be

Boeretang 200
B-2400 Mol

Alex C. Mueller

CNRS IN2P3

mueller@ipno.in2p3.fr

F-91406 Orsay

Introduction

The 21st century is coming with a number of challenges to a sustainable growth. In particular the fulfilment of the growing energy demand through the use of fossil fuels, as presently happens, has a limited future for considerations of resource management and the growing awareness of the risk of climatic change.

The European Commission's green paper: "Towards a European strategy for the security of energy supply" [1] clearly points out the importance to take into consideration all reasonably exploitable resources in Europe. Especially nuclear fission power should take a substantial share, provided that the problems of managing and stocking nuclear waste might be solved.

The strategy related to the closure of the fuel cycle depends on nuclear policies adopted by each European union member state. In any case, the transmutation of most of the long-lived radioactive waste is a promising solution, which could play a substantial role.

Both critical and subcritical reactors are potential candidates as dedicated transmutation systems. Critical reactors, however, loaded with fuel containing large amount of minor actinides (Americium and Curium) pose safety problems caused by unfavourable reactivity coefficients and small delayed neutron fraction. With regard to this latter problem, the subcriticality is particularly favourable and allows a maximum transmutation rate while operating in a safe manner.

The subcritical reactors are accelerator-driven systems (ADS) constituted by the coupling of a proton accelerator, a spallation target and the subcritical core.

The activities of the European Union and the member states in the frame of nuclear waste transmutation have been co-ordinated:

- Firstly, by the establishment of a European technical working group (ETWG) under the chairmanship of Prof. Carlo Rubbia, which has issued a road map [2] for preparing a demonstration programme to be performed. The recommendations of the technical working group are the need to design and operate, approximately in a decade, an experimental ADS at a sufficient large scale to become the precursor of the industrial practical scale transmuter. Such a facility, for which a common European effort is deemed necessary, is considered the fastest and most effective way to conclusively assess the potential and the feasibility of full scale industrial programme based on ADS; it is also assessed that in such a perspective the creation of an industrial platform is highly recommended.
- As a consequence of the ETWG recommendations, by the implementation of studies dedicated to the partitioning and transmutation of the nuclear wastes and sponsored by the European Commission. Among these studies, the project PDS-XADS is dedicated to the preliminary design studies of an experimental ADS. This concerns the design studies of the main components of an ADS: the accelerator, the spallation target and the reactor.

The PDS-XADS project

Objectives

The demonstration of the practicability of transmutation on an industrial scale requires to operate at a European level, an experimental ADS (XADS) which will demonstrate the coupling of the accelerator, the neutron spallation target and the subcritical core. Complementary to the demonstration of the basic phenomena involved in the ADS technologies, the preliminary engineering design studies of the XADS have to be performed in order to select the most promising technical concepts, to address the critical points of the whole system, to identify the research & development (R&D) in support, to define the safety and licensing issues, to preliminary assess the cost of the installation, and, then, to consolidate the road map of the XADS development. The assessment and comparison studies of the different conceptual designs of the main systems will allow to identify the most promising solutions which could be studied in detail in the next phases, and eventually realised.

A great amount of R&D and engineering activities have been already performed in Europe to demonstrate separate basic aspects of the ADS concept and to define conceptual reference configurations of the installation. Several different technological and design options have been considered and now studied in more details.

Taking into account that fast neutron spectrum is the a priori solution for transmutation purpose, the R&D efforts are focused on liquid metal-cooled ADS and gas-cooled ADS. The preliminary design studies are concentrated mainly on three concepts of the nuclear reactor part:

- a large gas-cooled concept (about 80 MW thermal – see Figure 3);
- a large lead-bismuth eutectic (LBE)-cooled concept (about 80 MW – see Figure 2);
- a smaller LBE-cooled concept (about 30 MW thermal); this concept is the MYRRHA concept initially developed by Belgian organisations (see Figure 4).

An alternative candidate is the sodium-cooled concept, but because of the considerable existing knowledge and validation on sodium technology, similar preliminary design studies have a lower urgency compared to the other concepts that are very innovative. The studies of a sodium-cooled concept are therefore, not included in the PDS-XADS project.

The spallation target is preferably a liquid heavy metal. LBE has been selected for this purpose. Two main concepts are envisaged: liquid heavy metal separated or not from the accelerator by a wall (called window) in contact with the heavy metal.

For the accelerator, the two envisaged types of machine are the cyclotron and the linac.

The purpose of the PDS-XADS project is to develop these configurations to a level sufficient to define precisely the supporting R&D needs, perform objective comparisons and recommend the solutions to be engineered in detail and realised.

Organisation of the PDS-XADS project

Twenty-five European organisations (Table 1) participate to the PDS-XADS project.

They represent the major European organisations in the frame of nuclear plant design (industrial companies), R&D in support to nuclear plant development (national research centres, labs and universities), accelerator design and development (industrial companies, research centres and universities).

The studies of the PDS-XADS project started in November 2001, for duration of three years. The budget of the project is about 12 M€, about 50% being funded by the European Commission, and 50% being paid by each participating organisation.

The PDS-XADS project is organised in order to integrate at the very early beginning of the conceptual design any constraint and request of the three main components of ADS.

The PDS-XADS project is split in five main workpackages (WP), the overall co-ordination being assured by Framatome-ANP SAS, France. Each WP is led by an adequate organisation taking into account the studies previously performed on these topics. The following workpackages are defined:

WP1: Global coherency (leadership: Commissariat à l'Énergie Atomique, France)

The first workpackage (WP1) is dedicated to the definition of the objectives and then the general specifications of the XADS. This is established consistently with the conclusions of the European road map and the recommendations of ETWG where the different radioactive waste policies of the European Union member states are taken into account. WP1 is in charge to achieve the definition of the missions of the XADS. It is also in charge of the definition of the methodologies and criteria for the comparison of the concepts under examination, and at the end of the project it will propose recommendations for future development as well as R&D needs. The recommendations for the choice of the reference concepts will be based on the studies of the LBE-cooled and the gas-cooled concepts, including also a sodium-cooled concept extrapolated from the available studies about advanced sodium-cooled fast neutron reactors. The studies of advanced sodium-cooled reactors are judged sufficiently developed for avoiding to perform specific XADS design studies, contrary to the cases of LBE-cooled and gas-cooled concepts.

WP2: Plant performance and safety

The workpackage WP2 is in charge to propose a safety approach for the XADS based on the European licensing requirements for future nuclear facilities. It has to establish common rules for defining the events to consider for the design. Then, it has to develop the calculation tools, to identify the R&D safety needs, and then to perform the preliminary safety evaluation of the XADS concepts. In order to organise the various tasks to perform in the safety area, WP2 is sub-divided in three sub-workpackages: WP2.1 (*leadership: Framatome-ANP SAS, France*) related to the general safety approach, WP2.2 (*leadership: Kungl Tekniska Högskolan, Sweden*) for the modelling of the phenomena important for the safety studies, and WP2.3 (*leadership: Empresarios Agrupados, Spain*) for the preliminary safety evaluation of the XADS concepts.

WP3: Accelerator (leadership: Centre National de la Recherche Scientifique – Institut National de Physique Nucléaire et de Physique des Particules, France)

The workpackage WP3 is in charge to provide the frame and the essential requirements for a concerted European effort for the design and eventually installation of an XADS high-intensity proton driven accelerator, which critically determines the overall performance of the system. It is the aim of WP3 to examine the relevant aspects concerning this accelerator. Thus, the planned task has to define an accelerator and beam transport line up to the spallation target. Linac and cyclotron type accelerators are investigated with the main emphasis on the specific XADS requirements:

- ADS-class accelerator characteristics such as reliability, availability, stability and reproducibility of power control, including shutdown and power limitation, and maintainability;
- The R&D needed for performance and cost optimisation on accelerator component critical to ADS-class characteristics;
- The choice for a reference accelerator and the beam transport up to the spallation target, including the medium to long-term extrapolation from an experimental to an industrial machine;
- The road map for the item above.

The inventory of specifications, generated jointly with the other workpackages, includes, both for linac and cyclotron, and in connection with the spallation target and the subcritical core the following characteristics: maximum beam current and energy, range of these parameters, current accuracy and energy control, associated time constant, performance of the beam shutdown system, reliability and availability, restart procedure, control of beam footprint on the target; beam losses along the line and associated shielding and time for access.

High-intensity accelerator technology is presently progressing due to the experimental and theoretical R&D activities made in various laboratories participating at the PDS-XADS project. The results from these important national programmes are used as basis for the definition of future ADS specific R&D needs to be performed. The commonly performed critical analysis of accelerator experts from the involved laboratories together with specialists from the industrial partners ensures that a viable road map and cost analysis both for the initial investment as for the operating costs can be performed for an XADS reference accelerator, including the ability to extrapolate to long-term industrial machines.

The initial work is concentrated on reliability and cost analysis and aims at identifying the components for which a future R&D programme would optimise these former two aspects.

An additional task of WP3 is to establish links between the specific accelerator studies, the specific spallation target studies, and the specific reactor studies. In particular the requirements and constraints from these components, related to availability, power variations, start-up and shutdown, repair and handling process, geometrical consistency have to be commonly examined and integrated in the design process.

WP4: Core and target

The workpackage WP4 is sub-divided in three sub-workpackages. WP4.1 (*leadership: Ansaldo, Italy*) related to the core studies of the LBE-cooled concept, WP4.2 (*leadership: National Nuclear Corporation Limited, UK*) related to the core studies of the gas-cooled concept, and WP4.3 (*leadership: Framatome-ANP GmbH, Germany*) related to the spallation target design studies. The core and spallation target studies of the MYRRHA concept are performed in the WP5.3.

WP5: System integration

The objective of the workpackage WP5 is the development of a consistent design of the main functional and mechanical equipment constituting the primary system of the reactor. WP5 is subdivided in three workpackages: WP5.1 (*leadership: Ansaldo, Italy*) related to the system integration in the primary system of the LBE-cooled concept, WP5.2 (*leadership: Framatome-ANP SAS, France*) related to the system integration in the primary circuit of the gas-cooled concept, and WP5.3 (*leadership: SCK•CEN, Belgium*) related to the system integration of the MYRRHA concept.

The European XADS specifications

The main missions of the XADS are first to demonstrate the operability of the ADS concept at a sufficient power level, secondly, to achieve the demonstration of the ADS technologies, and then, to use XADS as an irradiation tool.

Therefore the use of XADS should be done in two phases:

- Phase 1, which uses available fuel technology and is devoted to the demonstration of ADS concept and for irradiation purposes, in particular fuels dedicated to transmutation.
- Phase 2, which is devoted to the transmutation demonstration with a large number of minor actinide-based fuel elements. During this phase, XADS will be used more and more as demonstration of a transmuter.

In order to achieve these objectives, the key requirements of the XADS focus on a subcritical core operating with a fast neutron spectrum and a high neutron flux.

Additionally, the XADS must have a large flexibility in terms of subcriticality level and fuel technology, be robust and based on a sound and safe technology.

The XADS must have a minimum power level in order to demonstrate the feasibility of ADS at an industrial scale.

The demonstration of operability should be focused on the control of the accelerator and the subcritical core, the behaviour of the system during transients, the reliability of the system, especially the accelerator components.

Subcriticality

The subcriticality level has to be defined considering mainly anticipated safety requirements for a transmuter core. The reactor must be sufficiently subcritical for eliminating any risk of prompt criticality for a large range of normal and accidental events. As a consequence, a high-energy proton beam is needed, and that may be penalising from an economical and availability point of view. Therefore a properly balanced approach is needed.

In particular conditions, especially in shutdown conditions, the subcriticality level may be achieved by using neutron absorber systems. In power operations, control rods similar to those used in critical reactor should be avoided.

Power level

The XADS power level has to be sufficient to be representative of an ADS burner. The value of around 80 MW has been judged to be adequate for this purpose.

The technology demonstration of ADS transmuter is not the priority of the MYRRHA concept, which is an experimental facility dedicated to more basic aspects of ADS and irradiation purposes. Therefore, in the MYRRHA concept it is judged unnecessary to obtain so high power level. A value of around 30 MW has been judged to be optimised for MYRRHA.

In any case, exploitation of the generated power, even for self-operation of the accelerator, is not mandatory for the demonstration plant, but might be evaluated.

Fuel technology

In the first phase of the XADS, MOX fuel can be used for the demonstration and irradiation objectives. The demonstration of the transmutation will be done in the second phase with dedicated fuel. The validation of such a fuel having a high content of minor actinides could be done in the XADS during phase 1.

The capability to use during the first phase, existing MOX fuel from SNR-300 or SPX1 has to be investigated.

Accelerator

The optimisation of the proton beam energy for production of neutrons by spallation is in the range of 600 to 1 000 MeV. With such an energy, the current needed for producing the required power at the required subcritical level has to be between 5 and 10 mA.

Concerning the reliability and availability of the accelerator, the requirement is defined comparing with existing critical plants and taking into account the experimental characteristic of XADS. The objective is to limit the number of long duration beam interruptions (this means more than 1 second) to about 5 per year.

Spallation module

In order to contain specifically the spallation products generated during the operation of the target module, the spallation should be completely contained in a dedicated envelope. In particular, the spallation module has to be independent from the reactor primary circuit.

The conversion yield of an accelerated proton beam into spallation neutrons is most efficient with high-Z nuclei material; also, because of the high power generated in the spallation target by the colliding protons, a liquid metal target (lead-bismuth eutectic – LBE) is the reference solution.

The interface between the spallation target may be done either by a solid wall in contact with LBE (window concept), or directly through the free level of LBE (windowless option). In any case sufficient barriers have to be implemented for achieving the containment of the spallation products, even in case of failure of the window (in the window concept).

Accelerator of the XADS

Since the present conference is addressing in particular also the technological aspects of HPPA (high power proton accelerator), we will describe in this section in some more details the work which has been started within WP3. The organisations involved in these studies are *Centre National de la Recherche Scientifique – Institut National de la Physique Nucléaire et de la Physique des Particules (France)*, *Commissariat à l'Énergie Atomique (France)*, *Framatome-ANP (France)*, *Istituto Nazionale di Fisica Nucleare (Italy)*, *Ente per le Nuove tecnologie, l'Energia et l'Ambiente, (Italy)*, *Ansaldo (Italy)*, *Universität Frankfurt (Germany)*, *Forschungszentrum Jülich (Germany)*, *Framatome-ANP GmbH (Germany)*, *Ion Beam Applications SA (Belgium)* and *Instituto Tecnológico e Nuclear (Portugal)*. In practice, the work is carried out and organised through six “deliverables”, which are reports of well defined scope. Table 2 shows these, and provides some associated information.

Naturally, WP3 focuses its present work on the deliverable D9, “Requirements for the XADS accelerator & the technical answers”. Most important input is coming from WP1 (and in particular the deliverable D1 which defined the primary technical specification, see also the information given in the preceding sections). It has been already established, more generally for D1 and more specifically concerning the accelerator for D9, that the work of the ETWG constitutes a solid basis from which the more detailed studies can be started.

The ETWG has qualified the linear-type accelerator, which SCRF (superconducting radio-frequency) cavities for the high energy part as “the solution of choice” for high-power accelerator applications, that is for a power level which exceeds, say, 2 MW. Such a linac is schematically depicted in Figure 5. WP3 is presently investigating in more detail the arguments given and their relative weight. Besides the initial arguments: 1) that such a linac matches perfectly the required energy regime, and that its inherent modularity allows an easy upgrade to whatever energy finally demanded for industrial transmutation, 2) that the projected beam currents of such a linac very safely fulfil the industrial request, two other considerations emerge as being in particular support for an SCRF based linac:

- reliability, availability, maintainability;
- cost-optimisation of the operation.

Indeed, the initial studies carried out in WP3 confirm that SCRF technology has a very high reliability potential because several typical failures can be addressed by means of an adequate design philosophy:

- The outstanding performance which is presently observed with respect to the acceleration-gradients, better than 25 MV/m, e.g., for the elliptical cavities of the high energy section, allows to implement an extremely conservative over-design approach (in practice gradients about a factor of two smaller will be used) without reaching a prohibitive size of the accelerator. Present studies are focusing to maintain that conservative strategy for the other components, e.g. the couplers and the RF power supplies.
- This over-design will be accompanied with a high modularization (to which a linac intrinsically lends itself) of all components. This will allow to favour redundancy (“spare on-line”), and therefore, reliability and maintainability. In that respect, it is also discussed to operate simultaneously two independent front-ends.
- Pushing the concept of modularity, it is envisaged, in particular for the intermediate energy section, to actually use independently phased SCRF cavities. An associated fast control-system may allow to retune the cavities downstream in order to maintain good quality beam, even when a section is tripped (“fault-tolerant design”). Beam dynamics simulations are presently under way to assess quantitatively this highly attractive reliability measure, including also other tripped components of the linac (quadrupoles).
- The high modularization into power- and size-limited components will make a very active spare part policy possible, which needs to be associated with preventative maintenance measures.
- Another important aspect of maintainability is that the accelerator should have very low beam losses, in order to avoid activation of the structure and to permit easy human access (“hands-on maintenance”). Beam dynamics calculations show that SCRF cavities with their apertures being large with respect to the beam size do exhibit that required feature.

Concerning cost-optimisation it is clear that the over-design philosophy will induce certain additional costs. The high modularity is expected to give rise, on the other hand, to cost-savings because of industrial-type manufacturing, in particular for electronic and mechanical components. The use of SCRF technology, from an as low-energy regime as feasible, will also optimise the plug efficiency of the accelerator since this is the most efficient way to convert RF electrical power into beam power.

Although the superconducting linac solution is thus considered as the base-line option, WP3 is presently also assessing certain aspects of cyclotron technology. Indeed, we have come to the preliminary conclusion that a 600 MeV cyclotron may be technically feasible. However, we have disqualified ejection schemes that would use electrostatic deflectors or H^- stripping for the reasons of reliability and maintainability. The only realistic solution for the required intensity regime is thus acceleration of H_2^+ beams with ejection through stripping. In that case the required magnetic rigidity would lead, for conventional technology, to an accelerator twice the size of the PSI machine, or to a technically rather challenging superconducting cyclotron. In both cases there might be manufacturing problems, and it is not clear if the cost advantage which lower-intensity cyclotrons have, compared to linacs, is still valid. In the future, WP3 will elaborate a more quantitative assessment, including other considerations for reliability improvements of cyclotrons notwithstanding the present feeling favours in this aspect, as discussed above, the linac technology.

The beam-line connecting the accelerator to the spallation target is another important task. A preliminary design is presently evaluated to some detail. The beam would be directed vertically from above, by means of a doubly achromatic design with 45° bending magnets. A first finding is that the weight of the magnets could be kept below 15 tons, which greatly facilitates the handling and mounting. It is also shown that the focalisation system and a beam wobbling system, installed before the last bending magnet, matches the required beam size at the spallation target without the need of any other active device downstream of this last magnet.

A last observation is that the studies of WP3 keep in mind to identify the necessary R&D for the future, in particular in the context of funding demands within the next European programme (FP6). Although these evaluations have just started, it is already possible to anticipate that there will be a main focus to the qualification of full-scale accelerator components with respect to their reliability.

Conclusion

The European programme is a rationale approach allowing to select, then develop a European XADS. The PDS-XADS project involves the major nuclear and accelerator design organisations in Europe. The studies are starting now and no critical point has been identified. In particular, the first results on the accelerator part are very promising.

REFERENCES

- [1] Commission of the European Communities, Green Paper, “Towards a European strategy for the security of energy supply”, COM(2000) 769.
http://europa.eu.int/comm/energy_transport/library/livre-vert/livre-vert-en.pdf
- [2] “An European Road map for Developing Accelerator Driven Systems (ADS) for Nuclear Waste Incineration”, The European Technical Working Group on ADS – April 2001.
<http://itumagill.fzk.de/ADS/>

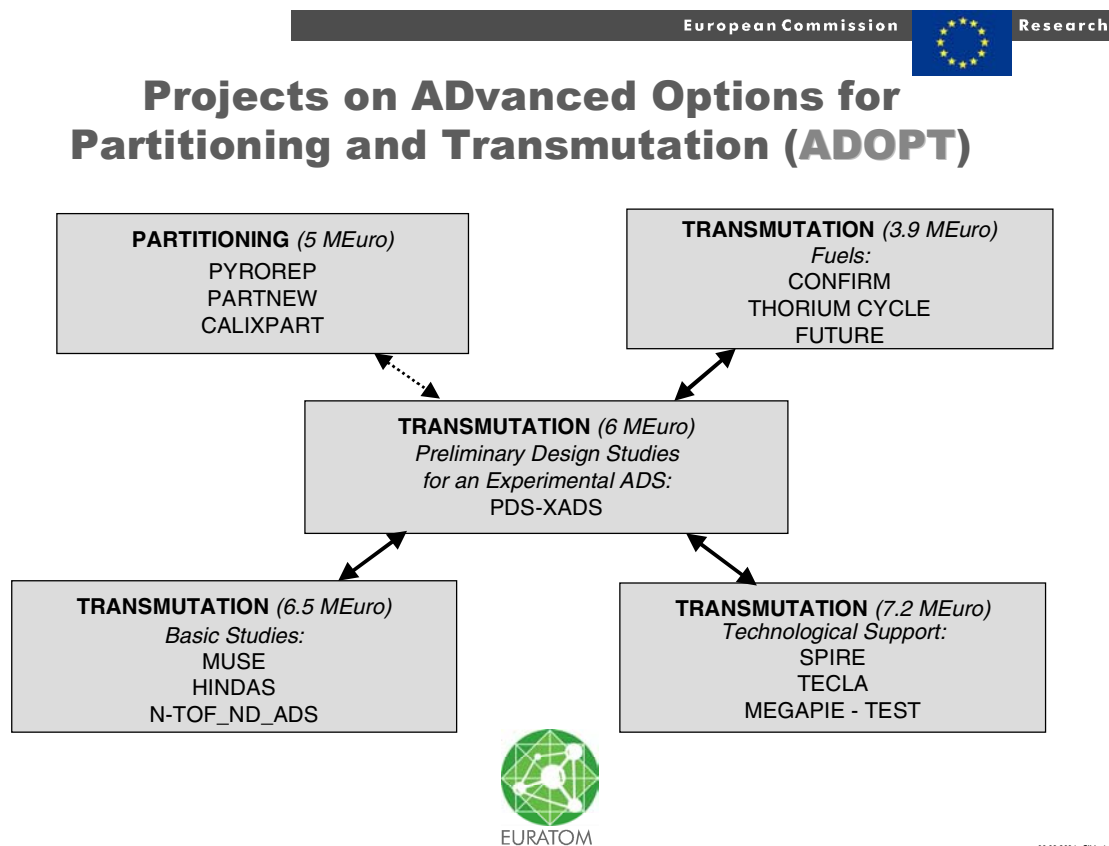
Table 1. Organisations participating at the PDS-XADS project

Organisations			
1	Framatome-ANP SAS	(FANP SAS)	F
2	Ansaldo	(ANS)	I
3	Tractebel SA	(TEE)	B
4	Empresarios Agrupados	(EA)	E
5	National Nuclear Corporation Limited	(NNC)	UK
6	Framatome-ANP GmbH	(FANP GmbH)	D
7	BNFL	(BNFL)	UK
8	Commissariat à l'Énergie Atomique	(CEA)	F
9	CIEMAT	(CIEMAT)	E
10	Centre National de la Recherche Scientifique – Institut National de Physique Nucléaire et de Physique des Particules	(CNRS)	F
11	University of Frankfurt	(UF)	D
12	EC-JRC-Petten	(JRC)	NL
13	Ente per le Nuove tecnologie, l'Energia et l'Ambiente	(ENEA)	I
14	FZK	(FZK)	D
15	Istituto Nazionale di Fisica Nucleare	(INFN)	I
16	University of Mining and Metallurgy	(UMM)	PL
17	Paul Scherrer Institute	(PSI)	CH
18	Nuclear Research & Consultancy Group	(NRG)	NL
19	Kungl Tekniska Högskolan	(KTH)	S
20	SCK•CEN	(SCK•CEN)	B
21	Universita Politecnica de Madrid	(UPM)	E
22	CRS4	(CRS4)	I
23	Instituto Tecnológico e Nuclear	(ITN)	PT
24	Ion Beam Application	(IBA)	B
25	Forschungszentrum Jülich	(FZJ)	D

Table 2. Deliverables

Deliverables No	Title	Responsible	Participants
D9	Requirements for the XADS accelerator and technical answers	CEA	ANS, CNRS, UF, INFN, ITN
D47	Accelerator: Feedback systems, safety grade shutdown and power control	CEA	CNRS, INFN, ITN
D48	Accelerator: Radiation safety and maintenance	CNRS	FANP GmbH, CEA, INFN
D57	Potential for reliability improvement and cost optimisation of linac and cyclotron accelerators	INFN	CEA, CNRS, ENEA, IBA
D63	Definition of the XADS-class reference accelerator concept and needed R&D	CNRS	CEA, UF, ENEA, INFN, ITN, IBA, FZJ
D80	Extrapolation from XADS accelerator to the accelerator of an industrial transmuter	INFN	FANP SAS, ANS, CEA, CNRS, IBA

Figure 1. Projects on advanced options for partitioning and transmutation (ADOPT)



Nota: The funding indicated is the contribution of the European Communities. It represents about 50% of the whole budget.

Figure 2. XADS – LBE-cooled concept

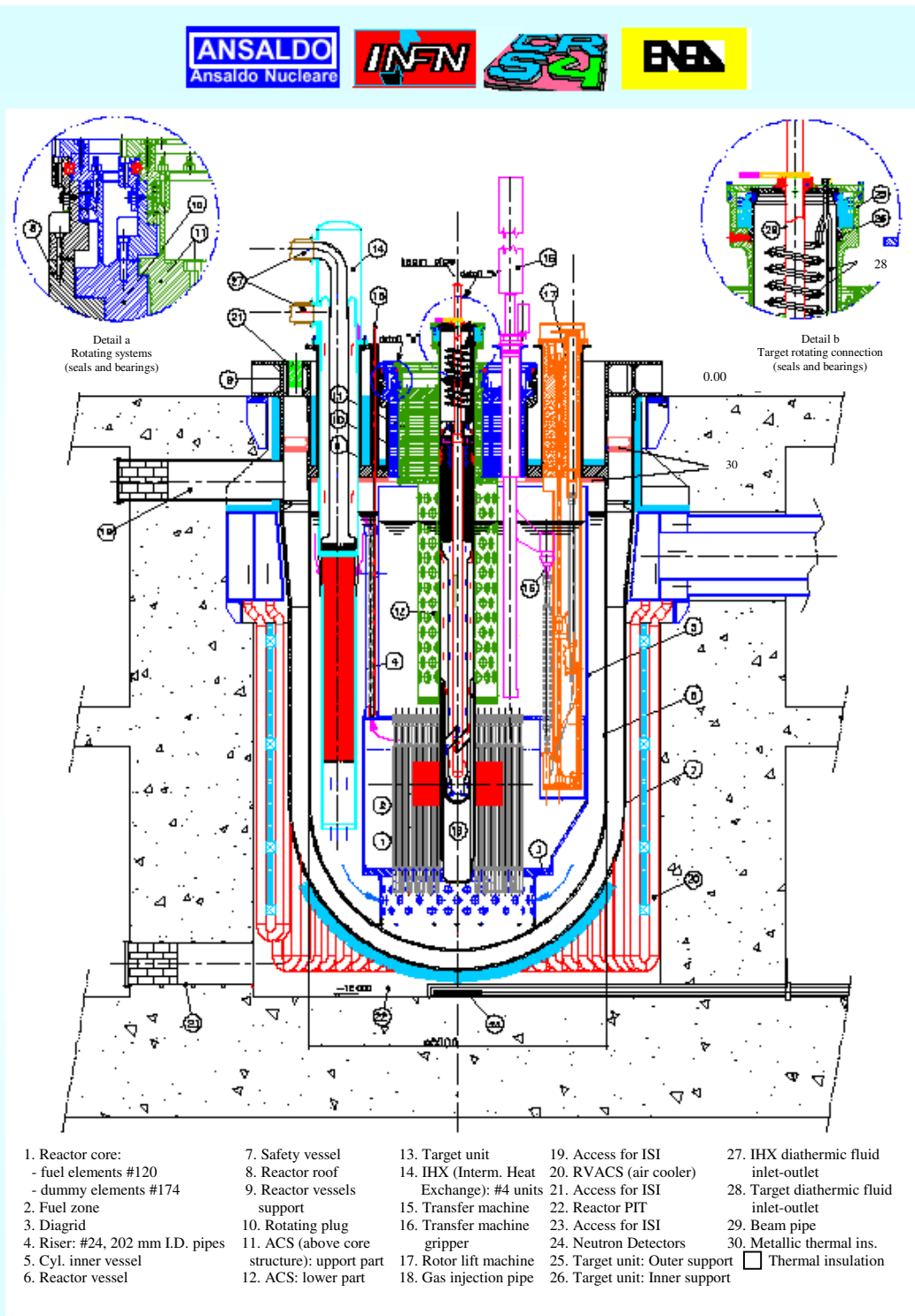


Figure 3. XADS – Gas-cooled concept

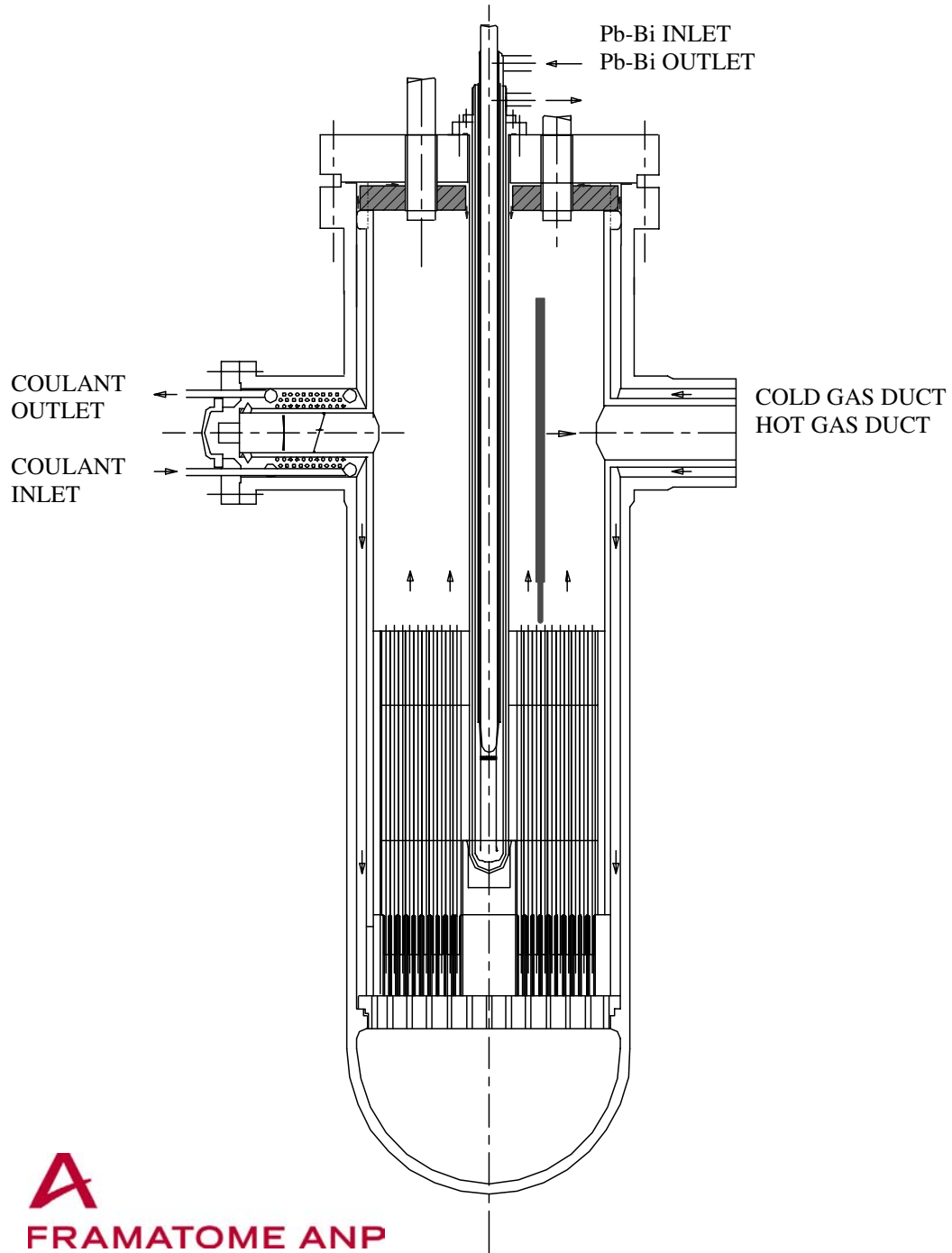


Figure 4. XADS – MYRRHA concept

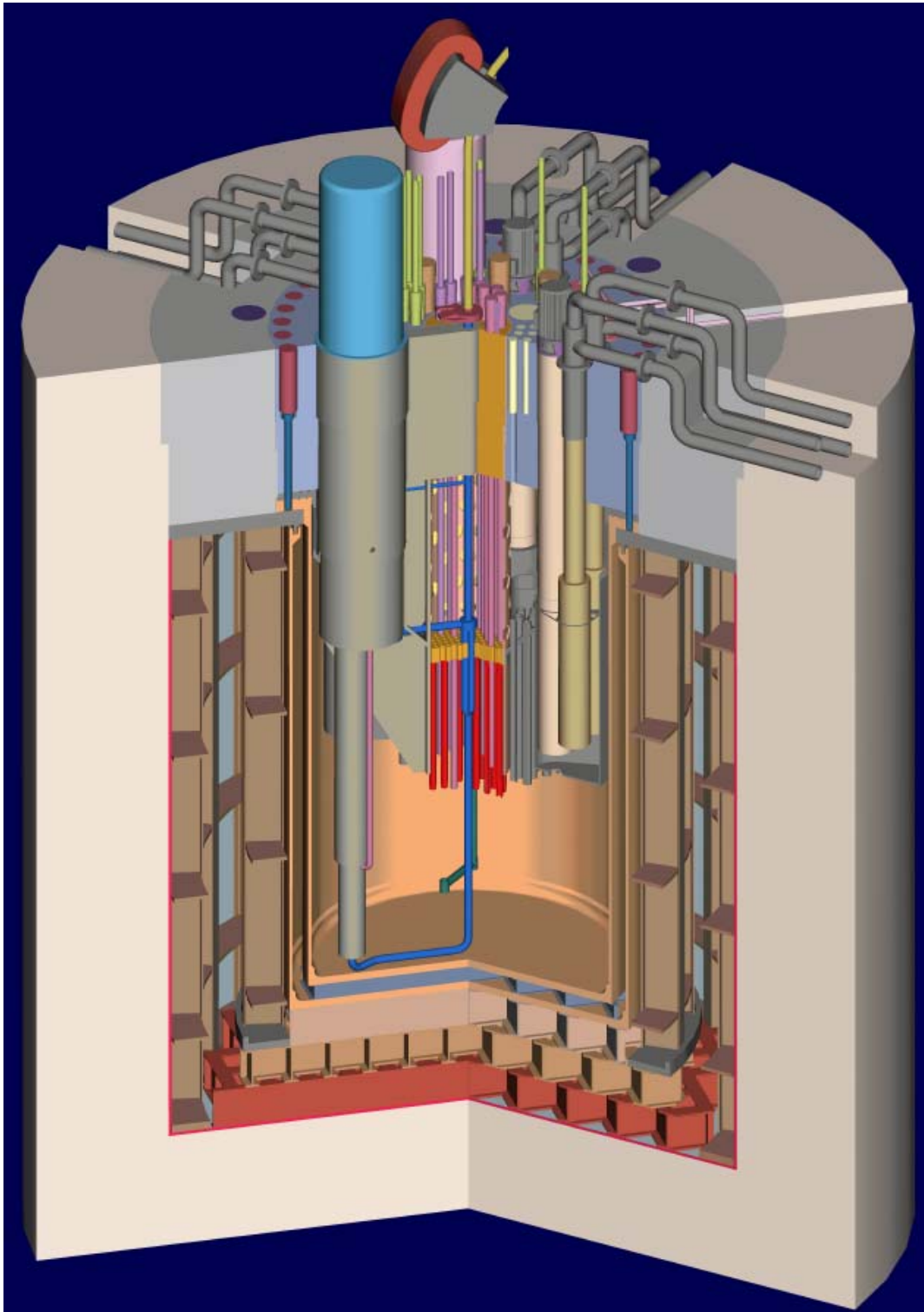
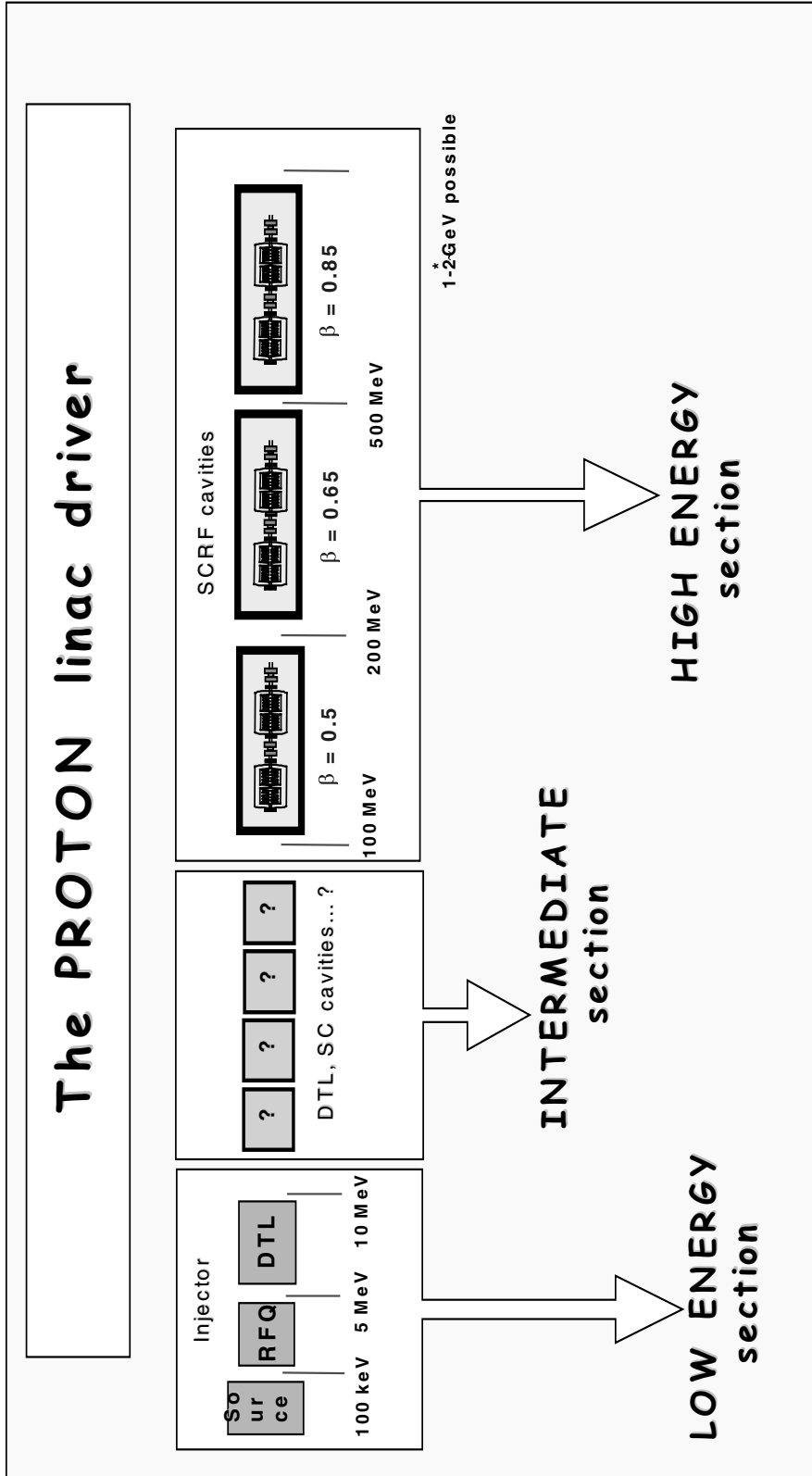


Figure 5. The PROTON linac driver



KOREAN R&D PROGRAMME FOR HPPA

Won S. Park, Yong S. Cho, Byung H. Choi

Korea Atomic Energy Research Institute

P.O. Box 105, Yusong

Daejeon, Korea

wonpark@kaeri.re.kr

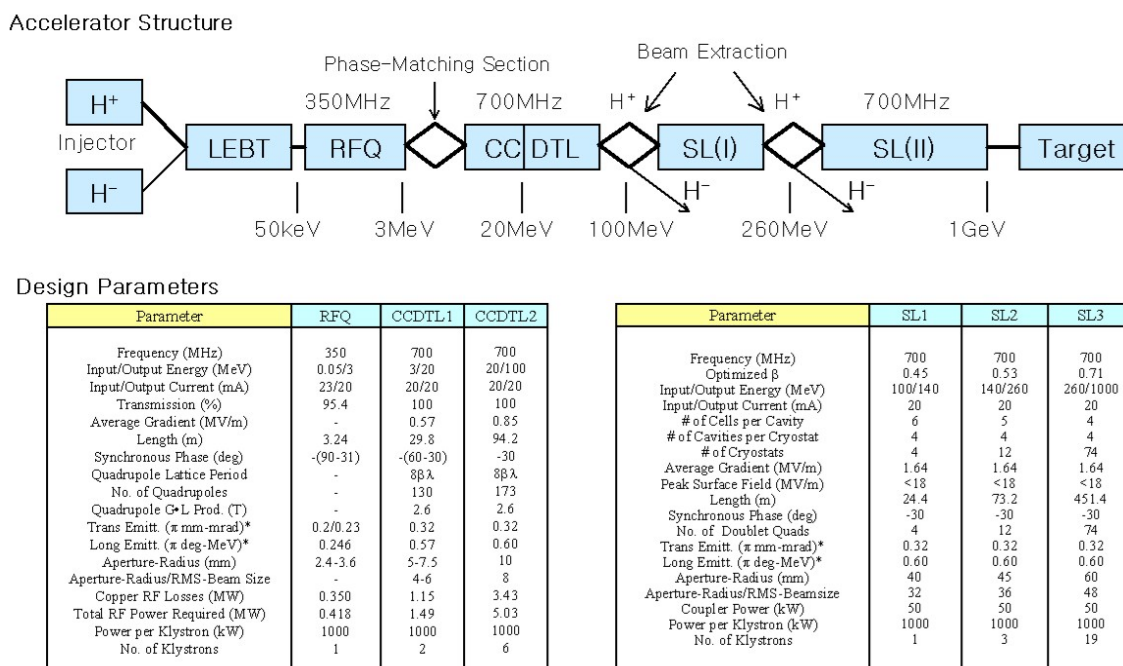
Abstract

KOMAC (Korea multi-purpose accelerator complex) programme has been being performed to build a 20 MW (1 GeV, 20 mA, cw) high-power proton linear accelerator to study basic researches, industrial applications, and nuclear transmutation since 1996. During the first phase from 1996 to 2001, the project was performed within the framework of national nuclear mid- and long-term R&D programmes. In this first phase, a proton linac from injector to 3 MeV RFQ with 1MW RF system in the KTF (KOMAC test facility) was developed. KOMAC programme was launched as one of national projects so called 21st century frontier R&D programme in the year of 2002. In the KOMAC project within the framework of 21st century frontier R&D programme, 100 MeV, 20 mA protons will be produced and many spin-offs of the accelerator technologies for industrial applications will be included such as nano-technology, bio-technology, etc.

Introduction [1]

KOMAC (Korea multi-purpose accelerator complex) had been proposed to build a high-power proton linear accelerator of 1 GeV and 20 mA since 1996. Figure 1 shows the accelerator structure and parameters of KOMAC. The major H^+ beam (18 mA and 1 GeV) will be used for nuclear waste transmutation and nuclear physics experiments while utilising the minor H^- beam (2 mA) for the basic research and medical therapy study.

Figure 1. Schematic layout of the KOMAC linac



KOMAC programme can be divided into two R&D phase based on its R&D fund sources. The first phase is from 1997 to 2001. During the 1st phase, KOMAC was performed as one of national nuclear mid- and long-term R&D programmes. KAERI had developed the proton accelerator technologies in KTF in the 1st phase. In the KTF, 3 MeV proton accelerator have been constructed and tested.

The 2nd phase of the KOMAC project will be from 2002 to 2008 and performed as one of 21st century frontier national R&D programmes.

1st phase programme of KOMAC

As the 1st phase of the project, we developed cw accelerating structure up to 20 MeV, and operated the accelerator in 10% duty pulse mode. After the initial operation, the cw operation of the accelerator will be tested. The 20 MeV proton accelerator was constructed in the KTF (KOMAC test facility), and will be commissioned in 2005. After the commissioning, KTF will provide the proton beam for the many industrial applications.

In the KTF, KAERI developed the proton injector, LEBT, 3 MeV RFQ, 20MeV DTL, and RF system. The proton injector was developed, and the 3 MeV RFQ will be constructed in 2002. Also we have a plan to develop the basic superconducting cavity technology in the KTF for the 2nd stage accelerator of the KOMAC.

Proton injector [2]

For 20 mA proton beam at the final stage, KOMAC requires the ion source with the proton beam current of 30 mA at the extraction voltage of 50 kV. Normalised rms emittance of less than $0.3 \pi \text{ mm} \cdot \text{mrad}$ is also required for good matching of ion beam into RFQ.

The system is composed of an accelerating high voltage power supply, ion source power supplies in a high voltage deck, gas feeding system, and vacuum system.

The injector has reached beam currents of up to 50 mA at 50 kV extraction voltage with 150 V, 10 A arc power. The extracted beam has a normalised emittance of $0.2 \pi \text{ mm} \cdot \text{mrad}$ from 90% beam current and proton fraction of over 80%. The proton fraction is measured with deflection magnet and scanning wire.

The beam can be extracted without any fluctuation in beam current, with a high voltage arcing in 4 hours. The cathode lifetime is about 40 hours. To increase the filament lifetime, it is necessary to lower the arc current or to change the tungsten filament to other cathode such as oxide cathode.

LEBT

Low-energy beam transport (LEBT) consists of two solenoids, two steering magnets, diagnostic system, beam control system, and funnel system to transports and matches the H^+ for 20 mA and H^- for 3 mA, beams from the ion source into the RFQ. The main goal of the LEBT design is to minimise beam losses. The design codes used are TRACE 3D and PARMTEQM. The PARMTEQM-simulated solenoid settings are $B=2 \text{ 800G}$ and $B=3 \text{ 900G}$, the RFQ transmission rate is more than 90%. Two solenoid magnets constructed are 20.7 cm long, 16 cm i.d., are surrounded by a low carbon steel and provide dc fields $\leq 5 \text{ 000G}$ on the axis. During the winter of 2000, we will test the LEBT to obtain a proper matching condition with the RFQ.

RFQ [3]

The KTF RFQ bunches, focuses, and accelerates the 50 keV H^+/H^- beams, and derives a 3.0 MeV beam at its exit, bunched with a 350 MHz. The RFQ is a 324 cm long, 4 vanes type, and consists of 56 tuners, 16 vacuum ports, 1 coupling plate, 4 RF drive couplers, 96 cooling passages, and 8 stabiliser rods. The RFQ is machined of OFH-Copper, integrate from separate four sections which are constructed by using vacuum furnace brazing. The fabricated RFQ is shown in Figure 2.

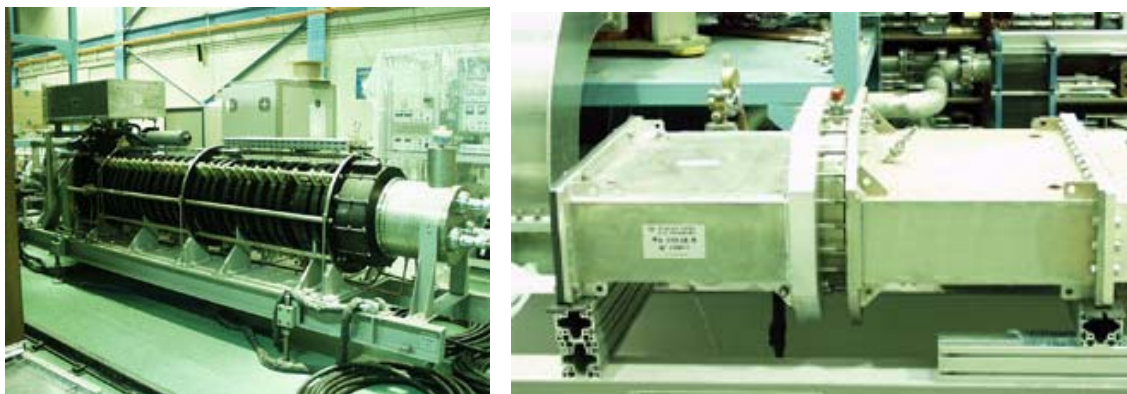
Figure 2. Fabricated RFQ cavity



High-power RF system

Two types of RFQ have been developed. The one is 0.45 MeV RFQ whose purpose is to check the basic RFQ technologies such as tuning, beam matching and so on, the other is 3 MeV main RFQ which was fabricated and vacuum tight checked already. The required RF power for 0.45 MeV RFQ is 110 kW CW and for 3 MeV is 417 kW CW respectively. The 1 MW, 350 MHz RF system has been developed to deliver a RF power to the RFQ. The high-power RF system consists of klystron, circulator, RF window, various waveguide components, klystron power supplies and cooling system. Recently all components of the RF system were prepared and are being tested.

Figure 3. 1 MW 350 MHz klystron and RF window



Low level RF system

The LLRF consists of a 350 MHz signal generator, a 160 W solid state amplifier, amplitude/phase control loops, and RF interlocks. The designed field stability in the RFQ cavity is within $\pm 1\%$ amplitude and $\pm 1.4^\circ$ phase using feedback control loops in the LLRF. For frequency control, another tuner controller module was used. The RF interlock signals comes from excessive reflected RF power, circulator arcs and window arcs.

DTL [4]

DTL will accelerate the 3 MeV 20 mA proton beam to the energy of 20 MeV. The structure design of DTL is based on the 100% duty factor.

For 20 MeV to 100 MeV, CCDTL cold models are fabricated to check the design, the tuning method, and the coupling coefficients and the fabrication method. The super-drilled coolant path is well fabricated, and this type cooling method will be used for the CCDTL construction. The field profile is measured with a bead perturbation method.

The design and fabrication technologies have been acquired, and the DTL for 2nd phase accelerator will be fabricated from the year of 2002.

Power supply system

The specifications of the high voltage power supplies for the KTF klystron are 100 kV, 20 A with the conditions that the voltage peak to peak ripple and the voltage regulation are less than 1%, and energy deposition in the klystron at the tube arc is less than 20 J. The power supply that meets the above conditions has been designed, manufactured and tested. The main components of the high voltage power supply are induction-voltage-regulator, transformer & rectifier tank for 12 pulses rectification, L-C filter, and ignitron crowbar. Voltage dividing resistors and a tetrode tube were used to provide variable high voltage to modulating anode of the klystron. The variable voltage modulating anode power supply gives the flexibility of klystron operation.

Cooling system

A 2 MW DI water cooling system for KTF RFQ and RF system was prepared as shown in Figure 5. The required cooling loops for RF system are circulator, RF load, RF window cooling loops and body, cavity, collector cooling loops for klystron. Because the coolant of the RF load is a mixture of water and ethylene glycol, a separate cooling loop for RF load with storage tank, pump and heat exchanger was installed. Also pump for pressurisation was installed in klystron body cooling loop, because the pressure of the DI water cooling loop was too low to supply enough flow to that cooling loop.

Status of KTF

In the KTF, we have developed the technologies for proton accelerators from low energy part. As a result of this development, we have constructed and tested 3 MeV proton accelerator system. Figure 6 shows the status of KTF. The 20 MeV accelerator in KTF will be constructed and commissioned in 2005. The experiences in KTF will be a basis for the 2nd phase accelerator of 100 MeV final energy.

Figure 4. High voltage power supply for klystron

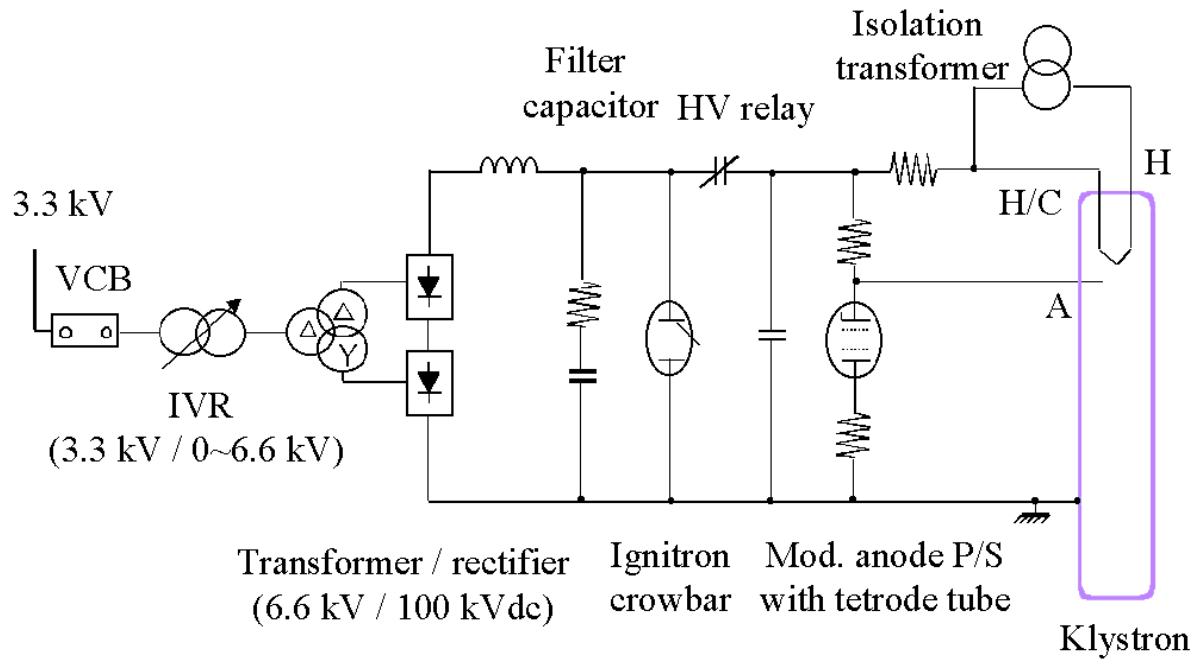


Figure 5. Facility for KTF

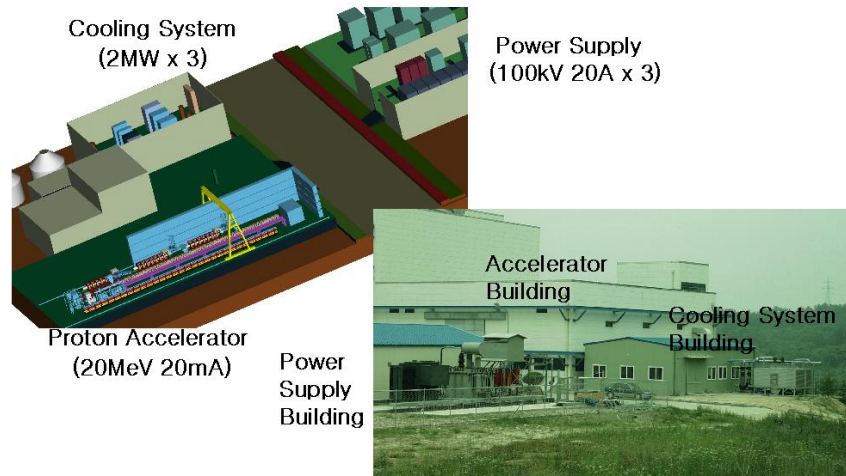


Figure 6. Status of KTF 20 MeV accelerator



2nd phase programme of KOMAC

Korean government launched “21C frontier R&D programme” to enhance national capability in science and technology. The 2nd phase KOMAC programme, “Proton engineering frontier project” had been approved as a frontier project.

The goals of 2nd phase KOMAC programme are as follows:

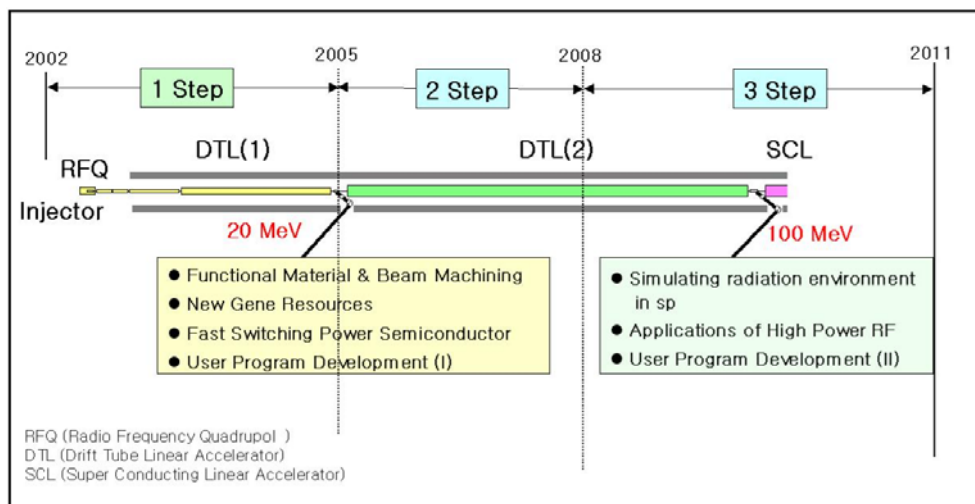
- Construction of 100 MeV proton linac.
- Development of beam utilisation’s and applications.
- Promotion of related industrial technologies.

The project schedule, the accelerator development, and beam utilisation plan are shown in Figure 7. The site will be selected after an intensive evaluation in June 2003.

The major beam utilisation and application areas are as follows:

- Functional material & beam machining.
- New gene resources.
- Simulating radiation environment in space.
- Fast switching power semiconductor.
- User programme development.

Figure 7. Time schedule of 2nd phase KOMAC



Development plan

The specifications of KOMAC 2nd phase accelerator are given as Table 1. The duty factor of the accelerator for the initial stage is 10%. But the final goal of the accelerator will be 100%. The technologies for the accelerator will be acquired in KTF. Also at this phase, the following technologies will be developed in KTF.

- Negative ion source.
- Superconducting cavity technology.
- Continuous beam sharing technology.

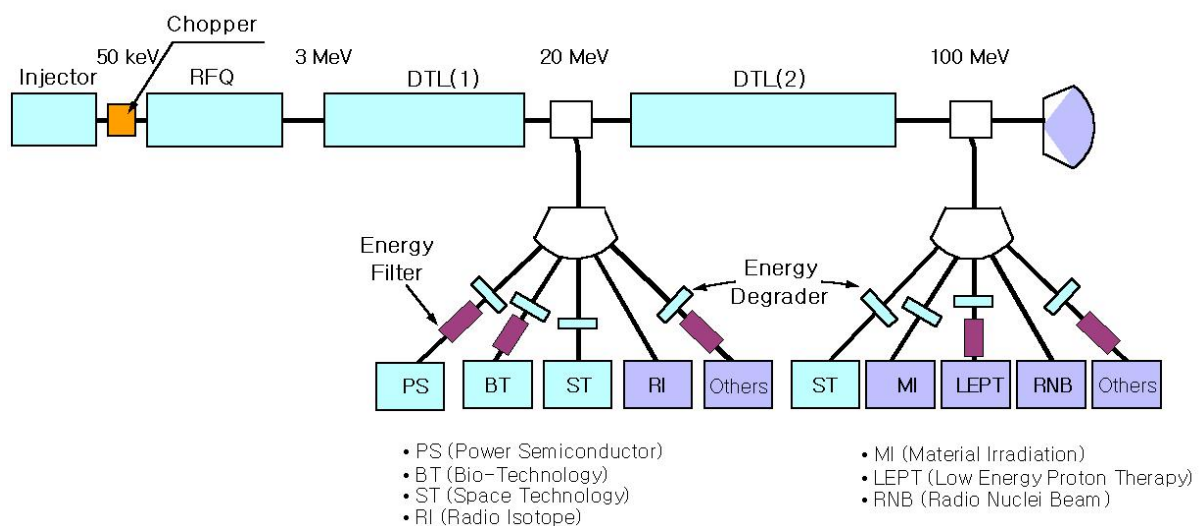
Table 1. KOMAC 2nd phase accelerator

• Ion	:	proton
• Proton injector	:	50 keV
• RFQ	:	3 MeV @ 350 MHz
• DTL	:	20 MeV @ 350 MHz
• CCDTL	:	100 MeV @ 700 MHz
• Max. beam current	:	20 mA
• Beam emittance	:	0.3 π mm · mrad (transverse) 0.4 π Deg. MeV (longitudinal)
• Duty	:	10% (initial stage), 100% (final stage)
• Beam switching	:	20 MeV & 100 MeV

Beam line for 2nd phase accelerator

For proton beam applications, the 2nd phase accelerator will supply beams with 20 MeV and 100 MeV. Figure 8 shows the schematic diagram for the beam line. The 50 keV beam from injector will be chopped with time-structure suitable for applications, and supplied via switching magnets at each energy stages.

Figure 8. Proton beam line for 2nd phase accelerator



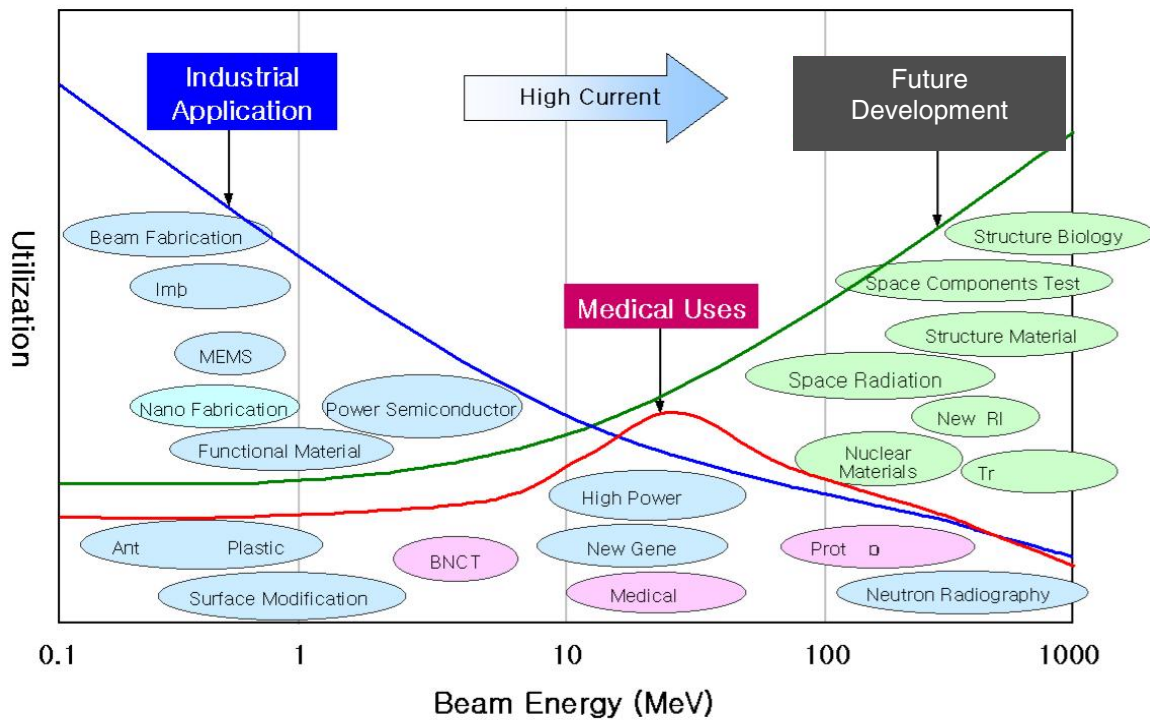
A possibility for further programme extension

Figure 9 shows the application areas of proton beam, and it is clear that for future needs of proton beam, an GeV accelerators are required. For GeV proton accelerator, as R&D of 2nd phase KOMAC project, the following technologies, that are the technical issues, will be developed:

- Negative ion source technology.
- Continuous beam sharing and control technology.
- Superconducting cavity fabrication and cryogenic technology.

With GeV accelerator, the KOMAC programme will be extended to spallation neutron source and its applications. The KOMAC user group is already formed. About a hundred of experts from the fields of material science, life science, nuclear science, physics and industry are joined in the group. Within the programme, the KOMAC project will support the user group who will be the major users of GeV accelerator for many application areas.

Figure 9. Role of high-power proton accelerator



Conclusion

KAERI is developing the KOMAC programme with two targets. One is to build an 1 GeV proton linac for an accelerator-driven transmutation experiments. Second is to develop spin-off technologies related with the accelerator technology and beam utilisation technology. In addition, KOMAC will be used as a Korea national research facility for basic science. In the 1st phase of KOMAC, the KTF accelerator which includes injector, LEBT, RFQ, CCDTL and RF system had been developed. In parallel, applications with keV and MeV proton beams are being developed such as ion irradiators, surface modification of polymers. In the 2nd phase, an 100 MeV linac and several beam lines of 20 MeV and 100 MeV will be constructed, and several applications with high current proton beams, and an user programme for future extension of the programme are planned. Also it is hoped that this accelerator will be useful for the nuclear data production.

Acknowledgement

The Korea Ministry of science and technology supports this work.

REFERENCES

- [1] Choi, B.H., *et al*, "Overview of the KOMAC project".
- [2] Proceedings of the 3rd International conference ADTTA'99 (1999).
- [3] Cho, Y.S., *et al*, "High-current ion source development for the Korea multi-purpose accelerator complex", *Rev. Sci. Instr.*, 71, 969 (2000).
- [4] Han, J.M., *et al.*, "Design and fabrication of the KOMAC RFQ", *Proceeding of PAC99*, New York, (1999).
- [5] Cho, Y.S., *et al*, "Cold model test of the KOMAC CCDTL cavities", *Proceeding of EPAC2000*, Vienna, (2000).

THE US ADVANCED ACCELERATOR APPLICATIONS PROGRAMME

Frank Goldner
US Department of Energy
Office of Nuclear Energy, Science and Technology
USA

The US Department of Energy (DOE) has invested over \$100 million in transmutation research and development over the past three years. The programme has evolved from an accelerator-based transmutation programme to a multi-tier reactor and accelerator based programme. These changes have resulted in a significant re-focus of the research and development programme as well as a name change to reflect the new direction. The advanced accelerator application (AAA) programme is now being renamed the advanced fuel cycle initiative (AFCI).

Research completed by the AAA programme in fiscal year 2002 points to a multi-phased programme, indicated in the last slide, consisting of two elements that would be conducted in parallel as part of an integrated research effort – an intermediate-term technology element (now being called AFCI Series One), which emphasises advanced technical enhancements to the current commercial nuclear power infrastructure; and a long-term technology element (now being called AFCI Series Two), which supports the introduction of next-generation nuclear energy systems to reduce the toxicity of nuclear waste.

AFCI intermediate-term development would address the issues associated with spent nuclear fuel disposition primarily by reducing the volume of material requiring geologic disposition through extraction of uranium. A second area of intermediate-term research and development will be development of proliferation-resistant processes and fuels to transmute significant quantities of commercially generated plutonium and other elements of concern (minor actinides) in reactors by approximately 2015. Successful implementation of these technologies would enable the United States to reclaim the significant energy value contained in spent fuel and significantly reduce the need for a second US repository.

AFCI long-term R&D would address issues associated with spent nuclear fuel as well as supporting fuel development requirements for a generation of new reactors possible in the 2030 and beyond time period. Specifically, this effort will support development of fuel cycle technologies that could sharply reduce the long-term radiotoxicity and heat load of high-level waste sent to a geologic repository. If successful, these technologies could enable the commercial waste stored in a repository to be no more toxic than natural uranium ore after approximately 1 000 years.

In general, we have found that there is reason to believe that the following objectives are attainable.

Reduce high-level nuclear waste volume: It is possible to develop and implement, by the middle of the next decade, proliferation-resistant technology to significantly reduce the volume of high-level nuclear waste from commercial spent fuel requiring repository disposal.

Reduce the cost of geologic disposal: Based on the analysis conducted by the Department thus far, the implementation of AFCI technologies could reduce the cost of spent nuclear fuel disposal in the first US repository by several billion dollars by permitting the use of fewer drip shields and waste packages and reducing the operation and transportation costs associated with those items. AFCI could also avoid the full cost of constructing a second repository under the scenario that anticipates new plant orders during the first third of the century.

Reduce inventories of civilian plutonium: It is possible to develop and deploy, by the middle of the next decade, advanced nuclear fuels that will enable the proliferation-resistant consumption of plutonium in existing LWRs or advanced gas-cooled reactors that may be available in the future.

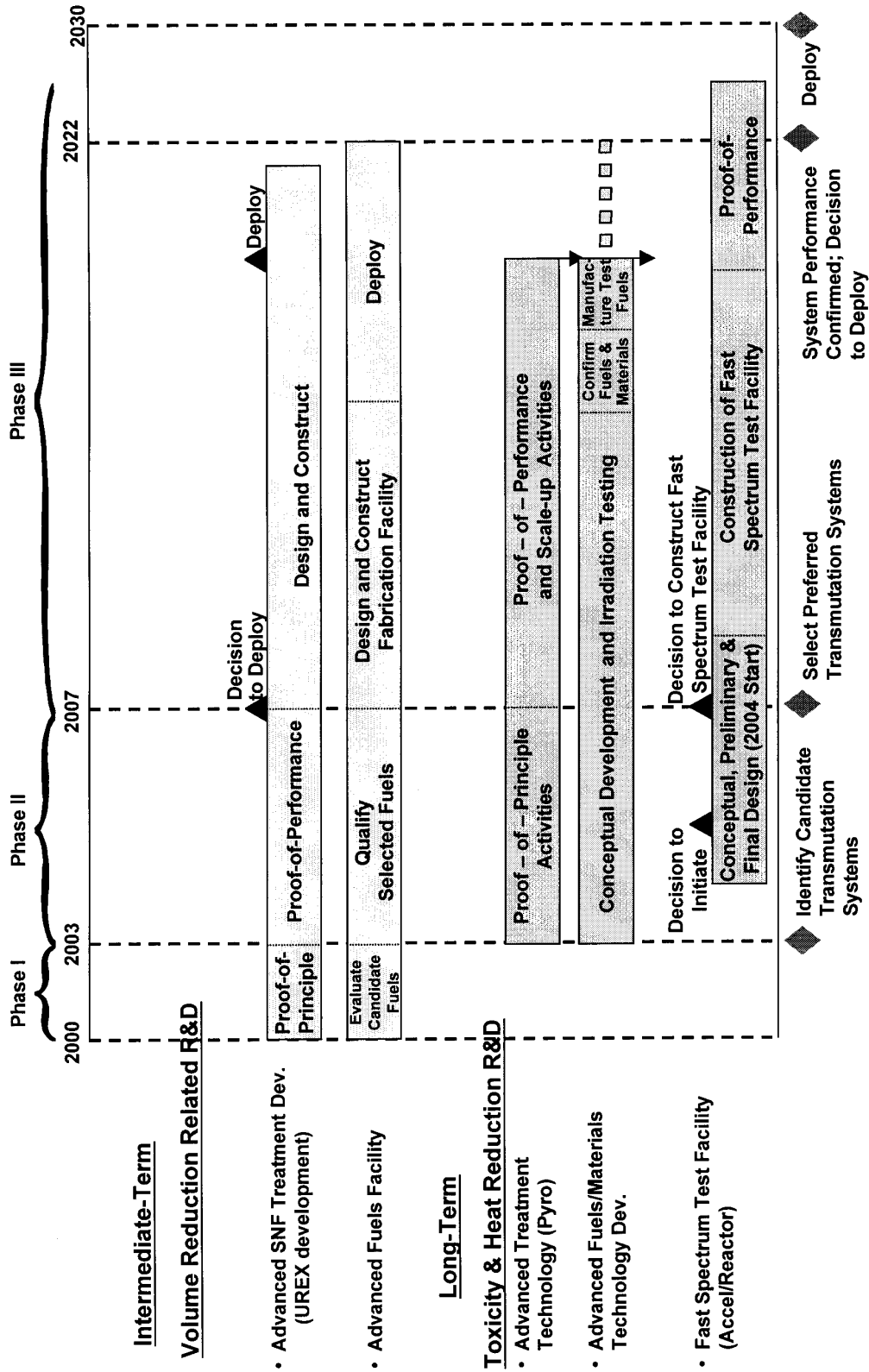
Reduce the toxicity of high-level nuclear waste: It is possible to develop and deploy, by approximately 2030, advanced proliferation-resistant treatment and transmutation technologies that

will both significantly reduce the volume of spent nuclear fuel and create waste forms sufficiently clean of long-lived, highly toxic species to reduce the time to reach the level of natural uranium from 300 000 years to approximately 1 000 years.

Bringing these technologies into use would require completion of a third phase of work (see Figure 1). In the case of AFCI Series One, successful completion of the second phase would enable the United States to initiate commercial deployment of these technologies by no later than 2015. The next generation technologies of AFCI Series Two would require significantly more time and research. Deployment could come only after a demonstration phase that could require new facilities in the United States or other countries, as well as satisfying potential requirements of reactors of the 2030 and beyond time period (i.e. Generation IV).

DOE believes AFCI could provide a significant contribution to achieving the Nation's energy and national security objectives by optimising nuclear energy systems in both the near and long term. This work can realise the vision anticipated by the *National Energy Policy* to explore advanced technologies to deal with spent nuclear fuel in co-operation with our international partners.

Figure 1. Potential follow on plans for the AAA programme



**RELIABLE LINAC DESIGN FOR
ACCELERATOR-DRIVEN SUBCRITICAL REACTOR SYSTEMS**

Thomas P. Wangler
Los Alamos National Laboratory
Los Alamos, NM 87544, USA

Abstract

Accelerator reliability corresponding to a very low frequency of beam interrupts is an important new accelerator requirement for accelerator-driven subcritical reactor systems. In this paper we review typical accelerator-reliability requirements and discuss possible methods for meeting these goals with superconducting proton-linac technology.

Introduction

High-power proton linacs in the megawatt beam-power range are considered an attractive choice for many applications requiring high average beam power. Applications of proton and deuteron linacs include accelerator-driven subcritical reactors for nuclear-waste transmutation, neutrino factories, fusion-materials studies, and injectors for spallation-neutron sources. Table 1 presents a survey of high-power linac projects, both proposed and already under construction. Also included are the parameters for the existing 800 MeV LANSCE proton linac, which has operated for almost 30 years.

Table 1. High power linac survey (H^+ , H^- , D^+)

Name	Ion	Pulse length (msec)	Rep rate (Hz)	Duty factor (%)	I_{bunch} (mA)	I_{Average} (mA)	Energy (GeV)	P_{Average} (MW)	Start date
LANSCE	H^+/H^-	0.625	100/20	6.2/1.2	16/9.1	1.0/0.1	0.8	0.8/0.08	ON
SNS	H^-	1.0	60	6.0	38	1.4	1.0	1.4	2006
CERN SPL	H^-	2.8	50	14.0	22	1.8	2.2	4.0	?
ESS short pulse	H^-	1.2	50	6.0	114	3.75	1.33	5+5	2010
ESS long pulse	H^+ or H^-	2/2.5	16.67	4.2	114/90				
FNAL 8 GeV	$H^+/H^-/e^-$	1.0	10	1.0	25	0.25	8.0	2.0	?
KEK/JAERI 400 MeV	H^-	0.5	50/25	2.5	50	0.7	0.4	0.28/0.14	2006
KEK/JAERI 600 MeV			25	1.25		0.35	0.6	0.21	?
TRASCO	H^+	CW	CW	100	30	30	>1.0	>30	?
IFMIF	D^+	CW	CW	100	2x125	2x125	0.040	10.0	2010
KOMAC (KAERI)	H^+/H^-	CW	CW	100	20	20	0.1(1.0)	2.0(20)	2011(?)
ATW	H^+	CW	CW	100	45	45	1.0	45	?

A historically important high-power proton-linac project (not listed in Table 1) is the accelerator production of tritium (APT) project, which took place during the decade of the 1990s. Figure 1 shows a block diagram of the APT linac design [1, 2, 3, 4]. Although the project was cancelled (identified as the backup technology to nuclear-reactor production of tritium in 1998), it established a new technology base for high-current CW proton-linacs. The accelerator used superconducting RF cavities at energies above ~ 200 MeV with transverse focusing provided by normal-conducting quadrupole doublets between cryomodules. The CW low energy demonstration accelerator (LEDA) facility [5] demonstrated the critical low-velocity part of the APT linac, including the DC injector and radio-frequency quadrupole (RFQ) technology at a 100 mA beam current, and a 0.67 MW beam power. High beam availability (90%) was an important feature of the APT design.

Superconducting elliptical cavities similar to those used in relativistic electron accelerators, but compressed longitudinally as required for the lower proton velocities, were designed and built for the APT high-velocity region, $\beta > 0.5$ (see Figure 2). These cavities have been successfully tested, providing at 10 MV/m twice the design value of the accelerating gradient [6]. More recently, superconducting spoke cavities (see Figure 3) are being designed and built to operate in the lower velocity range, $0.1 < \beta < 0.5$ [7]. This latter development allows the use of RF superconducting linac technology for proton kinetic energies above about 5 MeV, which constitutes the majority of the linac for most high-power proton linacs.

During the past decade, worldwide technology developments have made the use of superconducting RF technology more attractive for high-power proton linacs. Advantages of

superconducting linacs include lower operating costs, larger affordable bore radius (relaxing alignment, steering, and matching tolerances; reducing beam/loss and radioactivation; easing commissioning, and improving availability), installed redundancy (the linac can continue to operate even if an accelerating module fails), and worldwide industrial capability for fabrication of niobium superconducting cavities and cryomodules. Dramatic progress has occurred in several critical technical areas during the past decade, including higher accelerating gradients, higher power input-power couplers, and operating experience with pulsed electron beams (at the TESLA test facility). Furthermore, the performance of superconducting cavities is still improving. During the past 5 years all new high-power proton-linac projects have included superconducting sections. The spallation neutron source (SNS) [8] is scheduled in 2006 to become the first superconducting proton linac.

Figure 1. Block diagram of the APT linac design

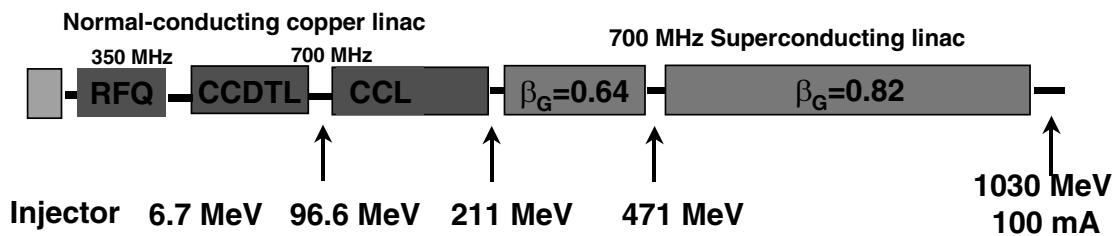


Figure 2. One of four 5-cell 700-MHz $\beta=0.64$ niobium elliptical accelerating cavities built for LANL by CERCA



Figure 3. New $\beta=0.175$ 2-gap 350-MHz niobium spoke accelerating cavity built for LANL by ZANON



Note: The cavity is shown with its end plates removed.

Accelerator requirements for ATW systems

The beam requirements for an accelerator-driven subcritical reactor system, such as an accelerator transmutation of nuclear waste (ATW) facility [9], vary for different projects. Typical ranges of values are listed in Table 2. The last two entries in Table 2 include approximate requirements for beam reliability (beam continuity) assuming for simplicity that the facility has beam scheduled for 100% of the time. The requirements for the frequency of beam interrupts are specified over two different time duration's. These two time duration's correspond to different constraints on ATW subcritical systems that deliver power to the grid [9]. First, beam interrupts of duration greater than about a second must be limited, to mitigate the integrated effects of thermal transients in the transmuter (subcritical reactor assembly) that shorten the transmuter lifetime. Second, beam interrupts of duration greater than ~10 minutes must also be limited to avoid long interruptions of power delivered to the power grid. In particular, interrupts of duration greater than ~10 minutes may require even longer (up to several days) transmuter restarts. Fortunately, the transmuter performance is unaffected by interrupts of duration less than about one second, which constitute the majority of accelerator interrupts. The beam-interrupt requirements in Table 2 must be considered as estimates, since these requirements are not precisely known at this time.

Table 2. Beam requirements for an ATW

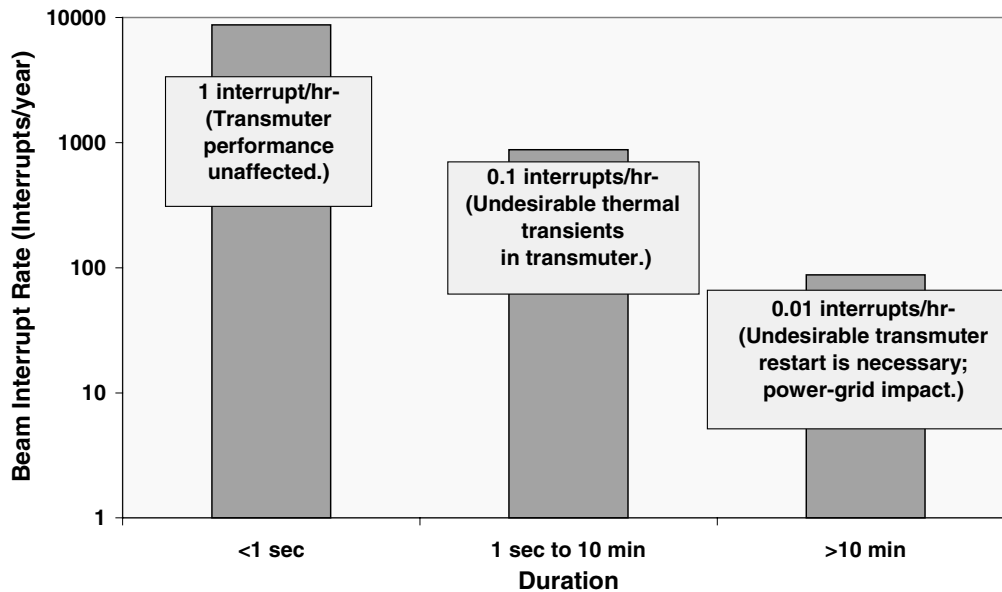
Parameter	Requirement
Energy (GeV)	0.6-1.5
Current (mA)	10-100
Beam power (MW)	10-100
Linac beam loss (W/m)	<1 W/m required and <0.1 W/m goal
Beam interrupts > ~1 s.	<100/year \approx 0.01/hr
Beam interrupts > ~10 min.	<2/year \approx 0.0002/hr

The actual interrupt spectrum for a modern proton linac like APT is expected to have characteristics similar to that shown in Figure 4. We note that the two beam interrupt requirements (for 1 sec. to 10 min., and >10 min.) in Table 2 lie considerably below, at least an order of magnitude below, the estimated performance levels shown in Figure 4. It should be emphasised that specification of beam-interrupt frequency requirements for accelerator operation has never been done before. Instead, beam availability (ratio of total beam delivery time to scheduled beam delivery time) has been the usual criterion. Modern accelerators can and do achieve high availability; the LANSCE facility achieves about 90% beam availability. But, an order of magnitude or more reduction in the frequency of beam interrupts to meet the ATW specifications would be a challenging new accelerator requirement.

Beam interrupts originate from many subsystems that comprise the overall accelerator system. Achieving a large reduction in the beam-interrupt frequency will probably require some major changes in design and operating philosophy. One idea is to adopt a new design and operating approach with respect to long-duration faults, which is to ride through the faults, rather than the present approach, which is to shut down the beam after each fault [10]. We believe that riding through faults would be most effectively implemented in a superconducting linac. What would be required for a superconducting linac is to leave the beam on after loss of an individual accelerating module. In this context, an accelerating module is defined as a subsystem including one or more superconducting cavities and the RF system that drives them. Based on experience, a failure is more often from some component in the RF system that supplies RF energy to the cavities, rather than the accelerating cavities.

The superconducting linac has several important features that may allow continued operation after a fault. First, the superconducting cavities typically have larger apertures, made economically affordable by the large, orders-of-magnitude reduction in RF power losses. The larger apertures provide extra margin against beam loss, even after faults that may have occurred in upstream beamline elements. Second, short superconducting cavities have a relatively small energy gain, so that loss of an accelerating module has a relatively small effect on the beam energy. The beam-energy reduction associated with loss of a module can be corrected by resetting the parameters of the downstream cavities, provided enough margin is available in the design. To provide this margin, one can install a few percent extra accelerating modules to allow compensation for loss of some modules during operation. After a fault, the downstream cavity parameters can be reset to restore the final energy. In addition, this compensation procedure can be expected to reduce the risk of beam losses that may result from the nonideal conditions caused by the fault. At the end of the run cycle, if not sooner depending on the situation, appropriate repairs would be made to the failed systems without having to shut off the beam. Although there is no obvious reason that this approach could not be made to work, nevertheless, there will be some faults, perhaps including some water, power, or beamline vacuum-system failures, for which shutting off the beam will probably be unavoidable.

Figure 4. Anticipated interrupt frequency spectrum for a proton linac like APT or ATW, integrated over three time duration's relevant to an ATW system



Note: The impact of the interrupts over each time scale is also described. Beam interrupt requirements must be limited only for interrupts with duration greater than about one second.

To be more specific, let us consider how we might respond to four common faults in a superconducting linac. First, consider that during normal operation the detection by installed diagnostics of an incipient RF window problem in the RF drive line between the RF generator and an accelerating cavity. For example, the computer-control system might detect arcing, temperature increase, or vacuum problems. In the conventional operating mode, the machine operators would shut off the beam, and immediately initiate repairs or replacement of components, in this case the window. This approach could result in a long downtime. The new approach would be to continue beam delivery, detune the cavity to prevent the beam-excited cavity fields from further damaging the window, activate a waveguide switch to isolate the RF window from the RF generator, and then reset the parameters of the downstream cavities to restore the correct final energy. The capability of doing all this very rapidly (<1 msec) to reduce the risk of beam losses during the transient period after detection of the fault would be ideal. But, if the beam apertures are large enough, beam losses that occur before the downstream cavities are retuned might be small, and such a rapid compensation response may not always be necessary.

Second, consider an RF system failure, such as that involving a fault in an RF generator or a circulator. The new approach, similar to that above, would be to continue beam delivery, turn off the RF generator, detune the cavities in that module, and reset the downstream-cavity parameters.

Third, consider a focusing-magnet failure. Other than the potential for infant mortality of a magnet during initial operations, this should be a very rare event. With only a single such failure, the large apertures of the superconducting cavities and solenoid magnets should allow us to continue beam delivery with no other immediate corrective action required. Likewise, a superconducting solenoid-magnet power-supply failure would be irrelevant, if the superconducting magnets operate in persistent mode.

In addition to a new operating philosophy, we would also anticipate a design philosophy with an increased emphasis on high reliability. It would be important for fault reduction to design all systems using more conservative voltages and power levels. Finally, it would be essential to anticipate an active, continuous-improvement programme after commissioning, to make high reliability the primary goal for long-term operation.

ATW design example

A 1-GeV CW superconducting linac-design concept for an ATW system is shown in Figure 5 [11, 12]. The 45 mA proton beam is bunched and accelerated to 6.7 MeV by the normal-conducting LEDA RFQ. This is followed by three sections of 350 MHz superconducting spoke resonators corresponding to geometric- β values equal to 0.175, 0.20, and 0.34. The beam energy at the end of the spoke-resonator section is 130 MeV. This is followed by three sections of 700 MHz superconducting 6-cell elliptical cavities corresponding to geometric- β values of 0.50, 0.64, and 0.82. Superconducting solenoid magnets installed in the same cryostats as the superconducting cavities are used for transverse focusing. The design requires maximum accelerating gradients of less than 7.2 MV/m, and a maximum input power-coupler capacity of 250 kW. The design concept uses 220 RF generators, 328 superconducting cavities, and 82 cryomodules. The total length of the linac is 513 m. The estimated power requirements are 96 MW ac-power for the RF system, and 11 MW ac power for the cryogenic refrigerator. The arrangement of cryomodules and accelerating modules is shown in Figs. 6 and 7 for the spoke cavities and the elliptical cavities, respectively. The design specifies one cavity per accelerating module for the spoke cavities and two cavities per accelerating module for the elliptical cavities. These choices are made, anticipating that they will allow continued beam delivery after loss of any accelerating module.

An initial beam-dynamics simulation study [12] with 10 000 macroparticles shows good performance with substantial margin for avoiding beam losses that could cause radioactivation in the accelerator. Figure 7 shows, as a function of energy, the rms and maximum beam sizes in the simulation together with the aperture radius. The large space between the aperture and the maximum beam size indicates a large margin for beam transport with minimal beam losses, which is ideal for an accelerator design that has good fault tolerance. More study is required for a quantitative assessment of the ability to maintain beam continuity when faults are present.

Figure 5. ATW superconducting linac design concept

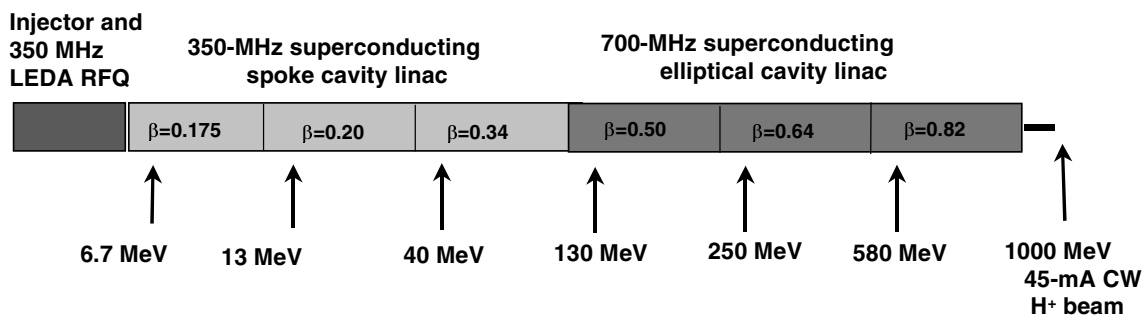


Figure 6. Block diagram of four spoke-cavity accelerating modules with cavities in one cryostat

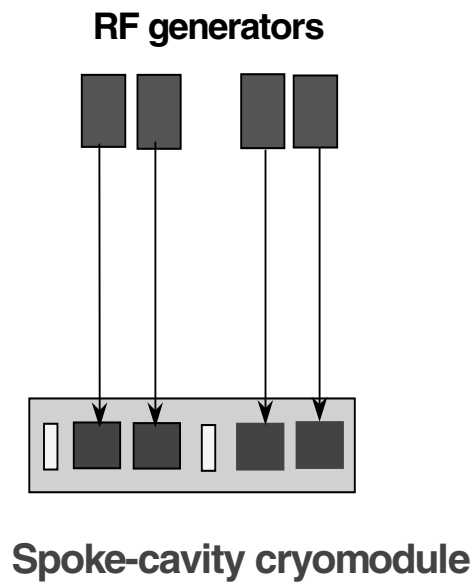


Figure 7. Block diagram of two elliptical-cavity accelerating modules with cavities in one cryostat

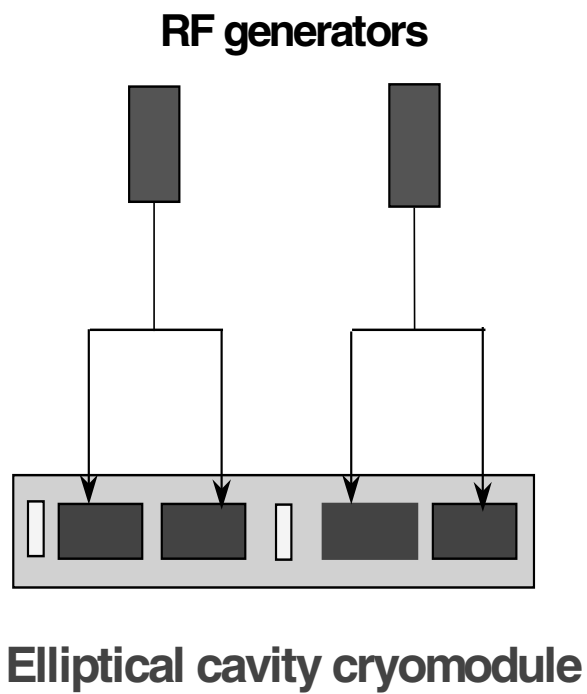
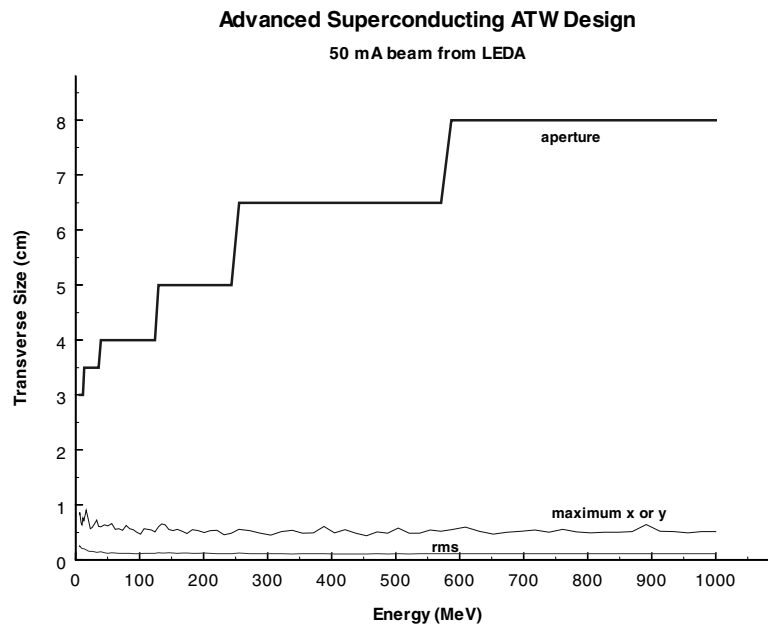


Figure 8. Beam size (rms and maximum) from multiparticle simulations and aperture radius plotted versus energy for the ATW superconducting linac design concept [12]



Necessity for system optimisation

Because of the challenging requirements for accelerator reliability, an overall system optimisation should be carried out, including both the accelerator and the transmuter. The question is whether the beam-continuity requirements described in Table 2 for the accelerator can be relaxed by different transmuter-design choices. To carry out such an optimisation, there is information that the transmuter designers need from the accelerator designers, particularly the spectrum of beam interrupts (frequency and duration) that can be expected. Likewise, there is information that the accelerator designers need from the transmuter designers. This includes an acceptable spectrum of beam interrupts for the different transmuter technologies, as well as the important question of what kind of accelerator maintenance schedule is compatible with transmuter operations.

Conclusions

There are many new proton-linac projects proposed for high-power applications. All specify high reliability and low-beam losses as requirements. The recent trend has been to use RF superconducting technology, because of the advantages of lower operating costs, larger affordable bore radius to minimise beam losses, and an installed redundancy so the linac can continue to operate even if an accelerating module fails. The applications for accelerators as drivers for subcritical reactors are particularly challenging because of the stringent requirements on beam continuity. We believe that superconducting linac concepts using short, large-aperture cavities, such as the ATW example presented in this paper, provide the best approach for improving accelerator reliability through a reduction of the frequency of beam interrupts. There can be no doubt that an R&D programme will be needed to address these new reliability requirements. In addition, accelerator-driven reactor projects, such as ATW, will need an overall system optimisation that includes an exploration of transmuter design options that might relax the accelerator reliability requirements.

Acknowledgements

The author acknowledges helpful discussions with R. Garnett, G. Lawrence, D. Rees, D. Schrage, and R. Sheffield.

REFERENCES

- [1] APT Conceptual Design Report, Los Alamos Report LA-UR-97-1329, 15 April 1997.
- [2] Lisowski, P.W., "The Accelerator Production of Tritium (APT) Project", Proc. 1997 Particle Accelerator Conf., Vancouver, pp. 3780-3784, May 1997.
- [3] Lawrence, G.P. and T.P. Wangler, "Integrated Normal-Conducting/Superconducting High-Power Proton Linac for the APT Project", Proc. 1997 Particle Accelerator Conf., Vancouver, pp. 1156-1158, May 1997.
- [4] Lawrence, G.P., "High-Power Proton Linac for APT; Status of Design and Development", Proc. XIX International Linac Conf., Chicago, IL, pp. 26-30, August 1998.
- [5] Smith, H., Vernon, J.D. Schneider, and R. Sheffield, "Low-Energy Demonstration Accelerator (LEDA) Test Results and Plans", Proc. 2001 Particle Accelerator Conf., Chicago, IL, pp. 3296-3298, June 2001.
- [6] Tajima, T., *et al.*, "Status of the LANL Activities in the Field of RF Superconductivity", Proc. 10th Workshop on RF Superconductivity, Tsukuba, Japan, September 2001.
- [7] Tajima, T., *et al.*, "Test Results of the LANL Beta=0.175 2-Gap Spoke Resonator", Proc. XXI International Linac Conf. (LINAC 2002), Gyeongju, Korea, August 2002.
- [8] Holtkamp, N., "The SNS Linac and Storage Ring: Challenges and Progress Towards Meeting Them", Proc. European Particle Accelerator Conf., Paris, France, June 2002.
- [9] "A Road map for Developing Accelerator Transmutation of Waste (ATW) Technology", report to Congress, DOE/RW-0519, October 1999.
- [10] Lawrence, G.P., "Reliability Considerations in Design of High-Power Linacs", 2nd OECD/NEA Workshop on Utilisation and Reliability of High Power Proton Accelerators, Aix-en-Provence, France, November 1999.
- [11] Wangler, T.P., "ATW Superconducting Linac Design Concept", inf. report, 12 March 2000.
- [12] Garnett, R., "ADTF Superconducting Linac Design", Los Alamos Group LANSCE-1 Report LANSCE-1:01-047, 1 May 2001.

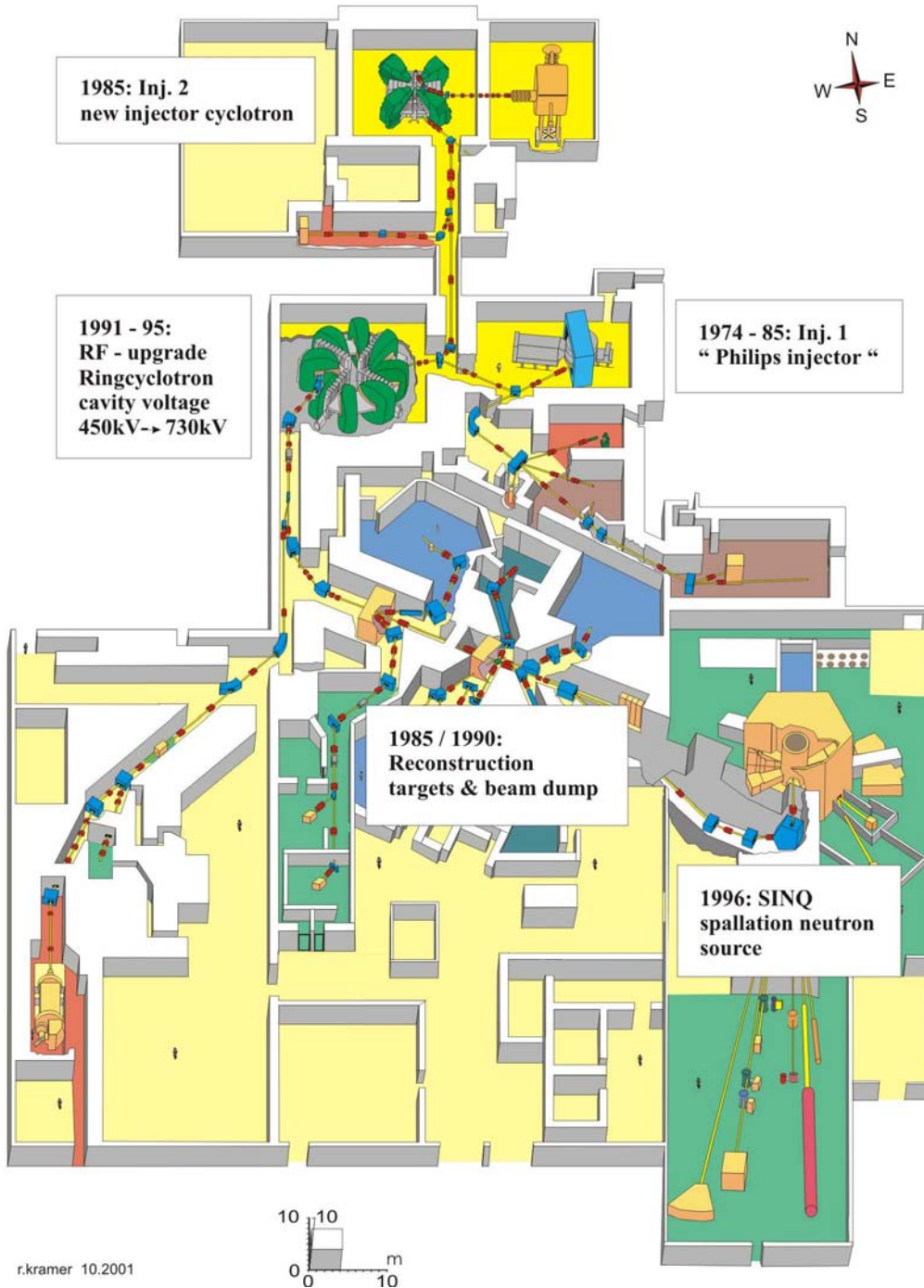
RELIABLE CYCLOTRON DESIGN

Th. Stambach, S. Adam, A. Mezger, P. Sigg, P.A. Schmelzbach
Paul Scherrer Institute (PSI)
Switzerland

Abstract

The beam delivery performance of the PSI cyclotron facility is presented. The facility operates routinely at a beam power around 1MW (590 MeV, 1.8 mA) as driver of the spallation neutron source SINQ. The beam statistics is discussed in detail with a focus on the causes for outage and beam interruptions. The facility has been built in 1974 for scientific purpose and been upgraded in several steps under economic limits. Hence several subsystems are not designed for highest reliability. It is found that a small number of events that are not typical for an ADS plant dominate the down time of the facility. The reliability and beam availability could be improved in the design stage. Important points are built-in diagnostics for a fast error location, optimal design for minimal repair times and measures to provide a high redundancy, possibly even with a farm of cyclotrons where one of them could act as spare accelerator.

Upgrade of the PSI accelerator facility

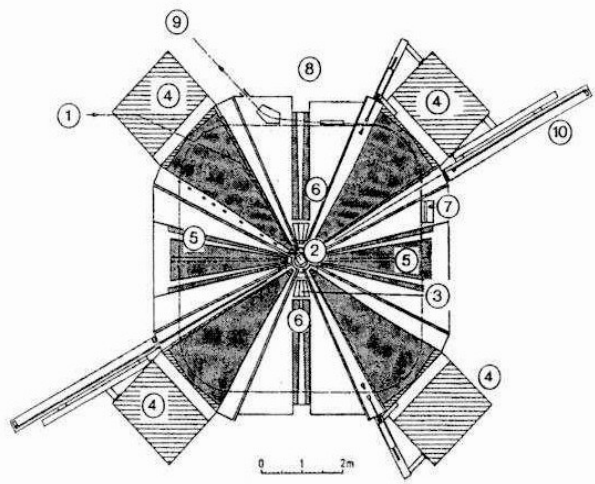


Beam intensity limitations

- PSI facility, 590 MeV/2 mA, driver for spallation neutron source

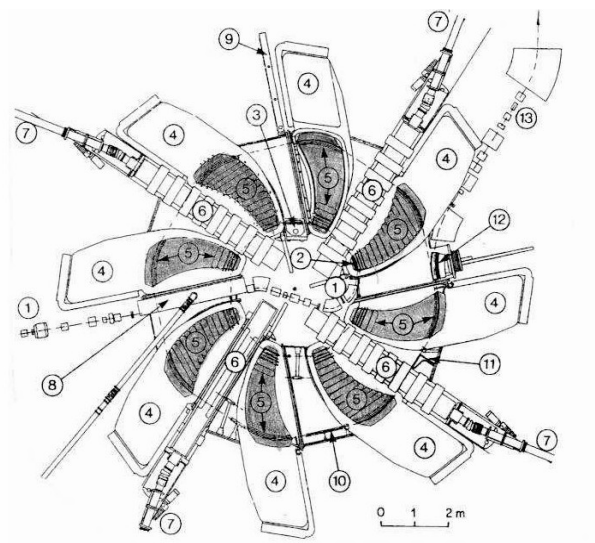
==>

Inj.2.: **2.2 mA** with 2 resonators
 turn separation doubled
 with 4 resonators



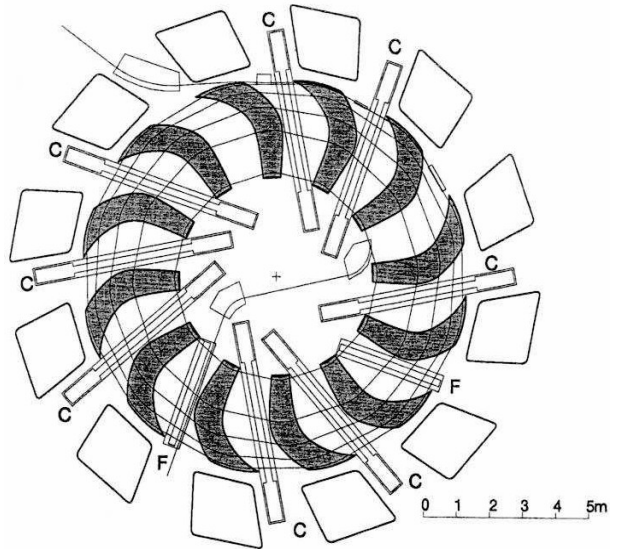
==>

Ring: **2 mA**
 longitudinal space charge
 (W. Joho, 1981)
 I_{\max} prop. to $\langle E_{\text{gain}} \rangle^3$
4 mA with 4 x 1 MV-cavities



==>

10 MW 1 GeV-cyclotron: **10 mA**,
 I_{\max} prop. to $\langle E_{\text{gain}} \rangle^3$
 8 x 1 MV-cavities



PSI beam time schedule

- beam production : March/April till Christmas
 pion production & spallation neutron source;
 on-line medical application (splitted beam).
- shutdown : January till March;
 upgrades, new projects & experiments;
 maintenance.
- weekly service : each Wednesday 08-22h
 routine maintenance (ion source filament);
 urgent repairs or development.

	1999	2000	2001
production beam time	5 750 h	5 260 h	4 390 h
shutdown, maintenance	2 080 h	2 200 h	3 540 h
unscheduled outage	650 h	840 h	450 h
delivered charge	8.3 Ah	8.5 Ah	7.1 Ah

==>

long shutdown periods are typical for a **research facility** like PSI, but not necessarily typical for ADS applications

PSI unscheduled outage April-September 1999

(As presented in Aix-en-Provence, all values scaled up to 1 y = 8 760 h.)

	Nb. of events	av. repair time	down time
CW	190/y	0.03 h	6 h/y (0.2%)
RF inj.2	170/y	0.45 h	76 h/y (0.9%)
ring	130/y	0.68 h	88 h/y (1.0%)
high voltage devices	8 200/y	14 s	30 h/y (0.3%)
magnets	10/y	35 h	350 h/y (4.0%)
PS, CTRL	330/y	0.28 h	91h/y (1.0%)
meson targets	50/y	0.08 h	4 h/y (0.1%)
support systems	100/y	2.40 h	239 h/y (2.7%)
beam protection	11 700/y	14 s	45 h/y (0.5%)
procedures & user	5 130/y	14 s	20 h/y (0.2%)
total per 8 760 h			950 h/y (10.8%)

==>

7.1% of down time was caused by only **9 events** of a nature not typical for a power plant environment

==>

2.4% was caused by remaining events

==>

1.2% caused by short beam interruptions

PSI unscheduled outage 2000/2001

(Analysed by A. Mezger)

All values scaled up to 1 y = 8 760 h of beam time.

	1999	2000	2001
beam trips (18 s)	100 h/y	228 h/y	112 h/y
meson targets	–	217 h/y	72 h/y
septum repairs	–	208 h/y	120 h/y
Cooling	210 h/y	160 h/y	88 h/y
Cockcroft-Walton	10 h/y	157 h/y	6 h/y
RF	160 h/y	142 h/y	64 h/y
vacuum	10 h/y	90 h/y	16 h/y
power supplies	50 h/y	62 h/y	54 h/y
site power	20 h/y	42 h/y	40 h/y
control	40 h/y	40 h/y	30 h/y
magnets	350 h/y	28 h/y	200 h/y
miscellaneous	–	18 h/y	94 h/y
personal safety	–	8 h/y	10 h/y
total per 8 760 h	950 h/y	1 400 h/y	906 h/y

==>

average down time for 1999/2000/2001 is **12%**, or 1 090 h/y (corresponding to 8 760 h operation)

==>

1.7% caused by **short beam interruptions**
10.3% component failure & **repair**

==>

the large differences confirm that down time is dominated by **single events** with generally **long repair times**

==>

reduction of repair time to **3.3%** to be **expected**, if we assume the best annual performance for every category

PSI facility: breakdown related to research activities

- The following categories in the list are due to the research nature of the PSI-facility:

targets	:	meson production target
site power	:	guaranteed in a nuclear power plant
miscellaneous	:	mostly user related
personal safety	:	for experimental facilities

	1999	2000	2001
meson targets	–	217 h/y	72 h/y
site power	20 h/y	42 h/y	40 h/y
miscellaneous	–	18 h/y	94 h/y
personal safety	–	8 h/y	10 h/y
total (for 8 760 h of beam time)	20 h/y	285 h/y	216 h/y

==>

<p>research activities account for 2%, or 174 h/y down time (scaled up for 8 760 h operation)</p>

PSI septum repairs

- Down time 2000/2001

	1999	2000	2001
septum repairs	–	208 h/y	120 h/y

- Electrostatic inflector or electrostatic deflector had to be **exchanged 5 times** in 2000/2001 (during 9 650 h operation), failure is related to voltage level & spark rate:

Inj 2 extr. (EID)	3.2 MV/m	300 discharges/y	no failure
Ring inj. (EIC)	7.4 MV/m	3 100 discharges/y	1 x failed
Ring extr. (EEC)	8.8 MV/m	4 300 discharges/y	4 x failed

- Average **repair time was 36 h**, essentially due to the fact:
 - the vacuum of the cyclotron has to be broken and restored;
 - that spare units are not stored in the cyclotron vault;
 - the shielding roof of the vault has to be removed;
 - spare units are available, but not preconditioned in the vault.

- The design accounts for high beam power, low beam losses and adequate handling under activated conditions, “**Wechselflaschen**” (shielded exchange & transport boxes) are provided for quick and “quasi-remote” exchange of the activated devices.

==>

today typically 1-2% average down time

==>

a long repair time can be avoided by having spare units readily available in the cyclotron vault, average **repair time** of 36 h could be reduced to **<10 h**, this would reduce down time to about **0.3-0.5%**

==>

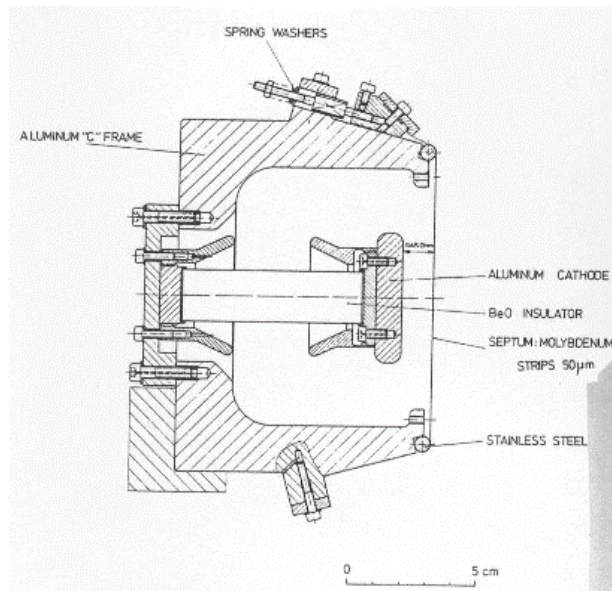
mean time between failure has to be improved, discharges and failures are **insufficiently understood**,

==>

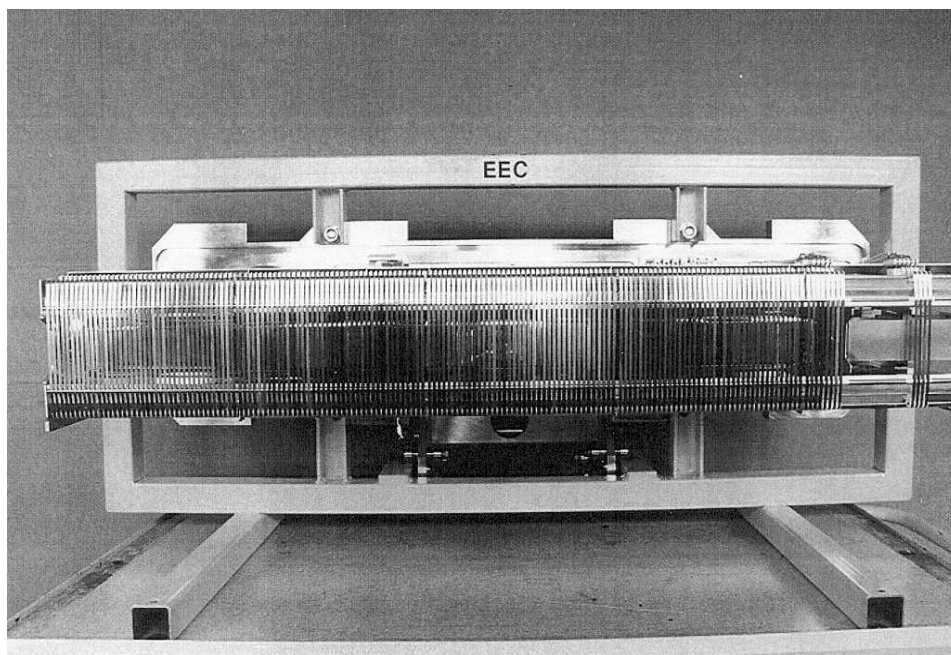
better fault diagnostics has to be provided.

PSI EEC: electrostatic extraction channel with foil septum

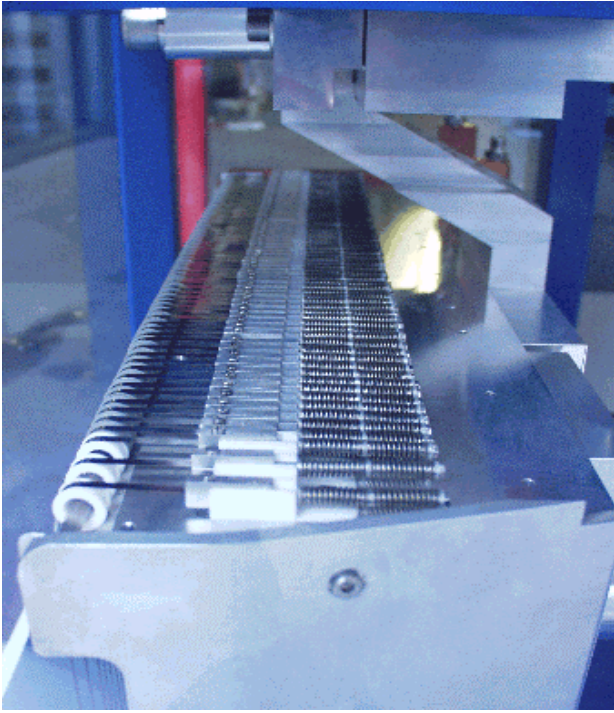
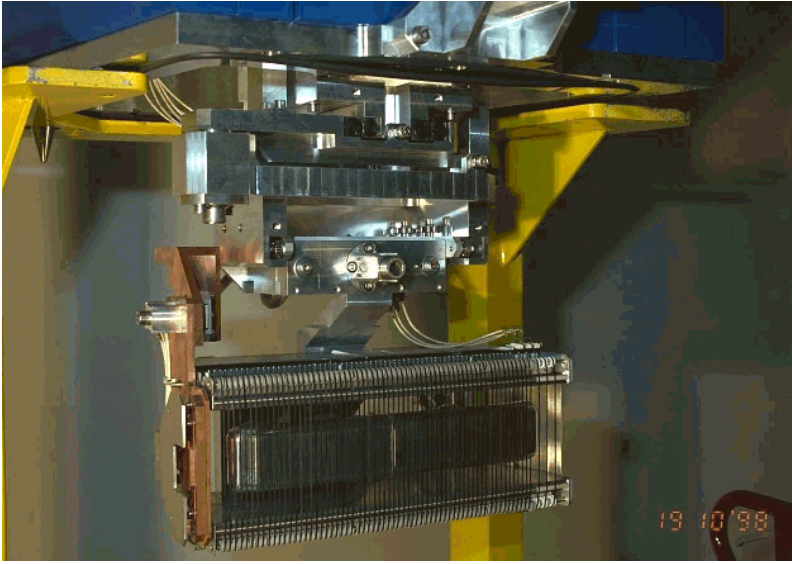
(M. Olivo, 7th Int. Conf. on Cycl. and their Appl. 1975.)



Cross-sectional view of the septum and C-frame. The stainless steel rods define a septum flatness of ± 0.02 mm. The C-frame is indirectly cooled from the support structure.



PSI EIC: electrostatic injection channel with foil septum



PSI facility: cooling and related problems

- Down time 1999/2000/2001

	1999	2000	2001
cooling	210 h/y	160 h/y	88 h/y
Cockcroft-Walton	10 h/y	157 h/y	6 h/y
magnets	350 h/y	28 h/y	200 h/y
vacuum	10 h/y	90 h/y	16 h/y
total (for 8 760 h of beam time)	580 h/y	435 h/y	310 h/y

- Dominated by single events (per 8 760 h)

1999	flood in the river serving water pumps	52 h	112 h
	corrosion in 25 y old bending magnet	132 h	285 h
	corrosion in 25 y old magnetic inflector	30 h	65 h
	ruptured groundwater pipe	16 h	35 h
2000	leaky Freon cooling for ion source dome	90 h	150 h
	15 y old vacuum seal injector cycl. leaky	27 h	45 h
2001	corrosion in 25 y old bending magnet	100 h	200 h
total	scaled up for 8 760 h of beam time	300 h/y	

==>

today typically 5.0% average down time (442 h/y)

==>

3.4% down time (300 h/y) is due to single events as listed above and related to **old equipment or upgrade** projects

==>

with proper **preventive maintenance** down time could be **reduced to 1.6%** or less

==>

preventive maintenance would also reduce the failure rate concerning shorter beam interruptions

PSI-facility: RF systems reliability upgrade

- 1991-1995 **high power upgrade** of the PSI facility:
 - RF cavity voltage raised from 450 kV to 730 kV peak;
 - final stage 800 kW final stage added to the RF amplifier chain;
 - RF power amplifiers reinstalled outside of the vault;
 - installations improved for fast exchange of amplifier stages.
- 1997-2001 ongoing **RF reliability improvement programme**:
 - detailed study on discharge mechanisms;
 - redesign of inductive high power coupler (window);
 - installation of spark detection in cavity coupler;
 - RF spark control logic, suppression of micro-sparks;
 - automatic pulsed restart after spark in cavities;
 - full event logging for better fault diagnostics.
- Down time 1999-2001

	1999	2000	2001
RF	160 h/y	142 h/y	64 h/y

==>

today typically **1.4%** average down time (122 h/y)

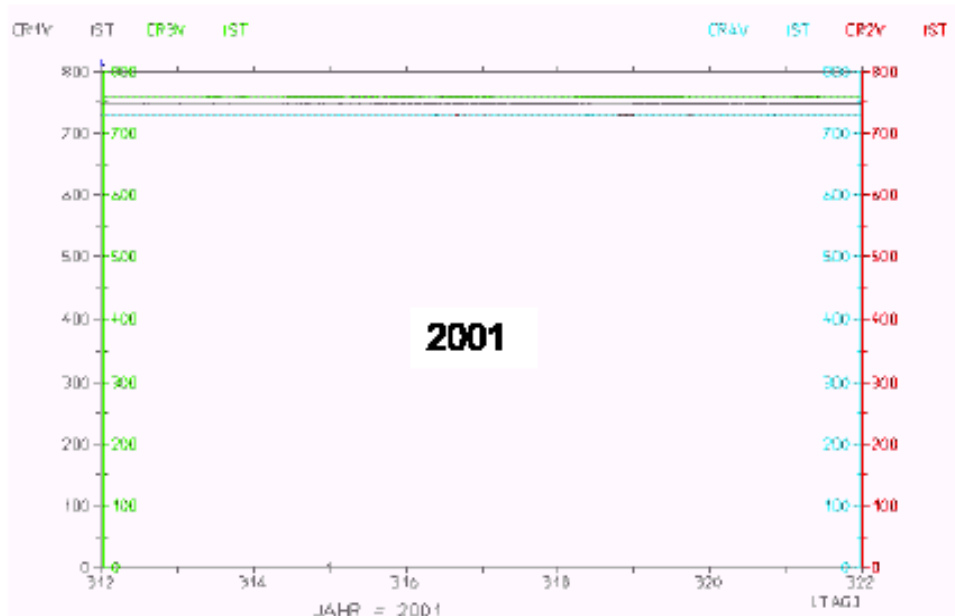
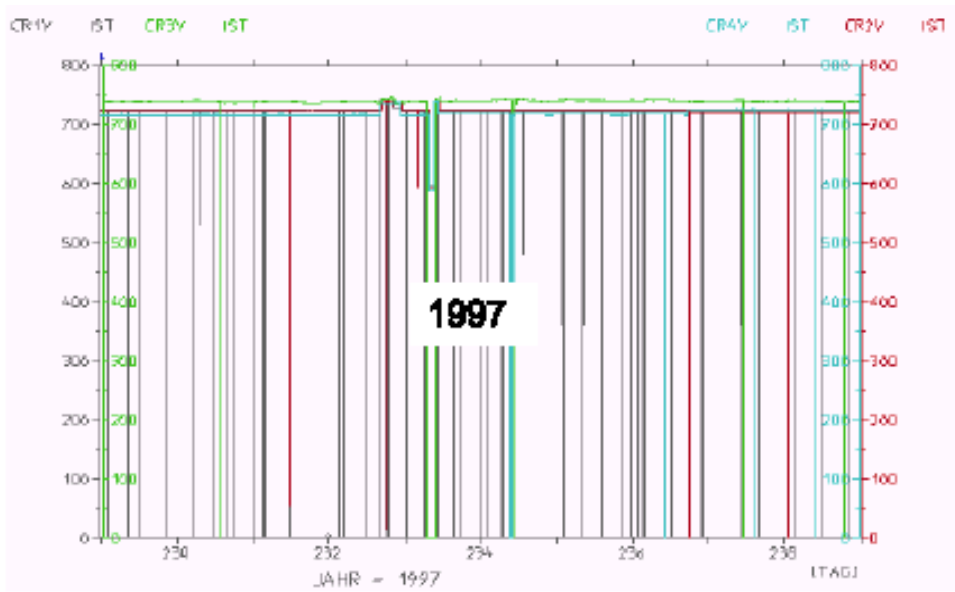
==>

reliability improvement effort has been very effective:

- enhanced failure rate after upgrade cured;
- understanding of discharge mechanism important;
- fault diagnostics and event logging necessary;
- **engineers** must be involved during routine operation.

590 MeV cyclotron cavity voltages

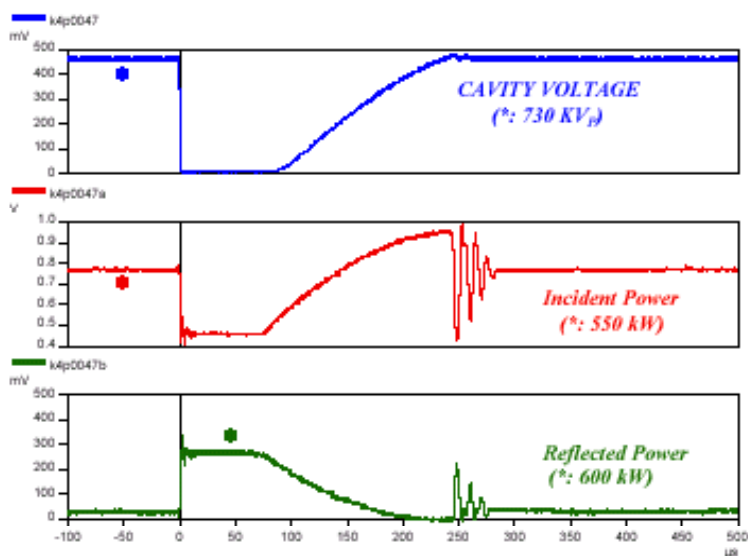
- Cavity voltages over a 10-day period in 1997 at 1.5 mA beam current before new RF-spark control came into operation, and the same voltages plotted over a 10-day period in November 2001 at 1.8 mA beam current (only interruptions longer than 1min duration are recorded).



RF systems, spark recovery in the 590 MeV cyclotron cavity

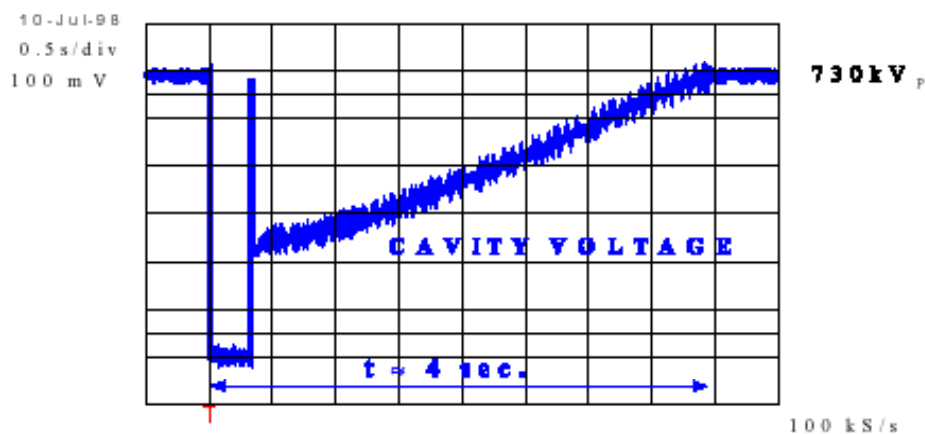
SELF-RECOVERING SPARK ("μ-spark") IN CAVITY

(RF power and beam stay on)

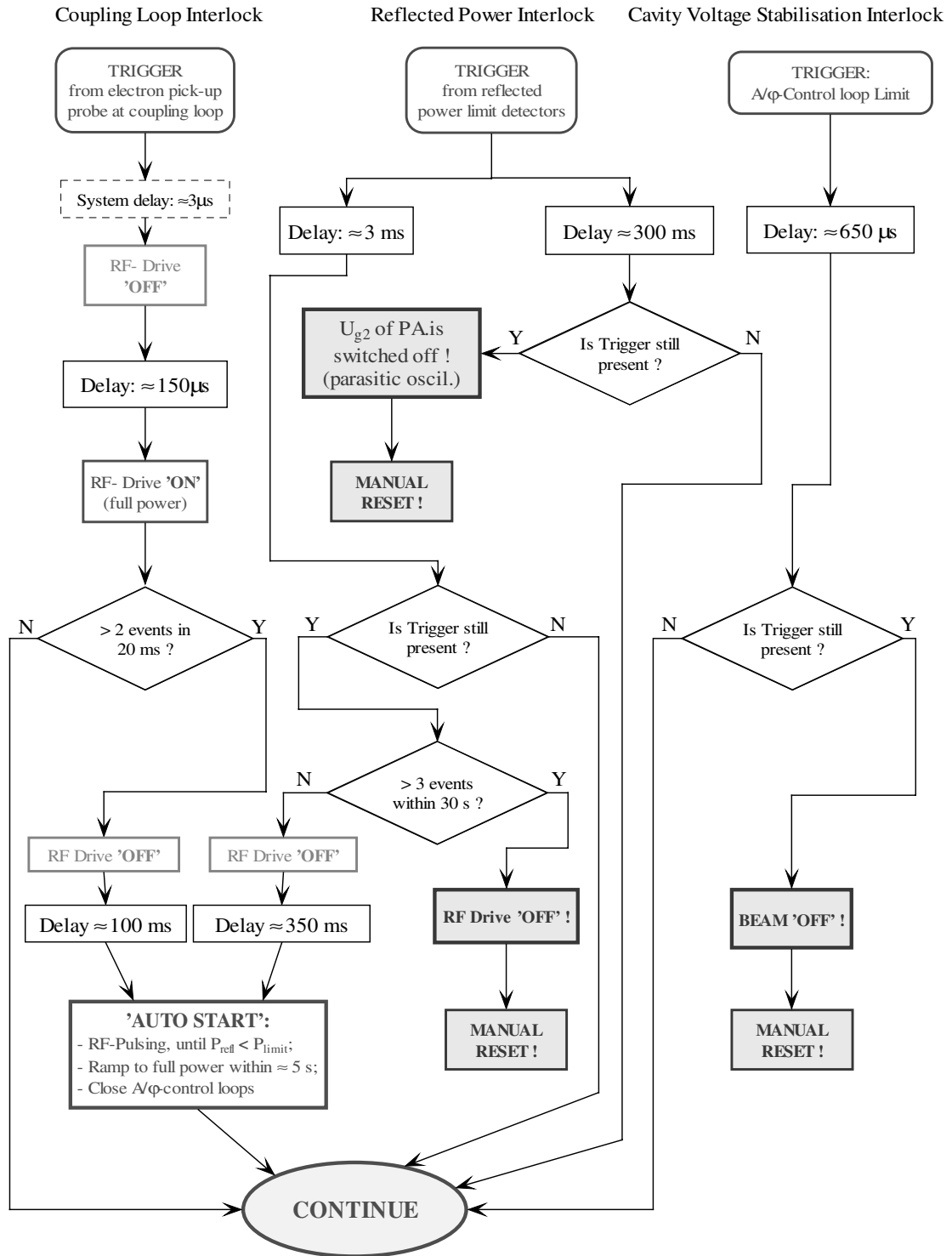


PULSING AND RAMPING PROCEDURE AFTER NON-RECOVERING SPARK IN CAVITY ('Auto-Start')

(Beam off after ≈ 1ms; RF turn-on after only one pulse)



RF systems, spark control procedures



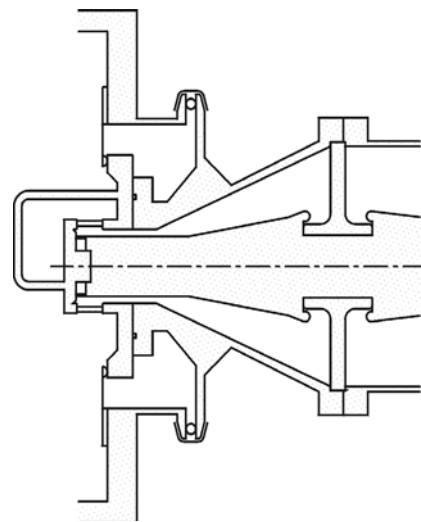
RF power coupler of the 50MHz-cavity

- Very complex discharge mechanisms:
 - 1st step: secondary electrons charge insulator surface of the window;
 - 2nd step: low power discharge at the boundary ceramics to metal;
 - 3rd step: evaporated metal cloud expands;
 - 4th step: metal vapour generates a powerful discharge in the loop.

- Old design

==>

Failure >200 kW



- New improved design

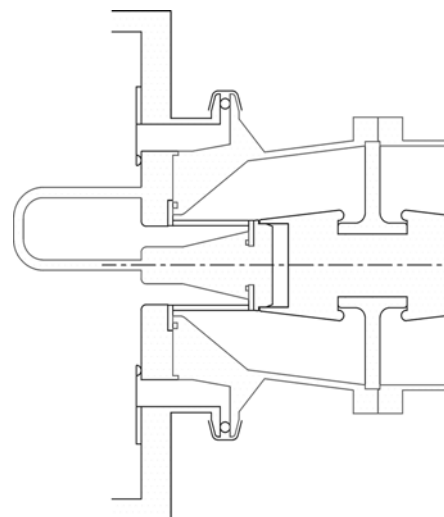
- proper 50Ω structure;
- ceramic out of RF-fields and wall current;
- low field strength on ceramic surface;
- ceramic easy to exchange.

==>

Good for 500 kW

==>

Lifetime to better than 4 y



PSI facility: power supplies and control systems

- Down time 1999/2000/2001

	1999	2000	2001
power supplies	50 h/y	62 h/y	54 h/y
control	40 h/y	40 h/y	30 h/y

- 40% of the down time 1999/2000/2001 is caused by single events with unduly repair times around 15 h (corresponding to 40 h/y)

==> **today typically 1.1% average down time (93 h/y)**

==> **failure rate** is a consequence of the complexity of the facility and the large **number of devices**

==> **built-in fault detection** can avoid down time through preventive maintenance and helps to reduce repair time

==> **repair time** can be **reduced** by modularity in the design, the availability of **spares and redundant systems**

==> down time could be **reduced** to less than **0.6%** (53 h/y) with built in fault detection and a proper spare part policy

PSI facility: beam trips, short beam interruptions <1 min.

beam trips	1999	2000	2001
number of trips	26 000/y	46 000/y	22 000/y
down time (14s-18s)	100 h/y	228 h/y	112 h/y

- Typical duration of a beam trip is below 20s, start-up is automatic, ramping time is adapted to thermal properties of the pion target, feed-forward techniques are used to adjust some critical parameters, on-line beam steering system keeps the beam on-axis during ramping.

==>

beam trips have caused about **1.7%** down time (147 h/y), but differences from year to year are large (1.1-2.6%)

Beam trips due to discharges in electrostatic devices

- **Discharges** contribute significantly to the number of beam trips
- Under **good conditions** the discharge rate is **10-15/day**, this corresponds to **0.2-0.3%** average down time (18-27 h/y)
- Under **bad conditions** the discharge rate can be as high as **100-500/day** this has caused **0.3-1.2%** average down time (25-100 h/y) (e.g. after venting the cyclotron vacuum chamber, in July/August 2000 two incidents have caused a higher discharge rate, metal evaporation after damage to RF spring-contacts of a badly mounted coupler and a hidden water leak on an extraction magnet)

==>

0.5-1.5% down time is caused by **short beam trips** after discharges in electrostatic devices

==>

in 2001 careful pre-conditioning has resulted in a lower rate

==>

discharge phenomena are not well understood, special effort needed to understand discharge mechanism and to improve failure rate and discharge rate of electrostatic devices

Beam trips due beam protection devices

- Beam loss monitors and beam transmission control produces a large number of fake-turn-off

==>

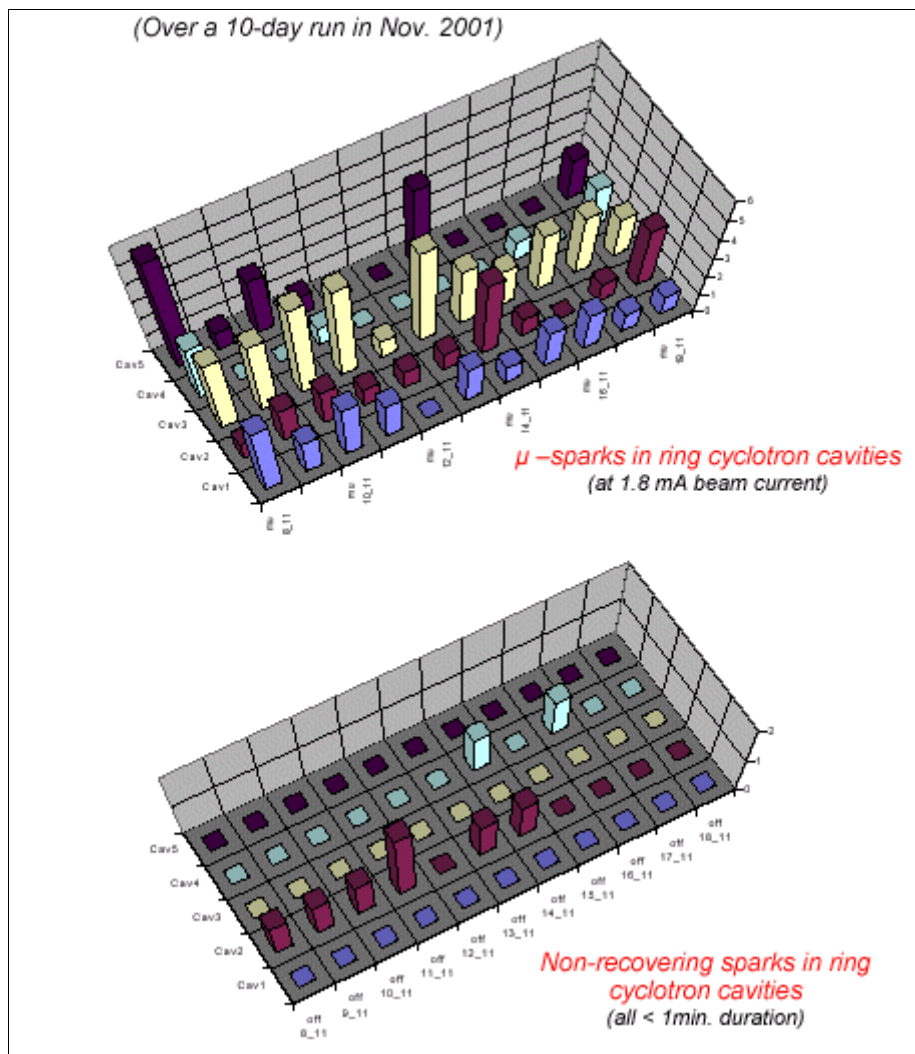
short beam interruptions from **beam protection** devices are estimated to cause **0.5%** down time

==>

interlock **levels** are set **too conservative** and in many cases much lower than needed to prevent damage, it is expected that down time could be **reduced to about 0.2%**

PSI, beam trips due to RF discharges

- Cavities operated below Kilpatrick limit, electric field <3.0 MV/m.
- Sparking rate of the Ring cyclotron RF-cavities (Cav. 1-4: 50 MHz; Cav. 5: 150 MHz).



==> **beam** is kept **on** after self-recovering **micro-sparks** <500μs, but beam loss on the electrostatic devices during micro-sparks may introduce discharges, rate about 10/day, **<0.2%** (18 h/y)

==> **non-recovering sparks** are **rare**, in some cavities none, cavity voltage is back on after 4 s, rate 1/day, **0.02%** (2 h/y)

Conclusion 1

==>

Reliability goal for a well designed ADS cyclotron is:		
	Down time	%
beam trips (18 s)	80 h/y	0.9
septum repairs	–	0.3
cooling/vacuum	140 h/y	1.6
RF	90 h/y	1.0
power supplies	30 h/y	0.3
site power	–	–
control	20 h/y	0.3
magnets	–	–
total per 8 760 h	380 h/y	4.4

==> we expect **3.5%** down time due to **component failure** and **0.9%** due to **beam trips**

==> There is a non-vanishing **risk** that one of the large components of the cyclotron with a **very long repair time** might fail

Conclusion 2

==>

several factors are in favour of an ADS solution with
a farm of e.g. 3-4 cyclotrons:

- better distributed neutron flux in the core
- better power distribution on the entrance window
- better possibility to adapt to changes in criticality
- higher reliability
- power swing with a beam trip is only half or one third
- redundancy in the case of large repairs
- redundant systems during regular maintenance
- less manpower needed for maintenance
- probably better power efficiency

and the price for three 10MW-cyclotrons is only about 1.5 x the cost of a 30 MW-machine, since the investment is dominated by the cost of beam power (30%)

Conclusion 3

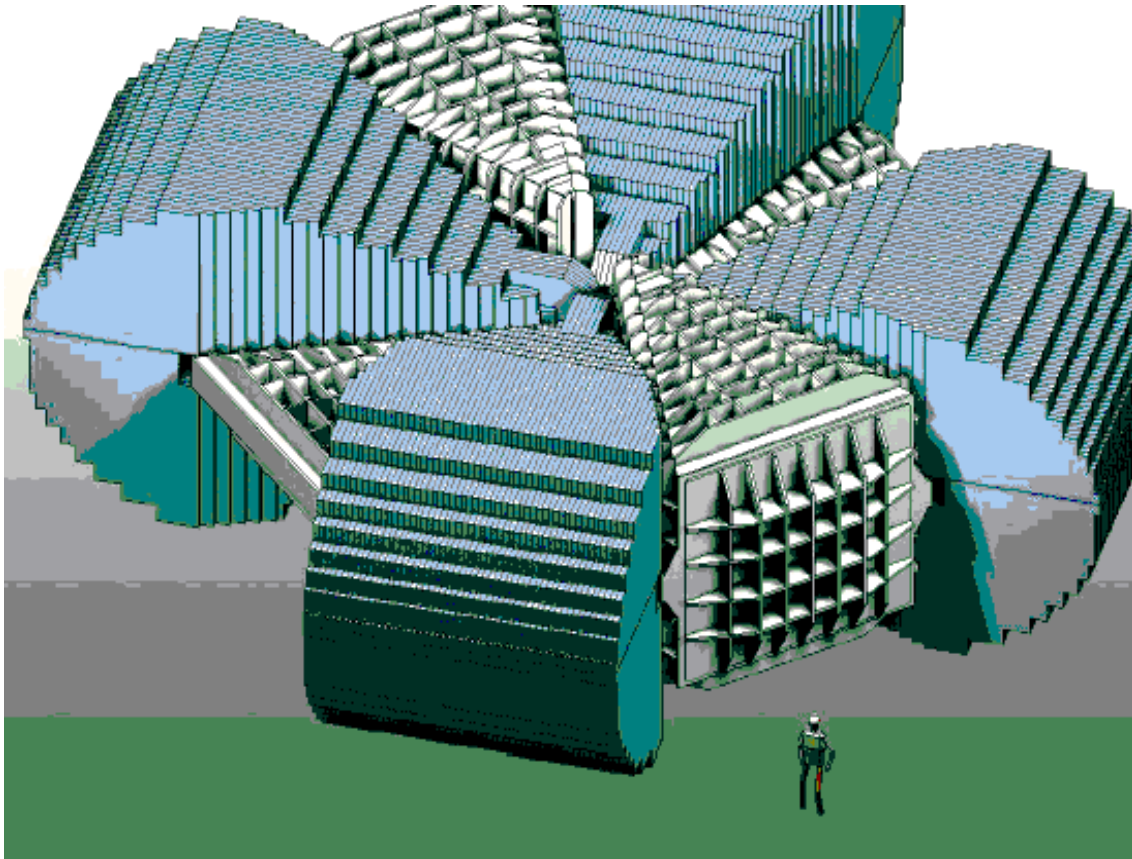
==>

use no electrostatic inflector & deflector

==>

keep RF voltage low

- e.g. The **MYRRHA** project (IBA/SCK CEN, Belgium) (ion beam application/Belgian nuclear research centre).
- **700 MeV H₂⁺**-cyclotron for 2.5 mA beam current extraction by stripping delivers a 5 mA proton beam at 350 MeV.
- large room temperature magnet with **6 Tm** bending power.



==>

economical solution for **1.75 MW** beam power

==>

3 month uninterrupted operation goal

TOWARDS RELIABLE HIGH POWER SPALLATION TARGET DESIGNS

Günter S. Bauer

ESS Projekt, Forschungszentrum Jülich
D52425 Jülich, Germany
g.bauer@fz-juelich.de

Abstract

Although the reliability issue is usually viewed from an accelerator point of view, performance of future ADS will also depend very strongly on the reliability of their target systems. In contrast to the accelerator field, very little experience exists in this respect, or even none at all for liquid metal targets, which are the concept of choice for most ADS projects. The present paper gives a selective overview of available experience and ongoing work in the field of high power spallation targets and discusses briefly the prospects of developing predictable and reliable liquid metal targets for high power applications.

Introduction

Future applications of the spallation process as a source of copious numbers of neutrons will be in the field of condensed matter research and in accelerator driven systems (ADS) with subcritical cores surrounding the spallation target. While both types of facilities will naturally thrive for high availability (as defined by the number of hours of operation per year), high reliability (as given by the time the source is actually functioning relative to the time it is scheduled to function) is an equally important concern. This is particularly true in ADS applications, where each interruption will not only cost money but will also contribute to fatigue in certain components and hence ultimately be one of the reasons for a limited life time. Although most of the concern with respect to reliability is with the driving accelerator, failure of the target system to function as designed might lead to serious trouble in terms of down times due to the likely need for remote maintenance and repair. Furthermore, the possibilities to introduce redundancy and low stress and fault tolerant designs in accelerator systems are much more obvious than in the target region [1]. It is also true, that much more experience exists with high current or high energy accelerators than with high power spallation targets. The physics and technology of spallation targets have been reviewed recently [2]. The present paper tries to point out what is available in terms of experience and test beds and what concepts exist and R&D is being done to go beyond the present state of the art. This is not meant to be a comprehensive review but rather to focus on some of the outstanding issues and developments.

SINQ as a forerunner to high power targets

Reliability of the SINQ target system

The world's most powerful existing spallation neutron source, SINQ, is located at the Paul Scherrer Institut in Switzerland [2], [3], [4]. This facility, whose primary mission is to serve neutron scattering for condensed matter science, started operation in 1997 at a beam power of less than 0.5 MW on target and is now approaching 1 MW as a result of continuing upgrading efforts. Understandably, this very effort to increase the power of the accelerated beam, together with the fact that the accelerator is a multiple use facility, compromises somewhat its reliability. This, however is exclusively true for the accelerator and beam transport system. The SINQ target itself excels by an availability around 99% in each given year, as can be seen from the chart given in Figure 1, which compares the weekly charge actually accepted by SINQ (hatched columns) to that offered by the accelerator (black columns).

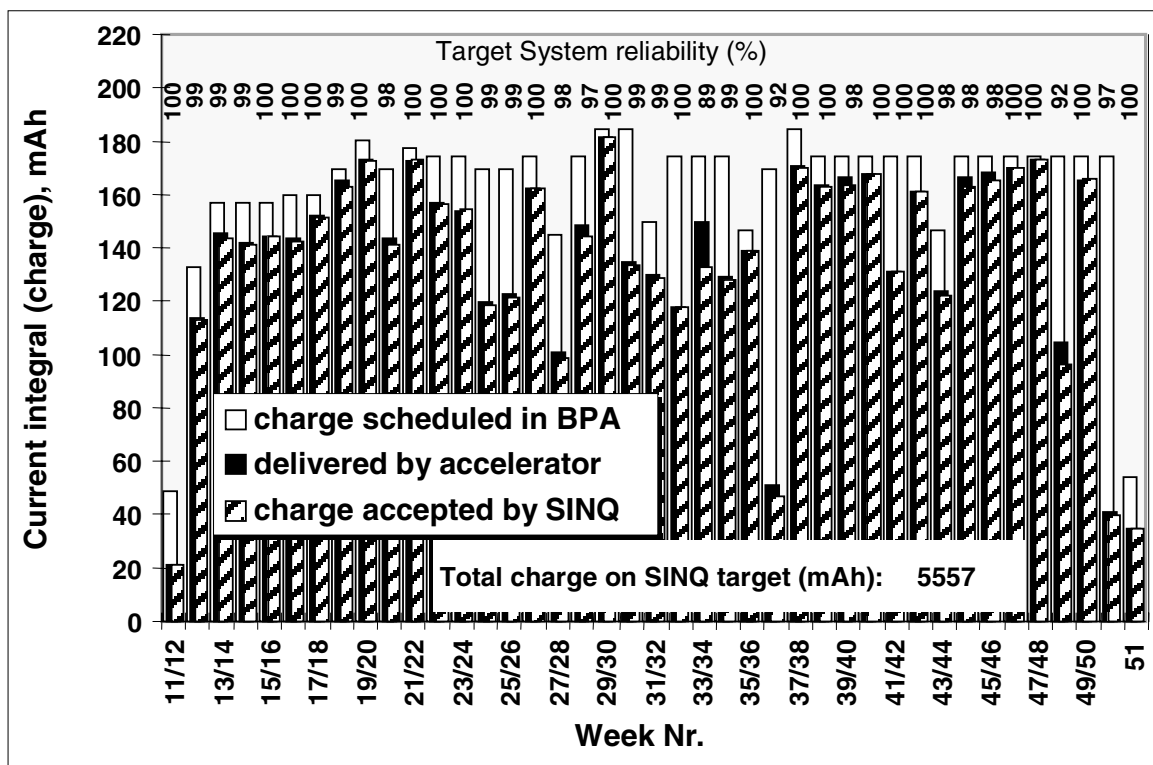
A similar chart given for the year 1999 in [2] shows the same picture, and also in 2001 the reliability was more than 99%. It should be noted that these figures include the liquid hydrogen cold moderator and its cryogenic system which is, in fact, one of the main reasons for time lost in SINQ operation, but is not relevant for an ADS. Other sources of occasional trouble are mostly peripheral systems such as non-availability of monitoring systems. The bottom line is that SINQ clearly demonstrates that at 1 MW beam power spallation targets can be very reliable. This is, of course partly due to a rather conservative design.

The SINQ target as a test bed

The SINQ target consists of an array of about 400 rods with 11 mm in diameter arranged in a piece of welded aluminium pipe of square cross section and cooled by heavy water in cross flow

(Figure 2). The rods were originally made of solid zircaloy for the commissioning and first production target. Taking advantage of positive experience with some test pieces inserted in the first production target, the rods for the following targets were made of lead encapsulated in thin (0.5 mm wall thickness) austenitic steel tubes. This resulted in a 50% increase in neutron flux in the moderator surrounding the target. The target is suspended in a double walled shell made from the alloy AlMg3, which has a separate water cooling. It is the radiation damage to this shell which is the most important factor in deciding on the service time of the targets.

Figure 1. Chart of charge scheduled, charge delivered and charge accepted by SINQ in 2000



So far the shell has been exposed to a total of 10Ah of beam, corresponding to an integrated peak proton load of ca. 300 mAh/cm² or 6.75*10²⁵ p/m². This shell has not yet been examined, but the decision to go to this load level was based on the findings from the examination of the previous one, which had been exposed to about half of that load (Figure 3).

Examining target components after use is not the only way in which the operation of SINQ helps to accrue a data base for the design of future high power targets. On the contrary, a large international collaboration has formed to support dedicated materials irradiation experiments in the SINQ target (STIP [5], SINQ target irradiation programme). In the frame of this program, up to 20 of the most highly loaded rods in the target are in fact not optimised neutron production rods, but are either assemblies of miniaturised test specimens of different types and materials or are solid rods of steel or test rods for future target concepts. Complete with thermocouples and dosimetry packages, these materials samples are removed from the targets and are examined by a variety of established methods to yield information on the effect of the very realistic irradiation conditions in SINQ on the properties of the various materials. Test methods are standard ones such as tensile tests, electron

microscopy, fracture toughness tests, etc., but also less common ones such as neutron radiography, small angle neutron scattering and internal strain measurements on radioactive specimens, which are possible at SINQ. As an example Figure 4 shows a neutron radiograph on an irradiated rod of martensitic steel encapsulated in a zircaloy tube. The dark spots are interpreted as hydride precipitates.

Figure 2. Schematic of the SINQ target (left) and target insert of the production target used in 2000/2001 before final mounting

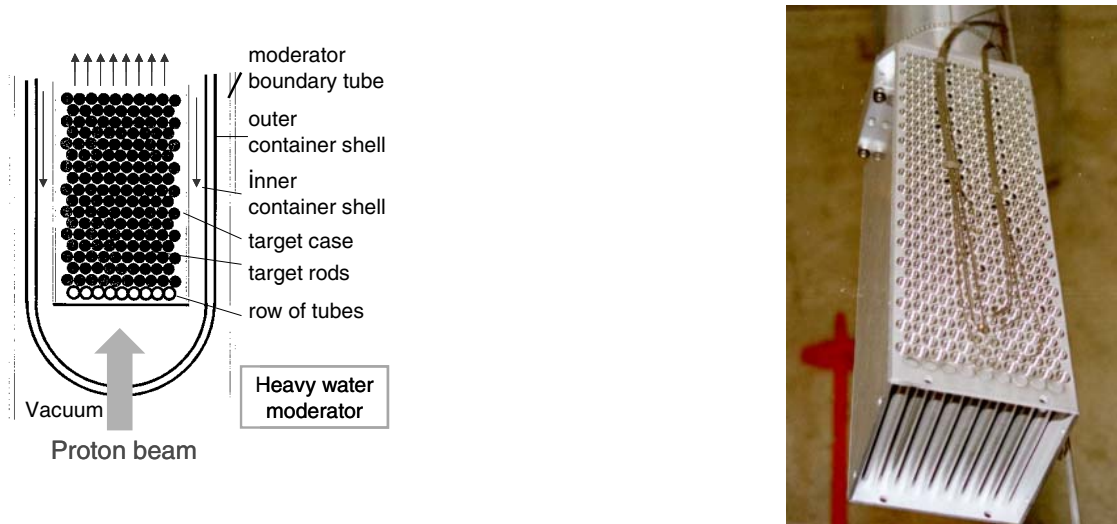
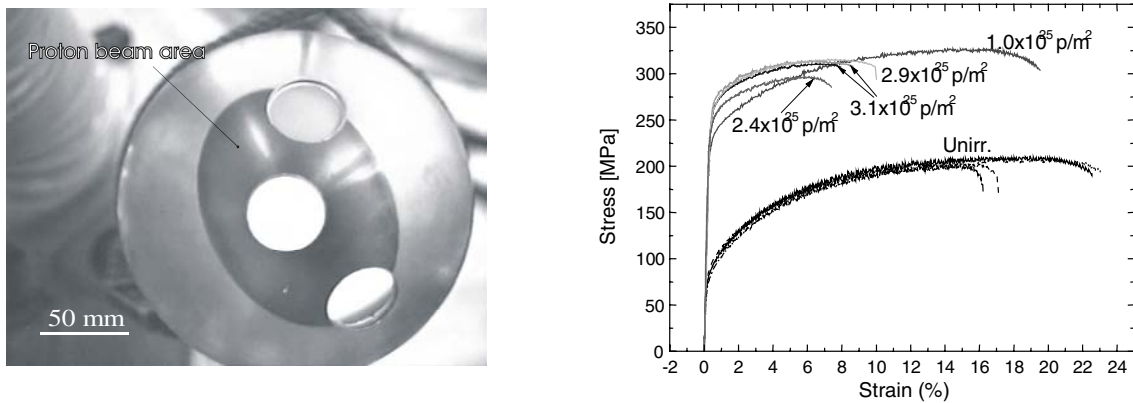


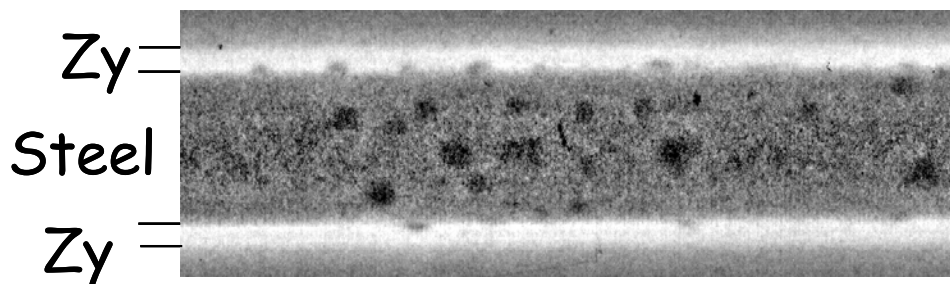
Figure 3. Bottom view of the second SINQ target shell used. The footprint of the beam is clearly visible (left). Samples were prepared from material drilled out of the AlMg3 shell and stress-strain curves were taken for pieces that had suffered different beam loads (right).



This seems to show that, while much of the hydrogen generated in the martensitic steel is released from this material, it is trapped in the zircaloy. This finding indicates that (a) there is little risk of hydrogen embrittlement of martensitic steel and, (b) caution must be exercised when choosing zircaloy as a structural material in regions where hydrogen production is high. (In fact, this is the main reason, why zircaloy is not being used as cladding material for the lead rods in SINQ until this question has been examined in more detail, despite its otherwise favourable properties.) It is worth

noting that much less hydride formation was observed in the zircaloy tube enclosing a rod of austenitic steel. This is in agreement with findings by other authors [6] that austenitic steels show higher solubility and lower diffusivity than martensitic ones and confirms the diagnostic power of neutron radiography on highly radioactive specimens.

Figure 4. Magnified section of a neutron radiograph taken of a test rod of martensitic steel that was irradiated in the SINQ target in a zircaloy (Zy) tube. The dark spots protruding into the zircaloy are interpreted as hydride lenses.

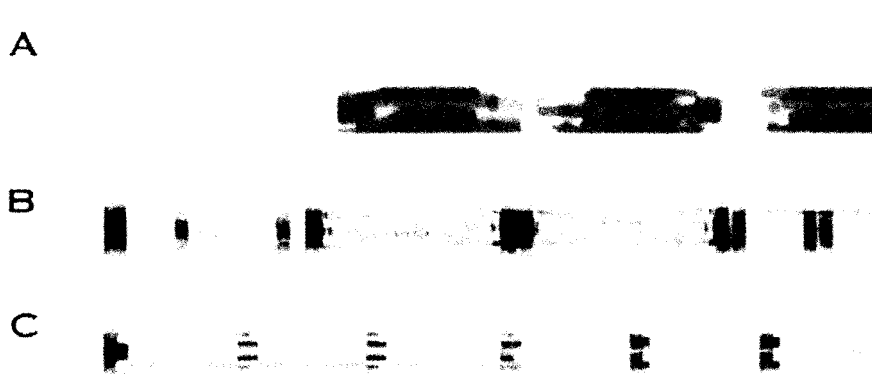


Another step forward: the MEGAPIE project

The above examples are meant to show how a data base is being accrued that will ultimately help to design spallation targets of high performance and that will allow to ensure the required reliability by properly assessing the service time of any target in view of its operating conditions. Given the existing experience, it must be said that at present the most reliable target concept for the Megawatt range of beam power is a solid rod target (cf. below). However, as the spallation source concepts demand higher and higher beam currents (and current densities for the sake of source compactness), liquid metal targets are the concept of choice for a variety of reasons. Not only is there no radiation damage in the target material, it is also not diluted by cooling channels and the presence of water in the target and core region can, in principle be avoided, which is important for a fast neutron system. However, to date no experience exists with all liquid metal targets, barring the fact that in the SINQ target the lead melts in some of the target rods during full power operation.

In an effort to demonstrate the feasibility of such a target, an international collaboration was initiated to design, build and operate the first high power liquid metal target, using the existing SINQ facilities. This collaboration, known as “MEGAPIE” (megawatt pilot target experiment) [7, 8] has, in the mean time, produced a full design of such a target including its auxiliary and ancillary systems as well as the related safety analysis report. It has also lead to considerable co-ordination in and strengthening of pertinent research on liquid metal corrosion, lead-bismuth technology, irradiation effects and the like, generating a broad data base and providing a lot of insight into the necessities and conditions for safe and reliable operation of such a system. As a precursor incorporating many of the features of the MEGAPIE target, a smaller experiment, called LiSoR (liquid solid reactions) has recently been put into operation to demonstrate the compatibility of molten flowing Pb/Bi with T91-type martensitic steel under irradiation with simultaneous application of stress [9]. First results of the LiSoR experiment will be obtained before the end of 2002. First results from irradiated target rods with steel specimens in stagnant Pb/Bi (and mercury) will be obtained from the imminent examination of test rods irradiated in the previous SINQ target (Figure 5).

Figure 5. Neutron radiographs of test specimens embedded in mercury (top) and Pb/Bi for irradiation in the SINQ target



The MEGAPIE target (Figure 6) employs two independent electromagnetic pumps for circulating the main Pb/Bi flow and to direct a separate bypass flow across the hemispherical beam window for improved cooling (by a factor of up to 5, as shown in off-line tests [10]). Important new fields in which a number of issues had to be solved are:

- the target fill-and-drain system;
- the heat removal control/auxiliary heating system that ensures a liquid state of the target material at all times and everywhere in the loop;
- the gas handling system and;
- the intermediate heat transfer system between the rather hot liquid metal and the practically unpressurised water cooling loop.

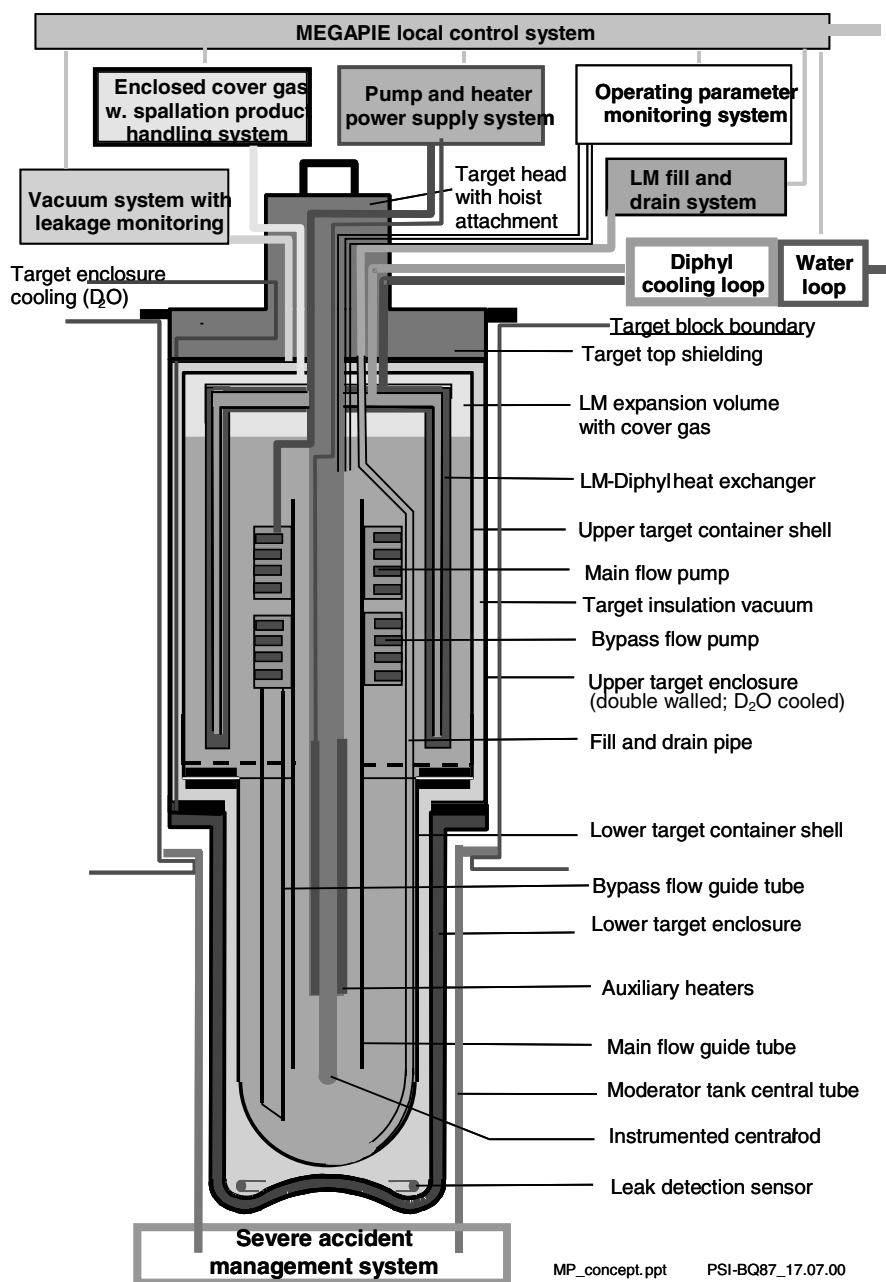
The target is heavily instrumented to provide as much data as possible during its operation.

MEGAPIE is planned to be inserted in the SINQ target block in early 2005 and to run for one year, i.e. about 5 Ah, before it will be removed for dismantling and careful inspection of its components. Its operation and post irradiation examination can be expected to be a major milestone on the route to reliable liquid metal targets.

R&D for the next generation spallation sources

Another field, to which a significant amount of research is being devoted by a different community is the development of high power targets for research spallation sources. These facilities are now aiming at a power level of 5 MW and will be operated in a pulsed mode. While this may seem to aggravate the issue, it may well be an important feature also for ADS, because beam pulsing is more and more entering the pertinent discussion [11] for a variety of reasons, such as easier diagnostics and monitoring, upgradability, easier use of multiple accelerator systems and the like. Irrespective of this, the power loads on the next generation spallation neutron sources will exceed that of MEGAPIE by about a factor of 3-4, which brings it closer to real ADS systems.

Figure 6. Schematic representation of the MEGAPIE target system



Note: Although highly simplified, the diagram shows the complexity of such a target and the large number of auxiliary systems necessary. Double enclosure (not shown) is provided for the cover gas and fill and drain system. “Severe accident management system” stands for a number of modifications made to the beam transport line in order to be able to recover from a spill of PbBi into the region below the target. (The beam enters the target from below).

Another feature that is different from current ADS concepts is the use of mercury as target material. While mercury is presently not considered as a candidate for ADS targets because of its low boiling point, it has a number of attractive and advantageous features that prompted the high power spallation source community to opt for this solution. Among them are its higher density, liquid state at room temperature (no risk of freezing), its lower corrosivity relative to Pb/Bi and the fact that it is

relatively easy to purify and does not produce alpha emitters of any significant life time. This makes the technology of mercury targets much easier – and hence probably also more reliable – than that of Pb/Bi targets. The high thermal neutron absorption cross section is not a disadvantage in a system that is designed for use of fast neutrons. In some cases it may even be an advantage due to removal of thermal neutrons from the system. A necessary condition for mercury to be considered as target material for ADS is complete separation of the core cooling and the spallation target loop, a concept which is making its way into more and more of the ADS designs proposed. The fact that the two loops will be on different temperature levels is not a concern, since there will be vacuum insulation between the two anyway.

Considering all this, the fact that both, mercury and Pb/Bi targets are presently being developed and the technologies will be available to choose from, is another positive feat in the quest for reliable spallation targets.

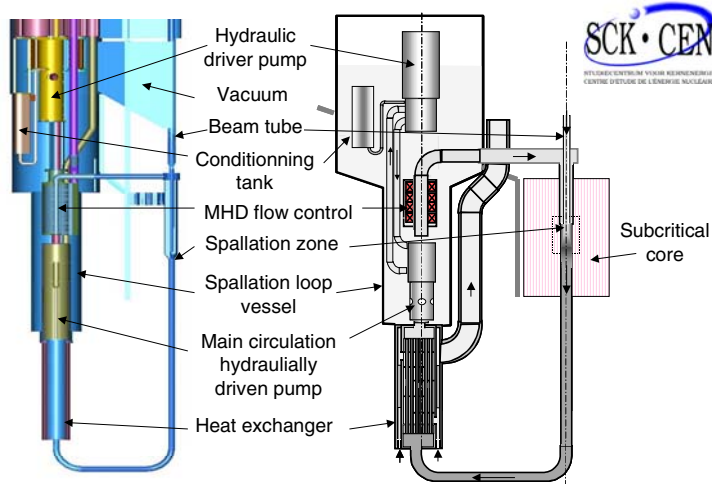
The most advanced of the next generation spallation source projects is the 1.4 MW SNS in Oak Ridge, TN, whose construction is progressing rapidly [12], followed by JSNS at JAERI, Japan [13], which has just started. ESS, [14, 15] with its two target stations of 5 MW beam power each would certainly be the most significant step forward, but is still awaiting approval.

The ultimate test: MYRRHA

The first project to combine a liquid metal target with a subcritical fast core at relevant power levels may be MYRRHA [16], an irradiation facility proposed by the Belgian SCK•CEN at Mol. This project foresees a flowing Pb/Bi target surrounded by a subcritical assembly that would produce up to 10^{15} fast neutrons per cm^2 per second and could also incorporate “thermal islands” in its core for thermal neutron irradiation. MYRRHA is planned to be fed by an accelerator of 350-400 MeV with a beam current of 4-5 mA. It is mainly this low proton energy which prompted the MYRRHA designers to embark on a target design, which is of special interest in the present context: a windowless Pb/Bi target with beam injection from above. A schematic representation of the loop is shown in Figure 7. The flow through the target is driven by the hydrostatic pressure due to the level difference between the surface of the Pb/Bi reservoir and the target position, The flow rate can be increased or decreased by an auxiliary MHD pump that can operate in forward or reverse direction with varying power, thus providing a large control margin. The heat exchanger is arranged in the return flow in front of (below) the main pump that maintains the liquid metal level in the reservoir. Due to unavoidable leakage to the main core cooling loop, which is also Pb/Bi, the main pump is hydraulically driven by a flow of Pb/Bi which is generated in a hydraulic driver pump above the level of the reservoir.

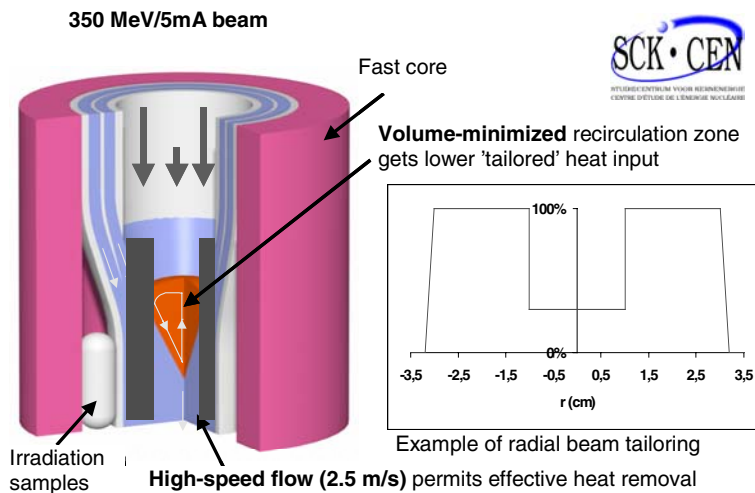
The actual target configuration proposed for MYRRHA is shown in Figure 8. Since it was found in full scale experiments with mercury that there is always a recirculation zone forming at the point of coalescence of the hollow liquid metal flow, which could also not be eliminated in model calculations by varying the parameters [17] it is proposed to use an intensity distribution in the proton beam that minimises heat input in this region. It is not clear, however, whether the problem can really be solved in this way. In a rather comprehensive study done for windowless targets for higher power (and hence larger cross sections) [18] it was found that a certain gas pressure level had to be maintained above the target to suppress the recirculation zone.

Figure 7. Scheme of the MYRRHA liquid metal loop



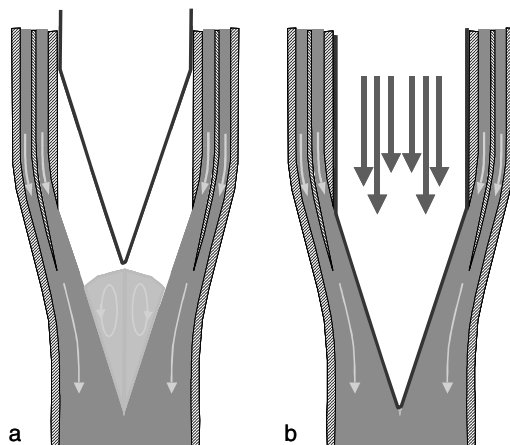
Note: In order to replace the target guide tube the whole loop will be lifted out of the Pb/Bi pool (core coolant) it resides in.

Figure 8. The MYRRHA windowless target design, employing high frequency steering of a pencil beam to generate an intensity distribution that avoids high heat load of the liquid metal in the recirculation zone



A window for the windowless?

Figure 9. Using a thin window might be a possibility to suppress the recirculation zone in a coalescing target. (a) window lifted above the liquid surface to illustrate situation without; (b) window fully inserted and hollow beam applied to minimise stress in the window tip



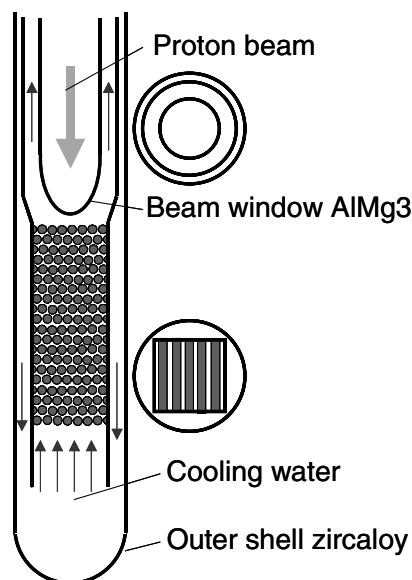
It is very likely that the problem of the recirculation zone is a fundamental one, which becomes the more serious, the larger the diameter of a windowless target, i.e. the larger the opening angle of the cone formed by the coalescing liquid. Once fluid is trapped in this recirculating volume, there is no way to predict, how long it will stay there, in particular since its buoyancy may increase due to heating by the beam. It is, therefore, likely that this will be a source of excessive evaporation of target material into the accelerator vacuum. This is not necessarily an unacceptable situation because there may be ways to condense the metal vapour and return it to the storage pool. MYRRHA, for example foresees a wide cross section for gas pumping between the region above the target and the space above the storage tank, whereas the beam vacuum pipe itself is of the smallest allowable cross section. Nevertheless excessive evaporation of Pb/Bi into this space would be a matter of concern because it might condense anywhere on the walls in an uncontrolled manner or, in the worst case, clog the cryopumps above the storage volume quickly, forcing much more frequent exchange than planned and hence impeding reliability. It might, therefore, be a good idea to consider inserting a thin window from above, which is shaped according to the ideal coalescence cone and whose sole function is to suppress the recirculation, as sketched in Figure 9.

Such a window would not have to sustain any significant pressure and would, therefore, not suffer any stress apart from the one generated by its own internal heating. It could, so to speak, be “floating” on the target surface. In order to ensure its proper cooling it might be made from very low Z material, e.g. beryllium or graphite for minimum internal heat generation and be pushed into the target by the weight of its shaft just enough to ensure proper metallic contact for good heat transfer. Using a “hollow” beam as envisaged for MYRRHA might still be a good idea to minimise the stress at the tip of the cone. Although there might be a need for frequent exchange of this window, this could be made an easy procedure which can be accomplished during scheduled shut downs of the accelerator, thus not affecting the availability but increasing the reliability of the system.

Conclusions

Reliability, but also availability as determined by the frequency and duration of necessary component changes, will be an important issue in the design of future spallation target systems. So far practical experience exists in the megawatt power regime with solid rod targets only. The design used at SINQ for beam insertion from below can be adopted, without too much extrapolation, to horizontal or vertical injection from above. In the latter case target exchange would have to be towards the proton beam line, making a design as sketched in Figure 10 a likely solution. This concept and its associated cooling loop can be considered a proven and reliable one, but has the disadvantage of relying on water cooling, which is undesirable in a fast neutron system.

Figure 10. The presently most viable target concept for high power application: an array of rods cooled by water in cross flow



Note: The water can be brought in from the top and flow out in an annulus between the beam tube and the inner forward flow guide tube.

Although MEGAPIE can be expected to demonstrate the principal feasibility of liquid metal targets with beam injection through a window under pressure from the inside, it may be anticipated that a lot more development work will be required to extend this concept to higher power and make it a reliable one in an industrial facility. The windowless target followed by the MYRRHA project will always have to fight the formation of a recirculation zone at the point of coalescence of the hollow part of the target. This will be the more serious an issue, the higher the target power and the necessary cross section and flow rate become. Inserting a flow guiding window, which would not have to sustain any significant pressure from the liquid metal may help in conjunction with a hollow beam that avoids putting a significant amount of heat into the tip of the window, but has, so far, not been studied in any detail.

REFERENCES

- [1] See various papers in this workshop series, e.g. Y. Cho, “Reliability and Availability of High Power Proton Accelerators”, pp. 227-237 and G.S. Bauer, “Concept of a fault tolerant Linear Accelerator as Proposed for the SINQ Project”, pp. 211-225, both: Proc. Workshop on Utilisation and Reliability of High Power Proton Accelerators, Mito, Japan (1998) OECD Proceedings.
- [2] Bauer, G.S., “Physics and technology of spallation neutron sources”, Nucl. Inst., Meth. in Phys. Res., A **463**, pp. 505-543, (2001).
- [3] Bauer, G.S., “Experience and Features of SINQ Relevant to ADS” in “Utilisation and Reliability of High Power Accelerators”, Proc. Workshop Aix-en-Provence 1999; NEA (2001).
- [4] Bauer, G.S., Y. Dai, and W. Wagner, “SINQ – Layout, Operation, Applications and R&D to High Power”, Annales de chimie – science des matériaux, in press (2002).
- [5] Dai, Y., and G.S. Bauer, “Status of the first SINQ irradiation experiment, STIP-1”, J. Nucl. Mat. 296, pp. 43-53, (2001).
- [6] Forcey, K.S., *et al*, J. Nucl. Mat. **160**,117, (1988).
- [7] Bauer, G.S., M. Salvatores and G. Heusener, “MEGAPIE, a 1 MW pilot experiment for a liquid metal spallation target”, J. Nucl. Mat. 296, pp. 17-23, (2001).
- [8] MEGAPIE (Groeschel) F. Gröschel, A. Cadiou, C. Fazio, Th. Kirchner, J.C. Klein, J. Knebel, G. Laffont, L. Ni, B. Smith, A. Zucchini, “The MEGAPIE Target– A Challenge for Materials”, presented at the IWSMT-5 Meeting, Charleston, to be published in JNM, May 2002.
- [9] Kirchner, T., Y. Bortoli, A. Cadiou, Y. Foucher, J.S. Stutzmann, T. Auger, Y. Dai, S. Dementjev, K. Geissmann, H. Glasbrenner, F. Gröschel, F. Heinrich, K. Kohlik, G. von Holzen, Ch. Perret, D. Viol, “LiSoR, a liquid metal loop for material investigation under irradiation”, presented at the IWSMT-5 Meeting, Charleston, to be published in JNM, May 2002.
- [10] Platnieks, G.S. Bauer, O. Lielausis and Y. Takeda, “Measurement of Heat Transfer at the Beam Window in a Mockup Target for SINQ Using Mercury”, Proc. ICANS XIV; ANL-98/33, pp. 382-395, (1998).
- [11] Callaway, T., R. Ryder, “Beam Reliability and Equipment Downtime Tracking – How LANSCE Closes the Loop”, this conference.
- [12] <http://www.sns.gov/>
- [13] <http://www.jaeri.go.jp/english/research/re06.html>
- [14] “The ESS Council”, *The ESS Project, vol. III: Technical Report*; available through: ESS Central Project Team c/o Forschungszentrum Jülich, D52425 Jülich, Germany, (2002).

- [15] <http://www.ess-europe.de/>
- [16] Aït Abderrahim, H., P. Kupschus, MYRRHA, A Multipurpose Accelerator Driven System (ADS) for Research & Development, March 2002 Pre-Design Report, SCK CEN, Mol R-3595 (2002).
- [17] Van Tichelen, K., P. Kupschus, B. Arien, H. Aït Abderrahim, “Design and Verification Experiments for the Windowless Spallation Target of the ADS Prototype MYRRHA”, this conference.
- [18] Belyakov-Bodin, V.I., V.N. Koterov, and V.M. Krivtsov, “Design of a Flowing Heavy Metal Target with a Free Surface for an Accelerator Driven Neutron Source”, Proc. 2nd Int. Conf. on Accelerator-Driven Transmutation Technologies and Applications, Kalmar, Sweden, 1996, ed. H. Condé, Upsala University, pp. 843-849, (1997).

THE DEMONSTRATION OF THE ADS CONCEPT

M. Salvatores
(ANL and CEA Cadarache)

A. D'Angelo
(ENEA)

D. Naberejnev
(ANL)

“Man is struck more from what he is missing than from what he has already got,
since when he feels well, he tends to loose conscience of himself.”

Goethe

Abstract

The issues related to the demonstration of the ADS concept are discussed. The need for experiments where the coupling of the subcritical core, the spallation target and the proton accelerator is realised at a significant power level, is underlined. Potential relevant approaches are also mentioned.

Introduction

Since the last workshop on the “Utilisation and Reliability of High Power Proton Accelerators”, held in Aix-en-Provence in November 1999 [1], some relevant development have taken place.

In Europe, a road map for developing ADS for nuclear waste incineration has been completed and published [2]. Moreover the 5th Framework programme of the EU has started, and a significant number of ADS-related projects are now going on.

In the USA, the AAA programme has produced a large amount of activities in the ADS field. In Japan, the joint project KEK-JAERI has also started.

The needs for the validation of the different components of an ADS dedicated to transmutation have been once more expressed in the different documents, and strategies towards the fulfilment of these needs have been further discussed.

In principle, three levels of validation can be specified.

- 1) validation of the different component concepts, taken separately (accelerator, target, subcritical core, dedicated fuels and fuel processing methods).
- 2) validation of the coupling of the different components in a significant environment, e.g. in terms of power of the global installation, using as far as possible existing critical reactors, to be adapted to the objectives.
- 3) validation in an installation, explicitly designed for demonstration (e.g. the XADS installation described in the European road map). This third step should evolve to a demonstration of transmutation fuels, after a first phase in which the subcritical core is loaded with “standard” fuel.

The first level of validation is presently underway in several programmes (e.g. for a high intensity proton accelerator). A typical example of an international initiative in the field of spallation targets is the MEGAPIE project [3]. Another example, in the field of the neutronics of the subcritical core, is the MUSE programme [4]. Experiments on dedicated fertile-free fuels begin to be planned or prepared, even if at a relatively slow pace.

As far as the required performances of the accelerator, the first level of validation is related to basic characteristics such as the reliability, as discussed at the previous workshops of this series.

The second and third level should take into account engineering requirements, which imply, e.g., not only the accelerator itself, but also the architecture of the beam line and the practical realisation of the coupling to the subcritical core.

This second level of validation, as defined above, should also give answers to problems such as reactivity monitoring and control at power, start-up and shut-down procedures, which do not require the availability of, e.g., an accelerator for a finalised design, but of a flexible tool, to make experiments which should give the proof of the robustness of the ADS concept, in view of its licensing, and operation.

The reliability issue and the first level of the ADS validation

This issue has been discussed, and a first valuable interaction among reactor core and accelerator designers has taken place at the Aix workshop in 1999.

Further work and assessments have been made, in particular in the frame of the European road map (see in particular Annexe IV of that report).

Since the target/subcritical reactor system should not be exposed to excessive thermal shocks induced by the proton beam trips, these trips should be reduced with respect to the present accelerator performances.

Of course, requirements for a demonstration ADS and for a future “industrial” installation are not the same.

However, up to now, firm quantitative recommendations have been rather scarce, due to the fact that a full detailed analysis requires the availability of a fairly detailed conceptual design of a specific ADS.

An order of magnitude of 10-100 “long” beam trips (i.e. interruptions $>10\div 20$ seconds) is often quoted.

In fact, for an ADS strictly devoted to the demonstration of the coupling of the components, the tolerable number of such “long” beam trips can be $\sim 1/\text{week}$, in order not to disrupt the normal performance of experiments.

The ongoing experimental programmes on HPPA, should allow to reach that goal in time with the development of an experimental demonstration of the ADS concept, as other papers at this workshop should confirm.

On the other side, existing accelerators will be used in the demonstration of specific components of an ADS. An outstanding example is the MEGAPIE project, aiming at the demonstration of the feasibility of a liquid Pb/Bi target at a significant level of power (~ 1 MW). The use of the PSI cyclotron will allow to reach a power level of 600-1 000 KW [3].

As far as beam trips, an order of magnitude of 10^4 is expected with that machine for the designed lifetime of the MEGAPIE target window. Preliminary calculations indicate that, to ensure that the cyclic load applied to the target window is lower than the critical load which could initiate fatigue crack, the design strain amplitude should be appropriately defined [5]. This of course has to take into account the effect of the liquid Pb/Bi environment.

It is interesting to note that, again for the MEGAPIE experiment, the use of an existing accelerator underlines the need for well controlled performances, related to the specific safety requirement of the liquid Pb/Bi target. This is the case of the tight control of the beam shape and focusing. In fact, the hypothetical presence of an unscattered proton beam, which has a much smaller spot size than the beam going normally through an intermediate graphite target, can give rise to severe heat deposition problems in the Pb/Bi target container [5].

The second level of ADS validation

Present design and parameter studies of ADS for transmutation indicate that a wide range of subcriticality regimes has to be envisaged. In fact most of designs require a subcriticality ranging from $K \sim 0.94 \div 0.95$ to $K \sim 0.99 \div 0.995$. In the “low” or in “high” K range, the dynamic behaviour of the ADS can be very different.

In fact, whatever the subcritical core reactivity feedback effects, in the “low” K range, the dynamic response of the system to, e.g., a reactivity insertion, will be dominated by the external source (“source dominated” mode). On the contrary, close to criticality, the dynamic behaviour will be imposed by the core feedbacks (“feedback dominated” mode). In this last case, the nature of the feedbacks, e.g. the value of the Doppler coefficient, will play an important role. This fact can make a difference (close to criticality) between a subcritical core loaded with standard or fertile-free fuel.

An example of such behaviour can be found in Figure 1, which was obtained for a PHENIX-type core made subcritical at different levels of K and for two values of the Doppler coefficient (“low” and “standard” Doppler coefficient).

This type of behaviour and the transition between the two modes, that can happen in the same core during the irradiation cycle due to burn-up reactivity swing, should be carefully investigated, in order to develop appropriate monitoring and control systems for the power distribution in the core, but also in order to choose appropriate reference subcriticality levels.

The validation of these phenomena should be an important part of the experimental programmes in support of the ADS concept development. Up to now, the kinetic behaviour of a subcritical core has been or is being validated essentially at zero power in the MUSE experiments [4], mentioned previously. The experiments will provide the necessary development of experimental techniques, in particular related to the reactivity control and monitoring.

However, in what we have called the “second” level of validation of the ADS concept, experiments are needed within a core at power, with a representative configuration of the spallation target, proton beam, and associated beam line.

The coupling of the ADS basic components

Very recently, exploratory studies have been or are being performed on the demonstration at full scale of the coupling of the ADS basic components, using an existing (low) power reactor.

These activities have been triggered by an original idea of C. Rubbia, who has proposed to use an existing TRIGA reactor at the ENEA centre of Casaccia in Italy.

The feasibility of the experiment (called TRADE: TRiga Accelerator Driven Experiment) has been assessed by a joint ENEA/CEA working group [6].

With respect to the problem of the dynamic behaviour, interesting results have been obtained [7], which show that the effect of the TRIGA feedback coefficients is such that they will show with significantly different amplitude, according to the subcriticality of the core (see Figures 2, 3 and 4). The power increase for reactivity insertions of 50 and 10 cents respectively, in 2 seconds, is shown at three different values of subcriticality. Experiments can then be envisaged to verify

experimentally the dynamic response of the core, together with the experimental determination of the relative subcriticality level.

The TRADE experiment is a full-scale demonstration experiment, since a proton accelerator should be used to supply protons to a spallation solid W target to be placed at the centre of the core. The power in the beam could be in the range 20-60 KW and the power in the core in the range 100-500 KW.

Similar experiments could be envisaged in a more simplified configuration, using e.g. the neutrons issued from (γ, n) reactions on a heavy metal (e.g. Uranium) target, to be put inside a low power flexible reactor like TREAT at Argonne-West. The accelerator to be coupled to the TREAT core, can be an electron accelerator, providing a beam power of 10-50 kW of e^- of ~ 50 MeV.

Exploratory study have indicated the potential of that approach [8]. In Figures 5 and 6, the power level behaviour is shown both for an hypothetical control rod reactivity insertion (1 000 pcm) and for an hypothetical external source increase of a factor 1.8. The effect is shown for several levels of subcriticality. Once again the expected behaviour in TREAT matches well the behaviour in an ADS.

As far as representativity, despite the fact that the proposed experiments are made in a thermal neutron spectrum environment and the preferred configurations of ADS for transmutation are related to fast neutron spectra, it is to show that the kinetic response to perturbation are identical in thermal spectrum reactors (with $\beta \sim 0.007$ and $T \sim 10^{-4}$ sec) or in fast spectrum reactors ($\beta \sim 0.002 \pm 0.003$, $T \sim 0.5 \times 10^{-6}$ sec), except for a shift to the lower frequencies for a thermal reactor.

The proton current/power relations

As far as the potential of an experiment like TRADE in TRIGA, the following example can be made.

As noted above, the proton current, power, and source importance are related. We can re-write the expression relating current, power, and reactivity as

$$P \sim \frac{S}{\left(\frac{1}{k} - 1\right)} \quad (1)$$

where it is assumed that the source is directly proportional to the proton current. This leads to a useful relation of perturbed quantities.

$$\frac{\delta P}{P} = \frac{\delta S}{S} + \frac{\delta k / k}{1 - k} \quad (2)$$

If we perturb the reactivity by a known amount (calibrated control rod), observe the change in power, then perturb the current to restore the original power, we can determine the subcritical k by

$$\frac{1}{1 - k} = \frac{\delta S / S}{\delta k / k} \quad (3)$$

An alternative is to oscillate an absorber of calibrated reactivity but maintain the current constant ($\delta S=0$). In this case, the relation is

$$\frac{1}{1-k} = \frac{\delta P / P}{\delta k / k} \quad (4)$$

Another aspect that must be studied is the effect of source importance on these relations. With the TRIGA experiments, one will be able to change the buffer region to optimise this parameter.

The third level of demonstration

The third level of demonstration of the ADS concept, should include its potential for radioactive waste transmutation in a fast spectrum in a fast spectrum.

In the European road map mentioned above [2], this level of demonstration is proposed within an installation of approximately 100 MW called XADS with a transition to an XADT, loaded at least in part with minor actinide (MA) fuel.

Of course, as far as Transmutation, this level of demonstration should be compatible with a full demonstration of MA-fuel fabrication, irradiation and reprocessing, to be performed on sizable amounts (e.g. tens of kilograms), with characterisation, beyond the laboratory scale, of material flows, including losses and the conditioning of the wastes.

This third level of demonstration needs a deployment of resources and funding well beyond what is needed in the first two levels of validation. In this respect, the completion of the experiments of the first and second levels at a relatively early time (~2006-2008) is mandatory to provide convincing arguments to decision makers for a possible deploying of the transmutation strategy based on ADS by ~2020.

Conclusions

The demonstration of the ADS concept, and its applicability to radioactive waste transmutation, requires a consistent series of experiments, in particular for the demonstration of the ADS components coupling in a representative configuration, both from the physics and from the engineering points of view.

It is presently emerging a strategy, using existing low power reactors, which would enable to provide a convincing demonstration of the viability of the concept at a relatively early time horizon (~2006-2008). In particular the TRADE experiment on the TRIGA reactor of ENEA-Italy, could be the final experiment of a series which includes the MUSE zero-power experiments with external source, the TREACS experiments on the TREAT low power reactor made subcritical and driven by an external neutron source provided by an electron accelerator which will induce (γ,n) reactions on a target placed at the centre of the core. With respect to these preliminary experiments, the TRADE experiment would provide a full-scale demonstration, including a proton accelerator with an associated beam transport line, which will be representative of the engineering architecture to be developed for a future ADS dedicated to transmutation.

A parallel effort will be needed to develop the MA-based fuels and the processing methods needed for multiple irradiations and recovery. In the same line, the development of HPPA should

continue also in parallel, to provide the demonstration of accelerator characteristics required for an industrial ADS (e.g. its reliability and control).

All these developments will enable to make a sound decision on the use of ADS for transmutation and allow the development of a full-scale prototype of ADS dedicated to transmutation by 2020.

REFERENCES

- [1] Proceedings of workshop “Utilisation and Reliability of High Power Proton Accelerators”, Aix-en-Provence, 22-24 November 1999, Nuclear Energy Agency, OECD, 2001.
- [2] “A European Road map for Developing Accelerator Driven Systems (ADS) for Nuclear Waste Incineration”, April 2001.
- [3] Bauer, G., M. Salvatores, G. Heusener, J. Nucl. Materials, 296, pp. 17-33, (2001).
- [4] Salvatores, M., *et al.* “MUSE-1: a first experiment at MASURCA to validate the physics of subcritical multiplying systems”, 2nd ADTT Conference, Kalmar, Sweden, June 1996.
- [5] Papers presented at the 3rd International Workshop on MEGAPIE, Bologna, March 2002.
- [6] “TRADE Final Feasibility Report – March 2002” by the Working Group on TRADE: TRiga Accelerator Driven Experiment.
- [7] D’Angelo, A., *et al.* to be published at P/T Inf. Exch. Meeting, KOREA.
- [8] Naberejnev, D., *et al.* to be published at PHYSOR 2002, KOREA.

Figure 1. Insertion of reactivity corresponding to 1/3 in 1 second behaviour of an ADS “PHENIX type” at three different levels of subcriticality and with two values of the Doppler coefficient

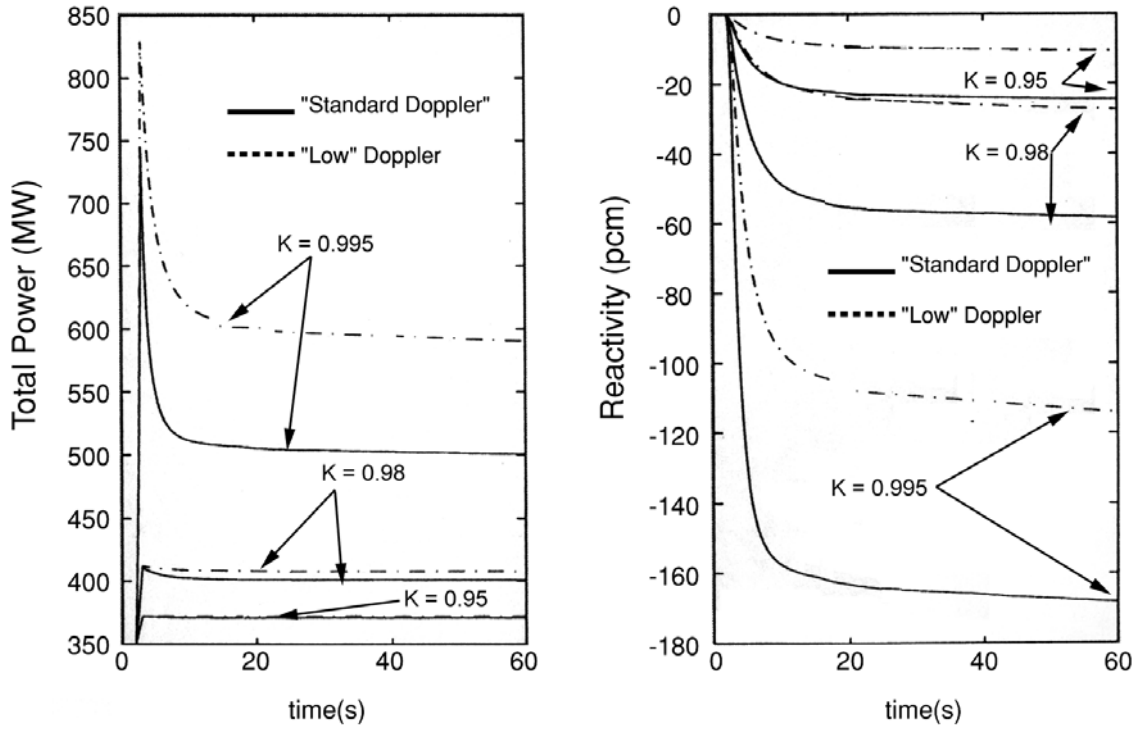


Figure 2. TRADE reference configuration (-3.81\$): reactivity insertions from 200 kW

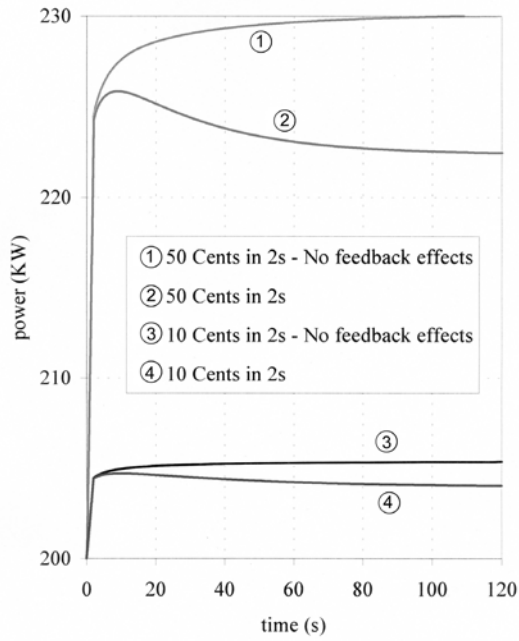


Figure 3. TRADE “High K” configuration (-1.74\$): reactivity insertions from 200 kW

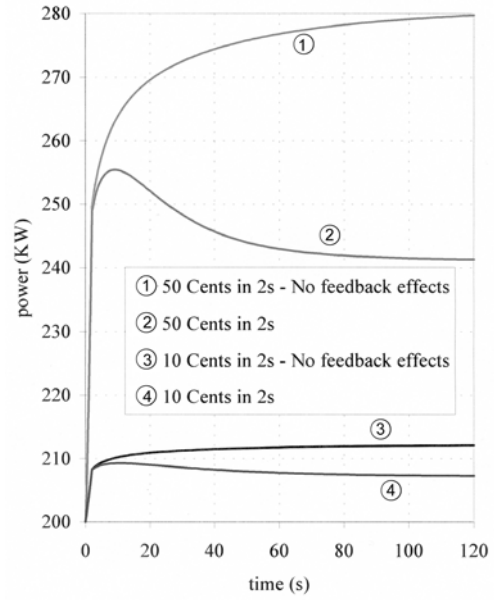


Figure 4. TRADE “Very high K” configuration (-0.72\$): reactivity insertions from 200 kW

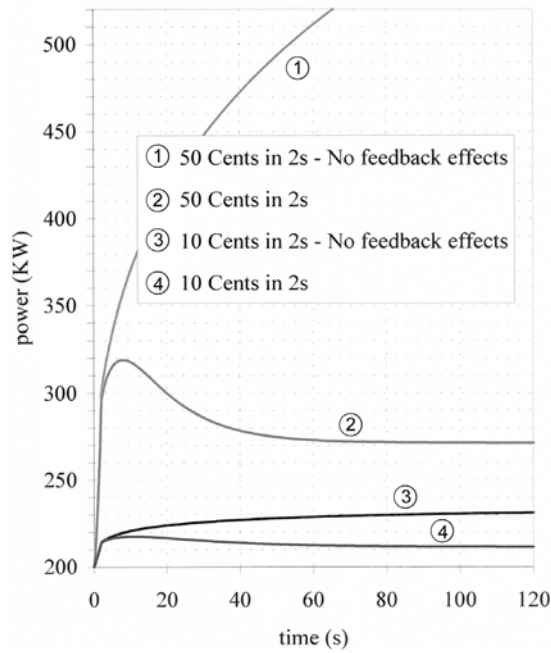


Figure 5. TREAT-initial reactor power 80 kW control rod transients. Insertions of 1 000 pcm of reactivity

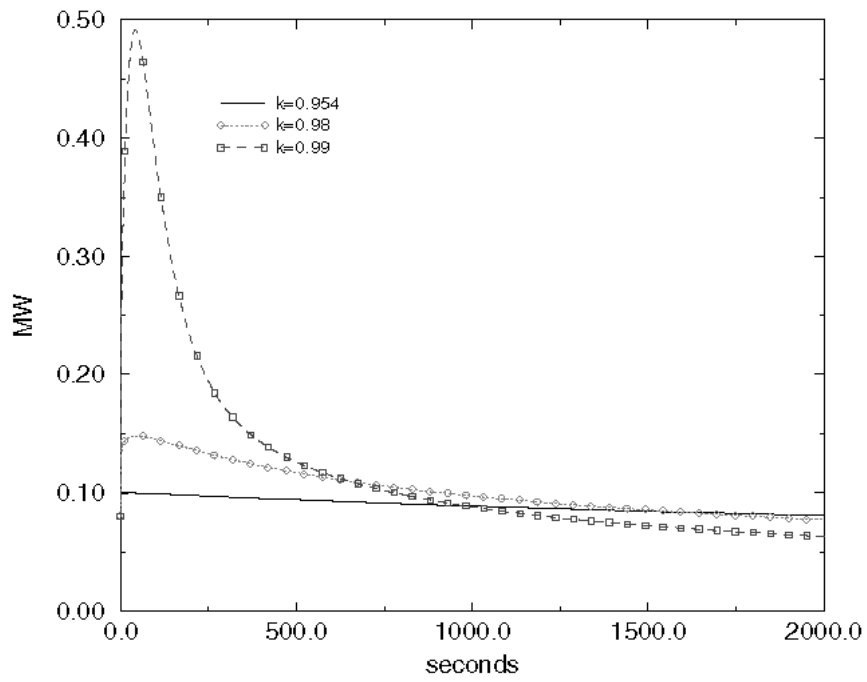
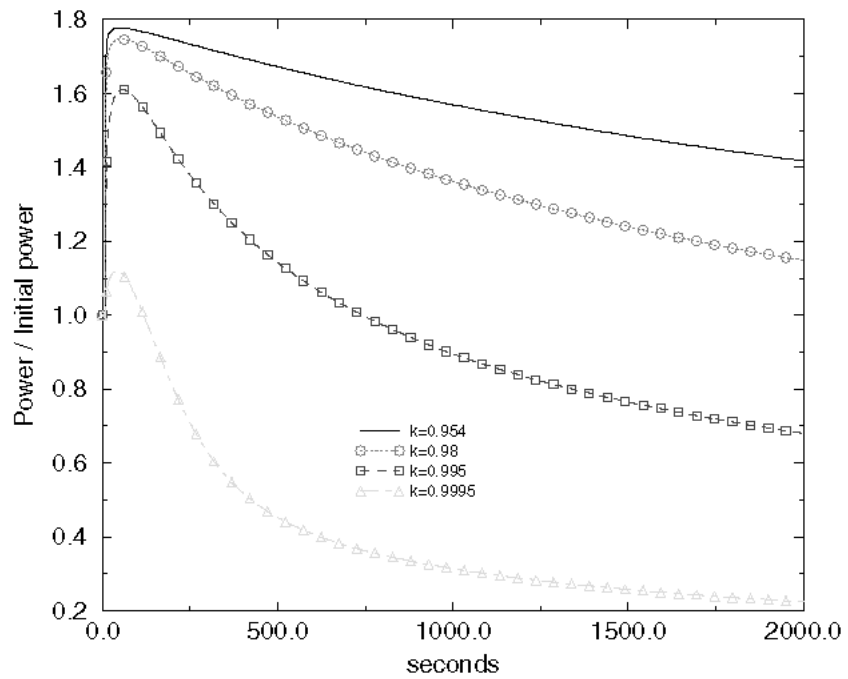


Figure 6. TREAT-initial reactor power 80 kW source transient $q=1.8 \times q$



THE MECHANICAL PROPERTIES OF 316L/304L STAINLESS STEELS, ALLOY 718 AND MOD 9CR-1MO AFTER IRRADIATION IN A SPALLATION ENVIRONMENT

S.A. Maloy, M.R. James, G. Willcutt, W.F. Sommer

Los Alamos National Laboratory, MS H809
Los Alamos, NM 87545

M. Sokolov, L.L. Snead

Oak Ridge National Laboratory, Metals and Ceramics Division
Oak Ridge, TN 37831-6151

M.L. Hamilton, F. Garner

Pacific Northwest National Laboratory
Richland, WA 99352

Abstract

The accelerator production of tritium (APT) project proposes to use a 1.0 GeV, 100 mA proton beam to produce neutrons via spallation reactions in a tungsten target. The neutrons are multiplied and moderated in a lead/aluminium/water blanket and then captured in ^3He to form tritium. The materials in the target and blanket region are exposed to protons and neutrons with energies into the GeV range. The effect of irradiation on the tensile and fracture toughness properties of candidate APT materials, 316L and 304L stainless steel (annealed), modified (Mod) 9Cr-1Mo steel, and Alloy 718 (precipitation hardened), was measured on tensile and fracture toughness specimens irradiated at the Los Alamos Neutron Science Center accelerator, which operates at an energy of 800 MeV and a current of 1 mA. The irradiation temperatures ranged from 50-164°C, prototypic of those expected in the APT target/blanket. The maximum achieved proton fluence was 4.5×10^{21} p/cm² for the materials in the centre of the beam. This maximum exposure translates to a dpa of 12 and the generation of 10 000 appm H and 1 000 appm He for the type 304L stainless steel tensile specimens.

Specimens were tested at the irradiation temperature of 50-164°C. Less than 1 dpa of exposure reduced the uniform elongation of the Alloy 718 (precipitation hardened) and mod 9Cr-1Mo to less than 2%. This same dose reduced the fracture toughness by 50%. Approximately 4 dpa of exposure was required to reduce the uniform elongation of the austenitic stainless steels (304L and 316L) to less than 2%. The yield stress of the austenitic steels increased to more than twice its non-irradiated value after less than 1 dpa. The fracture toughness reduced significantly by 4 dpa to ~ 100 MPa.m^{1/2}. These results are discussed and compared with results of similar materials irradiated in fission reactor environments.

Keywords: tensile testing, radiation effects, accelerator production of tritium (APT), stainless steel, Alloy 718, Mod 9Cr-1Mo.

Introduction

The US Department of Energy is investigating the use of an accelerator to produce tritium for national defence purposes. The accelerator production of tritium, APT, project design uses a 1.0 GeV, 100 mA proton beam to produce neutrons through the spallation of a tungsten target. The spallation neutrons are moderated and multiplied in a surrounding lead/aluminium/water blanket and captured by ^3He gas to produce tritium. Therefore, the structural materials in the APT target and blanket systems are exposed to a high energy proton and spallation neutron flux at energies up to 1.0 GeV [1]. This exposure causes displacement damage and the production and implantation of large quantities of hydrogen and helium in structural materials. The energy of this proton/neutron flux is high compared to the particle energies in a fission reactor. Thus the amounts of hydrogen and helium produced per dpa of exposure in the APT will be significantly greater than the amount of gas produced in a typical fission reactor. The temperature of the APT target/blanket, 50-160°C, is also significantly lower than most fission reactor environments. The combination of high particle energies, enhanced gas production and low operating temperatures may make irradiation induced degradation of the APT target/blanket materials differ significantly from the degradation previously experienced in fission reactors.

The effects of high energy proton and neutron irradiation on the mechanical properties of APT target and blanket structural materials were determined in an APT experiment which exposed mechanical test specimens to the 800 MeV, 1 mA Gaussian proton beam (where $2\sigma=3\text{cm}$) at the Los Alamos Neutron Science Center (LANSCE) [2]. Specimens were held in and near the proton beam in stainless steel envelopes to allow them to be irradiated without direct exposure to the cooling water. Because of the small size and high intensity of the Gaussian beam, specimens had to be small and thin to obtain a uniform flux and achieve prototypic APT temperatures (50-160°C)

Various mechanical properties including tensile, fracture toughness, etc. were measured on specimens after irradiation. This paper summarises the effect of high energy proton and neutron irradiation on the tensile and fracture toughness properties of Alloy 718, 316L and 304L and Mod 9Cr-1Mo. Each of these Alloys is a candidate structural material for the APT target and blanket.

Experimental

The S-1 tensile specimens, Figure 1A, were electro-discharge machined (EDM'd) from two thickness of sheet material, 0.25 and 0.75-1.0 mm. Sub-size compact tension specimens (Figure 1B) were EDM'd from 2 mm and 4 mm thick sheet material. Variations in specimen thickness coupled with the thickness effects on energy implantation and heat transfer provided a technique to irradiate materials to the same flux at different temperatures. The compositions of the different heats of material are shown in Table 1. The Mod 9Cr-1Mo specimens were machined from the same heat of material regardless of specimen thickness. The compact tension specimens were cut with one set having the crack parallel to the rolling direction and a second set having the crack perpendicular to the rolling direction. The as-machined Alloy 718 and Mod 9Cr-1Mo specimens were heat treated by first separately wrapping the specimens of each material in Nb foil packets and placing them in a quartz tube with a titanium ampoule which was back-filled with argon and sealed. The Alloy 718 specimens were annealed at 1065°C for 30 min. and air cooled. This was followed by ageing at 760°C for 10 hours furnace cooling to 650°C and holding for a 20 hour total furnace time, and finally air cooling. The Mod 9Cr-1Mo specimens were normalised at 1038°C for 1 hour and air cooled followed by a temper at 760°C for 1 hour and air cooling. The 304L and 316L materials were received in the annealed form, and no further heat treatment was performed. The Vickers hardness measurements at a

500 g load and grain size measured for each heat of material are shown in Table 2. The largest difference in hardness observed was between the two different heats of 304L stainless steel (174 kg/mm² at 0.75 mm thick and 159 kg/mm² at 0.25 mm thick).

The tensile and fracture toughness specimens were irradiated for six months at the LANSCE accelerator. After irradiation, the dose for each specimen was determined from analysis of pure metal activation foils placed next to specimens during irradiation. Details of the dose determination can be found in [3]. The fluence was first calculated using the Los Alamos High Energy Transport (LAHET) code system [4,5]. Then, the gamma spectra measured from the activation foils were used with the STAYSL2 code to adjust the calculated fluences. A mathematical fit of the position dependence of fluence was used to determine the fluence at each specimen position. The temperature for each specimen was determined by calculations that used measurements from thermocouples placed near each specimen to determine gap resistance between samples and cover plates. The details of this temperature measurement can be found in [6]. The calculated irradiation temperature varied from 50-164°C depending on specimen thickness and the location of the specimen with respect to centre of the proton beam.

The irradiated specimens were tensile tested in air (except for the 250 and 400°C tests on Mod 9Cr-1Mo) using an Instron machine equipped with a high temperature furnace. Except where noted, materials were tested at the irradiation temperature. Specimens were tested at an initial strain rate of 10⁻⁴/s. Load and displacement were measured and converted to stress and strain. The stress/strain curve for each specimen was corrected for machine compliance. The compliance-corrected stress/strain curves were used to determine 0.2% offset yield stress, ultimate stress, uniform elongation and total elongation. Fracture surfaces of selected tensile specimens were examined using a scanning electron microscope (SEM). These SEM micrographs were used to determine reduction of area by measuring the fracture surface area in relation to the area of the gage before testing. The fracture toughness was determined after irradiation by performing J-integral tests using an MTS testing machine in a hot cell. Procedures for testing followed ASTM E1737-96.

Results

Tensile testing

The tensile properties of Alloy 718 in the precipitation hardened condition, 316L and 304L in the annealed condition, and Mod 9Cr-1Mo in the tempered condition were determined after irradiation to a maximum dose of 13 dpa. The thickness of the samples were either 0.25 or 0.75 mm thick. Representative stress/strain curves of irradiated Alloy 718, given in Figure 2, show that the work hardening rate is essentially zero after only 0.09 dpa of exposure and does not recover as dose increases. The yield strength, shown in Figure 3, increases with dose up to 1 dpa and then gradually decreases out to 12 dpa. On the other hand, the uniform elongation drops almost immediately to less than 2% after 0.5 dpa and remains low for irradiation to 12 dpa.

Representative stress/strain curves for 316L/304L stainless steels specimens irradiated and tested at 50°C are shown in Figure 4. These curves show irradiation-induced increases in yield strength, losses in ductility and reductions in work hardening capacity. Test data, for all the 304L/316L stainless steel specimens, given in Figure 5, show a sharp irradiation-induced increase in yield strength. The irradiation-induced changes in uniform elongation are more complex, as shown in Figure 5. The non-irradiated uniform elongation ranges from 40-60%, and sharp decreases in uniform

elongation to less than 20% are observed after 0.01 dpa leading to a more gradual decrease out to 3-4 dpa where the uniform elongation decreases rapidly to less than 1%.

The effect of test temperature on the irradiated tensile properties of 316L/304L is shown in Figure 6A. Specimens irradiated to the same dose between 1 and 4 dpa were tested at increasing test temperature from 20 to 164°C. Uniform elongation shows a significant decrease with increasing test temperature between 20 and 164°C. Figure 6B shows the effect of test temperature on the stress/strain curve for materials irradiated to 9 dpa. Although the uniform elongation is the same at each temperature, there is a significant difference in the stress/strain curves after maximum load is reached.

Representative stress/strain curves for Mod 9Cr-1Mo after irradiation are shown in Figure 7. As observed for Alloy 718, the work hardening rate goes to zero after greater than 0.05 dpa of exposure. The data, for all tests performed on Mod 9Cr-1Mo at temperatures from 50-164°C, are plotted in Figure 8 and show that the yield stress sharply increases with dose and the uniform elongation drops precipitously to less than 1% after slightly more than 0.1 dpa of exposure.

The effect of test temperature was also evaluated on the irradiated tensile properties of Mod 9Cr-1Mo as shown in Figure 9. Because Mod 9Cr-1Mo is also a candidate material for the accelerator transmutation of waste program in which the target operates at higher temperatures, test temperatures up to 400°C in argon were investigated. The results show that uniform elongation is low (<1%) and does not significantly increase until the test temperature is raised to 400°C. A significant decrease of yield stress is also observed when testing at 400°C.

SEM analysis

The fracture surfaces of selected Alloy 718 and 316L and 304L austenitic stainless steel tensile specimens were observed using scanning electron microscopy. Figure 10 shows the fracture surface of an Alloy 718 specimen irradiated to 11 dpa. The fracture still appears ductile although the fracture is quite localised, i.e. the necked/fracture region is confined to a very small portion of the gauge section of the specimen. Reduction of area was also measured on this specimen and on others at lower doses. The results are shown in Figure 11. Although significant reductions in uniform elongation are apparent with increasing dose, very little change in reduction of area was observed. The reduction of area measurements were insensitive to test temperature (between 50 and 164°C) as well.

The fracture surface of a 316L stainless steel specimen irradiated to 9 dpa is shown in Figure 12. Fracture is also quite localised and the appearance is more ductile than that observed for Alloy 718. Reduction of area was also measured on this specimen and on other 316L and 304L stainless steel specimens. The results shown in Figure 10 reveal very little change in reduction of area for both stainless steels with increasing dose (and temperature between 50 and 164°C) while the change in uniform elongation with dose and temperature is quite large.

Fracture toughness

The change in fracture toughness with dose for precipitation hardened Alloy 718 and annealed 316L and 304L stainless steel is shown in Figure 13. The toughness for Alloy 718 dramatically decreases with increasing dose to half its non-irradiated value after only 2 dpa. The change in toughness is more gradual for the austenitic stainless steels tending to saturate at less than 100 MPa.m^{1/2} after 4-6 dpa of exposure. The change in fracture toughness with dose for Mod 9Cr-1Mo is shown in Figure 14. Significant decreases in fracture toughness are observed although there is large

scatter in the results. The highest toughness are observed for the crack perpendicular to the rolling direction for doses up to 3 dpa.

Discussion

Alloy 718

The mechanical properties of Alloy 718 in the precipitation hardened condition show two salient effects with irradiation in a high energy proton and neutron flux. First, the yield stress increases slightly while the uniform elongation and fracture toughness decrease dramatically after exposure to 0.5 and 2 dpa respectively. Second, the yield stress gradually decreases with increasing dose up to 12 dpa.

The dramatic decrease in uniform elongation and fracture toughness with increasing dose can be explained by the increase in the density of irradiation-induced defects with increasing dose, which hardens the material and increases its strength, producing a concomitant decrease in ductility and toughness. Black spot damage and Frank loop formation has been observed by Sencer *et al.* [7] in Alloy 718. Such damage is similar to what has been observed for irradiation of Alloy 718 in a fission reactor [8]. In addition, comparison of the change in uniform elongation with dose obtained in this study to that measured after irradiation in the high flux isotope reactor (HFIR) by Farrell *et al.* [9] shows very little difference in the results (Figure 15).

The decrease in the yield stress with increasing dose above 1 dpa may be explained by a second microstructural change observed by Sencer *et al.* [7]. In TEM studies, Sencer observed that the superlattice reflections for the strengthening precipitates, γ'/γ'' , disappear after irradiation to doses greater than 0.5 dpa in a high energy proton and neutron flux. Since the irradiation temperature is very low, making complete dissolution of the precipitates unlikely, he interprets the loss of these reflections, and the decrease in yield stress, as the results of irradiation-enhanced disordering of the hardening precipitates.

The fracture surfaces on the Alloy 718 specimens reveal very little change in fracture appearance and in measured reduction of area values with increasing dose. On the other hand, the uniform elongation drops significantly. The fracture still appears ductile but the localisation of the neck in the tensile specimens, and the shape of the stress/strain curve, suggests a very localised type of plastic flow, resulting in a small uniform elongation. Such strain localisation has commonly been caused by both hydrogen and irradiation embrittlement.

316L/304L stainless steels

The response of the mechanical properties of austenitic stainless steels, 316L and 304L, to irradiation in a high energy proton and neutron flux is a more gradual increase in yield stress concomitant with a decrease in uniform elongation and fracture toughness with increasing dose, (Figures 5 and 13). These changes occurring at low dose are attributed to increases in the density of irradiation-induced defects (black spot damage and Frank loops) with increasing dose as observed by Sencer *et al.* [7]. With increasing dose above 3 dpa, the uniform elongation dramatically decreases. Comparison of measured values of ductility, in this case, strain to necking, for LANSCE-irradiated vs fission neutron-irradiated 316 stainless steel at 20-100°C, does not show the same significant ductility decrease at 3 dpa, Figure 16. Strain to necking values equal uniform elongation values except in very

few cases where the maximum load does not coincide with the maximum elongation before necking occurs. Analyses by Oliver *et al.* [10] show that in addition to the displacement damage in these Alloys, they also retain up to 2 000 appm He and 2 500 appm H after irradiation in a high energy proton/spallation neutron spectrum. Such large amounts of retained gas may contribute to the observed differences in tensile properties.

A second effect is that increasing the test temperature from 20 to 164°C results in decreases in the measured uniform elongations (and strain-to-necking) in the 304L and 316L stainless steels for specimens irradiated to doses between 1 and 4 dpa. Figure 6B shows at higher doses, when a change in uniform elongation is not observed with increasing temperature, there is still a significant change in the shape of the stress/strain curve. A similar effect has been observed by Pawel *et al.* [11] in 316 stainless steel where a minimum uniform elongation (strain-to-necking) is observed for irradiation/testing performed around 300°C. It appears that data reported herein suggest that a minimum may appear at a lower temperature for irradiation in a spallation environment. However, more tests would be required at higher irradiation and test temperatures in a high energy proton/spallation neutron environment to confirm this effect.

The fracture surfaces on the 316L/304L stainless steel specimens still show a ductile appearance after irradiation to 9 dpa. Reduction of area also remains high at 9 dpa. Therefore, the low uniform elongation results from very localised fracture in a ductile mode.

Mod 9Cr-1Mo

The effect of increasing proton and neutron flux on the mechanical properties of Mod 9Cr-1Mo in the tempered condition is to decrease the uniform elongation and fracture toughness while increasing the yield stress. This can be attributed to the microstructural changes observed by numerous investigators as well as Sencer [12] which show an increase in black spot and Frank loop damage with increasing dose. Our results compare well with the results of Spatig *et al.* [13] for F82H who measured a $\Delta\sigma$ of 210 MPa at 25°C after a dose of 0.16-0.26 dpa for irradiation in a 590 MeV proton beam while we observe a $\Delta\sigma$ of 200-250 MPa after a dose of 0.12 dpa at 50°C. In addition, large scatter was observed in the measured fracture toughness values with increasing dose. Because the test temperature is very close to the brittle-to-ductile transition temperature (which will increase with increasing dose), such scatter is not surprising.

The effect of increasing test temperature on the tensile properties after irradiation to 3 dpa shows that the uniform elongation increases while the yield stress decreases as the temperature is raised from 250 to 400°C. This could be caused by annealing of radiation-induced defect clusters with increasing temperature.

Conclusions

The mechanical properties measured on Alloy 718 in the precipitation hardened condition, annealed 316L and 304L stainless steel and Mod 9Cr-1Mo in the tempered condition show the following effects after irradiation in a high energy proton/spallation neutron environment.

Alloy 718

- 4) The uniform elongation drops to less than 2% after only 0.5 dpa of exposure.
- 5) The yield stress increases slightly at low doses and then decreases with dose above 1 dpa of exposure.
- 6) The reduction of area shows very little change with increasing dose to 12 dpa.
- 7) The fracture toughness drops to less than 80 MPa.m^{1/2} after 2 dpa exposure.

316L/304L stainless steels

- 1) The uniform elongation gradually decreases with increasing dose but then abruptly drops at 3 dpa. Such an effect is not seen for irradiation in a fission spectrum and may be related to high retained helium and hydrogen in the material.
- 2) The yield stress increases with increasing dose to more than two times its unirradiated value.
- 3) For specimens irradiated to 1-3 dpa, increasing test temperature from 20-160°C results in decreasing uniform elongation.
- 4) The reduction of area does not significantly change with increasing dose to 9 dpa.
- 5) The toughness gradually decreases to less than 120 MPa.m^{1/2} after 5 dpa exposure.

Mod 9Cr-1Mo

- 1) The yield stress increases to over 900 MPa (30% increase) while the uniform elongation decreases to less than 2% after only 0.5 dpa exposure.
- 2) A slight increase (to over 3%) in uniform elongation is observed along with a decrease in yield stress when the test temperature is raised to 400°C.
- 3) The toughness drops quicker for the crack growth parallel to the rolling direction than observed for the crack growth perpendicular to the rolling direction

Acknowledgements

The authors would like to thank Manny Lopez and Toby Romero of LANL, Gary Whiting of PNNL and Wayne Bolinger and Gary Parks of ORNL for their expertise in handling and testing these tensile and fracture toughness specimens using manipulators in hot cells.

REFERENCES

- [1] Cappiello, M.W., and E. Pitcher, "Design and Operation of the APT Target/Blanket", *Materials Characterization*, **43**: pp. 73-82, 1999.
- [2] Maloy, S.A., W.F. Sommer, R.D. Brown, J.E. Roberts, J. Eddlemen, E. Zimmermann, and G. Willcutt, "Progress Report on the Accelerator Production of Tritium Materials Irradiation Program", *Materials for Spallation Neutron Sources*, The Minerals, Metals & Materials Society, ed. by L.K. Mansur M.S. Wechsler, C.L. Snead, and W.F. Sommer, pp. 131-138, 1998.
- [3] James, M.R., *et al.*, "Determination of Mixed Proton/Neutron Fluences in the LANSCE Irradiation Environment", *Proceedings: 2nd International Topical Meeting on Nuclear Applications of Accelerator Technology*, Gatlinburg, TN, pp. 605-608, 1998.
- [4] Prael, R.E. and H. Lichtenstein, *User Guide to LCS: The LAHET Code System*, Radiation Transport Group, Los Alamos National Laboratory: Los Alamos, NM., 1989.
- [5] Prael, R.E. and D.G. Madland, *LAHET Code System Modifications for LAHET 2.8*. Los Alamos National Laboratory: Los Alamos, NM., 1995.
- [6] Willcutt, G.J., *et al.*, "Thermal Analysis of the APT Materials Irradiation Samples", *Proceedings: Accelerator Applications '98*, Gatlinburg, TN: Am. Nucl. Soc., p. 254-259, 1989.
- [7] Sencer, B.H., *et al.*, "Microstructural Alteration of Structural Alloys by Low Temperature Irradiation with High Energy Protons and Spallation Neutrons", *Proc. Effects of Radiation on Materials, 20th Int. Symp. ASTM STP 1405*, Ed. by S.T. Rosinski, *et al.*, ASTM: West Conshohocken, PA.
- [8] Thomas, L.E., and S.M. Bruemmer, "Radiation-Induced Microstructural Evolution and Phase Stability in Nickel-Base Alloy 718", *Pro. 8th Int. Symp. Environmental Degradation of Materials in Nuclear Power Systems – Water Reactors*, American Nuclear Society, ed. by S.M. Bruemmer and A.R. McIlree, p. 772. 1997.
- [9] Farrell, K., in *Proceedings: Third Int. Workshop on Spallation Materials Technology*, Santa Fe, NM, ed. by W.F. Sommer *et al.*, Los Alamos National Laboratory, LAUR-00-3892, 1999.
- [10] Oliver, B.M., *et al.*, "Retention of Very High Levels of Helium and Hydrogen Generated in Various Structural Alloys by 800 MeV Protons and Spallation Neutrons", *Proceedings: Effects of Radiation on Materials, 20th International Symposium, ASTM STP 1405*, Edited by S.T. Rosinski *et al.*, ASTM: West Conshohocken, PA.
- [11] Pawel, J.E., *et al.*, "Irradiation Performance of Stainless Steels for ITER Application", *J. of Nuclear Materials*, **239**: pp. 126-131, 1996.

- [12] Sencer, B.H., “Structural Alloys Irradiated with Protons and Spallation Neutrons at Low Temperature Under High Helium and Hydrogen Evolution: Microstructural Evolution and Implications for Mechanical Properties”, PhD thesis, New Mexico Institute of Mining and Technology: Socorro, NM, p. 161, 2000.
- [13] Spatig, P., *et al.*, “Evolution of the mechanical properties of the F82H ferritic/martensitic steel after 590 MeV proton irradiation”, *J. of Nuclear Materials*, **258-263**: pp. 1345-1349, 1998.

Table 1. Elemental composition of materials used in APT irradiation in wt. %

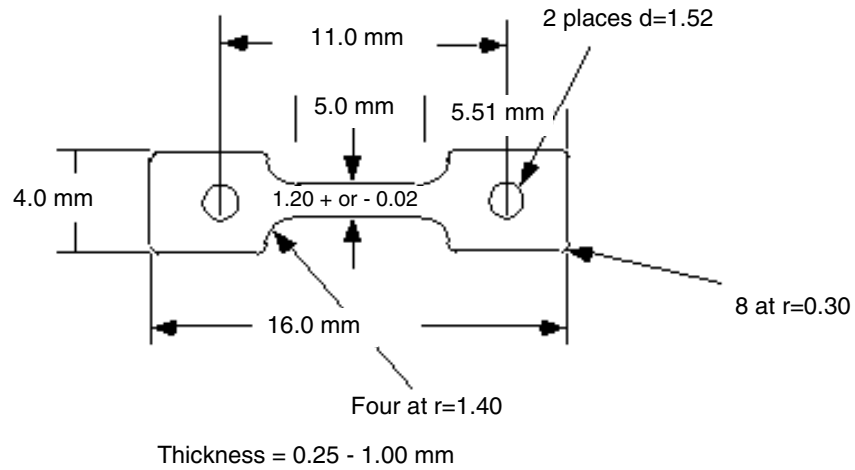
Material	Lot	Al	C	Cr	Cu	Fe	Mn	Mo	Ni	P	S	Si	Ti	Others
718 0.25 mm	E618	0.48	0.040	18.13	0.08	Bal	0.13	3.06	53.58	0.008	0.0010	0.11	1.030	Nb + Ta-4.98
718 0.75 mm	L426	0.54	0.050	18.13	0.05	Bal	0.21	3.01	52.70	0.005	0.0020	0.13	1.060	Nb + Ta-5.07; Co-0.4; B-0.004
718 2, 4 mm	G417	0.47	0.040	17.71	0.15	Bal	0.12	3.00	54.79	0.013	0.0010	0.13	0.980	Nb-4.98; Co-0.19; B-0.002
316L 0.25 mm	E835		0.019	17.26	0.26	Bal	1.75	2.57	12.16	0.022	0.0060	0.65		
316L 0.75 mm	L406		0.022	16.05		Bal	1.82	2.08	10.11	0.022	0.0002	0.48		
316L 2, 4 mm	D306		0.010	17.33	0.18	Bal	1.61	2.09	10.62	0.024	0.0190	0.43		Co-0.21; N-0.060
304L 0.25 mm	K953		0.020	18.23	0.38	Bal	1.77	0.33	9.68	0.026	0.0020	0.54		
304L 0.75 mm	L404		0.060	18.19	0.40	Bal	1.86	0.34	8.14	0.030	0.0003	0.48		
304L 2, 4 mm	K861		0.013	18.15	0.23	Bal	1.80	0.18	8.35	0.025	0.0100	0.43		Co-0.17; N-0.085
Mod 9Cr-1Mo	10148	.002	0.089	9.24	0.08	Bal	0.47	0.96	0.16	0.021	0.0060	0.28	0.002	V-0.21; Nb-0.054; Co-0.019; N-0.035; O-0.008

Table 2. Hardness and grain size of materials used in APT irradiation

Material	Thickness (mm)	Micro-hardness (kg/mm²)	Grain size (microns)
Alloy 718 (precipitation hardened)	4.00	486	65
	2.00	473	55
	1.00	458	30
	0.25	465	47
Mod 9Cr-1Mo (tempered)	4.00	293	27
	2.00	295	22
	0.75	283	21
	0.25	278	19
304L (annealed)	4.00	171	55
	2.00	175	65
	0.75	174	18
	0.25	159	15
316L (annealed)	4.00	159	32
	2.00	157	32
	0.75	149	21
	0.25	153	16

Figure 1. Schematic showing (A) the dimensions of the S-1 tensile specimen and (B) the dimensions of the sub-size disk compact tension specimen used for measuring the mechanical properties of materials after irradiation in a spallation environment

A.



B.

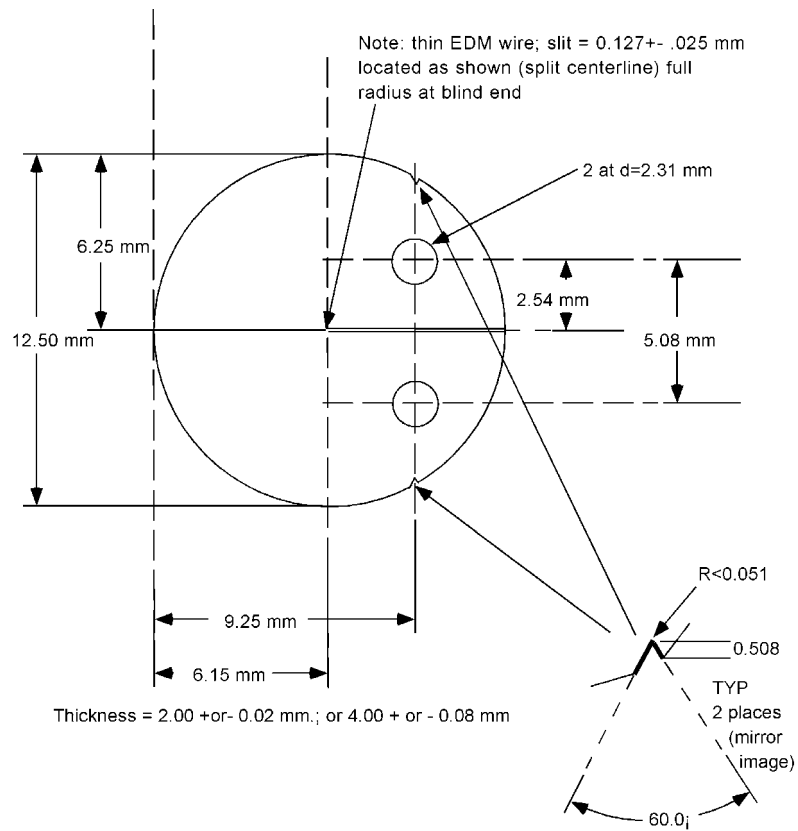


Figure 2. A representative plot of stress/strain curves measured on Alloy 718 in the precipitation hardened condition after irradiation in a spallation environment

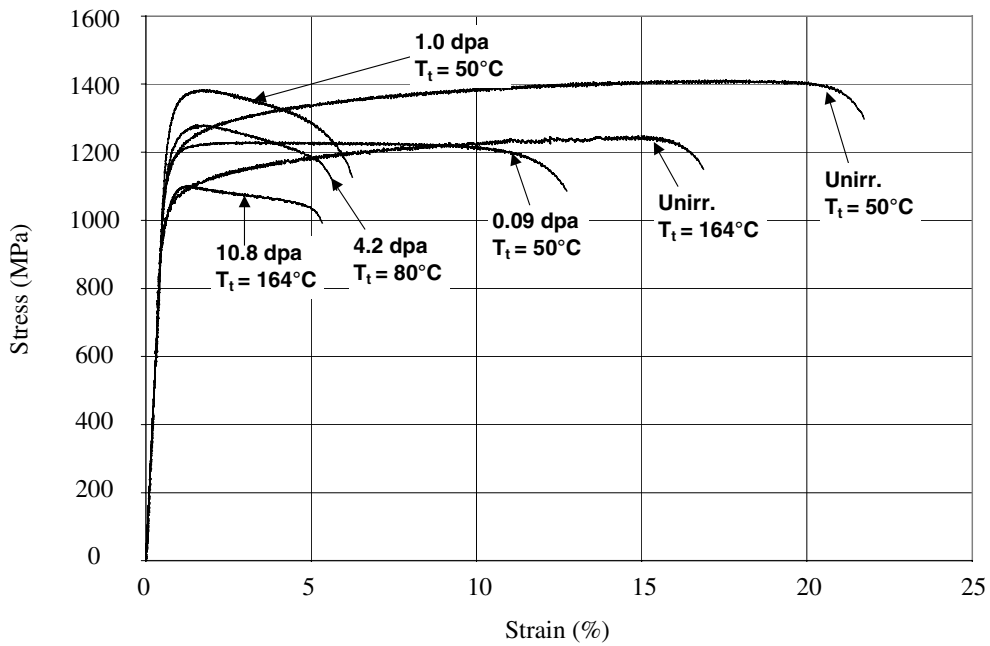


Figure 3. Graph showing the change in 0.2% offset yield stress and uniform elongation in Alloy 718 after irradiation in a spallation environment ($T_t = T_{irr} = 50-160^\circ\text{C}$)

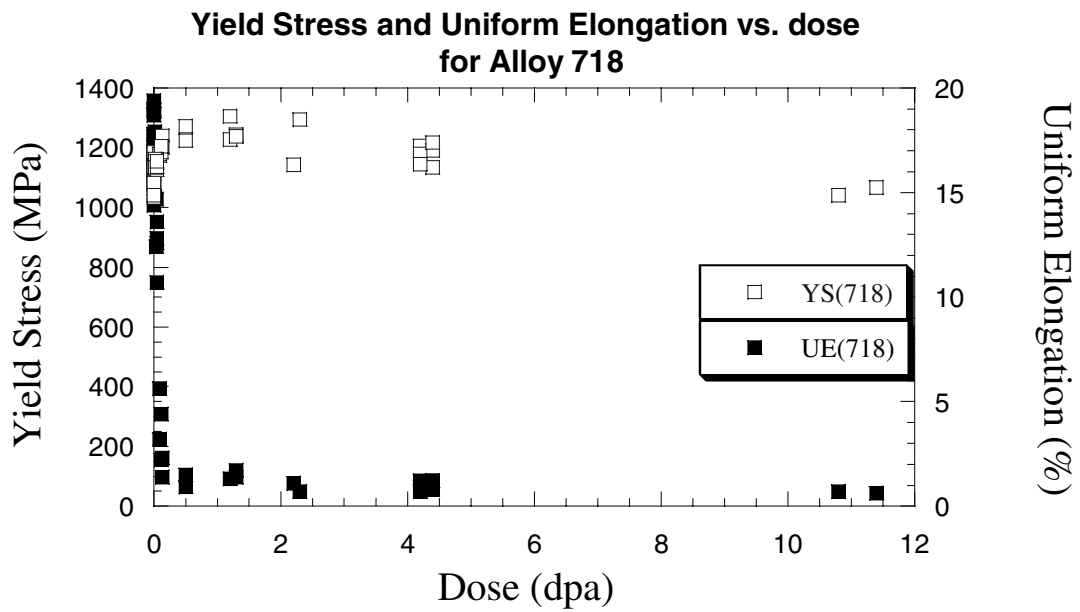


Figure 4. A representative plot showing stress/strain curves measured on annealed 316L stainless steel after irradiation in a spallation environment

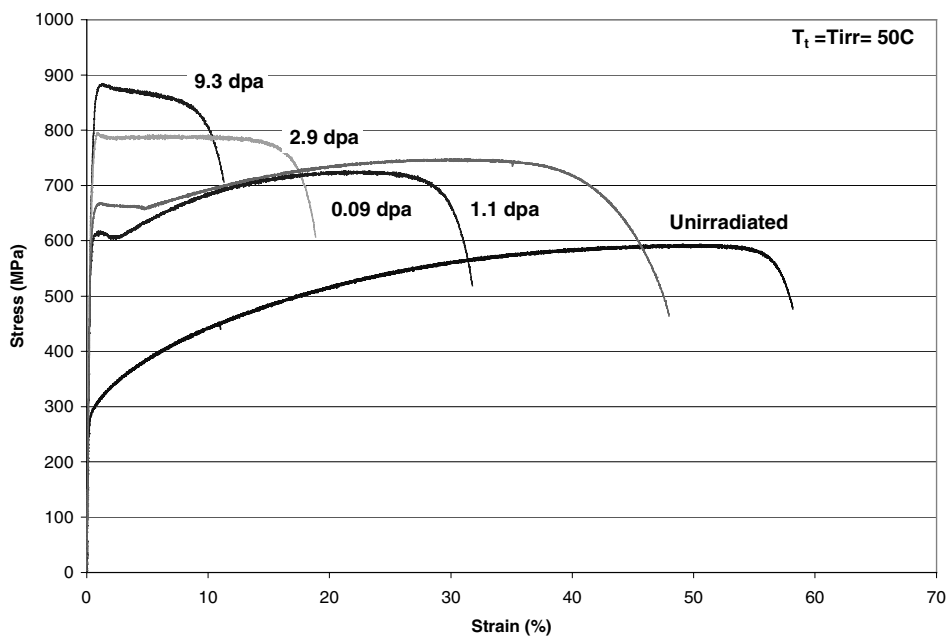


Figure 5. A graph showing the change in uniform elongation and 0.2% offset yield stress with dose after irradiation in a spallation environment ($T_t = T_{irr} = 50\text{-}160^\circ\text{C}$)

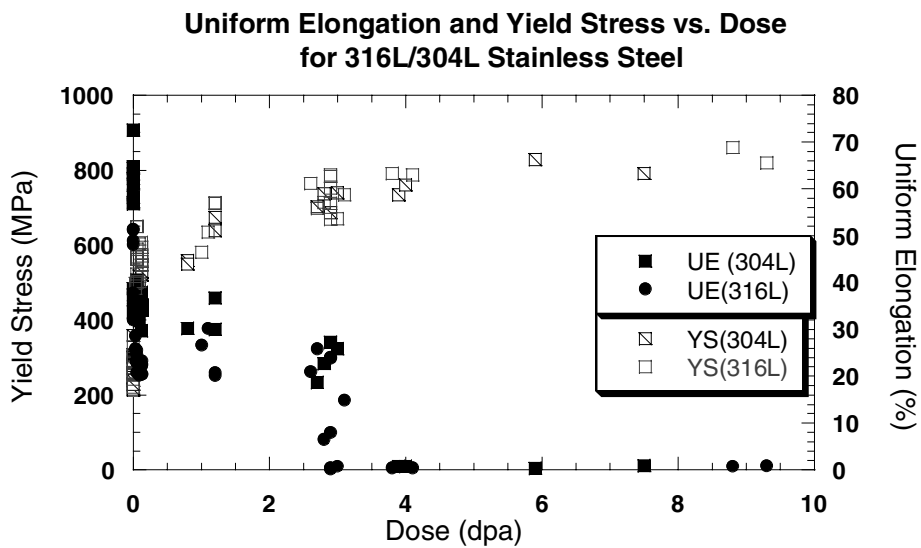
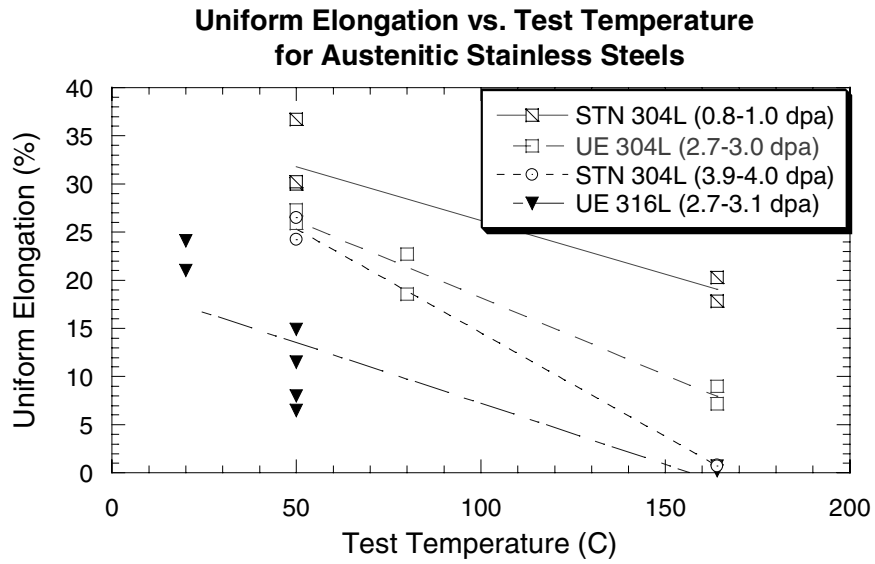


Figure 6. (A) Graph showing the decrease in uniform elongation or strain-to-necking with increasing test temperature after irradiation to 1-4 dpa in a spallation environment and (B) stress/strain curves showing the effect of test temperature after irradiation to 9 dpa in a spallation environment

A.



B.

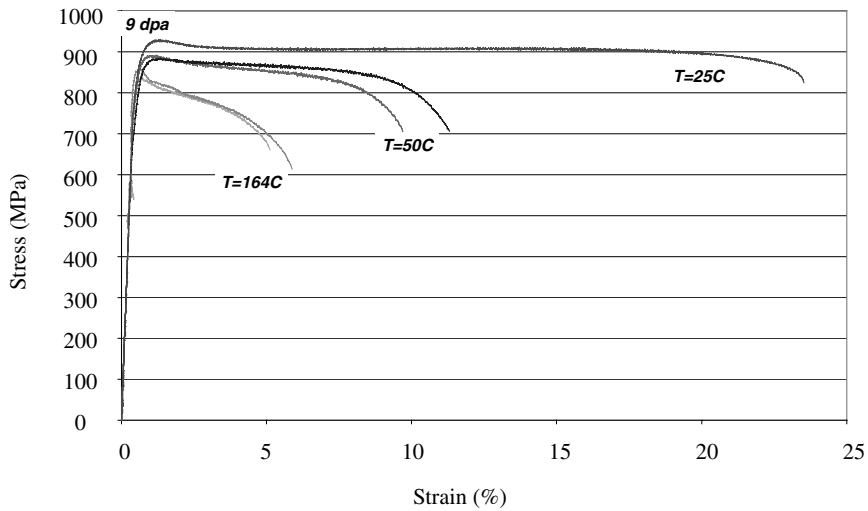


Figure 7. A representative plot showing stress/strain curves for Mod 9Cr-1Mo after irradiation in a spallation environment

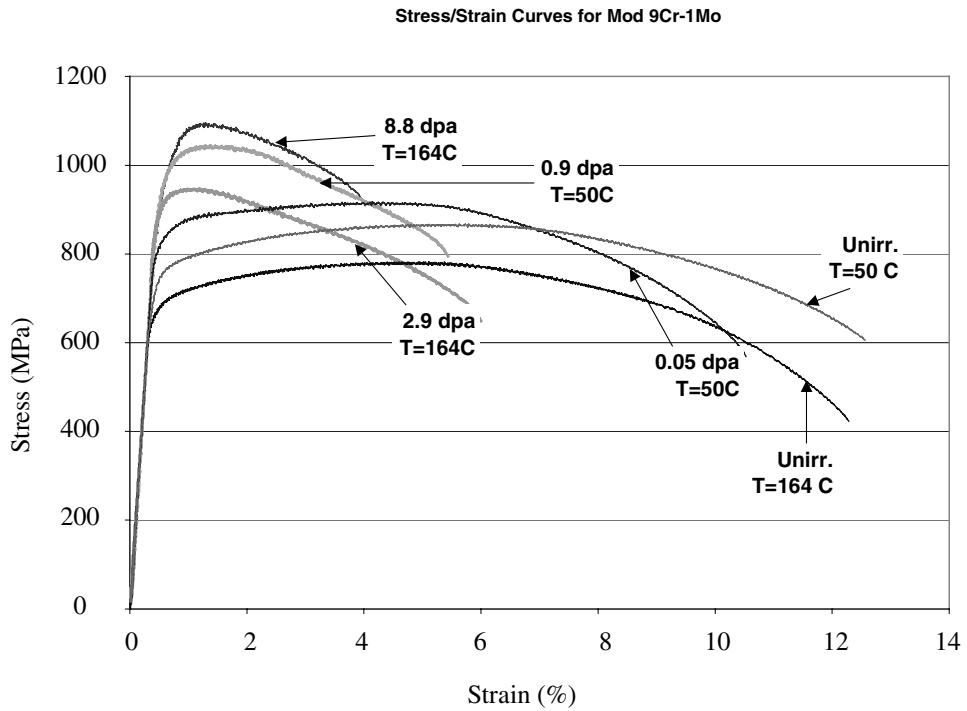


Figure 8. A graph showing the change in 0.2% offset yield stress and uniform elongation with increasing dose after irradiation in a spallation environment (Tt=Tirr=50-160°C)

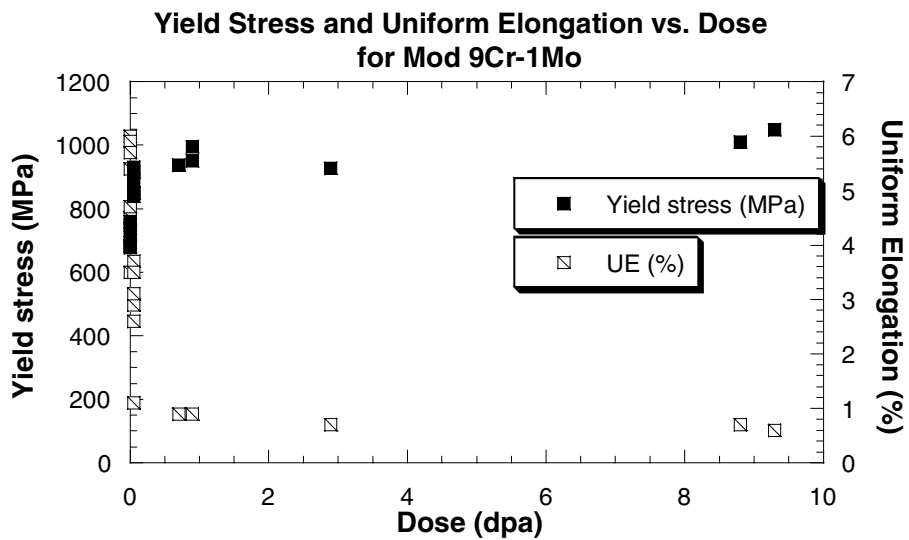


Figure 9. A graph showing the change in 0.2% offset yield stress and uniform elongation with increasing test temperature for specimens irradiated to 3 dpa in a spallation environment (Tirr=35-50°C)

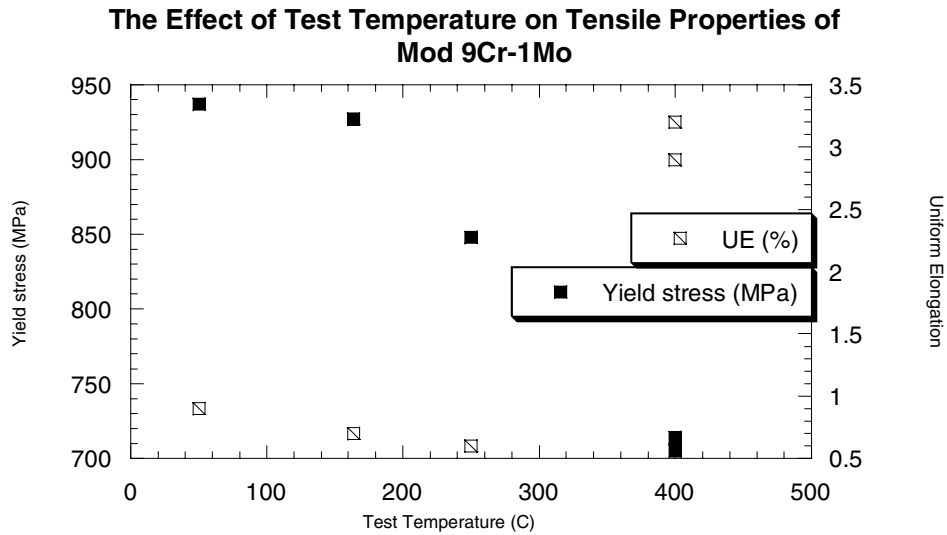


Figure 10. Scanning electron micrographs showing the fracture surface of an Alloy 718 tensile specimen after irradiation to 11 dpa in a spallation environment (Tt=Tirr=150-160°C)

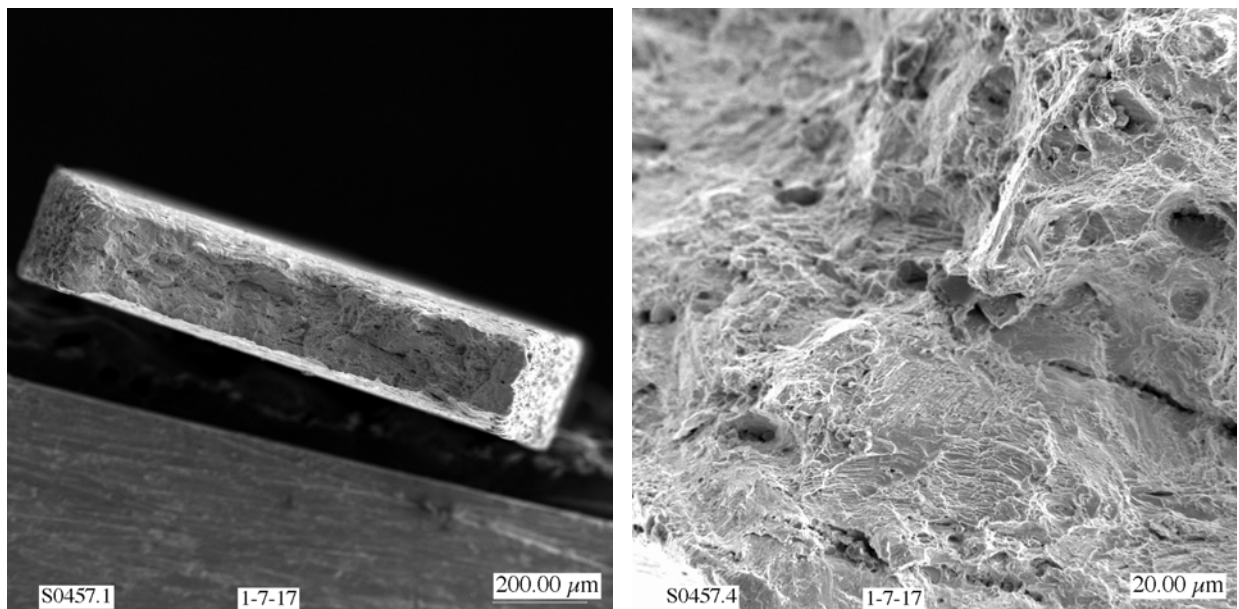


Figure 11. Graph showing reduction of area plotted vs. uniform elongation for precipitation hardened Alloy 718 and annealed 304L and 316L stainless steel (Tt=Tirr=50-160°C)

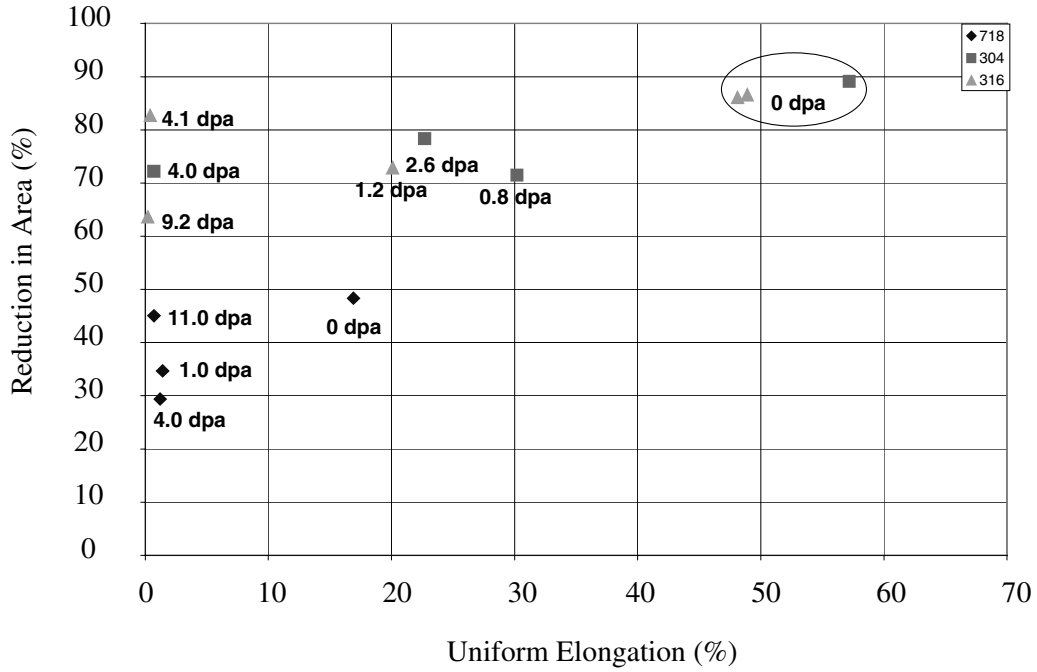


Figure 12. Scanning electron micrographs showing the fracture surface of a 316L tensile specimen after irradiation to 9 dpa in a spallation environment Tt=164°C, Tirr=72°C

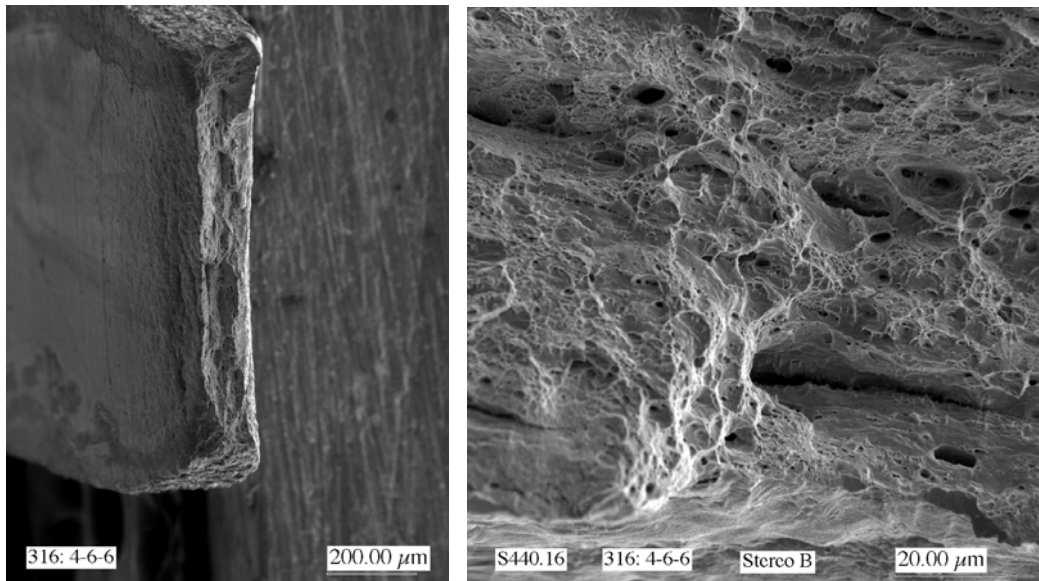


Figure 13. Graph showing the variation of fracture toughness with dose for precipitation hardened Alloy 718 and annealed 316L and 304L stainless steel after irradiation in a spallation neutron spectrum ($T_t=T_{irr}=50-160^\circ\text{C}$)

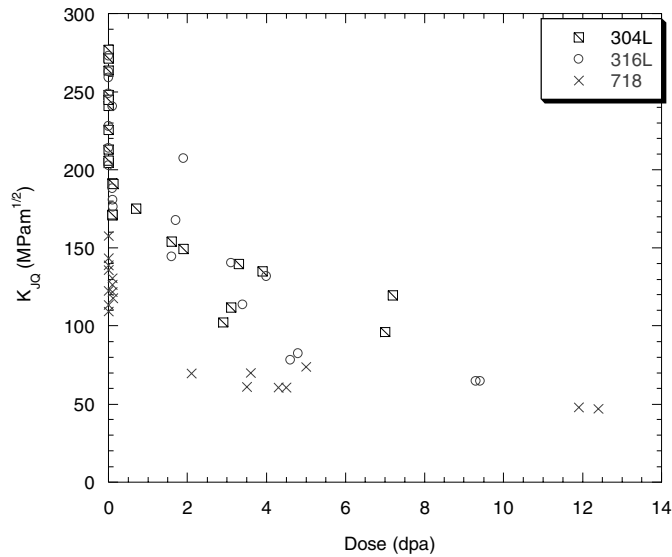


Figure 14. Graph plotting fracture toughness vs. dose for Mod 9Cr-1Mo after irradiation in a spallation neutron spectrum ($T_t=T_{irr}=50-160^\circ\text{C}$)

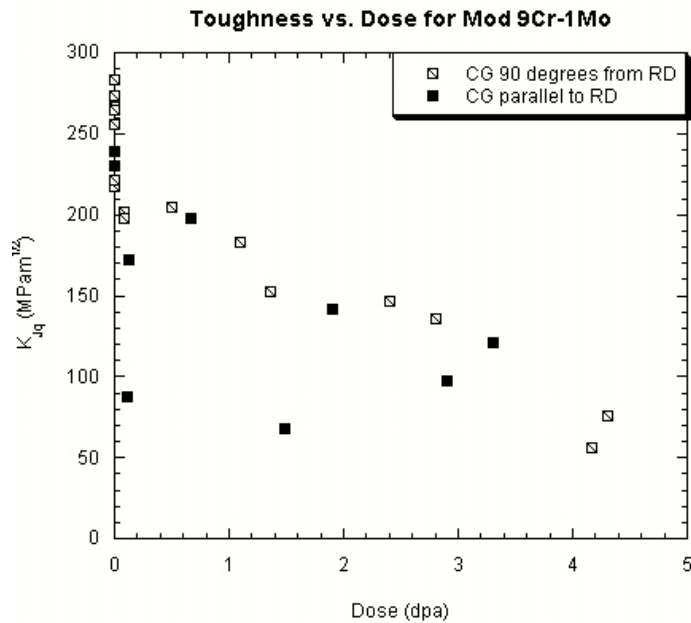


Figure 15. A graph comparing the uniform elongation measured on Alloy 718 in tension after irradiation in an accelerator to similar doses irradiated in the high flux isotope reactor (Tt=Tirr=20-50°C)

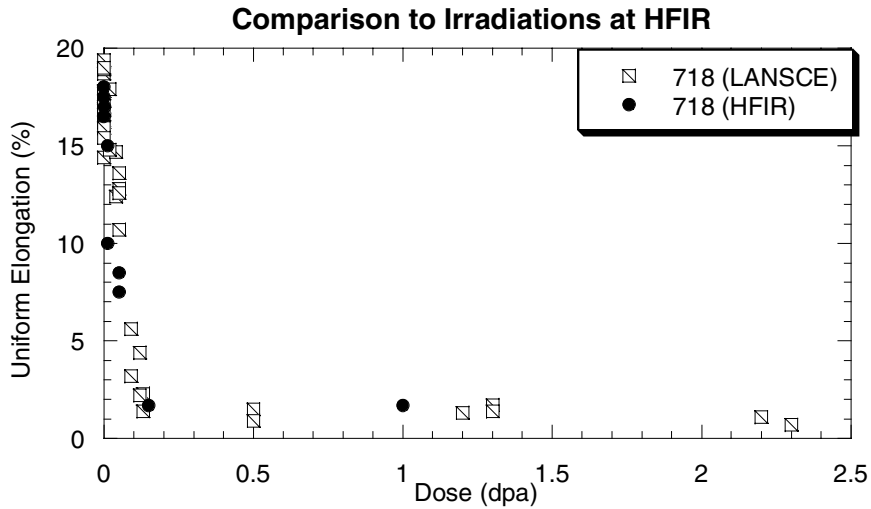
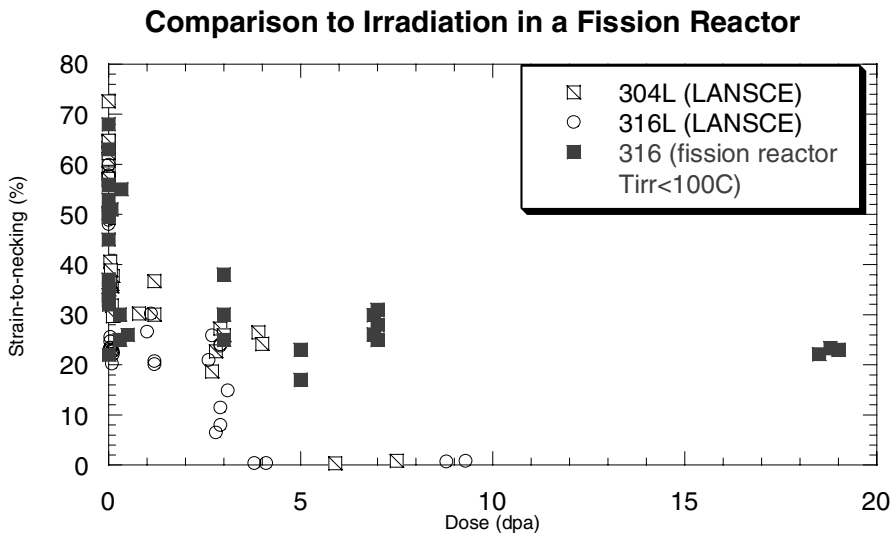


Figure 16. A graph comparing the strain-to-necking measured on 300 series stainless steels after irradiation in the LANSCE accelerator to those measured after irradiation in a fission reactor [11] at low temperatures (<100°C) (Tt=Tirr=50-80°C for LANSCE data)



SESSION II

Accelerator, target/window/materials and multiplier

Chair: R. Sheffield

RELIABILITY TESTS OF THE HIGH-POWER PROTON SOURCE SILHI AT CEA/SACLAY

R. Gobin, P.-Y. Beauvais, D. Bogard, R. Ferdinand, P. Mattéi
Commissariat à l'Énergie Atomique, CEA Saclay, DSM-DAPNIA
91191 Gif-sur-Yvette Cedex, France

Abstract

In France, the IPHI demonstrator project (injector of protons for high intensity) is developed by a CEA/DSM – CNRS/IN2P3 collaboration for several applications based on the use of high power proton accelerators. The IPHI RFQ is designed to accelerate a 100 mA proton beam from 95 keV to 5 MeV. The construction of the segmented 8 m long RFQ is under progress. The particles are injected from the SILHI (high intensity light ion source) ECR source. SILHI has been producing intense beams since 1996. A new extraction system and new control system led to large improvements in term of intensity, beam line transmission, stability. Moreover, automatic restart procedures allow to minimise the beam off time. More than 130 mA are now routinely produced at 95 keV with a proton fraction higher than 80%. Several long run tests have been performed to measure the source reliability and to improve the mean time to repair. This article will report a summary of the reliability tests pointing out the influence of the last improvements. The source will be installed on the IPHI site within the next months.

Introduction

CEA and CNRS have undertaken an important R&D programme on very high beam power light-ion accelerators (MW class) for several years. The two French research agencies are interested among others by applications such as accelerator-driven system (ADS), new generation of exotic ion facilities or neutrino and muon production for high-energy particle physics. The R&D programme is essential since the performances requested by these projects are one to two order of magnitude higher than those achieved by the most powerful existing accelerators. Severe beam loss limitations are necessary to allow hands-on maintenance. The necessity to achieve a very high availability with a reduced number of beam trips add new constraints which make the R&D effort even more indispensable to have a realistic view of the new generation of high-power accelerators.

The strategy carried by the CEA–CNRS collaboration has been to restrict the R&D programme to a limited number of essential subjects with a maximum overlap on the different projects. The R&D effort is then concentrated on three topics:

- 1) IPHI a prototype of linac front end up to 10 MeV with beam currents up to 100 mA CW,
- 2) construction and test of $\beta < 1$ superconducting cavities,
- 3) improvement of the codes for accurate beam dynamics calculations.

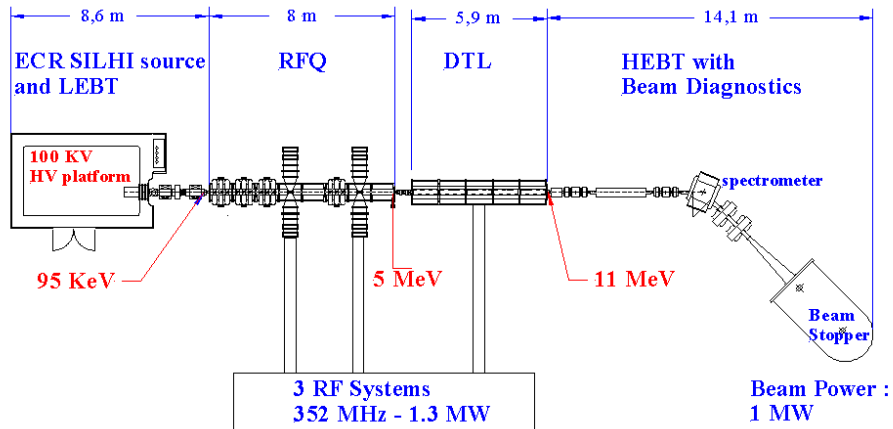
IPHI is foreseen to be the front part of a high power proton accelerator (HPPA) [1]. It includes an ECR source, a RFQ and a DTL to provide beam energies up to 10 MeV. Since 1996, SILHI has been regularly producing intense proton beams, in cw or pulsed mode, with performance close to the request [2]. A new extraction system has been designed to minimise beam losses on the extraction electrodes by reducing the initial divergence. New reliability tests were performed to analyse EMI-hardened device improvements as well as automatic procedures. In 2001, a 162 hour test has been successfully achieved; the beam availability reached 99.8%.

IPHI general layout

The Figure 1 represents the general layout of the IPHI prototype. The ions are produced at 95 keV by the ECR ion source located on a HV platform. The 2 LEPT solenoids allow the beam matching at the 5 MeV RFQ entrance. The DTL (not yet funded) will increase the energy up to 10 MeV. The diagnostics line will be first installed at the RFQ exit to characterise the beam at intermediate energy.

The IPHI site is now ready to receive the different parts of the prototype. Two 352 MHz klystrons are already arrived from CERN to power the RFQ (construction under progress). The first RFQ segment is under mechanical and RF tests after brazing. The seven other segments will be built within less than 2 years. The SILHI experiments stopped at the end of April and the source will be installed on the IPHI site within few months.

Figure 1. General layout of the IPHI project



Proton source performance

SILHI is an ECR ion source operating at 2.45 GHz. The RF power is produced by a 1.2 kW magnetron source and is fed to the source via standard rectangular wave-guides with a four stub automatic tuning system and a three section ridged wave-guide transition. A new set of the 5-electrode extraction system allows beam losses limitations and the source is now currently producing beam intensity higher than 120 mA with a proton fraction close to 85%.

The emittance measurement unit is an aperture-slit method made of a 0.2 mm diameter Tantalum sampler and a Wien Filter. It allows species beam emittance analysis at the exit of the accelerator column (0.53 m from the plasma electrode) or at the end of the LEBT (4.5 m from the plasma electrode). The $r-r'$ rms normalised emittance values turn out to be lower than $0.2 \pi \cdot \text{mm} \cdot \text{mrad}$ at the exit of the source for a 100 mA proton beam. A significant emittance growth has been observed at the end of the LEBT (nominal values of $0.3 \pi \cdot \text{mm} \cdot \text{mrad}$). This emittance growth did not depend on the extraction configuration. The critical parameters seemed to be the beam focussing depending on the solenoid current.

To minimise possible breakdown and to optimise the reliability, different developments and technical choices were adopted. The following list presents several items developed in this framework:

- Quartz window protected behind a water cooled bend.
- Electrode shape optimisation to minimise the electric field and the spark rate.
- Large safety margins on all power supplies (HV and others).
- Optimisation of power supplies air or water cooling.
- Separate cable path and shielding for signals and power.
- Galvanic insulation of analogue and digital signals.
- Use of EMI hardened devices especially for all sensitive electronics and PLC.

- Development of beam current feedback.
- Development of EPICS automatic start/restart procedures.
- Development of specific beam diagnostics.

LEBT space charge compensation analysis indicated the significant contribution of secondary electrons by means of beam losses on the walls, interceptive diagnostics or gas adding. A small amount of heavy gas (Ar or Kr) allow a better space charge compensation.

Source reliability tests

Three 100 hours long runs have been performed with the previous extraction system to analyse the source reliability. The source was continuously operated for 5 days and the reliability-availability respectively reached 94.5%, 97.9% and 99.96%. In October 1999, only one beam trip occurred at the beginning of the 104 hours test for 2.5 min, and 103 hours uninterrupted running time was achieved.

Table 1 summarises the 5 run reliability tests performed since the source produced its first beam in 1996.

Parameters	December 97	May 99	October 99	March 01	June 01
Energy (keV)	80	95	95	95	95
Intensity (mA)	100	75	75	118	114
Duration (h)	103	106	104	336	162
Beam off number	53	24	1	53	7
MTBF (h)	1.75	4.00	n. a.	≈6.00	23.10
MTTR (mn)	6.00	5.30	2.50	≈18.00	2.50
Uninterrupted beam (h)	17.00	27.50	103.00	25.00	36.00
Availability (%)	94.50	97.90	99.96	95.20	99.80

This table shows the reliability-availability can reach higher than 99.5% with a very low number of beam off within a whole week. The mean time to repair is largely too long for continuous injection in a ADS and improvements will have to be again achieved to match the requests. As a bad running gives more information than a good one, the following paragraphs comment the March 2001 test where the availability only reached 95.2%.

In the framework of the CEA participation to the IFMIF programme, a new long CW test was planned for a 4 weeks duration. Since the source remote control is completely updated with the EPICS system, automatic procedures and home internet network connections allow us to leave the source working without any operator locally.

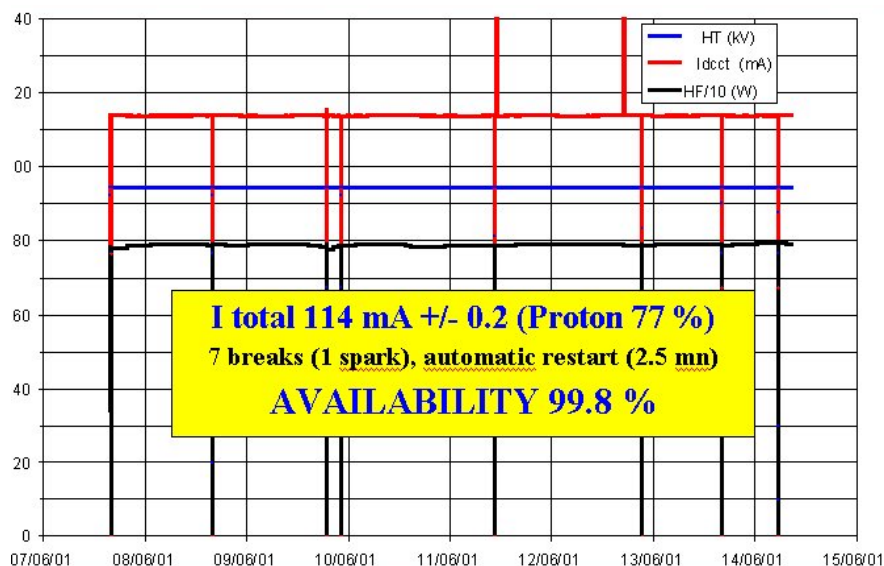
The run began with a 97 mA proton beam (118 mA total and 84% proton fraction) extracted at 95 kV. Too many breakdowns occurred. In the same time, the servo control loop which keeps constant the extracted beam current progressively increased the RF power, indicating changing beam characteristics. The proton fraction dropped from 84 to 63%. Beam line residual gas analysis revealed an oil contamination.

Even though this reliability test did not reach the expected results, it gave us valuable information summarised hereinafter.

- Beam line pollution leads to rapid beam quality degradation.
- The O₂ cleaning beam seems very efficient to improve the proton fraction but after the cleaning, the spark rate did not decrease.
- The automatic restart procedures which take 2.5 min, were not completely adapted to all the situations especially if a spark occurs during the restart period.

After cleaning of the accelerator column and new conditioning, a 114 mA (+/- 0.2) – 95 keV beam was produced for 162 hours with a 77% proton fraction (Figure 2). Seven beam off occurred mainly due to plasma extinction (only one spark). The 7 restarts were automatically operated and took 2.5 min each. The availability reached 99.8%.

Figure 2. 162 hour long run

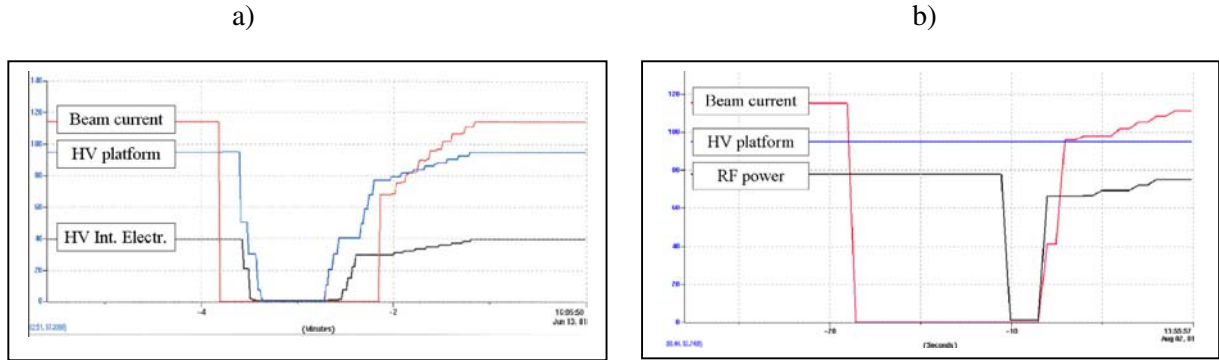


After automatic procedure improvements achieved with the EPICS control system, beam off for as short as 20 seconds occur when only plasma extinguishes. The Figure 3 shows 2 different automatic restarts: a) the beam stop is due to a HV spark and the HV power supplies switched down; b) the beam stop is only due to plasma extinction and switching down and up the RF power allow us to recover the beam.

A fast analogue feedback should be developed to again minimise the beam off duration in case of plasma extinction. Less than few hundred ms duration could be expected. At present time, spark very often lead to power supplies switch down and do not allow faster restart than 2.5 minutes.

The beam noise is in the 1 to 1.4% range. This noise was mainly due to the 19 kHz coherent oscillations transferred to the plasma from the magnetron RF switched power supply. A 3 GHz klystron will be tested to minimise the beam noise. The non Gaussian distribution of the noise do not allow any more to speak of a +/- range but in a full range beam noise.

Figure 3. Automatic restart: a) After spark (2.5 min beam off)
b) After plasma extinction (20 s beam off)



Conclusion

To summarise the SILHI reliability analysis, the different tests have been performed with a higher intensity than expected by the ADS HPPA. More than 800 hours of continuous operations gave us lots of information to optimise the source behaviour. Several weak points have been discovered and solved.

No spark occurs without beam after specific accelerator column conditioning. The use of EMI hardened devices enhanced dramatically the source performance. Sparks now do not lead to power supplies failures or PLC reboots. Moreover short experiments indicated a lower spark rate with a lower beam intensity as well as with pulsed beam. These results will have to be confirmed by specific runs planned after the move of the source on the IPHI site.

The SILHI beam characteristics are close to the RFQ requests and the first 5 MeV beam is expected in 2004.

Table 2 summarises the SILHI source performance. In deuteron, the duty factor was limited by neutron production.

Particles	Proton		Deuteron	
	Requests	Status	Request	Status
Energy [KeV]	95	95	95	100
Intermediate electrode [kV]	55	56	?	50
Proton, Deuteron current [mA]	100	108	140	129
Total current [mA] / (<i>I max</i>)	110	130 (157)	155	135 (166)
Proton, Deuteron fraction [%]	>90	83	>90	96
Plasma electrode diameter [mm]	–	9	–	9
Current density [mA/cm ²]	140	204	243	212
Availability [%]	AHAP	>99	AHAP	–
RF forward power [W]	<1 200	850	<1 200	900
Duty factor [%]	100	100	100	0.2*
H ₂ , D ₂ gas flow [sccm]	<10	5	<10	1
Beam noise rms. [%]	2	1.2	2	1.2
rms normalised emittance [$\pi \cdot \text{mm} \cdot \text{mrad}$]	0.2	0.11 @75 mA	0.2	–

REFERENCES

- [1] Beauvais, P.Y., *et al.* "Status report on the Saclay high intensity proton injector project (IPHI)", EPAC 2000 Conference proceedings, Vienna, Austria.
- [2] Gobin, R., *et al.* "High intensity ECR ion source (H+, D+, H-) development at CEA/Saclay", ICIS 2001 Conference, Rev. Scien. Instr., Volume 73, n° 2, (922).

OPERATIONAL EXPERIENCE WITH A 352 MHZ 5-CELL ACCELERATING STRUCTURE FOR THE HIGH ENERGY SECTION OF THE TRASCO LINAC

E. Chiaveri, R. Losito, S. Calatroni
CERN, 1211 Geneva 23, Switzerland

R. Ballantini A. Chincarini, G. Gemme^{*}, R. Parodi
INFN Genova, Via Dodecaneso 33, 16146 Genova, Italy

D. Barni, A. Bosotti, C. Pagani, P. Pierini
INFN Milano, LASA, Via Fratelli Cervi 201, I-20090 Segrate, Italy

Abstract

The five-cell module, $\beta=0.85$, built at CERN for the TRASCO project was fully tested at the CERN SL/CT test bench. The cavity, built using the standard niobium on copper technique, was previously tested in a vertical cryostat, showing Q_0 and accelerating field exceeding the design goal of the TRASCO project ($Q_0 = 2.5 \times 10^9$ and $E_{acc} = 5.5$ MV/m @ 4.5 K). After this successful test the cavity was equipped with all the LEP-II cavity ancillaries, and tested in a horizontal cryostat. The behaviour of the fully equipped cavity substantially confirmed the results of the preliminary production tests in the vertical cryostat. No multipacting activity was detected confirming the soundness of the design and the quality of the surface treatment. After the low power test of the TRASCO module the cavity was powered through the main coupler up to 250 kW, using one of the LEP 1.3 MW klystrons. The obtained accelerating field was ~ 7 MV/m, exceeding by 30% the design value of 5.5 MV/m.

* gianluca.gemme@ge.infn.it

Introduction

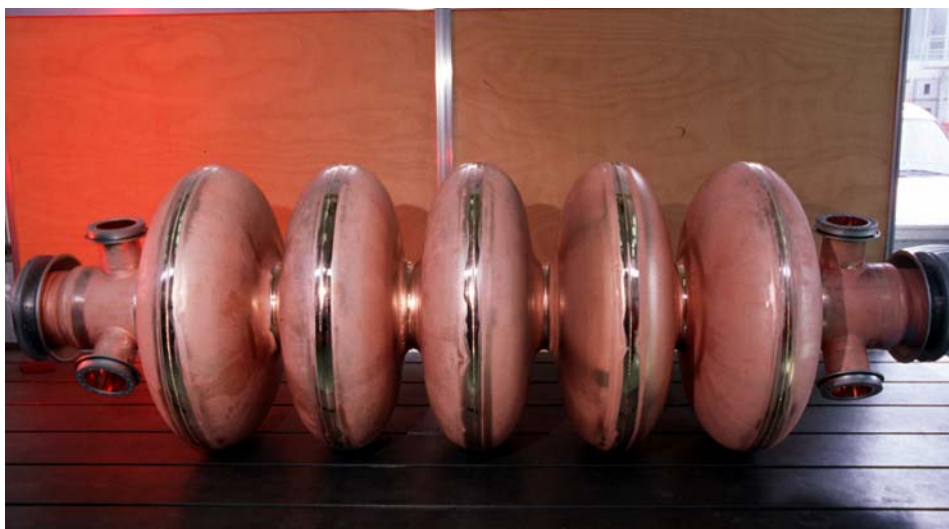
The TRASCO project is an R&D effort jointly supported by ENEA (the Italian agency for the development of new energy sources) and INFN (the Italian organisation for the research in subnuclear and nuclear physics) [1, 2]. The project is funded by the Italian government through a grant for the technological transfer to the Italian industries. The aim of the project is the design, test and production of critical components of an accelerator driven sub-critical nuclear reactor for the transmutation of long-lived radio nuclides produced in standard light water nuclear power plants. INFN is responsible for the design of the high current (25-30 mA), high energy (100 MeV to 1 GeV) proton accelerator driving the intense neutron source used to keep running the fission process in the sub-critical nuclear reactor.

As a first step in the development process we decided to use already existing components for the RF system and to use for the cavity construction the state of the art techniques proven in mass production. For the aforementioned reasons the first cavity prototypes were designed at the frequency of the LEP-II superconducting cavities: 352.2 MHz. Therefore we signed an agreement with CERN for the construction and test of a five-cell prototype cavity to take full advantage from the experience gained by the SL/CT group at CERN during the development, construction and installation of the LEP-II modules. Under this agreement, CERN built and tested a full scale prototype of the $\beta=0.85$ five-cell accelerating cavity on the geometry defined by INFN [3]. Due to the reduced length of the proton cavity with respect to the LEP (electron) geometry the sputtering process had to be modified.

INFN provided the design of the accelerating cavities [3], and the needed support for the ESCA-Augur analyses eventually needed in the process of adapting the sputtering process to the new cavity geometry. We decided to build a cavity terminated with standard LEP type cut-off tubes equipped with a main coupler port and a full set of ports for the high order mode couplers.

After the performance test of the cavity in a vertical cryostat [4], we decided to extend the INFN-CERN agreement to the test in a machine ready configuration.

Figure 1. The $\beta=0.85$ TRASCO cavity after construction



Cavity production

The cavity was built forming the half-cells by spinning starting from a OFHC copper sheet 3.5 mm thick according to the standard LEP cell production. The full cavity is then assembled using 8 equal half-cells for the body of the module plus two different half-cells at each end to obtain the needed field flatness for an optimum distribution of the fields in the cavity. The half-cells of both types were formed then deep electro-chemically polished to remove the first copper layer which has a heavily distorted crystal lattice. This lattice distortion is produced both by the cross rolling process used in the formation of the copper sheet, and by the spinning procedure employed for the half-cell production.

The experience gained during the LEP cavities production has shown that poor copper crystal lattice properties will always lead to sputtered niobium films with poor RF quality (mainly producing high RF losses and low accelerating fields). The electron beam welded cavity is shown in Figure 1.

Figure 2. The 5-cell cavity ready for the sputtering cathode insertion



Niobium film coating

The coating of the accelerating structure was done using a slightly modified LEP cavity procedure to adapt the sputtering process and to cope with the shape of the shortened $\beta=0.85$ cavity. This step of our programme was greatly helped by the experience gained by the SL/CT group in the reduced β programme developed at CERN in the previous years.

In particular, the sputtering magnetron was shortened to reduce the dimension of the sputtering source and to increase the landing angle of the niobium atoms on the copper surface. The iris and wall

region the cavity shape were already optimised by INFN to improve even more the deposition angle, and, consequently, the quality of the film. The final geometry has been chosen by taking into account both the geometry requirements for the efficiency of the sputtering process described above and the overall electromagnetic performances of the cavities. This final optimisation compromise lead only to a minor decrease in the R/Q factor of the cavity with respect to the maximum obtainable. Figure 2 shows the 5-cell cavity in the CERN clean room waiting for the installation of the sputtering cathode.

After the sputtering the cavity was mounted on the test cryostat for the measurement of the quality factor Q_0 and of the maximum accelerating field. In the vertical test the cavity met the TRASCO goal at the first run, only needing a mild helium conditioning to reach to the maximum field. The results of the vertical test are reported in Figure 3.

Figure 3. Q_0 versus field @ 4.5 K and 2.5 K for the five-cell cavity (vertical test)

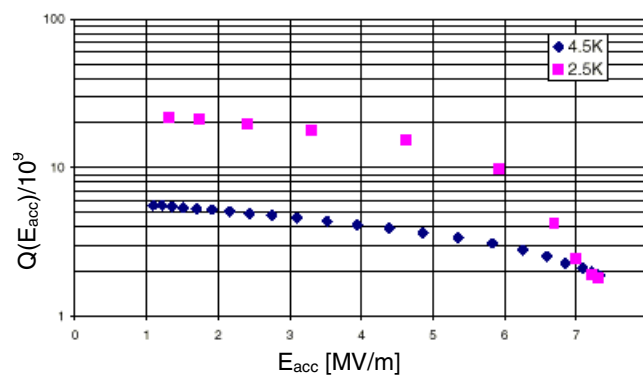
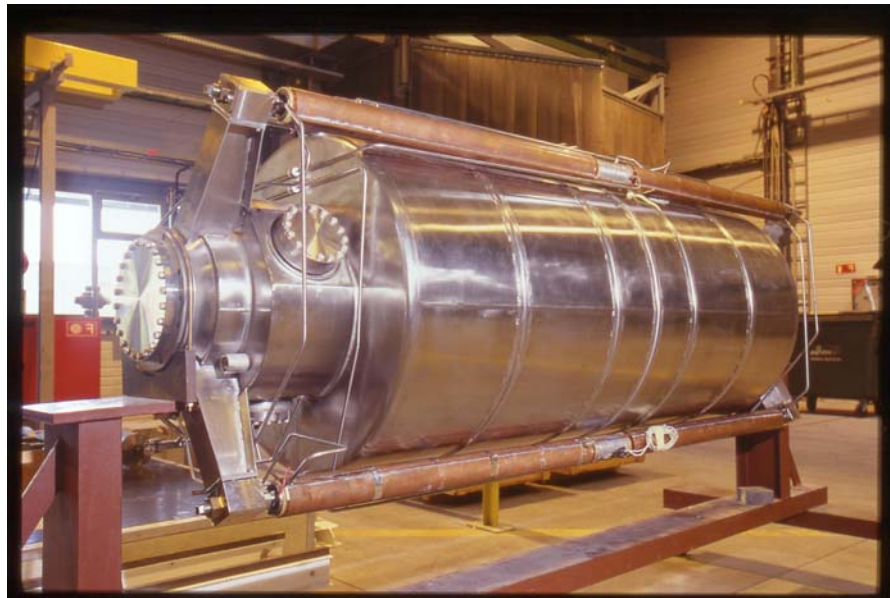


Figure 4. Five-cell cavity inserted in the LHe vessel and equipped with the tuners



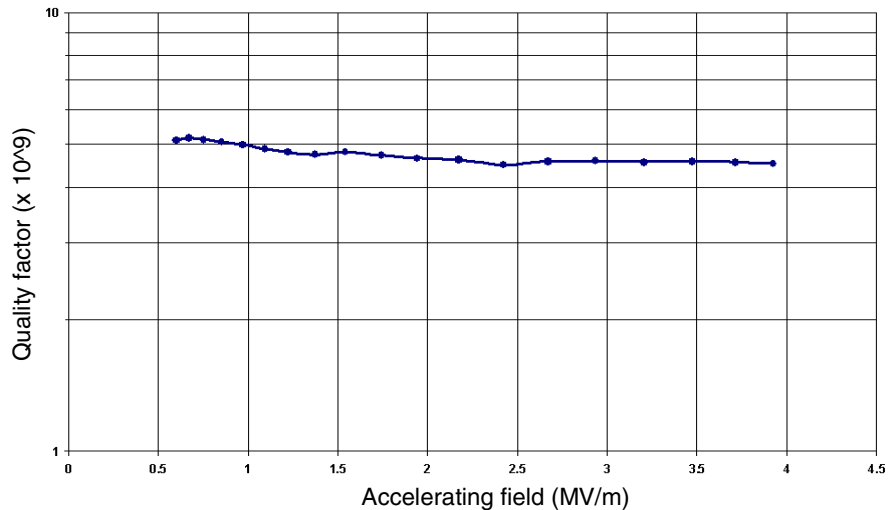
Horizontal cryostat

After the completion of the vertical test, we decided to fully exploit the possibilities of the cavity testing it in a machine-ready condition, using a modified LEP cavity cryostat. For this reason the INFN-CERN agreement was extended to include this part of testing and the needed development for the tooling.

The cavity, fully equipped with a LEP-II main coupler, HOM couplers, fast and slow tuners, was inserted in a stainless steel skin forming the helium vessel (Figure 4).

After the installation of the couplers, in the CERN clean room, the module was inserted in a standard LEP-II skin cryostat, the thermal super-insulation was added and the completed module installed in the SM18 vault for the high power tests.

Figure 5. Preliminary Q_0 versus accelerating field measurements. The maximum available RF Power limited the accelerating field.



RF tests

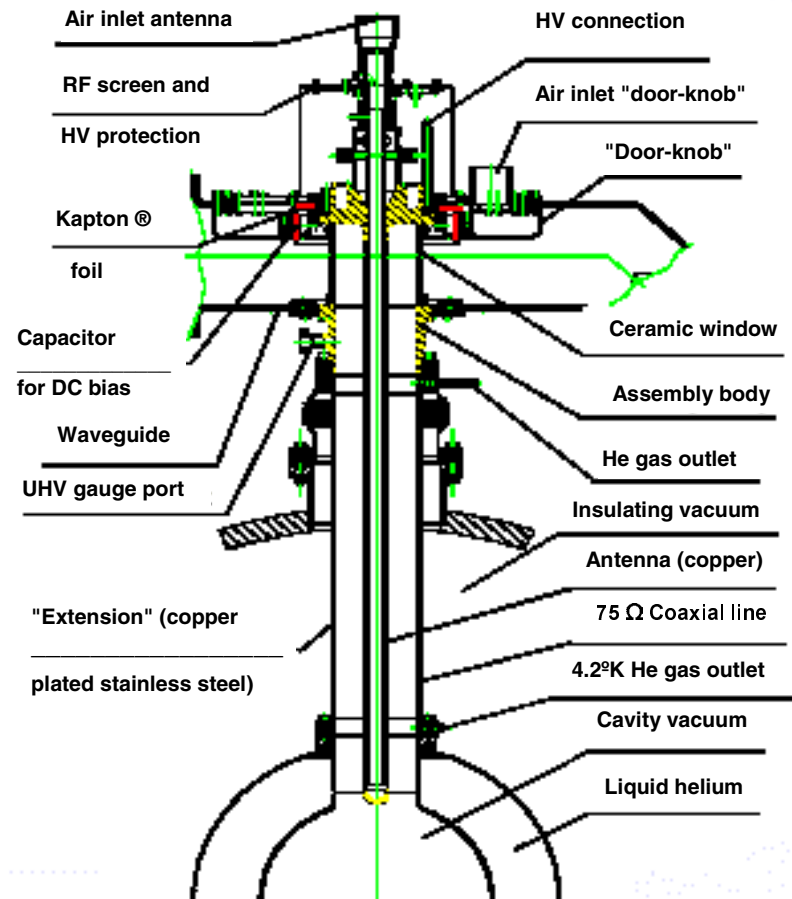
The RF test were originally planned for May 2001 and performed in August 2001, due to the higher priorities of other CERN activities (mainly related to LHC) that needed the use of the cryogenic and test infrastructure. During the test, one of the tuner windings burned, preventing us from tuning the cavity sharp resonance to the operating frequency of the RF klystron used for the high power tests. Consequently, we decided to perform a low power test, using a wide band amplifier, to check the overall behaviour of the module.

The results of this test were quite encouraging, as shown Figure 5. The cavity Q_0 at low field was the same of that reached in the vertical tests and the maximum obtained field was around 4 MV/m (limited by RF power availability), with only a small Q_0 versus field degradation, light electron emission and no need for cavity conditioning up to this field.

High power test

After installation of a new tuner on the cavity, the accelerating module was connected to the 1.3 MW CW klystron, using the standard LEP-II coupler shown on Figure 6.

Figure 6. Layout of the 75 W fixed coupler used in the tests of the TRASCO module



Details of the coupler design have already been reported in earlier publications [5, 6]; therefore, only a short summary of the main topics will be given here.

A fixed coupler of the open-ended coaxial type is used, with the option of applying a DC bias, if required, to suppress multipacting barriers.

The coupler consists of five room temperature functional parts: a waveguide input, a "door-knob" waveguide-coaxial transition, a ceramic window, an air cooled inner conductor (also called *antenna*) coupled to the cavity RF field, and an outer conductor equipped with an electron pick-up and a port for the vacuum gauge.

A helium gas cooled “extension” extends the outer conductor inside the cryostat down to the cavity port. Modified ConFlat[®] vacuum seals are used at the connecting flanges to provide low loss RF UHV joints.

A DC bias up to 2.5 kV can be applied to the inner conductor to suppress multipacting (MP) and to reduce the RF conditioning time.

As shown in Figure 6 a coaxial capacitor at the “door-knob” in the high RF current region, together with an additional capacitor (a copper plated Kapton[®] foil) between the antenna base and the waveguide, are used in order to guarantee the ground insulation for the DC bias.

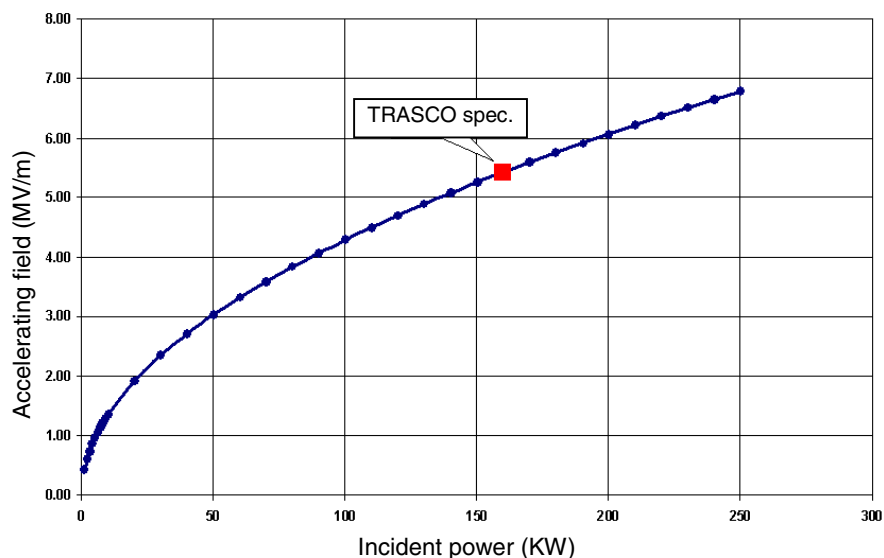
RF conditioning of the coupler

The ceramic windows of the coupler were baked out under vacuum for 24 hours at 200°C on the cavity before the cool down. This procedure efficiently improves the conditioning of the couplers [7]. Then the cavity was cooled down to 4.3 K and the CERN standard conditioning procedure applied.

Initially, the RF pulsing without cooling the extension, and then RF power cycling with the extension cooled down by a counterflow of cold helium gas. The RF power cycling is controlled by a double feedback loop (analogue loop and digital control loop) adjusting the RF power level as a function of the vacuum level.

Being the coupler one of the spare LEP-II coupler (stored for 3 years in dry nitrogen) the conditioning of the surface was rather long but straightforward. We were able to smoothly increase (even if slowly) the RF power up to 250 kW in 6 working days without incurring in any severe vacuum activity related to multipacting barriers.

Figure 7. Module field versus RF power



The first strong vacuum instability, with sudden burst of pressure, was encountered just at the 250 kW level, corresponding to 7 MV/m accelerating field, 30% higher than the design field of 5.5 MV/m foreseen for the operation of the TRASCO module. Note that in this situation, in the absence of any beam loading, nearly all the incident power is reflected from the cavity and the coupler is withstanding both the incident and reflected power load. The module field versus the CW incident power is shown in Figure 7.

The operating experience with the LEP-II modules suggests to use the DC bias for multipacting suppression if any further increase of the RF power is foreseen. Safety and reliability considerations suggest not to increase the complexity of the system, to avoid a possible build up of sources for instabilities leading to system failures. For the above mentioned considerations, we decided not to press any further the system, (already exceeding the design) and to check for the system reliability.

The incident power was set a whisker lower than the onset power of the multipacting barrier detected at 250 kW, and kept constant within few % by the standard RF stabilisation loop used for the LEP cavities. The “long term” test at full power lasted 72 hours; during this run the field in the cavity was 7 MV/m with a steady coupler vacuum of 5×10^{-10} mbar and a temperature near the RF ceramic window around 50°C. No field instabilities were experienced or any action was needed to keep the module running. The test ended as scheduled with a smooth shutdown of the cavity lowering the power to zero with a 2 hours ramp down time. This slow ramp down time, by far slower than the minimum ramp down required to avoid thermal stresses in the coupler window, was used to check for multipacting levels at low field possibly reappearing some time after initial coupler conditioning.

Conclusions

The first test of the cavity module has been encouraging, showing no degradation of the cavity RF characteristics from the vertical test stand to the complete linac module test

The full power tests showed an operating field of 7 MV/m, exceeding by 30% the TRASCO design field.

A 3 days long run of the cavity at 7 MV/m was successfully completed without any degradation of the field level and any need of intervention to restore the module operation. The test run was ended according to the schedule to release the cryogenic resources to scheduled tests of LHC magnets. It is worthwhile to note that the reached input power level of 250 kW, in this test almost fully reflected, would allow the acceleration of the nominal TRASCO beam of 30 mA, at the nominal accelerating field of 5.5 MV/m and a synchronous phase of -30° .

Acknowledgements

The TRASCO collaboration wish to thank all the CERN SL/CT group for the invaluable help in the construction, preparation, and testing of the TRASCO linac module.

In particular we wish to thank A. INSOMBY and O. ABERLE for the module construction and the installation of the coupler.

REFERENCES

- [1] The TRASCO_AC Group, “Status of the High Current Proton Accelerator for the TRASCO Program”, INFN Report INFN/TC-00/23, December 2000, <http://wwwsis.lnf.infn.it/pub/INFN-TC-00-23.pdf>.
- [2] Pagani, C., D. Barni, G. Bellomo, P. Pierini, R. Parodi, Proceedings of the Linear Accelerator Conference, Chicago (IL), 1998.
- [3] Barni, D., A. Bosotti, C. Pagani, P. Pierini, S. Visonà, G. Gemme, R. Parodi, Proc. of the EPAC 98 Conference, Stockholm, p. 1870, 1998.
- [4] Chiaveri E., R. Losito S. Calatroni, A. Daccà, G. Gemme, R. Parodi, D. Barni, A. Bosotti, C. Pagani, G. Varisco, Proc. of the 9th Workshop on RF Superconductivity, Santa Fe (NM), (paper WEP034), 1999.
- [5] Tuckmantel, J. *et al.*, “Improvements to RF power couplers for the LEP2 superconducting cavities”, PAC, Dallas TX, 1995.
- [6] Haebel, E., H.P. Kindermann, M. Stirbet, V. Veshcherevich, “Status of RF power couplers for superconducting cavities at CERN”, EPAC, Sitges, 1996.
- [7] Haebel, E., H.P. Kindermann, M. Stirbet, C. Wyss, V. Veshcherevich, “Gas condensation on cold surfaces, a source of multipacting discharges in LEP2 power couplers”, 7th Workshop on RF Superconductivity, Gif-sur-Yvette, 1995.

**BEAM RELIABILITY AND EQUIPMENT DOWNTIME TRACKING
HOW LANSCE CLOSSES THE LOOP**

N.T. Callaway, R.D. Ryder
Los Alamos National Laboratory
Los Alamos, New Mexico, USA

Abstract

LANSCE uses a semi-automated accounting system to track how well we meet our stated beam delivery goals. When an equipment failure prevents delivery of the desired beam to our customers, the first order cause is identified and an accurate measurement of the downtime is recorded. For equipment downtimes of significant duration, we investigate the causes and make recommendations that will hopefully eliminate or mitigate the impact of similar downtimes in the future.

Introduction

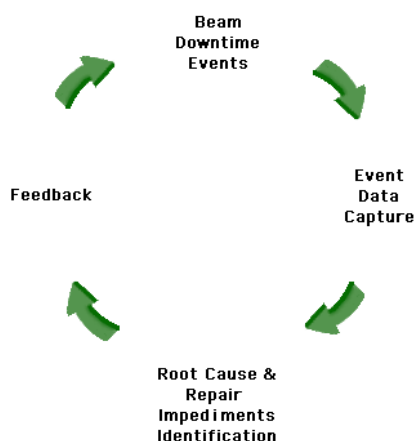
The Los Alamos Neutron Science Center (LANSCE) is comprised of an 800 MeV, half-mile long, proton linear accelerator (linac), multiple high-energy beam transport lines, a proton accumulator or proton storage ring (PSR), neutron production targets (1L and 4D), and neutron as well as proton experimental areas. A negatively charged, pulsed proton ion beam (H-) is produced in the H- injector and transported to the two-stage linac. There it is accelerated to 800 MeV and directed into the beam switchyard. The switchyard bends the beam either north to the Line-X experimental areas or south to the PSR (and 1L target) and the weapons neutron research (WNR) 4D target.

Beam delivery to the PSR/1L Target and WNR target runs continuously during scheduled neutron production periods. The PSR receives twenty Hz of 625 μ sec duration H-beam pulses from the linac. Each pulse has a micro-pulse structure of 250 nsec duration pulses. The PSR accumulates the micro-pulses contained in each 625 μ sec pulse into a single 250 nsec duration high-intensity pulse. These pulses are then extracted from the PSR and directed to the 1L neutron production target.

WNR receives up to one hundred Hz of H- beam directly from the linac. The beam is transported from the switchyard, through Line-D, then to the WNR 4D neutron-production target for use by WNR experimenters.

Beam delivery to Line-X experiments is provided on an “on demand” basis (in contrast to Line-D’s continuous beam delivery). Initially, the facility is aligned and tuned for beam delivery to a Line-X experiment, then when the experimenters indicate they are ready, a “shot” of beam is produced and accelerated to the experiment.

Beam delivery to the experimental areas requires the coordinated operation of many different systems. We classify our systems according to their general functionality, e.g. cooling water, vacuum, low level RF, high power RF, magnets, magnet power supplies, pulsed power, control computers, etc. An equipment failure in any of these systems will typically interrupt beam delivery. The frequency and duration of these equipment failures negatively impacts our beam delivery reliability. The goal of the LANSCE beam reliability and equipment downtime tracking system is to reduce the frequency of equipment failures and their duration.



This goal is achieved through a four-step process. The process is initiated when scheduled beam delivery is interrupted (beam event). We accurately record the frequency and duration of beam events and their apparent cause. Next, if a beam event lasts for a significant duration, we investigate its root cause and any impediments encountered during restoration efforts. Corrective actions are recommended based upon the results of this investigation.

This process is a modified implementation of classic continuous process improvement (CPI). It is cost efficient and ensures incremental improvement to our beam reliability by “closing the loop” between equipment downtime tracking and beam reliability improvement.

Event data capture

Our beam event data capture system has achieved a good balance between computer automation and manual input by our facility operators. The tracking system is based on beam non-availability events, i.e. if the facility is incapable of delivering the scheduled quality or quantity of beam to an experimental area a beam event is recorded. During continuous-delivery operation, the start of a beam event is identified by the automated comparison of the beam current being delivered to an area with the scheduled current. If the beam current falls to one half of that scheduled, the facility operators are notified and a beam event duration timer starts. During shot-mode operation, automated identification of a beam event start is impractical because there is no scheduled current and no actual beam current except during the shot. We investigated the use of automated accelerator-equipment-readiness monitoring during shot mode as a means of identifying the start of a beam event but abandoned this approach since its accuracy never achieved an acceptable level. We identify the start of beam events during shot mode beam delivery by asking the facility operators to monitor the status of the facility. If a change in the facility readiness occurs that would prevent the delivery of a requested shot, they manually initiate a beam event (computer channel toggle) and the event duration timer starts.

When the facility is again capable of shot-mode beam delivery the operators manually end the beam event (computer channel toggle). In continuous delivery mode, the beam event ends when the beam current delivered exceeds half of the scheduled current.

When a beam event ends, the event timer stops and the operators are prompted to enter the apparent cause of the event, the responsible system, and the affected area into the computer-based central control room log (CCRLog). The CCRLog invokes a menu driven interface for the operators to assign the class of system responsible for the event and the area in which it occurred (injector, linac, Line-X, Line-D, etc.). Additionally, the CCRLog inserts special characters into the entry to assist with automated identification of various components of the CCRLog entry. This creates consistency in the records and facilitates automated extraction of the event-related information at the end of the shift. Figure 1 shows example CCRLog entries for a beam event.

Approximately thirty minutes after the operators close out the CCRLog at the end of their shift an automated computer process extracts, formats, and saves the beam event data. Valuable information concerning beam reliability, equipment availability, failure frequency for a class of equipment, and outage duration statistics is extracted from this data.

Two types of analysis are performed on this data. Overall facility reliability is determined as well as the reliability of classes of systems. This analysis is useful for identification of chronic problems and equipment reliability trends.

Figure 1. CCRLLog entries example for a beam event

```
09:09 |NSC out of production| H- 80KV arcdown. Power supply
will not recover to 80KV, contacted the source crew.
09:19 |NSC back in production|>>10m<{INJ}[LINAC]
The 80KV arcdown caused IBSM1Y to run up to above 1,000mA.
Reset the magnet to 0mA.
```

A second type of analysis is performed if the duration of the event is considered to be significant (currently the threshold for “significant” is three hours) and involves performing root-cause determination and repair impediment identification.

Root cause(s) and repair impediments identification

Beam events that last longer than three hours are relatively rare at LANSCE [1]. They typically account for less than four percent of the total number of events; however, prior to 2001 they accounted for more than fifty percent of the total beam downtime. Their significant impact on beam reliability makes it imperative that we identify the root cause(s) of these types of outages and any impediments to timely restoration of normal beam operation.

When a beam event lasts longer than three hours we begin a root cause investigation by interviewing the personnel involved. To avoid the implication that we are looking for a place to affix blame, we explain to the personnel involved that the reason for the investigation is to find any “lesson learned”.

During the interviews we attempt to determine the following:

- 1) What happened? Typically the operators have a different perspective than the system experts and the experts have a different perspective than management, etc.
- 2) Was the duration of this event typical for this type of problem? If the answer to this question is yes, extra focus should be given to preventing reoccurrence of this class of outage.
- 3) Were adequate resources available? Most long beam events involve extended troubleshooting and/or repairs. Was the appropriate diagnostic equipment available? Were spares readily available? Were sufficient personnel available to assist? Was system documentation available and up-to-date?
- 4) What could we do differently next time to reduce the duration of the downtime?
- 5) How can we prevent or reduce the frequency of this class of outage?
- 6) Were there any impediments to restoring normal operation?

Questions one and two are basic fact-gathering questions. They also serve to refresh recollections about the beam event.

Questions three through five are designed to reveal key process improvement points. They draw directly on the expertise of the personnel involved to provide valuable feedback for process improvement.

Question six is a summary-antithesis of questions three through five – it asks the same question but in the opposite way. Because of this, it frequently yields insights that were not previously revealed.

These interviews provide feedback into the system from the operators, system experts, and managers that may otherwise have been lost. For example, before we began conducting interviews a system expert may have had an idea for reducing the frequency or duration of a class of outage that involved changes to the operator's training programme. Without the interviews it was unlikely that these changes would have been suggested or implemented. Now, however, a mechanism exists for cross-team/group incremental process improvement.

These interviews also reinforce the institutional priority of beam reliability improvement in a positive way.

Based on information gathered in the interviews and elsewhere, we identify specific actions that will reduce the duration of similar class outages. Sometimes the corrective action may be a simple procedure change, other times the interviews will highlight a fundamental resource availability problem that must be addressed by upper level management.

Feedback

Daily, during beam delivery periods, the LANSCE-6 reliability team posts charts in the operations building lobby and on the LANL intranet that indicate how well we are meeting our beam reliability goals. We also post side-by-side comparisons of system availability performance.

Weekly we summarise the previous week's beam reliability data and report this to LANSCE division management.

At the end of each beam operation month we produce beam reliability reports for each experimental area. These reports contain graphs and tables detailing the beam delivery and equipment availability statistics for the month. These tables can be used to quickly identify systems that are experiencing chronic beam reliability problems. A section at the end of these reports contains the analysis of events that lasted longer than three hours.

These greater-than-three-hour outage investigation reports contain a description of the event, its root cause, contributing factors, an analysis of the various aspects of the outage, corrective actions that have been taken and any additional recommended corrective actions. The recommendations are based on input from the personnel involved with the beam event and knowledgeable third party evaluation of the event as a whole.

These recommendations address actions necessary to reduce the likelihood of similar occurrences (root cause) and actions that will mitigate the impact of similar outages in the future (restoration efficiency). We try to ensure that the recommendations are practical and workable. In cases where the cost to benefit ratio may be questioned, the recommendation is stated in those terms.

After the reports are reviewed by the personnel involved in the beam event, they are placed on the LANL intranet and the appropriate operations, support, and management personnel are notified.

The monthly reports provide an accurate measurement of how well we are meeting our beam reliability goals. Equally important, they provide a view of the issues associated with meeting these goals. Understanding the issues associated with meeting our reliability goals allows our managers to make better informed resource allocation decisions and allows operations and support personnel to implement corrective actions that will incrementally improve the reliability of the entire facility.

Summary

LANSCE achieved its design energy in 1972. Since then the facility has grown and adapted to the changing expectations of our customers and sponsors. Through this time one demand has remained consistent – the facility must operate reliably. As our facility enters its fourth decade, proper resource allocation to achieve satisfactory beam reliability remains challenging. The beam reliability and equipment downtime tracking system provides LANSCE management with the necessary information to make informed resource allocation decisions. Resource allocation, however, is not the only essential aspect of beam reliability improvement. Feedback from the system experts, operators, and managers provides information necessary for incremental process improvement. Initiating actions based on feedback from those involved with facility operations “closes the loop” between tracking and recording facility operation data and actually improving beam delivery reliability.

REFERENCES

- [1] LANSCE beam availability reports for 1995 through 2002.

COMMENTS TO ACCELERATOR-DRIVEN SYSTEM

Taka aki Matsumoto
Hokkaido University
Sapporo 060-0813, JAPAN
mtmt@qe.eng.hokudai.ac.jp

Abstract

Accelerator-driven system (ADS) that was a subcritical nuclear reactor driven by a high power proton accelerator was recently studied by several large organisations over the world. This paper described two comments for ADS: philosophical and technological ones. The latter was made from a view point of micro ball lightning (BL) that was newly discovered by the author. Negative and positive aspects of micro BL for ADS were discussed.

Introduction

High energy proton beams of about 1 GeV provided an intensive neutron source by spallation reactions with a target. Those neutron sources were actually applied to fundamental researches such as neutron scattering and irradiation facilities, in which high neutron flux beams were continuously required [1]. Furthermore, an idea of refreshment of spent nuclear fuels by a similar proton accelerator was early proposed [2]. On the other hand, the author proposed the nuclear incineration of a minor actinide by a high power proton accelerator [3]. And the idea progressed to a hybrid system of an accelerator and a nuclear reactor, called ADS [4]. ADS was recently studied by several large organisations over the world [5]. Here, the nuclear reactor was to be operated under a subcritical condition so that it could be essentially free from run away accidents.

This paper described two comments for ADS: philosophical and technological ones. The latter was made from a view point of micro BL that was recently discovered by the author during electrical discharge experiments. Since micro BL was easily generated anywhere in laboratory as well as in natural fields, appropriate cares should be taken to effects of micro BL on ADS. However, positive aspects of micro BL was also discussed.

Philosophy for ADS

In general, it was important to have a solidified philosophy, especially when we wanted to perform R&D for a large scale system. For ADS, why did we try to combine a nuclear reactor with an accelerator? This question should strongly arise by considering a fact that a large number of nuclear reactors were already producing electricity and greatly contributing to civilian lives over the world. Many specialists of nuclear reactor would be reluctant to have a more complicated system like ADS.

Here, we should review developments of nuclear reactor. We had a future review from light water reactor (LWR) to fast breeder reactor (FBR). This review was not accepted at the present time. Even if the review was authorised, it seemed to the author that LWR and FBR stood on the nearly same stage in a long eyed history of nuclear reactors. Since the history of nuclear reactor was not so long, it would be difficult to have a long eyed review. Now, it would be useful to apply analogy in order to review a new thing.

A good analogy would be to see the history of ship that was a nearly long as that of human being. In an ancient period, a wooden log or canoe were a good transport tool. Later, they learned to use wind energy for transport and sailing boats appeared. Controlling sail, they could make boats run. Furthermore, sailing boats were replaced by steam boats that were driven by supplying energy from outside. Steam boats could run even on a day with no wind and more safely carried many people and heavy packages. Moreover, steam boats opened new feasibility, for example, running over and under water.

Today's nuclear reactors were very similar to sailing boats. By moving control rods, we operated nuclear reactors. But they could not only be operated under a subcritical condition but also run away in a super critical condition as sailing boats often wrecked on a stormy day. ADS that was driven by external energy would correspond to steam boats, and open new feasibility in future like steam boats did.

Technological comments from micro BL

The reliability of ADS was being examined from various aspects of technology [5]. Here, a technological comment was described from a very different aspect: micro BL [6]. Micro BL could be very easily generated in laboratory as well as in natural fields. Two kinds of micro BL (external and internal) were discussed, related to the reliability of ADS.

Brief review of micro BL [6]

Micro BL could be easily generated when a large number of electrons were charged over an atomic or molecular cluster. The majority of the electrons were scattered out with their repulsive force, but some portion of them covered the surface of the cluster. Here, the electrons were assumed to be interconnected to each other. Such special state of the electrons could cause several curious properties of micro BL.

First, the bonding of the interconnected electrons was so strong that nuclear reactions easily occurred in the cluster. Since micro BL was a strongly coupled multi body system, new kinds of nuclear reaction became possible, called electro-nuclear reactions (ENRs). There were several ENRs that were found so far, depending on the strength of the bonding. Among them, the most significant one was electro-nuclear collapse (ENC) that could be induced by the electromagnetic force. And ENC could be followed by electro-nuclear regeneration (ENG) that regenerated conventional elements. Light elements such as carbon, oxygen and hydrogen were regenerated by ENC of heavy elements such as lead and cadmium.

Secondly, micro BL showed an extraordinary penetration of non-conductive materials such as plastic. This was also caused by the interconnected electrons of micro BL that had few free electrons to interact with electrons contained in the materials.

Thirdly, micro BL could be generated by other physical effects such as compression, friction, irradiation and ultrasonic vibration. When these effects were mixed with electrical discharge, the formation of micro BL could be accelerated. It was recently found that a large number of micro BL could be generated during violent natural phenomena such as lightning, earthquake and volcanic eruption.

Negative effects of micro BL

There were two kinds of micro BL that could potentially damage ADS: external and internal ones. A huge number of external micro BL were often generated outside an ADS facility during violent natural phenomena. Some portion of them could easily enter the ADS facility, because micro BL had the property of extraordinary penetration through non-conductive materials such as concrete. Alternatively, micro BL could enter the ADS facility through leading wires of electricity, because they could run through the wires. The invading micro BL could damage electrical devices by their high density charges and microscopic explosions of their nuclear collapse.

On the other hand, the internal micro BL could be generated in a target system by different processes: two potential processes were considered. First, losing their kinetic energy, proton beams became hydrogen atoms or molecules that could be accumulated in a small local point in the target. Those hydrogen could very easily form micro BL and induce nuclear collapse that generated jet like reactions. This might have caused a pit erosion that was a severe problem for the target. Secondly,

micro BL also could be generated by little cavity. For a coolant fluid with a severe condition, little cavity could be often generated by rapid changes of temperature and pressure. When little cavity collapsed, micro BL could be effectively generated and damage a coolant vessel.

Positive aspects of micro BL

We could expect some positive aspects of micro BL for ADS, if we apply the curious properties of micro BL. First, an extremely high current accelerator of proton beams might be obtained. As we wanted to obtain a much higher power proton accelerator, a space charge effect became a severe problem. However, micro BL that could contain a large number of protons, more than 10^{15} protons, was strongly bonded by the interconnected electrons and fairly stable.

Two different kinds of micro BL acceleration were proposed [7]:

1. acceleration after micro BL was formed, and
2. coincidental combination of accelerated proton and electron beams.

The latter method could be applied to ADS without a large modification of the conventional proton accelerator.

Secondly, micro BL had the property of extraordinary penetration so that the window problem might be reduced to some extent.

Discussion

The idea of ADS was born about ten years ago and the study started by large organisations. Design considerations were focussed in hybrid systems of the conventional proton accelerator and nuclear reactor. So design changes to the both devices were required to be small as possible. However, as the study progressed in future, our consideration would go to a direction of designing accelerators and nuclear reactors that could be the most suitable to ADS. For example, ADS with a large heat capacity by using materials such as graphite might be considered in order to compensate frequent trips of the accelerator.

New hybrid systems could be born only by combining the conventional accelerator and nuclear reactor. If one of them or both will be replaced with new ones in the next steps, we could expect that such hybrid systems would become revolutionarily new [8]. The application of micro BL might be one of good candidates.

REFERENCES

- [1] See Proceedings of International Conference of Advanced Neutron Source (ICANS).
- [2] Takahashi, H. *et al.*, BNL-28779, (1980).
- [3] Matsumoto, T., “Calculations of a Proton Accelerator Driven Incineration Reactor”, Proc. of International Conference of Emerging Nuclear Energy Systems (ICENES’89), Karlsruhe, p. 75, (1989).
- [4] Matsumoto, T., “Renaissance of Research”, Genjitu (in Japanese) published by Kyoto Univ. Research Reactor Inst., Vol. 71, p. 6, (1988).
- [5] For example, Proceedings of this conference (2002).
- [6] Matsumoto, T., “Steps to the Discovery of Electro-Nuclear Collapse: Collected Papers (1989-1999)”, private publication, (2000).
- [7] Matsumoto, T., “Acceleration Methods of Itonic Clusters”, Proceedings of Linear Accelerator Meeting in Japan, Himeji, p. 77, (2000).

R&D STATUS OF SUPER-CONDUCTING PROTON LINAC AND THE KEK/JAERI HIGH INTENSITY PROTON ACCELERATOR PROJECT

Nobuo Ouchi

JAERI

Tokai-mura, Ibaraki-ken, 319-1195, JAPAN

Abstract

R&D work of a super-conducting proton linac has been continued since 1995 in JAERI for the neutron science project and the current KEK/JAERI high intensity proton accelerator project. In the cavity development work, we obtained good performance, high field and high quality factor. As the next step of the R&D, a prototype cryomodule was fabricated. The cooling and high power RF tests of the cryomodule were performed successfully. The RF test is being continued to obtain stable accelerating field in the pulsed operation. In the high intensity proton accelerator project, the super-conducting linac is planned in the energy region from 400 to 600 MeV and the beams will be delivered towards the transmutation experimental facility (TEF). TEF consists of two facilities; the transmutation physics experimental facility (TEF-P) and the target test facility (TEF-T). This paper provides the R&D status of super-conducting proton linac and the high intensity proton accelerator project concerning the super-conducting linac and TEF.

Introduction

JAERI proposed the neutron science project (NSP) since 1995 for neutron science, nuclear physics, neutron irradiation, RI beam science and engineering study of nuclear waste transmutation [1]. The accelerator for the NSP was designed to be a 1.5 GeV linac and two storage rings, and the maximum beam power was intended to be 5 MW. Super-conducting structure was chosen for the high-energy part of the linac from 0.1 to 1.5 GeV.

High energy accelerator research organisation (KEK) also planned the Japan hadron facility (JHF) for neutron science, muon science, exotic nuclei science, fundamental particle physics and neutrino oscillation experiment [2]. It was planned that the JHF comprises a 50 GeV main synchrotron, a 3 GeV rapid cycling synchrotron and a 200 MeV linac.

In 1999, JAERI and KEK agreed each other to bring the NSP and the JHF into one project because both projects have common features which are summarised in a single key word; “high power proton accelerators” [3]. The joint project is named high intensity proton accelerator project, which consists of a 600 MeV linac, a 3 GeV synchrotron, a 50 GeV synchrotron and experimental facilities. A super-conducting proton linac and a transmutation experimental facility are planned in the project.

R&D work of the super-conducting proton linac for the NSP has been performed since 1995 in collaboration with KEK. In this work, development of super-conducting cavities and cryomodule has been performed. After the establishment of the joint project, the R&D target is shifted from the NSP toward the high intensity proton accelerator project.

R&D status of super-conducting proton linac in JAERI is presented in this paper. The super-conducting proton linac and the transmutation experimental facility in the high intensity proton accelerator project are also presented.

R&D status of super-conducting proton linac

As the first step of the R&D work, development of super-conducting cavity for a proton linac has been performed. Prior to the cavity development, infrastructure was prepared in JAERI, i.e., a cryostat for the cavity test, a clean room for cavity assembly, a high pressure water rinsing system and a furnace for heat treatment. In the cavity development, 600 MHz single-cell and multi-cell cavities were fabricated and tested. As the next step, a prototype cryomodule has been developed.

Cavity development

600 MHz single-cell cavities of β (ratio of the beam velocity to the light velocity)=0.5, 0.89 and 5-cell cavities of β =0.5, 0.89 and 0.6 were fabricated and tested. Two 5-cell cavities of β =0.6 have been installed in the prototype cryomodule. Pure niobium sheets (RRR~200) of 3 mm thickness were used for the cavity fabrication. The fabrication process consists of deep drawing, trimming and electron beam welding. The welding for some cavities was carried out in the KEK workshop.

As for the surface treatment, barrel polishing and electro-polishing were applied for the cavities. Typical removal thickness were 10~50 μm and 30~100 μm for the barrel and electro-polishing, respectively. After the polishing, heat treatment at 750°C for 3 hours was performed in order to degas hydrogen absorbed during the electro-polishing. As for the 5-cell cavities, pretuning was performed to

adjust resonant frequency and field flatness, and then electro-polishing of 10~30 μm was applied. After the final electro-polishing, high pressure water rinsing at 8-9 MPa for 1-2 hours and cavity test (vertical test) at 2K were performed. In the case that the cavity performance was not sufficient, the electro-polishing and/or the high pressure water rinsing were carried out again.

Figure 1. Test results for single-cell cavities

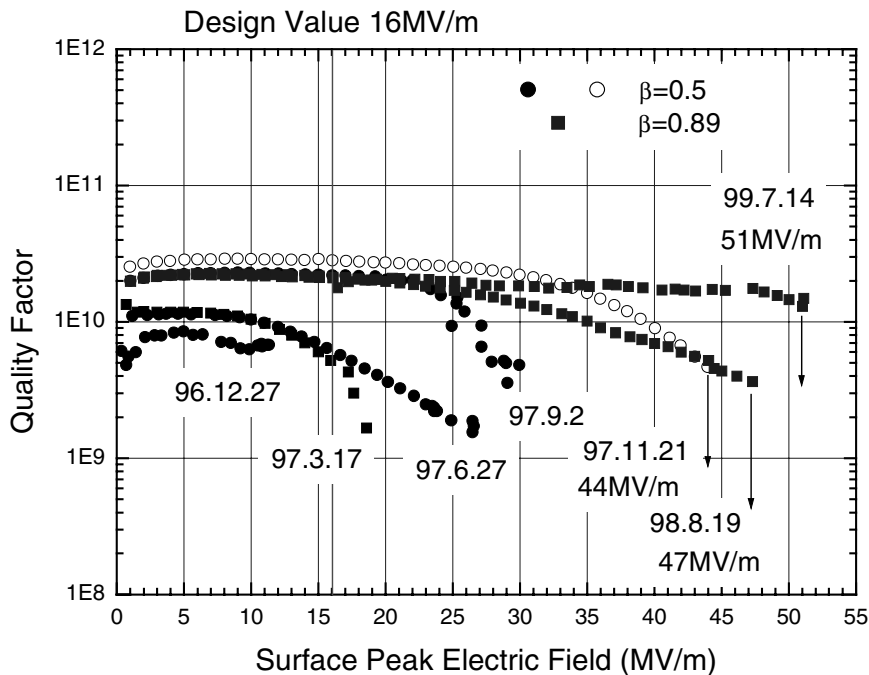
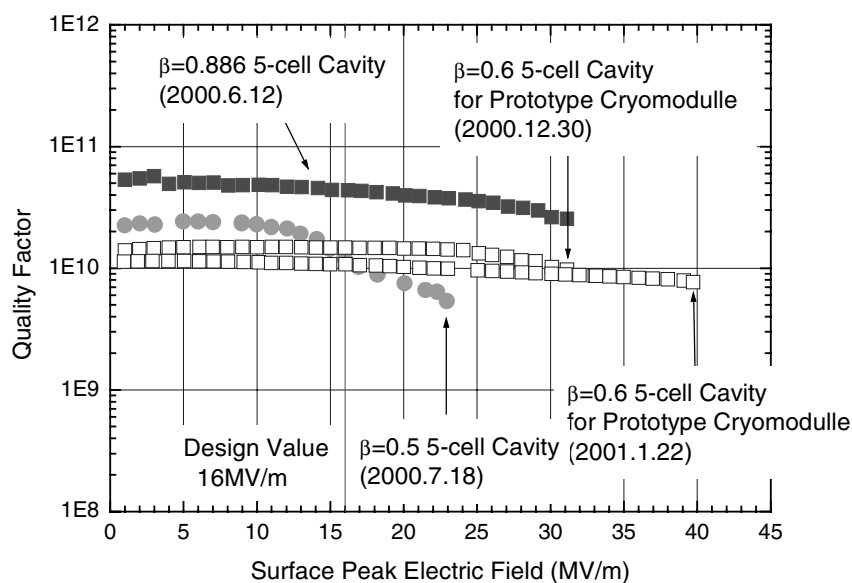


Figure 1 shows the results of the cavity test for the single-cell cavities, where two cavities of $\beta=0.5$ and a cavity of $\beta=0.89$ were fabricated and tested. The first test was made at the end of '96; the cavity performance was not good, low field and low quality factor, because of improper condition of the high pressure water rinsing. The high pressure rinsing was repeated two times and the surface peak field reached 27 MV/m, which exceed our design value of 16 MV/m (June 1997). The electro-polishing was carried out and high quality factor about $2E11$ was obtained (September 1997). For the second cavity of $\beta=0.5$ and the cavity of $\beta=0.89$, surface peak field of 44 MV/m and 47 MV/m were obtained in each first test, respectively [4].

Figure 2 shows the results for the 5-cell cavities. For the cavities of $\beta=0.5$ and 0.89, surface peak field of 23 and 31 MV/m were obtained, respectively. For the first cavity of $\beta=0.6$, surface peak field of 31 MV/m was obtained, where temperature was increased at the power coupler port. Therefore, for the second cavity, chemical polishing ($\sim 5\mu\text{m}$) was applied at the RF ports. Then the field increased to 40 MV/m for the second cavity as shown in Figure 2 [5].

In the super-conducting linac for the NSP, surface peak field of the cavities was designed to be 16 MV/m and we obtained much higher. Therefore, the design field in the high intensity accelerator project is increased to 30 MV/m.

Figure 2. Test results for 5-cell cavities



Design and development of 972 MHz cavity for the high intensity proton accelerator project is in progress. First test of the single-cell cavity of $\beta=0.725$ was performed and surface peak field of 38 MV/m was obtained. As for the multi-cell cavity, surface treatment and pretuning of a 9-cell cavity are in progress now and the first result will be obtained soon.

Prototype cryomodule

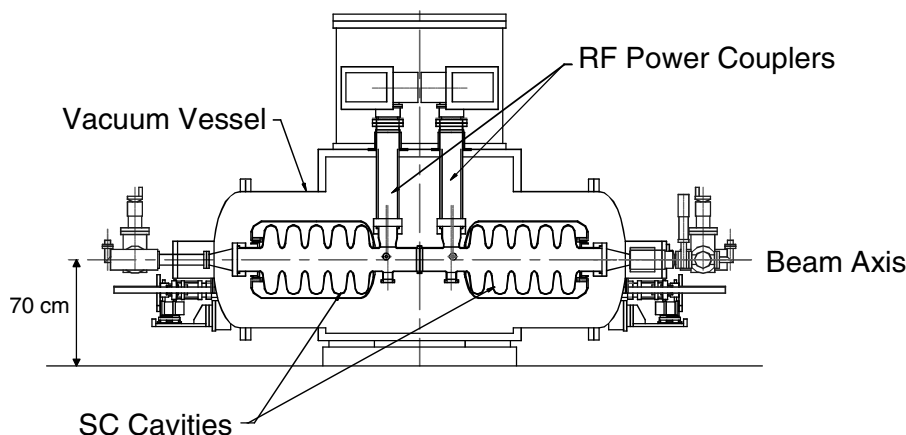
As the next step of the R&D work, a prototype cryomodule was fabricated. One of the objectives of the cryomodule development is demonstration of total performance of a superconducting proton linac. Cavity installation process into a cryomodule is key issue to avoid particle contamination in the cavity which causes field emission in the high field operation. Cavity support and tuning system are important to reduce Lorentz force detuning and to control cavity field. Cryogenic performance such as heat leak and control of the liquid helium pressure is also important for operating cost and stable operation. The other objective is demonstration of stability for accelerating field in a pulsed operation [6]. For the high intensity proton accelerator project, pulsed operation is planned and pulsed Lorentz force due to the electromagnetic field of the cavity leads dynamic detuning and then disturbs the stability of the field.

Cryomodule design and assembling

Figure 3 shows the schematic view of the cryomodule [7]. The cryomodule includes two 5-cell cavities of $\beta=0.6$ as described above. Jacket type liquid helium vessel is applied as shown in Figure 3. The jackets are made of stainless steel. The joint between niobium and stainless steel has been performed by the HIP (hot isostatic pressing) method, where copper plate of 1mm thick is used as an insertion material between niobium and stainless steel. Two jackets are connected through a reservoir tank located above the jackets. The volumes of each jacket and the reservoir tank are about 80 and

30 liters, respectively. The cryomodule is designed to achieve 2K operation. Liquid helium at 4.2K is fed from a Dewar vessel and cooled down by a heat exchanger and a JT valve to 2K. Thermal intercepts at 4.2K are located at beam pipes, RF input couplers and a cavity support in order to reduce heat leak to the 2K jackets. Thermal shield at 80K is also located between a vacuum vessel and 4K thermal intercepts. A coaxial type RF power coupler is installed for each cavity. Magnetic shield of the Permalloy (2 mm in thickness) is placed on the inner surface of the vacuum vessel.

Figure 3. Schematic view of the prototype cryomodule



Connection of the two cavities and beam pipes were performed in a class-10 clean room in order to avoid particle contamination. Cavity installation into the cryomodule, power coupler installation and leak tests of the cavity were also carried out in a class-100 clean room.

Test results

Cooling time from room temperature to 4K was about 2 days. The cooling of thermal intercept needs long time. Improvement of conductance for the thermal intercept can reduce the cooling time. Cooling time from 4K to 2K was short enough to be about 3 hours.

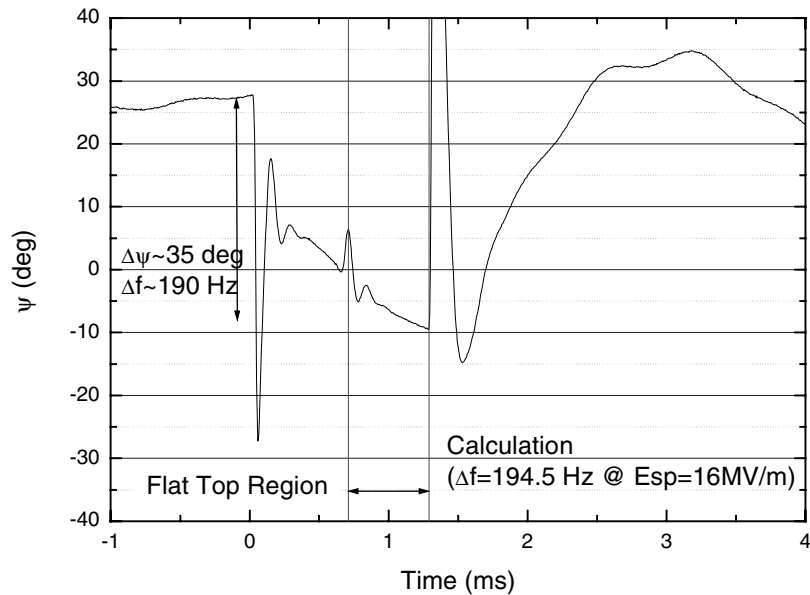
Heat leak of the liquid helium jacket was designed to be 1.7W, however, the measured results were about 10W at both 4K and 2K. The reason of this disagreement is not clear; cooling of the thermal intercept is not sufficient or the design has some problems.

Loaded Q's of the two cavities were measured to be 1.25E6 and 1.13E6. The design value for the loaded Q was 1.6E6, which was calculated using the MAFIA code. The disagreement between measured and calculated values was considered due to the uncertainty of the calculation. We are planning to make recalculation using the HFSS code to achieve more accurate estimation.

Tuning sensitivities of the cavities were measured to be 193 and 184 Hz/mm, which are agreed with the design value of 194 Hz/mm. Frequency shift sensitivities for the liquid helium pressure were also measured in the cool down from 4K to 2K. The measured results were 682 and 716 Hz/kPa, which are agreed fairly well with the calculated results of 888 Hz/kPa.

Measurement of the Lorentz force detuning is one of the most important issue for the cryomodule test. The detuning is proportional to square of the accelerating gradient (E_{acc}). The detune constants were measured in the CW operation; 9.4 and 15.6 Hz/(MV/m)² for the two cavities. The calculated value is 9.0 Hz/(MV/m)² and one of the measured results agrees well but the other is not. The reason is not clear and re-measurement is necessary.

Figure 4. Dynamic detune angle measured in a pulsed operation



As for the high power test of the cryomodule, surface peak field of 10 MV/m and 16 MV/m were achieved successfully in a CW and a pulsed operation. As an example of the high power test, Figure 4 shows the dynamic detune angle (ψ) in a pulsed operation at the condition of rise time of 0.7 ms, flat top of 0.6 ms, repetition rate of 50 Hz and surface peak field of 16 MV/m at the flat top. Fast fluctuations at the beginning of the rise time, beginning and end of the flat top in Figure 4 were due to the response of the feedback loop in the low level RF control system. Slow fluctuation was due to the Lorentz force detuning. The variation of the detune angle from the beginning of the pulse to the flat top was about -35 deg, which corresponds to the detuning of about -190 Hz. The experimental result for the Lorentz force detuning agreed with the calculated value of -194.5 Hz at surface peak field of 16 MV/m.

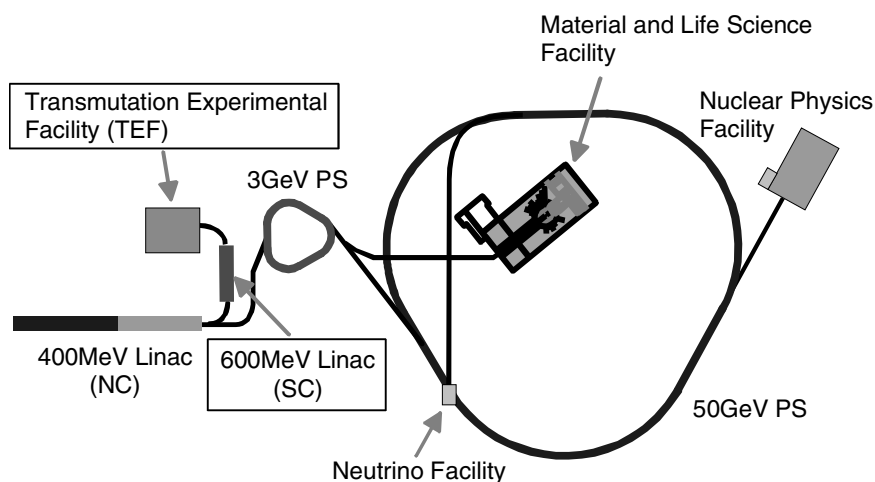
Final goal of the test is demonstration of stable accelerating field in the condition of two-cavity operation by one RF system, which is the scheme designed for the high intensity proton accelerator project as described in the next section. Optimisation of low level RF control system is in progress now.

High intensity proton accelerator project

Overview of the project

Figure 5 shows a schematic view of the accelerator complex of the high intensity proton accelerator project. The accelerator consists of a 600 MeV linac, 3 GeV and 50 GeV synchrotrons. Fundamental particle, nuclear physics and neutrino experiments are planned with proton beams from a 50 GeV synchrotron at the nuclear physics facility and the neutrino facility. The neutron science, muon science and exotic nuclei science will be studied with 3 GeV proton beams at the material and life science facility. R&D of ADS is planned using 600 MeV beams at the transmutation experimental facility (TEF). The linac up to 400 MeV consists of normal conducting structures and its repetition rate is 50 Hz. The 25 Hz pulses will be injected into the 3 GeV synchrotron and the other 25 Hz pulses will be led to a super-conducting linac. Therefore, the super-conducting linac will be operated only for the TEF and flexible experiments will be available for the super-conducting linac and the TEF. As the 400 MeV linac accelerates negative hydrogen beams for the injection to the 3 GeV synchrotron, the super-conducting linac also accelerates negative hydrogen beams.

Figure 5. Schematic view of the high intensity proton accelerator project



The project is divided into two phases. In the first phase, the 400 MeV linac, the two synchrotrons, the material and life science facility and the nuclear physics facility are constructed. The Phase-I already started in 2001. In the second phase, the super-conducting linac, the TEF and the neutrino facility are planned. The Phase-II will be start at 2004.

Super-conducting proton linac

Table 1 summarises the parameters of the super-conducting linac [8]. The linac consists of 11 cryomodules containing two 9-cell 972 MHz cavities. Quadrupole magnets provide focusing with a doublet lattice located in a room temperature region between cryomodules. The room temperature region also contains beam diagnostics and vacuum system.

Grouping of cavity β has not been fixed yet. It is considered that one or two groups are enough because the beam β does not increase so much in the energy region from 400 to 600 MeV. The grouping will be determined with the consideration of the beam dynamics.

Table 1. Parameters for the super-conducting linac

Energy	400-600 MeV
Frequency	972 MHz
β	0.71-0.79
No. of cell	9 cell/cavity
No. of cavity	2 cavity/cryomodule
No. of cryomodule	11 cryomodules
Length	57.7 m
Surface peak field	30 MV/m
Accelerating field (Eacc)	9.7-11.1 MV/m
Synchronous phase	-30 deg
No. of klystron	11
Total RF power (peak)	10 MW
Loaded Q	$\sim 5E6$

The surface peak field of the cavity is designed to be 30 MV/m. The accelerating fields of the cavities are in the range between 9.7 and 11.1 MV/m, which depend on the beam β . The length of the accelerating section is 57.7 m. Additional length of about 20 m is necessary for the beam matching section at the upstream region of the accelerating section.

RF system is designed so as to drive two cavities with one klystron. Vector sum control of two cavities is studied in the test of the prototype cryomodule. Total RF power is 10 MW and RF powers for each klystron and power coupler are about 1 MW and 500 kW, respectively.

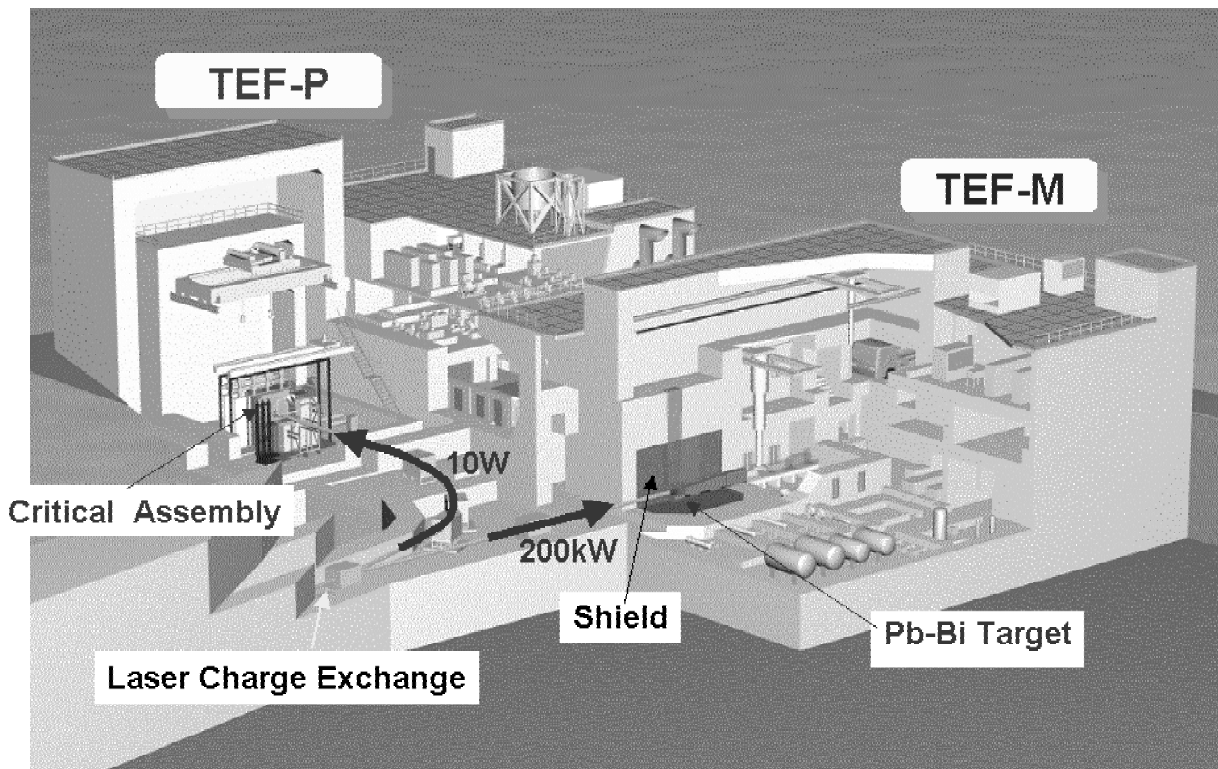
Transmutation experimental facility

The transmutation experimental facility (TEF) consists of two buildings; the transmutation physics experimental facility (TEF-P) and the ADS target test facility (TEF-T). Figure 6 shows the conceptual view of the TEF [9].

TEF-P is a zero-power critical facility, which operates with a low power proton beams less than 10 W to investigate the reactor physics and the controllability of ADS. The maximum fission power is preliminary decided as 500 W. The critical assembly is designed with referring to the fast critical assembly (FCA) in JAERI/Tokai for the reuse of the nuclear fuel in FCA. The design is the horizontal table-split type critical assembly with a rectangular lattice matrix. Low current proton beams are extracted by a laser charge exchange technique from the high intensity negative hydrogen beams of 200 kW, where most of the beams are introduced into the TEF-T. The negative hydrogen beams are exposed by a YAG-laser, which can strip one electron from the negative hydrogen, so as to change small amount (below 10W) of negative hydrogen to neutral one. The negative and neutral hydrogen are then separated with a bending magnet. The neutral hydrogen is converted to the proton by a stripping foil and the beams are introduced into the TEF-P. The pulse width of the proton beams is controlled by changing the duration of the laser exposure in the range from 1 ns to 0.5 ms. Demonstration of the charge exchange system is scheduled in 2002 using 2 MeV negative hydrogen

beams at JAERI. The measurement of transmutation rate of MA is also planned using fission chambers in the TEF-P, in which very short pulses about 1ns are necessary to apply time-of-flight technique.

Figure 6. Conceptual view of the transmutation experimental facility (TEF)



TEF-T is a material irradiation facility, which can accept a maximum 200 kW/600 MeV beams into the spallation target of the Pb-Bi eutectic target. The R&D items performed in the TEF-T are (1) investigation of irradiation damage and lifetime of the window and structural material, (2) investigation of compatibility of material with flowing liquid metal under the irradiation of high power proton beams and (3) demonstration of the liquid metal spallation target system. The proton beam size of 4 cm in diameter at the target position is designed so as to achieve average beam density about 30 mA/cm², which is expected for the real ADS plant. The Pb-Bi eutectic is filled into cylindrical vessel of 15 cm in diameter and 60 cm in length made of stainless steel. The cylindrical volume of 4 cm in diameter and about 8 cm in length can be used for the material irradiation tests, where more than 10 dpa/year can be achieved. The maximum temperature and flow rate of Pb-Bi target are designed to be 450°C and 2 m/s, respectively. The target vessel is mounted on a movable trolley and can be withdrawn to an access cell, where replacing target cell, cleaning up residual Pb-Bi and picking up irradiated test pieces are carried out.

Summary

R&D work of the super-conducting proton linac is continued since 1995. As the first step of the R&D, super-conducting cavities have been developed and good performance of the single- and multi-cell cavity has been obtained. As the next step, the prototype cryomodule has been developed in order to demonstrate the total performance as the super-conducting accelerating system. The cooling and high power test of the cryomodule has been performed successfully. Further test is planned to demonstrate stable accelerating field in a pulsed operation.

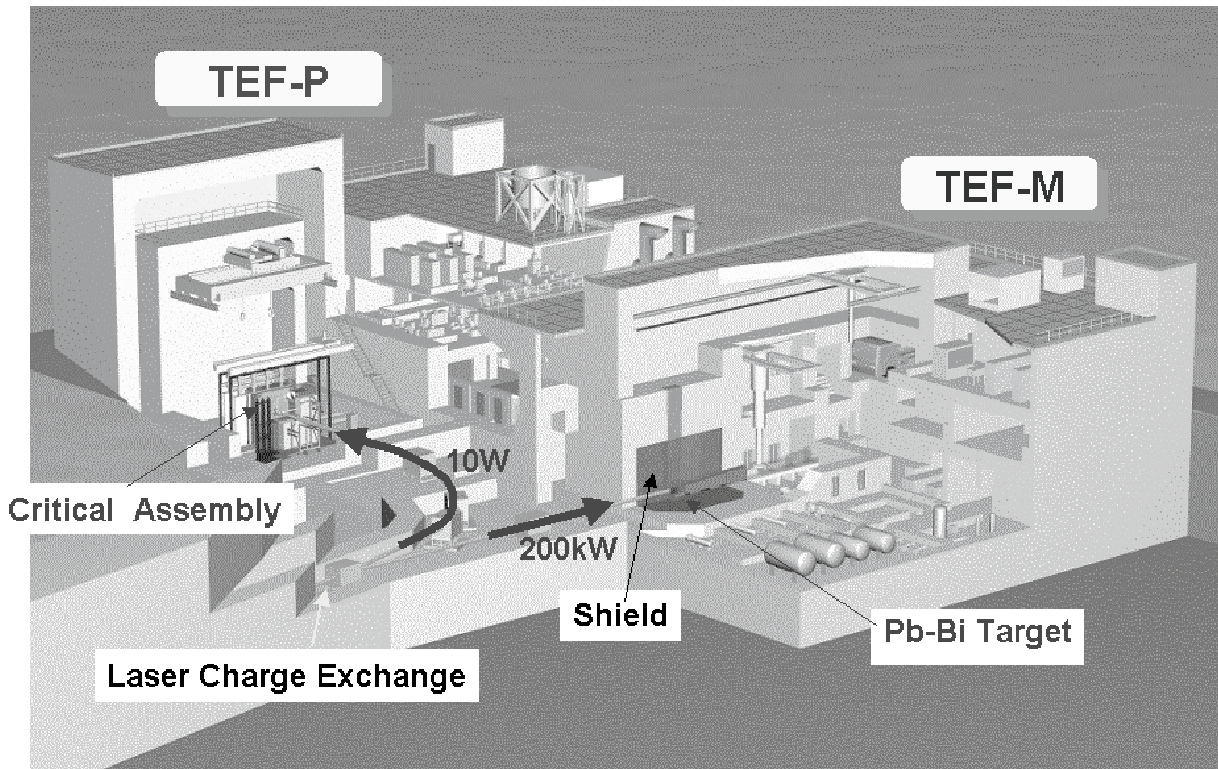
In the high intensity proton accelerator project promoted by JAERI and KEK, the super-conducting proton linac and the transmutation experimental facility are planned. The super-conducting proton linac covers the energy range between 400 and 600 MeV for the transmutation Experimental facility. Investigation of reactor physics and target material for the ADS will be performed in the TEF-P and TEF-T, respectively. These facilities are planned in the second phase of the project.

REFERENCES

- [1] Mizumoto, M. *et al.*, "A High Intensity Proton Linac Development for the JAERI Neutron Science Project", Proc. of LINAC98, Chicago, USA (1998).
- [2] Yamazaki, Y., "The Japan Hadron Facility Accelerator", Proc. of APAC98, Tsukuba, Japan, p. 314 (1998).
- [3] Yamazaki, Y. *et al.*, "Accelerator Complex for the Joint Project of KEK/JHF and JAERI/NSP", Proc. of PAC99, New York, USA, p. 513 (1999).
- [4] Ouchi, N. *et al.*, "Development of Super-conducting Cavities for High Intensity Proton Accelerator in JAERI", IEEE Trans. on Applied Super-conductivity, vol. 9, No. 2, p. 1030, (1999).
- [5] Takeda, O. *et al.*, "Performance of 600MHz 5-cell Super-conducting Cavities for Prototype Cryomodule at JAERI", Proc. of SRF2001, Tsukuba, Japan, PR013, in press.
- [6] Ouchi, N., "Pulsed SC Proton Linac", Proc. of LINAC2000, Monterey, USA, WE205 (2000).
- [7] Ouchi N. *et al.*, "600 MHz Prototype Cryomodule for High Intensity Proton Linac at JAERI", Proc. of SRF2001, Tsukuba, Japan, PT029, in press.
- [8] Hasegawa, K. *et al.*, "System Design of a Super-conducting Linac for the High Intensity Proton Accelerator Project (KEK/JAERI Joint Project)", Proc. of SRF2001, Tsukuba, Japan, PS003, in press.
- [9] Oigawa, H. *et al.*, "Conceptual Design of Transmutation Experimental Facility", Proc. of GLOBAL2001, Paris, France (2001).

beams at JAERI. The measurement of transmutation rate of MA is also planned using fission chambers in the TEF-P, in which very short pulses about 1ns are necessary to apply time-of-flight technique.

Figure 6. Conceptual view of the transmutation experimental facility (TEF)



TEF-T is a material irradiation facility, which can accept a maximum 200 kW/600 MeV beams into the spallation target of the Pb-Bi eutectic target. The R&D items performed in the TEF-T are (1) investigation of irradiation damage and lifetime of the window and structural material, (2) investigation of compatibility of material with flowing liquid metal under the irradiation of high power proton beams and (3) demonstration of the liquid metal spallation target system. The proton beam size of 4 cm in diameter at the target position is designed so as to achieve average beam density about 30 mA/cm², which is expected for the real ADS plant. The Pb-Bi eutectic is filled into cylindrical vessel of 15 cm in diameter and 60 cm in length made of stainless steel. The cylindrical volume of 4 cm in diameter and about 8 cm in length can be used for the material irradiation tests, where more than 10 dpa/year can be achieved. The maximum temperature and flow rate of Pb-Bi target are designed to be 450°C and 2 m/s, respectively. The target vessel is mounted on a movable trolley and can be withdrawn to an access cell, where replacing target cell, cleaning up residual Pb-Bi and picking up irradiated test pieces are carried out.

THE USE OF NEG VACUUM PUMPS ON THE LEDA RFQ¹

Robert Valdiviez, Dale Schrage
Los Alamos National Laboratory

Stewart Shen, Keith Kishiyama
Lawrence Livermore National Laboratory

Abstract

The low energy demonstration accelerator (LEDA) radio frequency quadrupole (RFQ) accelerator utilises non-evaporable Getter (NEG) vacuum pumps on each of the six vacuum waveguides that couple RF power into the RFQ. The RFQ produces a 6.7 MeV proton beam at 100 mA under a CW condition. The peak RF power consumption of the RFQ is in the neighbourhood of 2.2 MW for 100 mA, CW beam operation [1]. The RF power is divided approximately equally amongst six waveguides, with each waveguide conducting a peak of approximately 367 kW of RF power. Each waveguide incorporates a vacuum pumping package that consists mainly of a NEG pump and a turbo pump. The NEG is the main pumping unit with a hydrogen pumping speed of about 1 300 liters/sec. The performance of the NEG pumping units has been found to be very reliable at maintaining a waveguide vacuum level of approximately $2.0E-7$ Torr under full power operating conditions. RFQ conditioning and operational tasks have been supported well by this vacuum pumping design. This paper will discuss the details of the waveguide vacuum pumping design, the NEG testing conducted to support the design, and the operational experience with the NEG pumping units.

1. Work sponsored by the U.S. Department of Energy.

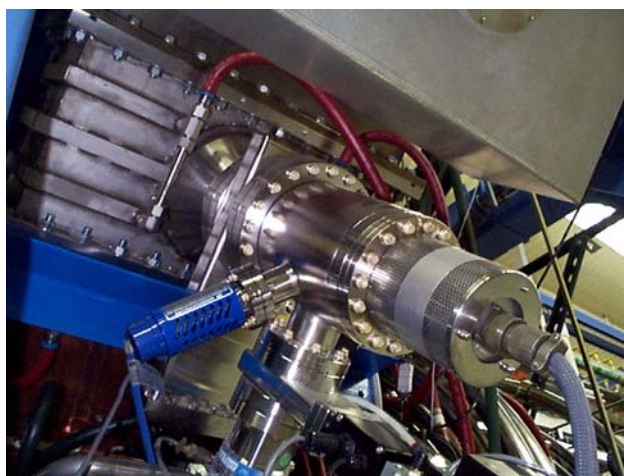
Introduction

NEG vacuum pumps are noted for their high pumping speed of hydrogen [2]. The main constituent to pump in the RFQ and waveguide vacuum space is hydrogen, making this a good application for a NEG pump. The NEG pump cartridge design allows for a relatively compact unit to be fastened to the waveguide. The spaces surrounding the RFQ and waveguide are congested with equipment, so a compact design of the pumping units was necessary. In addition, since the NEG pump uses no moving parts there is no vibration input to the waveguide. The pumping unit assembly on the waveguide does include a small turbo pump. The rotors of turbo pumps are balanced to very close limits, so no problematic vibration input was added by the turbo pump either. Vibration in the waveguides can be directly transferred into the RFQ since they are mechanically coupled solidly to each other.

The waveguide arrangement used to transition from an RF window to an RF port of the RFQ starts with a rectangular cross-section waveguide of half-height WR2300 dimensions and transitions to the RF port dimensions using a tapered ridge-loaded waveguide design [3]. The RF coupling slot in the end of the waveguide is approximately 0.060 inch in height and 3.5 inch wide. This small slot that provides RF coupling between the waveguide and the RFQ inner space is too restrictive to allow the RFQ vacuum pumping system to also pump the waveguides effectively. For this reason a separate vacuum pumping unit is placed on each of the six RF waveguide assemblies. The pumping unit is located immediately down-stream of the RF window assembly, and pumps both the RF window vacuum volume and the waveguide vacuum volume. Figure 1 is a photograph of one of the vacuum pumping assemblies mounted on a waveguide assembly.

The performance and lifetime of the RF window is strongly dependent upon the pressure that is maintained in the vacuum side of the window. This trend was demonstrated during the extensive high-power RF testing and conditioning of the 1.0 MW rated RF windows [4]. The vacuum pumping design of the window and waveguide volumes has to reliably maintain a vacuum pressure level on the order of $4.0\text{E-}7$ Torr or better at the window under full power operation. Under conditioned full-power operation the gas load in any waveguide volume is predicted to be approximately $4.0\text{E-}9$ Torr-liter/sec-cm².

Figure 1. NEG vacuum pumping assembly on an RF waveguide

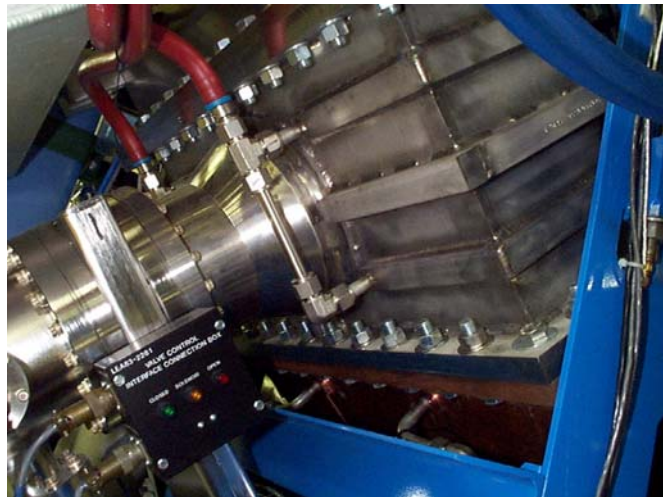


Waveguide and NEG pumping assembly design

The vacuum waveguide that connects an RF window to a port on the RFQ is comprised of three different sections. The first section is a rectangular waveguide that connects the RF window to the first section of tapered waveguide. The other two waveguide sections are tapered in cross-section, and incorporate an internal horizontal ridge and side cavities for RF coupling.

The rectangular section of waveguide is made of copper plated stainless steel. The power loss in this waveguide is approximately 0.05 W/cm^2 , and is high enough that water cooling channels are included in the design. This waveguide section has an RF grill machined in the lower plate. A vacuum housing adapter is welded to the outside of the lower waveguide plate, covering the RF grill. The RF grill prevents any substantial leakage of RF power into the vacuum assembly. The vacuum pumping assembly is bolted to this vacuum housing adapter. Figure 2 highlights the waveguide rectangular section and the vacuum assembly connection location.

Figure 2. Rectangular waveguide and vacuum pumping assembly connection



The two tapered waveguide sections are connected in series and to the RFQ. The total length of the tapered ridge geometry required to make the transition and coupling is divided into two axial sections. This division makes the fabrication and installation of the tapered section more manageable. The waveguide cross-section tapers in two dimensions creating an increasingly restrictive volume. The waveguide cross-section decreases as it moves away from the vacuum pumping location, creating a restrictive volume near the end of the waveguide where it couples to the RFQ. Even with the greater geometric restriction at the waveguide end a large over-all molecular conductance exists for the tapered waveguide section. The side cavities of the waveguide create a rather open volume along the sides of the ridge, allowing for a large molecular conductance. Figure 3 shows the internal geometry of the ridge-loaded tapered waveguide. Figure 4 is a section view of the rectangular waveguide.

The vacuum pumping assembly on each waveguide consists of a NEG pump, turbo pump, ion gage, and a small back-fill valve for gas filling of the assembly. An 8 inch high-vacuum valve separates the vacuum pumping assembly from the waveguide vacuum volume.

Figure 3. Section view of ridge-loaded tapered waveguide

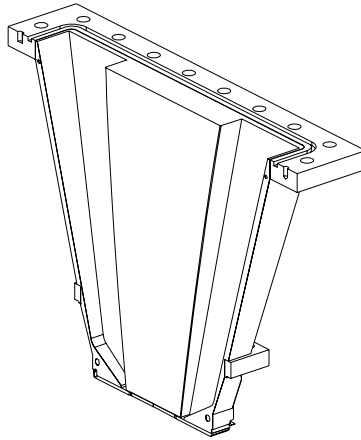
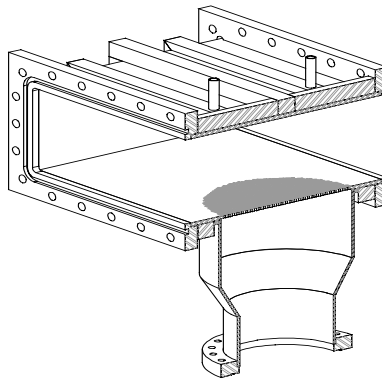


Figure 4. Section view of rectangular waveguide



The NEG pump is the main component of the vacuum pumping assembly. The NEG pump chosen for this design is a SAES CapaciTorr B1300 cartridge pump using ST185 material blades as the getter material. The bare cartridge (no vacuum housing surrounding it closely) has a hydrogen pumping speed of approximately 1 300 liters/sec as stated by the manufacturer. The NEG cartridge subassembly is mounted to a vacuum flange. The cartridge flange is mated to the cylindrical body of the vacuum assembly, and the body in turn mates to the waveguide vacuum housing adapter.

The NEG cartridge is shown in Figure 5. The B1300 cartridge resides inside of a 6 inch diameter tube. This configuration was expected to restrict the hydrogen pumping speed of the cartridge containing the ST185 getter material to about 1 200 liters/sec. Accounting for the molecular conductances of the vacuum housing adapter and the RF grill the effective hydrogen pumping speed at the waveguide side of the RF grill was predicted to be approximately 755 liters/sec.

Figure 5. NEG Cartridge with ST185 getter material blades



The turbo pump on the assembly is a Varian model V70LP pump. The pump has nominal pumping speeds of 70 liters/sec for nitrogen, and 45 liters/sec for hydrogen. The turbo pump provides two main functions for the NEG pump i) remove gases that are driven off during NEG material regeneration, and ii) remove the non-getterable gases during normal operation. The noble gases are not pumped by the ST185 Getter material.

NEG pump testing

The NEG pump underwent pumping speed and sorbing capacity testing [5]. The testing was conducted to test the suitability of this type of vacuum pump for the waveguide vacuum pumping environment. The gas loading on the pump during RFQ conditioning was expected to be substantial. A high gas sorbing capacity with little degradation in pumping speed was desired from the waveguide vacuum pump in order to not interrupt RF power conditioning activities with frequent pump regenerations.

The average hydrogen pumping speed for a new NEG B1300 cartridge with ST185 Getter material was measured to be 1380 liters/sec. The NEG pump was housed in a 6.0 inch diameter body for the pumping speed tests. The NEG pump sorbed approximately 2 Torr-liters of hydrogen during each pump speed test. These test results show that the predicted effective hydrogen pumping speed at the waveguide side of the RF grill is near 823 liters/sec.

The sorbing capacity testing involved testing the hydrogen pumping speed of the NEG pump as it sorbed 1.0 standard liter (760 Torr-liters) of hydrogen without any regeneration being performed. The same NEG cartridge as was used in the pump speed testing was also used in the sorbing capacity testing. The hydrogen pumping speed degraded slightly as the pump ingested the hydrogen gas load, dropping only to 1 150 liters/sec after sorbing almost 1.0 standard liter of hydrogen. This sorbed gas load corresponds to approximately 2 000 hours of operation at full RF power for 100 mA beam operation. These test results indicated that the NEG pump would function as needed in the waveguide vacuum pumping application.

Control and operation of the waveguide pumping assembly

The control of the waveguide pumping assemblies on the RFQ waveguides involves controlling the operation of the high-vacuum valves and the operation of the high vacuum pumps. The control system also controls the regeneration cycles used on the NEG pumps.

While it is possible to operate the NEG pump at elevated temperatures in order to have much higher pumping speeds the NEG pumps in this application are operated at room temperature. Operation at elevated temperatures was rejected for safety considerations. If the vacuum is broken with room air the oxygen will react with the hot ST185 getter material and allow the getter material to combust. With operation at ambient temperature the control system was not required to provide temperature control of the NEG pump. The NEG pumps undergo high temperature operation only during regeneration. During regeneration the vacuum valve between the vacuum pumping assembly and the waveguide remains closed, and the control system logic prevents the valve from being opened during the regeneration cycle.

The regeneration cycle for the NEG pumps was modified slightly from the recommended regeneration temperature-time profile provided from SAES. During pump testing it was found that a regeneration cycle of 550°C for 90 minutes produced higher subsequent pumping speeds. SAES originally recommended 500°C for 45 minutes. The temperatures are relative since the measuring thermocouple in the pump assembly is located near to, but not in direct contact with the NEG material. The ramping-up of the NEG temperature took place over approximately two hours. The ramp-up is paced primarily by the ability of the auxiliary pumping device, in this design the V70 turbo pump, to maintain the vacuum space pressure near 1.0E-4 Torr during the regeneration cycle. The NEG pump should not be exposed to too high of a pressure during regeneration. Maintaining a vacuum in this range also helps reduce the heat loss to the room.

The ion gage that is located on the waveguide pumping assembly is used only when the waveguide isolation valve is closed, as in during NEG pump regeneration. During RF operation of the RFQ an ion gage located on the RF window assembly is used to control RF power on or off depending on the pressure level of the vacuum that is measured very near to the window. For normal RF operation the vacuum trip level as measured by the RF window ion gage is set to near 5.0E-7 Torr.

Protection of the NEG material can be achieved in one of two ways. The NEG canister can be back-filled with clean dry nitrogen that passivates the NEG material. Any gas that comes into contact with the NEG material will not be pumped. The NEG material can be reactivated by putting it through a regeneration cycle. Argon gas can also be used to back-fill the NEG canister, but it will not passivate the NEG material. Argon will act simply as a heavy cover gas to blanket the NEG material in the canister. Since the argon is not pumped by the NEG material it is not depleted within the contained volume. The argon must be pumped out by an alternate means, in this design by the turbo pump, to re-establish the vacuum volume and allow the NEG pump to function.

Operational performance of the NEG vacuum pump

The waveguide vacuum pumping assembly with the NEG pump incorporated has provided reliable service throughout the RFQ operation. No major problems have been encountered with the operation or maintenance of the NEG pumps. No adverse conditions have been placed on the RFQ, RF window, or any other component due to the presence of a NEG pump in the vacuum system.

The RFQ RF power conditioning activities started with only four of the six waveguides conducting RF power into the RFQ. Each waveguide pumping assembly contained a new NEG pump canister that had been activated using the regeneration profile of 550°C for 90 minutes.

A little more than a month's time passed during the RFQ conditioning process before a total RFQ RF power level of 1 MW was reached. During this time the NEG pumps were regenerated once, at approximately the half way point in time to the sustained 1.0 MW operation. Table 1 lists the main events in the first two months of RFQ conditioning activities that are relevant to the NEG pump performance. The waveguide pressure continually declines as the conditioning progresses, as would be expected. The NEG pump is shown to initially produce a base pressure of 6.0E-9 Torr when isolated from the waveguide volume. A good base pressure was reached after each subsequent regeneration, indicating that the NEG pumps had experienced no damaging events. The base pressure improved slightly with time most likely due to the vacuum assembly surfaces undergoing some cleaning as more time under vacuum lapsed. There is no measurable degradation in the NEG materials ability to be regenerated to its original pumping capability in this operational time frame.

The NEG pump regeneration operations were performed at times that were convenient for the conditioning activities. No waveguide pressure degradation was observed that indicated that a regeneration was necessary. The regenerations used were pre-emptive tasks that were intended to prevent waveguide pressures from rising due to a decreased pumping ability and thus interfering with the RF power conditioning activities.

The RFQ steady operation that followed the conditioning phase experienced no problems with the waveguide vacuum pumping assembly operation. Reliable vacuum pumping of the waveguides has been provided by the NEG pumps throughout the various beam activities and experiments involving the RFQ.

Table 1. NEG pump performance during RFQ conditioning

Date	Ave WG press., Torr (RF power off)	Ave NEG base press., Torr	Total RFQ power reached, MW
11-18-1998	6.0E-7	6.0E-9	–
11-19-1998	Started RFQ conditioning	–	–
11-26-1998	1.0E-7	5.0E-6	–
12-3-1998	Regenerated NEG pumps	–	–
12-3-1998	7.0E-8	5.0E-9	–
12-24-1998	5.0E-8	–	1.0
1-4-1999	Regenerated NEG pumps	–	–
1-4-1999	5.0E-8	4.0E-9	–
1-13-1999	2.0E-8	–	1.2

Summary

The NEG vacuum pump assembly has served the RFQ high power conditioning and steady-state operations well. The SAES CapaciTorr B1300 NEG pump using ST185 getter material has provided a robust pump design for this application.

REFERENCES

- [1] Young, L., "High Power Operations of LEDA", Linac2000 Conference Proceedings, paper TU201.
- [2] della Porta, P., "Gettering, an Integral part of Vacuum Technology", SAES Getters S.p.A., Technical Paper TP-202.
- [3] Valdiviez, R., "The Mechanical Design and Fabrication of a Ridge-Loaded Waveguide for an RFQ", Linac'98 Conference Proceedings, p. 597.
- [4] Cummings, K., "Results and Lessons Learned From Conditioning 1 MW CW 350 MHz Coaxial Vacuum Windows", Linac'98 Conference Proceedings, p. 938.
- [5] Kishiyama, K., "Testing of Vacuum Pumps for APT/LEDA RFQ", Linac'98 Conference Proceedings, p. 624.

CORROSION MEASUREMENTS ON APT PROTOTYPIC MATERIALS IN THE LANSCE HIGH-POWER PROTON BEAM AND APPLICABILITY TO OTHER SYSTEMS

**R.S. Lillard, G.T. Chandler¹, P.D. Ferguson², F.D. Gac, M.R. James,
S.A. Maloy, M.A. Paciotti, L.S. Waters, G.J. Willcutt**

Los Alamos National Laboratory

¹Westinghouse Savannah River Company

²Oak Ridge National Laboratory

Abstract

The corrosion rates of several “corrosion resistant” materials behave in a similar manner even under the intense radiation of the LANSCE high-power beam. A second observation was made, showing that the corrosion rates saturated under high instantaneous radiation intensity in corrosion experiments conducted for the accelerator production of tritium (APT) programme. The LANSCE H⁺ beam is not prototypic of the proposed APT production plant in several respects. The instantaneous proton flux in the APT production plant beam is about 10 times that of the LANSCE beam. The small transverse APT beam spot is rastered to spread the power density over the area of the target, and as the beam rasters, it creates a pulsed character to the beam at a specific location. In order to develop correlations that would enable extrapolation of the corrosion data to the proposed APT production plant, the experimental programme included measurements over a range of average beam currents, measurements at high and low instantaneous beam current, and measurements at various combinations of pulse width and repetition rate. The correlations that were developed are based on an approximately linear dependence of corrosion rate on average beam current (average radiation intensity) and the saturation effect observed at high instantaneous radiation intensity. For a given transverse beam profile and for the same average beam current, the correlations predict the highest corrosion rate in a dc beam and the lowest corrosion rate in the lowest duty cycle beams. In the case of the APT extrapolation, the predicted corrosion rates were a factor of 5 lower than for a dc beam depositing the same average power density. The measured corrosion rates and the formulated extrapolations are applicable to water-cooled targets and components in proton beams.

Introduction

Corrosion experiments for the accelerator production of tritium (APT) programme were conducted with the high-power LANSCE H⁺ beam which is not prototypic of the proposed APT production plant in several respects. The instantaneous proton flux in the APT production plant beam is about 10 times that of the LANSCE high-power beam. The small transverse APT beam spot is rastered to spread the power density over the area of the target. As the beam rasters, it creates a pulsed character to the beam at a specific location, similar to the LANSCE beam. Thus, the corrosion programme included measurements over a range of average currents, measurements at high and low instantaneous power density, and measurements at various combinations of pulse width and repetition rate in order to develop correlations that would enable extrapolation of corrosion data to the conditions in the production plant.

Corrosion data

Corrosion rates of Alloy 718, 316L stainless steel, and aluminum Alloy 6061-T6 located in the intense LANSCE H⁺ beam have been measured as part of the APT programme [1]. Two other corrosion resistant materials, Alloys 625 and C276, were also included in the irradiation as alternate materials. Figure 1 shows the layout of the corrosion probes with respect to the proton beam flux profile which is approximately Gaussian in both transverse dimensions with σ 's of 1.85 cm. Surprisingly, both of the candidate materials and the alternates located in the proximity of the 340 μ A beam showed similar corrosion behavior as seen in Figure 2. The 316L SS probe within Tube 40 is out of the proton beam and has a lower corrosion rate than the others shown in Figure 2.

A general feature of the data and is that corrosion rates increase with average proton beam current (Figures 3 and 4). Specifically, corrosion rates increase with average beam current as a power law, and the exponent is not far from 1.0 for all the materials studied [1]. These data are referred to in the text as the "average beam current series". Beam parameters are given in Table 1.

Table 1. Proton beam parameters for corrosion data for Figures 3 & 4, the average beam current series

Average current (mA)	Peak current (mA)	Repetition rate (Hz)	Gate length (μ s)	Duty cycle
0.010	16	3	200	0.00060
0.036	16	10	200	0.00200
0.100	16	10	625	0.00625
0.340	16	36	625	0.02250

Note: Duty cycle is repetition rate times gate length.

It was noticed early, from the preliminary online results, that the corrosion rates did not fall off transversely to the beam centerline as steeply as did the current density of the proton beam. Referring to Figure 5, it is seen that proton beam power falls faster than do the corrosion rates. In addition, Probes 35 and 38 of the same material (316L SS) located at the same transverse distances from the beam centerline exhibit significantly different corrosion rates.

The influence of duty cycle

A second set of measurements, termed the “duty cycle series”, explored a range of beam delivery parameters (instantaneous proton beam current,¹ proton pulse width, and repetition rate). The purpose of this series was to extrapolate the corrosion observations to conditions in the production plant. The duty cycle experiment employed two peak currents, the maximum available 16 mA and another ten times smaller (1.6 mA). The average current was held constant by increasing the repetition rate for the 1.6 mA run by a factor of 10. The experiment found approximately a factor of two lower corrosion rate for the 16 mA instantaneous current than for the 1.6 mA case, suggesting a saturation effect; for example, additional protons above a threshold flux do not add to the corrosion kinetics. Corrosion efficiency is introduced in [2] as part of the discussion of corrosion measurements in pulsed beams.

Table 2. Corrosion rates for Alloy 718 (Tube 33) as a function of average beam current, peak current, gate length, and repetition rate

Peak current (mA)	Average current (mA)	Beam pulse width (μ s)	Repetition rate (Hz)	Corrosion rate (μ m/y)
16.0	0.010	600	1	0.17
16.0	0.010	200	3	0.17
16.0	0.033	200	11	0.23
1.6	0.010	625	10	0.26
1.6	0.010	200	31	0.35
1.6	0.035	605	35	0.38
1.5	0.030	220	100	0.55

Note: The electrochemical impedance spectroscopy (EIS) technique averages the corrosion rate over the surface of the probe. Throughout the text, tube number and probe number are used interchangeably.

Data presented in Table 2 explored pulse width, repetition rate, and peak current. Consider subsets of Table 2 where average beam current and pulse width are constant. It is seen that high instantaneous beam current has a lower corrosion rate for the same average beam current. See [2] for specific operating conditions for these measurements. According to these data, a corrosion efficiency (taken as 1.0 at low instantaneous radiation intensity) drops to approximately 0.5 at the highest available instantaneous radiation intensity.

It might be anticipated that the corrosion rate during the beam pulse is greater than the rate between beam pulses. And, in fact, we show evidence for transient effects in corrosion: The 1.6 mA peak current corrosion rates measured at 0.010 mA average are very interesting. Data were taken with the same corrosion probe at the same peak beam current and the same average beam current, where only the pulse length (and repetition rate) changed. A saturation-like effect, similar to the high instantaneous beam current saturation, is seen. Evidently, the saturation effect extends in time. The smaller corrosion rate was observed for the longer pulse length, constituting the discovery of a time constant in the process. The time constant can be thought of as a persistence, i.e., the radiation-induced effect must persist for a length of time in order to explain the observation. For example, corrosion near

1. There is underlying micro pulse structure comprised of sub-nanosecond width pulses at 5 nanosecond spacing, but this time structure is not considered in this analysis. Peak current and instantaneous current are therefore used interchangeable in the text.

the tail end of the 600 μ s beam pulse is apparently suppressed by the presence of beam about 600 μ s earlier in the same beam pulse. Corrosion transient modeling described in [2], replicates the trends in the Table 2 data by including a relaxation time for the corrosion rate after the beam pulse.² The fact that the identical effect is not seen at 16 mA peak beam current could be attributed to an already saturating corrosion effect due to the high instantaneous beam current.

Empirical correlations

In order to extrapolate to the APT plant conditions or other situations, interpretations of corrosion incorporate the observation that corrosion rates increase with average beam current as a power law under conditions where the instantaneous beam current is constant. An expression is constructed that seeks to find a common explanation for the influence of the duty cycle described above, the transverse fall off of corrosion rate (Figure 5), and saturation at high beam intensity (i.e., corrosion efficiency). Qualitatively, the probes in the center see more intense beam than the off-axis probes, the corrosion rate for them is suppressed by the corrosion efficiency, giving rise to a broader transverse distribution (Figure 5).

To find such an expression it was first necessary to calculate the particle distributions and their respective energies. Complete three dimensional geometry of the corrosion insert and the proton beam parameters were input to the MCNPX code, and detailed computations of radiation intensity were computed for each corrosion probe.

Since we do not know which particle type(s): proton, photon, neutron, is (are) primarily responsibility for the radiation-enhanced corrosion observed in these experiments, we are not sure which of the MCNPX predictions should be used to correlate with the measured corrosion rates. The differing spatial distributions of the particles might form a basis for deciding which are involved in corrosion. In fact, neutron and/or photon power densities (Table 3) correlate with trends in corrosion rate (Figure 2). However, there are not a sufficient number of corrosion measurements to evaluate different weightings of each particle type in determining corrosion rate. Therefore, the simplest descriptor of radiation intensity, the total energy deposited for all particles combined, is the one exploited in this paper. (See Discussion section regarding Probes 35 and 38.)

Table 3. Results from radiation transport calculations for tubes containing 316L SS samples

Probe #	Relative proton flux	Relative neutron flux	Relative photon flux
35	72.7	38.0	35.2
36	127.0	52.7	46.2
38	70.9	43.8	37.3
40	6.0	13.5	13.2

Note: Flux was averaged over the tube length and summed for all particle energies. The relative fluxes permit comparison between corrosion probes but not between particle types.

2. It is not demonstrated conclusively that the corrosion rate itself undergoes a transient, but some physical change leading to corrosion does have a transient behavior.

The corrosion rate is formulated as an average over the length of the probe of the local power density³ times the efficiency ϵ which is a function of the instantaneous power density:

$$CR = a \sum_i P^{0.95} \epsilon(P_i) \quad (1)$$

where

- CR is the average corrosion rate of the probe in $\mu\text{m}/\text{y}$,
- a is the conversion factor from power density to corrosion rate in $\mu\text{m}/\text{y}$ per W/cm^3 ,
- P is the local time-averaged power density in W/cm^3 ,
- ϵ is the corrosion efficiency and is a function of the instantaneous power density, and
- P_i is the instantaneous power density and is equal to:

$$P_i = \frac{P}{\text{Duty Factor}} \quad (2)$$

where the *duty factor* is equal to the pulse width in seconds multiplied by the repetition rate in Hz. (e.g., Table 1). This expression reproduces the overall characteristics of the experiments plotted in Figure 3 (the beam current series). The experiments performed at different beam currents found that the corrosion rate for 316L SS increases nearly linearly with average beam current (the dependence is a power law with exponent 0.95) where instantaneous beam current was always constant [1]. Since the power density at any point in the probe is directly proportional to average beam current, the exponent 0.95 can be applied to P as given by Equation 1.

Correlations between total power density and corrosion rate were made for the 316L SS data because these probes were located directly on the beam centerline as well as several cm from centerline, allowing the corrosion rates to be analysed over a wide range of P . The set of corrosion measurements for 316L SS considered in this analysis were conducted at an average beam current of $340 \mu\text{A}$, a pulse width of $625 \mu\text{s}$, and a repetition rate of 36 Hz . A functional form for ϵ was created and trial values assumed in order to complete the prediction of corrosion rate from Equation 1. The predictions of Equation 1 were then fitted to the measured corrosion rates for each 316L SS probe [1] by varying the parameters for ϵ and the value of the conversion factor, a .

The 16 and 1.6 mA peak current data of Table 2 would be prime information for the proposed fit because the factor of 10 change in P_i would be valuable in fitting the dependence on P_i . But since Table 2 applies entirely to Alloy 718 Probe 33, the data cannot be included directly in the fitting procedure for 316L SS probes. Taking advantage of the similarity between the Alloy 718 and 316L under radiation, a *ratio* of Alloy 718 corrosion rates from Table 2 could be included. The $600 \mu\text{s}$, $10 \mu\text{A}$ average-current data was selected, and the corrosion rate ratio between the two peak currents

3. It must be considered whether temperature increase due to higher power density is responsible for the increasing corrosion rates. This possibility has been examined and it was concluded that the calculated probe surface temperatures cannot account for the large increase in corrosion rates seen in Figure 3.

was included in the fit, that is, Equation 1 was required to predict the experimental ratio. According to Equation 1, when ε is multiplied (weighted) by a P distribution such Probe 33 in Figure 6, the corrosion rate is suppressed in the center of the probe. Figure 7 displays a typical fitted corrosion efficiency distribution over the length of Probe 33 for two peak currents.

A single-parameter function for ε that fits the 316L SS data at 340 μA is an exponential with decay constant of 0.000063 per W/cm^3 , while the conversion a was found to be 0.114 μy per W/cm^3 . Figure 8 shows ε and the scale of the instantaneous power density with an arrow marking the maximum extent of the experimental data. The saturation effect leading to Figure 8 suggests a continued drop in ε , however, since there is little theoretical or experimental guidance, there is little merit in attempting to extrapolate a long way to the high instantaneous power. Alternately, other functions were examined that have excellent fitting behaviour over the range of available data but extrapolate as a constant corrosion efficiency at high instantaneous power density.

$$\varepsilon = 0.2 + \frac{0.8}{1 + \left(\frac{P_i}{7846}\right)^{1.39}} \quad (3)$$

The expression was selected (Figure 9) that tracks the exponential out to the limit of the experimental information and then places an arbitrary asymptotic limit of 0.2 on the corrosion efficiency. The extra fitting variables are for the convenience of having a definite formula for corrosion efficiency and do not detract from the ability of the exponential to fit ε with one variable.

The measured corrosion rates for Probes 35 and 38 differ by 38% (Figure 2), and these are averaged for the fit because the computed P for these are nearly identical as previously discussed. We note here that Table 5 does predict a difference between Probes 35 and 38 based on neutron or photon flux, although not as great as measured. (See Discussion.)

Another variation taken adds a constant corrosion rate to Equation 1 and treats it as a fitting variable, resulting in greatly improved quality of fits. The preferred value for this constant corrosion rate is 0.73 $\mu\text{m}/\text{y}$. Although not strongly motivated, this constant can be thought of as the corrosion rate at a location where the power density is zero, such as an out-of-beam region where water chemistry effects dominate [3, 4].

Extrapolation to the APT production plant beam conditions

The instantaneous power density under APT production plant [5] conditions is determined from the beam raster that sweeps a spot beam uniformly over the APT target. Any location in the complex raster sees a repetitive pulse train of eleven 50 μs wide pulses spaced by 4.1 ms where the amplitude of the pulses varies as a Gaussian with a σ of 4.65 ms. As an approximate comparison, the maximum instantaneous power densities in the pulse train are 10 times higher than are present on the corrosion probes. Therefore, according to Figure 9, the corrosion efficiency is about 0.2 and rises to 1 when the rastered beam spot is far from the location in question. Equation 1 now becomes a sum over the individual pulses in the train:

$$\text{Corrosion Rate} = 0.73 + 0.114 \sum_{\text{pulses}} P^{0.95} \varepsilon(P_i) \quad (4)$$

The corrosion data from the beam current series (Figure 3) supports the premise that the corrosion rate is additive for pulsed beams, and the duty-cycle series supports the premise that corrosion rate is additive for different peak current beam pulses, once accounting is made of ϵ .

Figure 10 summarises the effect of the beam time-structure on local corrosion rate. With no time structure (dc beam) the local corrosion rate would follow the upper curve. The middle curve (LANSCE beam) shows the behavior of corrosion as the beam current is increased, ending up at a 0.34 mA and a time-averaged power density of 300 W/cm^2 . The lower curve is the predicted corrosion rate for the APT rastered beam from Equation 4 as the average power density is increased to maximum (at the design current of 100 mA). The corrosion rates at low power density all initially follow the dc beam case and then increase more slowly as the corrosion mechanism begins to saturate.

From Figure 10, the APT rastered beam is predicted to produce a corrosion rate of $20 \text{ }\mu\text{m/y}$ in the 316L SS cladding [5] of the tungsten target cylinders.

Predictions for corrosion probe examinations

The EIS method is ideally suited to determining the corrosion performance of the APT candidate materials:

1. It is a sensitive on-line method for measurement under specific controlled beam conditions and water chemistry parameters.
2. A number of materials can be examined under the identical conditions, enabling the correlations drawn in this report.
3. Aqueous corrosion is electrochemical in nature and so it is natural to utilize an electrochemical technique where the corrosion current determines directly the rate of loss of structural metal.

Nevertheless, post-irradiation examination of the corrosion probes was carried out in attempt to confirm the EIS measurements. Equations 3 and 4 predict the corrosion distribution over the lengths of the 316L SS probes (Figure 11) during the measurement period of approximately 10 days. Predicted corrosion in the center of the probe is only $0.3 \text{ }\mu\text{m}$. Moreover, the probes accumulate corrosion over the entire period of irradiation which lasted 2 months, and during most of this time other APT experiments located upstream of the corrosion experiment heavily interacted the core of the proton beam, leaving the predicted corrosion distribution shown in Figure 12. The sum of Figures 11 and 12, is the predicted corrosion over the course of the entire irradiation and is a fairly flat distribution. Even small relative changes along the length were difficult to discern,⁴ and diametrical variations, measured in the hot cell, could not detect corrosion of the center of the probes with respect to the ends within a measurement uncertainty of $2.5 \text{ }\mu\text{m}$.

The 304L SS cover plates for the materials irradiation experiment [6] offer a more sensitive test since they saw a narrow proton beam profile for a longer period of time (6 months). Using Equations 3 and 4 and computed power densities, predictions for the corrosion that should occur over the length of the cover plates are presented in Figure 13. However, measurements of the cover plates (Table 4)

-
4. Corrosion rates measured with EIS are the rate of loss of structural metal; in general, it is not determined whether corrosion will result in a build up of oxide scale or a decrease in thickness. Corrosion can increase a probe diameter due to oxide buildup or decrease it if the oxide sluffs off.

could not detect corrosion of the center of the plates with respect to the ends within a measurement uncertainty of 5 μm and thus present a discrepancy with Figure 13.

Table 4. 304L Cover plate thickness measurements

304L Envelope designation	Thickness at end (mils)	Thickness at centre (mils)	Thickness at end (mils)
Control	9.5	9.6	9.5
1-5	9.8	9.8	9.7
2-5	9.5	9.6	9.4
4-5	9.4	9.2	9.1

Note: The thickness measurement of envelope 4-5 was compromised by the presence of corrosion products on the inside of the plate due to water leaking inside the envelope.

Based on the data and analysis presented, there is good confidence that the corrosion distribution should be peaked in the center of the cover plates. Looking at Figure 5, corrosion is peaked on the probe that is in the centre of the proton beam. Thus, there is every reason to believe that the 304L cover plate corrosion should peak in the center as well.⁵

Some of the possibilities that could reconcile the predictions of Figure 13 and the measurements of Table 4 are the following:

1. The cover plates were cooled with a different water system than that used for the corrosion experiment, with largely unknown characteristics.
 2. The cover plates formed an envelope for the materials radiation effects samples and were welded around the perimeter of the envelope, forming a water-tight seal in most instances. Evidence of corrosion was observed on the insides of the cover plates as seen by discolorations and distinct outlines of the material test samples.⁶ This would increase the thickness in the center where the evidence of corrosion on the inside of the cover plates was the greatest.
 3. Corrosion was as predicted but left an oxide that maintained the thickness. This one is unlikely since the cover plates were still shiny on the outside, the side in the flowing water stream. An oxide of the thickness predicted in Figure 13 should leave a discoloration.
 4. The cover plate estimate includes an extrapolation of Figure 3 to 1 mA average current. Possibly, the curve begins to roll over faster than the power 0.95, i.e., an increasing saturation with average current.
 5. The corrosion profile is actually peaked, but the EIS predictions are too high, leaving the peaking undetectable.
-
5. It is conceivable that the corrosion is due to intermediate lifetime radiolysis products lasting long enough to skew the corrosion distribution to a sigmoid-like one that does not peak in the center. But this distribution would then show up in the Table 4 as a thinning in the center and at the downstream end (in the water flow sense). To be a viable model, the products would have to react before reaching Probe 40 in the next manifold section.
 6. Nitric acid may have formed in the humid air trapped inside the envelopes during welding.

Discussion

Modifications to corrosion rates derived solely on power density may be necessary because the operable corrosion mechanism may be responsive to differing radiation fields the APT plant, e.g., the fact that the neutron flux is higher in the APT production plant than in the LANSCE experiments that were used to derive Equation 4 and Figure 10.

Proposed explanations for the radiation-enhanced corrosion can be categorized by response/recovery times. We know that the initial effects of the radiation (scattering, ionization, excitation, displacement damage, etc.) occur very rapidly. And we have seen a time constant (the order of 1 ms) in our data that motivated the transient modeling studies [2], but we do not know the type of radiation responsible for the time constant nor the explanation of the corrosion enhancement. The existence of a transient implies that the corrosion rate increases in some way to the beam pulse and then recovers, and we shall examine the time scales of the effects that are usually mentioned for explaining radiation effects in corrosion in order to look for transients.

1. Radiation can strongly influence reaction rates by breaking bonds that ordinarily have to wait for thermal energy, thus accelerating the kinetics of allowed reactions. In this capacity, any ionizing radiation will cause this effect to occur, and the power density would be a good predictor for the effect. In the point defect model (PDM) of passive oxides [7], the reaction rate constants at the barrier layer interfaces enter into the film growth rates (corrosion). While the reaction rate constants would return to normal after the beam ceases, a persistence or relaxation back to steady state may occur in the vacancy concentrations set up within the barrier layer by the increased reaction rates.
2. Water radiolysis products are produced very rapidly, and all ionizing radiation contributes to these processes. Assuming that water is present on the solution side of the barrier layer, radiolysis radicals can dramatically increase the production and consumption of the cation and anion vacancies that transport metal and oxygen ions through the barrier layer. As with radiation effect 1, above, the reaction rates would return to normal after the beam ceases, but relaxation back to steady state may occur in the vacancy concentrations set up within the barrier layer by the increased reaction rates on the solution side of the barrier layer.
3. Electrical properties of the semi-conducting barrier layer, such as conductivity, are affected by radiation, for example, by the creation of electron-hole pairs, and in this capacity any ionizing radiation will cause this effect to occur. The main point is that these carriers die off after the radiation goes off, with no obvious persistence effect. These carriers play a role, but do not appear to be rate limiting in the PDM.
4. Lillard and Daemen have seen that proton irradiation alters the dielectric properties of the passive oxide film in tungsten [8] which suggests changes in the oxygen transport properties through the oxide film and therefore changes in corrosion rate. In the PDM, the electron donors in the semi-conducting barrier film are the defects themselves, the oxygen vacancies. Intense proton and neutron fluxes produce copious numbers of point defects, some of which form vacancies that directly affect metal and oxygen ion transport. Short time scale relaxation of this structural damage is not known but conceivable.
5. Experimentally, we have seen that the recovery after the first beam exposure is not complete since the corrosion rate does not return to the pre-beam condition. We were able to look on the time scale it takes to make a measurement (20 minutes). Some “permanent” damage has apparently occurred, unlike the electronic changes that disappear after beam is off. Just as

with the effect described in 4, this is suggestive of structural damage to the passive oxide layer, induced by nuclear scattering, i.e., neutron damage to semiconductor materials. This structural damage also changes the electrical properties of the passive oxide layers, determined to be highly doped semiconductors [7]. As for a relaxation effect, one is the corrosion itself that reconstitutes the layer. For a very thin barrier film, it is possible to “repair” it through corrosion on the time scale needed.

A related issue, the Probe 35-38 discrepancy, also bears discussion. The corrosion rate measured for Probe 38, Figures 2 and 5, has 38% higher corrosion rate than that measured for Probe 35 even though the power density is the same. Dominated by the protons, the power density is the same because the probes are the same distance from the beam axis. The photon flux ratio of Probes 38 and 35 is in the right direction but only “accounts” for 5% out of the 38% discrepancy (Table 3). Neutron flux therefore is a better predictor than the gamma flux, “accounting” for 15% out of the 38% discrepancy (Table 3). The fourth described radiation effect, above, is the one to try here. As a matter of practicality, we propose to use the material damage parameter, displacements per atom (dpa) in the metal as a predictor for corrosion rate. The dpa accumulation rate, which includes the effects of neutrons and protons, might not be the operable radiation effect on corrosion, but it might well be proportional to the operable effect (e.g., defect density, oxygen vacancies). However, this most promising avenue is not anticipated to be fruitful in explaining the discrepancy because the material damage directly in the beam is dominated by the protons and is influenced only to a small extent by the neutrons because of the lower neutron flux relative to the proton flux at the locations of Probes 35 and 38.

Of the five radiation effects mentioned above, some are predicted well by power density alone and others are a consequence of nuclear scattering of protons and neutrons. For applications and/or locations where neutrons are prevalent, we recommend scaling up the predictions of Equations 3 & 4 by dpa accumulation rates. For the APT production plant with its higher neutron flux, this amounts to a factor of 2 increase in corrosion rate.

Conclusions

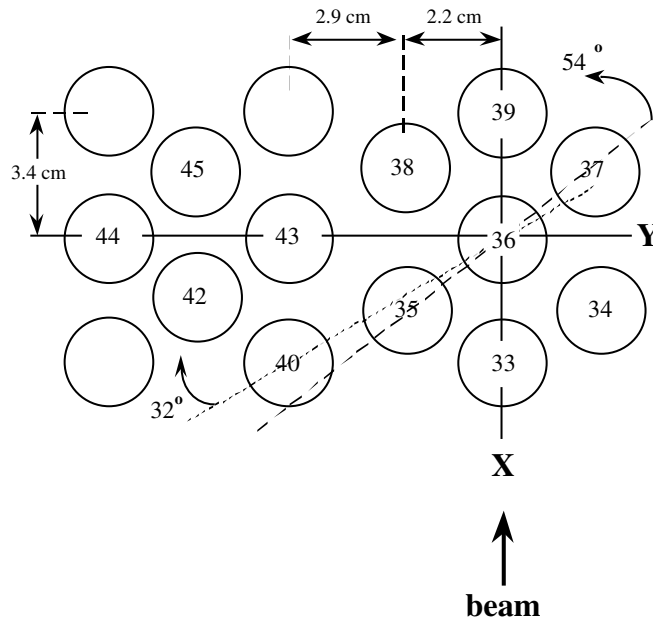
Correlations between corrosion rate and radiation intensity computed by MCNPX have been found for 316L SS and permit extrapolation to the raster beam conditions in the APT production plant. The formula makes use of the observation that the corrosion efficiency drops as the instantaneous radiation intensity increases, thus reducing corrosion projections in the rastered beam of APT. Using total power density as the measure of radiation intensity, a corrosion rate of 20 $\mu\text{m}/\text{y}$ is projected for 316L SS. As a result of the corrosion efficiency, the rastered APT beam has a factor of 5 lower corrosion rate than would be obtained for an expanded dc beam that was once considered for APT targeting.

The discovery of a time constant is significant, as is the finding of a saturation effect at these high power densities. The time constant found, in one interpretation, is the order of the widths of the beam pulses (600 μs) and suggests both theoretical consideration and further pulsed beam studies.

REFERENCES

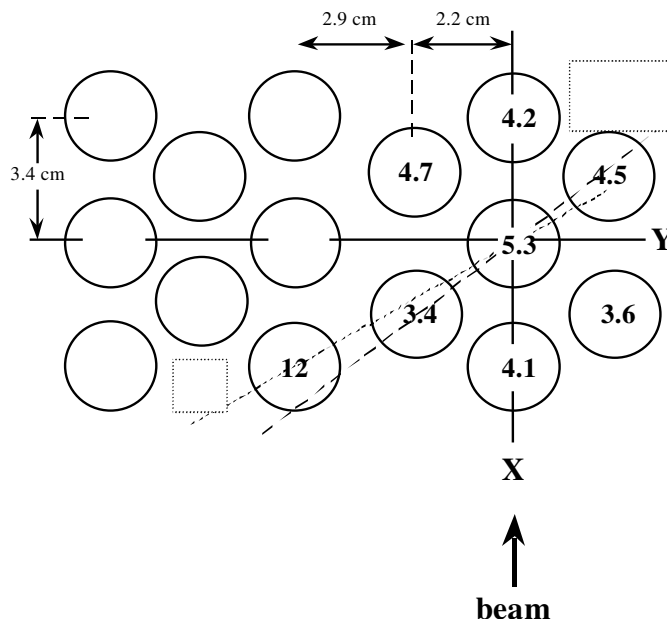
- [1] Lillard, R.S., F. Gac, M. Paciotti, P. Ferguson, G. Willcutt, G. Chandler, and L.L. Daemen, "The Effects of High Energy Proton Radiation on the Corrosion of Materials", *Effects of Radiation on Materials: 20th International Symposium, ASTM STP 1405*, S.T. Rosinski, M.L. Grossbeck, T.R. Allen, and A.S. Kumar, Eds., American Society for Testing and Materials, West Conshohocken, PA, 2000.
- [2] Lillard R.S., and M. Paciotti, "A Model for Analyzing Corrosion Data from Pulsed Proton Beam Irradiation Experiments", Accepted for publication in JOM.
- [3] Lillard, R.S., D.L. Pile, and D.P. Butt, "The Corrosion of Materials in Water Irradiated by 800 MeV Protons", *Journal of Nuclear Materials*, 278, (2000), 277-289.
- [4] G.T. Chandler, K.A. Dunn, M.R. Louthan Jr., J.I. Mickalonis, F.D. Gac, S.A. Maloy, M.A. Paciotti, W.F. Sommer, Jr., and G.J. Willcutt Jr., "Corrosion Testing in Support of the Accelerator Production of Tritium Program (U)", *Proceedings of the 2001 NACE International Annual Conference CORROSION 2001*.
- [5] Cappiello, M. and E. Pitcher, "Design and Operation of the APT Target/Blanket", *Materials Characterization* 43:73-82 (1999).
- [6] Maloy, S.A., M.R. James, G.J. Willcutt, W.F. Sommer, W.R. Johnson, M.R. Louthan, M.L. Hamilton, and F.A. Garner, "The Effect of High Energy Protons and Neutrons on the Tensile Properties of Materials Selected for the Target and Blanket Components in the Accelerator Production of Tritium Project", *Effects of Radiation on Materials: 20th International Symposium, ASTM STP 1405*, S.T. Rosinski, M.L. Grossbeck, T.R. Allen, and A.S. Kumar, Eds., American Society for Testing and Materials, West Conshohocken, PA, 2002.
- [7] Macdonald, D.D., "Passivity – the key to our metals-based civilization", *Pure Appl. Chem.*, Vol. 71, No. 6, pp. 951-978, 1999.
- [8] Lillard, R.S., and L.L. Daemen, "The Influence of Radiation on the Passivity of Tungsten", *Electrochimica acta*, 147, (June 2002).

Figure 1. A schematic of the tube array irradiated at the LANSCE A6 target station



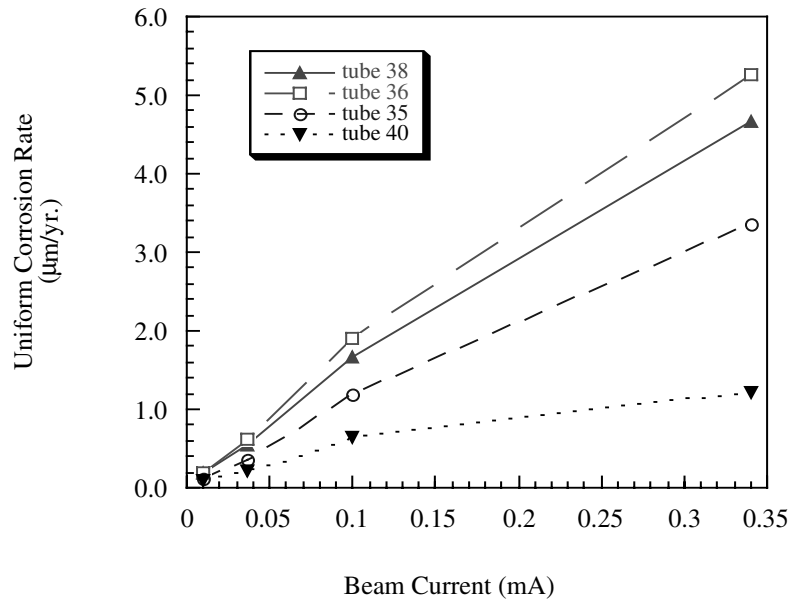
Note: Three of these tubes contained Alloy 718 corrosion samples, Tube 33, Tube 39, and Tube 45. Tubes 36, 35, 38, 40 contains 316L probes. Tube 34 contains an Alloy 625 probe, and Tube 37 contains an Alloy C276 probe.

Figure 2. The same tube array of Figure 1 where corrosion rates in $\mu\text{m}/\text{y}$ are displayed inside the circles representing the water tubes



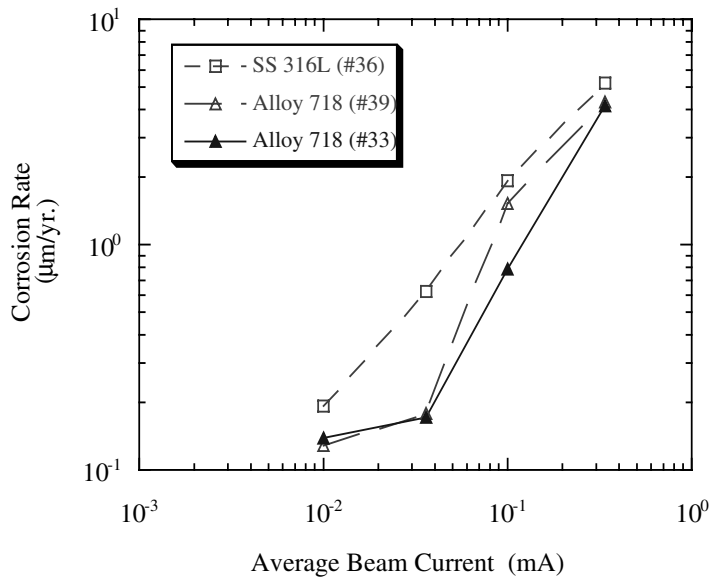
Note: The point is that all of these corrosion resistant materials in proximity to the beam have similar corrosion rates. Beam current is $340 \mu\text{A}$.

Figure 3. Corrosion rate as a function of average beam current for 316L SS probes [1]



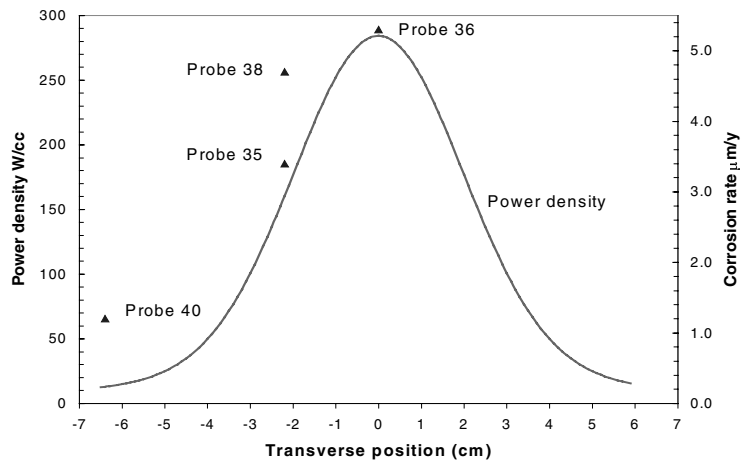
Note: Refer to Figure 1 for tube locations. The peak current is the same for all data points.

Figure 4. Corrosion rate as a function of average beam current



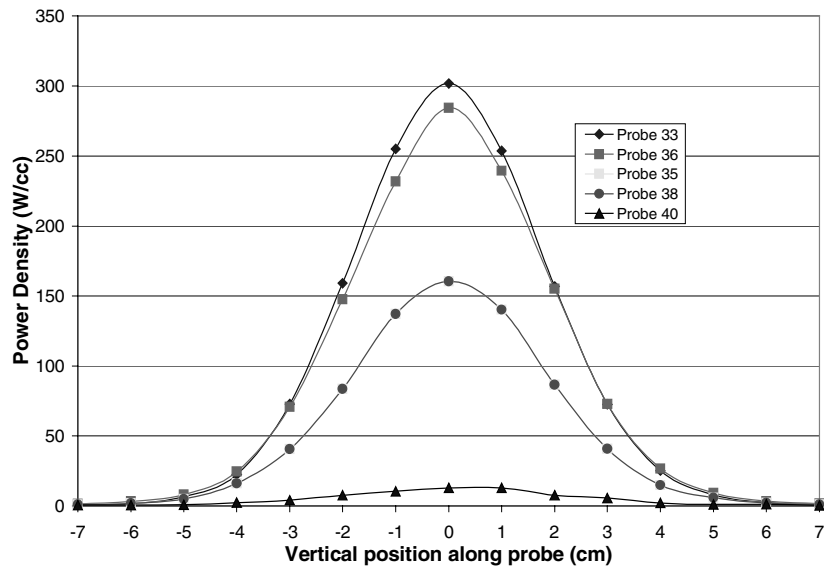
Note: The peak current is the same for all data points.

Figure 5. Comparison of the power density profile (solid curve) and corrosion rates (points) for 316L SS probes



Note: The corrosion rates do not fall off as rapidly as the power profile. Probes 35 and 38 differ substantially. The horizontal position of the vertically mounted probes is plotted.

Figure 6. Time-averaged power density as a function of the vertical position along the length of the probe



Note: Zero cm is the centre of the proton beam. Probe 33 is Alloy 718 and the others are 316L SS. Probes 35 and 38 are transversely equidistant from the centre of the beam and the power curves are nearly identical.

Figure 7. Corrosion efficiency variation along the length of Probe 33 for two instantaneous proton beam currents

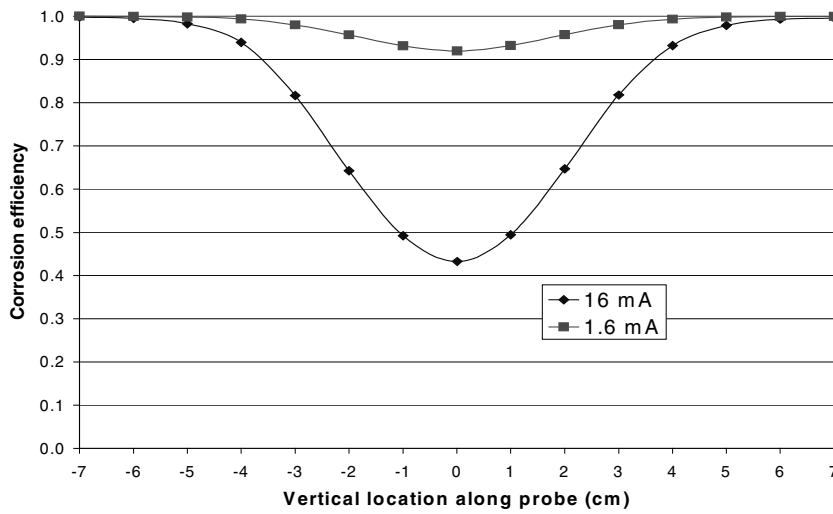
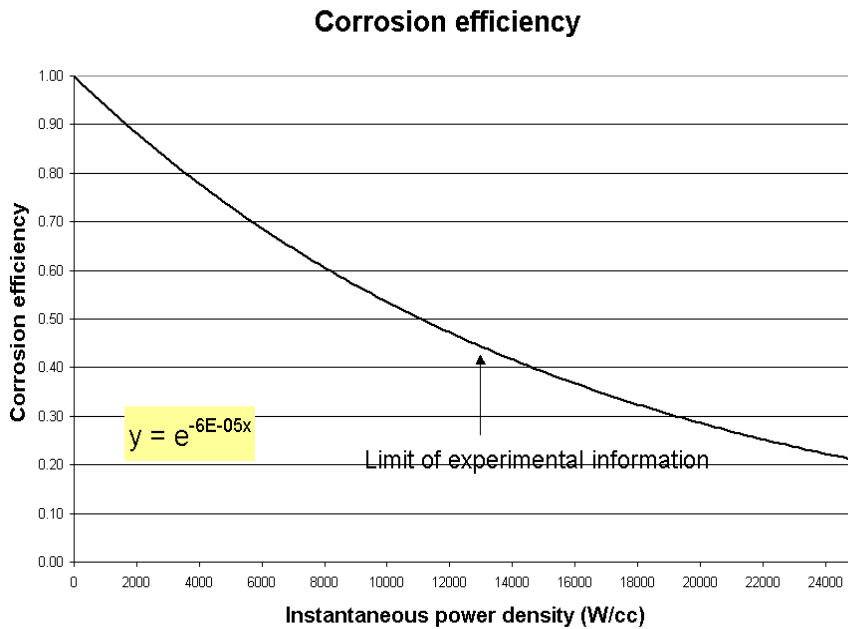
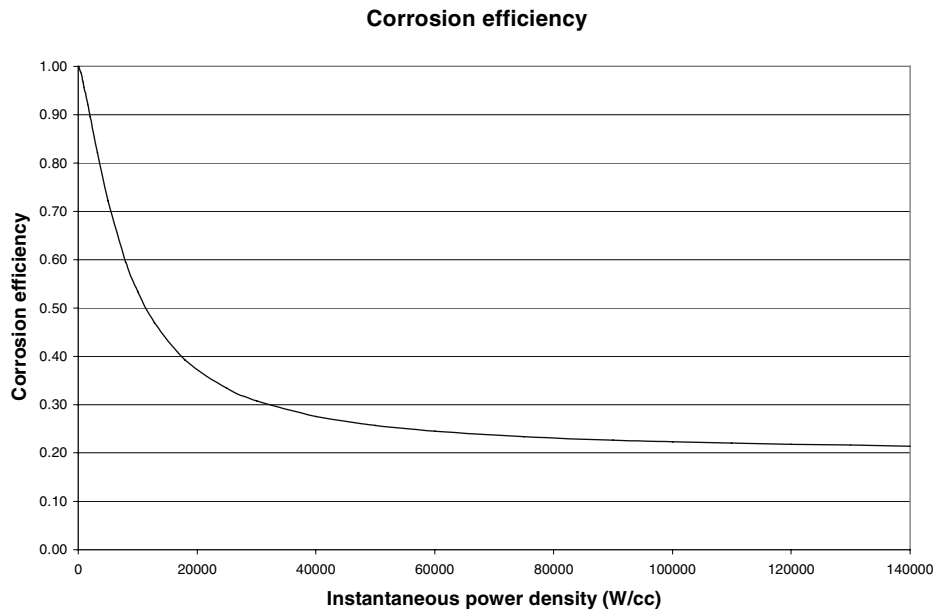


Figure 8. Corrosion efficiency as function of instantaneous power density



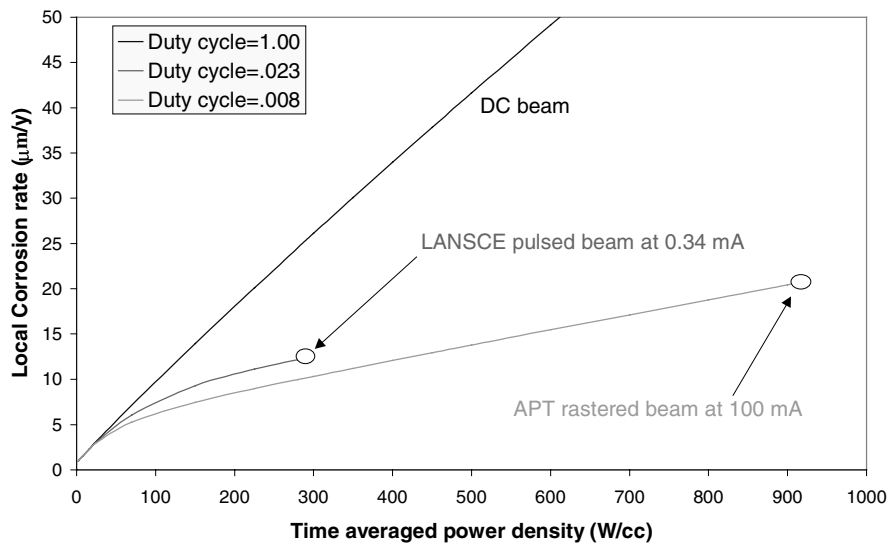
Note: No experimental information is available beyond an instantaneous power density of 13 000 W/cc. Data points do not appear because the contribution from each probe is a range of instantaneous power density, with a shape like Figure 6.

Figure 9. Extrapolated corrosion efficiency as function of instantaneous power density



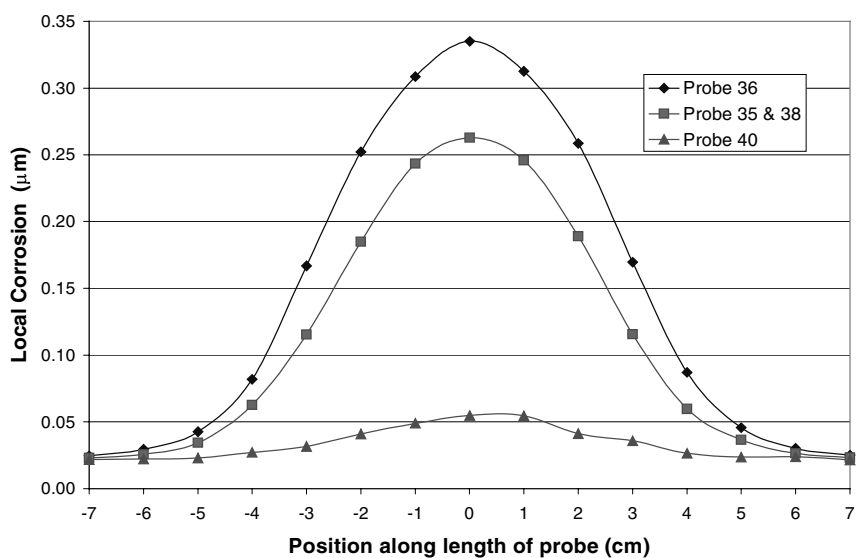
Note: This function tracks Figure 8 to the limit of the experimental information.

Figure 10. Corrosion rate as a function of average power density for different beam duty cycles



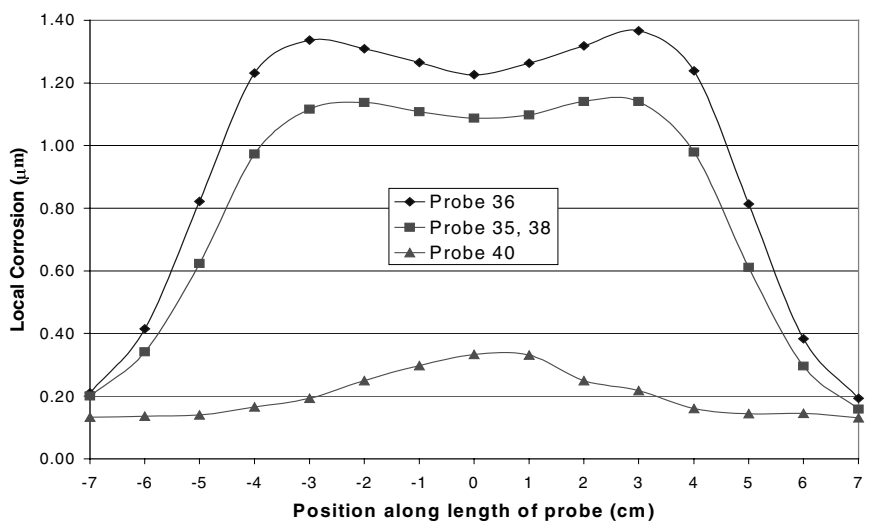
Note: The rollover of corrosion rate is due to the corrosion efficiency.

Figure 11. Corrosion profile for Probes 36, 35, 38, and 40 as predicted by the corrosion formula



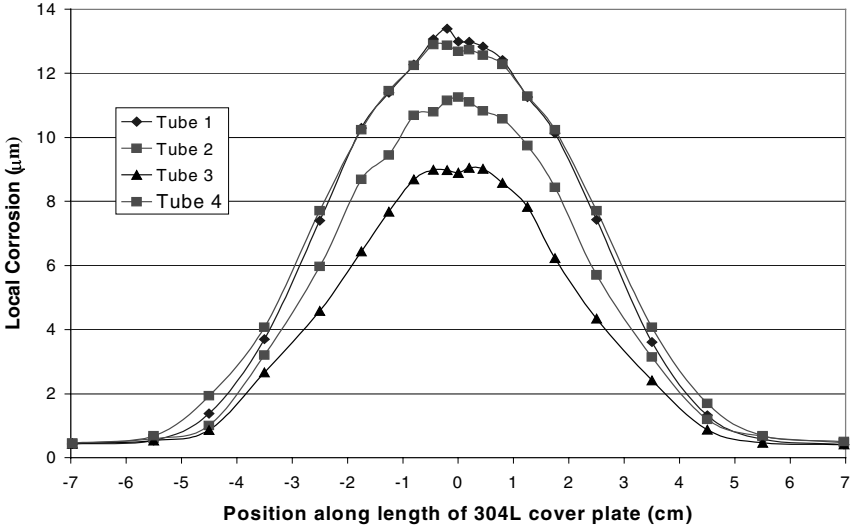
Note: 340 μA is impinging on the corrosion experiment with no other material upstream – 10 days irradiation time.

Figure 12. Corrosion profile for Probes 36, 35, 38, and 40 as predicted by the corrosion formula



Note: 950 μA is impinging on the full array of APT experiments, with the corrosion one being last. The central dip is due to the protons interacting with the horizontal tungsten elements upstream of the vertically oriented corrosion probes – 2 months irradiation time.

Figure 13. Predicted corrosion of the 304L cover plates (envelopes) that kept the cooling water from contacting the APT materials irradiation samples – 6 months irradiation time



**PRELIMINARY MEASUREMENTS FROM A THICK LEAD-BISMUTH
TARGET USING 800 MEV PROTONS**

M.R. James¹, R.T. Klann², G.L. Morgan¹, E.J. Pitcher¹, M.A. Paciotti¹, J.M. Oostens³

¹Los Alamos National Laboratory

²Argonne National Laboratory

³Campbellsville University

Abstract

One of the major environmental issues facing the world is the safe, long-term storage of large amounts of plutonium and other actinides from retired weapons and the nuclear power industry. An accelerator-driven subcritical assembly is being explored as a way to burn these wastes. Such a system would use a beam of high-energy protons impinging on a target of lead-bismuth liquid eutectic for neutron production. Proper calculation of the neutron yield from such a target is required for the design of a surrounding subcritical assembly. To gather data on the neutron production, we irradiated a thick (10 cm radius, 50 cm length) target of lead-bismuth in the “Blue Room” facility at the Los Alamos Neutron Science Center. The target was irradiated with a 24 nA beam of 800 MeV protons, and the neutron spectra was measured at various locations along the target using both time-of-flight spectroscopy and activation foils. In addition, activation foils were placed downstream of a tungsten target (target 4) in a well-characterised neutron environment to establish the spectral unfolding technique. The experimental configuration and some preliminary results of these experiments are presented in the current work.

Introduction

To measure the neutron yield from a target of lead-bismuth eutectic (LBE) and to confirm the MCNPX [1] code predictions, we began an experimental programme in the Los Alamos Neutron Science Center (LANSCE) “Blue Room” (also known as WNR target 2). This programme would consist of neutron spectrum measurements using varying sizes of LBE targets irradiated with an 800 MeV proton beam. The measurement techniques would be both time-of-flight (TOF) spectroscopy and activation foils to measure the neutrons at various locations on the target. The TOF technique would measure the angular component of the neutron spectrum at various locations from the target, and the foils would be used to measure the total neutron spectrum across all angles at point locations along the target surface. The first phase of the experimental programme was started in December 2001 with irradiation of an LBE target having a radius of 10 cm. TOF measurements were made along two flight paths, and several sets of activation foils were placed on the target to gather spectral information at various locations. The initial results of that experiment are reported in this paper. Further experiments are planned for two targets having a radius of 5 and 20 cm, respectively.

Experimental set-up

The target was fabricated as a cylinder of LBE (44.5% lead and 55.5% bismuth) with a radius of 10.16 cm and a length of 50 cm. The target was weighed after fabrication, and a density calculation verified that no major voids were present from the casting process. The target was placed on a translation table capable of being controlled remotely to change the position of the target along the proton beam axis. In this way, the field of view of the TOF collimators would cover different longitudinal regions of the target. Two TOF flight paths were utilised to measure the neutron spectrum, and 13 foil packets were assembled and placed on the target to quantify the neutrons at specific locations. A schematic of the configuration is given in Figure 1. The foil packets consisted of foils of aluminium, gold, bismuth, cobalt, copper, iron, indium, lutetium, niobium, nickel, and titanium. Rhodium, terbium and cadmium-covered gold foils also were included in several packets to test their use in the spectrum unfolding process. Counting of many of the foils was performed at the LANSCE Staging Area, where two high-purity germanium (HPGe) detectors were controlled by a PC running Gammavision™. After acquisition of the gamma spectra, the files were converted to a format usable by PCGAP [2] for analysis.

The target was positioned in the Blue Room, and the proton beam was aligned to the centre of the front surface. On the first day, a short irradiation was conducted (~2.4 h at 24 nA, 1.41×10^{15} 800 MeV protons delivered) with one foil stack in place to test the data gathering process and to confirm dose rate estimates for foil handling. The foil stack was removed, and counting was initiated at a counting facility located at the LANSCE staging area. These preliminary results confirmed that measurable activities were produced in the foils with the existing experimental protocol. The next day the target with a “full” instrumentation set of 11 foil stacks was irradiated. These foil stacks were placed along the top of the target at 10 cm intervals (plus one foil stack that was positioned 5 cm from the front face). Foil stacks also were placed at 90 degree intervals around the target at the 10 cm axial location. After 4 h of beam at 24 nA, 2.27×10^{15} protons were delivered, the beam was stopped, and the foils were retrieved. Two foil stacks (at the 20 cm and 40 cm axial locations) were left on the target for the remainder of the TOF phase of the experiment.

Some foils were initially counted at the LANSCE Staging Area counters, primarily the bismuth foils. All foils were then sent to the C-INC group at Los Alamos National Laboratory for further counting. At the end of the TOF phase of the experiment, the two remaining foil stacks were retrieved

from the target. These foils were on the target as it received $\sim 1.65 \times 10^{16}$ protons over a 38 h period. The foils from these stacks were counted at the LANSCE Staging Area counters

Two foil stacks also were irradiated in a target station downstream of the nearby target 4 facility. Target 4 is a tungsten target that produces a hard spallation-neutron spectrum for neutron experiments. The advantage was that the neutron spectrum had been well characterised for this location; therefore, the foils' activation could be compared to a known spectrum. Two stacks were used to increase the amount of foil material because the flux was very low ($\sim 3 \times 10^5$ n/cm²/s) in this location. The foils were irradiated for ~ 98 h for a total integrated neutron fluence of $\sim 1.5 \times 10^{11}$ n/cm² and then withdrawn and counted at the staging area facility.

Preliminary results

Initial analysis of the foils was conducted for the target 4 irradiation. The activities of various isotopes were determined for the various materials. The overall activity of the foils was very low, and many foils showed few, if any, isotopes from irradiation. For the isotopes that were measured, the level of activity at the time of the count was quantified and the activity adjusted back to the end of the irradiation (time-zero) and then adjusted to a "saturation" activity based on the beam current history of the irradiation. A set of reactions was built up and analysed using the STAY'SL [3] code. The starting spectrum used was supplied by the LANSCE-3 group [4]. Twenty-eight reactions from nine foils eventually were used to reconstruct the neutron spectrum in STAY'SL. A list of the reactions and their relative match to the fitted spectrum is given in Table 1.

In Table 1, the measured activity is the computed saturation activities for each reaction and the approximate level of uncertainty. Estimated Activity is the result of folding the fitted spectrum with the cross section for the given reaction and represents the "ideal" saturation activity. The % Diff column shows how the measured activity differs from this estimate. The Chi is a measure of the magnitude of the difference that also has uncertainties from the measurement and cross section factored in. The 90% Energy Range are the upper and lower energy bounds where 90% of the activity of the reaction is produced.

The foil activities are mostly within +/-20% of the expected values based on the resultant spectrum. Some reactions show significant deviation from the expected values. For example, the Co(n,4n)Co-56 reaction differs significantly from the expected level of activity. In this case, high levels of background for the ⁵⁶Co peaks make quantification somewhat uncertain. A similar problem plagues the analysis of the ²⁰²Bi because overlap from ²⁰²Pb gammas interferes with quantification of the isotope. However, assignment of larger errors to these uncertain isotopes allows them to be carried through the calculation and the spectrum to be analysed.

Figure 2 shows the previously measured neutron spectrum and the one derived from analysis of the foils. The two show relatively good agreement. A low-energy tail extending into the epithermal region can be seen. It was necessary to reconstruct this part of the spectrum to balance activities from the low-energy threshold reactions. The other foil packets also have been counted, and the isotopes contained have been identified and quantified. Those results still are being compared to estimated spectra from the target computed with MCNPX. The values for the spectra in Figure 2 are given in the Appendix.

The TOF results have been analysed, and the preliminary results are available from the preliminary experimental report [5].

Table 1. Foil results from target 4 irradiation

Reaction	Measured activity (decays/atomx10 ²⁴)	Error (%)	Estimated activity (decays/atomx10 ²⁴)	% Diff	Chi	90% energy range	
AL27(N,*)NA24	5.53E+03	5	5.48E+03	0.9	0	7.00E+00	2.40E+02
FE(N,X)MN54	1.46E+04	15	1.03E+04	29.6	2.4	4.00E+00	3.60E+02
FE(N,*)48V	1.12E+03	15	1.36E+03	-21.7	0.5	6.40E+01	5.20E+02
CO59(N,P)FE59	2.92E+03	15	2.69E+03	7.7	0.2	4.00E+00	2.00E+01
CO59(N,NA)MN54	4.41E+03	25	5.11E+03	-15.8	0.2	3.20E+01	4.60E+02
CO59(N,2N)CO58	3.00E+04	10	3.02E+04	-0.7	0	1.30E+01	2.20E+02
CO59(N,4N)CO56	1.09E+03	19	1.98E+03	-81.3	3.5	4.40E+01	4.00E+02
CU(N,*)58CO	4.77E+03	15	4.87E+03	-2.2	0	3.60E+01	4.60E+02
LU(N,X)LU169	8.83E+03	10	1.01E+04	-14.7	0.2	5.60E+01	2.00E+02
LU(N,X)LU170	1.43E+04	15	1.49E+04	-3.8	0	4.40E+01	2.60E+02
LU(N,X)LU171	2.44E+04	7	2.21E+04	9.3	0.2	3.60E+01	2.40E+02
LU(N,X)LU172	2.42E+04	5	2.26E+04	6.6	0.1	2.80E+01	2.40E+02
LU175(N,G)LU176	2.54E+04	20	2.48E+04	2.4	0	9.20E-03	2.00E+00
AU197(N,G)AU198	1.82E+04	5	2.11E+04	-15.6	1.3	1.20E-02	3.00E+00
AU197(N,4N)AU194	2.82E+04	5	2.49E+04	11.6	0.5	2.80E+01	3.80E+02
AU197(N,2N)AU196	6.63E+04	5	6.23E+04	6.1	0.2	9.00E+00	2.20E+02
IN115(N,N')IN115	4.97E+04	15	6.77E+04	-36.2	2.6	1.00E+00	1.10E+02
IN115(N,G)IN116	3.38E+04	5	2.98E+04	11.8	2.5	1.20E-02	3.00E+00
TB(N,9N)TB151	3.72E+03	15	3.53E+03	5.2	0.1	8.00E+01	3.20E+02
TB(N,7N)TB153	1.19E+04	15	7.69E+03	35.5	5.6	6.00E+01	1.80E+02
TB(N,6N)TB154	9.02E+03	15	9.32E+03	-3.3	0	4.80E+01	1.60E+02
TB(N,5N)TB155	1.70E+04	15	1.77E+04	-4.3	0.1	3.60E+01	1.50E+02
TB(N,4N)TB156	2.05E+04	5	2.11E+04	-2.8	0.3	2.80E+01	1.40E+02
BI(N,11N)BI199	5.72E+03	20	4.66E+03	18.4	0.3	1.10E+02	4.80E+02
BI(N,8N)BI202	3.20E+03	30	6.51E+03	-103.2	4	7.60E+01	3.60E+02
BI(N,7N)BI203	1.10E+04	5	9.17E+03	16.4	0.9	6.00E+01	3.60E+02
BI(N,6N)BI204	1.10E+04	5	1.07E+04	2.9	0	5.20E+01	3.20E+02
BI(N,5N)BI205	2.10E+04	5	1.80E+04	14.3	0.7	4.00E+01	2.80E+02
BI(N,4N)BI206	2.44E+04	5	2.28E+04	6.6	0.1	2.80E+01	2.40E+02

Summary

The preliminary results for foil analysis in the target 4 beamline showed good agreement with the established spectrum for that location. Although some reactions are very divergent, most show good agreement with the known neutron spectrum in that location. This determination establishes confidence in the spectral unfolding technique with the current foil materials in a spallation neutron environment, especially in the case of the bismuth and terbium foils that do not have much history in their use. Work continues on the analysis of the foils from the LBE target irradiated in the Blue Room to characterise the spectrum at various locations on the target surface.

Further information about the experimental set-up and initial results can be found in the preliminary report [5].

Future work

In addition to continued analysis of the foils from the December irradiation, a further irradiation of targets and conditions is planned for July 2002 and December 2002. It is expected that targets having a radius of 5, 10, and 20 cm will be irradiated under a variety of beam conditions and that the neutron spectra will be measured with a combination of TOF and activation foil techniques.

These results will ultimately be compared to predictions from the MCNPX code to gather information on the accuracy of the physics and transport of the protons and neutrons from LBE targets.

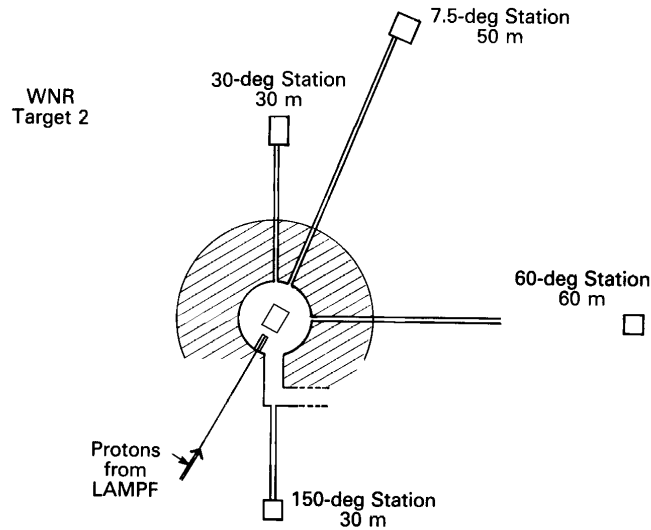
Acknowledgements

This work has benefited from the use of the Los Alamos Neutron Science Center at Los Alamos National Laboratory. This facility is funded by the United States Department of Energy under Contract W-7405-ENG-36. The authors also would like to acknowledge the contributions of Valentine Tcharnotskaia and Keith Woloshun for their invaluable work in the target fabrication and assistance during the experiment.

REFERENCES

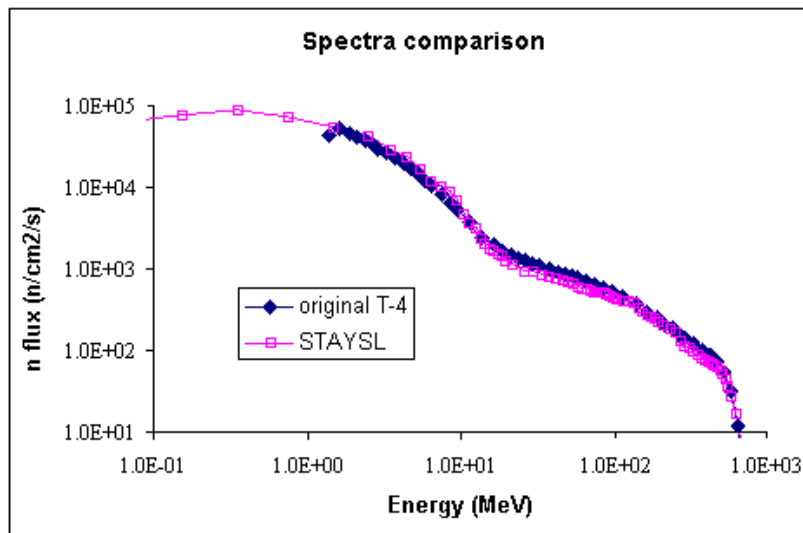
- [1] Hughes, H.G. et al., "Recent Developments in MCNPX," *ANS Proceedings of the 2nd International Topical Meeting on Nuclear Applications of Accelerator Technology*, Gatlinburg, TN, 20-23 September 1998, pp. 281-286.
- [2] Killian, E.W., and L. V. East, *J. of Rad. and Nuc. Chem.*, v. 233 (#1-2), pp. 109-114, 1988.
- [3] Perey, F.G., "Least squares dosimetry unfolding: The program STAY'SL", ORNL/TM-6062, ENDF-254 (October 1977).
- [4] Takala, B., LANSCE-3, LANL, private communication.
- [5] Klann, R.T., M.R. James, G.L. Morgan, K.A. Wolshun, E.J. Pitcher, M.A. Paciotti, J.M. Oostens, and V. Tcharnotskaia, "Neutron Leakage from a Lead-Bismuth Target: Report of Preliminary Results", Los Alamos National Laboratory report, in preparation.

Figure 1. A schematic of the LANSCE “Blue Room” (WNR target 2), with the relative locations of the target and the TOF beam tunnels shown



Note: The LBE target was placed in the centre of the room. (*This figure is not to scale.*)

Figure 2. Comparison of the measured spectra with spectra derived from activation foils results in the target 4 irradiation facility



Note: The solid diamonds are the previously characterised neutron spectrum, and fission chambers and the spectrum resulting from analysis of the activation foils are the open squares.

Appendix

Table of neutron spectra from Figure 2
 (The last column shows the ration in the measured flux to the
 estimated flux from the STAYSL analysis.)

Energy (MeV)	Measured (n/MeV/cm2/s)	STAYSL (n/MeV/cm2/s)	Ratio (measured/STAYSL)
7.63E-02	5.83E+04	6.65E+04	0.88
0.15	7.00E+04	7.96E+04	0.88
0.35	9.00E+04	9.27E+04	0.97
0.75	8.00E+04	7.40E+04	1.08
1.50	5.00E+04	5.49E+04	0.91
2.50	4.00E+04	4.41E+04	0.91
3.50	2.57E+04	3.00E+04	0.86
4.50	1.85E+04	2.37E+04	0.78
5.50	1.34E+04	1.71E+04	0.78
6.50	9.57E+03	1.21E+04	0.79
7.50	8.26E+03	1.04E+04	0.79
8.50	7.26E+03	9.02E+03	0.80
9.50	5.69E+03	6.99E+03	0.81
10.50	3.96E+03	4.81E+03	0.82
11.50	3.47E+03	3.77E+03	0.92
12.50	2.97E+03	3.19E+03	0.93
13.50	2.23E+03	2.36E+03	0.94
14.50	1.96E+03	2.05E+03	0.96
15.50	1.78E+03	1.83E+03	0.97
16.50	1.69E+03	1.71E+03	0.99
17.50	1.60E+03	1.59E+03	1.01
18.50	1.51E+03	1.49E+03	1.02
19.50	1.43E+03	1.26E+03	1.13
22.00	1.31E+03	1.14E+03	1.14
26.00	1.13E+03	9.70E+02	1.16
30.00	1.12E+03	9.51E+02	1.18
34.00	1.05E+03	8.84E+02	1.19
38.00	1.00E+03	8.36E+02	1.20
42.00	9.50E+02	7.92E+02	1.20
46.00	9.00E+02	7.48E+02	1.20
50.00	8.50E+02	7.06E+02	1.20
54.00	8.00E+02	6.65E+02	1.20
58.00	7.50E+02	6.26E+02	1.20
62.00	7.10E+02	5.95E+02	1.19
66.00	6.90E+02	5.82E+02	1.19
70.00	6.60E+02	5.61E+02	1.18
74.00	6.30E+02	5.40E+02	1.17
78.00	6.20E+02	5.36E+02	1.16
82.00	6.10E+02	5.32E+02	1.15
86.00	5.95E+02	5.23E+02	1.14
90.00	5.60E+02	4.96E+02	1.13
94.00	5.40E+02	4.81E+02	1.12
98.00	5.20E+02	4.66E+02	1.12

Energy (MeV)	Measured (n/MeV/cm2/s)	STAYSL (n/MeV/cm2/s)	Ratio (measured/STAYSL)
105.00	4.85E+02	4.36E+02	1.11
115.00	5.14E+02	4.24E+02	1.21
125.00	4.96E+02	4.06E+02	1.22
135.00	4.81E+02	3.88E+02	1.24
145.00	4.43E+02	3.33E+02	1.33
155.00	4.05E+02	2.96E+02	1.37
165.00	3.67E+02	2.68E+02	1.37
175.00	3.42E+02	2.57E+02	1.33
185.00	3.23E+02	2.38E+02	1.36
195.00	2.97E+02	2.18E+02	1.36
210.00	2.78E+02	1.99E+02	1.40
230.00	2.53E+02	1.80E+02	1.41
250.00	1.93E+02	1.64E+02	1.17
270.00	1.50E+02	1.26E+02	1.19
290.00	1.35E+02	1.13E+02	1.19
310.00	1.25E+02	1.03E+02	1.21
330.00	1.15E+02	9.44E+01	1.22
350.00	1.05E+02	8.56E+01	1.23
370.00	9.80E+01	7.95E+01	1.23
390.00	9.20E+01	7.43E+01	1.24
410.00	8.80E+01	7.14E+01	1.23
430.00	8.40E+01	6.89E+01	1.22
450.00	7.90E+01	6.57E+01	1.20
470.00	7.30E+01	6.15E+01	1.19
490.00	6.50E+01	5.55E+01	1.17
510.00	5.90E+01	5.11E+01	1.15
530.00	5.00E+01	4.40E+01	1.14
550.00	4.10E+01	3.66E+01	1.12
580.00	3.00E+01	2.73E+01	1.10
620.00	1.80E+01	1.67E+01	1.08
660.00	1.00E+01	9.49E+00	1.05
700.00	6.00E+00	5.80E+00	1.03
740.00	2.40E+00	2.36E+00	1.02
780.00	5.00E-01	4.99E-01	1.00

GAS PRODUCTION CROSS-SECTION MEASUREMENTS AT LANSCE

Robert C. Haight, Matthew Devlin
Los Alamos Neutron Science Center
Los Alamos National Laboratory

Abstract

We are measuring the production cross sections for hydrogen and helium production by neutrons from threshold to 100 MeV on structural materials of importance to the advanced accelerator application programme. Our approach is to measure the isotopes of hydrogen and helium as they are emitted in the nuclear reactions such as (n,xp), (n,xd), and (n,xalpha). The data include not only the production cross-sections but also the angular distributions and energy spectra of the emitted particles. These benchmark data also test nuclear reaction model calculations. Progress to date is reported.

Introduction

The goal of this project is to measure hydrogen and helium production on structural materials proposed for the AAA programme in the neutron energy range up to 100 MeV. At present there are few data above 20 MeV for such important elements as iron, chromium, nickel, and molybdenum. New evaluations that extend to higher energies [1] are based to a great extent on nuclear model calculations. The data in these new evaluations, especially for the structural materials, invite tests and validation.

We have begun a programme to measure these cross sections on elemental constituents of structural materials. This work is a continuation of measurements made up to 60 MeV on other materials such as silicon [2] and cobalt [3].

Our method is to detect protons, alpha particles and other isotopes of hydrogen and helium emitted in reactions induced by neutrons at the WNR/LANSCE spallation neutron source. Schematically, the measurement approach is shown in Figure 1, where the correspondence of these microscopic measurements is made to the materials environment. Protons, deuterons, tritons, ^3He and alpha particles are emitted in reactions of the neutrons with the constituent elements of the material. In a component that is more than a few millimeters thick, most of these light charged particles stop in the material itself, although a few with high enough energy will exit the component and stop in neighbouring material. For our experiments, we select thin foils of the material of interest so that all of the light charged particles can escape with little energy loss. We are thereby able to measure not only the production cross sections for the isotopes of hydrogen and helium, but also the energies of the emitted particles and their angular distributions. Although these latter two quantities do not affect the hydrogen and helium production, they are of importance in validating nuclear model calculations because they serve as further constraints on the models. With improved models, the production cross sections can be calculated with more confidence, and this is important for reactions that are difficult to measure in the laboratory.

Another important feature of our experiments is that the data are obtained for the full range of incident neutron energies simultaneously. Figure 2 illustrates the technique. The WNR/LANSCE neutron source is a pulsed source based on short (sub 1 ns) bunches of 800 MeV protons that are incident on a tungsten neutron-production target. The resulting neutrons are collimated into small neutron beams, which then pass along flight paths to the experimental stations. For these measurements, we place samples 15 meters from the neutron source and use time-of-flight techniques to deduce the energy of the neutron that induced the reaction. As shown in the figure, the faster neutrons arrive at the sample first and are followed by lower energy neutrons.

From our previous work [2], we show in Figures 3 and 4 the type of data we expect to obtain. Spectra of alpha particles emitted from silicon are shown in Figure 3 for four bins of incident neutron. The total production cross section for alpha particles is obtained by integrating the over the emitted energies. For silicon, the production cross section for alpha particles, which is very nearly the total helium production cross section, is shown in Figure 4 over the range of incident neutron energies from threshold (about 6 MeV) to 60 MeV. Nuclear model calculations from the GNASH code are also shown in Figure 3 and 4. In this case, the experimental validation of the calculations shows good agreement between the model calculations and the data.

Experimental set-up

The test chamber is an evacuated chamber 55.9 cm in inside diameter to accommodate the test materials and the detectors. The apparatus is located on the 30 degree right beam line at the LANSCE/WNR spallation neutron source and is 15 meters from the neutron source. The chamber and the detector layout are shown in Figure 5.

Detector systems for the emitted charged particles are deployed at 4 angles with respect to the incident neutron beam direction. The angles are chosen to cover much of the full angular range so that the angle-integrated production cross-section can be reliably determined from the differential data. The detectors are coincidence counters consisting of low-pressure gas proportional counters followed by silicon surface barrier detectors and thick CsI(Tl) detectors to stop the most energetic hydrogen and helium nuclei. Signals from these detectors undergo preliminary processing near the chamber, and then the processed signals are transported to further electronics and a data acquisition system in a nearby building.

Progress to date

In this quarter (January-March, 2002) we have analysed the data taken in November and December 2001. These data were to commission the detector station, shielding, detectors and the data acquisition system. For this commissioning, we used an iron sample and concentrated on the proton emission (hydrogen production) at several angles. Detection of protons from the target is challenging because protons are easily produced by neutron interactions with shielding materials. Typical data are shown in Figure 6. A measure of the quality of data is the signal-to-background ratio. The signal-to-background ratios have been found to be 6:1 in the forward angles and 3.5:1 at 90 degrees at $E_n=100$ MeV. At lower neutron energies, the signal to background ratios are significantly better. These results show that the measurement programme is possible as planned. Some improvements in the shielding are indicated to make the measurement programme even more solid, and we are pursuing them.

To obtain beam time for the production measurements beginning in August 2002, we prepared a request for beam time. The LANSCE programme advisory committee is at present reviewing this proposal, along with many others. We expect no problem with this review because, to our knowledge, there are no other requests to use this detector station.

We have made significant progress in increasing the staffing of this project. We have hired a new postdoctoral fellow who will join our group in July 2002. Two beginning graduate students will be with us this summer to develop improved detectors and to help in conducting the experimental runs.

Summary

The production cross sections for hydrogen and helium are being investigated up to 100 MeV incident neutron energy on structural materials of importance to the advanced accelerator application programme. Initial runs have proven the practicability of the approach. In the next running period, beginning in July 2002, production runs will be made on iron and other materials as chosen by the AAA programme.

REFERENCES

- [1] Chadwick, M.B., P.G. Young, S. Chiba, S.C. Frankle, G.M. Hale, G. Hughes, A.J. Koning, R.C. Little, R.E. MacFarlane, R.E. Prael, and L.S. Waters, "Cross Section Evaluations to 150 MeV for Accelerator-Driven Systems and implementation in MCNPX," Nucl. Sci. and Eng. **13**, 293 (1999).
- [2] Bateman, F.B., R.C. Haight, S.M. Sterbenz, M.B. Chadwick, P.G. Young, and S.M. Grimes, "Light Charged-particle Production from Neutron Bombardment of Silicon: Role of Level Densities and Isospin", Phys. Rev. C **60**, 064609-1 (1999).
- [3] Grimes, S.M., C.E. Brient, F.C. Goeckner, F.B. Bateman, M.B. Chadwick, R.C. Haight, T.M. Lee, S. M. Sterbenz, P. G. Young, O. A. Wasson, and H. Vonach, "The $^{59}\text{Co}(n,\alpha)$ Reaction from 5 to 50 MeV", Nucl. Sci. Eng. **124**, 271 (1996).

Figure 1. Relationship of gas production in materials to our approach to measuring the production rate

Gas production by neutrons in materials

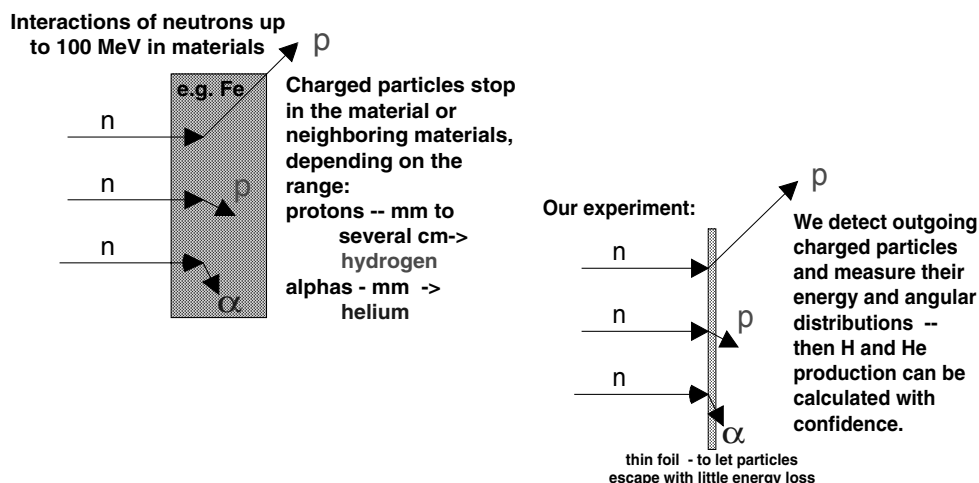
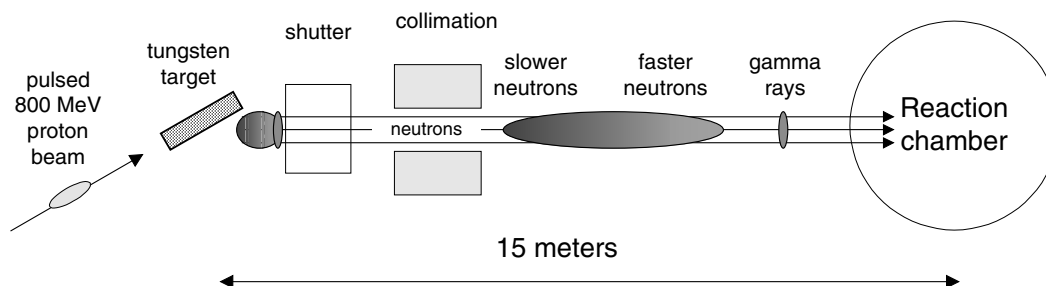


Figure 2. Time of flight technique

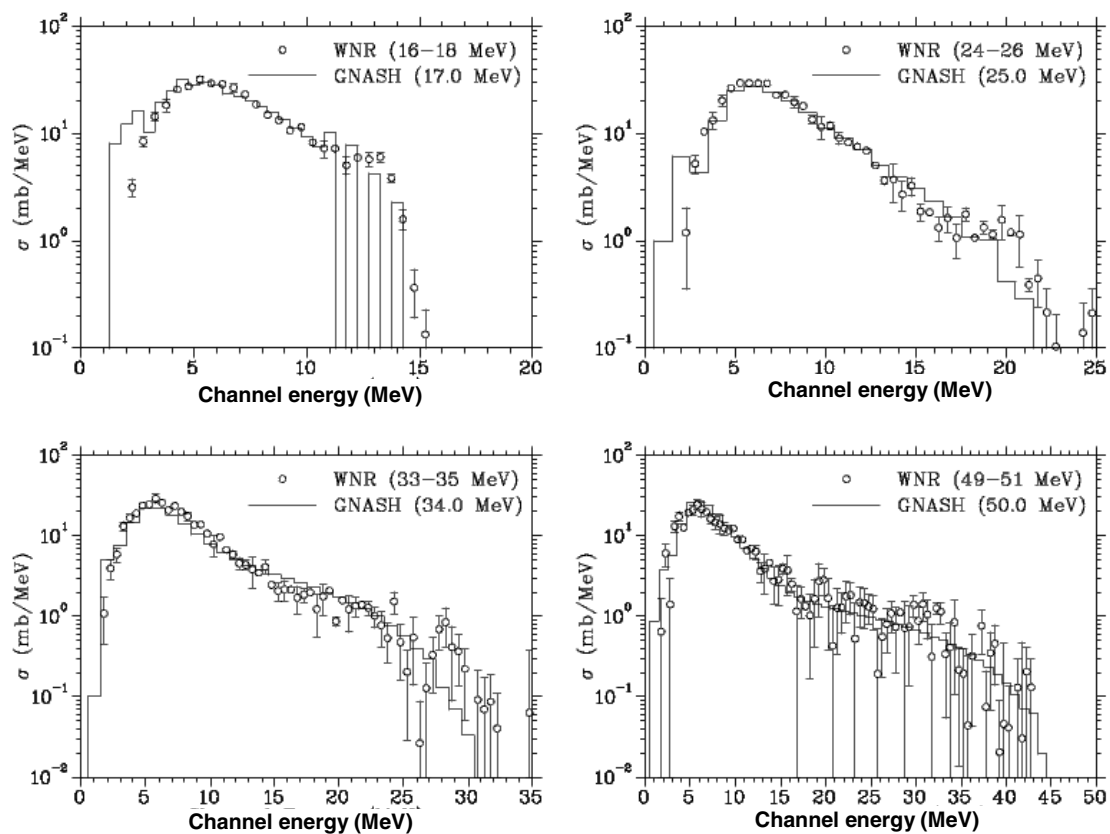
Time of flight over the flight path identifies the energy of the neutron that induces the reaction



Note: The incident proton beam is pulsed with a burst width of less than 1 ns. Neutrons, produced in the tungsten target by spallation reactions, are collimated into a neutron beam that travels 15 meters mostly through air before reaching the reaction chamber. Gamma rays from the source reach the reaction chamber first and are followed in turn by fast neutrons and then by the slower neutrons. The neutron time of flight is measured by a “start” timing pulse, derived from the proton beam and a “stop” pulse from detectors in the reaction chamber.

Figure 3. Spectra of alpha particles emitted from silicon bombarded by neutrons in four energy ranges

Si(n, α) Angle-integrated cross sections



Note: These data are integrated over the angle of emission. Nuclear model calculations (GNASH) are shown as the histogram lines [2].

Figure 4. Excitation function of the cross-section for alpha-particle emission from silicon in neutron-induced reactions [2]

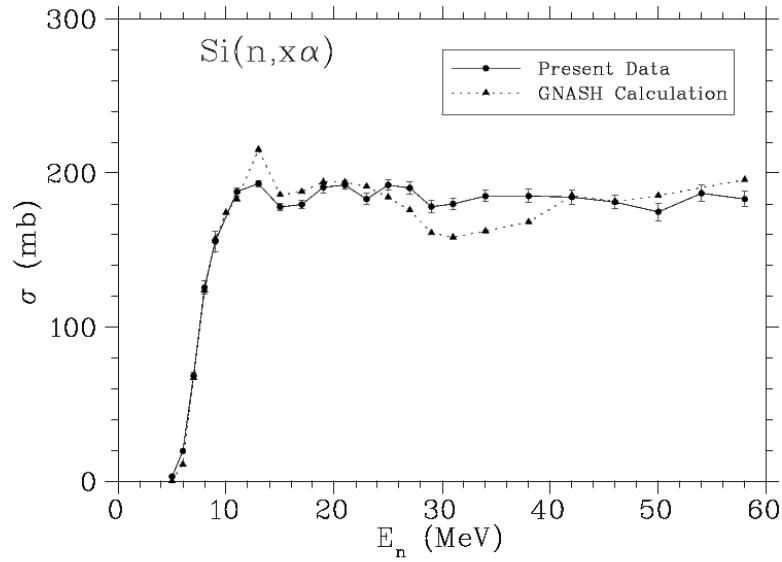


Figure 5. Layout of apparatus for measuring neutron-induced hydrogen and helium production showing collimation for the neutron beam, target position, and array of detectors

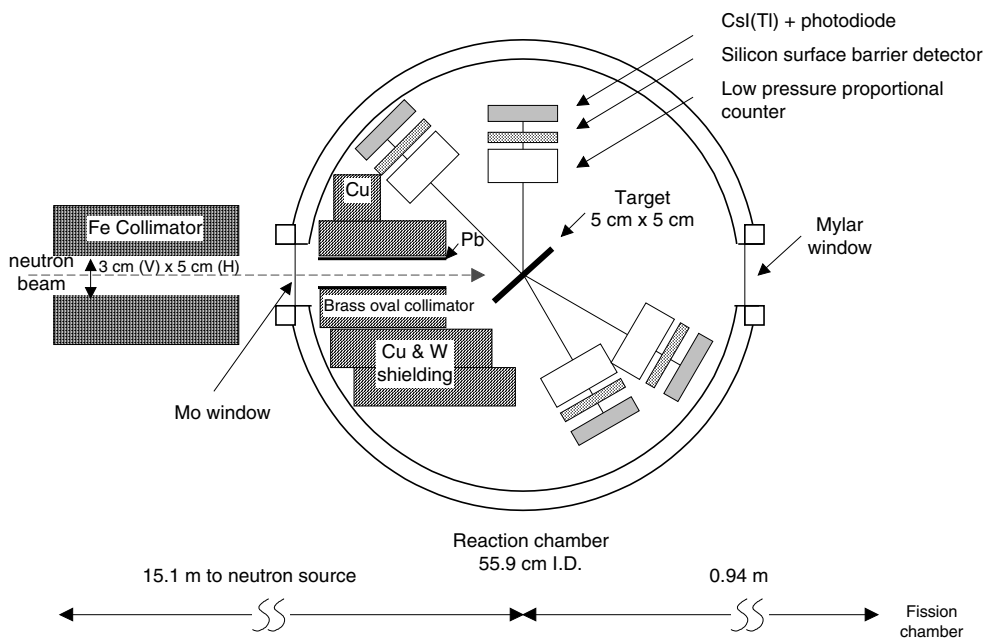
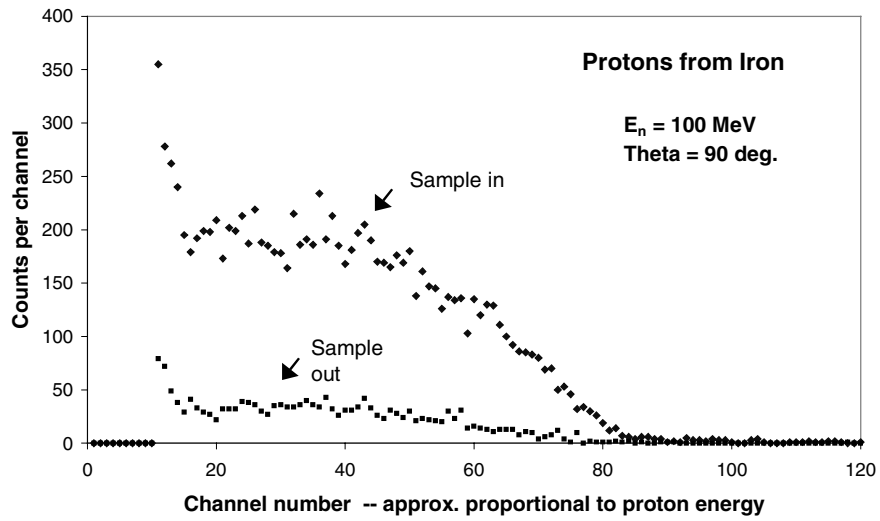


Figure 6. Sample-in and sample-out measurements of proton production from an iron sample at a neutron energy of 100 MeV



Note: The signal-to-background ratio is good at this neutron energy and significantly better at lower incident neutron energies.

THERMAL-HYDRAULIC DESIGN ANALYSIS OF A 5 MW SODIUM-COOLED TUNGSTEN TARGET

X. Cheng¹, P.J. Finck², J. Roglans-Ribas,² T. Schulenberg¹

¹Forschungszentrum Karlsruhe
Postfach 3640, 76021 Karlsruhe, Germany

²Argonne National Laboratory
9700 South Cass Avenue, Argonne, IL 60439, USA

Abstract

One of the main objectives of the ADTF (accelerator-driven test facility) is the demonstration of the feasibility of the accelerator-based transmutation of nuclear waste. A pre-conceptual design of an accelerator-driven, sodium-cooled subcritical multiplier assembly has been developed with a thermal power of 100 MW. A high-energy proton beam (600 MeV/5 MW) is fed to the spallation target for neutron production. In the design configuration with a solid target with tungsten plates, the subcritical assembly core and the target form two parallel flow paths cooled with sodium. The present thermal-hydraulic analysis focuses on the following aspects:

- Cooling capability of the beam window.
- Cooling capability of the tungsten plates.
- Passive decay heat removal.

The effect of important design parameters on the thermal-hydraulic behaviour of the target has been investigated. Based on the results achieved, reference thermal-hydraulic designs of the sodium-cooled tungsten target are proposed. Measures are recommended and assessed to enhance the thermal-hydraulic performance of the target under both normal operating conditions and passive decay heat removal conditions.

Introduction

The proposed accelerator-driven test facility (ADTF) within the advanced accelerator application programme of the US Department of Energy is envisioned as a major nuclear research facility with multiple testing and production capabilities [1]. One of the main objectives of the ADTF is the demonstration of the feasibility of the accelerator-based transmutation of nuclear waste. For this purpose, an accelerator-driven subcritical multiplier (SCM) is being designed with a thermal power of 100 MW [2]. A high-energy proton beam (600 MeV/5 MW) is fed to the spallation target for the neutron production. Two different designs of the spallation target have been considered, i.e. a heavy liquid metal (HLM) target or a sodium-cooled tungsten target. In the HLM target, liquid lead-bismuth eutectic (LBE) is used as the spallation material and the coolant as well. One of the major concerns of a LBE target is the big deficiency in reliable technology of operating a lead-bismuth cooled facility.

Although solid tungsten targets have been constructed for some other purposes, the heat deposition density in the present application is much higher than in the cases studied in the past. In the ADTF test facility with a solid target, the subcritical reactor core and the target form two parallel flow paths with common circulating pumps. The thermal-hydraulic behaviour of the target under normal operating conditions as well as under passive decay heat removal conditions need to be investigated. The present analysis focuses on the following aspects:

- Cooling capability of the beam window. The beam window is made of steel and separates the accelerator-related devices from the reactor island. A high heat deposition density in the beam window makes the cooling capability of the window one of the most challenging tasks of the target design.
- Cooling capability of the tungsten plates. Thin tungsten plates are used as the spallation material, which are covered with steel cladding. A sufficient cooling capability has to be provided to both the tungsten plate and the cladding.
- Passive decay heat removal. In a solid target, decay heat is released in the solid materials located in the spallation zone. A safe removal of the decay heat under natural convection conditions is one of the design requirements.

This paper summarises the thermal-hydraulic analysis carried out to date. Based on the results achieved, a reference design of a sodium-cooled tungsten target is proposed. The effect of important design parameters on the thermal-hydraulic behaviour of the target has been investigated. Measures are recommended and assessed to enhance the thermal-hydraulic performance of the target under both the normal operating condition and the passive decay heat removal condition. To complete the design of the solid target, structural analyses should be performed and integrated with the thermal-hydraulic analyses.

Boundary conditions

The main characteristics and requirements of the solid tungsten target are summarised as follows [2]:

- Proton energy : 600 MeV
- Beam power : 5 MW
- Beam diameter : 16.2 cm
- Coolant : sodium
- Spallation material : tungsten
- Radial beam power distribution : uniform
- Sodium inlet temperature : 360°C
- Maximum coolant velocity : 5 m/s
- Maximum window temperature : 600°C
- Maximum cladding temperature : 600°C
- Window and structural material : stainless steel (HT9)

The heat released in the active part of the solid tungsten target is about 3.7 MW. For the present analysis, the heat deposition rate in the beam window and in the structure material is assumed to be 50% of that in tungsten at the same location. Sodium is assumed to be transparent to the proton beam. Based on the experience available, the maximum velocity of sodium should be lower than 5.0 m/s. From thermal stress consideration the maximum temperature of the beam window, as well as the cladding material, has to be kept below 600°C. The sodium inlet temperature is the same as the temperature at the core inlet (about 360°C). The four centre rings of the SCM core are left open to accommodate the spallation target, which has an outer diameter of 34 cm. At the conceptual design phase, many options are still open related to the design of the reactor core. In general, it was agreed that the existing sodium systems technology gained at EBR-II should be applied to ADTF as far as possible [2]. In the reference proposal, a fuel pin of EBR-II type (MK-III) has been proposed. The fuelled length of the EBR-II fuel pin is about 36 cm. Therefore, the length of the spallation zone should be smaller than 36 cm.

Target proposals

Two design configurations were proposed, as shown in Figures 1 and 2. Table 1 summarises some reference parameters of both configurations.

Table 1. Reference parameters of both configurations

Configurations	Horizontal plates	Vertical plates
Number of tungsten plate [-]	55	6 x 28
Thickness of the tungsten plates [mm]	3.00	4.00
Cladding thickness [mm]	0.15	0.15
Flow channel width [mm]	2.50	3.00
Diameter of beam window [mm]	200	200
Thickness of beam window [mm]	2.50	2.50
Effective heat transfer coefficient across the gap [kW/m ² K]	5.00	5.00

In the first design, the tungsten plates are placed horizontally in the spallation zone, whereas in the second design the tungsten plates are arranged vertically. Both designs have a single flow path, i.e. the coolant cools at first the tungsten plates and then the beam window. In the reference proposal of the horizontal configuration, the total number of tungsten plates is 55. The thickness of each tungsten plate is 3 mm. This gives a total tungsten thickness of 165 mm for beam damping. The flow channels between two tungsten plates have a height of 2.5 mm. This gives a total height of the channels of 135 mm. In this case, the total height of the spallation zone is about 320 mm. The tungsten plate has a circular shape with two extended wings. The diameter of the circle is 200 mm, and the outer diameter of the wings is 330 mm, which is identical to the inner diameter of the guard tube. The wall thickness of the guard tube is 5 mm. The diameter of the vacuum beam tube is 200 mm. The beam window has a hemispherical shape with a thickness of 2.5 mm. A cladding is required for the tungsten plates for structural purpose and to retain spallation products. The thickness of the cladding should be as small as possible. A thickness of about 0.15 mm is used for the reference proposals. The effect of the cladding thickness on the cooling capability has to be assessed. In the wing region, the thickness of the tungsten plates could be reduced, to provide sufficient space for a gas plenum accommodating spallation gas.

A perforated plate is located close to the beam window, to achieve a desirable flow distribution close to the window and to provide a sufficient cooling capability of the beam window. The porosity distribution of the perforated plate should be optimised. If required, a perforated plate is put at the target inlet, to guide the inlet flow smoothly to the riser annuli and to minimise flow recirculation in the inlet region. The pressure drop through the target assembly should match the pressure drop through the multiplier fuel assemblies.

Figure 1. Horizontal configuration

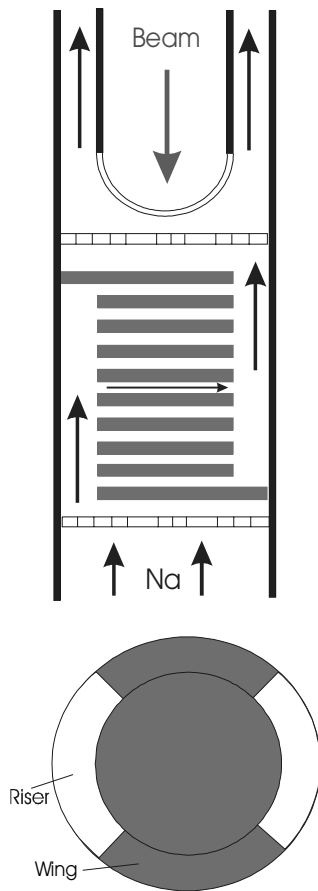
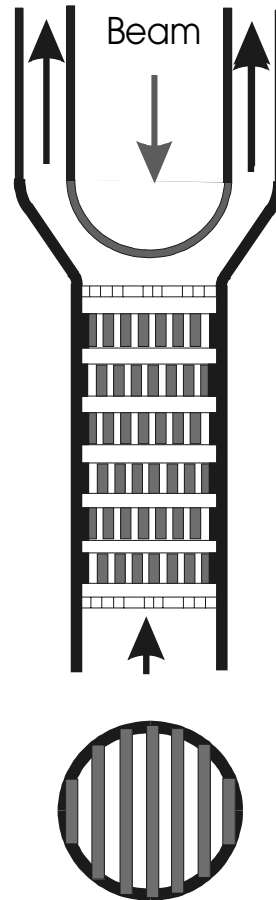


Figure 2. Vertical configuration



The mass flow rate of sodium into the target is 40 kg/s. This gives an average sodium temperature rise of 70°C. The average sodium velocity in the riser and in the channels is 3.4 m/s and 2.2 m/s, respectively, below the maximum acceptable velocity of 5 m/s.

In the second proposal, the tungsten plates are placed vertically in the spallation zone. The thickness of the plates is 4 mm, and the height of the plates is 55 mm. The channels between plates have a width of 3 mm. The entire spallation zone is axially divided into six sub-zones. Each sub-zone contains a tungsten plate bundle with 28 plates. The six tungsten plate bundles are staggered, so that for each proton there is at least 165 mm of beam damping depth of tungsten. The gap between each sub-zone is about 5 mm. The total height of the spallation zone is 355 mm. The lower part of the guard tube has an inner diameter of 200 mm. The total flow area is about 0.018 m². This gives an average velocity of about 2.6 m/s, also below acceptable limits. The flow area in the beam region is about 0.012 cm². The temperature increase in the beam region might be about 30% higher than the average value.

Results and discussion

This study analyses the thermal-hydraulic behaviour of the target under both normal operating conditions and passive decay heat removal conditions. The effect of the following parameters has been studied:

- Thickness of the tungsten plate.
- Thickness of the cladding.
- Thermal resistance of the gap between the cladding and the tungsten plate.
- Width of the flow channels.
- Porosity distribution of the perforated plates.

Horizontal configuration under normal operating conditions

Under normal operating conditions, the flow behaviour in the target and the cooling capability of both the spallation zone (tungsten plate and cladding) and the beam window are investigated.

Spallation zone

The spallation zone consists of an inlet riser, an outlet riser and 55 flow channels. Thermal-hydraulic behaviour in the spallation zone has been analysed using a one-dimensional approach. Figure 3 shows the coolant velocity in different channels for the reference parameters. The channel number is ordered from the top down to the bottom, i.e. channel 1 is the channel closer to the beam window. It is seen that the coolant velocity both in the upper part and in the lower part is higher than in the middle region. However, this velocity difference is small, less than 1%.

Figure 4 shows the maximum temperature of the coolant, the cladding and the tungsten plate in different flow channels. The results show that the maximum cladding temperature in the entire spallation zone is about 520°C, well below the design limit (600°C). A large temperature drop (about 500°C) across the gap between the cladding and the tungsten plate is obtained. In this analysis, the effective heat transfer coefficient of the gap was 5.0 kW/m²K, corresponding to a helium gas layer with a thickness of about 20 µm.

Figure 3. Flow velocity in different channels

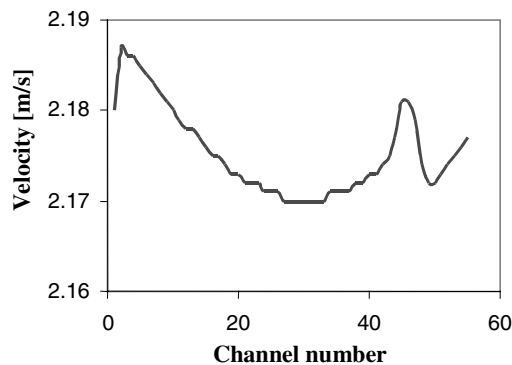


Figure 4. Maximum temperature in different flow channel

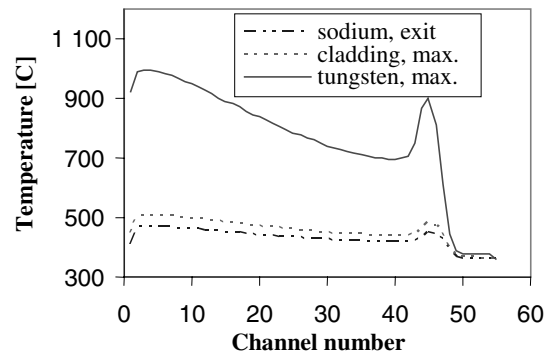


Figure 5. Effect of the tungsten plate thickness on the maximum temperatures

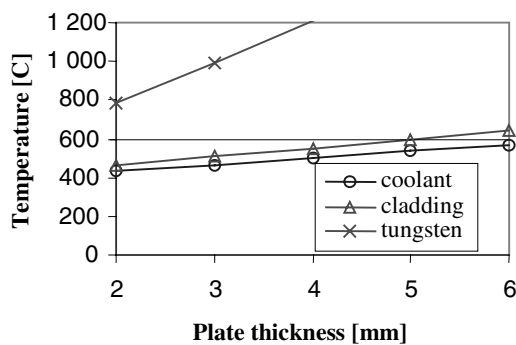
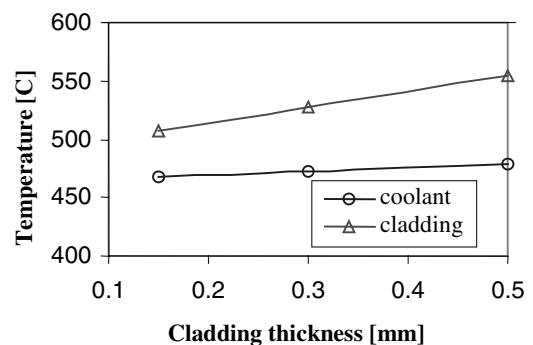


Figure 6. Effect of the cladding thickness on the maximum temperatures



- Thickness of the tungsten plate

The upper limit of the thickness of the tungsten plate is determined by the maximum temperatures in the spallation zone. Figure 5 shows the maximum temperature of the coolant, the cladding and the tungsten plate versus the plate thickness. At a thickness of 5 mm, the cladding temperature exceeds the design upper limit (600°C). The selection of the lower limit of the plate thickness is mainly based on the consideration related to the target construction and to the total beam damping length. A smaller plate thickness leads to a larger number of plates, to provide sufficiently large beam damping length. At the same time, the flow channel width has to be reduced accordingly, to keep the total height of the spallation zone within the fuel pin length (36 cm). A plate thickness of 2 mm requires a channel width of about 1.5-2.0 mm. The construction of both the thin tungsten plate and the narrow flow channels would be a challenging task. Furthermore, the thermal expansion and deformation of the plates have to be taken into account, to avoid local flow reductions and excessive local temperature peaks. Based on the above considerations, a plate thickness of 3.0 mm and a channel width of 2.5 mm have been proposed for the horizontal configuration.

- Thickness of the cladding

The thickness of the cladding affects mainly the cladding temperature. Figure 6 shows the maximum coolant temperature and the maximum cladding temperature versus the cladding thickness. The cladding material (HT-9) used in this study has a high thermal conductivity. Even with a cladding thickness of 0.5 mm, the cladding temperature is still below 600°C. If another material, e.g. SS316, is used as the cladding material, the thermal conductivity is reduced by about 35%. In this case, a cladding thickness of 0.5 mm would be the upper design limit.

The selection of the cladding thickness is also dependent on the tungsten plate thickness. For a larger plate thickness, the upper limit of the cladding thickness will be reduced. A combined design optimisation of all the geometric parameters is necessary for the final design of the target.

Beam window

For the analysis of the cooling capability of the beam window, only the upper part of the target is considered, i.e. the region above the uppermost tungsten plate, as indicated in Figure 7. Due to the non-symmetric arrangement, flow modelling must be three-dimensional in this region. However, for this preliminary analysis, this region is simplified to an axis-symmetric 2-dimensional domain, as shown in Figure 8. Coolant is assumed to enter the domain in the annular gap. Some geometric parameters are summarised as follows:

- Inner radius of the beam tube (R1) : 100 mm
- Thickness of the beam window (D4) : 2.5 mm
- Inner radius of the guard tube (R2) : 165 mm
- Distance between the tungsten plate and the perforated plate (D1) : 100 mm
- Distance between the perforated plate and the beam window (D2) : 30 mm
- Thickness of the perforated plate (D3) : 5.0 mm

The diameter of the tungsten plate is identical to the diameter of the beam window, i.e. 200 mm. The perforated plate is divided into three zones, as shown in Figure 9. In the central region there is a single hole with a diameter of D5. In the middle range, $D5 \leq D \leq D6$, and in the outer region, $D6 \leq D$, two different porosity values are assumed, ε_1 and ε_2 .

A thickness of 2.5 mm for the beam window is selected based on the previous experience gained in the design of both the ISTC target [4] and the MEGAPIE target [5]. As window material, HT9 is selected due to its high thermal conductivity and favourable corrosion resistance properties. Assuming that the sodium coolant temperature at the inlet of the target is 360°C and the heat released in the spallation zone is 3.7 MW, a temperature rise of 70°C is obtained through the spallation zone. The sodium temperature at the inlet of the computation domain is 430°C. The inlet velocity of sodium is 1.0 m/s. For this numeric analysis, the CFD code CFX-4.4, has been used.

Figure 7. 3-D Flow domain close to the beam window

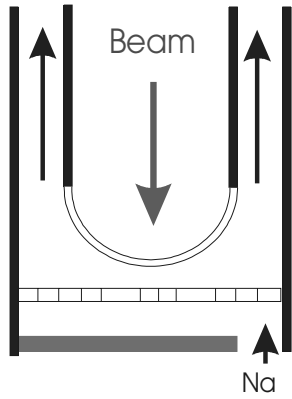


Figure 8. Simplified computational domain for the 2-D CFX calculation

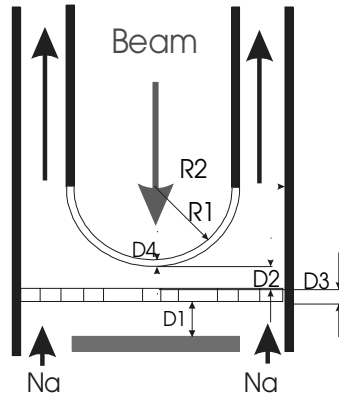
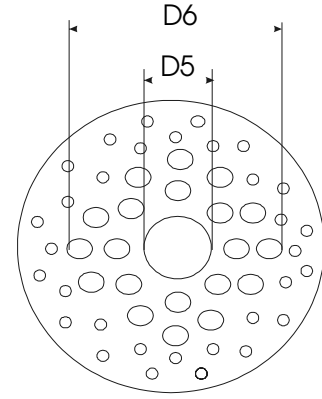


Figure 9. Perforated plate



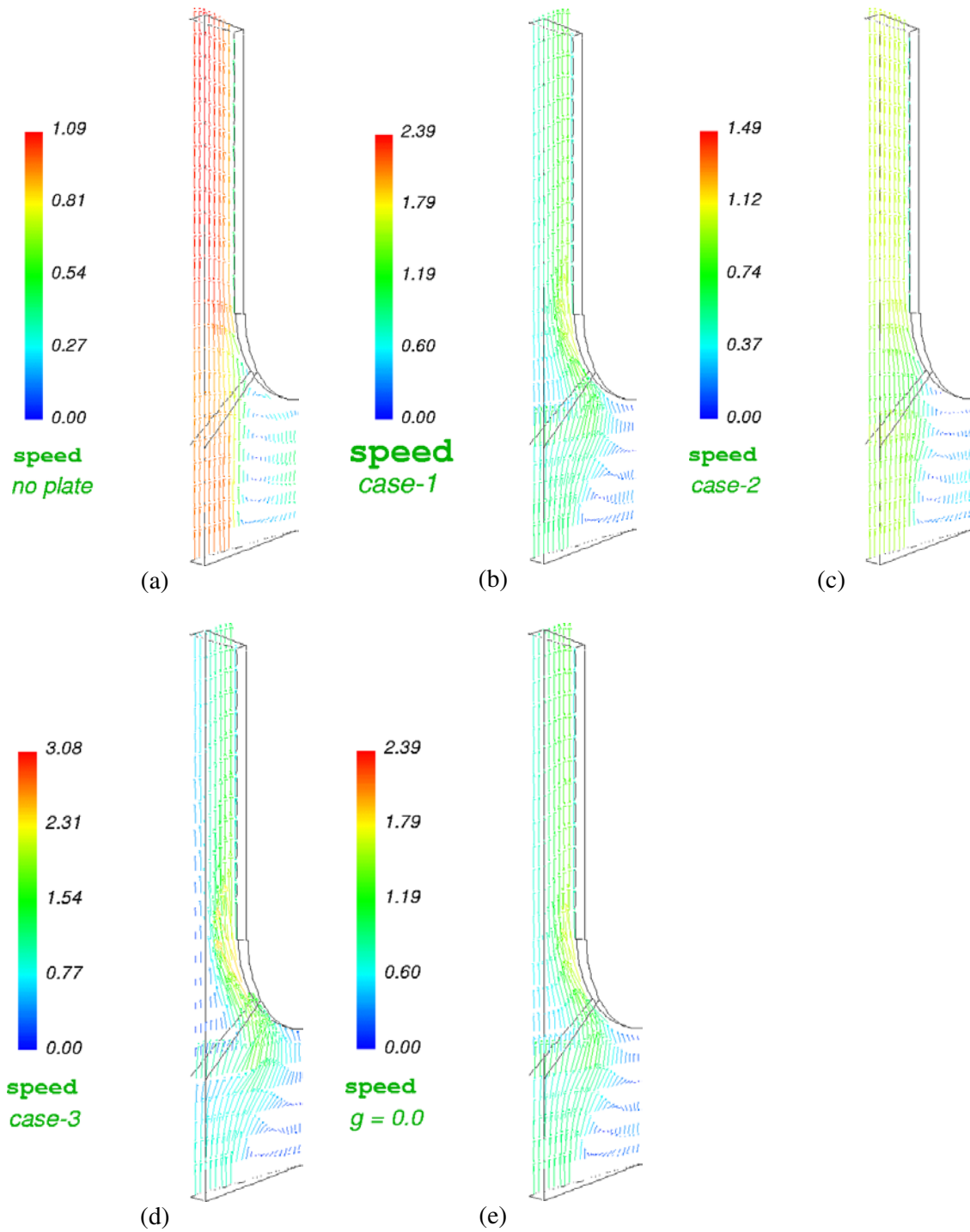
Five different cases have been analysed, as summarised in Table 2. The effect of the distribution of perforated plate porosity is investigated with the first four cases, whereas in the fifth case, the gravitation acceleration (g) is set to be zero, to analyse its effect on the heat transfer behaviour. The diameter of the central hole ($D5$) is 60 mm. The outer diameter of the middle region ($D6$) is 200 mm.

Table 2. 2-D CFD results

	Input data			Results			
	ϵ_1	ϵ_2	g	V_{max} [m/s]	U_{rev} [m/s]	T_{max} [C]	ΔP [Pa]
Case 1	0.5	0.2	9.8	2.39	-0.37	549.87	1145
Case 2	0.5	0.5	9.8	1.49	-0.38	647.32	290
Case 3	0.5	0.1	9.8	3.08	-0.30	545.40	2286
Case 4	no perforated plate		9.8	1.09	-0.46	648.71	115
Case 5	0.5	0.2	0.0	2.39	-0.37	549.87	1145

Figure 10 shows the velocity fields in the five different cases. The main results are summarised in Table 2. For all cases a flow re-circulation zone occurs in the region below the perforated plate and close to the symmetry axis. In the case without a perforated plate, coolant entering the annular gap flows mostly straight ahead. In the cases with perforated plates, coolant is partially forced to flow towards the central region. The smaller the porosity ϵ_2 , the stronger the coolant flow towards the window centre, and the higher the maximum sodium velocity in the computational domain. However, both the size of the flow re-circulation zone and the maximum reversal flow velocity are reduced with the reduction of porosity in the outer region.

Figure 10. Velocity field in five different cases



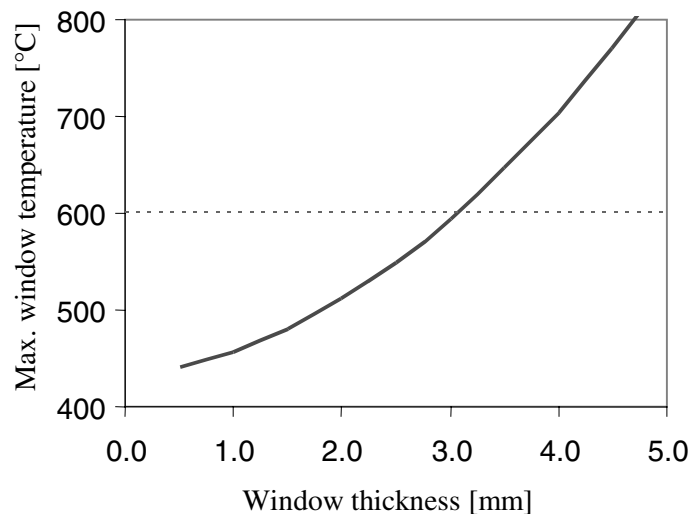
In the case without a perforated plate, there is a large hot zone close to the window centre. The maximum window temperature is about 650°C . A significant reduction in this hot zone is achieved for the cases with a porosity of the outer region smaller than 20%. The maximum temperature of the

window is reduced to about 545°C. It is seen in Table 2 that the gravity acceleration has no effect on either the velocity field and the temperature field.

- Window thickness

The thickness of the beam window is one of the key parameters affecting the maximum window temperature. By neglecting the heat conduction in the circumference direction, the estimated maximum window temperature is shown in Figure 11 for the case 1 versus the beam window thickness.

Figure 11. Effect of the window thickness on the maximum window temperature



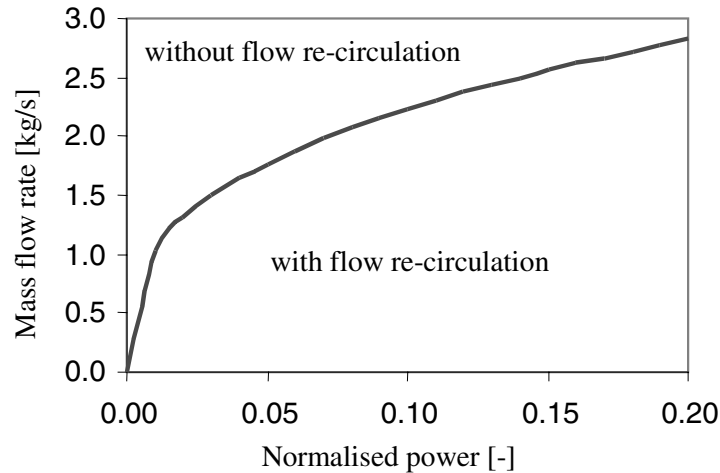
It is seen that the window temperature reaches the design criteria (600°C) at a window thickness of about 3.0 mm. Thus, the proposed reference design assumes a window thickness of 2.5 mm. According to the experience gained during the design of the ISTC target and the MEGAPIE target, a window thickness of about 2.5 mm should be sufficient to withstand thermal and mechanical stress load. Nevertheless, structural analysis will be needed to assess the safety margin.

Horizontal configuration under passive decay heat removal conditions

Spallation zone

One of the important design criteria of the solid target is the feasibility of passive decay heat removal, i.e. the decay heat has to be safely removed by natural convection of sodium. Under natural convection conditions, the coolant velocity in the upper part of the target will be lower than that in the lower part of the target. Under some conditions, flow reversal in the upper part may occur. For the reference proposal, the boundary line (critical line) for the onset of flow re-circulation has been derived, as illustrated in Figure 12. In this figure, the heat generation rate is normalised to the nominal value (3.7 MW). The design of the spallation target has to provide sodium flow rate above the critical line under natural convection conditions.

Figure 12. Critical line for the onset of flow re-circulation



The mass flow rate through the target under passive decay heat removal conditions depends on the design of the reactor core, the primary loop and the target itself. For the present analysis, the following data are taken (pressure drops are similar to that of EBR-II [2]):

- Thermal power of SCM : 100 MW
- Thermal power of the target : 3.7 MW
- Pressure drop over the reactor core : 0.27 MPa
- Pressure drop over the primary loop (no core) : 0.07 MPa
- Mass flow through the target : 40 kg/s
- Mass flow through the active core : 720 kg/s
- Mass flow through the entire primary loop : 810 kg/s
- Elevation difference between the active core and the upper plenum : 1.0 m
- Elevation difference between the active core and the heat exchanger : 3.7 m

The decay heat fraction in the spallation zone (tungsten plate), which is defined as the ratio of the decay heat to the nominal power, should be lower (to approximately 25%) than in the reactor core [3]. Due to the lack of reliable data, two different values of the decay heat fraction are studied for the target, i.e. 100% and 25% of the decay heat fraction in the reactor core.

Figure 13 shows the mass flow rate through the target versus the decay heat fraction. For comparison, the critical mass flow rate is also indicated in this figure. For a decay heat fraction of 25% of that in the core, the mass flow rate is well above the critical value. A nearly uniform distribution of the velocity is obtained (see Figure 14). In this case, a sufficient cooling capability of the spallation zone is provided. For a 100% decay heat ratio, the mass flow rate through the target is close to, but smaller than, the critical value. Flow re-circulation in the upper part of the spallation target takes place (Figure 14). Coolant and cladding temperature will exceed acceptable values.

Figure 13. Mass flow rate into the target under natural convection conditions
(F_q : decay heat ratio)

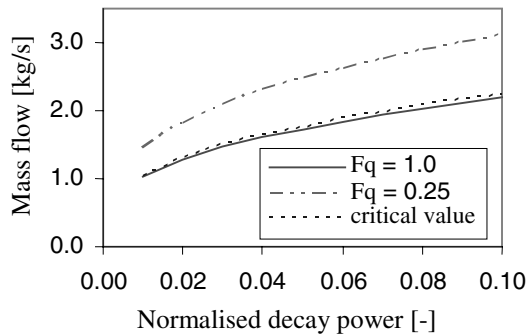
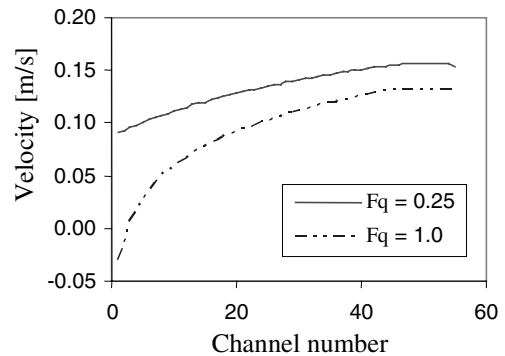


Figure 14. Velocity in different flow channels under natural convection conditions
(core decay heat fraction=5%)



A possibility to achieve a more uniform distribution of the coolant flow in the spallation zone, is the introduction of additional hydraulic resistance at the inlet of each flow channel. Figure 15 shows the velocity distribution in the flow channels for a flow restriction with a hydraulic resistance of 10 inserted into each flow channel. In this case the assumed ratio of the decay heat fraction is 100%. Compared to the case without an additional hydraulic resistance (Figure 14), the velocity distribution is much more uniform. A sufficient cooling capability for the spallation zone is obtained (Figure 16).

Figure 15. Velocity in each flow channel with additional hydraulic resistance
(core decay heat fraction=5%)

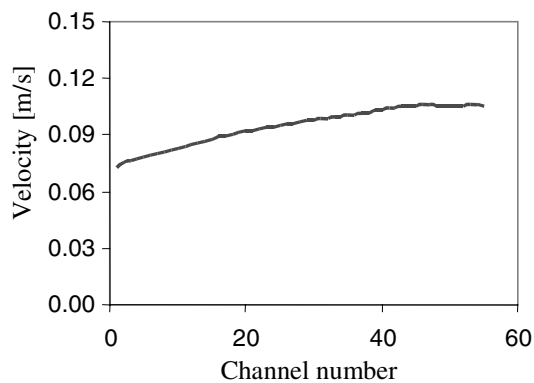
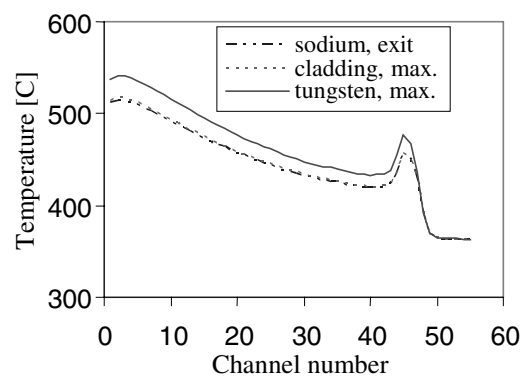


Figure 16. Temperatures in each flow channel with additional hydraulic resistance
(core decay heat fraction=5%)



Beam window

The total mass flow rate into the spallation target under natural convection conditions (see Figure 13) is supplied to cool down the beam window. This mass flow rate is sufficient to safely remove the decay heat from the beam window.

Vertical configuration

For the time being, no detailed analysis has been carried out for the vertical configuration. The main challenge of this design is to provide sufficient large beam damping depth (at least 16 cm), and at the same time to keep the total height of the spallation zone below 36 cm. To cope with this boundary condition, the gap between the plate bundles is small, i.e. 5 mm in the reference proposal. This would cause a high pressure drop over the spallation zone. It is worth mentioning that this restriction will disappear if the target is used in a subcritical reactor with fuel pin with a larger fuelled region.

A similar cooling capability for both the spallation zone and the beam window is expected in the vertical configuration as in the horizontal configuration. A perforated plate located close to the beam window is recommended, to enhance the coolant mixing and to achieve a more uniform temperature distribution of the coolant before it cools down the beam window. Detailed analysis of the cooling behaviour and the design optimisation of the perforated plate should be carried out in the next phase.

In the vertical configuration, passive decay heat removal is not a serious concern. No local flow re-circulation is expected under passive decay heat removal conditions. The mass flow rate established under natural convection conditions will be sufficient to cool down both the spallation zone as well as the beam window.

Summary

In this study, two different configurations have been proposed for a sodium cooled tungsten target for the accelerator-driven test facility (ADTF). Detailed thermal-hydraulic design analysis has been carried out for the horizontal configuration. The effect of important design parameters has been investigated.

Under normal operating conditions, a sufficient cooling capability has been achieved for both the cladding and the tungsten plate, if the cladding thickness is less than 0.5 mm. The cooling capability of the spallation zone under passive decay heat removal conditions is one of the key limitations of this design. A significant improvement can be achieved by inserting additional hydraulic resistance into the flow channels. The CFD calculations performed so far indicates a sufficient cooling capability of the beam window if the perforated plate for flow distribution is properly designed.

Detailed 3-D CFD analysis is required in the future to optimise the geometrical arrangement of the upper part of the target, including the perforated plate. The feasibility of the proposed target designs needs to be assessed related to neutron-physics, thermal-mechanics and material consideration.

A similar cooling capability of both the spallation zone and the beam window is expected in the vertical configuration as in the horizontal configuration. A safe decay heat removal under natural convection conditions is easily realised in the vertical configuration.

Acknowledgement

The work was carried out during the assignment of the first author at the Argonne National Laboratory from May 2001 to May 2002. The colleagues of the Engineering Simulation Section of RAE have provided important support in performing the CFX-4.4 calculation.

REFERENCES

- [1] Los Alamos National Laboratory, *et al.* ADTF, Request for Approval of Mission Need, Critical Decision-0, AAA-TP0-ADTF-01-0006, February 2001.
- [2] ADTF Design Team, Private Communication, Argonne National Laboratory, May 2001-May 2002.
- [3] Mohamed Y., A. Gohar, Private Communication, 2001.
- [4] Yefimov, E., The main results of feasibility study of liquid metal targets and the working plan on the project #559, Kick-off meeting on the ISTC project #559, February 1998, Obninsk.
- [5] Salvatores, M., G. Bauer, G. Heusener, The MEGAPIE Initiative – Executive Outline and Status as per November 1999, Paul Scherrer Institut, 1999.

SESSION III

Test facilities and control/safety/shutdown

Chair: Ph. Finck

**SAFETY ANALYSIS OF NA AND PB-BI COOLANTS
IN RESPONSE TO BEAM INSTABILITIES**

M. Eriksson, J. Wallenius, J.E. Cahalan*, K. Tucek, W. Gudowski
Royal Institute of Technology, Department of Nuclear and Reactor Physics
10691 Stockholm, Sweden
*Argonne National Laboratory, Reactor Analysis and Engineering Division
9700 South Cass Ave., Argonne, IL 60439, USA

Abstract

A comparative safety study has been performed on sodium vs. lead/bismuth as coolant for accelerator-driven systems. Transient studies are performed for a beam overpower event. We examine a fuel type of recent interest in the research on minor actinide burners, i.e. uranium-free oxide fuel. A strong positive void coefficient is calculated for both sodium and lead/bismuth. This is attributed to the high fraction of americium in the fuel. It is shown that the lead/bismuth-cooled reactor features twice the grace time with respect to fuel or cladding damage compared to the sodium-cooled reactor of comparable core size and power rating. This accounts to the difference in void reactivity contribution and to the low boiling point of sodium. For improved safety features the general objective is to reduce the coolant void reactivity effect. An important safety issue is the high void worth that could possibly drive the system to prompt criticality.

Introduction

Both sodium and lead/bismuth are considered as coolant candidates in accelerator-driven systems. At RIT a global safety study of accelerator-driven systems is performed to investigate neutronic and transient characteristics of lead/bismuth vs. sodium as primary coolant and the performance of oxide, nitride, and metallic fuels for various accident initiators and core sizes. In the present analysis we benchmark the two coolants for oxide fuel in the response to a sudden beam excursion. This type of accident initiator is unique to accelerator-driven systems and is open to considerable question. One of the most questionable items is the nature of the initiating circumstances; for example; what is the maximum beam load change that could possibly occur and at what speed can this transition materialise? The outcome will depend strongly on the details of these conditions as well as on the time over which the beam remains on. In the following paper, the beam is presumed to double in strength in an instant and remain on for an unspecified time. The extreme nature of this assumption is subject to debate. However, the analysis of accidents that appear incredible is an important part of the design of a safe reactor. Much can be learned from simulated severe accidents. The purpose of the present paper is to measure the strengths and weaknesses of two particular coolants, independent of probability, or even possibility, of occurrence.

Model and assumptions

The benchmark is performed using a common design, set of assumptions, and computational methods. The continuous energy MCNP simulation code is applied to the neutronics analysis. A 3-D pin-by-pin model is defined. Oxide fuel is adopted being diluted with zirconium dioxide. In order to flatten the power distribution, the core is subdivided into two regions with varying content of ZrO_2 . We have adopted a Pu to TRU ratio of 40% at BOL since this composition minimises reactivity losses over a large number burnup cycles [1]. The Pu/TRU ratio is kept constant. The plutonium isotopic vector corresponds to the discharge from spent MOX fuel (5% ^{238}Pu , 38% ^{239}Pu , 30% ^{240}Pu , 13% ^{241}Pu , and 14% ^{242}Pu). The americium composition consists of two thirds ^{241}Am and one third of ^{243}Am . The analysis aimed at increasing the core diameter through an increase in pin pitch while holding the pin diameter and core height constant. Pitch-to-diameter ratios are varied in the range from $P/D=1.25$ to 2.25 (constant $D=8$ mm). To compensate the reactivity loss when P/D is increased the fraction of ZrO_2 is adjusted (from core average of 30% at $P/D=2.25$ to 70% at $P/D=1.25$) in order to preserve $k_{eff}=0.97$. A summary of design parameters is presented in Table 1.

Transient analysis is performed with the aid of the SAS4A safety code [2]. A primary heat transport system is defined and represented by the core, primary pumps, the shell side of the heat exchangers, connecting piping, and compressible pool volumes with cover-gas surfaces. Coolant passage through the core is modelled by a single thermal and hydraulics channel. The feedwater system is assumed to remove heat at 100% for all time. Thus, when the power increases above nominal, there will be a mismatch in heat production and heat removal and the net effect is core inlet temperature rising with time. The point kinetics approximation is used for calculating transient power. A value of β_{eff} equal to 0.20% is assumed, a representative value for a minor actinide burner. The coolant flow rate in a lead/bismuth-cooled reactor is limited by erosion/corrosion damage of structural material. At present the flow rate of lead/bismuth is taken to be 2.5 m/s. No such limitation exists for the sodium-cooled reactor where the main concern in the past has been to limit pumping power requirement. For that reason a sodium flow rate of 5 m/s is adopted. Transient response is calculated assuming intact core geometry; i.e., fuel pins and coolant channels are well defined, precluding the possibility for insertion of large reactivity values by core compaction. Temporal and spatial void distributions are calculated. Reactivity feedbacks are modelled by coolant density changes and an

assumed Doppler constant of $Tdk/dT = -38$ pcm. As will be seen, the Doppler coefficient has negligible influence on the operational behaviour. The void reactivity coefficient and the prompt neutron lifetime are determined from static neutronic analysis, as discussed in the next section. In a preliminary study, a uniform void coefficient is used. Structural reactivity feedback phenomena (e.g. radial and axial core expansion) have been excluded considering the low responsiveness of a source-driven system to reactivity changes [3]. Under the present conditions, structural expansion introduces reactivity changes that are small with respect to the void effect. It is recognised, however, that such reactivity feedback effects may affect the calculated performance values.

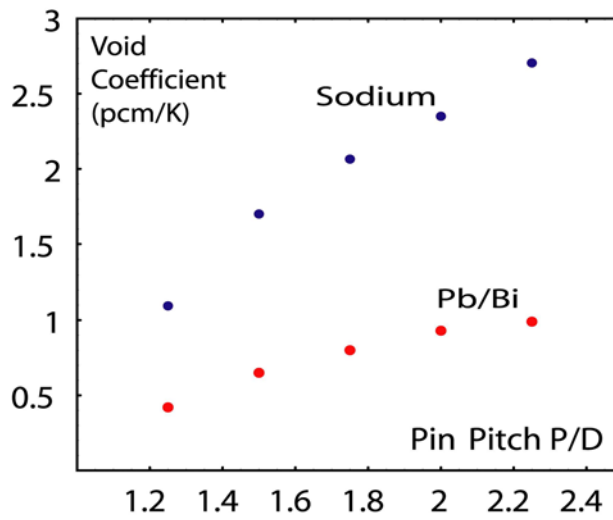
Table 1. Design parameters

Characteristic	Value
Core power	800 MWth
Average linear power	16 kW/m
Core coolant inlet temperature	573 K (Pb/Bi and Na)
Coolant flow rate	2.5 m/s (Pb/Bi) and 5.0 m/s (Na)
Fuel composition	$(Pu_{0.6}Am_{0.4})O_2 + ZrO_2$
Fuel porosity	10%
Core height	1.00 m
Fission gas plenum height	1.50 m
Outer fuel radius	3.45 mm
Inner cladding radius	3.50 mm
Outer cladding radius	4.00 mm
P/D	Varied from 1.25 to 2.25
Doppler constant (Tdk/dT)	-38 pcm
k_{eff} (eigenvalue)	0.97
β_{eff}	0.20%

Neutronics analysis

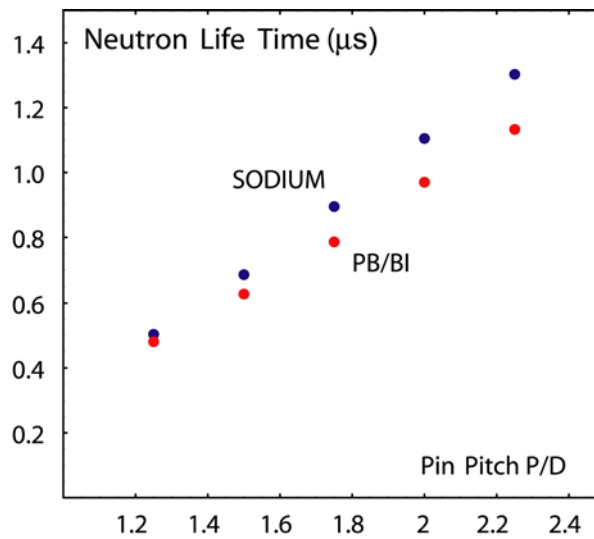
Following coolant voiding there is hardening of the spectrum caused by a decrease in neutron scattering. Removal of coolant also results in higher neutron leakage. Hardening of the neutron spectrum and increased neutron leakage are the two dominating physical phenomena contributing to the void reactivity effect. In general, hardening of the spectrum leads to a positive reactivity component due to an increase in the number of neutrons released per neutron absorbed in the fuel while increased leakage gives rise to a reactivity loss since more neutrons may escape the core. The void reactivity effect has been calculated for the present system and is illustrated in Figure 1. The void coefficient is expressed as a function of pitch-to-diameter ratio. The void coefficient is obtained by calculating the k -eigenvalue at a given density and then performing a second calculation but with a density corresponding to a temperature increase of 200 degrees Celsius. The density is changed uniformly over the core and the upper plenum. Figure 1 indicates that the negative reactivity effect associated with increased neutron leakage is not sufficient to offset the positive reactivity contribution of a harder spectrum. The spectrum effect becomes more positive as P/D increases. As a result, the void reactivity coefficient becomes increasingly positive at higher P/D. It is observed that both coolants possess a significant positive void reactivity coefficient. However, the void coefficient tends to be more positive for sodium because of higher moderating power and an influential scattering resonance in ^{23}Na at 3 keV. In the energy region above 100 keV, the fission-to-capture ratio for ^{241}Am rises more rapidly than for ^{239}Pu . For that reason, the void coefficient becomes more positive if the fraction of americium is increased and the fraction of plutonium is correspondingly decreased.

Figure 1. Void reactivity coefficient [pcm/K]



The prompt neutron lifetime was calculated using MCNP. As expected, the prompt neutron lifetime increases with increasing P/D, corresponding to a softer spectrum and longer distance travelled by neutrons up to their point of absorption. Note that the average neutron lifetime in the lead/bismuth-cooled core exceeds $1\mu\text{s}$ for high pin pitches ($P/D > 2.0$).

Figure 2. Prompt neutron lifetimes



Failure criteria

In order to predict core damage a set of failure criteria has been postulated, those are listed in Table 2. Several difficulties exist in attempting to provide failure criteria for the existing system. The principal difficulty is the uncertainty in the operating performance of the fuel and structural materials. Chemical and mechanical interactions between the fuel, cladding, and coolant, as well as irradiation performance, etc. are not well known. Validation of failure criteria will require the availability of experimental test data. Nonetheless, preliminary safety margins can be established as a first estimate to envelop worst-case conditions. The fuel is assumed to be stable up to the melting point, which is a reasonable assumption for sub-stoichiometric oxide fuel. The fuel melting point as well as thermophysical properties vary with the stoichiometry. Present fuel properties correspond to an oxygen-to-metal ratio of 1.93. The failure temperature is based on the melting point of PuO_2 [4] and AmO_2 [5] together with the melting point of diluent ZrO_2 , applying Vegard's law. The maximum cladding temperature is constrained by mechanical considerations. The primary cladding loading is the internal gas pressure; fuel-cladding mechanical interaction is neglected. We have assumed a maximum internal pin pressure of 10 MPa in steady-state as a result of pressure build-up by the continuous release of fission gases. Under transient conditions the pressure may increase even further causing an increase in the loading of the cladding. Simultaneously, the cladding loses its strength at elevated temperatures. The cladding failure temperature is determined from correlations based on the calculated hoop stress and the failure temperature measured in cladding burst tests (20% cold-worked type 316 austenitic stainless steel) [6]. The transient burst temperature is representative for fast transients where the temperature is rapidly increasing until the cladding fails, providing less time for creep-type deformation.

Table 2. List of failure temperatures

Failure mechanism	Failure temperature	Comment
Melting of oxide fuel	2 886K	$0.11(\text{Pu}_{0.6}\text{Am}_{0.4})\text{O}_2+0.89\text{ZrO}_2$
Cladding burst temperature	1 333K	20% CW SS316, 5.56°C/sec, hoop stress 100 MPa.

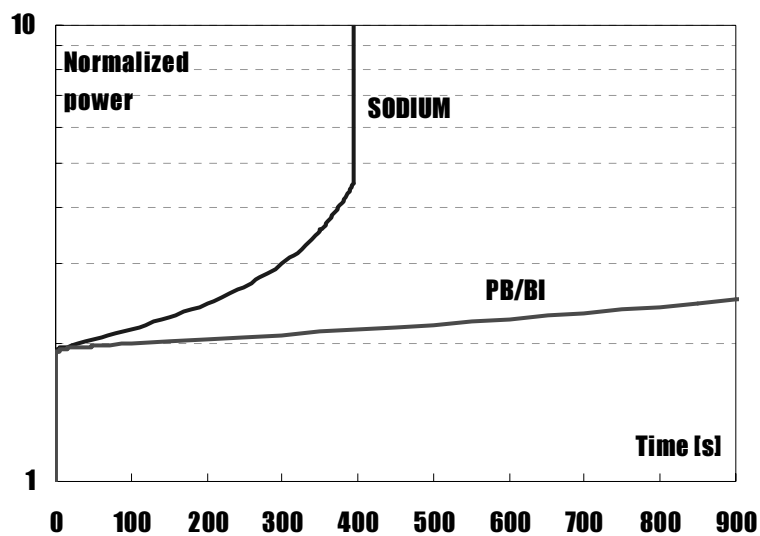
Transient analysis

Transient response has been examined for an unprotected transient overpower (UTOP) event. It is assumed that the intensity of the external neutron source is *promptly increased by twice the initial value*. Reactor shutdown is disregarded. It is possible to imagine that a control system failure or simply inadvertent operation of the accelerator could lead to an accidental increase of beam power. However, it is important to acknowledge the highly hypothetical nature of the accident under discussion.

Transient power is displayed in Figure 3. For the case displayed the pitch-to-diameter ratio is 1.50. The magnitude of the initial burst is the same, independent of the coolant. The steady-state power will multiply by a factor of S/S_0 if the source strength is stepped from S_0 to S . The speed of the transition is determined by the prompt period. Delayed neutrons do not appreciably slow the response.

Following the prompt jump, the power changes as a result of reactivity feedbacks. Coolant void reactivity feedbacks contribute to the course of the accident by adding reactivity. The small negative reactivity feedback associated with the Doppler effect does not influence the course of the accident. Differences in transient behaviour between lead/bismuth and sodium result primarily from the difference in boiling point and void reactivity effect. Coolant density changes provide modest changes in reactivity compared to the full void reactivity effect, which may introduce significant positive reactivity values. This causes the reactivity insertion rate to be considerable larger in the sodium-cooled core. Void generation, and thus positive reactivity insertion, is abrupt in the vicinity when boiling starts. Sodium boiling begins at the core outlet and develops axially downward. In the sodium-cooled core, the void effect adds enough reactivity to bring the reactor to a prompt critical state, with possible severe safety consequences. Prompt critical conditions are established about 400 seconds after accident initiation. Large positive reactivity insertions are potentially possible due to lead/bismuth voiding as well. However, it is seen that the high boiling temperature for lead/bismuth (1 943K) compared to sodium (1 154K) makes voiding less probable even though there are other ways of voiding the coolant besides boiling, i.e. large scale steam generator failure or possibly sudden gas release from ruptured pins. Voiding could possibly occur in severe loss of coolant accidents, such as tank rupture, however this must be regarded as extremely unlikely. It should be recognised that structural damage most likely occurs before boiling is encountered in a lead/bismuth-cooled reactor.

Figure 3. Normalised reactor power, P/D=1.50

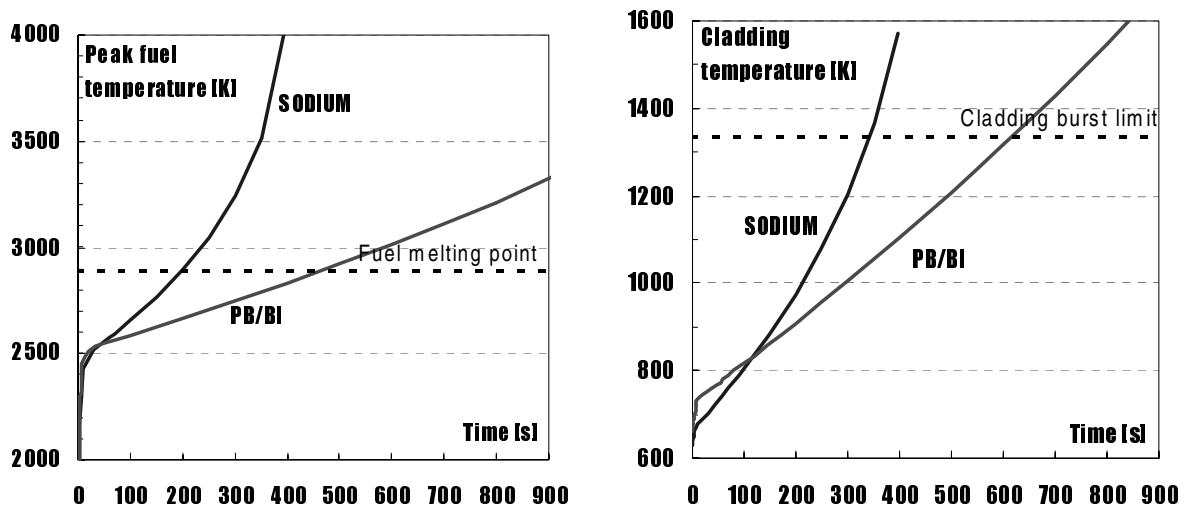


In Figure 4 peak fuel and cladding temperatures are shown for the case P/D=1.50. Since no time is required for heat transport, the fuel suffers a rapid temperature rise. The amount of beam input determines whether there is immediate fuel damage or not. Subsequent heat-up occurs as a result of positive feedback from voiding and insufficient heat removal capability. The steam generators are assumed to remove heat at a rate of nominal power, resulting in increasing core inlet temperature as the transient proceeds. Sharp fuel temperature increase is calculated in the sodium case, as a result of a significant void reactivity insertion. The failure criterion for the fuel is exceeded in 200 seconds and the cladding is expected to reach its burst temperature in 350 seconds. The fuel fails prior to the initiation of sodium boiling (~350 sec) and this might disable the reactor before boiling and prompt criticality occurs. However, it is difficult to determine the consequences of fuel melting. In the sodium

case, cladding failure is predicted to occur by burnout. Cladding failure occurs simultaneously with sodium boiling. It is recognised that a substantial change in the nature of the accident may occur at the onset of fuel or cladding damage. Therefore, extrapolation beyond the actual failure points is subject to considerable uncertainty.

The assumption of constant heat rejection rate is conservative. In an overpower accident it is likely there will be some increase in the heat removal above 100%. Taking this into account would yield less pessimistic results. In reality, the feedwater system would try to maintain the correct coolant temperature returning to the core, and if it is not able to do so, the feedwater system would trip and issue reactor shutdown. It should be recognised that for both coolants considered the grace period is in the order of several minutes, which, in principle, provides considerable time for a well-designed safety system to act.

Figure 4. Peak fuel temperature (left) peak cladding temperature (right), P/D=1.50



The calculation is repeated for a range of pitch-to-diameter ratios. In Figure 5, the grace period is calculated for different P/D's. The grace period is measured in seconds. The grace time decreases somewhat at large pitches, a consequence of higher void coefficient for larger P/D. From the very basis of the assumptions, the choice of coolant does not change the inevitability of reaching a failure point; the timing of failure is different, however. The Pb/Bi cooled core features twice the grace time compared to the sodium-cooled core with the same P/D and power rating. The calculation revealed a small margin to prompt criticality at large pitches (sodium case). It was found that rapid sodium vaporisation and expulsion occurred at the onset of boiling. Prompt criticality could possibly occur in less than 1 sec ($P/D > 1.50$) once sodium boiling is initiated.

Oxide fuel temperatures are sensitive to linear power ratings. The allowable linear power is limited by the melting point. The low thermal conductivity of oxide fuel is compensated somewhat by a high melting point. Figure 6 illustrates the sensitivity of grace time on linear power. The calculation was performed for $P/D=1.50$. It should be recognised that different power ratings correspond to different core total powers in Figure 6. The number of fuel pins is fixed while the steady-state linear power is varied. In the reference case the linear power is 16 kW/m corresponding to a total reactor power of 800 MWth. The mode of failure differs; fuel failure dominates at high linear powers while

cladding failure supersedes as the mode of failure at low linear power (<14 kW/m). The grace period provides an indication of the time available for a safety system to act. It was found that the safety performance of oxide fuel deteriorates rapidly with increasing pin power rating. At high linear power immediate fuel damage may occur, providing little time for a protection system to respond. It is possible to extend the grace period by derating the oxide fuel, but it has some obvious penalties.

Figure 5. Grace period as a function of pin pitch, linear power=16 kW/m

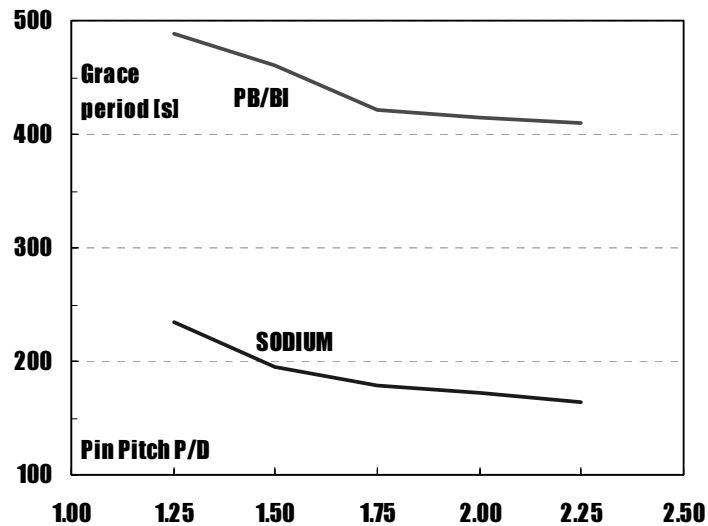
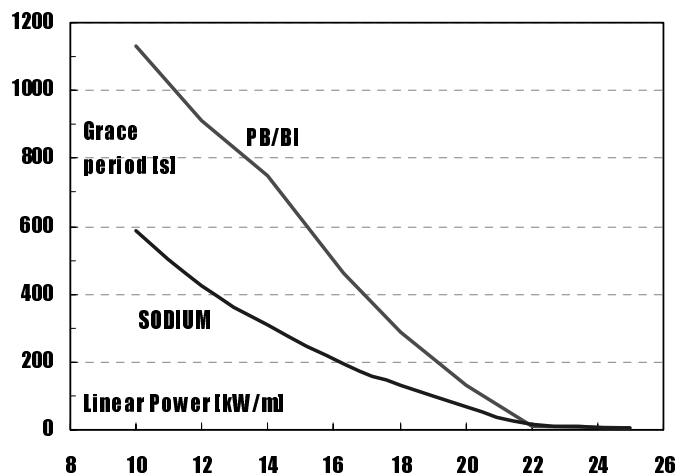


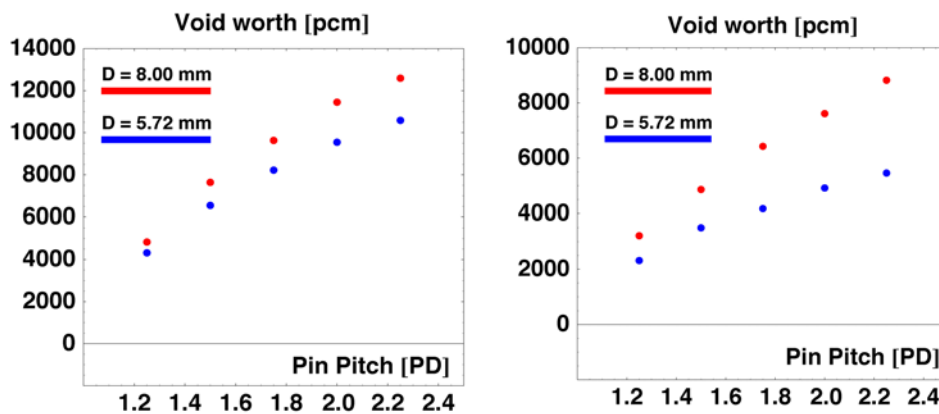
Figure 6. Grace period as a function of linear power rating, P/D=1.50



The characteristics that have the greatest effect in the present analysis are the differences in boiling point and void coefficient. While the boiling temperature is fixed, the void coefficient can change significantly with design parameters. The void reactivity effect is the result of several physical

phenomena and various methods have been proposed for reducing the void worth by design [7]. One possible way of void worth reduction is to reduce the pin size. The net result is shown in Figure 7, where the void worth of lead/bismuth and sodium, respectively, is calculated as a function of P/D. The coolant void worth is determined by removing all coolant from the core and the upper plenum. The results suggest that a significant reduction in the void worth is achievable using smaller pin diameter. Reducing the void worth is an essential design objective. Large values of the void worth may present a difficulty in the licensing of minor actinide burners because of the risk for severe damage to the plant and public safety.

Figure 7. Sodium (left) and lead/bismuth (right) void worth as a function of P/D
(Pin diameter is a parameter)



Summary

Comparison was made of the safety performance of sodium vs. lead/bismuth as primary coolant in a minor actinide burner reactor. The systems were benchmarked for oxide fuel. Neutronic investigations were made on the void reactivity effect for a range of pitch-to-diameter ratios. Transient behaviour for a beam overpower event and the time-to-failure were compared.

A strong positive void coefficient was found for both sodium and lead/bismuth. The considerable void effect is attributed to a high fraction of americium (60%) in the fuel. It was found that void reactivity insertion rates increases with P/D. In response to the particular accident under discussion, the Pb/Bi-cooled core featured twice the grace time compared to the sodium-cooled core. The essential difference is attributed to the difference in boiling point and void reactivity contribution. An important safety issue is the high void worth that could possibly drive the system to prompt criticality. The problem is the result of the present fuel composition and it exists in both the sodium-cooled reactor and the lead/bismuth-cooled reactor. To some degree, this may be counter-balanced with proper core design, e.g. smaller pitch and pin diameter. For improved safety features, the general objective is to reduce the coolant void reactivity effect. The sodium-cooled core was found to have a smaller safety margin to prompt criticality. The high boiling temperature of lead/bismuth makes voiding less probable. The low effective thermal conductivity of oxide fuel results in high fuel temperatures and imposes constraints on the allowable linear power. Derating the oxide fuel could enhance the safety performance, but it has some obvious penalties.

REFERENCES

- [1] Takizuka, T. *et al.*, “Studies on accelerator-driven transmutation systems”, Proc. 5th Information Exchange Meeting on Actinide and Fission Product Partitioning and Transmutation, EUR 18898 EN, OECD/NEA, 1998.
- [2] Cahalan, J.E., A.M. Tentner, and E.E. Morris, “Advanced LMR Safety Analysis Capabilities in the SASSYS-1 and SAS4A Computer Codes”, Proc. of the International Topical Meeting on Advanced Reactors Safety, Pittsburgh, 17-21 April 1994.
- [3] Eriksson M. and J.E Cahalan, “Inherent Shutdown Capabilities in Accelerator-driven Systems”, *Annals of Nuclear Energy*, Vol. 29/14, pp. 1689-1706, (2002).
- [4] Cordfunke, E.H.P., R.J.M. Konings, G. Prins, P.E. Potter, and M.H. Rand, “Thermochemical Data for Reactor Materials and Fission Products”, Elsevier Science, Amsterdam, 1990.
- [5] Katz, J.J., G.T. Seaborg, and L.R. Morss, “The Chemistry of Actinide Elements”, 2nd Ed., Vol. 1 and 2, Chapman and Hall, London, 1986.
- [6] Hunter, C.W., Fish, R.L., Holmes, J.J., “Mechanical Properties of Unirradiated Fast Reactor Cladding During Simulated Overpower Transients”, *Nucl. Technol.* 27(3), pp. 376-388 (November 1975).
- [7] Khalil, H.S. and R.N. Hill, “Evaluation of Liquid-metal Reactor Design Options for Reduction of Sodium Void Worth”, *Nucl. Sci. Eng.*, 109, 221-266 (1991).

**ACTIVE AND PASSIVE SAFETY CONTROL PERFORMANCE
IN SUBCRITICAL, ACCELERATOR-DRIVEN NUCLEAR REACTORS**

James E. Cahalan

Argonne National Laboratory
Reactor Analysis and Engineering Division
9700 South Cass Avenue
Argonne, Illinois 60439 USA
jecahalan@anl.gov

Marcus Eriksson

Royal Institute of Technology
Department of Nuclear and Reactor Physics
10691 Stockholm, Sweden
marcus@neutron.kth.se

Abstract

Traditional safety performance requirements for nuclear reactors have been developed for critical reactors, whose kinetics characteristics differ significantly from subcritical, accelerator-driven nuclear reactors. In a critical nuclear reactor, relatively small amounts of reactivity (negative or positive) can produce large changes in the fission rate. In subcritical reactors, the self-multiplication (k) decreases as the subcriticality ($1-k$) increases, and the responsiveness to small reactivity changes decreases. This makes subcritical nuclear reactors less responsive to positive reactivity insertions than critical reactors. Also, larger negative reactivity insertions are needed in subcritical reactors to shut down the fission chain if the neutron source remains. This paper presents the results from a computational analysis of the safety performance of subcritical, accelerator-driven nuclear reactors. Coupled kinetics and thermal-hydraulics models are used to quantify the effectiveness of traditional protection and control system designs in subcritical reactors. The analyses also quantify the role of inherent, passive reactivity feedback mechanisms in subcritical reactors. Computational results are used to develop conclusions regarding the most favourable and effective means for reactor control and protection in subcritical, accelerator-driven nuclear reactors.

Introduction

Accelerator-driven subcritical nuclear reactor designs are being considered for transmutation of long-lived radioactive nuclides produced in commercial nuclear power reactors during operation and discharged with the spent fuel. The objective of this transmutation process is to lessen spent fuel storage requirements by converting heavy radioactive nuclides, primarily plutonium and higher actinides, into lighter, shorter-lived nuclides. Plutonium will fission in conventional light water reactors, but the higher actinides have small thermal neutron fission cross sections, and are more efficiently destroyed in fast spectrum nuclear reactors.

Accepted safety design requirements for critical nuclear reactors dictate that the reactor shall be designed to have an inherent, prompt, negative reactivity feedback mechanism to counter any insertion of positive reactivity that makes the reactor supercritical. A supercritical reactivity excursion can raise the reactor power to a level that results in coolant boiling or fuel melting, and subsequently the potential for harm to the public by release of radioactivity. A prompt negative fuel temperature reactivity feedback is normally achieved by adjusting the fuel composition so that in increasing temperature transients, the effective capture cross section increase due to Doppler broadening of resonances dominates the increase of the fission cross section. For a feed stream of higher actinides, such an adjustment of the fuel composition may not be consistent with mission requirements, since the fertile nuclides that provide a negative Doppler feedback also transmute into heavy, long-lived nuclides.

Subcritical nuclear reactor designs driven by a spallation neutron source targeted by a high-power proton accelerator have been proposed for transmutation of higher actinides. In these designs, the accelerator becomes the controller of the reactor neutron kinetics. The level of subcriticality provides a margin for inadvertent positive reactivity insertions, compensating for the possible absence of a prompt negative Doppler effect. From a safety standpoint, a deeper level of subcriticality provides a larger margin of safety for positive reactivity insertion. However, from an operational performance standpoint, a lesser level of subcriticality provides greater reactor self-multiplication and a higher reactor power from a given neutron source strength. Therefore, the decision on the level of initial subcriticality involves a trade-off and optimisation among competing factors.

The potential reactor kinetics implications of the level of initial subcriticality are illustrated in Figure 1. This figure shows the reactor power history, normalised to unity at the initial steady state, in response to insertion of an amount of reactivity corresponding to the effective fraction of delayed neutrons in a liquid sodium-cooled fast reactor operated at various levels of subcriticality. (Criticality is measured by the ratio of the population of self-multiplication neutrons of a given generation to the population on the prior generation, exclusive of any source neutrons. In equilibrium, this ratio, called the effective multiplication factor “ k ”, is unity and the multiplication process is self-sustaining. When k is unity, the reactor is critical. If k is less than unity, the chain reaction will die away without an external source of neutrons, and the reactor is subcritical). The reactivity is inserted as a linear ramp beginning at 50 s and terminating at 150 s, and all reactivity feedbacks have been neglected. For the initially critical reactor and the design with the smallest subcriticality ($k=0.999$), the reactor becomes supercritical during the reactivity insertion and the power rises exponentially to a level that raises the coolant temperature to coolant boiling, where the simulation was ended. However, for the higher levels of subcriticality ($k=0.99$ and $k=0.98$), the reactor remains subcritical, and the power increase stops when the reactivity insertion ceases.

The results shown in Figure 1 illustrate the safety advantage of subcritical operation in response to reactivity insertion when the level of subcriticality is greater than the amount of inserted reactivity.

Based solely on safety goals, it would seem desirable to make the initial subcriticality as large as possible, i.e. to make the initial multiplication factor, k , as small as possible. However, the numerous and complicated factors determining the optimal level of subcriticality can not be summarised in a single analysis. There are multiple considerations that impact control and protection systems design choices, operating conditions and procedures, and ultimate safety margins. Some of the reactor kinetics aspects involved in the design decision process will be explored and discussed in this paper.

Shutdown system design

One of the issues under discussion in the area of safety design features concerns the role of control rods for power shutdown. In nuclear reactors, it is customary to include special-purpose shutdown control rods for emergency power shutdown. Current regulatory standards require two independent and diverse shutdown systems, each capable of stopping the fission process in the event the other system fails. These control rods contain a material that is a strong absorber of neutrons, typically boron. Strong neutron absorption interrupts the chain reaction process, which dies away completely with time if the multiplication factor from one generation of neutrons to the next becomes less than unity. The stronger the inserted neutron poison, the greater the multiplication factor is degraded, and the faster the fission power decays.

In a subcritical, source-driven reactor, the primary emergency power shutdown system will likely be a trip, interruption, or diversion of the beam, thus terminating the source neutrons and extinguishing the fission process. Shutdown absorber control rods have been proposed for the second, independent shutdown system. In a subcritical reactor, the relative poisoning strength of a given mass of neutron absorber is determined by the degree of initial subcriticality, as measured by how fast and how far that amount of absorber will reduce the fission power. As the initial subcriticality becomes larger, the relative importance of self-multiplication decreases, and the relative importance of the source increases. Because the absorber shutdown system functions by interrupting the chain reaction process, the effectiveness of a given amount of absorber material decreases as the initial subcriticality increases. This performance characteristic is illustrated in Figures 2 through 5.

Figures 2 through 5 contain results from reactor kinetics simulations of a nuclear reactor operated in subcritical mode at three different levels of subcriticality, and also as a critical system. The calculations reported in Figures 2 through 5 show the kinetic behaviour resulting from insertion of differing amounts of neutron absorber material into a reactor operating with $k=0.98$, 0.99 , 0.999 , and 1.0 , respectively. In these calculations, the amount of neutron absorbing material is measured in terms of a unit of reactivity corresponding to the effective fraction of delayed neutrons. In the reactor considered here, the effective delayed neutron fraction is 0.002 , and this amount of reactivity is one dollar ($1\text{\$}$) of reactivity.

Figure 2 shows the kinetic behaviour of the reactor with $k=0.98$. At the initial steady state, the reactor is operating with an external source of neutrons that just balances the subcritical reactivity state to yield an equilibrium neutron population from one generation to the next. At 5 s , different amounts of absorber material are instantaneously inserted, and the curves in the figure show the time history of the reactor power following the negative reactivity insertions. For comparison, the fraction of the reactor power coming from decay of fission products, called decay heat, is also shown. Energy from fission product decay will appear following shutdown regardless of continuing fission energy, and is a thus measure of the effectiveness of shutdown. Figure 2 indicates that several hundred dollars of negative reactivity are necessary to bring a subcritical reactor with $k=0.98$ from normal power to near decay heat power if the external neutron source continues to operate (i.e. failure of the primary shutdown system). For a critical reactor physicist, this is a very large amount of reactivity, since it is

customary in critical reactor design to limit the amount of reactivity in any single control rod to one dollar. Such a limit is assumed in order to prevent the possibility of criticality on prompt neutrons alone following the inadvertent withdrawal of a single control rod. Imposing the same requirement of making a diverging power excursion impossible in a subcritical reactor would necessitate that no single control rod could bring the system to criticality with the source present.

Figure 3 shows the effect of decreasing the initial subcriticality by increasing the initial k to 0.99. This tends to make a given amount of negative reactivity more effective in reducing the power. However, many tens of dollars of reactivity are required to bring the reactor power to near the decay heat level.

In Figure 4, the initial k has been raised to 0.999. The computed results show that power reduction to decay heat in this case can be achieved rapidly with a few tens of dollars of control material at this level of subcriticality. For the sake of reference, the behaviour of a critical system (initial $k=1.0$), is shown in Figure 5. In terms of minimising the amount of reactivity needed for shutdown, the critical system is optimal, with a requirement of about ten dollars or less, depending on other factors such as the capacity of the post-shutdown heat removal system.

The results shown in Figures 2 through 5 indicate that designing a reactivity-based shutdown system in a subcritical reactor involves a trade-off between the initial subcriticality and the amount of reactivity needed for shutdown. There are physically-based limits on both of these quantities. First, the permissible level of initial subcriticality is based on the conceptual principle and requirements associated with the goal of subcritical reactor operation, namely, to avoid the possibility of supercritical reactor kinetics for accidental positive reactivity additions. The level of initial subcriticality is set by the safety requirement for the magnitude of the positive reactivity addition that must be accommodated before supercriticality results. Also, the subcriticality level is determined considering accelerator performance and the strength of the neutron source. Deeply subcritical operation requires a significant increase in accelerator capability to supply the neutron source needed to overcome the associated degradation of self-multiplication. In addition, the level of initial subcriticality can not be reduced beyond the threshold established by the achievable performance of instrumentation and control systems in normal operation. Second, the total amount of shutdown reactivity is limited by the allowable reactivity in each control rod, and the practical limit on the number of control rods. The allowable reactivity per rod is based on an accepted industry design principle based on making supercriticality impossible given the inadvertent withdrawal of a single shutdown control rod. The upper physical limit on a single rod's reactivity worth is set by the amount of control material that can be contained in the volume allocated to one control rod. The practical limit on the number of control rods is set by the reactor geometry and by the number of locations available for control assemblies. In addition, there is an economic incentive to reduce the number of costly, safety-grade control rod assemblies.

In summary, there are significant challenges facing the reactor designer in arriving at a satisfactory shutdown control system employing absorber control rods in an accelerator-driven subcritical nuclear reactor. For subcriticality levels that meet conceptual goals and performance requirements in normal operation, the amount of negative reactivity required for power shutdown may be very large, and may exceed realistic physical limits.

Start-up system design

In the preceding section, the role of control rods for emergency shutdown was considered, and it was shown that very large control reactivity requirements exist for shutdown to decay heat levels for

source-driven subcritical systems. However, the same results show that much smaller amounts of reactivity can change power levels substantially. For example, Figure 2 shows that for the system with $k=0.98$, only 10\$ of negative reactivity are required to reduce the power to near half its initial value. Starting from the reduced power level, the same amount of positive reactivity would bring the reactor to full power. This indicates that conventional control rods could be used for power manoeuvring required for burn-up compensation and load changes, possibly including start-up operations.

Existing sodium-cooled reactor design and operating procedures provide guidance on power manoeuvring and start-up system requirements. In normal start-up and shutdown operations in a liquid-metal cooled reactor, the rate of coolant temperature change is limited to control temperature gradients in structural members and the resulting internal stresses. (The impact of beam reliability on coolant system design is addressed in [1]). In the experimental breeder reactor-II (EBR-II) reactor start-up procedure [2], bulk sodium temperature changes in the tank are limited to 10°F (~5.6°C) per hour. The fast flux test facility (FFTF) start-up procedure [3] limits coolant hot leg temperature changes to 50°F (~28°C) per hour. These limits have been established in a design process considering not only structural member strength requirements, but also the features and capabilities of the primary coolant pump control system and the reactor power control system. Both EBR-II and FFTF have conventional centrifugal pumps driven with electric motors in the primary coolant system. Both EBR-II and FFTF employ conventional moveable control rods for power manoeuvring. EBR-II control rods contain fuel, and FFTF control rods contain absorber material. Although these designs and performance requirements are strictly relevant only to their original application, they do indicate general ranges for realistically achievable control rod speed of motion and reactivity worth characteristics.

Based on the apparent reactivity requirements for power manoeuvring and experience with sodium-cooled reactor design and operation, it seems likely that conventional control rods could be used for power regulation in subcritical reactor operation. In addition, the apparent rate of reactivity change required seems to be achievable with conventional control rod drive mechanisms.

Unprotected reactivity insertion accident response

In design basis accident sequences, the reactor protection system functions and the accident sequence terminates without damage to the plant or danger to the public. In liquid metal-cooled fast reactor safety assessments, it is customary to consider the consequences of protection system failure as a test of containment capability and a measure of safety margin beyond the design basis. For the accelerator-driven subcritical reactor design, one such beyond design basis scenario considers the system response to an inadvertent positive reactivity insertion with failure of the reactor scram system. In such a sequence, the system response is determined by the thermal, hydraulic, mechanical, and neutronic performance characteristics of the plant in off-normal operating conditions.

The subcritical reactor design considered here is based on the design analysed in [4]. The design consists of a metallic-fuelled, liquid-sodium-cooled, fast subcritical reactor with a nominal operating power of 840 MWt. The coolant system configuration is taken to be typical for a pool-type primary system. For the purpose of the analyses reported here, the reactor was assumed to have reactivity feedbacks from changes in 1) fuel temperature, 2) coolant temperature, and 3) structural temperature.

The fuel temperature reactivity feedback was assumed to be associated with the Doppler effect. The value of the Doppler coefficient, $T dk/dT$, was treated parametrically by assuming values of -0.0005 and -0.00005 to cover the range typical for fuel compositions with a small but negative Doppler effect.

The coolant temperature reactivity feedback was assumed to be associated with the change in coolant density. The value of the coolant density feedback coefficient was assumed to have values corresponding to full coolant voiding reactivity worths of -3% and $+3\%$ to cover the range typical for a small, high leakage, sodium cooled fast reactor.

The structural temperature reactivity feedback was assumed to be associated with radial core expansion associated with thermal expansion of the above-core subassembly load pads. As in the FFTF core restraint design, thermal expansion of these load pads tends to spread the core apart and introduce negative reactivity. For the analyses report here, a single radial core expansion reactivity coefficient of $-0.0016\%/K$ was assumed.

The positive reactivity insertion assumed in these analyses was 1% ($\Delta k=0.002$) at a rate of $0.01\%/s$ beginning at 50 s of transient time. The results for the case of no reactivity feedback for various initially subcritical effective multiplication factors are shown in Figure 6. For the highest value of k (0.9995), the reactivity insertion takes the reactor supercritical, and the power increases until the coolant heats to the boiling point. For the other subcriticality levels, the reactivity insertion leaves the reactor subcritical, and the rapid power increase stops with the end of the reactivity insertion. Because there are no reactivity feedbacks, the power continues to slowly approach an asymptotic maximum value with a time constant determined by the combined effects of the build-up and decay of the delayed neutron precursors and of the nuclides contributing to gamma heating.

Figure 7 presents the results for the reactivity insertion with the most unfavourable combination of assumed reactivity feedbacks: a positive coolant void worth of $+3\%$, the small Doppler coefficient of $-0.00005\%/K$, and the nominal radial core expansion feedback. The reactivity feedbacks are not sufficient to prevent super-criticality for the high multiplication case. The remaining cases stay subcritical, and in the long term the power slowly approaches an asymptotic minimum value.

In the next Figure 8, results are presented for the larger Doppler coefficient and the positive coolant void worth. The results are only slightly different from the results in Figure 7, indicating that even the larger Doppler coefficient considered here is so small that it has little effect.

Lastly, Figure 9 presents results for the larger Doppler coefficient and the negative coolant void worth of -3% . As the plotted curves show, the change in coolant void worth feedback limits the net reactivity sufficiently to prevent coolant boiling in the highest multiplication case ($k=0.9995$). In fact, in this case the negative reactivity feedbacks are sufficiently strong to take the system subcritical again once the reactivity insertion stops, and the reactor power decreases afterward.

The results of this parametric analysis of the unprotected reactivity insertion accident sequence indicate that passive reactivity feedbacks can provide beneficial protection against progression into severe accident conditions (coolant boiling, fuel melting), even in sequences in which the reactor is temporarily supercritical. However, it is clear that the most significant factor in preventing super-critical transients is the level of initial subcriticality compared to the reactivity insertion.

Unprotected beam excursion accident response

Accelerator-driven system designs have been proposed in which the power decrease associated with fuel burnup over one reloading cycle is compensated by increasing the beam strength. This implies a beam control system capable of regulating the beam intensity, and brings into question the reactor response to combined beam control and protection system failures. To study this accident sequence, the same initial conditions and parametric reactivity feedback variations employed in the

previous (unprotected reactivity insertion) section were assumed for a beam increase to 180% of the initial value. It should be noted that such a transient will not progress into coolant boiling conditions for the design studied, since a power increase to at least 400% must occur to raise the coolant to the boiling point in a liquid-sodium cooled reactor.

Figure 10 shows the results for the case of a beam increase to 180% at 50 s with no reactivity feedbacks for various levels of subcriticality. Recall that the higher the self-multiplication (the larger values of k), the greater the fraction of neutrons from fission, and the less the fraction of neutrons from the source. Hence, for the same reactor power the neutron source is smaller for the higher self-multiplication cases. In Figure 10, this contributes to the slow response of the near-critical case ($k=0.9995$), since for this case the source is very small and the time constant for adjustment to the asymptotic condition is very long. On the other hand, for the highly subcritical cases, the source constitutes a larger fraction of the total neutron population, the system time constant is shorter, and the step increase in the source more immediately brings the power near the asymptotic value.

Figure 11 presents the results for the beam excursion with most unfavourable assumed reactivity feedbacks: a positive coolant void worth of +3\$, the small Doppler coefficient of -0.00005\$/K, and the nominal radial core expansion feedback. Compared to Figure 10, the moderating influence of the reactivity feedbacks is evident, especially for the near-critical case ($k=0.9995$).

Figure 12 presents the results for a positive coolant void worth and the larger Doppler coefficient. The additional negative feedback provides a small increment in retarding the power increase compared to Figure 11, with the most significant effect in the near-critical case.

Figure 13 shows the results for a negative coolant void worth of -3\$ and the larger Doppler coefficient. Compared to Figure 12, the additional negative coolant feedback reactivity provides further reduction in the peak transient power.

The results for the parametric analysis of an unprotected beam excursion accident sequence indicate that passive reactivity feedbacks will act to limit the overall transient power increase and to bring the reactor back into balance with the heat rejection level. The degree of limitation is more significant and timely for initial conditions that are nearer to critical, and the impact of the passive feedbacks decreases for cases that begin far from critical. This is to be expected, since the magnitude of the reactivity feedback is proportional to the temperature increase and limited by the magnitude of the temperature increase. A fixed amount of negative reactivity feedback will have less influence in limiting reactor power as the initial subcriticality becomes larger, and the feedback reactivity becomes a smaller fraction of the net reactivity.

Conclusions

This paper presents discussions and analysis results concerning the safety characteristics of sodium-cooled, accelerator-driven, subcritical fast reactors, with a focus on design features and their performance in normal operation and in accident sequences. Specific design features considered here include shutdown control rods and inherent reactivity feedbacks in unprotected accident sequences.

Reactor kinetics analyses of subcritical reactors operating initially at various levels of subcriticality show that such designs provide significant safety margin and protection against severe accident progression in reactivity insertion accident sequences, so long as the amount of inserted reactivity does not result in supercritical reactor conditions. The question then becomes the degree

of initial subcriticality, and this design choice is influenced by a number of safety, economic, and performance considerations.

Specific analyses of secondary shutdown reactivity requirements indicate that the amount of reactivity needed for initial subcriticality levels around 1% or more may be so large that the use of control rods may be impractical. Hundreds of dollars of reactivity will be required to lower the reactor power to near decay heat levels if the beam continues to operate, and it may not be possible to find a poison material of sufficient strength and compactness. In contrast, the reactivity requirements for routine power manoeuvring (i.e. burnup swing compensation, load following, or startup from stand-by) are relatively modest, in the neighbourhood of a few tens of dollars, and control rods could be used for routine power manoeuvres.

Parametric analyses of passive reactivity feedback effects in reactivity insertion without scram accident sequences indicate that such feedbacks can be effective in preventing supercritical transients and severe accident progression for some combinations of initial and feedback conditions. In general, the passive reactivity feedback effects are most effective for low subcritical initial conditions (high k , near critical), in which the amount of reactivity coming from the passive feedbacks is significant compared to the initial subcritical reactivity. However, the primary factor in preventing supercritical reactor kinetics remains the level of initial subcriticality in comparison to the magnitude of inserted reactivity.

A study of passive reactivity effects in unprotected beam excursion accidents also quantifies the role of passive reactivity effects in limiting reactor power excursions and in reducing the reactor power after the beam excursion. Once again, the passive reactivity feedback effects are most effective for nearer-to-critical initial conditions, and less effective for highly subcritical systems. For these later systems, the thermal margin provided by the sodium coolant, equivalent to more than 400% of the normal full power, prevents short-term severe accident progression.

REFERENCES

- [1] Dunn, F.E., "Thermal Response of the Multiplier of an Accelerator-driven System to Beam Interruptions", these proceedings.
- [2] "Experimental Breeder Reactor II (EBR-II) System Design Descriptions", Volume I, General Facilities.
- [3] "Fast Flux Test Facility (FFTF) System Design Description for Reactor Plant Control System", SDD 90, Chapter 4, Operation.
- [4] Hill, R.N. and H.S. Khalil, "Physics Studies for Sodium Cooled ATW Blanket", Proc. IAEA TCM on Core Physics and Engineering Aspects of Emerging Nuclear Energy Systems for Energy Generation and Transmutation, Argonne, Illinois, November 28-30, 2000.

Figure 1. Reactor response to reactivity insertion for various multiplication factors

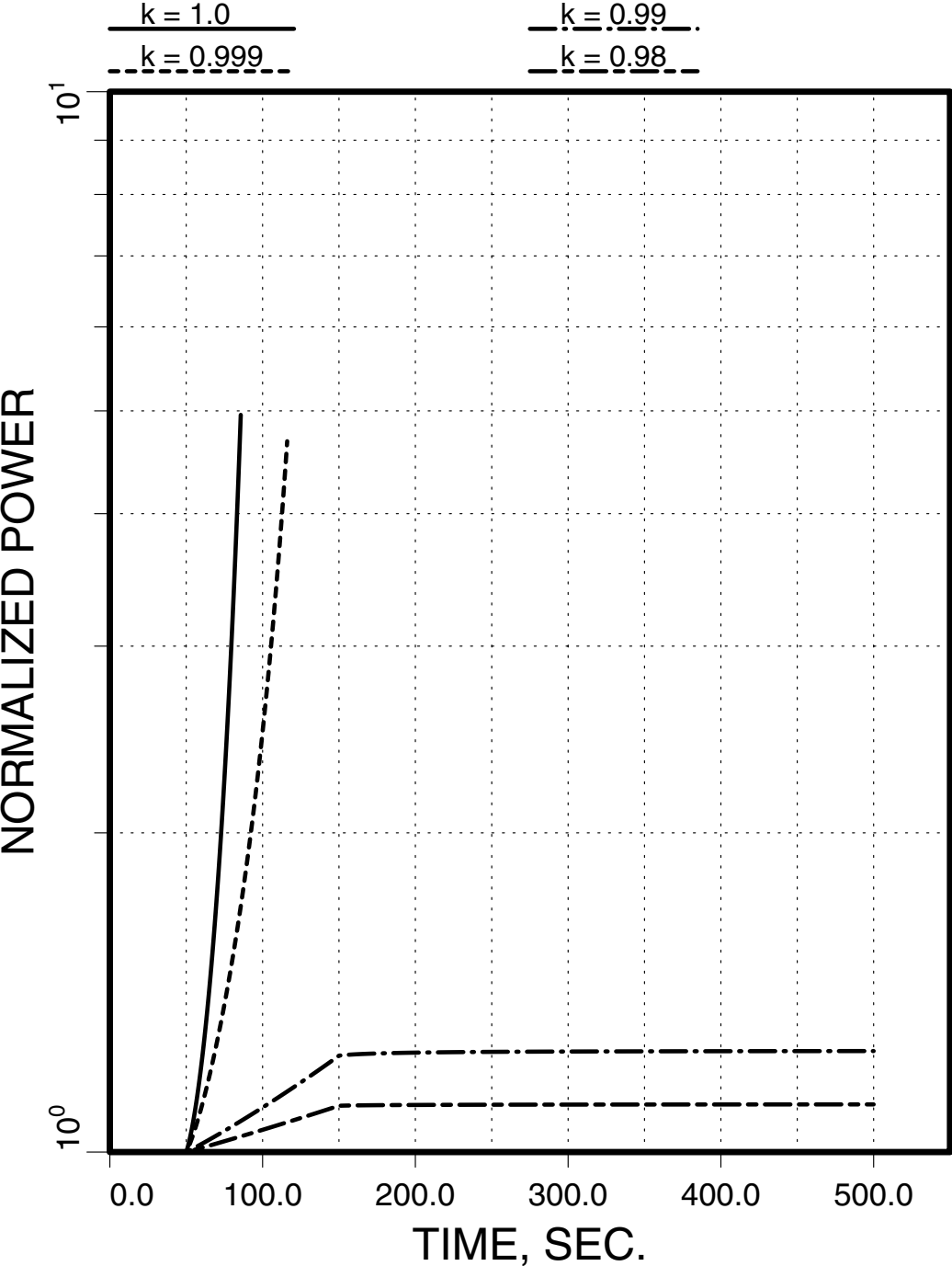


Figure 2. Shutdown reactor kinetics behaviour for initial $k = 0.98$

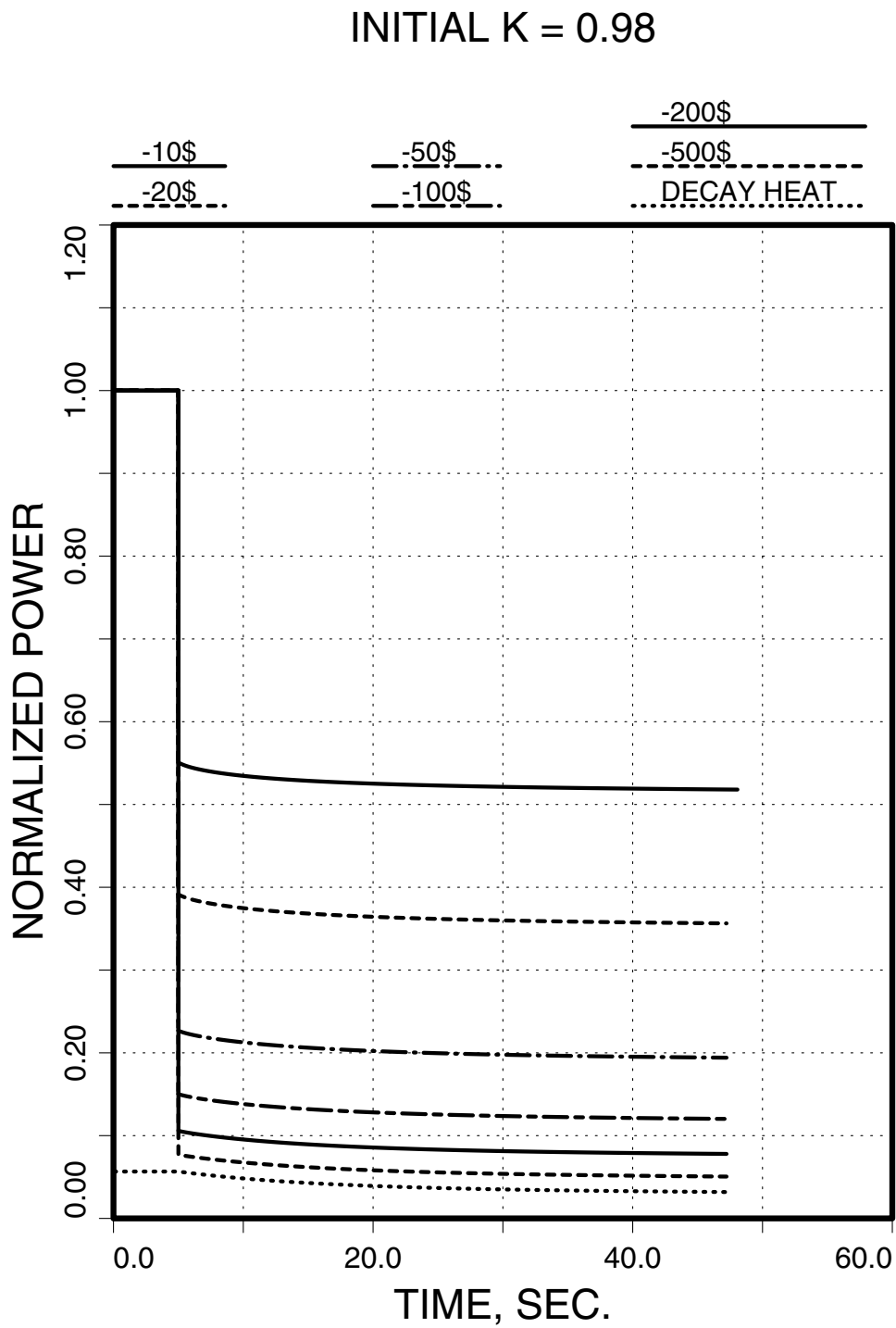


Figure 3. Shutdown reactor kinetics behaviour for initial $k = 0.99$

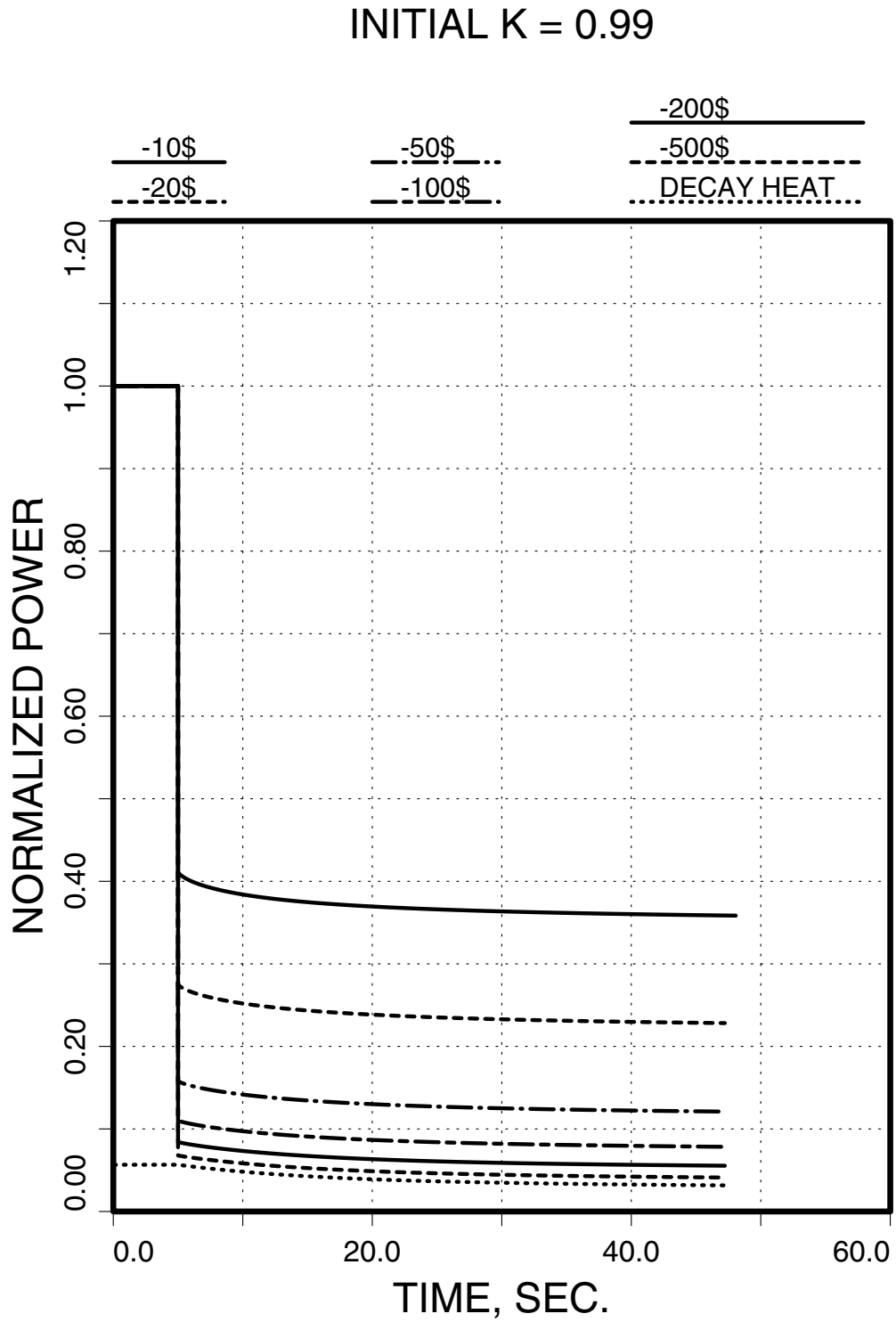


Figure 4. Shutdown reactor kinetics behaviour for initial $k = 0.999$

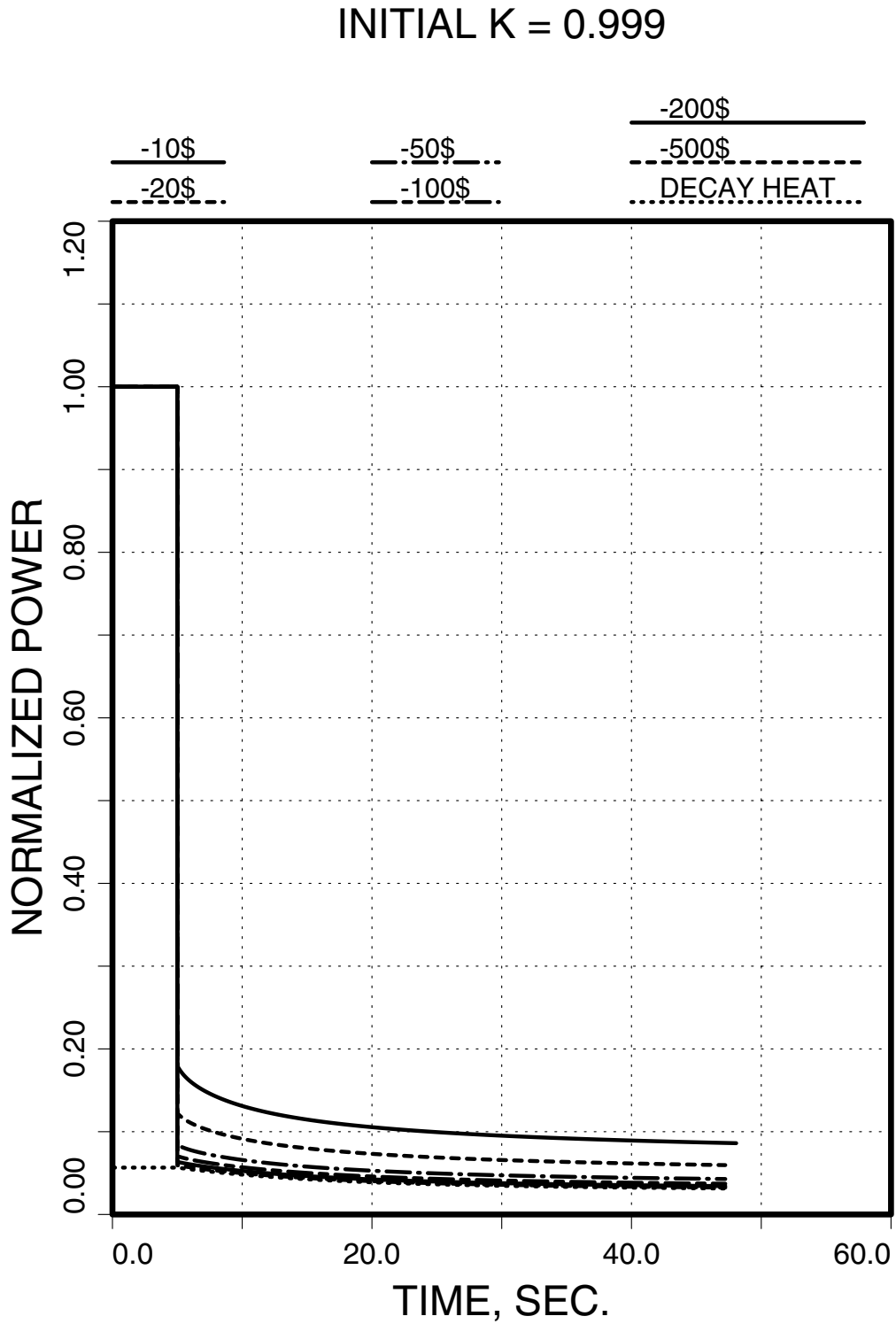


Figure 5. Shutdown reactor kinetics behaviour for initial $k = 1.0$

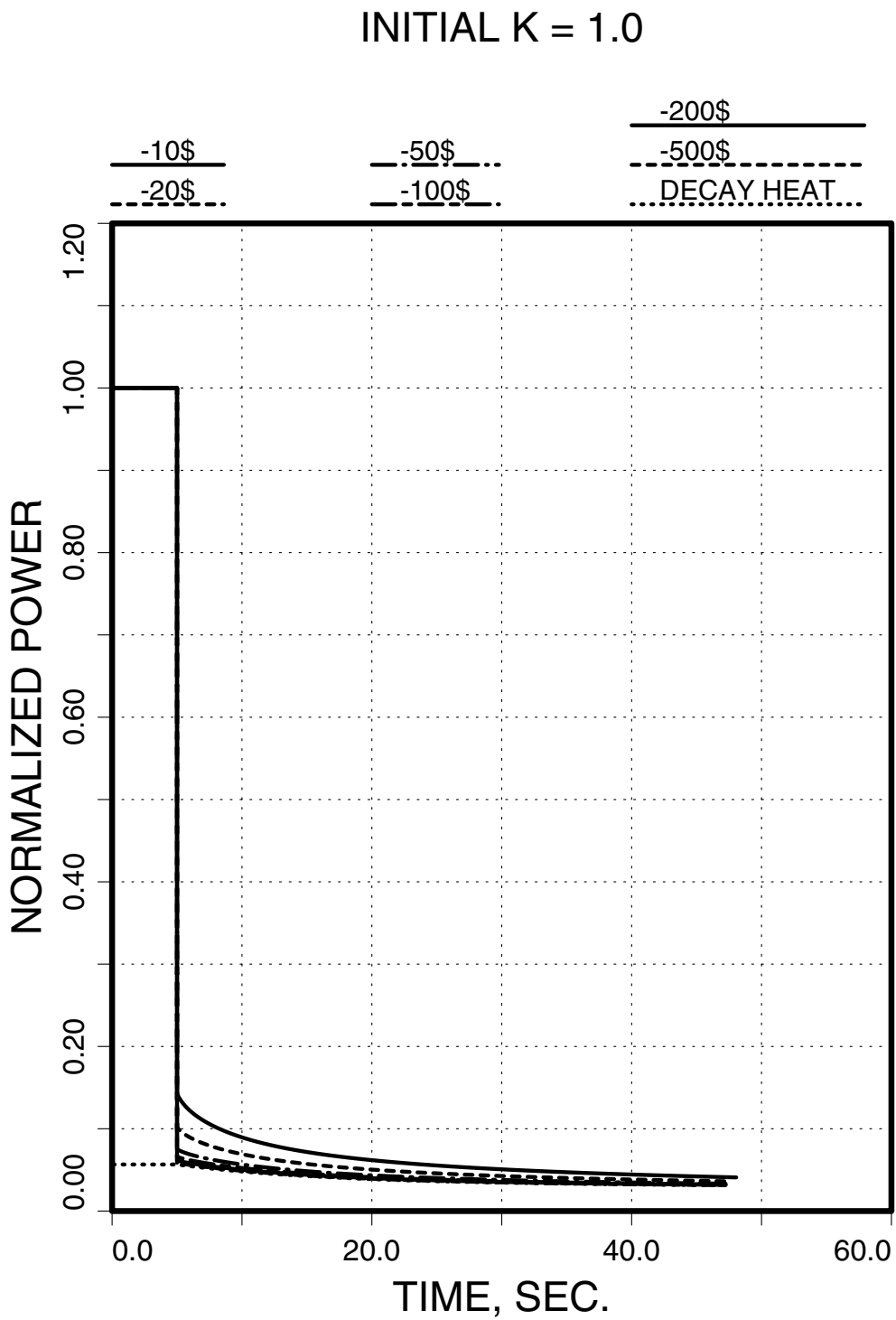


Figure 6. Reactivity insertion analysis results for no reaction

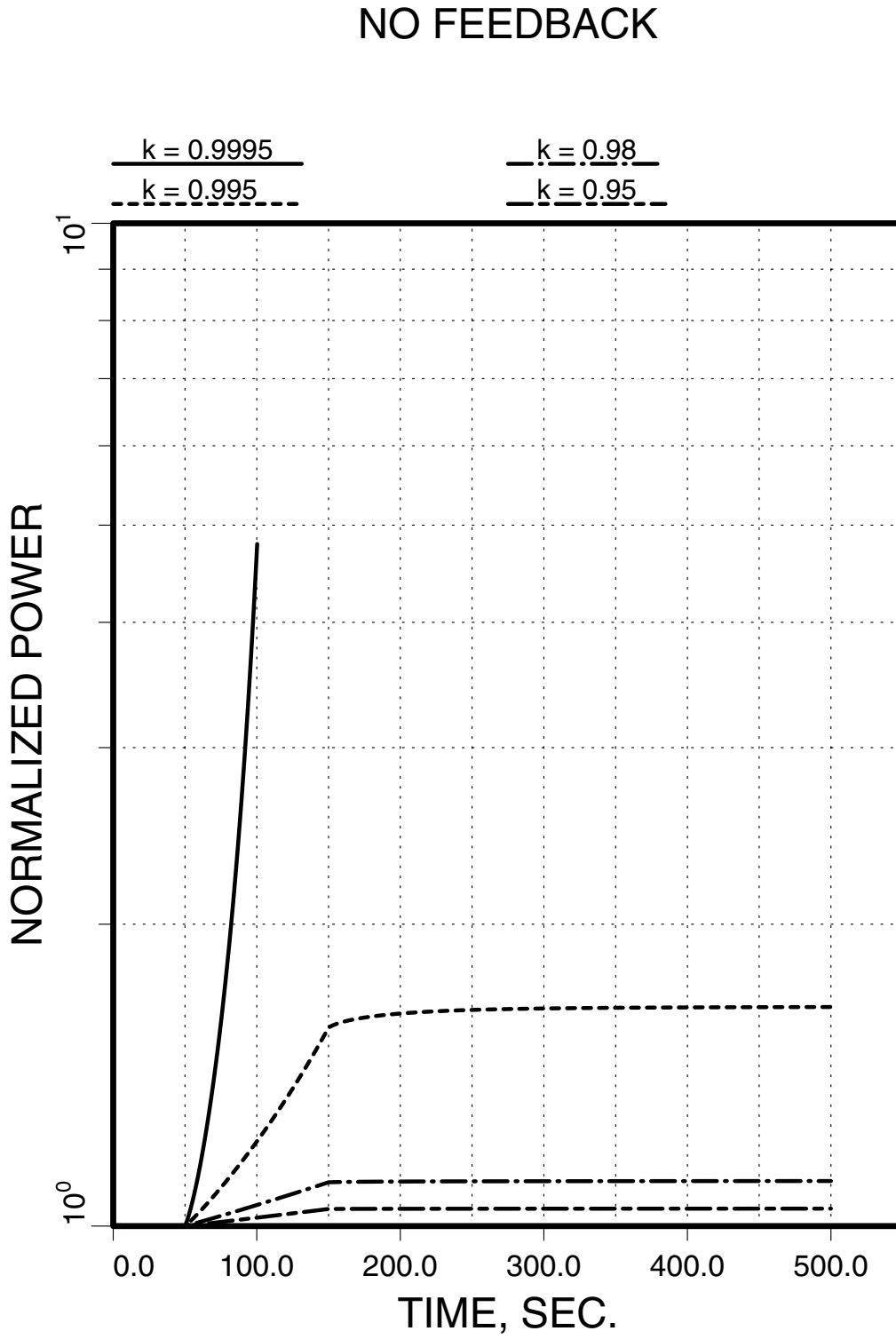


Figure 7. Reactivity insertion analysis results for positive void and small Doppler

REX -0.0016 $\$/K$, DOPP -0.00005, VOID +3.0 $\$$

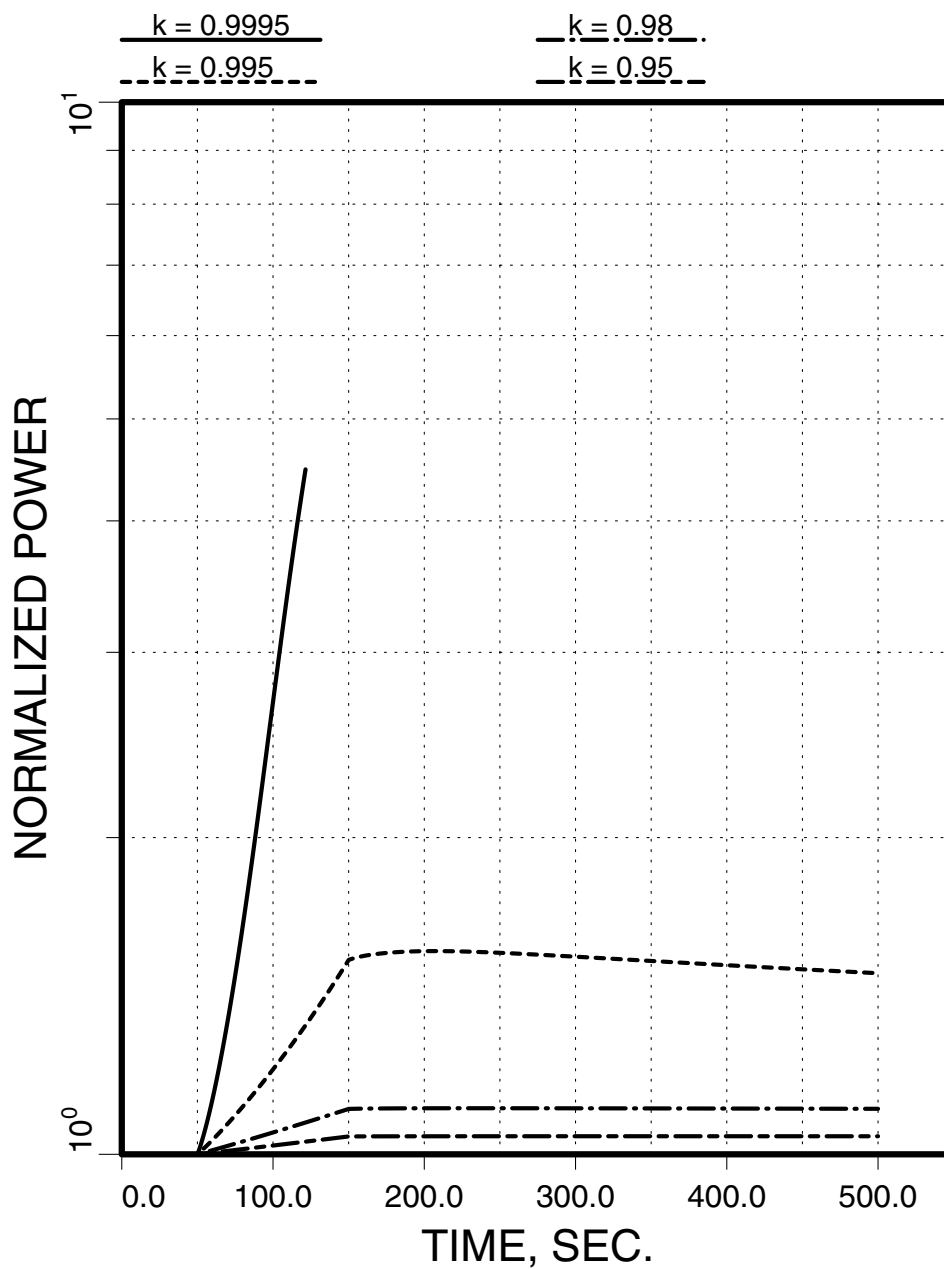


Figure 8. Reactivity insertion analysis results for positive void and large Doppler

REX -0.0016 \$/K, DOPP -0.0005, VOID +3.0\$

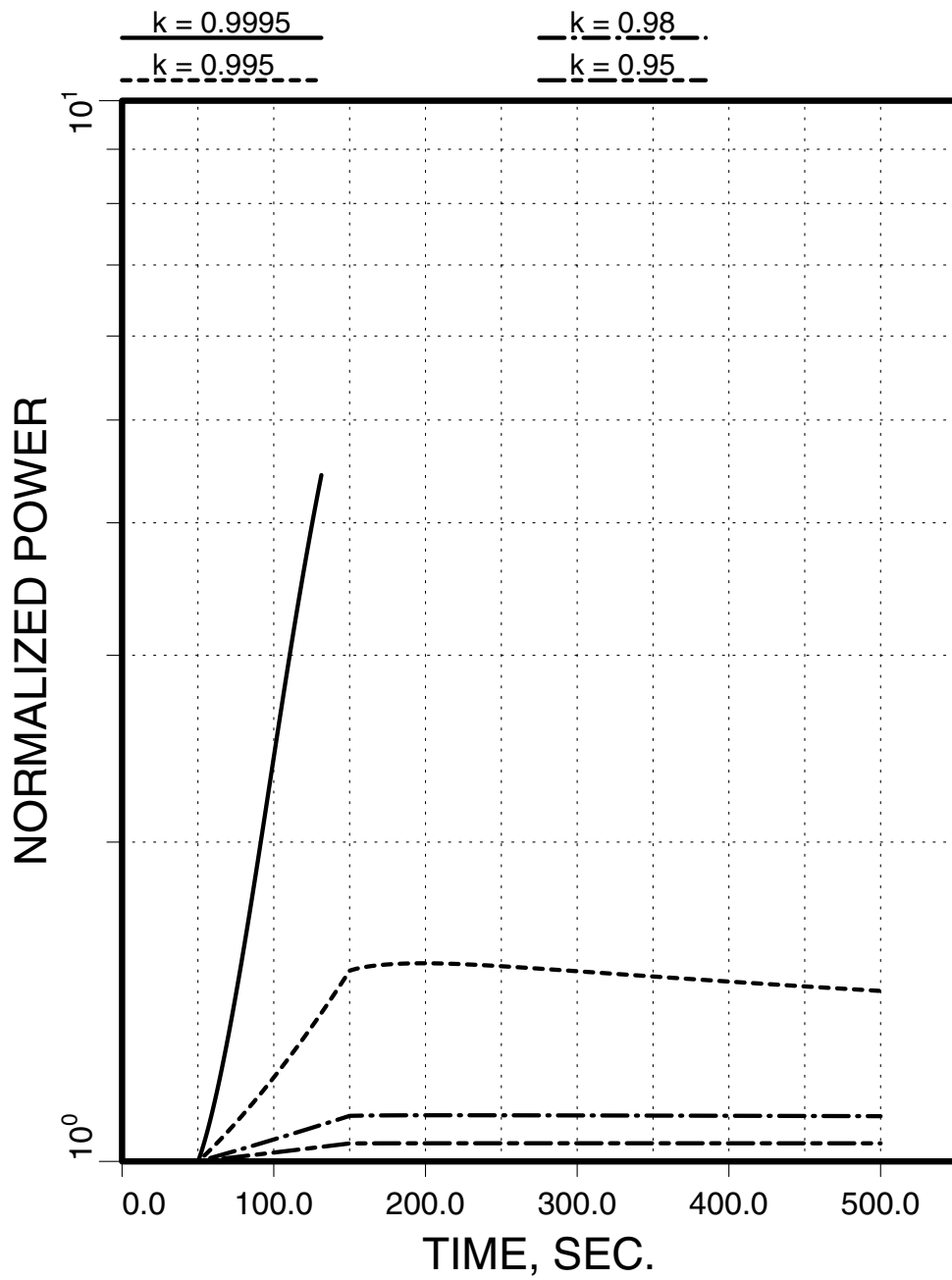


Figure 9. Reactivity insertion analysis results for negative void and large Doppler

REX -0.0016 \$/K, DOPP -0.0005, VOID -3.0\$

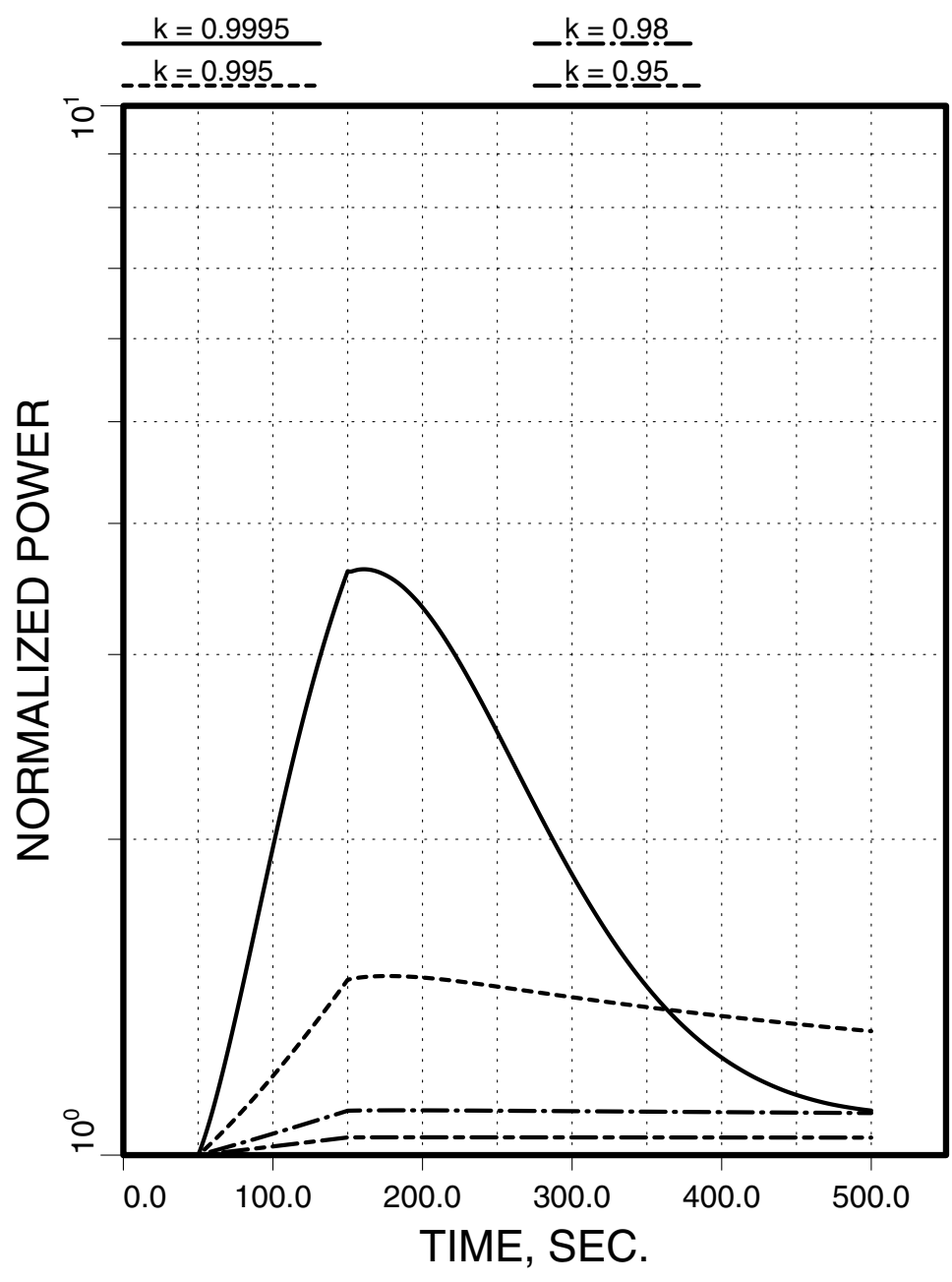


Figure 10. Beam excursion analysis results for no feedbacks

NO FEEDBACK

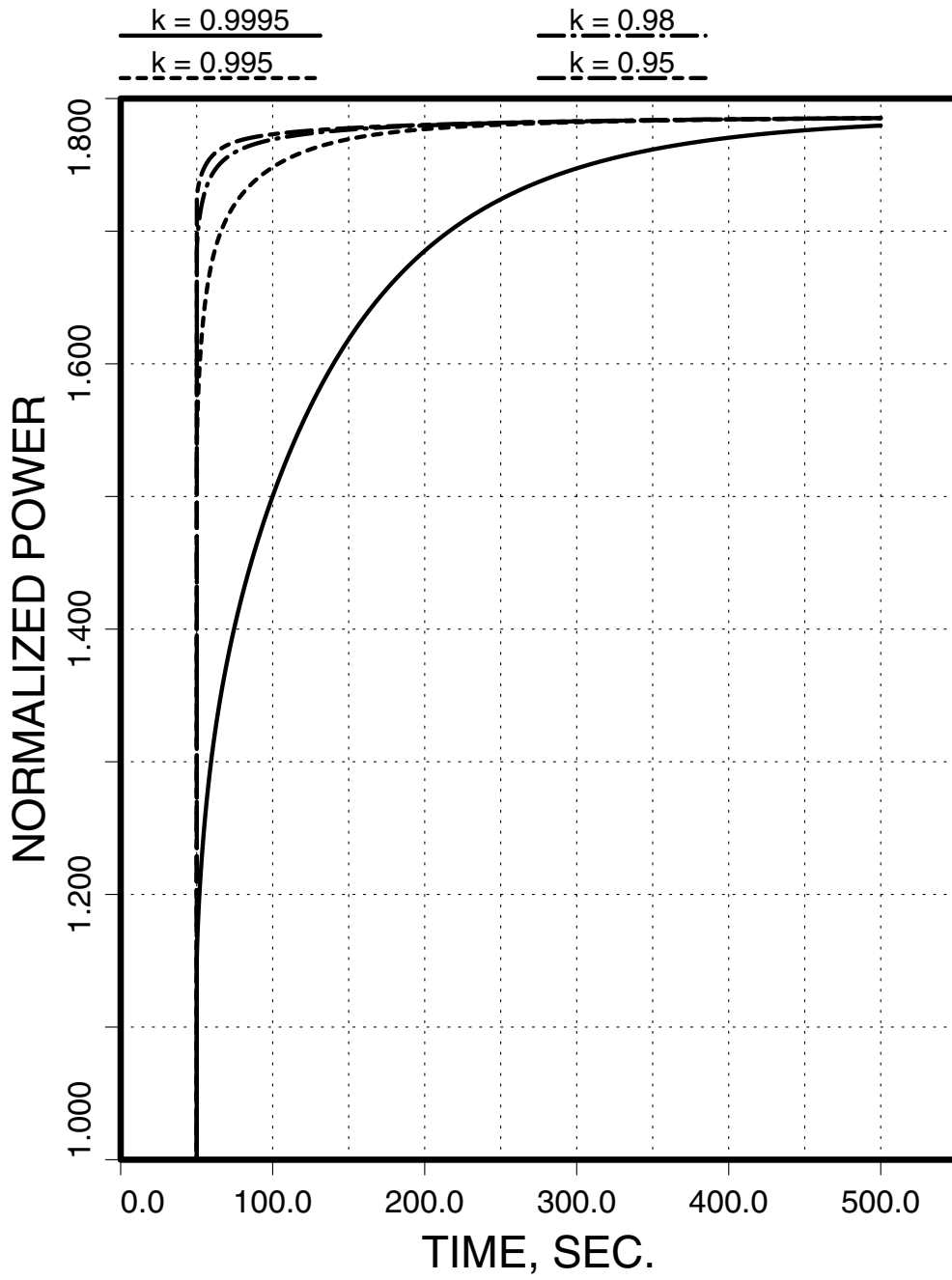


Figure 11. Beam excursion analysis results for positive void and small Doppler

REX -0.0016 \$/K, DOPP -0.00005, VOID +3.0\$

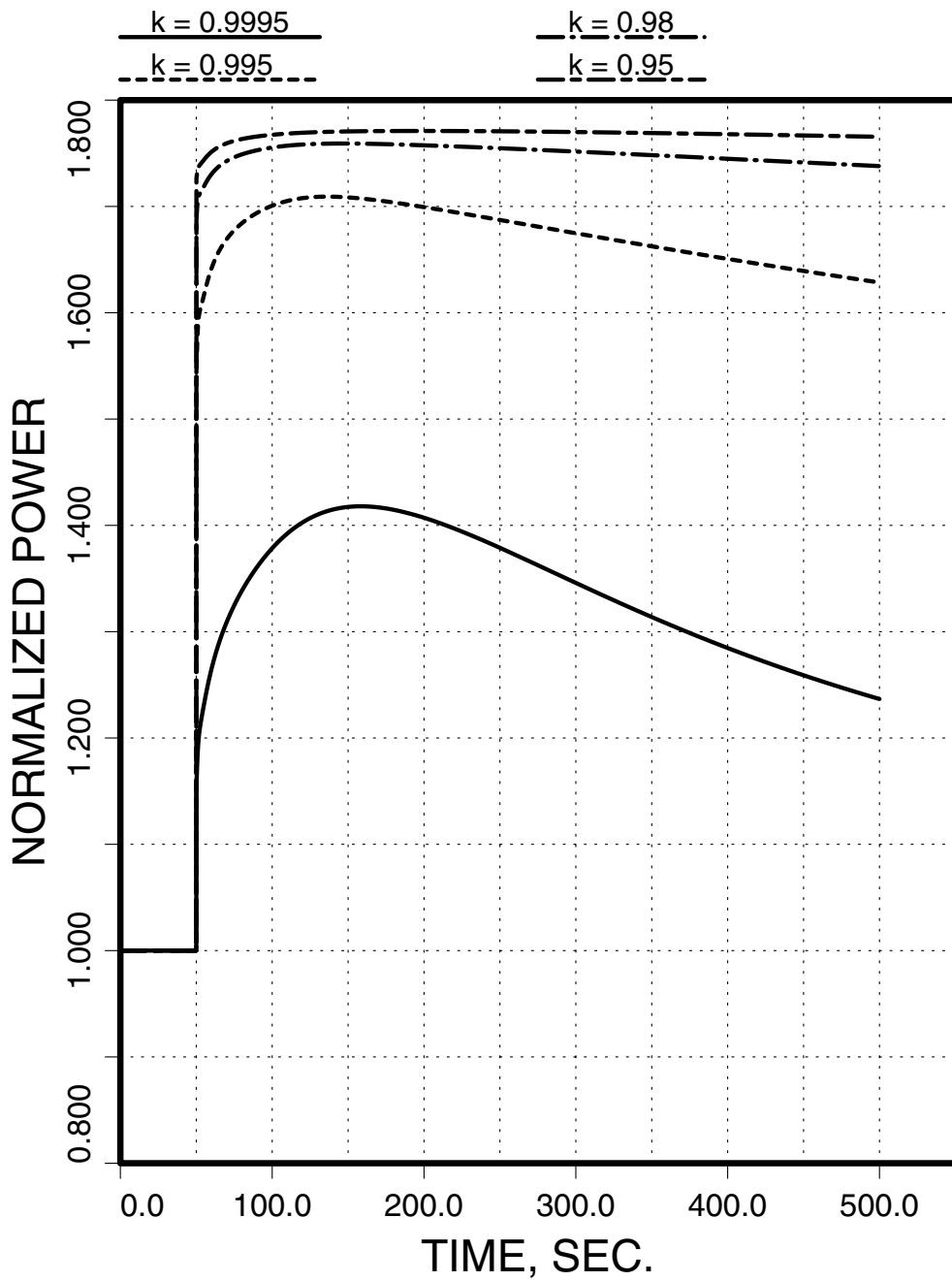


Figure 12. Beam excursion analysis results for positive void and large Doppler

REX -0.0016 \$/K, DOPP -0.0005, VOID +3.0\$

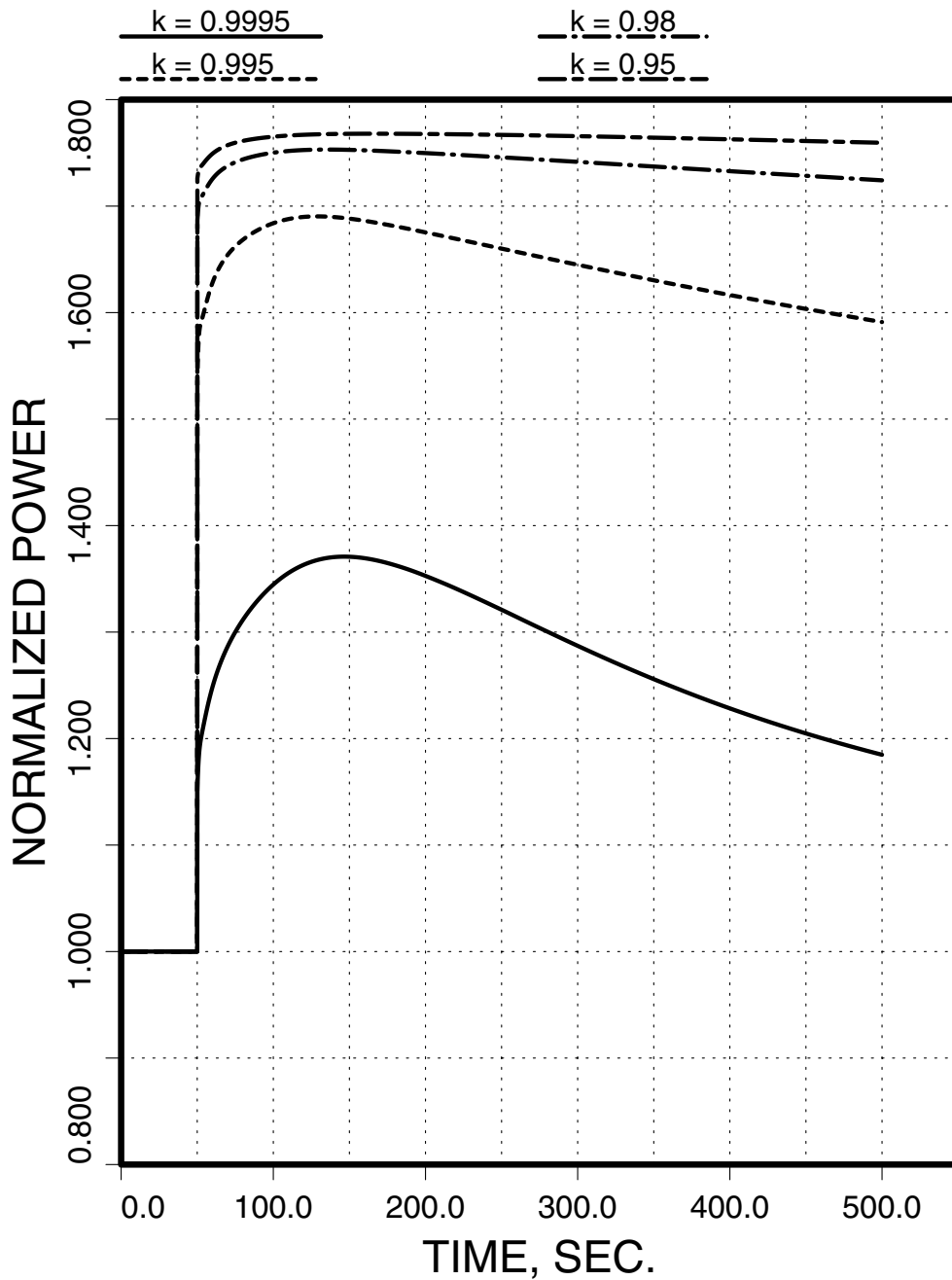
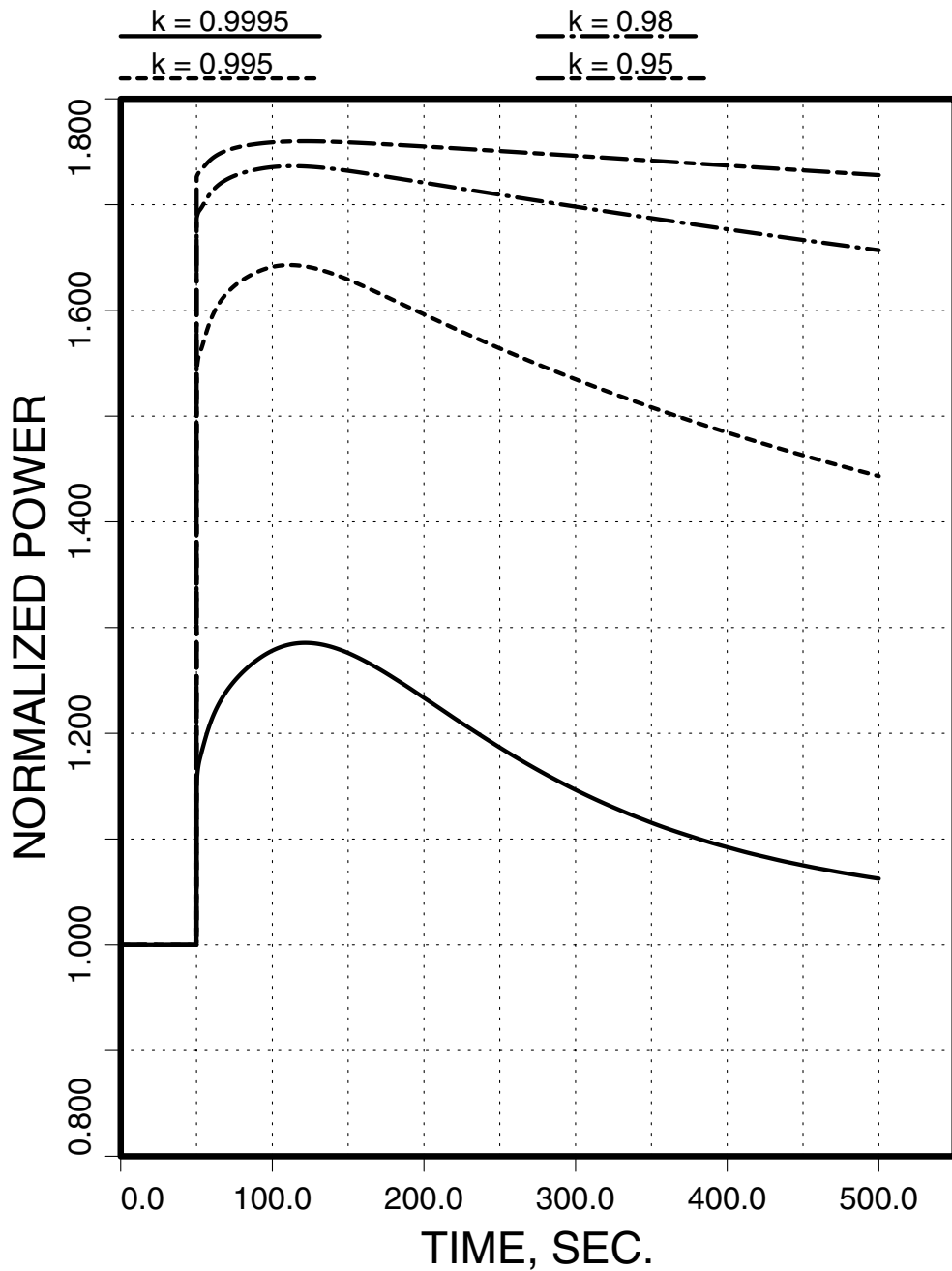


Figure 13. Beam excursion analysis results for negative void and large Doppler

REX -0.0016 \$/K, DOPP -0.0005, VOID -3.0\$



OPERATING REQUIREMENTS FOR A PROTON BEAM ACCELERATOR TO COUPLE WITH A SUBCRITICAL SYSTEM

Alberto Negrini, Giuseppe Proto

Ansaldo Nucleare, Division of Ansaldo Energia S.p.A.
Corso Perrone 25, 16161 Genova, Italy

Abstract

The design of the coupling between a high power proton accelerator and a subcritical multiplier is a complex task involving different engineering disciplines dealing with beam control, spallation target physics and its cooling, the dynamics of the coupled beam-target-core system. The performances of these coupled systems have to be addressed for a number of conditions, from normal operation to transients and accidents. The paper reports the main findings from a study which intended to assess the choice of beam basic parameters and its specifications to work under normal operating conditions. Taking as reference facility the cyclotron driven 80 MW_{th} LBE cooled XADS reference configuration developed by a group of Italian organisations led by Ansaldo, the study aimed to determine suitable operating ranges and conditions for the proton beam in order to link the accelerator operating requirements to actual needs and limits of the target and of the driven subcritical system, as well as to fix operating bounds and set points as design input for the control system of the accelerator and the beam transport line. In particular, a 3-step beam start-up sequence for driving up the XADS to full power has been proposed for mediating the response of coupled systems very different in nature and governed by an underlying fast-acting physics. General requirements for beam variability and focalisation have been also worked out to comply with stability figures of nuclear plants and with the specific target design and plant layout features of the XADS.

Introduction

Following a preliminary design developed in 1998, which was based on a former conceptualisation of the energy amplifier [1] made by CERN, the reference configuration [2] of the lead-bismuth eutectic cooled experimental ADS (LBE-XADS) has been worked out in the period 1999-2001 by a group of Italian organisations led by Ansaldo with the aim of assessing the industrial feasibility of a small-sized industrial demonstration plant version of the ADS.

The design activity has been accomplished by the XADS Italian consortium (Ansaldo, ENEA, INFN, CRS4, CIRTEN, SIET and SRS) under the aegis of the MURST (the Italian Ministry of University and of the Scientific-Technological Research), which funded a comprehensive programme based on two main applied research tasks for the design of the target and the subcritical multiplier (Ansaldo, ENEA, CRS4, CIRTEN, SIET and SRS) and for the conception of the accelerator system and development of its components (ENEA and INFN).

The activity is now progressing in Italy, still with the support of MURST, for assessments of the lead-bismuth technology in the large scale CIRCE LBE experimental facility and, with the support of the 5th EU RTD framework programme, on the comparison of a gas and LBE cooled XADS.

A few key choices of the XADS intend to delimit the number of arbitrary variables and to overcome any potential drawback linked with the adoption of more advanced, however prototypical solutions. The LBE-XADS design philosophy aims to show how an industrially conceptualised ADS plant can be reasonably simple and feasible without having to rely on critical technological ventures other than those inherent with it, notably the accelerator-core coupling and the use of the Pb-Bi eutectic for sustaining the neutron flux and recovering the heat from the fuel core.

This basic approach can be summarised as follows:

- 1) small sized, though significant and scalable, core power level of 80 MW_{th};
- 2) LBE operating spallation target designed to consistently match fuel core size and power;
- 3) moderate coolant temperature (300±400°C) for lessening corrosion and thermal loads;
- 4) fuel type based on proven FR's (U, Pu) MOX;
- 5) unextended in-core residence time fuel duty to safely assess behaviour in poorly proven LBE;
- 6) core k_{eff} range (0.97±0.93, BOL-EOL) suitable to maintain adequately safe subcriticality margin during normal operation and foreseeable DBA's, while keeping a moderate demand on beam power;
- 7) enhanced natural circulation core cooling in normal operation and passive evacuation of residual core power under transients/accidents;
- 8) proton accelerator design upgrading from proven technologies and operating experience for mean beam energy and moderate power;
- 9) limited footprint of the XADS dedicated accelerator to reduce complexity and costs.

These prerequisites set forth for the LBE-XADS intend to give enough confidence for design solutions to work with the challenging peculiarities of the ADS concept and are also reasonably tailored to the main tasks that a relatively small experimental plant is required to address:

- a) demonstration and acquisition of operating experience on the coupling between a HPPA with a subcritical core;
- b) operating data and experience for LBE cooling technology (heat evacuation, corrosion);
- c) performances and duty of a HPPA as coupled to a subcritical driven system.

The prerequisite (5) above and related (3-4) lead to delimit the in-core residence time of the fuel batch to a maximum of 2-3 years, or 25 000 hours EFP, in order to control the drawbacks due to potential fuel degradation in a corrosion active and at high hard neutron flux environment. The limitation of the fuel irradiation time and the maximum coolant temperature at 400°C (which gives rise to about 500°C peak cladding temperature) are expected to keep the possible cladding corrosion effects below acceptable limits. The three years maximum core cycle length and the moderate fuel power density delimit the fuel core cycle average discharge burn-up to about 25 GWd/ton (35 GWd/ton batch peak), which is however consistent in that the demonstration of massive burning is not considered a prominent objective for the XADS. Conversely, designing a much higher BU system (4÷5 times more are targeted in large FR's) would require substantially higher core power (as this relates to the fuel fission density) with attentive management of large reactivity changes, innovative fuel design, larger and complex plant, all these options being much beyond the scope of a first experimental plant. Rather, high BU performances for incineration of TRU's and of selected fission products could be eventually tested into prototypical single fuel assemblies or in small clusters after mastering a due operating experience with the XADS.

The LBE cooled XADS

The LBE XADS [3] can be schematically divided into some conceptual blocks: the spallation target, the subcritical core, the primary loop, the secondary loop and the auxiliary systems.

The target

Two design solutions, “window” and “windowless”, are studied for the target, each with LBE acting both as spallation target and cooling fluid separate from the primary eutectic by a retrievable mechanical structure, the target unit, which is centred inside a core cavity to evenly deliver the source spallation neutrons to the surrounding fuel.

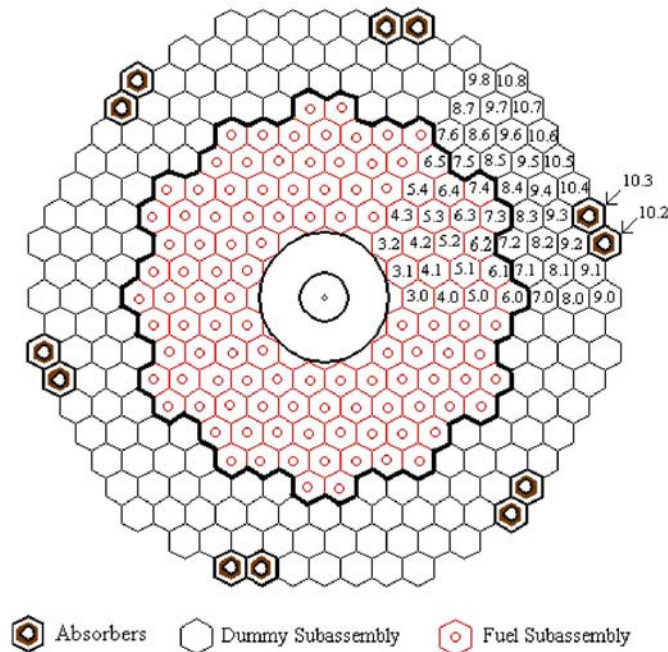
The window target configuration consists of a mechanical barrier of material fairly transparent to neutrons and protons, engineered to withstand pressure and thermal loads. The LBE flows by natural circulation as it is heated up by the proton beam in the lower part of the target unit centred at the core mid-plane, while it is cooled down in the upper part where the heat is evacuated through a heat exchanger by means of a diathermic fluid.

In the “windowless” target configuration (Figure 1) a spallation LBE free surface is exposed to the beam vacuum, balanced by about 1m LBE head. The beam impinges directly on the eutectic, which is forced to circulate downwards by means of a density mismatch originated and controlled by an injection of cover gas in the uprising LBE flow.

The fuel core

The fuel core (Figure 2) consists of an annular pattern of 120 fuel assemblies, for a total of 3,65 tons of MOX fuel, which surrounds the inner target cavity. The assemblies are all alike, each loaded with 90 fuel pins which have the same cross dimensions and fuel MOX composition as the standard Superphénix reload fuel (but with slightly higher enrichment, 23% Pu, to set an operational $k_{\text{eff}}=0.97$ at nominal power and BOL). The fuel pin cluster is enclosed into a hexagonal wrapper; the lattice is about 40% larger while the active fuel length is slightly shorter (87 vs 100 cm) than SPX. The fuel core is surrounded by a buffer region of 174 non-fuelled dummy elements filled-up by LBE, whose purpose is softening the hard neutron spectrum to relieve the fast fluence on the fixed structures around the core.

Figure 2. The LBE XADS core cross-section [2]



The buffer region adds up LBE thickness to the coolant flowing in the downcomer of the primary loop: a substantial core reflector is thus available for improving the overall neutron economy by a sort of diffusive neutron cloud around the core. The core boundary neutron leakage is so minimised to as low as 1-2% without need of specific reflector structure which is on the contrary requested in FR's based on different coolants. The LBE is in fact a highly diffusive and fairly transparent (slowly-lethargising and low-absorbing) means for neutrons which undergo thousands of collisions against Pb-Bi nuclei while slowly relaxing from fast down to thermal energies. The long wandering neutrons tend to be kept and attenuated inside the LBE volume whereas they would rather escape, while rapidly slowing down, in light, low-A liquids, or gas coolants.

A practical result of such a higher neutronic sustainability in LBE (survivability with high energy spectrum) directly reflects the possibility of making substantially wider fuel pin lattice in LBE cooled systems: due to reduced friction losses, this also helps sustaining natural circulation regimes and diminishes pressure head requirements when assisted pumping or natural circulation enhancement is needed.

Moreover, the core buffer allows a very flexible management for irradiation testing of prototypical FA's containing different kind of fuels or LLFP's and for positioning neutron absorbers to lower $k_{\text{eff}} < 0.95$ before starting the core refuelling outages.

A core multiplication factor of 0.97 (at core rated power, BOL) is considered sufficiently low to ensure the safe operation of the LBE XADS without need of shutoff rods. During the irradiation cycle, the core reactivity drops with a rate of about 0.004%/day due to the fuel depletion. The depletion rate is mainly related to the fuel type (both for composition and enrichment) and to the neutron spectrum. It also depends on the general core design and performances, as these relate to the fuel lattice, the overall fuel core loading and the power density. Due to the criteria fixed on the maximum residence time for delimiting the exposure of the fuel to a potentially degrading environment, the total core cycle reactivity depletion does not exceed a 4%, i.e. the operating multiplication factor reduces from 0.97 at BOL to 0.93 at EOL.

The primary loop configuration

The use of lead-bismuth eutectic in the XADS allows retaining neutronic properties similar to lead, but its remarkably lower melting point consents to operate at moderate temperatures. Some experience on the LBE corrosion chemistry and protection methods for the structural steels is already known and can be more readily developed in out-of-pile testing facilities like the large scale CIRCE experimental loop [4].

Nevertheless, the major drawback of using the LBE eutectic is the formation of the 138 days $T_{1/2}$ α -emitter ^{210}Po from bismuth, which requires a purification system for draining this radiotoxic exhaust from the cover gas at the top of the primary loop (PL).

The PL configuration is the pool-type, rather than the loop-type, as this design allows to pool within the main vessel all the primary coolant with the spallation target and the core structures, as well as the four intermediate heat exchangers (IHX). Conversely, a loop-type option with LBE coolant is hardly practical as this would involve quite huge and heavy piping, complex and costly design and seismic problems. The pool-type is also the preferred solution for large sodium-cooled reactors and the design experience gained with them can be suitably transferred to LBE.

As the highly diffusive, low-lethargising neutronics exploitable with the LBE allows making large fuel pin lattice, with pitch-to-pin diameter ratios in the range 1.5÷2 vs ~1.2 of FR's, the coolant pressure drops across the core can be kept below a few tenths of bar, i.e. an order lower than sodium-cooled FR's.

The prerequisite of developing a substantial cooling by natural circulation can be hence readily met (thanks also to the small XADS power) as a pool-type loop configuration can provide inherently large flow area with simple design of the primary system. However moderate, the flows developable by natural circulation can be in any case sufficient for evacuating the XADS residual power and are besides suitable for limiting the LBE corrosion-erosion on structural materials.

The space saved from the lack of a cumbersome pumping mechanics can be made available on the roof of the primary loop for components which are specific add-ons of the XADS, like the beam-pipe and the spallation target structure.

The exploitation of a completely natural circulation in the primary coolant would conversely present some demanding design requirements and constraints, which refrain from fully undertaking such a design philosophy: 1) a substantial reactor vessel height for developing enough head to drive purely natural circulation, which would add distance between the bending magnet and the spallation target; 2) an attentive minimisation of pressure losses through the core and the IHX, impacting on optimal performances; 3) an inherently poor controllability of the LBE flow-rate limiting the flexibility of operating conditions.

As a result of mediating between the countervailing merits and drawbacks of natural vs forced circulation, while keeping as a safety requirement the removal of the core residual heat by natural convection alone, it has been decided to design a flow enhancement system based on the injection of a few percent volume of PL cover gas into the bottom of the riser above the XADS core. The PL design then includes 24 risers where the reduced density lifting thrust of the two-phase LBE - gas mixture is added to that of the core heating to the LBE upstream flow. The admixed gas is stripped into the PL cover atmosphere when the LBE flow turns down at the pool surface. The total head is the natural buoyancy of the hot LBE stream above the core added by the gas injection density lightening, as weighted against the single-phase cold flow in the PL downcomer at the PL vessel wall after the IHX.

During normal operation the natural convection head is a 20% of that assisted by the gas injection, but the natural circulation alone is more than sufficient, after power shutdown, to cool the core and is able, in any case, to remove the core power during possible abnormal transients where the active head runs-out but the proton beam is not switched-off (in this case the coolant temperature rises 100°C more, doubling from 100 to 200°C, i.e. from 400 to 500°C at the core outlet). Such a temperature increase would not be a major concern in itself, as it can be sustained for a long time by the PL and vessel structures without need of specific design countermeasures, it would nevertheless impair the prerequisites set forth on corrosion mitigation in the LBE environment.

On the other hand, exploitation of higher natural heads for more moderate LBE temperature increments would require rising the height of the hot head a few times and/or enlarging the core size. These measures, besides hindering the operating flexibility, would make the PL and the whole XADS facility huger and costly, very disproportional compared to the aims an experimental facility is expected to accomplish.

As for the beam, an extended distance of the spallation zone, centred at the core mid-plane, from the beam controlling optics located above the PL cover top, would make the necessary beam spot precision more difficult to achieve.

The secondary system – BOP configuration

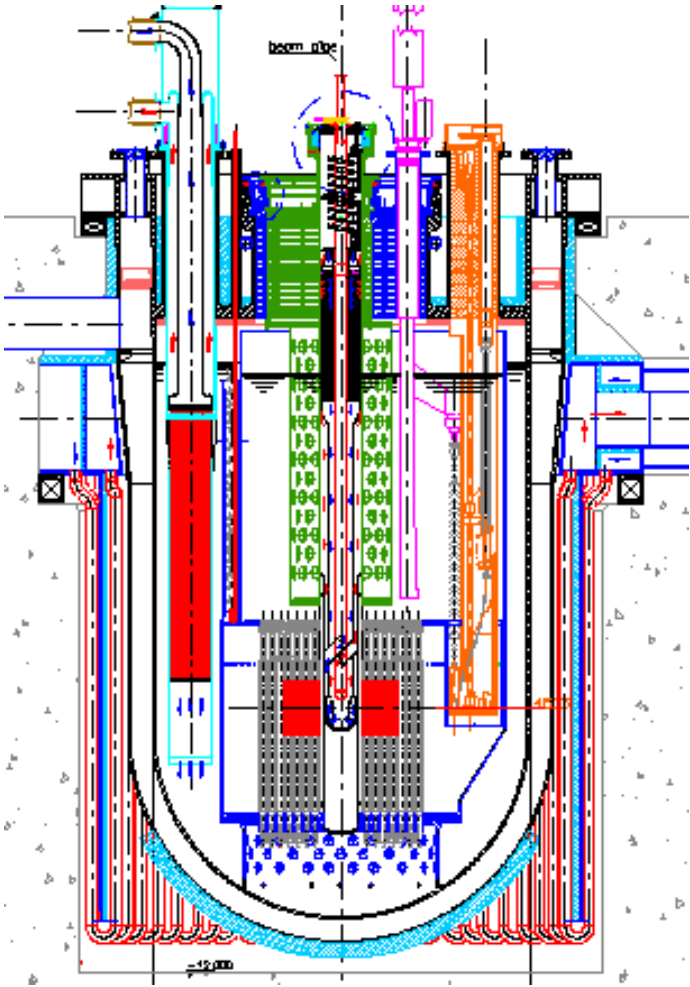
The two loops secondary system is thermally coupled to the PL through four IHX's so to transfer the operational core heat to the outer environment.

Each secondary loop, besides two IHX's, includes three heat exchangers arranged in series for rejecting heat to the external atmosphere via finned tubes and is operated through a circulation pump. The thermal cycle temperatures, 280-320°C cold-hot leg, are consistent with the synthetic diathermic fluid used as the coolant for this circuit. While assuring good compatibility with the hot LBE in case

of leaks from the IHX (no fast chemical reactions are foreseen), this choice allows to keep high enough temperature levels in the SS without pressurisation due to the low vapour pressure of the organic fluid. In spite of the lower thermal properties, the overall heat transfer capability of the SS fluid is comparable to that of LBE. The much lighter, non-corrosive, organic fluid can be in fact pumped at high speed and its comparably high heat capacity allows a 50 times lower mass compared to that required for cooling also the SS by LBE.

Conversely, the largely different coolants thermal property and the much longer SS flow path, compared to the PL, may require quite slow ramp-rates, during beam start-up/shut-down transients, for controlling temperature mismatches between the two loops, giving rise to oscillations in the SS due to its much larger thermal time constant.

Figure 3. The LBE XADS PL cross-section [2]



Refuelling

The fuel handling system is similar to those of sodium FR's, but specific design must be implemented for fuel assemblies tending to float in the high density LBE. There are two handling machine equipment's, one for the in-core service, another providing for transferring the fuel assemblies into flasks, and eventually into casks as intermediate storage.

The refuelling operations require to disassemble the beam pipe from the spallation target structure, in order this can be extracted up from the core and PL. The whole beam controlling optics, with the huge bending magnet, must be disconnected and moved apart. As the target extraction inserts positive reactivity, the in-core handling machine is preventively used for shifting a dozen of neutron absorbers (which are parked by the core buffer outer edge in normal operation) inwards to the core periphery in order to diminish the k_{eff} below the safety value of 0.95.

Table 1. Main LBE XADS data by plant area [3]

Plant area	Reference solution
Plant power	80 MWth core
Target options	a) windowed b) windowless
Core subcriticality	1) rated power: 0.97 (BOL) > k_{eff} > 0.93 (EOL) 2) refuelling: k_{eff} < 0.95
Fuel	(U, Pu) MOX
Primary system Coolant circulation	- pool type with 4 IHX's - enhanced natural-circulation
Secondary system	2 organic fluid loops evacuating heat to air by 6 finned exchangers
Thermal cycle	300 C at core inlet, 400 C at core outlet
Reactor roof	Metallic plate
Main and safety vessel	Hung from a cold annular beam
Structural materials	Vessels and internals: 316 L Target and fuel: 9Cr 1 Mo
In-vessel fuel handling	one rotating plug + one fixed arm + one rotor lifting machine
Secondary fuel handling	Flask, encapsulator, canister, Lifting & transport to water pool
Nuclear island	Solid basement on seismic supports
Plant safety	Full passive decay heat removal

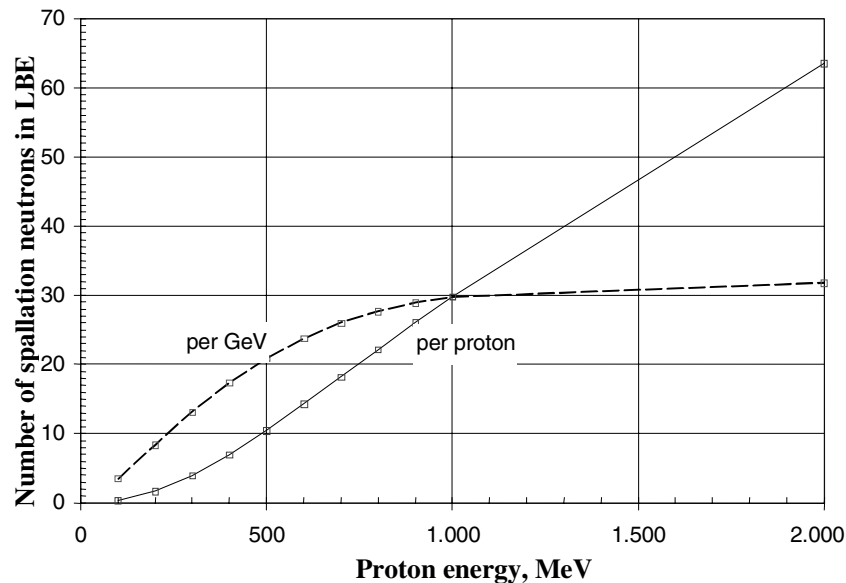
Beam needs for the LBE XADS

The prerequisites set forth on the small sized core power (80 MW_{th}) are indeed addressing, through the well known relationship, $P_{thcore} = G \cdot P_{beam}$, a beam power level of a few MW's for a reasonable gain, G , of the order of 20. The gain factor, expressed as:

$$G = \frac{n_y}{1-k} \frac{k}{v} \gamma = \frac{G_o}{-\rho} \quad (1)$$

is a mild function (some tens percent) of the fuel type and of neutron energy spectrum through ν (number of neutrons per fission) and γ (energy released by fission), a fair function (linear to asymptotically constant) of the neutron spallation yield, n_y , per unit energy of the impinging proton beam (Figure 4) and a strong function of the fuel core subcriticality margin, $\rho = (k - 1)/k$, as this may evolve during the foreseen core cycle length. In equation (1) the source importance is not explicit as this is about ~ 1 , i.e. not exploited in the spallation cavity design considered for the LBE-XADS.

Figure 4. Neutron yield by proton spallation in LBE



The initial subcriticality level and the core reactivity change, along with an assumed cycle length, are then crucial parameters for defining the beam parameters. The operational subcriticality level is established in order to keep away from the critical state ($k_{\text{eff}} = 1$) with adequate margin under operational and accidental (DBA) conditions which lead to wide temperature changes or positive reactivity insertions. Allowances for a safety margin of $\Delta k = 1\%$ and for k measurement error (0.6%) are applied to the criticality limit, so that the actual upper limit for the multiplication factor becomes $k = 0.984$ for normal operation and DBA's. Core cooling from operating down to ambient temperatures plus target-beam pipe flooding by LBE or earthquake loading (1.4% total including Doppler, coolant density and thermo-structural effects) accounts for the widest reactivity insertions predictable under DBA conditions for the LBE-XADS. The core multiplication factor limit for normal operation at full power and BOL is thus set at $k_0 = 0.97$ (i.e. a subcriticality margin of $\rho_0 \sim -3\%$). Accidents like those involving large core compaction may be ascribed to beyond design accident scenarios which, as based on the core and fuel assembly design, may worth about $0.5 \div 0.6\%$, so that they can be eventually included in the safety margin of 1%.

As seen above, the core cycle reactivity change accounts for a 4%, so that the minimal contribution of the reactivity ($-1/\rho$) to the gain factor in (1) is about 13 at core EOL, whereas it is as large as 32 at BOL.

The basic spallation gain factor G_o is directly proportional to the neutron yield n_y through the ratio of γ (200 MeV/fission) to ν (~ 3 for the MOX fuel considered), so that it keeps the same asymptotic trend of n_y (which leads to about 32 neutrons/GeV beyond 1 GeV).

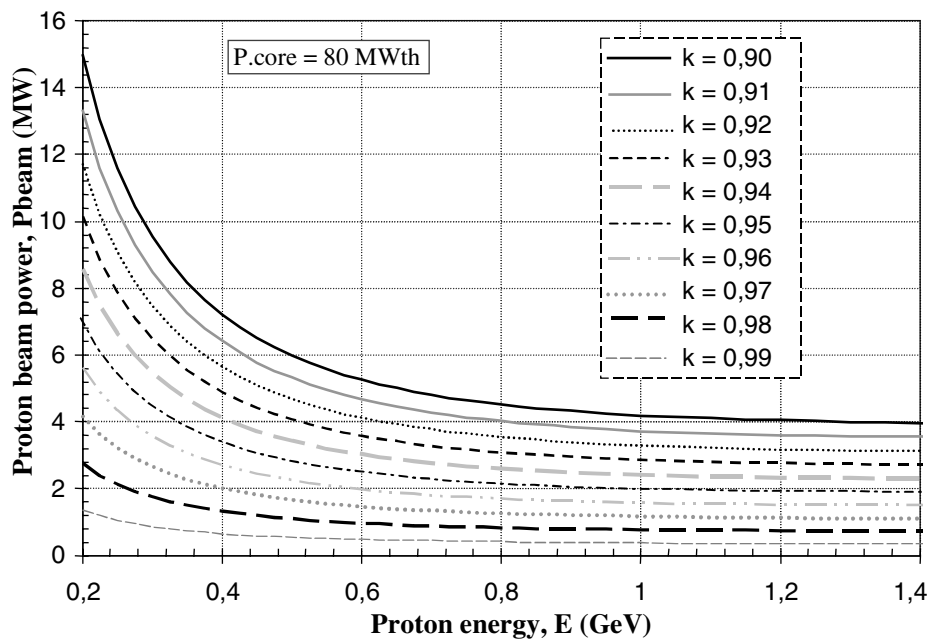
The effective gain is however driven by the level of the actual subcriticality during core irradiation, so that the resulting beam power function:

$$P_{beam} = P_{th_{core}} \frac{-\rho}{G_o} \quad (2)$$

can be assessed by Figure 5, which shows, for a given core thermal power, the requested beam power as a decreasing function of the proton energy for different levels of core subcriticality.

This figure clearly shows that it is not generally worth going beyond 1 GeV proton beams, as the reduction of the requested beam power would be quite negligible due to the steady trend of the power function curves in the high energy region. For the operating k_{eff} levels of the LBE XADS in particular, the curves already start on asymptotic trend in the proton energy range between 600÷800 MeV, with beam powers only 25÷10% higher than those at 1 GeV. The power curves trend is instead rather sloped at 400 MeV, with beam power levels 70% higher than at 1 GeV, and markedly rises at lower energies.

Figure 5. Requested beam power for a 80 MW_{th} core as a function of proton energy and k-level

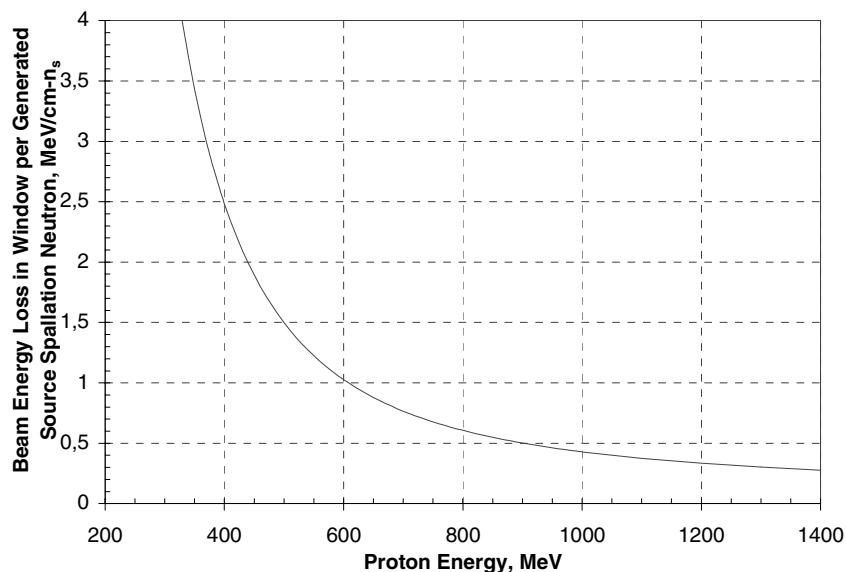


A number of additional issues are considered for selecting the most convenient beam energy: 1) the beam losses (window target design), 2) the range of the proton beam in the spallation target LBE bulk surrounded by the fuel core, 3) the hard spallation neutron fluence on the fixed structures (core barrel and diagrid), 4) the beam magnetic rigidity which is proportional to the beam momentum and sizes the deflection optics, 5) the shielding requirements.

The energy losses through the beam window show a marked decrease with the proton energy (Figure 6), which lessens the operating temperatures. However, the differences between $0.6 \div 1$ GeV may be still manageable for beams of the order of a few MW's and, in fact, a 502°C maximum window temperature is calculated [2] for the LBE XADS window target configuration. Conversely, the steep increase of losses for proton energy as low as 400 MeV (2.5 higher than at 600 MeV) would most likely prevent the use of windows, requiring windowless target instead.

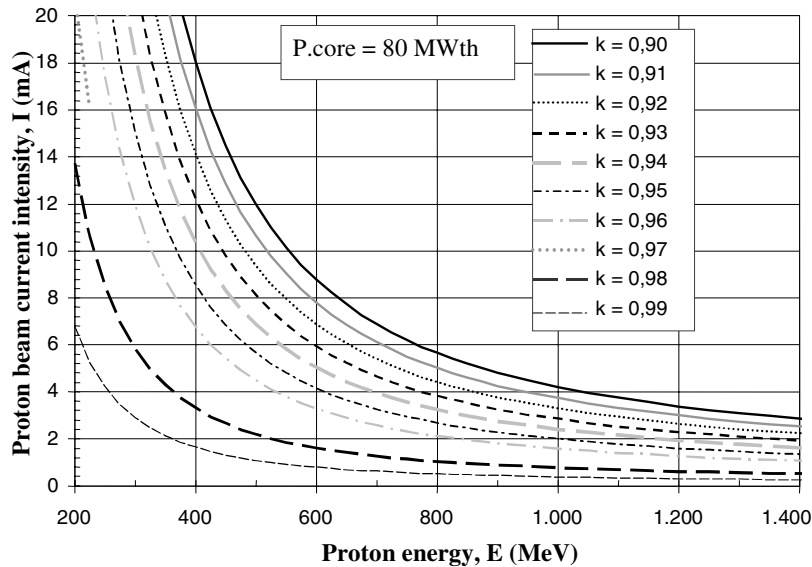
While point 1) above plays in favour of the higher proton energies, all the others may represent disadvantages. An excessive beam range would in fact stream neutrons to a poor match with a relatively short active fuel length (less than 1 m for the XADS small core), as the spallation cavity has to be kept wide enough both for cooling and to lessen the hard fluence on the fuel assemblies and keep the core fixed structures at a distance (the fuel assemblies are lengthened at the foot to put farther the core diagrid). The range of a 600 MeV proton beam in LBE (~ 30 cm, centred at core mid-plane) is in fact about 1/3 of the fuel core height, so that the spallation neutron flux, spreading as an almost homogeneous point source, well matches the surrounding core. Higher beam energies with more extended beam ranges would couple with much longer fuels, that is, in principle, with larger cores (external radii should also increase consistently) with much larger fuel loading, adequate for quite high core powers. Higher beam energies would also more likely require larger sizes for the PL in order to keep fast fluence impact below limits. Moreover, size and weight of the beam deflection optics proportionally increase with energy, which is adding other drawbacks in terms of room space and supporting structures needed for huge magnets.

Figure 6. Proton beam energy loss (ionisation) in target window per spallation neutron formed in LBE



All these issues concur, together with the limited core power and burn-up extension of the LBE-XADS, to relieving somewhat the requirements on the proton beam to sustain the subcritical core. Under the XADS prerequisites it has been thus possible to identify, inside the range of the practicable proton acceleration energies, a reasonable upper bound of 600 MeV, which (Figure 5) results in a proton beam power of 3.6 MW's at core EOL conditions ($k = 0.93$).

Figure 7. Requested beam current for a 80 MW_{th} core as a function of proton energy and k-level



The beam current demand is then 2.5 mA at BOL and 6 mA at the end of core cycle, as it can be observed from Figure 7. As the beam current curves show much sharper trend than power ones, they are less suitable than the beam power curves in Figure 5 for assessing the needed beam features.

The LBE XADS accelerator

As discussed in the previous section, the low power size chosen for the demonstration facility, as well as the moderate fuel core burnup, do not eventually require making extremely powerful neutron source for sustaining the LBE XADS subcritical core, so that the basic accelerator features have been specifically selected on the basis of the prospect of a first low-power experimental facility.

The prerequisites set forth in points (8) and (9) have furthermore induced to explore the feasibility of a cyclotron system as the most appealing solution due to its relative inherent compactness, which would eventually limit the overall costs.

Conversely, linacs systems appeared to draw substantial disadvantages related to costs for plant complexity, extensive site and shielding. They also appear to sur-dimension the effective accelerator needs, at least in the XADS domain (while a large scale demonstration scenario would probably challenge the inherent technological limits of cyclotron systems).

It is incidentally pointed out that, when considering cyclotron systems, alternate designs could envisage the use of multiple low-energy devices connected in parallel for supplying high currents. On the basis of a 350 MeV – 5 mA cyclotron [5] for instance, it could be possible to arrange a 3-cyclotrons system (as results from Figures 5 and 7) to fulfil the spallation source needs of the LBE-XADS. The feasibility apart of matching a 3-cyclotrons compounded beam under reliable operation, the use of a windowless target would appear quite mandatory in that case (3.5 times power losses in comparison with the 600 MeV, Figure 6). The windowless target however recognised as the far preferred solution, the windowed design has to be kept as back-up, while the development of the windowless is

still in progress, so that the only viable choice remains, for the time being, on a single high energy – moderate current beam delivering system.

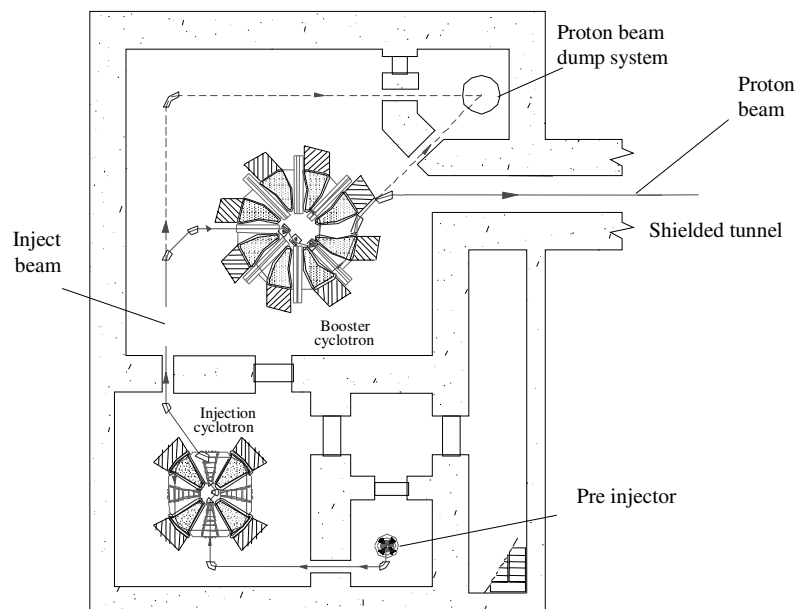
The design of the cyclotron system for the LBE XADS has been carried out in collaboration with the INFN-LNS of Catania [6] for outlining a conceptual scheme of the accelerator layout and to identify the major components and related performances. The system is based on the following features:

- H^+ ions accelerated to 600 MeV energy for up to 6 mA output current (3.6 MW maximum beam power output);
- accelerating system based on two main cyclotron stages working in series, pre-injected by a small, low-energy cyclotron

The INFN-LNS conceptualisation of the LBE-XADS cyclotron system is closely connected with that of the PSI facility, with the aim of basing on well-known and proven design solutions for which a fair operating experience already exists. The basic parameters for the LBE-XADS accelerator system have been selected within a reasonable upgrading of the PSI device, keeping in mind the possible improvements that could be made available by means of the current accelerator technology.

The layout of the two-stage cyclotron, designed in NC technology, the shielding walls included, is a roughly square footprint of about 30 to 40 m side (Figure 8).

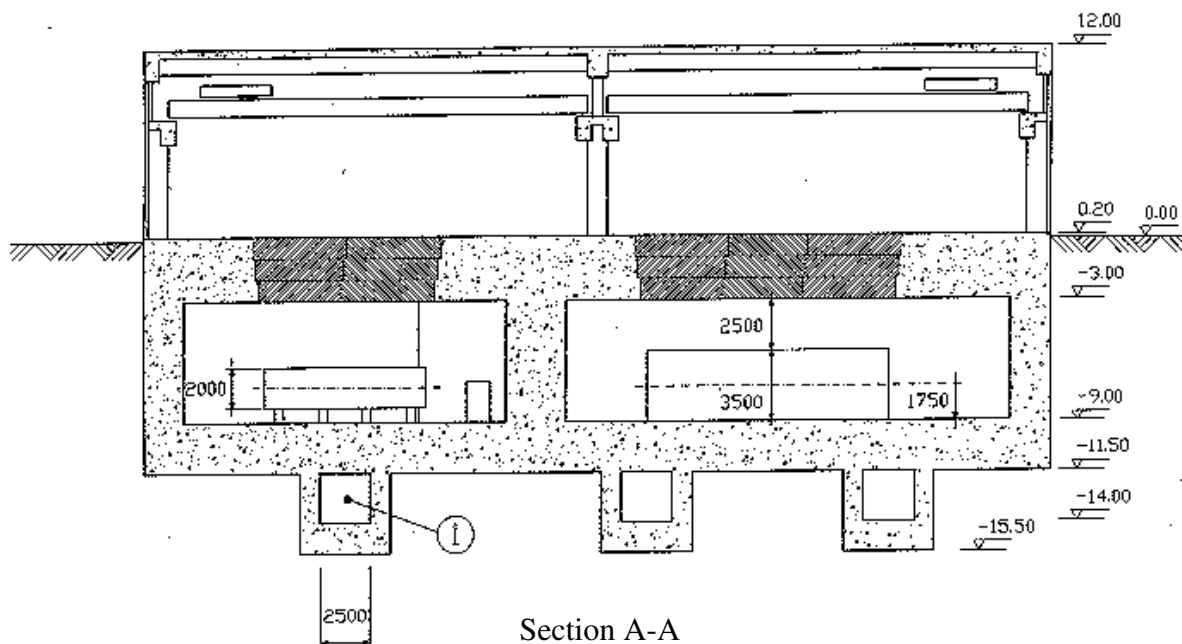
Figure 8. Accelerator system layout



The accelerator occupancy area is substantially related to the beam energy [7], both for the extension of the acceleration devices and shielding, whereas the beam intensity would play a minor role (beam current losses are in any case limited to a maximum value, which can be as conservative as 1 nA/m [8]). As the beam follows a spiralling path in the cyclotron, the accelerating efficiency in terms of energy gain per unit of used footprint (MeV/m) can be many tens of times that of a linac. The moderate building scale dependence of a cyclotron facility has to be weighted-up vs. a linac construction, which is affected in much larger proportion by the beam energy.

In order to limit the concrete wall thickness, a suitable option is to house the ion source, the pre-injector and the two accelerating stages underground, whereas the control room and service systems are placed at the ground floor (Figure 9). A thick shielding floor is between the two levels, with heavy blocks closing the apertures for the accelerator components handling and servicing. The accelerator building height to the ground is about 12 m with the service hoist cranes assembled under the roof, so that the overall accelerator facility is visualised as half grounded 30x40 m side solid, which appears in good proportion with the rest of the LBE XADS plant (~40x80 m) plant. The requirement of maintaining the overall plant installation inside a relatively compact and reasonably delimited plot plan is then fulfilled.

Figure 9. Accelerator building (vertical section)



The low-energy beam section (Figure 8) includes [6] the 100 keV ion source delivering up to 30 mA protons, the beam buncher segmenting the continuous source into RF bunched beam (CW beam at about 50 MHz) and the compact magnet injector cyclotron (CIC), which is accelerating a 12 mA beam up to 5.5 MeV. After cleaning and shaping, the beam is injected in the intermediate acceleration stage (ISSC, or injector cyclotron) which rises the energy up to 100 MeV; due to beam halos losses in the early turns, the final beam current is almost halved to 6 mA. The final stage is the separated sector magnets ring cyclotron (RC, booster cyclotron) which accelerates the protons up to 600 MeV. By-pass transport lines to a beam dump cavity have been foreseen both for the ISSC and the RC in order to safely exhaust the beam power without interacting with the XADS core when performing adjustments and testing on the accelerating lines.

Beam operating requirements

The control of the ADS core power can be actuated either by beam or reactivity changes, as shown by differentiation of the core to beam power equation:

$$\frac{\delta P_{th_{core}}}{P_o} \approx \frac{\delta P_{beam}}{P_{beam_o}} - \frac{\delta \rho}{\rho_o} \quad (3)$$

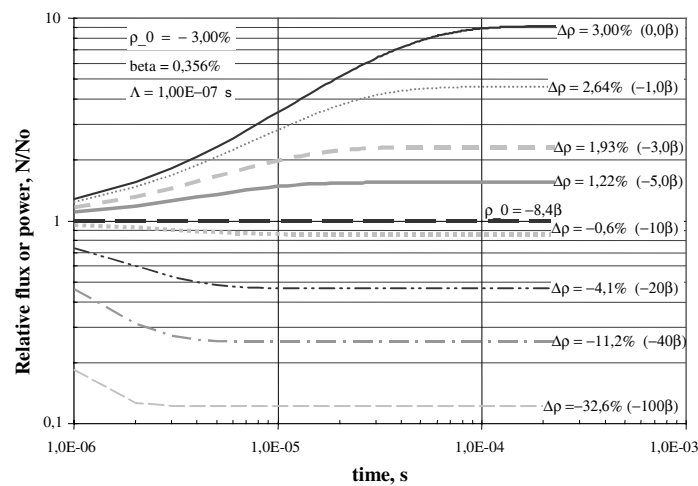
where the energy dependence of the gain factor G , through the spallation yield n_y (1), is neglected as small. Since reactivity controlling devices are not foreseen for operating the LBE-XADS and the beam power is controlled by the beam current only (being the proton energy a fixed parameter of the accelerator complex) the core power changes are directly related to the beam current changes:

$$\frac{\Delta P_{th_{core}}}{P_o} = \frac{\Delta I_{beam}}{I_o} \quad (4)$$

Because of the prompt neutron kinetics of a subcritical system, any beam current change from the accelerator, which directly affects the yield of the spallation neutron source in the target, is reacted almost instantaneously by the core multiplication, quite insensitive to delayed fission neutrons effects for enough large ρ_o . The core neutron flux, and the fission power accordingly, are subject to change at the same, potentially fast, rate of the beam intensity, which may constitute an actual drawback for the LBE XADS operability and safety. The thermal time constants of the core and PL are in fact much slower (from a few to some hundreds seconds) in comparison with the fission power period ($10^{-5} \div 10^{-4}$ s) to which they are coupled (see Figure 10, a simplified neutron point kinetics approximation from [8]).

Thus, following any change of beam power or core reactivity, continuous recursive adjustments of the fast beam control could be needed for offsetting mismatched feedbacks and damping oscillations from the slow responding thermal system. Abrupt power changes may also apply major thermal-mechanical loading on the fuel and PL components, impairing either their toughness or endurance.

Figure 10. Power transient of the subcritical core ($\rho_o = -3\%$) following fast reactivity injections



In critical reactors, the mechanically actuated control rods and the delayed neutrons kinetics (tens of seconds, depending on reactor type) are slow means naturally matching the core heat transfer dynamics. Conversely, the intrinsically fast response of the beam power and core kinetics in the ADS may be mediated to the slow response of the thermal system by means of slow actuating devices, which can be either mechanical or rate-controlled in the case of neutron absorbers and beam current regulation respectively.

The absence of operating neutron absorbers, justified by the limited cycle reactivity span of the LBE XADS, avoids the implicated DBA accidents but may require controlling the beam injection rate to match, or envelope, the time constants of the coupling thermal systems.

The condition for an overall homogeneous system dynamics in normal operating transients can then involve a crucial designing for the beam intensity variation rate to make it suitable for the thermal inertias of the coupling systems. As a viable option, the beam intensity injection rate control can be fixed in emulation of the mechanically controlled absorbing rods and implemented by means of inherently safe electronics to prevent any malfunction, or misuse, in ensuring its reliability as rate-regulated system. Under this perspective, the emergency fast beam shut-off apart, the potential flexibility of a beam control to supply different rates, however useful and attractive for some operating instances, should not be exploited under the safety viewpoint.

In addition to fixing an adequate beam injection rate, a flexible manoeuvring procedure should also try to match at best the functional characteristics of the different coupled systems (the accelerator complex, the target, the core-PL and the SS-BOP) under the widest operational transient conditions, i.e. the system start-up and shut-down shifting the core state between hot stand-by and rated power.

Earlier design of beam windows cooled by natural or assisted flows have ascertained how arbitrary beam injection rates may peak the window temperature to damage at still moderate power levels (Figure 11). A first small step may then turn useful to initiate the beam power start-up sequence in order to trigger a small LBE flow in the spallation target, suitable for smoothing the window temperature on the following beam power injections. As the main rise to the rated power level is being performed at a fixed ramp-rate, a 3-steps sequence [8] is eventually assumed for the LBE XADS start-up to normal operation:

- 1) **turn-on step:** from hot stand-by zero power up to a $1\div 1.5\%$ of core rated power (i.e. $\sim 1 \text{ MW}_{\text{th}}$);
- 2) **unrestricted ramp step:** from previous step up to $10\div 15\%$ core power (i.e. $\sim 10 \text{ MW}_{\text{th}}$);
- 3) **fixed ramp-rate step:** at $0.1 \text{ \%}/\text{s}$, $0.0001 (\Delta P/P)/\text{s}$, power change rate from the $10\div 15\%$ level up to the rated core power of $80 \text{ MW}_{\text{th}}$.

Hold-times, of optional occurrence and duration, may interleave the sequence, whenever needed, depending on accelerator-core or PL-SS operation requirements (Figure 12). The aims for a 3-step sequence are:

- to set a flexible procedure for the joint start-up of quite different coupled systems;
- to let a low power operation adequate for running sufficient beam currents to reliably stabilising the control of accelerator parameters prior to drive the whole system towards higher power levels;

- to delimit the eventual need of running early beam rises at unrestricted rates to power levels of limited impact for the driven complex.

The initial 1% power surge ($30\div 80\ \mu\text{A}$ beam BOL-EOL), besides triggering convective flows in the different cooling systems, may turn to be useful for providing a low-load feed for setting the accelerator system at low-power stand-by conditions. The XADS may be thus set at start-off to power conditions without either major restrictions for the accelerator or impact for the driven system.

As seen, the first small step may allow the next ramp to 10 MW_{th} core power (i.e. up to $0.3\div 0.8\ \text{mA}$, BOL-EOL) at a fairly unrestricted rate (dotted line of Figure 12). This condition may apply to the core and PL system at least, while PL-SS transients matching to avoid temperature instabilities in the SS would require slow rates (solid line of Figure 12). Nevertheless, an unrestricted ramp rate option may be helpful for the accelerator complex to adjust and steady its control conditions at substantial power level (near to $1\ \text{mA}$ beam at EOL), so that the subsequent ramp to rated power may perform under most reliable conditions for the LBE-XADS whole system.

Safety requirements are anyway expected to ask that, prior to any beam injection, the flows in the different cooling systems (target, core, PL and SS) have to be already started and operated normally.

As for beam stability, the accelerator control may be expected not very tight during this stabilisation step and a $10\div 20\%$ power variability should be acceptable at this low level of the start-up sequence (i.e. $10\text{ MW}_{\text{th}} \pm 2\text{ MW}_{\text{th}}$ tolerance).

Figure 11. Window temperature transient on 12.5% beam power (EOL) for different injection rates

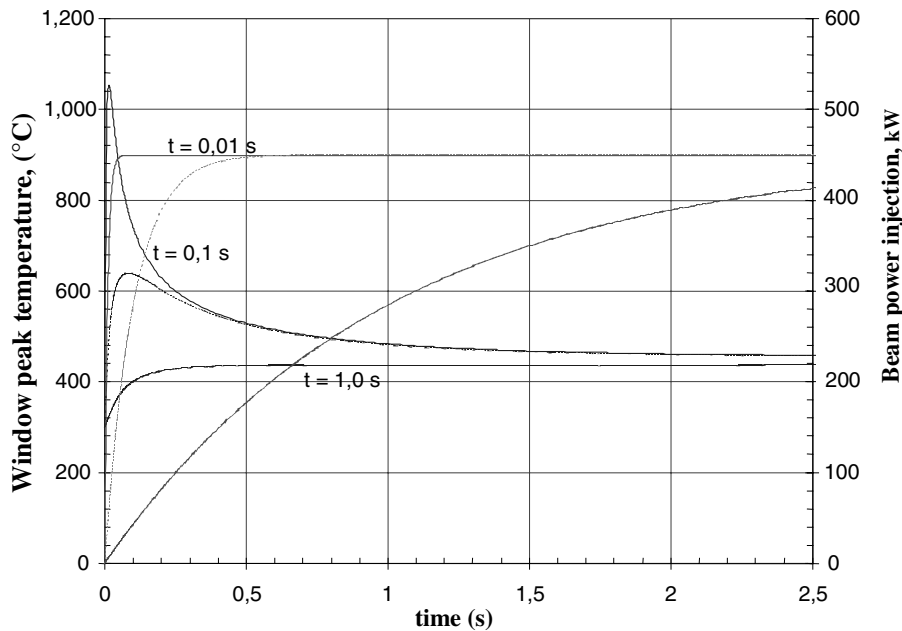
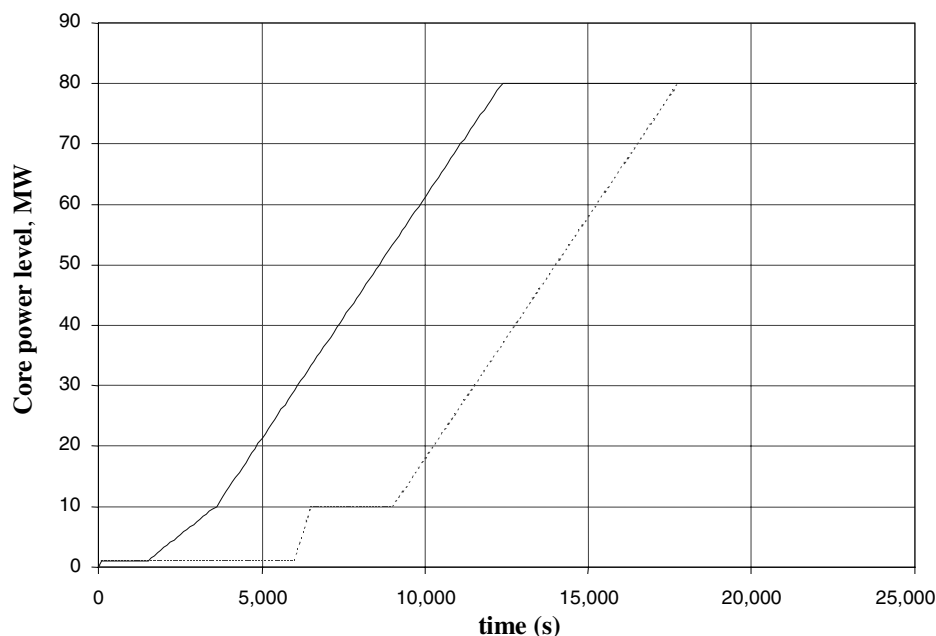


Figure 12. 3-step beam injection start-up sequences



The 3rd step of the start-up sequence is performed under fairly slow ramp-rate control of the beam intensity, which intends comparing to the reactivity insertions controlled by absorber rods in fast reactors. When starting the ramp at the level of 10 MW_{th} core power, it takes about 2.5 hours to get the nominal level of 80 MW_{th} by a rate of 8 kW/s. As the core power increases driven by the beam ramp, the core reactivity diminishes a 0.74% from hot stand-by to full power conditions (set at $k_0 = 0.97$), that is about a tenth of the beam change. The reactivity feedbacks have then secondary effects on power start-up, their small negative addition being compensated by the beam.

Conversely, if the core rise to power were to be driven by reactivity, once the beam has been started and set to the rated current (2.5 mA at BOL), a 30% worth change (Figure 10) would need to be released by neutron absorbers for a 10÷100% power step. While the addition of control rods to a small XADS may significantly increases the PL construction complexity (Figure 3), their inherent liability to reactivity initiated accidents is also an unavoidable drawback (restraining worth to less than $\sim 10\beta$ to avoid prompt-criticality events would diminish the efficacy to above 50÷60% of core power).

The 1/10 000 ($\Delta P/P$)/s rate for the beam ramp step is based on typical rates of reactivity insertion following inadvertent withdrawal (at its natural speed) of a control rod: a few cents/s or $\Delta k_{\text{eff}} = 0.0001 k_{\text{eff}}/s$ are assumed for a typical FR fuel with $\beta \approx 0.003 \div 0.004$ in [9]. This same rate applies to power changes, as $P(t) = P_0 \exp(-t/T) \rightarrow \Delta P/P_0 = t/T \sim t \cdot \Delta k/l$ for an infinite critical lattice, where $T = \Delta k/l$ is the reactor period and l the neutrons mean life (prompt+delayed).

When the 0.01%/s power rate is applied in equation (3), which is an approximation for small reactivity changes vs larger subcriticality, equivalent rates can be alternately found, for the BOL ÷ EOL subcriticality levels, both for reactivity changes, as $\Delta\rho \sim \Delta k = 1.1 \div 2.5 \text{ %/hr}$ (for $-\rho_0 = 3 \div 7\%$ respectively), and beam current variations:

$$\frac{\Delta I}{I_0} / s = 0.01\% / s = \pm 0.25 \div 0.6 \mu A / s \quad (5)$$

The lower value of 0.25 $\mu A/s$ applies to fuel core under the highest reactivity conditions at BOL, when the core response is more sensitive to beam rate injections. In order to avoid misoperations involving safety issues, one beam rate only should be applied for all conditions from BOL to EOL and, preferably, the lower, bounding, one at BOL of 0.25 $\mu A/s$, even if this would double the ramp duration at EOL.

However, the beam rate must be considered as just one component of the rise to power (equivalent to the steady uncontrolled withdrawal of a control rod bank in a FR). Depending on various requirements as fuel conditioning, transients matching for different cooling loops, set points for operating condition check-out and overrun limitation, etc. the actual start-up control procedure of the LBE-XADS may be managed to last as flexible as needed by interleaving ramp steps with time lapses at constant power.

Beam shut-off under normal operating conditions may just reverse the start-up control procedure. This allows to smoothly fade the elevated beam power for a soft relieving of the impact of the thermal-mechanical loading in the fuel core and PL structures.

The same beam rate is also applied for controlling the LBE-XADS power changes at the rated level in order to avoid the aforementioned instable control situations and abrupt thermal loading on structures. Set points, adjustable along with core cycle, may also delimit maximum beam insertions for preventing control errors or misoperation.

It is finally observed how the design flexibility of a control system based on electronic circuitry rather than on mechanical devices should allow to optimise the beam rate for best operation of the LBE-XADS under both performance and safety viewpoints.

Beam stability requirements

Besides the operating criteria, a few key parameters for beam quality have to be identified as relevant to the accelerator-core functional coupling.

A wide beam variability margin (10÷20%) may be allowed for the first two steps of the start-up sequence when the core power level is still low, so that the impact on the plant is minor. Conversely, beam instabilities during the rate-controlled power changes must be substantially restricted and an effective control of the beam should be in place.

The power stability range may be assumed to narrow from a 10÷20% of the 10% ramp step, up to a $\pm 1 \text{ %}$ allowance at the nominal power level of 80 MW_{th}.

During normal operating conditions in fact, nuclear reactors generally account for limited instabilities of the power level, which are restricted to a few percent ($\pm 2 \text{ %}$, [10]). On the other hand,

accelerators are reported capable of supplying a stable and reliable beam by varying the current at the injector in CW systems (cyclotrons) or by adjusting pulse width and repetition rate in linacs [11]. These adjustments would be controlled by automatic regulation systems to assure the necessary beam stability for operation at stable thermal power.

As an extension of equation (3), the differentiation of the XADS core power into source and multiplication terms is applied for assessing stability conditions:

$$\left(\frac{\delta P}{P}\right)_{core\ power} = \left(\frac{\delta S_n}{S_n}\right)_{neutron\ source} + \left(\frac{\delta M_f}{M_f}\right)_{system\ energy\ multiplicity} \quad (6)$$

This distinguishes two main contributions to the core power variability, one for the neutron source ($S_n = I/e \cdot n_y(E) \cdot E = P_{beam} \cdot n_y / e$, with e the elementary charge), linked to beam related parameters (E , I , n_y), another for the energy multiplicity in the system ($M_f = 1/(-\rho) \cdot 1/v \cdot \gamma$), linked to variables affected by coupled neutronics - thermal-hydraulics feedback. The neutron multiplicity, function of the reactivity level ρ , is the most affected by coolant flow-temperature changes, whereas the neutron fission probability, $1/v$, and the energy release per neutron induced fission, γ , are less influenced.

On a simple even sharing basis, a $\pm 1\%$, or $\pm 1.4\%$ by square-rooting, variability range can be attributed to the neutron source and to the nuclear chain generation system. The allowance for source variability could be eventually extended to a larger range, e.g. to a $\pm 2\%$, should the system variability be assessed as fairly limited in itself, e.g. to about $\pm 1\%$, such to result in an overall instability span at rated power reasonably inside a $4 \div 5\%$, being the two variability terms squared-compounded.

The energy variability cannot be neglected, as in (3-4), when deriving the neutron source perturbation, the beam-related XADS variability expression is then:

$$\left(\frac{\delta S_n}{S_n}\right)_{neutron\ source} = w_{fE} \frac{\delta E_{beam}}{E_o} + \frac{\delta I_{beam}}{I_o} \quad (7)$$

where w_{fE} is an energy dependent factor weighting the energy variability term, so that, while the neutron source is proportional (through the yield n_y) to the beam power, its variability is not.

The w_{fE} beam energy-dependent weighting factor is assessed by the spallation yield n_y (neutrons/GeV) from the curve fitting of Figure 4 [8] as:

$$n_y = a \left[1 - e^{-bE^c} \right] \rightarrow w_{fE} = \left[1 + \frac{bcE_o^c}{e^{bE_o^c} - 1} \right] \quad (8)$$

and, based on the fitting coefficients a , b , c (31.783, $2.145 \cdot 10^{-4}$ and 1.3707 respectively) it is equal to 1.64 at the rated proton beam energy of $E_o = 600$ MeV.

Equation (7) shows that the source stability figure is shared between the relative variability's of beam energy and current, as given by the ratio of the sign-dependent, time-fluctuating, instant “ δ ” values to the nominal “ o ” values:

$$\pm \frac{\delta S_n(t)}{S_{n_o}} = \pm w_{f_E} \frac{\delta E(t)}{E_o} \pm \frac{\delta I(t)}{I_o} \quad (9)$$

Fluctuations may be integrated over an arbitrary time period to assess the root-mean-square of the neutron source variability and, considering beam energy and current truly independent from each other, as it may be expected on a first order basis, it is found:

$$\begin{aligned} \left(\frac{\Delta S_n}{S_n} \right)_{rms} &= \sqrt{\frac{1}{N} \sum_i^N \left(\left(\frac{1}{S_n} \frac{\delta S_n}{\delta E} \right) \delta E + \left(\frac{1}{S_n} \frac{\delta S_n}{\delta I} \right) \delta I \right)_i^2} \\ &= \sqrt{\left(\left(\frac{1}{S_n} \frac{\delta S_n}{\delta E} \right) \Delta E \right)_{rms}^2 + \left(\left(\frac{1}{S_n} \frac{\delta S_n}{\delta I} \right) \Delta I \right)_{rms}^2} \end{aligned} \quad (10)$$

This equation represents the general relative error propagation formula, where the adding-up for $N \rightarrow \infty$ makes the sign-dependent cross terms likely to cancel out on a statistical unbiased basis.

The differential of the source $S_n(I, n_y, E)$, equation (7), and the above discussed allowable stability range lead by equation (10) to express the condition:

$$\left(\frac{\Delta S_n}{S_n} \right)_{rms} = \sqrt{w_{f_E}^2 \left(\frac{\Delta E}{E} \right)_{rms}^2 + \left(\frac{\Delta I}{I} \right)_{rms}^2} \leq \pm 1 \div 1.4\% \quad (11)$$

that is the source *rms* variability is equivalent to the square root of the sum of beam energy and current one's squared, the energy term being weighted by an energy dependent factor based on the yield expression. Due to the w_{f_E} factor, the neutron source variability does not equalise that of beam power, which is given by the square root of the simple sum of energy and intensity *rms*'s squared.

On assuming that the beam energy and intensity variability's may be equivalent $[(\Delta E/E)_{rms} \equiv (\Delta I/I)_{rms}]$ in equation (11) taken at the higher bound of $\pm 1.4\%$, the beam power *rms* variability would be a 74 % of the source': $(\Delta P/P)_{rms} = 0,736(\Delta S_n/S_n)_{rms}$, i.e. ± 37 kW at the maximum rating of 3.6 MW. Conversely, an even sharing between the two terms in the square root, would credit a $\pm 0.61\%$ and $\pm 1\%$ variability ranges for the beam energy and current respectively. The allowable variability range of beam power would be then $\pm 1.17\%$ (about 84% of the source'), or ± 42 kW at the maximum beam rating.

Due to their distinctive techniques in forming and controlling, beam energy (connatural to accelerating devices) and current intensity (broad-range adjustable operating parameter) may be expected to have, or be allowed to have, quite different intrinsic stability characteristics. Therefore, some kind of criterion needs to be assessed for distinguishing constraints between the two beam parameters, more specifically, by delimiting that more critical under the viewpoint of beam trajectory stability, i.e. the beam energy, as eventually affected by transport line requirements.

It is finally underlined that the variability's here considered intend to apply to fluctuations of the mean values of beam parameters, in connection with the core performances they may affect. Energy dispersion and radial intensity distribution across the beam spot, which are more strictly dependent on design details of the accelerator and of the beam line optics, are not reported here. In practice, beam current (or energy) instability may be evaluated as:

$$\pm \frac{\Delta I}{I} (\%) = \frac{I_{max} - I_{min}}{I_{max} + I_{min}} \times 100 \quad (12)$$

where I_{max} and I_{min} are monitored over a given time period to assess a maximum variability range. By statistical assessment the time trend of averages and deviations can be used to compound tolerance limits at given percentiles.

Beam focalisation requirements

The different contributions to be ascribed to energy and current variability's in equation (11) may be assessed by relations between energy stability and focalisation requirements accounting for randomly occurring beam spotting variations.

The turn separation (11÷15 mm) at the beam extraction radius (4.45 m) of the RC [6] and a beam spot width assessed as a half of that ([8] as based on beam parameters of [6] and beam width correlation from [12]), may hint an assessment for a possible maximum energy shift, which could ever theoretically occur at the RC outlet.

To this end, the beam rigidity is derived from the cyclotron formula, $mv^2/r = qvB$, as:

$$B \cdot r = \frac{m}{q} v = \frac{m_o}{q} \gamma \cdot \beta \cdot c = \frac{1}{300} \sqrt{(E_k (E_k + 2E_o))} \quad (13)$$

which is applicable for protons ($E_o = 938$ MeV) and gives 4.06 T·m rigidity for $E_k = 600$ MeV beam.

Relative variations of beam bending radius, $\delta r/r$, can be derived by differentiation of (13):

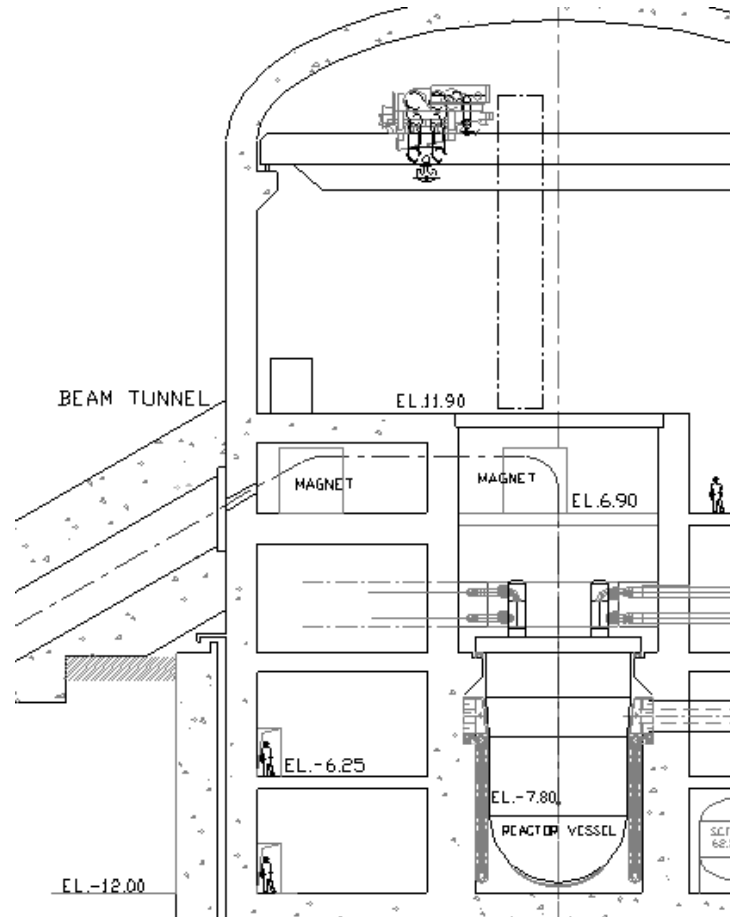
$$\frac{\delta r}{r} = \frac{E_k + E_o}{E_k + 2E_o} \frac{\delta E_k}{E_k} - \frac{\delta B}{B} = 0,62 \frac{\delta E_k}{E_k} - \frac{\delta B}{B} \quad (14)$$

At high saturation values the magnetic field variations may be fairly small, so that beam radius variability's may be considered mainly a function of the beam energy changes. Then, assuming a possible beam path deviation of a half of the outer turn separation, a 7 mm shift on a 4.45 m extraction radius would imply a maximum energy swing of $\pm 0.25\%$ (± 1.5 MeV) on the average proton beam kinetic energy.

A $\pm 0.25\%$ beam energy stability figure, linked, as seen, to some, however conservative, assumption on how the beam could be assumed to exceedingly shift at the RC outlet, would still represent less than a half of the one assessed in Section "Beam stability requirements" by an even sharing between energy and current. The beam transport line, whether capable to accept such presumed energy variations, should not excessively modify them up to the delivery in the spallation target.

The beam stability can be assessed in practice by means of a focalisation requirement which consider the actual path of the beam line through the layout of LBE-XADS (Figure 13).

Figure 13. LBE XADS beam line across plant



The nuclear block arrangement drawing shows a 15 m proton beam “free-flight” distance between the down bending magnet and the spallation target in the core. The most appropriate focalisation requirement can be hence that any beam energy variability, which may occur under normal operating conditions, must not lead to beam deviations at the bending magnet exit such to impact with the beam line duct or any other spallation target structure [8].

On a 15 m beam path range, the present design of the LBE-XADS windowless and window target allows for a maximum side-gap of 2 cm only between the beam footprint edge and target structure: a 8 cm beam spot transversal scanning inside a 12 cm LBE flow duct and 16 cm beam dish inside a 20 cm pipe are in fact designed for the windowless and window target respectively.

The beam shift at the target level following an energy swing δE_k from the nominal value E_{k_0} which perturbs the beam bending radius of Δr , i.e. from r_o to r_o' , is:

$$\begin{aligned}\Delta x &= \Delta s + L \operatorname{tg} \theta = \left(r_o' \cos \theta - r_o \right) - \Delta r \cos \alpha + L \frac{\Delta r \operatorname{sen} \alpha}{r_o' \cos \theta} \cong \\ &\cong \frac{\Delta r}{r_o} \left[(1 - \cos \alpha) r_o + L \operatorname{sen} \alpha \right]\end{aligned}\quad (15)$$

where Δs is the beam lateral shift at the exit of the bending magnet, $L = 15 \text{ m}$ the beam range to target, θ the trajectory deviation, α the beam bending angle and r_o the bending radius at the nominal energy of 600 MeV ($r_o = 2.71 \text{ m}$ for a magnetic field of 1.5 T). In the case of a 90° beam bending and neglecting field perturbations, equations (13-14) allow to assess the beam shift as:

$$\Delta x = \frac{\Delta r}{r_o} (r_o + L) = 0.62 \frac{\delta E_k}{E_k} (r_o + L) \leq 2 \text{ cm} \quad (16)$$

Based on this condition, the maximum allowable beam energy variability is then:

$$\left(\frac{\Delta E}{E} \right)_{rms} \approx \pm 0.18\% \Rightarrow \Delta E_{rms} = \pm 1.1 \text{ MeV} \quad (17)$$

which corresponds to a maximum allowable deviation angle $\theta \approx \operatorname{tg} \theta = \Delta r / r \approx \Delta x / (r_o + L)$ of about $4'$.

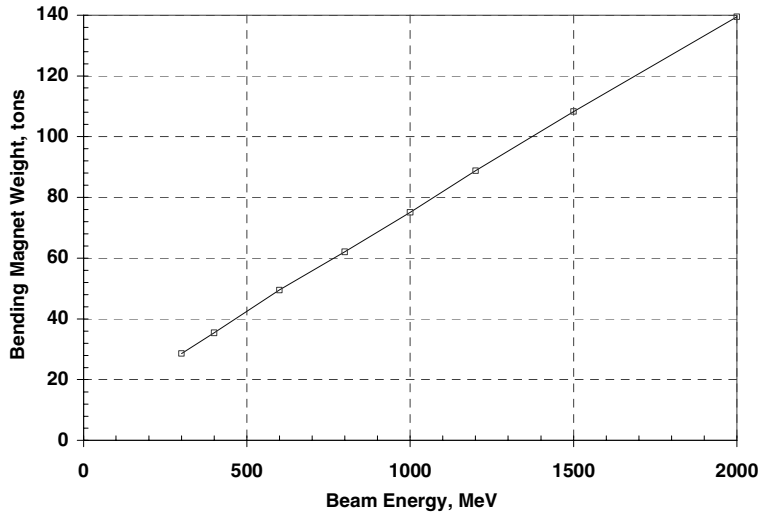
The condition expressed by equation (17) is quite tight, more restrictive than the $\pm 0.25\%$ considered as possible extreme energy swing at the RC outlet. In the case of a double 45° bending arrangement, with beam refocused between the two magnets but unconditioned at the exit of the second bending directed down to target, the resulting beam shift would be a 64% of that at 90° , allowing a little larger energy variability, i.e. of 0.28 % or $\pm 1.7 \text{ MeV}$, and a deviation angle of $6'$.

Neglecting the magnetic field contribution ($-\delta B/B$) to $\delta r/r$ in equation (14) may be reasonable when the field is well inside the saturation region, as for the sector magnets with $B_{\text{fill}} = 2.09 \text{ T}$ [6]. The orbits controlling field should be in fact more stable than the accelerating field in the cavities. Should any magnetic field variability be comparable to beam energy, the allowance set in equation (17) would then reduce accordingly. This a fortiori applies to the beam bending magnet operating at the lower field of 1.5 T.

The allowances above are therefore upper bounds for the beam energy variability, on condition that the bending system one's are minor. This much depends on the specific design of beam transport and delivery to the target unit, which is underway to date. The optimisation of the beam line scheme of Figure 13 would require to split the 90° bending and also an adequate optics to control the overall deflection path.

Conversely, the substantial encumbrance of a beam bending system and its impact on the layout and containment have to be kept in mind: Figure 14 shows an estimation (including neither stabilisation optics nor infrastructures) of the weight (steel + copper) of "C" shaped 90° bending magnet system as a function of the beam energy (50 tons for a 600 MeV beam).

Figure 14. 90° beam bending magnet weight



The energy variability allowance assessed on beam focalisation requirements by equation (17) allows now to determine a more precise condition, as based on the source variability equation (11), for the beam current variability as well:

$$\left(\frac{\Delta I}{I}\right)_{rms} \leq \pm \sqrt{(1.4\%)^2 - w_{f_E}^2 \left(\frac{\Delta E}{E}\right)_{rms}^2} = \pm 1.37\% \quad (18)$$

which is applicable in the case of a 90°, one-turn, beam to target bending (0.18% energy allowance), whereas it would be a $\pm 1.32\%$ in the case of a 45° bending (0.28% energy allowance).

Due to the quite restrictive requirement on the energy variability, which is bound, as seen, to the beam line transport to target configuration itself, the allowance for the beam current variability can be in practice as ample as the source variability is allowed to be.

Summary and conclusions

The feasibility design of a small-size lead bismuth eutectic cooled ADS (the 80 MW_{th} core power LBE-XADS) performed by a group of Italian organisations led by Ansaldo and supported by the MURST (the Italian Ministry of university and of the scientific technological research) under the prospects of the development of an industrial size plant has prompted the attention on some specific new requirements for the HPPA.

This first work has been intended to draw some basic criteria for a methodology to approach the problem of the coupling between a HPPA with a subcritical system, keeping in mind requirements under the viewpoint of the substantial upgrading to which a full-scale operational ADS would have to respond.

The specific requirements for a HPPA to couple with the LBE-XADS, which, together with others, such as the toughness to beam trips, may ask for a substantial re-addressing for design and operating criteria to which accelerators mainly devoted to R&D were accustomed to, are summarised in Table 2 below.

Table 2. Accelerator-core coupling parameters

<i>Accelerator-core coupling</i>	
Spallation neutron yield, n/p	~14
k_{eff} , BOL÷EOL	0.97 ÷ 0.93
Gain factor G, BOL÷EOL	54 ÷ 22
<i>Beam parameters</i>	
Proton energy	600 MeV
Beam current, BOL÷EOL	2.5 ÷ 6 mA
Proton beam momentum	1 219 MeV/c
<i>Beam operating changes</i>	
Beam control rate at power	+/- 0.25 μ A/s
<i>Beam start-up sequence</i>	
1) turn-on step	1÷1.5% P_o
2) unrestricted ramp step	10÷15% P_o
3) fixed ramp-rate step	0.01% P_o/s
<i>Overall plant power stability</i>	
range at full power (80 MW _{th})	4 %, 3.2 MW _{th}
<i>Beam stability at full power</i>	
Power	± 1.38%
Energy	± 0.18% ± 1.1 MeV
Current	± 1.37%

As seen from the table, fairly tight limits have been inferred for the beam parameters variability when adopting stability figures which, whereas assumed comparable to standard nuclear plants, have to be tailored to an actual ADS layout (i.e. the LBE-XADS) and to specific functional requirements.

A substantial, interdisciplinary work would be then needed in the future in the field of the design and assessment of the operational coupling of a HPPA to subcritical system in order to address requirements and prescriptions which, besides assessing the issues linked to the ADS operation and control, they could in turn give more useful indications for the design criteria of the different XADS systems and components as well as allowing to better identify their functional requirements, while also providing the safety analysis with more focused and practical assumptions.

Abbreviations

BOL / EOL	beginning of life / end of life
BOP	balance of plant
BU	burn up
CIC	compact injector cyclotron
CW	continuous wave
DBA	design basis accident
EFP	equivalent full power
FR	fast reactor
IHX	intermediate heat exchanger
ISSC	intermediate separated sector cyclotron
LBE	lead bismuth eutectic
LLFP	long lived fission product
MOX	mixed oxide fuel
NC	normal conductive
PL	primary loop
RC	ring cyclotron
SPX	Superphénix
SS	secondary system
XADS	experimental accelerator-driven system

REFERENCES

- [1] Rubbia, C., *et al.*, “Conceptual Design of a Fast Operated High Power Energy Amplifier”, CERN/AT/95-44(ET), September 1995.
- [2] Cinotti, L., *et al.*, “XADS Pb-Bi Cooled Experimental Accelerator Driven System – Reference Configuration – Summary Report”, ANSALDO ADS1SIFX0500, Rev. 0, June 2001.
- [3] Cinotti, L., *et al.*, “Conception and Development of a Pb-Bi Cooled Experimental ADS”, ANS Winter Meeting, Reno 12-15 November 2001.
- [4] Turrone, P., ENEA-Bologna (I), L. Cinotti, Ansaldo-Genova (I), *et al.*, “The CIRCE Test Facility”, ANS Winter Meeting, Reno, 12-15 November 2001.

- [5] Abderrahim, H, *et al.*, SCK•CEN, Y. Jongen, *et al.*, IBA, “MYRRHA, a Multi-purpose ADS for R&D as First Step Towards Waste Transmutation – Current Status of the Project”, OECD-NEA 6th International Exchange Meeting on Actinide and Fission Product Partitioning Transmutation, Madrid, Spain, 11-13 December 2000.
- [6] Calabretta, L., *et al.*, INFN-LNS, “An Accelerator Complex to Drive a Demonstrative Subcritical Reactor”, OECD-NEA Workshop on Utilisation and Reliability of HPPA’s, Aix-en-Provence, France, 22-24 November, 1999.
- [7] Klein, J.C., *et al.*, “Structural Activation, Energy Deposition and Shielding Calculations due to Proton Beam Losses in a High Power Proton Linear Accelerator”, OECD-NEA Workshop on Utilisation and Reliability of HPPA’s, Aix-en-Provence, France, 22-24 November, 1999.
- [8] Negrini, A. “Design Specification – Performance Requirements for an Accelerator to couple with a Subcritical System”, ANSALDO Internal Report ADS1SNPX0191, Rev. 0, June 2000.
- [9] Rief, H., JRC CEC Ispra (I), H. Takahashi, BNL Upton NY (US), “Control of Accelerator Driven Subcritical System Fuelled by Actinides”, Proceedings of a TCM, Vienna, 29 November-2 December 1993 International Atomic Energy Agency, Vienna (Austria) IAEA-TECDOC 783.
- [10] Carlucci, B., Framatome Lyon (F), A.C. Mueller, CNRS-IN2P3, Orsay (F), M. Napolitano, INFN Naples (I), A.P. Navarro, LAESA Zaragoza (ES), “Report of the TWG sub-group on Accelerators for ADS”, Internal doc. of The European Working Group on ADS, March 2001.
- [11] “A European Roadmap for Developing Accelerator Driven Systems (ADS) for Nuclear Waste Incineration”, The European Working Group on ADS, April 2001.
- [12] Stammach, Th., *et al.*, “The feasibility of high power cyclotrons”, Nuclear Instruments and Methods in Physics Research B 113, 1-7, 1996.

SAFE SHUTDOWN OF ACCELERATOR-DRIVEN SYSTEMS

Brent E. Boyack, Michael W. Cappiello, Kemal O. Pasamehmetoglu

Advanced Accelerator Applications Technology Development Office

Los Alamos National Laboratory, USA

Abstract

Accelerator-driven systems have been and are being considered for several applications in which a spallation target is coupled to a subcritical multiplier or high-powered blanket. Examples are the accelerator production of tritium and accelerator transmutation of waste. Of primary importance for any accelerator-driven system is the need to demonstrate the safe shutdown of the system. In the United States, insights regarding the evolving design and regulatory requirements for the safe shutdown of accelerator-driven systems can be developed by considering the safety philosophies and approaches of the US Department of Energy (DOE) and the US Nuclear Regulatory Commission (NRC). Both the DOE and NRC approaches to safety emphasise the use of multiple layers of protection to prevent or mitigate the unintended release of radioactive material to the environment. In addition, however, there is a clear movement to employing simplified, inherent, and passive, means to accomplish safety functions in new reactor designs. In general, the use of inherent or passive safety features assures that the response to any upset condition is controlled by basic, inherent, physical processes, such as the expansion of metals with increasing temperature rather than the functioning of engineered components. In this changing design and regulatory environment, the challenge is to identify and employ basic, inherent, and passive physical processes to ensure the safe shutdown of accelerator-driven systems. In this paper we review the design and regulatory environment and explore several design approaches featuring both the functioning of engineered components and inherent features to produce the safe shutdown of accelerator-driven systems.

Introduction

Accelerator-driven systems (ADS) are being considered for use in the transmutation of spent nuclear fuel and for isotope production. In these systems, a proton accelerator is coupled to a spallation neutron source that in turn is surrounded with either a power producing blanket or isotope production targets or moderators for conditioning the neutrons. Within the US, examples are the accelerator production of tritium (APT) [1, 2], the spallation neutron source (SNS) [3], the accelerator-driven test facility (ADTF) [4] and accelerator transmutation of waste (ATW) [5] systems. Common to each of these systems is the use of a high intensity proton accelerator and a spallation neutron source for driving the desired reactions within a receiver, be it tritium production as in the APT, neutron generation for scientific studies as in the SNS, or the transmutation of highly radioactive wastes as in the ATW.

If the receiving system is a subcritical reactor, as is the case, for example, in the ATW, a highly reliable means of shutting down the beam is essential. In effect, beam shutdown is required to ensure that anticipated transient and potential accident sequences cannot be further aggravated by a failure to terminate delivery of the beam and its associated energy to the receiving system.

A significant safety characteristic of accelerator-driven systems is that the driving energy source, the beam, can be rapidly and easily terminated. It has also been determined that it is important that reliable means of terminating the beam operation on demand be provided. Therefore, highly reliable, active systems for terminating beam delivery have been designed. The APT target/blanket beam shutdown (TBBS) system is an example of one such design.

Hazards analysis of the APT revealed that the principal accelerator-related risks to the public are failures to terminate the beam and misfocusing accidents [6]. The APT safety objective was to ensure that no design basis accident could result in a “beam on” condition. Accordingly, the beam shutdown system was designated as a safety class system.

Safety class beam trips were provided for the following design basis accidents: loss of flow, flow blockages, loss of coolant, loss of heat sink, and helium tube breaks. For each design basis accident requiring a safety class beam shutdown, two independent and diverse detection, signal processing, and actuation trains were required. Each train was composed of three functional elements, a sensor network, logic solvers, and a beam shutdown mechanism. Each train was required to be single-failure proof. The conditional probability of failure for the safety-class TBBS was required to be less than 10^{-6} /year.

Additional requirements were placed upon the signals to be used for beam shutdown.

- First, the sensors were required to be located in the primary heat removal systems for the target and blanket.
- Second, a minimum of one type of signal was required to feed one train (Train 1) and another diverse signal type was required for the second train (Train 2).
- Third, exceeding the setpoints for any signal type on either train required a beam shutdown.
- Fourth, loss of any signal or loss of power to the instruments required an automatic beam shutdown.

The resulting signal types selected for the safety class TBBS are shown in Table 1.

Table 1. Signal types for the APT main beam shutdown systems

Target Train 1 signal type	Target Train 2 signal type	Blanket Train 1 signal type	Blanket Train 2 signal type
Pump current	Pump speed	Pump current	Pump speed
Cold-leg flow rate	Hot-leg flow rate	Cold-leg flow rate	Hot-leg flow rate
Cold-leg ΔP fluctuations	Hot-leg ΔP fluctuations	Cold-leg ΔP fluctuations	Hot-leg ΔP fluctuations
	Pressuriser pressure		Pressuriser pressure
Pressuriser level	Pressuriser level	Pressuriser level	Pressuriser level
Cold-leg pressure	Hot-leg pressure	Cold-leg pressure	Hot-leg pressure
Heat exchanger (HX) temperature	HX exit temperature	HX temperature	HX exit temperature
Pressure fluctuations	HX inlet temperature	Pressure fluctuations	HX inlet temperature
Boiling noise	HX ΔT	Boiling noise	HX ΔT

The external safety review of the beam shutdown system was not taken to a formal conclusion by the Defense Nuclear Facilities Safety Board (DNFSB) before the APT project was terminated. However, based upon the preliminary reviews that were conducted, the DNFSB concurred that the beam shutdown system design was acceptable.

The APT beam shutdown system briefly described above relies on *active* components, e.g., components whose functioning depended on an external input such as actuation, mechanical movement or supply of power [7]. Although not explicitly required by regulatory bodies at this time, there is an increasing emphasis on including inherent and passive safety features in a design. Designs employing inherent and passive safety features emphasise the use of natural forces, (e.g., gravity, self-correcting neutronic feedback) and de-emphasise systems which require large amounts of electricity, rapid automatic response, complex logic, or high energy [8].

Institutional perspectives on passive safety

As defined by the International Atomic Energy Agency (IAEA), a passive component has no moving part and its functioning does not depend upon an external input [7]. Very few systems are totally passively safe. To recognise the range of possibilities, the IAEA defined four categories of passivity, summarised in Table 2 [8].

In 1986, the US Nuclear Regulatory Commission (NRC) issued a statement of policy on the regulation of advanced nuclear power plants [9]. The Commission considered the term “advanced” to apply to reactors that are significantly different from current generation light water reactors ... and to include reactors that provide enhanced margins of safety or utilise simplified inherent or other innovative means to accomplish their safety functions. The Commission stated its expectation “that advanced reactors will provide enhanced margins of safety and/or utilise simplified, inherent, passive,

or other innovative means to accomplish their safety functions”. The Commission stated a number of attributes that could assist in establishing the acceptability or licensability of a proposed advanced reactor design. Two are repeated here because of their applicability to ADS designs. The Commission is seeking “highly reliable and less complex shutdown and decay heat removal systems. The use of inherent or passive means to accomplish this objective is encouraged (negative temperature coefficient, natural circulation)”. The Commission also endorsed “simplified safety systems which, where possible, reduce required operator actions...”. It should be stated that the advanced reactor policy statement did not specify new regulations.

Table 2. Categories of passivity

Characteristic	Category A	Category B	Category C	Category D
Sensor signal inputs	No	No	No	Yes
External power sources or forces	No	No	No	No
Moving mechanical parts	No	No	Yes	Either
Moving working fluid	No	Yes	Yes	Yes
Example	Core cooling via radiation or conduction to outer structural parts	Heat removal by natural circulation to elevated heat exchangers	Rupture disk or spring-loaded valve for over-pressure protection	Core flooding following primary system depressurisation by an active system

The US Department of Energy (DOE) does not explicitly require passive or inherent safety features [10]. However, the DOE clearly is fostering work on reactor concepts that use both inherent and passive safety features. One such example is the DOE-sponsored effort on small modular reactors (SMRs) [11]. The SMRs all make greater use of inherent safety features than do existing larger commercial plants. For example, inherent safety may be achieved through fuel designs that are able to withstand extreme temperatures without loss of the fuel’s integrity. Almost all of the design concepts rely on natural circulation of the coolant in emergency modes and many SMRs additionally rely on natural circulation for cooling of the core during normal operation.

DOE perspectives regarding inherent safety features are summarised in a report to congress [11]. The report notes that traditional nuclear reactor safety systems have usually been referred to as “active engineered safety system”, because they involve engineered components that are required to perform some action in response to reactor conditions or operator commands. Even though many such active systems can partly rely on natural physical phenomena, such as gravity, they also involve electrical or mechanical operations that have finite probabilities, albeit small, of failure. Inherent safety is described in the report to congress as being fundamentally different. In general, the use of inherent safety features assures that the reactor response to any upset condition is not determined by the functioning of engineered components, but is controlled instead by basic, inherent, physical phenomena such as the expansion of metals with increasing temperature, or the use of buoyancy to provide flow and cooling by natural circulation. For the report to congress, inherent safety is viewed as a condition that is achieved without operation or functioning of any device that is susceptible to failure. The use of inherent safety principles is thought to further reduce or eliminate the likelihood

and consequences of a reactor accident, and make reactor design and operation simpler. The use of inherent safety features is “considered very important”.

A final insight into the safety-related trends in nuclear reactors comes from the DOE’s Generation IV initiative and the technology goals for Generation IV nuclear energy systems [12]. The goal designated safety and reliability-2 states “Generation IV nuclear energy systems will have a very low likelihood and degree of reactor core damage”. The supporting text for the goal states “Additional means, such as passive features to provide cooling of the fuel and reducing the need for uninterrupted power, have been valuable factors in establish this trend [*i.e., trend to lower core damage frequencies*]. The evaluation of passive safety should be continued and passive safety features incorporated into Generation IV nuclear systems whenever appropriate”.

In summary, there are strong incentives to utilising inherent passive features in new reactor designs, particularly with respect to safety. Passive concepts have the potential to: (1) simplify the design and make it cheaper to build, operate, and maintain; and (2) increase the real safety of the plant through systems which are less complex and more reliable since they rely on phenomena and processes that are naturally related to the operational or accident behaviour of the plant [8].

Candidate ADS beam shutdown approaches

Given that passive systems utilising inherent characteristics have the potential to deliver significant economic and safety benefits, ADS design teams must make every effort to incorporate these features. In the remainder of this paper, passive shutdown concepts previously identified for several ADS designs are summarised. In addition, several other candidate approaches to ADS beam shutdown are described. To varying degrees, each of the approaches described is best described as a concept rather than as a proven design approach at this time.

We emphasise that active systems such as those previously described for the APT system would remain as the primary means of beam shutdown in an ADS. The primary objective of the passive systems utilising inherent characteristics described in the following paragraphs is accelerator beam shutdown should the active systems fail to perform as designed. Thus, this passive safety approach partially supplants the traditional engineered devices by exploiting passive systems or inherent characteristics. These concepts are implemented to assure safe response, even if the engineered systems, which require assured sources of power and high reliable active sensing and switching equipment were to fail [13].

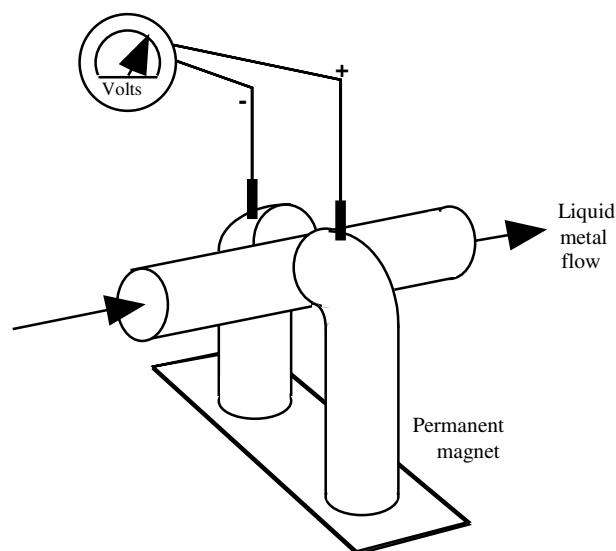
Carlsson and Wider have evaluated a melt-rupture disk concept for two ADS designs, one operating at 80 MWt and the second at 250 MWt. [14], each undergoing a combined loss-of-heat-sink and loss-of-flow accident with a failure to terminate delivery of the beam to the target. An immediate consequence of this accident will be an increase in the ADS primary coolant temperature. The passive safety design feature is an integral melt-rupture disk incorporated in the beam tube at a level below the surface of the ADS primary coolant. Once the coolant exceeds the design limit for the melt-rupture disk, e.g., 873K, The disk will fail and coolant will enter the vacuum tube and fill the tube to a level above the top of the active core. Thus, the impact point of the proton beam will move upward out of the core and the spallation neutron production in the target region is reduced to zero. Rather than terminating the beam, this concept significantly lengthens the time for a subsequent active action to terminate the beam.

Several concept categories for terminating beam delivery in an ADS are being considered at Los Alamos National Laboratory.

The first concept category focuses on shutdown system designs in which beam delivery to the reactor is terminated by interrupting the accelerator power supply. This approach envisions no moving mechanical parts in the shutdown system but does utilise sensor signals that are generated as an inherent feature of passive sensing devices.

As an example of this approach, consider an unprotected loss-of-flow accident (ULOF) in a large ATW. The flow-sensing device is an electro-magnetic flow meter. This meter has no power source and no moving parts; its primary components are a permanent magnet and associated wiring to carry the current. The normal flow of the liquid metal coolant through a metered pipe induces a small electrical current (Figure 1). Following a ULOF, the flow is reduced and the current is also reduced. The sensor current is not sufficiently large to be used directly in terminating the accelerator beam. However, the signal would be amplified and then delivered to the accelerator injector. Following the ULOF, the injector current, responding to the inherent current reduction in the electro-magnetic flow meter, would fall below the level at which the injector could continue to operate. A fail-safe connection would be used for the amplifier and injector, i.e., should the amplifier or associated wiring fail, the accelerator beam would be terminated.

Figure 1. Category 1 beam termination: electro-magnetic flow meter for ULOF accident



The system described in the previous paragraph does not fit directly into any of the passive system categories of Table 2. However, it is clear that the inherent characteristics of a passive sensing device can be used, with one intermediate active step, the amplifier, to terminate the beam delivery for the ULOF sequence.

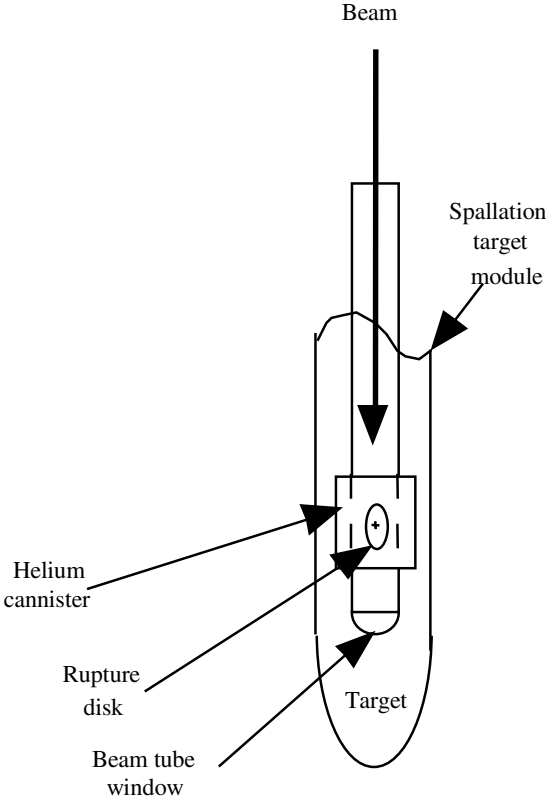
Different sensors would be required for other accident sequences, e.g., a loss-of-heat sink and loss of coolant scenarios.

The second concept category for accelerator beam termination requires the breaking of the beam tube vacuum and the subsequent rapid transport of vapour, gas, or liquid through the beam tube at acoustic speeds to the RF cavities of the accelerator. The introduction of any of these substances into

the cavity will cause arcing and the ability of the accelerator to accelerate protons to high energy levels.

As an example of this approach, consider an unprotected loss of heat sink (ULOHS) scenario. The passive device would be a pressurised canister of compressed helium gas immersed in the primary coolant but connected to the beam tube through a rupture disk (Figure 2). As the ULOHS scenario progressed, the primary coolant temperature would increase, as would the pressure of the helium in the canister. Once the helium pressure had risen to a predetermined value, the rupture disk would break and the helium would exhaust into the beam tube. The helium would proceed up the beam tube at acoustic speeds, enter the RF cavities and cause arcing that would effectively terminate beam injection.

Figure 2. Category 2 beam termination: pressurised gas canister for ULOHS scenario



Another example of this second category would be to design the beam tube window to fail due by design during the ULOHS scenario. The liquid metal coolant would then rise in the beam tube until the static and dynamic pressures balanced. This upward movement of liquid in the beam tube would have two effects. First, as the liquid metal rapidly moved into the beam tube, the spallation source would rapidly move upward, possibly out of the target/blanket region. Second, some of the liquid metal coolant would be vaporised and proceed up the beam tube, enter the RF cavities, and cause

arcng that would effectively terminate beam injection approximately 1 second after failure of the beam tube window.

Four concepts for safe shutdown of accelerator-driven systems have been discussed. A brief summary of the key features of each of these concepts is provided in Table 3. The feasibility of designing highly reliable beam shutdown systems was demonstrated for the APT. Active beam shutdown systems such as those designed for the APT will continue to be the primary means of beam shutdown because are highly reliable and because they have the least impact on subsequent ADS recovery and operation. The remaining three concepts rely to varying degrees on the inherent safety features directly associated with the response of an ADS to a given accident. These concepts all display varying degrees of passivity when referred to the IAEA defined four categories of passivity summarised in Table 2. One or more of these concepts, as well as other passive concepts that will evolve as ADS designs progress, will likely be deployed as a complement to the active beam shutdown systems, thereby benefiting from the positive features of both approaches.

Table 3. ADS beam shutdown concept summary

Concept	Accidents protected	Passivity category	Comments
Active beam termination systems of the type designed for APT	All	None	Highly reliable, first-line systems with failure to terminate beam probability of less than $10^{-6}/\text{yr}$.
Beam tube rupture disk to primary coolant or beam tube window failure by design	All transients resulting in an increase in primary coolant temperature	Category C	Increases time for subsequent active or passive system beam termination. Vaporised of liquid metal coolant will migrate up beam tube at acoustic velocity and terminate RF cavity operation. Extensive post-accident cleanup required
Electro-magnetic flow meter	All loss-of-flow accidents	Category D	No moving mechanical parts. An eternal power source is required for the amplifier. Amplifier is designed such that any failure will terminate the beam.
Rupture disk to pressurised gas canister	All transients resulting in an increase in primary coolant temperature	Category C	Gas will migrate up beam tube at acoustic velocity and terminate RF cavity operation.

Conclusions

Of primary importance for any ADS is the need to demonstrate the safe shutdown of the system to prevent severe damage and the release of radioactive material to the environment. Active systems have been designed for the safe shutdown of an accelerator. However, there is a clear movement in both the design and regulatory sectors to employ simplified, inherent, and passive, means to accomplish safety functions in new reactor designs. To date, no beam shutdown system based largely

on passive devices and utilising inherent features of an ADS design has been demonstrated. Several concepts have been discussed in the literature and these have been summarised in this paper. Two additional concept categories for accelerator beam termination have been described and discussed in this paper. The first concept category focuses on shutdown system designs in which beam delivery to the reactor is terminated by interrupting the accelerator power supply. For this concept, we conclude that the inherent characteristics of a passive sensing devices can be coupled with minimal intermediate active equipment to terminate accelerator beam delivery. The second concept category for accelerator beam termination requires the breaking of the beam tube vacuum and the subsequent rapid transport of vapour, gas, or liquid through the beam tube at acoustic speeds to the RF cavities of the accelerator. Realisations of designs within this concept are more passive and more fully utilise inherent characteristics of the ADS design.

Nomenclature

ADS	accelerator-driven system
ADTF	accelerator-driven test facility
APT	accelerator production of tritium
ATW	accelerator transmutation of waste
DFNSB	Defense Facilities Nuclear Safety Board
DOE	United States Department of Energy
HX	heat exchanger
IAEA	International Atomic Energy Agency
NRC	United States Nuclear Regulatory Commission
SMR	small modular reactor
SNS	spallation neutron source
TBBS	target/blanket beam shutdown
ULOF	unprotected loss-of-flow
ULOHS	unprotected loss-of-heat sink

REFERENCES

- [1] Lisowski, P.W., "The Accelerator Production of Tritium Project", Proceedings of the 1997 Particle Accelerator Conference, Vancouver, B.C., Canada, 12-16 May 1997, pp. 3780-3784.
- [2] APT Conceptual Design Report, Los Alamos National Laboratory document LAUR 97-1329 (15 April 1997).
- [3] Appleton, B.R., "The National Spallation Neutron Source (NSNS) Project", Proceedings of the 1997 Particle Accelerator Conference, Vancouver, B.C., Canada, May 12-16, 1997, pp. 20-23.
- [4] Cappiello, M., *et al.*, "System Studies for the ADTF: Target and Materials Test Station", Los Alamos National Laboratory document LA-UR-01-5253 (2001).
- [5] Bennett, D., *et al.*, "Compendium of Initial Point Designs for Accelerator Transmutation of Radioactive Waste", Los Alamos National Laboratory document LA-UR-01-1817 (Feb. 2001).
- [6] "APT Preliminary Safety Analysis Report", Los Alamos National Laboratory draft document PPO-POO-G-PSA-X-0001.
- [7] IAEA Safety Glossary, "Terminology Used in Nuclear, Radiation, Radioactive Waste and Transport Safety", International Atomic Energy Agency, Version 1.0 (April 2000).
- [8] Garland, W.J., "Nuclear Reactor Safety", McMaster University Course Notes (February 1998).
- [9] "Regulation of Advanced Nuclear Power Plants: Statement of Policy", United States Nuclear Regulatory Commission, 51 FR 24643 (July 1986).
- [10] "Nuclear Safety Management", Code of Federal Regulations 10 CFR Part 830 (Jan. 10, 2001).
- [11] "Report to Congress on Small Modular Nuclear Reactors", US Department of Energy, Office of Nuclear Energy, Science and Technology (May 2001).
- [12] "Technology Goals for Generation IV Nuclear Energy Systems", Generation IV Roadmap NERAC Subcommittee (13 April 2001).
- [13] Wade, D.C., "Safety Consideration in Design of Fast Spectrum ADS for Transuranic or Minor Actinide Burning: A Status Report on Activities of the OECD/NEA Expert Group", Proc. 6th Information Exchange meeting on Actinide and Fission Product Partitioning and Transmutation, Madrid, Spain (Dec. 11-13, 2000), EUR 19783 EN, OECD/NEA, Paris, France (2001).
- [14] Carlsson, J. and H.U. Wider, "Decay Heat Removal from an Accelerator-driven System", Proceedings of the Global 2001 International Conference on Back-end of the Fuel Cycle: "From Research to Solutions", Paris, France (9-13 September 2001).

THEORETICAL AND EXPERIMENTAL EVALUATION OF THE WINDOWLESS INTERFACE FOR THE TRASCO-ADS PROJECT

D. Barni, P. Michelato, D. Sertore
INFN Milan – LASA – Italy

A. Bonucci, R. Giannantonio
SAES Getters S.p.A. – Italy

P. Turrone
ENEA – Bologna – Italy

L. Cinotti
ANSALDO – Italy

Abstract

TRASCO-ADS is a national funded programme in which INFN, ENEA and Italian industries work on the design of an accelerator-driven subcritical system for nuclear waste transmutation. TRASCO is the Italian acronym for transmutation (TRASmutazione) of waste (SCOrie).

One of the most critical aspects of an accelerator-driven system (ADS) is the interface between the UHV environment of the accelerator and the pressurised system of the spallation target (a contained plenum of Pb-Bi eutectic at 400°C with a gas ceiling at about 1 bar). The “window” is the physical interface between the two environments. Thermo-mechanical and radioprotection issue pointed out that the window is a critical issue.

The windowless interface consists of a system where the spallation target and the linac are separated only by a progressive dynamic pumping system that connects the vacuum of the linac accelerator and the coolant flow of the spallation target. Theoretical consideration and calculation results are presented in this paper. The need for a validation of the model gave the motivation for an experimental set-up whose results are also presented.

The extrapolation to the full system needs accurate analysis for a compliant dimensioning of the system in the interface region.

Introduction

Research and development as well as design activities on a subcritical reactor driven by an external neutron source generated by high energy protons impinging on heavy nuclei are in progress in several countries following the Rubbia proposal [1]. Such system, called accelerator-driven system (ADS), aims to fission transuranics and to transmute selected long lived fission fragments.

The Italian TRASCO programme [2] aims to study the physics and to develop the technologies needed to design an accelerator-driven system (ADS) for nuclear waste transmutation. TRASCO is the Italian acronym for transmutation (TRASmutazione) of waste (SCOrie).

The proposed R&D programme investigates all the main subsystems of an ADS (accelerator, window/target and subcritical reactor).

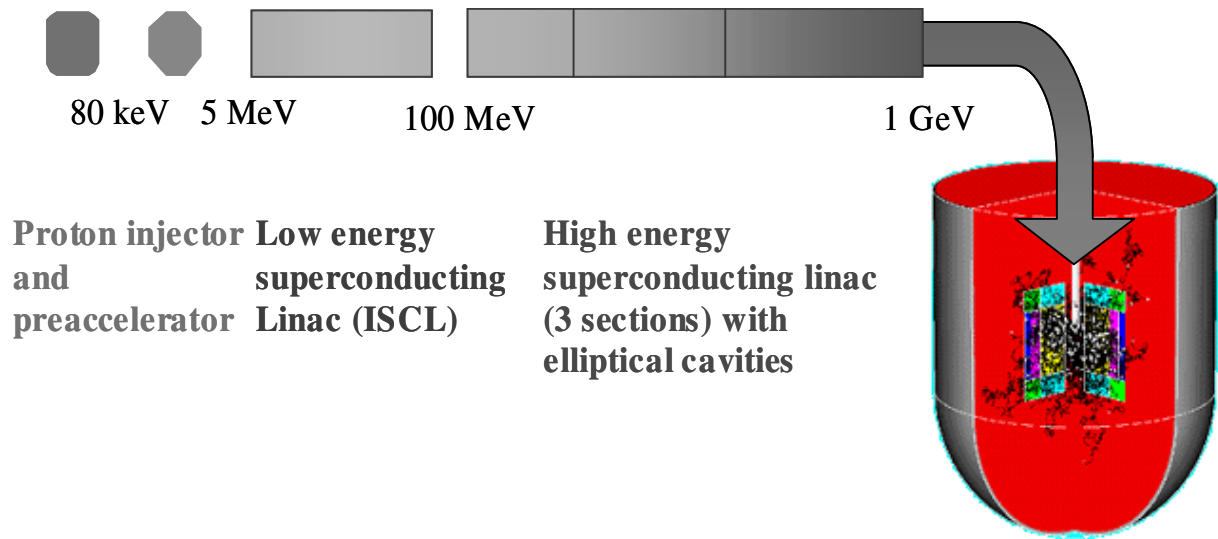
TRASCO

The programme consists of two main parts, regarding, respectively, the accelerator and the subcritical system as shown in Figure 1. Although ENEA and INFN will be jointly responsible for the whole programme, INFN will essentially manage the first part, and ENEA the second part. Besides ENEA and INFN, a few qualified Italian firms and other Italian public research institutions (namely, Universities and INFN, the National Institute for Physics of Matter) participate in the project.

The main objectives of the research programme are:

- Conceptual design of a 1 GeV – 30 mA proton linac [3].
- Design and construction of the proton source and of the first section of the RFQ, as well as of some prototypical cavities concerning the superconductive linac [3].
- Development of methods and criteria for neutronics, thermal-hydraulics and plant design for an EA-like subcritical system, as well as some specific aspects related to the safety analysis of this type of nuclear installation.
- Materials technologies and development of components to be used in a plant in which lead or lead-bismuth eutectic (LBE) acts both as a primary target and as a coolant.
- Experiments to validate and verify proposed technologies for materials compatibility with lead and lead-bismuth Alloys.

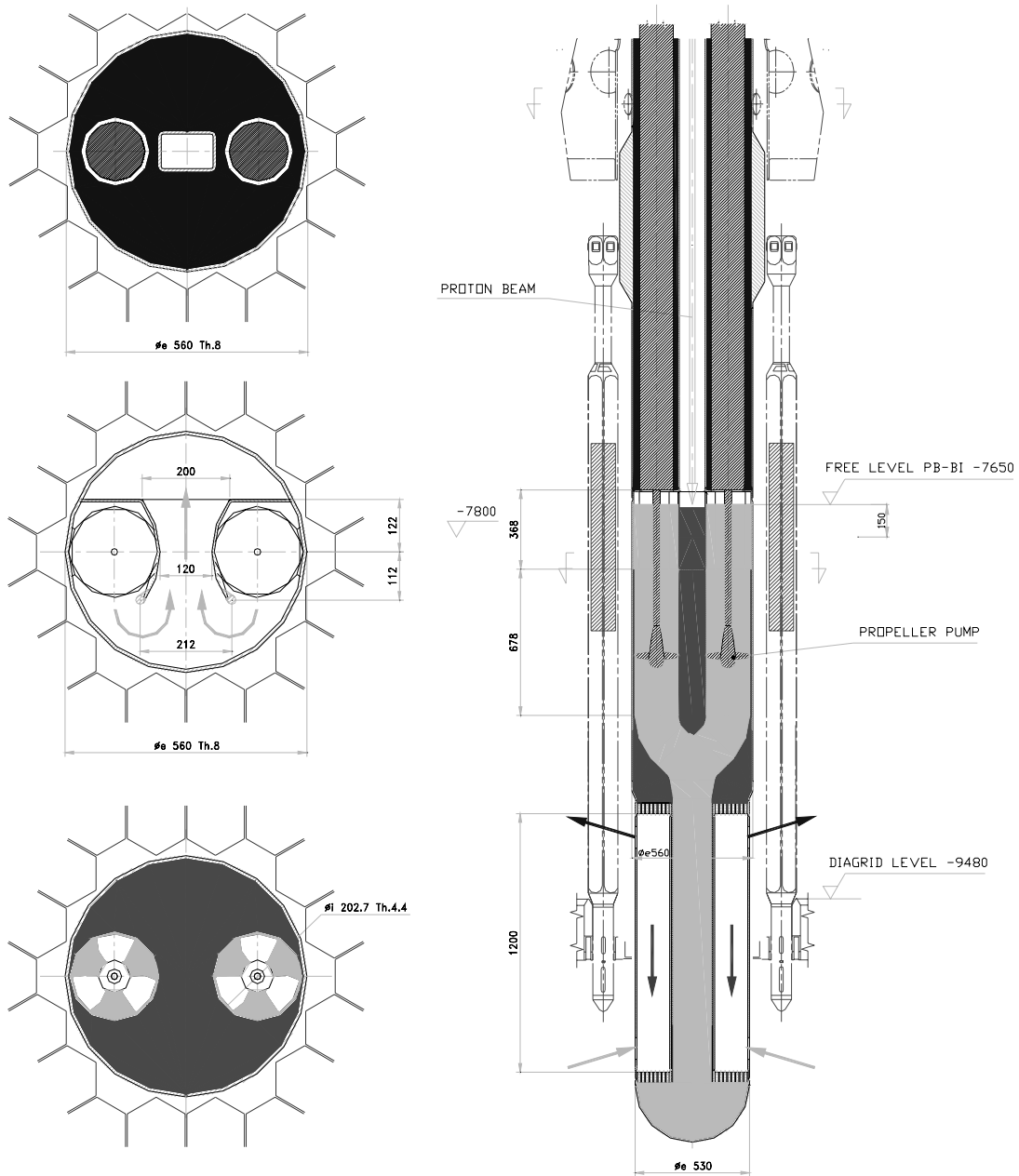
Figure 1. Schematic view of TRASCO layout from the proton source to the subcritical core



TRASCO – windowless

The TRASCO reference configuration [2] foresees two target options: the hot window target and the windowless target. The present paper refers specifically to the windowless target solution where the high vacuum condition required for the vacuum pipe of the proton beam have no structural separation from the flowing LBE that shows a free surface at the impinging protons. The beam impinging the free surface of the LBE will deposit on the liquid metal roughly 80% of its power and the hydraulic circulation has to be shaped so to keep the free surface temperature around 450°C. The windowless target solution for the ADS is illustrated Figure 2. Two propeller pumps force LBE, cooled by the heat exchangers, through the target area. LBE flows in the interaction area orthogonal to the proton beam axis providing a more efficient heat removal and a lower temperature of the free surface.

Figure 2. Conceptual drawing of the LBE circulation in the windowless configuration
 (In the centre-left picture, arrows indicate LBE flow directions in the interaction region)



The vacuum technology should cope with the requirement of producing a good vacuum condition along the proton beam line and of protecting the accelerator against contamination from vapours and gases released from the LBE free surface. The expected outgassing rates for TRASCO linac + reactor operational parameters are summarised in Table 1.

Table 1. Expected gases and vapours load for the TRASCO windowless configuration from the different sources: spallation nuclear reactions, LBE evaporation from the free surface and control of LBE oxide concentration

	Outgassing rate [g/year]	Source
PbBi – LBE	11 500	Evaporation (T = 450°C)
Po	Still unknown	Nuclear reaction
Hg	150	Nuclear reaction
H ₂	6	Nuclear reaction
H ₂ O	48	Oxidation control
He	4	Nuclear reaction

Vacuum system design

The design of the vacuum system for the windowless solution must deal with complex geometries, vapour condensation and gas dynamics.

A suitable numerical approach has been developed to keep into account all these effects. To validate this new tool and to tune the free parameters in the model and experimental measurement campaign has been carried out.

Numerical approach

Usually, vacuum science and technology faces the problem of computing the partial pressure distribution in a vacuum system. Gas (molecular) flows are then derived from partial pressures using the kinetic theory of gases. Gases typically present inside UHV systems are released from the inner walls of the pipes due to desorption phenomena (*i.e.* these gases are not evolved by the corresponding liquid phases). Stainless steel or aluminium pipes release H₂, H₂O and CO whose partial pressures are easily measured by means of standard manometers. The measure of partial pressures of LBE components cannot be properly carried out using ordinary manometers. Also, as LBE is not in thermodynamic equilibrium with its own vapour, vapour pressure is not unequivocally defined.

We decided to develop a suitable numerical model to directly compute the distribution of gas fluxes in the interface pipeline. Due to the rather complex geometry of the system, the method of angular coefficients has been chosen [5]. A finite-element method is used to discretise the system that is divided in elements where the density of the total emitted molecular flux (v) can be assumed constant. For every element (labelled by the subscript i), we can write:

$$v_i = v_{0i} + (1 - \varepsilon_i)v_{inc\ i} \quad (1)$$

where:

- v_{0i} is the molecular flux density generated by the i -th surface (*e.g.* the thermal gas desorption flux);

- v_{inci} is the flux density incident on the elementary area dF_i ;
- ε_i is the adsorbed fraction of incident flux, usually accounting for:
 1. the *reflection coefficient*, which determines the probability that a molecule that is incident on the surface will leave it, dwelt on it during a time of the order of the oscillation period of the crystal lattice;
 2. the *coefficient of stimulated gas desorption* which determines the number of gas particles desorbed from the surface under the action, for instance, of a fast molecule that struck the surface;
 3. the *sticking coefficient*, which determines the probability of prolonged retention by the surface (greatly exceeding the oscillation period of the crystal lattice) of a gas molecule that has reached it;
 4. the *condensation coefficient*, which determines the probability of prolonged retention of the surface of a similar molecule that has struck it due to a condensation event.

We can write v_{inci} as:

$$v_{inci} dF_i = \sum_{j=1}^n \varphi_{j \rightarrow i} v_j dF_j \quad (2)$$

where $\varphi_{j \rightarrow i}$ is the mean *angular coefficient* from the j -th surface to the i -th surface and n is the number of elements. Using a well-known property of the view factors, we can write:

$$v_{inci} = \sum_{j=1}^n \varphi_{i \rightarrow j} v_j \quad (3)$$

$$v_i = v_{0i} + (1 - \varepsilon_i) \sum_{j=1}^n \varphi_{i \rightarrow j} v_j$$

We obtain a system of n unknowns consisting in the fluxes emitted from the elementary surfaces. This way, the adsorbed fluxes can be easily calculated as:

$$v_{adsi} = \varepsilon_i \sum_{j=1}^n \varphi_{i \rightarrow j} v_j \quad (4)$$

We have calculated the view factors with the software tool ANSYS 6.0 [6], able to solve thermal radiation problems (that require the evaluation of the same view factors needed in our model).

Experimental set-up

To test the numerical tool previously described, we have arranged two different UHV experimental set-up in different configurations to measure the property of liquid LBE and its dynamic in a vacuum environment at different temperatures. The first approach directly measures the weight loss from a LBE sample, while the second studies the evaporation rate at different temperatures and the vapour dynamics.

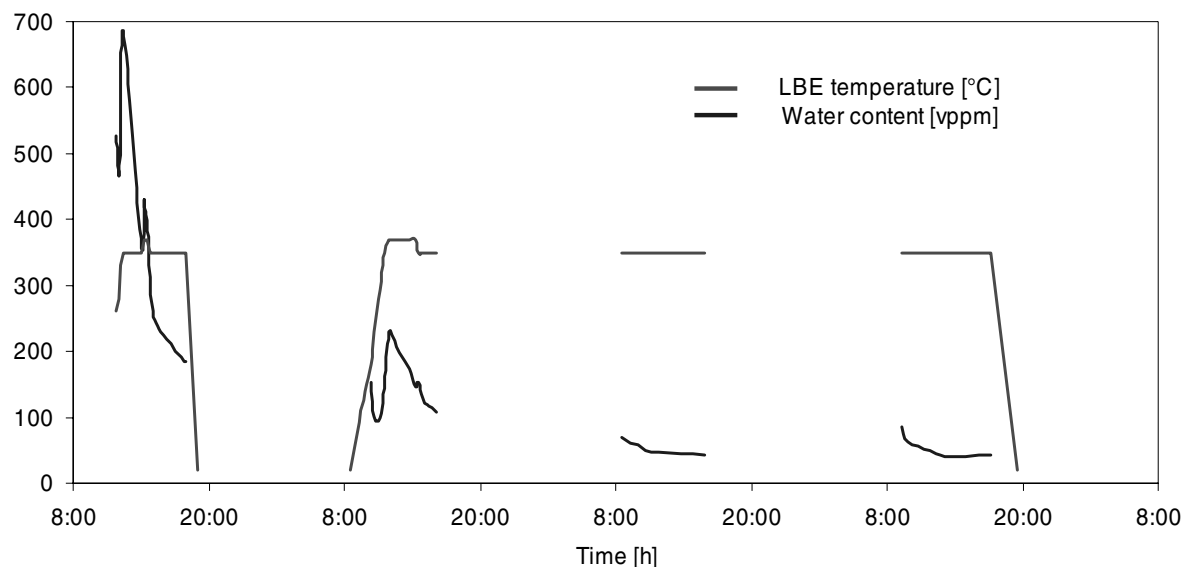
LBE preparation

Solid LBE (pure at 99.99%) from ingot was melted under Argon to reduce oxidation.

A gas mixture of Argon with 5% of Hydrogen has been later injected into the liquid LBE to reduce oxides, originally present in the ingot, to metal with production of water. The measurement of outgoing water is in relation to the oxides concentration in the LBE. This process has been carried out discontinuously during four days up to 370°C as shown in Figure 3. The final content of water is about 40 vppm with ~20 vppm expected from the carrier gas (Ar).

The same gas mixture at an overpressure of 300 mbar (@ 350°C before cooling) has been left at the end as protecting gas in the container.

Figure 3. Water vapour content into the gas outlet (volume ppm) during deoxidation of the LBE
(The stable final water content indicates the end of the deoxidation process)



Weight loss measurements

To experimentally evaluate the evaporation rate of LBE at different temperatures, a suitable apparatus was designed.

The evaporation rate was measured by means of a gravimetric method. A specimen, typically weighing about 40 g was prepared by cutting an LBE ingot. The solid sample was then positioned inside a Petri quartz crucible held in position through a ¼ in tube also containing the sample thermocouple hanging over the LBE free surface at a distance of 10 mm. The system was then sealed and set under high vacuum conditions. The upper part of the quartz bulb ($f=63$ mm, height=400 mm) was kept at room temperature. After a first outgassing at low temperature (250°C), the sample was rapidly heated up to the desired value (450°C and 560°C). The sample was then allowed to evaporate under vacuum for 15 h. After a fast cool down, the sample was then weighed to evaluate, by difference, the amount of Alloy lost due to evaporation.

Evaporation and vapour dynamics measurements

To pump over a LBE liquid surface, an UHV oven able to reach 650°C has been connected to a 2 m long vacuum pipe (CF 63) whose temperature can be controlled up to 200°C. Two microbalances (quartz oscillator thickness monitor) fitted in the vacuum pipe can be inserted at 685 mm and 1 685 mm distance over the LBE liquid surface monitoring the deposition rate with an active area of 50 mm² and 0.1 nm resolution. The microbalances are cooled by water flow. The pumping system consists of a turbo molecular pump unit (300 ls⁻¹), two ion gauges and a residual gas analyser. The base pressure, after a bake-out, is $2 \cdot 10^{-7}$ mbar. Due to complex geometry of the system this measurement is used in according with the numerical approach of the problem.

Experimental results

The experiments were made by positioning a single microbalance (upper microbalance, located at $z=z_1=1$ 685 mm and lower microbalance, located at $z=z_2=685$ mm) or both microbalances to study the shadow of one on the other. In the following we denote $v_{ads,S}(T, z=\{z_1, z_2\})$ the deposition rate measured in a single microbalance experiment and $v_{ads,D}(T)$ the deposition rate measured in a double microbalance experiment, where T is the LBE temperature.

We expect the ratio $R=v_{ads,S}(T, z=z_2)/v_{ads,S}(T, z=z_1)$ to be independent on the evaporation rate of the melt *i.e.* on the LBE temperature because it depends just by the geometrical factors, that can be computed by angular coefficient method, and by the free parameter ϵ .

The interface system is modelled schematically as represented in Figure 4. We assume that $\epsilon=\bar{\epsilon}$ both for the microbalance surface and for the pipe inner walls and that $\epsilon=1$ for the LBE surface. Also, we assume that the flux v_0 generated by microbalance surface and by the pipe inner walls is equal to zero, since these surfaces operate at room temperature.

Figure 4. Model of the interface system

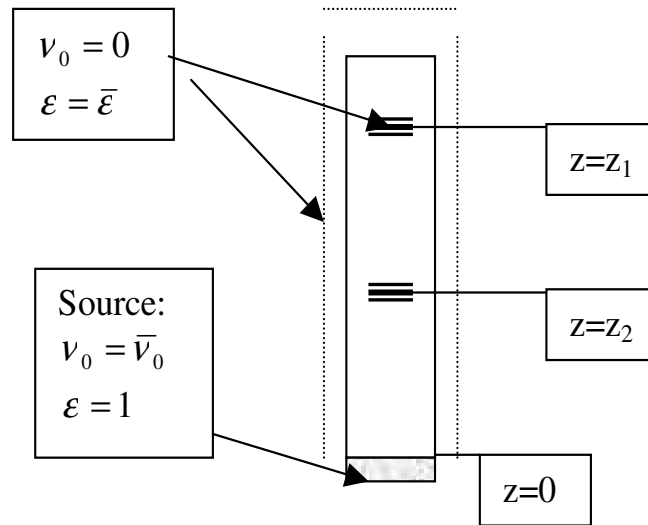
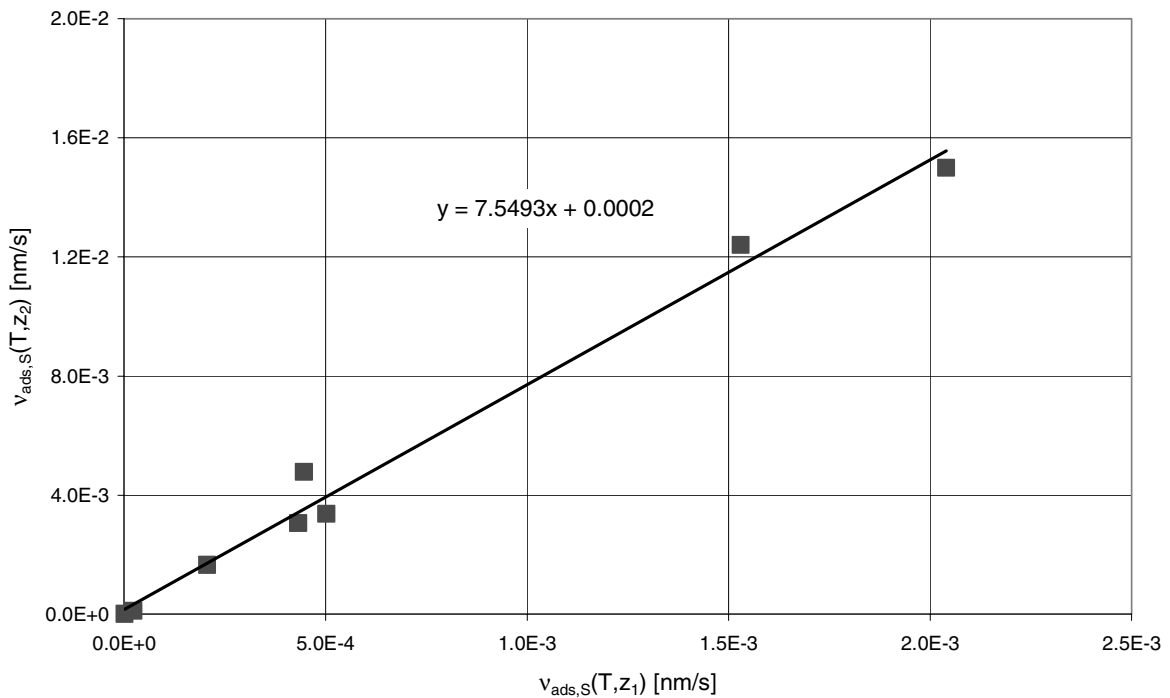


Figure 5. Experimental values of $v_{ads,S}(T, z=z_2)$ and $v_{ads,S}(T, z=z_1)$ drawn at several different LBE temperatures
(The slope is the ratio R independent on evaporation rate)



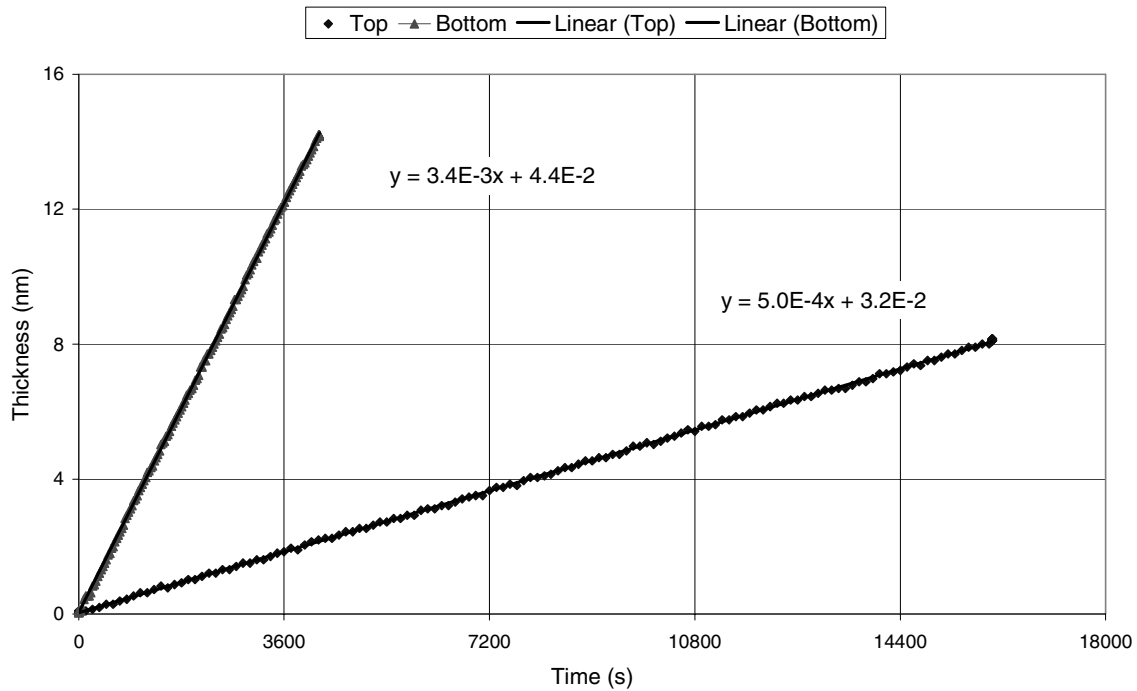
An evaluation of the ratio R from the experimental values of $v_{ads,S}(T, z=z_2)$ and $v_{ads,S}(T, z=z_1)$ drawn at several different LBE temperatures is given in Figure 5.

Experiments confirmed that R is independent on the LBE temperature. We could properly describe the whole set of experimental data by optimising the coefficient ε . The measured value of $R \cong 7.54$ corresponds to a calculated value $\varepsilon \cong 0.27$.

We could predict the outcome of the double microbalance experiments, *i.e.* the ratio $R_D = v_{ads,D}(T, z=z_2) / v_{ads,D}(T, z=z_1)$, assuming that $\varepsilon \cong 0.27$. A value $R_D \cong 18.5$ was computed, to be compared with the experimental mean value $R_D \cong 18.4$.

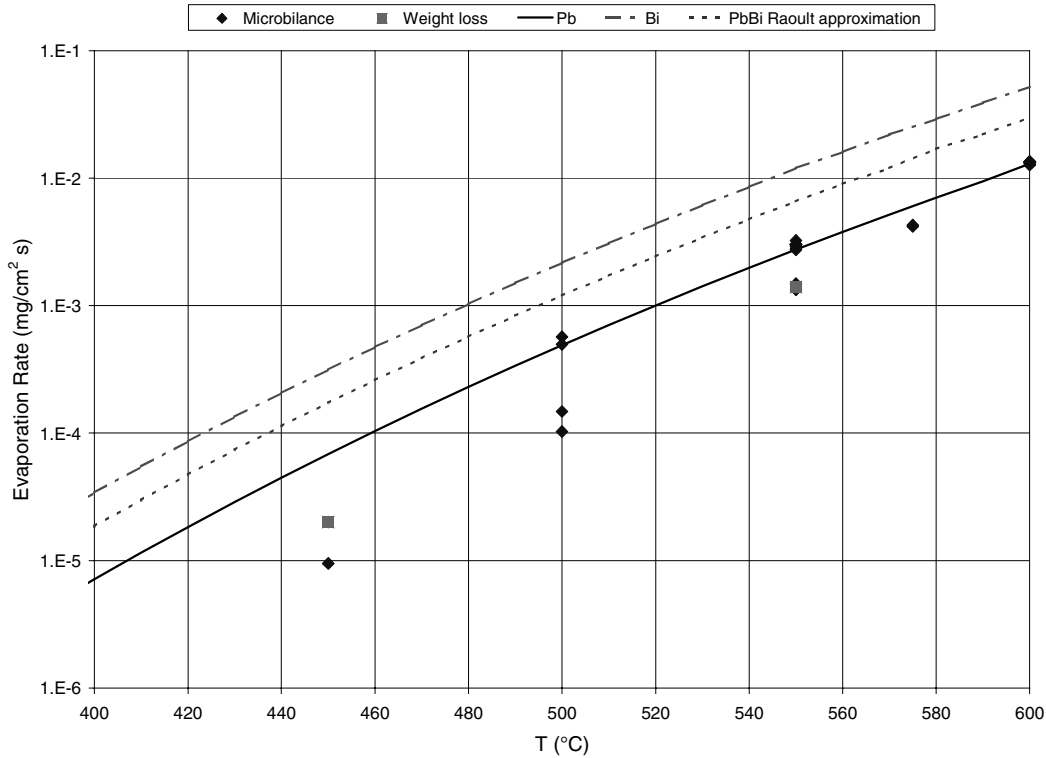
Once obtained a reliable value for ε , the computation of the evaporation rate of the LBE can be accomplished using the calculated $v_{ads}(T) / \bar{v}_0(T)$ ratios, where $v_{ads}(T)$ can be a condensation rate on the bottom or on the top microbalance in a single or in a double microbalance experiment. As an example Figure 6 shows a typical test at 550°C.

Figure 6. Deposition rate from LBE at 550°C on both microbalances as measured using the evaporation apparatus



We have compared the calculated $\bar{v}_0(T)$ values, deduced from the microbalance measurements, with the evaporation rates measured using the experimental weight loss apparatus described in previous paragraph and with data available on the literature [7]. These data refer to single-component liquid/vapour systems. Unfortunately, no reliable liquid/vapour data are available for the LBE system. As a first approximation (to be verified), we can assume the Raoult law to be valid for LBE, so that we can compute LBE evaporation rate using the pure liquid lead and pure liquid bismuth evaporation rates (of course, LBE composition is known).

Figure 7. Comparison between the calculated $\bar{v}_0(T)$ values and the pure lead, pure bismuth, Raoult-based LBE and weight loss LBE evaporation rates



A comparison between the calculated $\bar{v}_0(T)$ values from microbalance, the pure lead, pure bismuth, Raoult-based LBE and weight loss LBE evaporation rates is shown in Figure 7. The agreement between the data reported for lead and the values measured questions the validity of the Raoult's approximation in the case of liquid LBE.

Conclusion

A suitable numerical tool has been developed to study the gas and vapour evolution for the windowless interface of TRASCO. This new tool needs experimental data on liquid LBE in an UHV environment not available in literature. For this reason, an UHV experimental set-up has been built that allows to measure weight loss and evaporation rate from free surface of liquid LBE at different temperature.

The free parameter for the dynamics of the gas in the tube is mainly the adsorption constant ϵ that influences strongly the gas dynamics in the system. From the evaporation measurements on the microbalances, we computed it to 0.25. Once ϵ has been set, we have evaluated the evaporation rate and compare it with data reported in literature. A good agreement with lead data has been obtained, that disagrees with Raoult law.

The future plan is to study in deeper details the properties of liquid LBE in UHV condition to continue the validation of the numerical model, checking the adsorption at different temperature, in view of a complete design of the windowless interface between linac and reactor.

REFERENCES

- [1] Rubbia, C. *et al.*, “Conceptual Design of a Fast Neutron Operated High Power Energy Amplifier”, CERN/AT/95-44(ET), 1997.
- [2] <http://trasco.lnl.infn.it> or <http://rin365.arcoveggio.enea.it/ads>.
- [3] The TRASCO_AC Group, “Status of the High Current Proton Accelerator for the TRASCO Program”, INFN Report INFN/TC-00/23, available from <http://wwwsis.lnl.infn.it/pub/INFN-TC-00-23.pdf> and references cited therein, December 2000.
- [4] Celona, L., *et al.*, “TRIPS: The high intensity proton source for the TRASCO project”, Review of Scientific Instruments, Vol. 71, No. 2, p. 771, (2000).
- [5] Saksaganskii, G.L., “Molecular Flow In Complex Vacuum Systems”, Gordon and Breach Science Publishers.
- [6] ANSYS is a registered trademark of ANSYS Inc.
- [7] Roth, A., “Vacuum Technology”, 3rd Ed. North-Holland, Chapter 4.1.3.

DESIGN AND VERIFICATION EXPERIMENTS FOR THE WINDOWLESS SPALLATION TARGET OF THE ADS PROTOTYPE MYRRHA

Katrien Van Tichelen, Peter Kupschus, Baudouin Arien, Hamid Aït Abderrahim
SCK•CEN, Boeretang 200, B-2400 Mol, Belgium
myrrha@sckcen.be

Abstract

SCK•CEN, the Belgian Nuclear Research Centre, works on the conceptual design and basic engineering of a multipurpose ADS for R&D, dubbed MYRRHA, a small high-performance irradiation facility with fast neutron fluxes up to 1.10^{15} n/cm²/s to start operation in about 2010. It is to serve for demonstrating the ADS concept and to be used for research on structural materials and nuclear fuel, liquid metals and associated aspects, reactor physics and subsequently on applications such as waste transmutation, radio-isotope production and safety of subcritical systems.

Specific to the MYRRHA ADS system is the choice for a windowless spallation target at the centre of the subcritical core. Apart from the space limitations and material property short-comings, the current and power density figures would make the design of a solid window for the spallation source next to impossible: the chosen 5 mA at the relative low energy of 350 MeV leads to a current density of order 150 $\mu\text{A}/\text{cm}^2$ (as far as we know at least a factor of 3 higher than any window design that has been attempted to meet). This is the main reason for adopting the windowless design for MYRRHA which has as a consequence that the free surface ultimately has to be compatible with the vacuum requirements of the beam transport system of the accelerator. The total beam energy will be dumped into a volume of ca 0.5 l leading to a heating power density of ca 3 kW/cm³. In order to remove this heat from the LM with an average temperature increase of 100°C on top of the temperature of the inlet flow of 240°C a total flow rate of 10 l/s at an average flow speed of 2.5 m/s is required. It is suggested from estimates that the evaporation from “hot spots” with elevated temperatures beyond the average 340°C – close to the free surface in the re-circulation zone (and these are the only ones of interest for the vacuum compatibility problem) – is then still acceptable. The design investigations are therefore directed to assess and minimise the re-circulation zone inherent in the free surface formation under the geometry and flow requirements.

This paper will summarise the design programme for the windowless design of the spallation source at the centre of the subcritical core. It will include the main findings reported in (Van Tichelen, 2000) and (Van Tichelen, 2001) and the future programme for the optimisation of the windowless design. These design activities include both experiments and CFD calculations and their interaction.

In summary, the design of the MYRRHA spallation target is very challenging: a Pb-Bi flow pattern with a free surface needs to be established within the geometrical constraints, adequate to remove the very concentrated heat deposition of the proton beam so that the thermal and vacuum requirements are met. A number of the design activities have been and are being performed to study the flow behaviour and to obtain an adequate design. The results of these activities, although not yet totally conclusive, look very encouraging to yield the desired target configuration.

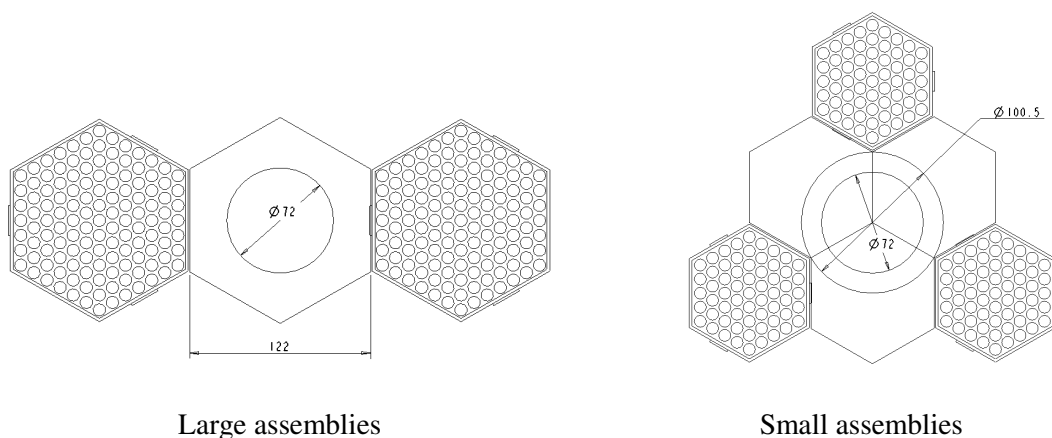
Introduction

At the heart of an accelerator-driven system is the spallation target. It is the neutron source providing primary neutrons that are multiplied by the surrounding subcritical core (SC). The primary neutrons are produced by the spallation reaction of heavy target nuclei under impinging high-energy protons generated by a suitable particle accelerator. The amount of spallation neutrons depends on the initial energy of the incident particle and on the atomic number of the target nuclei. For instance, for a lead target bombarded with 350 MeV protons one expects a yield of 6 n/p (thick target) (Aït Abderrahim, 2001) and for the Pb-Bi eutectic liquid metal (LM) the same yield is expected.

Due to the high Z efficiency, a heavy metal is the most appropriate solution for the target. Moreover, because of the very high power density one arrives at due to space limitations when optimising the subcritical core performance, a liquid metal remains the only option permitting to remove the heat by forced convection.

The MYRRHA subcritical core consists of hexagonal assemblies of MOX fast reactor-type fuel pins with an active length of 600 mm placed centrally in a LM pool (Aït Abderrahim, 2000/2001). Two configurations – that are different with respect to the size of the hexagon – are currently studied. In the “large assembly” configuration, one single central hexagon is removed. In the small assembly configuration, three central hexagons are removed. This is shown in Figure 1. A more detailed figure showing all features described in this section can be found in (Aït Abderrahim, 2001). Both configurations leave a gap around the spallation target’s flow return tube (of 72 mm ID, 80 mm OD) – being filled with the SC liquid Pb-Bi coolant. The outside dimensions of this gap are constrained by the neutronic performances of the core: in order to obtain the required fast neutron fluxes for high flux irradiation samples to be placed in this gap – e.g. for minor actinide transmutation investigations – the gap width is restricted to the dimensions shown in Figure 1 (Malambu, 2000). Above the region of the spallation source – which, with its ca 13 cm axial length, is centrally placed in the SC’s 60 cm active length – the feeder downcomer and a nozzle, taking the liquid to the centre position, can use the full space created by removing the above hexagon(s). It is clear that in the “small assembly” configuration the feeder section is more difficult. For the moment, the investigations have been focused on the “large assembly” case. In the future a dedicated effort will be made to design the redistribution of the flow through the three inlet sections of the “small assembly” case. The position of the target in MYRRHA is shown in Figure 2 in plan view.

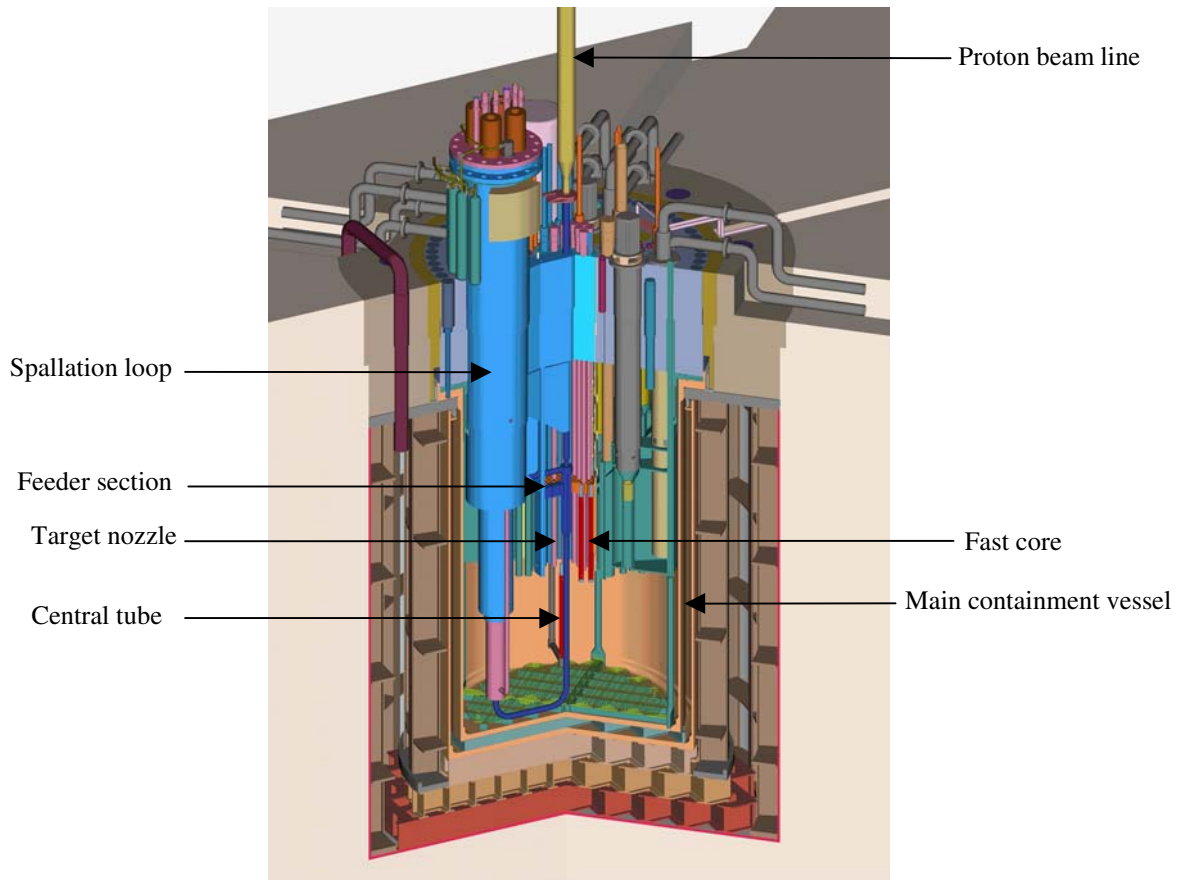
Figure 1. Dimension of the central gap for the spallation target in the hexagonal core of MYRRHA



With the above space limitations it is intended to deliver the 5 mA protons in form of a pencil beam scanning the available surface inside the 72 mm ID in such a way that it best matches the re-circulation pattern of the free surface and according provisions are foreseen in the ion optics of the accelerator. Apart from the space limitations and material property short-comings, also the current and power density figures would make the design of a solid window for the spallation source next to impossible: the chosen 5 mA at the relative low energy of 350 MeV leads to a current density of order $150 \mu\text{A}/\text{cm}^2$ (as far as we know at least a factor of 3 higher than any window design that has been attempted to meet). This is the main reason for adopting the windowless design for MYRRHA which has as a consequence that the free surface ultimately has to be compatible with the vacuum requirements of the beam transport system of the accelerator. The total beam energy will be dumped into a volume of ca 0.5 l leading to a heating power density of ca $3 \text{ kW}/\text{cm}^3$. In order to remove this heat from the LM with an average temperature increase of 100°C on top of the temperature of the inlet flow of 240°C a total flow rate of 10 l/s at an average flow speed of 2.5 m/s is required. It is suggested from estimates that the evaporation from “hot spots” with elevated temperatures beyond the average 340°C – close to the free surface in the re-circulation zone (and these are the only ones of interest for the vacuum compatibility problem) – is then still acceptable. The investigation is therefore directed to assess and minimise the re-circulation zone inherent in the free surface formation under the above geometry and flow requirements.

To summarise, the challenge in the MYRRHA spallation target design is to create a Pb-Bi flow pattern with a free surface within the geometrical constraints, adequate to remove the heat deposited by the proton beam so that the thermal and vacuum requirements are met.

Figure 2. The position of the spallation target in the MYRRHA system



Design programme

To gain insight in the characteristics and expertise in the creation of an adequate free surface flow, SCK•CEN has developed a roadmap of experiments with increasing correspondence to the real situation. This roadmap is supported and guided by computational fluid dynamic (CFD) calculations. The CFD calculations are also used to investigate the flow pattern and temperature profile in the presence of beam heating which cannot be simulated experimentally at this stage.

Since to-scale experiments with Pb-Bi eutectic LM are more difficult to conduct due to its high melting temperature, water and mercury are used as simulating fluids in the first and second instance. Indeed, the analysis of the relevant dimensionless numbers (Re , Fr and We for a free surface flow under gravity in which surface tension might play a role) shows that Pb-Bi lies within the span of these liquids. In view of this, the optimisation of nozzles can be done using the relatively easy-to-handle water and mercury and confirmation experiments have to be carried out using Pb-Bi.

From the Prandtl number that describes the heat transfer capability of the liquids, it is clear that LM experiments remain indispensable for analysing the thermal aspects.

First water experiments at UCL

In June 1999 an R&D programme started in collaboration with the thermal-hydraulics department of Université Catholique de Louvain (UCL, Belgium). Within this R&D programme, water experiments on a one-to-one scale under atmospheric pressure were performed. Due to equipment limitations and the initial lower specification of the beam, most experiments were performed at a flow rate of 5 l/s.

As result of the experimental investigations (Van Tichelen, 2000 and Seynhaeve, 2000), a stable free surface at different fluid levels could be established. The experiments showed the necessity of taking provisions to suppress possible swirl creation in the central tube originating from the feeder section. The experimental nozzle and the resulting free surface are shown in Figure 3. Also shown is a comparison between LASER Doppler velocimetry (LDV) measurements of the velocities in the entrance region and the output of CFD calculations.

In the centre where the down coming flow meets, a so-called re-circulation zone or “hydraulic jump” is formed. Experiments introducing dye in the flow have shown that the residence time of fluid particles in the re-circulation zone is on the brink of being critical. This has important implications on the fluid temperatures at the free surface when the beam heating will be present.

Minimising the residence times by minimising the re-circulation zone is seen as a major tool to handle the surface heating. Moreover, by minimising the re-circulation zone to a small region in the centre, one can shape the proton beam in such a way that it avoids direct heating of this zone (hot spot avoidance). This is done by wiggling in the kHz range a pencil beam over the free surface to create a time-averaged hollow profile which leaves a hole in the centre and deposits the major part of the heat in the main high velocity flow.

The water experiments did not allow this optimisation as at a certain minimisation level air from the atmosphere above is entrained in the flow leading to two-phase conditions with entirely different flow properties. This limited the usefulness of the water experiments under atmospheric pressure, however, some confidence was taken from the co-incidence of the experimental and CFD flow field evaluation in the re-circulation region.

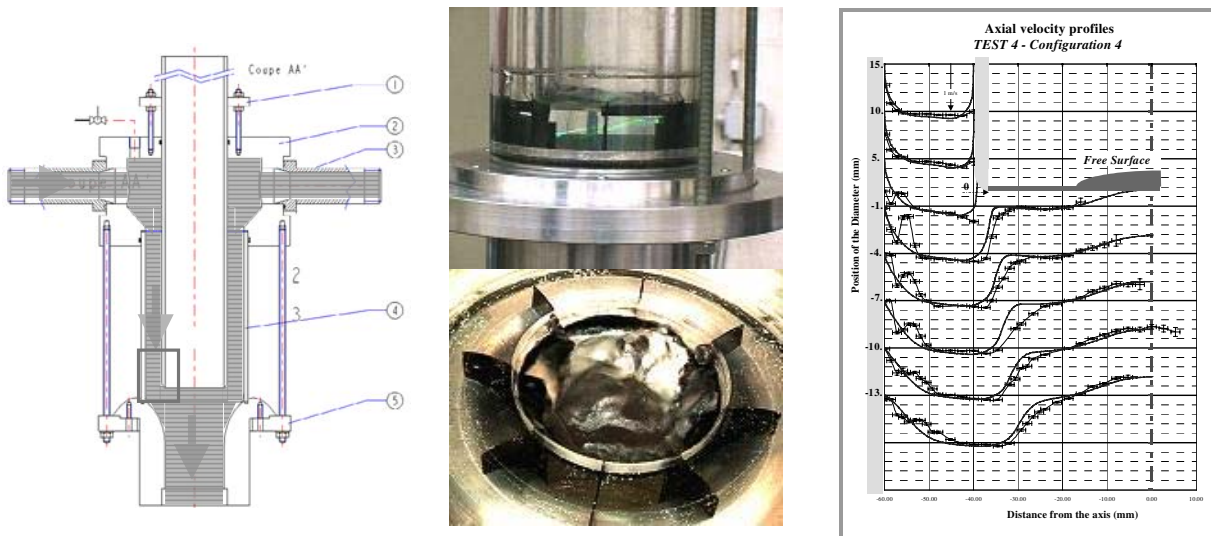
Hg experiments at IPUL

To eliminate the possibility of air entrainment and to step forward in the approach towards the assessment, a to-scale experiment using liquid Hg at a flow rate of 10 l/s and under adequate vacuum conditions has been conceived by SCK•CEN and carried out at the Institute of Physics (IPUL) of the University of Latvia in Riga, Latvia.

The experimental loop (shown in Figure 4) at IPUL contains 8 ton of liquid mercury and is in this way an even match to the later MYRRHA loop. Its main parts are an MHD pump, a loop main valve, a heat exchanger to remove the pump heat losses to the mercury, a test section and an MHD flow meter. The MYRRHA module is inserted in the test section.

To remove or add small amounts of mercury from or to the otherwise closed loop, a cylinder was installed and connected to the loop through a feeding line with a valve at the outlet of the module and a bleeding line with a valve at the inlet of the nozzle. A vacuum system was added to the loop at the top of the module to establish vacuum above the free surface – typically to less than 0.1 mbar.

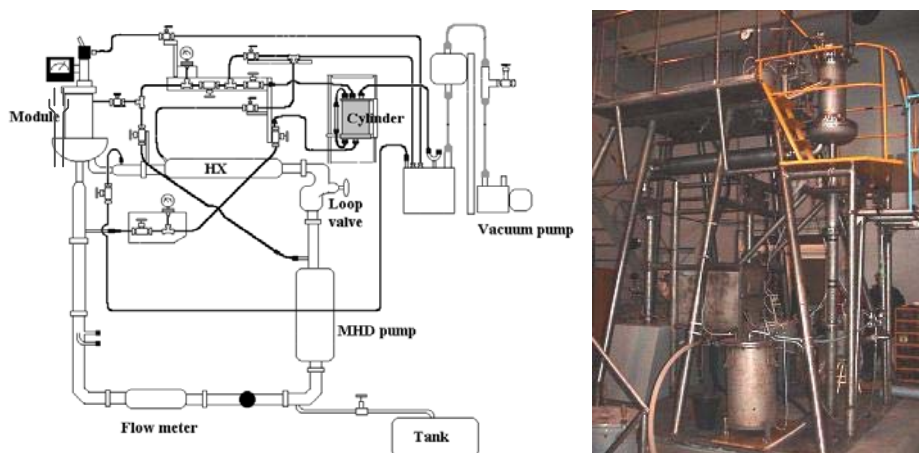
Figure 3. The nozzle in the water experiment



The nozzle tested at UCL gave a lot of useful information but could never be used in the final spallation loop. The free surface of spallation is in the real situation not the lowest point in the loop. Therefore, the flow through the nozzle feeder should be drag limited in order to prevent the fluid from falling down. As the feeder section in the UCL was relatively short, the large gap width of 20 mm did not influence the experiments. In reality, the feeder section will be of the order of 2 m and the liquid would fall down. By reducing the gap width, one can increase the drag to prevent the fluid acceleration by gravity.

However, a reduction of the gap width should not lead to increased flow velocities in the downcomer. It was experienced that a large difference between the velocity in the feeder and in the central tube, leads to a much 'noisier' free surface due to the sudden and forced deceleration of the fluid.

Figure 4. Hg experimental loop at IPUL, Latvia



With respect to the second point, it was decided to design a nozzle with a large feeder cross-section in order to eliminate the velocity mismatch, but to insert an intermediate septum to keep the drag limitation of the first point.

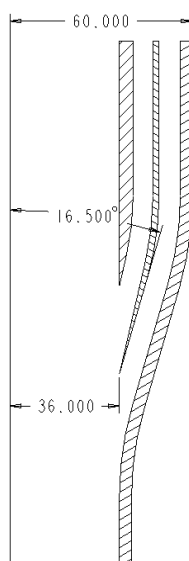
To maximise the useful space for irradiation samples, a large entrance angle into the central tube is most favourable. In this way, the samples can be positioned close to the highest flux region.

However, experiments showed that it was necessary to reduce high inward radial acceleration and velocity of the flow in the entrance region in order to reduce cavitation and to be able to reduce the large Hg dome. This is done by reducing the entrance angle of the nozzle.

It is important to stress here that by using the term “cavitation” we mean strictly the phenomenon of the LM flow detaching from the wall (with subsequent re-impingement onto the wall); we do not at this stage combine this in any way with the surface-corrosive action of cavitation as seen in a number of other technological areas.

These considerations led to the nozzle with a double-gap (DG) feeder cross-section equal to the cross-section of the central tube and an entrance angle of 16.5° shown in Figure 5.

Figure 5. Nozzle DG16.5



Experiments showed that this nozzle DG16.5 has indeed the desired potential. Cavitation is absent in all experiments which allows us to position the free surface arbitrarily by adding or removing Hg to/from the loop. A conical shaped flow pattern with a reduced re-circulation zone at the centre can be obtained. The conical flow has a velocity of about 2.5 m/s and is expected to be capable of removing the heat deposited by the proton beam (according to CFD calculations).

Below a certain value for the level, droplet spitting occurs. This is of course to be avoided as the droplet might evaporate and jeopardise the vacuum of the beam line. In the future, we will estimate to which extent (if at all) droplet formation can be tolerated. An optimisation process needs to be carried out to minimise the formation. One should also mention that due to a difference in surface tension, the behaviour of Hg and Pb-Bi with respect to the droplet formation will probably be different

and – backed by some indicative and qualitative experience in other laboratories – it is expected that the formation will be lower for Pb-Bi.

Figure 6 shows on the left a picture of the surface in an intermediate position. The conical shaped main flow at ~ 2.5 m/s and the re-circulation region can clearly be seen. In the middle, a picture of the surface at a lower position is shown where the re-circulation region had disappeared completely and a V-shaped free surface was obtained. In this lowest free surface position, significant spitting of Hg droplets from the surface was present. At the level shown in the right picture, the spitting disappeared almost completely.

In all cases, the flow was slightly asymmetric with a elliptic shaped re-circulation region. This was due to a small asymmetry of the nozzle and is to be avoided in the final configuration because it complicates the possible later beam shaping for hot spot avoidance.

In conclusion, the last experimental campaign at IPUL has proven that our sought after the “ideal” configuration leads to a solution. Further fine-tuning and investigation is however required in four areas:

- Entrance angle optimisation to maximise the useful space for irradiation samples in the high-flux region outside the target head.
- Optimisation of re-circulation region with regard to droplet formation and suitability of hot spot avoidance.
- Optimisation of axial symmetry of re-circulation region.
- Minimisation of cavitation.

Mercury experiments are too cumbersome to do this fine-tuning. Since the earlier experiments have confirmed the expected hydrodynamic similarity of water and Mercury, the optimisation is done using water after which we will go back to Hg for confirmation of the water results.

In parallel with these experiments, numerical simulations using CFD codes are performed aimed at reproducing the existing experimental results and giving input for the optimisation of the nozzle geometry in the experiments. All free surface simulations are performed using the VOF-mode of the FLOW-3D code (Hirt, 1981).

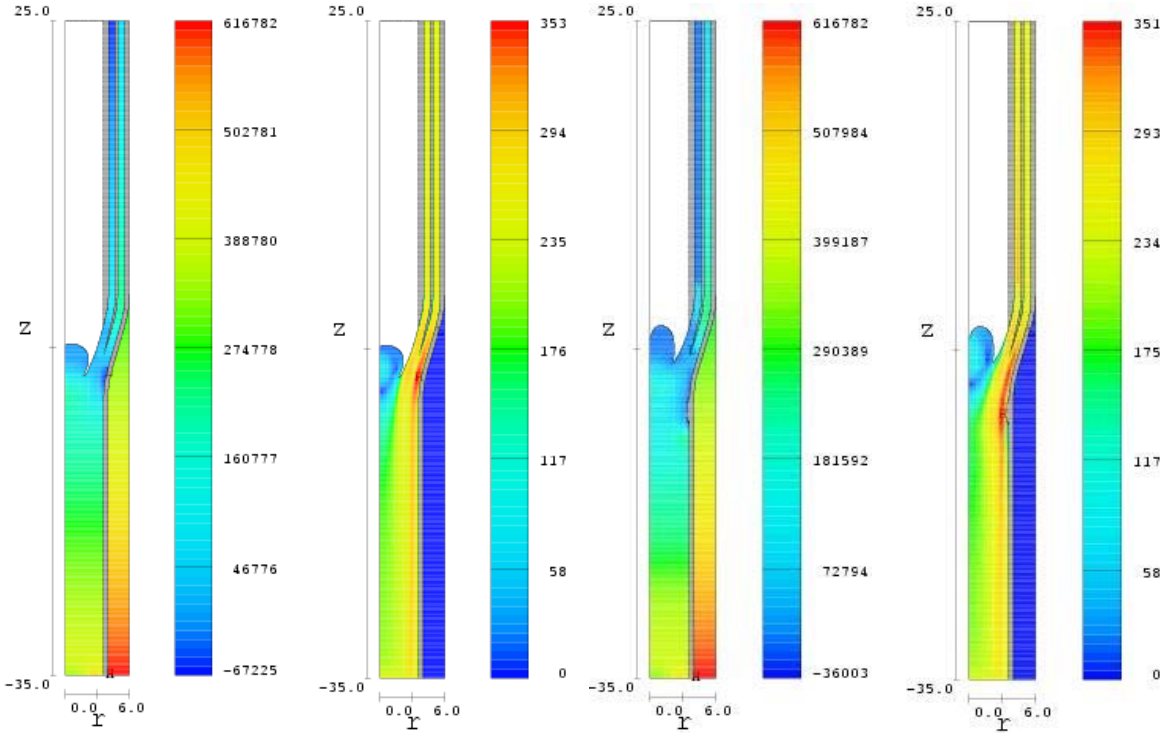
Figure 6. The free surface at three different positions in the Mercury experiment



Figure 7 shows the result of the CFD simulations for the DG16.5 nozzle. For the two pictures at the left hand side the non-cavitation model was switched off. At the entrance of the central tube, a small zone with negative pressures occurs. As the region above the free surface was fixed to zero pressure because of the vacuum, these negative pressures are not physical. Correspondingly, a large acceleration of the fluid takes places in this zone. These unphysical results led to believe that cavitation would occur in the nozzle at these very places.

An indication for correctness of this conclusion was found when the cavitation model was turned on. The results are given in the pictures at the right hand side of Figure 7. One clearly sees the fluid detaching from the wall at the entrance of the central tube. A zero pressure cavitation region is formed. The exact appearance and extent of this region can however not be predicted by the code.

Figure 7. DG16.5: Pressure and velocity fields for the non-cavitation model and the cavitation model (units: g-cm-s)



The detachment of the fluid from the wall seems to be limited. In the corresponding experiments no cavitation could be observed. This leads us to conclude that we are at the brink of cavitation for the DG16.5 nozzle.

The main shortcoming of the CFD codes in general is their inability to reliably predict the height (and corresponding fluid velocities) of the free surface dome. In FLOW-3D the overestimation of this height is limited in comparison with other CFD codes, but still it is unacceptable for the reliable prediction of the heat removal capabilities of the free surface flow.

The same is true for the codes' inability to simulate the observed phenomenon of droplet spitting at the surface.

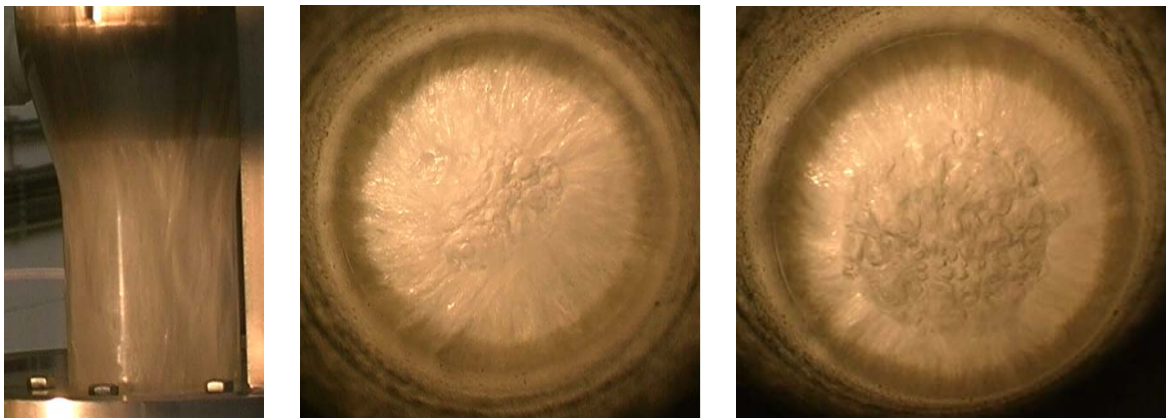
Currently, we are conducting in collaboration with NRG (The Netherlands) a large programme to assess and improve the capability of different existing CFD codes to correctly predict the flow field at the free surface. FLOW-3D is the most promising and our efforts are focused on this code. These efforts are already far developed but not yet conclusive. If it will appear that the current CFD codes are not sufficiently reliable in predicting the flow field at the free surface, an elaborate measurement programme will be necessary to determine the fluid velocities in the re-circulation region. These velocities will then serve as input to the CFD code for subsequent heat transfer calculations. Here CFD simulations are indispensable since experimental simulations are not yet possible due to the absence of an adequate proton beam.

Second water experiments at UCL

As stated above, a second campaign of water experiments is conducted in order to address the main four areas of remaining optimisation: entrance angle, re-circulation and droplet formation, asymmetry and cavitation.

In view of this, the existing water loop at UCL has been enhanced. A flow rate of 10 l/s is now possible. The pressure above the free surface can be reduced to a vacuum pressure of ca 20 mbar absolute. To be able to investigate the effects of various modifications, the nozzles are made insertable, with a high dimensional accuracy to avoid asymmetry and with a drag limited inlet flow. A plexiglas measurement section is present for optical analysis and cavitation detection. Velocity field measurements are foreseen using Laser Doppler velocimetry at first instance and using ultrasonic techniques at second instance. The lifetime of eddies near the surface will be estimated with transient colour injection and a fast laser camera.

Figure 8. The free surface at two different positions in the water experiment



Recently, a similarity check has been performed which showed the same results for the successful DG16.5 nozzle of the Mercury experiments with the same features provided boiling of the water is avoided by raising the vacuum pressure up to around 22 mbar. Some pictures of the results are shown in Figure 8 for two different free surface levels.

Different modifications are currently being prepared to approach a solution to the remaining problems. If these are successful, a full characterisation of the velocity fields will be performed. The successful configuration then will be re-tested with Mercury.

Besides for the optimisation of the nozzle itself, the water loop will be used to design and test the three-inlet configuration for the “small assembly” case. In this case, the flow coming from three inlet sections has to be redistributed over the full circumference of the nozzle. The flexibility and visibility of the water loop make it well suited for this study.

Future steps

As the spallation target design is a crucial point for the MYRRHA project, final confirmation experiments are foreseen to be performed with the eutectic LM at similar temperatures.

Pb-Bi experiments at FZK

In view of this, a collaboration with Forschungszentrum Karlsruhe (FZK, Germany) has been negotiated and the technical interface has been agreed, aiming at inserting a to-scale model of the MYRRHA spallation target similar to the one in the Mercury loop in their KALLA-THEADIS Pb-Bi loop. This Pb-Bi loop is in size similar to the Mercury loop but in complexity closer to the MYRRHA spallation loop: it has two free surface levels and a mechanical impeller pump at nominal flow rate. This will ultimately yield also data on loop control parameters and corrosion-like phenomena (Sobolev, 2001). The start of the experiments is foreseen for this fall.

Pb-Bi experiments at ENEA

A second campaign of Pb-Bi loop experiments is foreseen to be performed in the CHEOPE loop in collaboration with ENEA (Bologna/Brasimone, Italy). A to-scale model of the MYRRHA spallation target will be inserted in the existing CHEOPE experimental vessel together with a MHD pump, a configuration that will correspond to the minimum closed loop configuration of a MYRRHA like spallation circuit with no deduction by other loop problems. The first tests are now envisaged for fall 2002.

For the further proof-of-principle, the proton beam heating needs to be applied once the suitable “ideal” flow field has been established, tested and determined in the different experiments. As already said, since it is not possible at this stage to simulate this heating experimentally, CFD simulations with for instance FLOW-3D have to be used for this purpose. In the ideal case, the CFD code will be able to predict the flow field and the temperature field at the same time. If not, the measured experimental flow field will be enforced into the code and the temperature field will be calculated.

Spallation loop

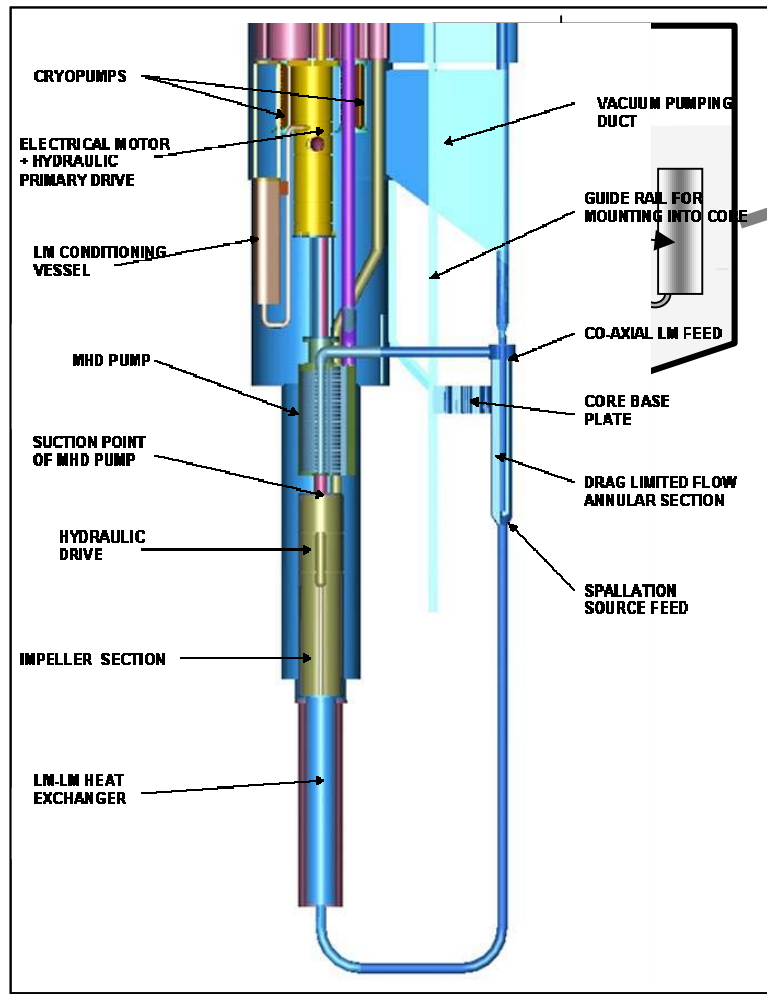
Lay-out

The LM free surface does not only form the spallation target but also forms the interface to the proton beam line and ultimately the accelerator vacuum. Therefore, the spallation loop will not be

directly part of the subcritical core coolant system but will be closed in itself. Figure 9 gives a schematic lay-out of the spallation loop together with its technical lay-out.

The LM starts from the upper reservoir that also features the second and upper free surface and flows mainly by gravity through the (double) annular gap into the annular nozzle. As already stated, this gap is sized in such a way that the flow is drag-limited to about the same velocity with which the flow will leave the downstream tube after the nozzle.

Figure 9. Spallation loop schematic and technical lay-out



The heated coolant from the target will follow the U-shaped tube to the return column, will pass the LM-LM heat exchanger (whose secondary coolant is the subcritical core main coolant) and will be taken up by the mechanical impeller pump situated at a level in the loop that is sufficiently low for the correct suction pressure to be maintained. The pump determines the velocity of that part of the loop; it returns the LM to the upper reservoir at a rate of 10 l/s.

An auxiliary MHD pump working in series with the impeller pump and capable if required to operate in 2-quadrant mode (i.e. accelerating and decelerating), will permit to balance the nozzle inlet and outlet flow and thus to control the free surface level. The pump is in line with the impeller pump but its entrance is open to the reservoir of which the level is about 2 m higher. This way there is a guaranteed minimum of suction pressure and the MHD pump is partially de-coupled from the impeller pump. For the detection of this level, a pre-requisite for putting the MHD pump into feedback, a LIDAR system is foreseen.

The full spallation loop will contain about 500 l of LM, its active part likely only 120 l and the branch from the entrance of the MHD pump to the upper free surface will contain about 25 l of LM (Aït Abderrahim, 2002).

Loop dynamics

The proposed scheme for the dynamic control of the spallation loop is the inter-linking of a fast feed-back loop – in which the LIDAR level measurement is determining the current of the MHD pump necessary to keep the spallation free surface level constant – with the slow loop of the main impeller pump. The MHD pump therefore has to cope with transient and other influences in the time domain of say 10^{-2} to 10 s (PID loop) whereas the main pump works in the time domain 1 s to infinity (PI loop).

The fastest thermal transient in the loop is the certainly a beam trip on the 10^{-6} s scale. In this case, the hot column runs with 2.5 m/s through ~6 m of pipe (up to the LM-LM heat exchanger, with very little exchange of heat to the tube wall) whereas cold LM is filled up at the top, generating a linear contraction of the column over a time of $6[m]/2.5[m/s]=2.4$ s. With the temperature volumetric expansion coefficient of Pb-Bi of $\sim 1.5 \cdot 10^{-4}$, this leads to a linear expansion of LM in the tube: for a ΔT of 100°K and 6 m column length, this leads to roughly a contraction of 9 cm in 2.4 s or a speed change of 0.0375 m/s. The MHD pump should therefore manage to keep the level constant during the (arbitrary) trip period in order that the beam can be switched on at any time.

The dynamics of this process is well within the parameter range in which one could expect successful feed-back operation provided the power of the pumps will comply. The required speed variation is of order $0.0375[m/s]/2.5[m/s]=1.5 \cdot 10^{-2}$. On the drag limited section of the annular down-comer this speed variation is proportional to the $\Delta p/p$ that is applied in the respective time frame. Assuming that the flow in the upper arm would be drag limited and compensate the height potential of the 2.5 m LM column between the upper and spallation free surface at 1.5% less than the nominal speed, the pump would have to exert of a bias pressure of about 0.015×2.5 bar ≈ 40 mbar in order to bring the flow up to nominal speed. This would require a power equivalent of 40 W.

Acceleration forces dwarf these values: to accelerate the 250 kg column to ~ 0.05 m/s in about 10^{-2} s requires an instantaneous power level of 1.25 kW. If we extend this feed-back time to $5 \cdot 10^{-2}$ s the power falls back on the 250 W level, with a temporary mismatch of the surface position of order 5 mm (which would be acceptable).

Assuming a realistic efficiency of 15% of an MHD pump with a conducting medium as poorly as Pb-Bi, the required average power bias would be of order 500 W. Taking into account the instantaneous power levels, these dynamics would require that the pump can handle and the inverter power supply can deliver ± 2 kW.

A similar analysis can be performed for the transient in which the beam is switched on using the same time scale. It leads to the same conclusions for the MHD pump powers.

The impeller pump needs essentially to overcome the friction forces of the main circuit plus the potential energy according to the height difference between the spallation free surface and the upper free surface. The resulting pressure drop is the former 2.5 bar plus the pressure drop that is mainly concentrated in the heat exchanger (that is not yet dimensioned). Taking a conservative value of 2.5 bar for the latter, we arrive at a maximum total of 5 bar and the above mass flow rate of 10 l/s, leading to a required 5 kW. Since we want to employ an indirect drive with an auxiliary hydraulic circuit driven by an electrical motor on top of the large column, the overall efficiency of these impellers (assumed to be of order 70% and there are now three in a row) of 35%. So, the required motor power for the main pump is of order 10-15 kW.

One can conclude from these considerations that for the MHD pump and the impeller pump the problem of the dynamic load seems manageable (Aït Abderrahim, 2002).

Conclusion

The design of the MYRRHA spallation is very challenging: a Pb-Bi flow pattern with a free surface needs to be established within the geometrical constraints, adequate to remove the very concentrated heat deposition of the proton beam so that the thermal and vacuum requirements are met.

A number of the design activities have been and are being performed to study the flow behaviour and to obtain an adequate design. These design activities include both experiments and CFD calculations and their interaction.

So far, there is no evidence that the “windowless” design cannot be made to work and there is a solid optimism that the remaining issues can be resolved. The most severe issue to be tackled is the elimination of the hot spot problem but even here are quite a number of options available to minimise the problem.

The conceptual design of the spallation loop and a first assessment of its dynamic behaviour has been performed and did not reveal points that might be critical.

In summary, the results of our design activities, although not yet totally conclusive, look very encouraging to yield the desired target configuration.

Another effort at SCK•CEN, not discussed here, is dealing with the vacuum and accelerator compatibility of the configuration (Sobolev, 2001 and Aït Abderrahim, 2002).

REFERENCES

- Aït Abderrahim, H., Kupschus, P., Jongen, Y., Ternier, S., *MYRRHA, A Multipurpose Accelerator-driven System for R&D, First Step towards Waste Transmutation*, SCK•CEN, Mol, BLG 841 (2000).
- Aït Abderrahim, H., Kupschus, P., Malambu, E., Aoust, Th., Benoit, Ph., Sobolev, V., Van Tichelen, K., Ariën, B., Vermeersch, F., Jongen, Y., Vandeplassche, D., *MYRRHA, A Multipurpose Accelerator-driven System for R&D*, this conference (2001).
- Aït Abderrahim, H., Kupschus, P., *MYRRHA, A Multipurpose Accelerator-driven System (ADS) for Research & Development*, March 2002 Pre-Design Report, SCK•CEN, Mol, R-3595 (2002).
- Hirt, C.W., Nichols, B.D., “Volume of Fluid (VOF) Method for the Dynamics of Free Boundaries”, *Journal of Computational Physics* 39, 201 (1981).
- Malambu, E., “Neutronic Performance Assessment of the MYRRHA ADS Facility”, SCK•CEN, Mol, R3438 (2000).
- Seynhaeve, J.-M., Winckelmans, G., Bolle, L., Jeanmart, H., *MYRRHA project: R&D Collaboration between SCK•CEN and UCL/TERM: Phase 1 and 2*, Université Catholique de Louvain, Louvain-la-Neuve (2000).
- Seynhaeve, J.-M., *MYRRHA project: R&D Collaboration between SCK•CEN and UCL/TERM: Phase 3*, Université Catholique de Louvain, Louvain-la-Neuve (2000).
- Sobolev, V., Van Dyck, S., Kupschus, P., Aït Abderrahim, H., *Researches on Corrosion Mitigation in MYRRHA multipurpose ADS for R&D*, this conference (2001).
- Van Tichelen, K., Kupschus, P., Aït Abderrahim, H., Seynhaeve, J.-M., Winckelmans, G., Jeanmart, H., Roelofs, F., Komen, E., *MYRRHA: Design of a Windowless Spallation Target for a Prototype ADS*, Proc. of the 10th Int. Conf. Emerging Nuclear Energy Systems, Petten (2000).
- Van Tichelen K., Kupschus P., Ariën B., Aït Abderrahim H., Kljukin A., Platacis E., *Design and Verification Experiments for the Windowless Spallation Target of the ADS Prototype MYRRHA*, Fourth International Meeting on Accelerator-driven Transmutation Technologies and Applications, Reno, Nevada (2001).

RADIOPROTECTION CALCULATIONS FOR THE TRADE EXPERIMENT

L. Zanini¹, A. Ferrari, A. Herrera-Martínez, Y. Kadi
CERN, CH-1211 Geneva 23, Switzerland

C. Rubbia, N. Burgio, M. Carta, A. Santagata
ENEA, 00196 Roma, Italy

L. Cinotti
Ansaldo Nucleare, 16161 Genova, Italy

for the TRADE collaboration²

Abstract

The TRADE project is based on the coupling, in a subcritical configuration, of a 115 MeV, 2 mA proton cyclotron with a TRIGA research reactor at the ENEA Casaccia Centre (Rome). Detailed radioprotection calculations using the FLUKA and EA-MC Monte Carlo codes were performed during the feasibility study. The study concentrated on dose rates due to beam losses in normal operating conditions and in the calculation of activation in the most sensitive components of the experiment.

Results show that a shielding of 1.4 m of barytes concrete around the beam line will be sufficient to maintain the effective doses below the level of 10 μ Sv/h, provided that the beam losses are at the level of 1 nA/m.

The activation level around the beam line and in the water will be negligible, while the spallation target will reach an activation level comparable to the one of a fuel element at maximum burnup.

1. Luca.Zanini@cern.ch.

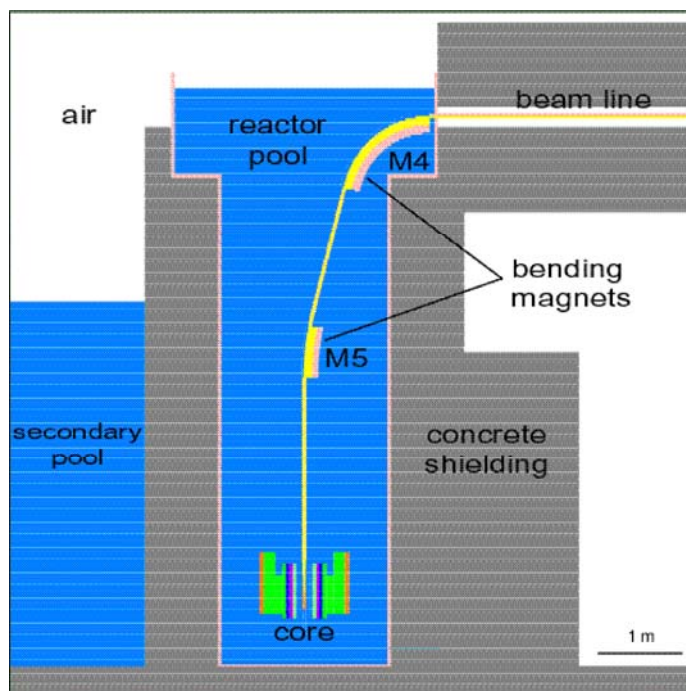
2. The working group on TRADE: TRIGA accelerator-driven experiment (ENEA, CEA, Ansaldo): TRADE Final Feasibility Report, Rome, March 2002.

The TRADE experiment

The European roadmap towards the experimental demonstration of ADS indicates a number of experiments that should allow testing the different components of such a system [1]. Dedicated experiments are included in the roadmap for the study of the accelerator (IPHI, TRASCO), the target (MEGAPIE), the subcritical core (FEAT, TARC, MUSE). In this framework, an experiment providing the first coupling between an accelerator and a subcritical reactor is very useful from both licensing and experimental point of views. In fact, such an experiment will demonstrate the operation of an ADS system, from start-up to nominal power level, to shutdown, and will allow studying the relation between proton current and reactor power, the neutron source importance and reactivity effects.

Carlo Rubbia suggested to carry out this pilot experiment at the ENEA-Casaccia site where a 1 MW TRIGA research reactor is operating [2]. A cyclotron accelerating protons to 115 MeV, with a maximum current of 2 mA, will be built on the side of the reactor building. The reactor core will be modified, by replacing the central fuel rod with a spallation target of tungsten and by removing some other fuel rods (in particular the inner ring). The proton beam will be sent through a beam transport line to the reactor core, and will produce neutrons by spallation in tungsten.

Figure 1. View of the geometry of the TRADE experiment as implemented in the FLUKA calculations



Such an experiment presents additional radioprotection problems with respect to a normal reactor, because of the presence of the proton beam. In particular, one has to consider the following radioprotection issues: *i*) interaction of the proton beam with the target; *ii*) beam losses along the beam transport line in normal operating conditions; *iii*) radiation release in accident cases different from those of a conventional reactor.

In the following section we treat these cases concentrating in particular in the first two topics. The third point has been treated extensively in [3].

Simulations

Monte Carlo simulations were performed using the FLUKA [4] and EA-MC [5] codes. In order to study the beam-target interaction and the radiation release in accident cases, a full model of the TRIGA reactor including the additional features of the TRADE experiment was implemented. The geometry used in the simulations is shown in Figure 1. Two bending magnets, labelled M4 and M5, which divert the proton beam to the reactor core, were included. Before the M4 magnet a straight section of the beam line approximately 10 m long is foreseen to transport the beam from the accelerator to the reactor building. The same geometry was implemented in EA-MC in order to study by means of burnup calculations the activation of the target, of the water and of the air.

The problem of the radiation due to beam losses in normal conditions was treated differently. In this case, we followed two calculational schemes, one based entirely on FLUKA and a coupled FLUKA-EA-MC. In both schemes 110 MeV protons were generated distributed along the length of the beam tube and propagated outwards. The calculations were done for 10^6 protons and scaled to 1 mA current.

Beam-target interactions

The distribution of neutrons generated in the spallation target unit and surrounding core structures is given in Figure 2. Spallation neutrons are produced in a region extending radially up to 5 cm from the centre of the core, that is a few cm before reaching the fuel elements. The neutron spectra from spallation and fission are different, and in the spallation more high-energy neutrons are produced; their average kinetic energy is of the order of 3-4 MeV. These neutrons are rapidly slowed down by the water moderator before reaching the core internal structures, therefore they do not represent a major problem in terms of radiation damage. We note that a few thermal neutrons, up to 10^9 n/cm²/s/mA, will stream along the beam tube and slightly irradiate ($1.3 \cdot 10^{-5}$ Gy/s/mA) the lower permanent magnet, situated approximately 3 m above the core. On the other hand, the neutron leakage through the top of the reactor pool is negligible. We conclude that the shielding already present around the TRIGA reactor is sufficient to shield against the neutrons due to beam-target interactions.

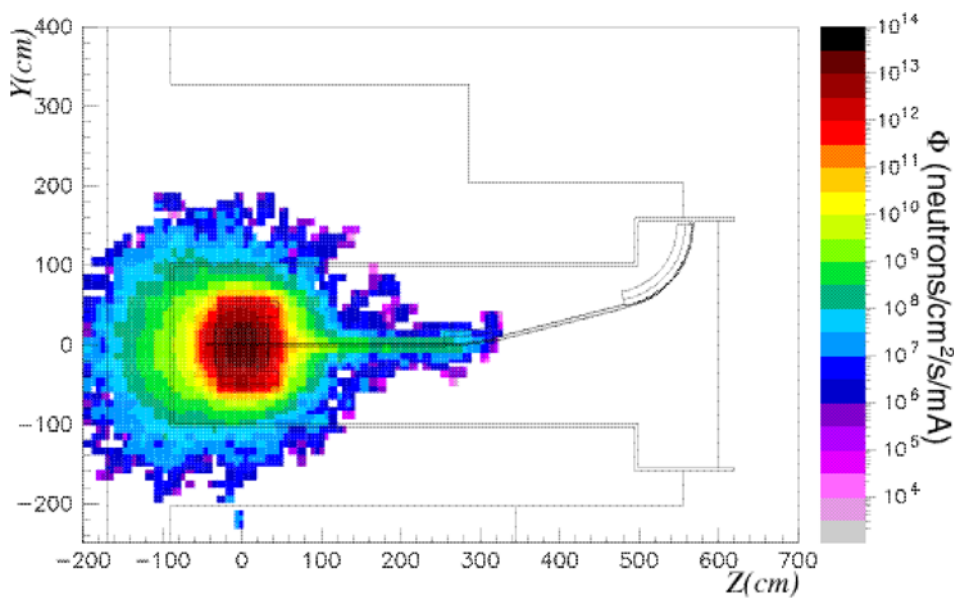
Concerning γ radiation, the photon flux reaching the top of the reactor pool is higher than the neutron flux, up to 10^4 γ /cm²/s/mA. However, this flux does not constitute a problem in terms of effective dose. In [3] the results concerning this case are reported in more detail.

Radiation due to beam losses during normal operation

The most delicate aspect of the TRADE experiment is the coupling between the accelerator beam line and the reactor core. The beam is transported from the cyclotron to the reactor building through a shielded beam line. It is important to ensure that during the experiment the radiation released outside of the beam line does not exceed the allowable limits of exposure. This radiation originates from beam losses due to protons escaping from the beam line in normal operating conditions, and generating spallation neutrons in the beam tube and in the shielding. Typically, in the straight section of the beam line, the beam losses are expected to be of the order of 10^{-6} /m of the beam current. This will be the case for the portion of the beam line, approximately 10 m long, going from

the accelerator to the reactor. On the other hand, when the beam is bent, like in correspondence to the M4 magnet (see Figure 1), the losses are expected to be higher, of the order of $10^{-4}/\text{m}$. Thus, the shielding will have to be carefully designed around the bending magnet. Since this part of the beam line is not yet designed, we concentrate here on the study of the shielding in the straight section of the beam line.

Figure 2. Neutron flux distribution ($\text{n}/\text{cm}^2/\text{s}/\text{mA}$) following the impact of the proton beam on a solid tungsten target in the TRADE experiment



In Figure 3 the essential components of the straight section of the beam line are shown. The beam pipe is made of aluminium or stainless steel, and has a thickness around 0.5 cm. Its inner radius must be bigger than 1.3 cm, which will be the radius of the proton beam. After a gap, which will have to be big enough to accommodate, the focusing quadrupoles, the concrete, in type and amount to be determined, is placed for shielding.

We have studied different shielding options by comparing the results using concrete with and without boron and barium. The effect of the variation of the thickness of the shielding on the effective dose has been determined. More complex shielding combinations have also been considered. The effect of the material and thickness of the beam line on the escaping neutron flux has also been investigated.

Variation of the shielding thickness and composition

In the calculations we used the ordinary concrete and the barytes concrete, as well as ordinary concrete with addition of boron to absorb thermal neutrons. The density of the normal concrete and of the normal concrete with boron is $2.35 \text{ g}/\text{cm}^3$, while the density of the barytes concrete is $3.54 \text{ g}/\text{cm}^3$. The chemical compositions of the different concretes are given in Figure 4.

Figure 3. The components of a 1 m long straight section of the beam line with the shielding

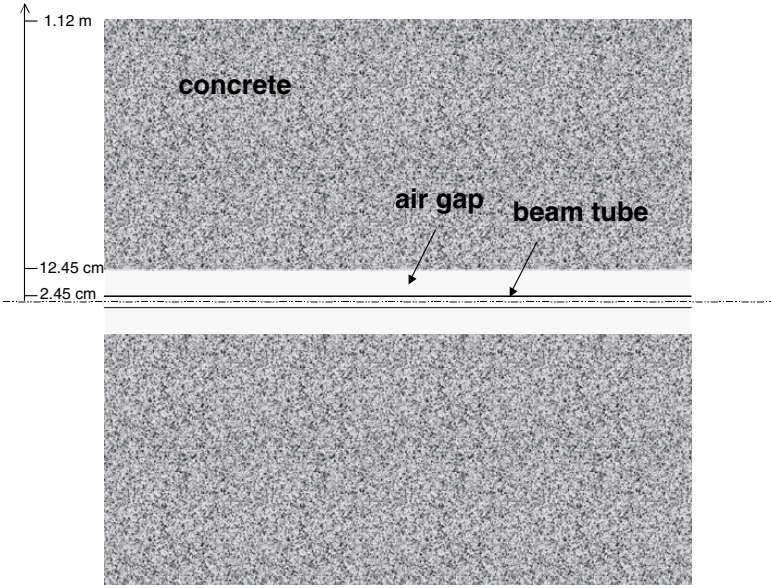
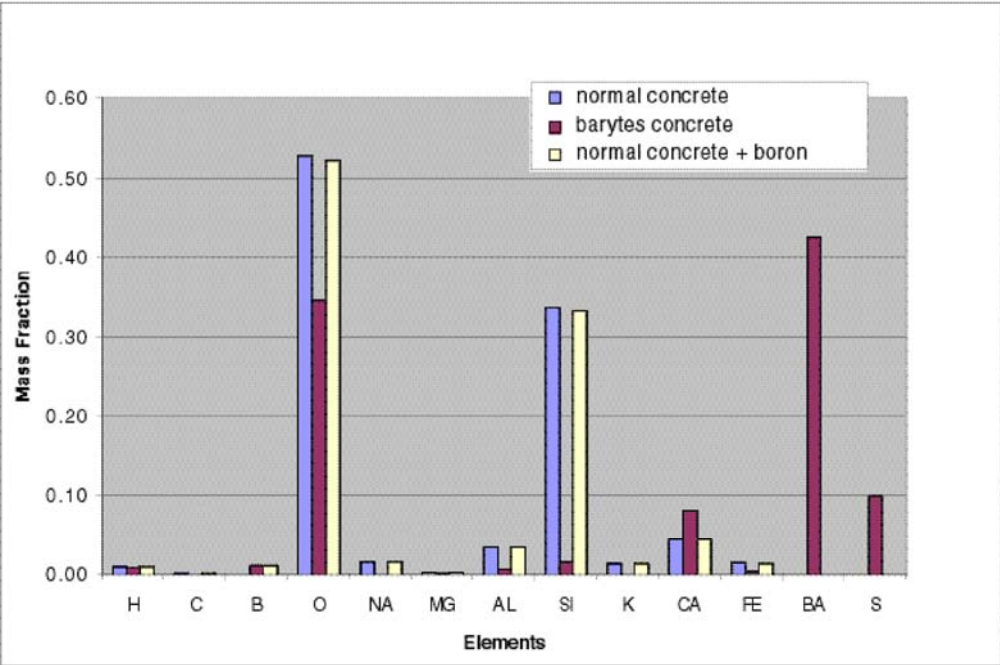


Figure 4. Chemical composition of the three different concrete materials used (in weight fraction)



1) The first study was done on the concrete thickness, varying the thickness of barytes concrete using 1 m, 1.4 m and 2 m radius. The neutron flux escaping the shielding in the three configurations is given in Figure 5. Increasing the thickness of the shielding by 40-50 cm gives a reduction in the flux, uniform at all the energies, by a factor of 10. In Table 1 the integral fluxes of escaping neutron above and below 20 MeV of energy are given. We also indicate the total neutron yield (the number of neutrons produced per primary proton), and the yields in the beam pipe and in the concrete. The yield in the concrete does not increase with the concrete thickness, indicating that practically all the source neutrons are produced within the first meter of shielding.

Table 1. Main neutronic parameters versus shielding thickness for barytes concrete and an aluminium beam pipe (0.8 cm thick) per 10 nA of beam losses

Shielding thickness (m)	Flux of escaping neutrons (n/cm ² /s) <20 MeV	Flux of escaping neutrons (n/cm ² /s) >20 MeV	Total neutron yield	<20 MeV neutron yield	Yield in beam pipe	Yield in concrete shield
1.0	38.0	18.0	0.202	0.167	0.035	0.132
1.4	4.0	2.0	0.201	0.167	0.032	0.135
2.0	0.2	0.1	0.203	0.169	0.033	0.136

The particle fluxes obtained using FLUKA and EA-MC were consistent. The effective doses were calculated with FLUKA using Pelliccioni conversion coefficients [6]. In Figure 6 the spatial distribution of the effective dose for 1 mA of beam loss with a shielding of 1 m of barytes concrete is represented. Assuming beam losses of 10 nA (i.e. 1 nA/m×10 m) we obtain in this case the corresponding dose rate of 100 µSv/h, which is 10 times the allowable dose rate in the reactor building for unlimited exposure of personnel. The dose is essentially due to neutrons (90% of the total). Therefore, it is necessary to have a thickness of concrete of at least 1.4 m.

2) The next test was performed by considering different types of concrete. Figure 7 shows the neutron fluxes in the concrete shield in the three cases. As shown, the presence of boron eliminates the thermal peak and reduces the flux of epithermal neutrons. The spectra in the case of barytes concrete and concrete with boron are similar. However, for the barytes concrete the flux below about 3 MeV is higher, while there are less high-energy neutrons. Clearly, in this case the higher density of the barytes concrete plays a role in slowing down more high-energy neutrons. The increased flux below 3 MeV is due to the (*n,Xn*) reactions in barium and to the higher spallation neutron yield.

Figure 5. Variation of the neutron flux spectra escaping the beam transfer line as a function of the thickness of the concrete shield

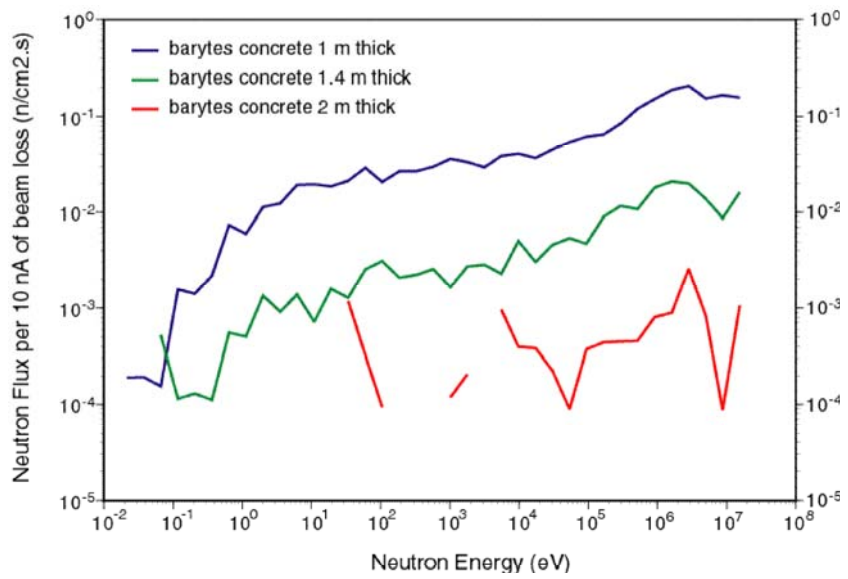


Figure 6. Estimation of the particle dose rate to human body escaping the beam transfer line per mA of beam losses, in the shielding configuration with 1 m thick barytes concrete

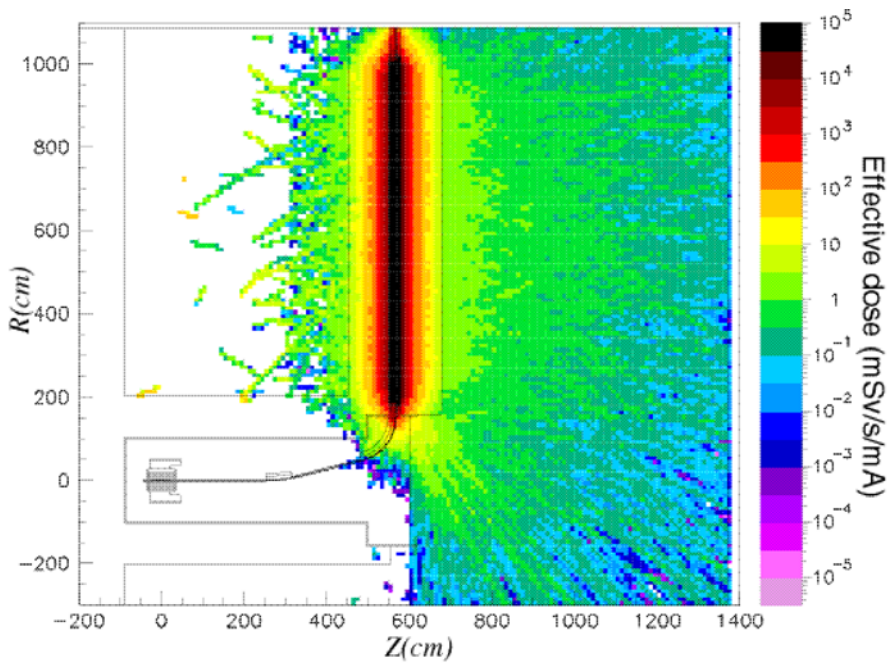


Figure 7. Neutron flux spectra for different compositions of the concrete shielding (1.4 m thick) per 10 nA of beam loss

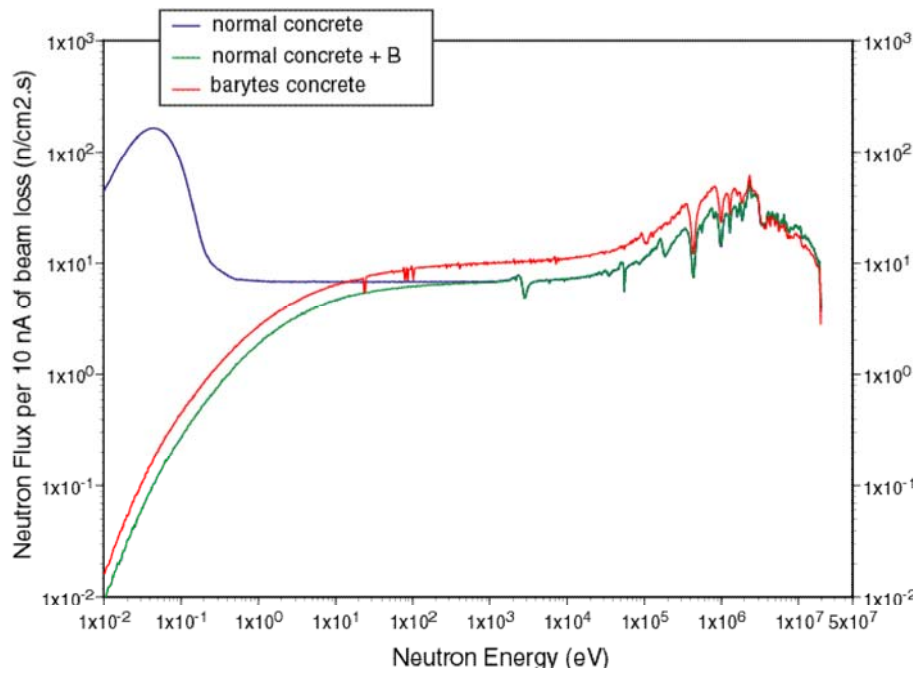


Table 2. Main neutronic parameters versus concrete composition (1.4 m thickness) and an aluminium beam pipe (0.8 cm thick) per 10 nA of beam losses

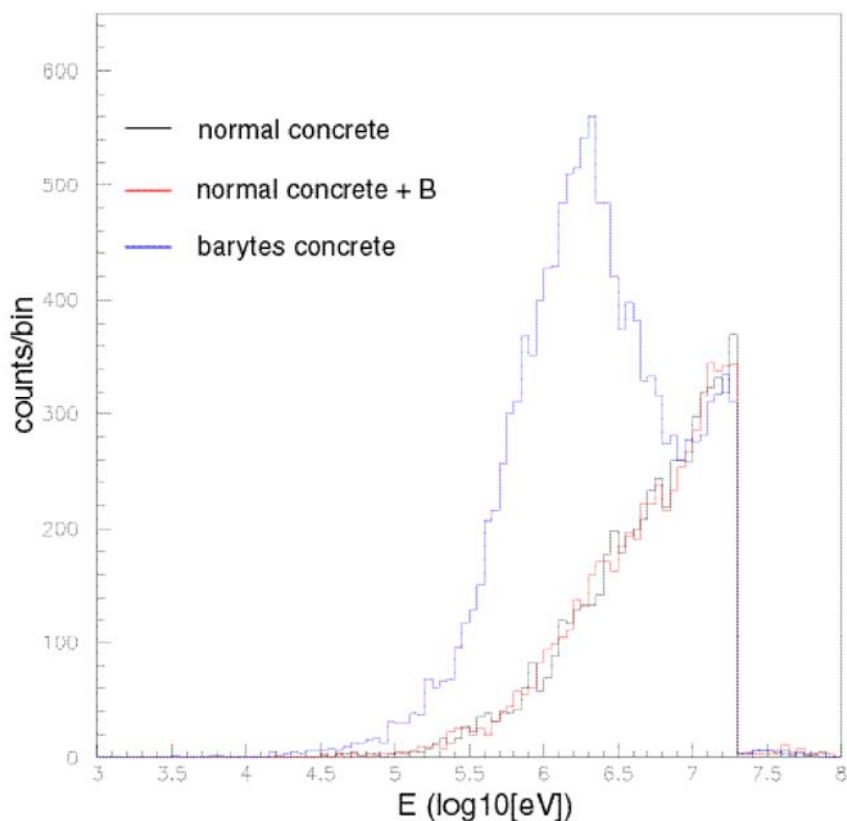
Concrete	Flux of escaping neutrons (n/cm ² /s) <20 MeV	Flux of escaping neutrons (n/cm ² /s) >20 MeV	Total neutron yield	<20 MeV neutron yield	Yield in beam pipe	Yield in concrete
normal	17	6	0.127	0.095	0.033	0.062
normal + B	7	5	0.127	0.094	0.032	0.062
barytes	4	2	0.201	0.167	0.032	0.135

Consequently, the flux of escaping neutrons above and below 20 MeV depends strongly on the type of concrete. The values of the integral flux for escaping neutrons above and below 20 MeV are given in Table 2. The flux with the barytes concrete shielding is roughly a factor 4 lower than the flux with the normal concrete.

This result is achieved despite a neutron yield about 40% higher in the case of the barytes concrete. This effect was investigated by looking at the spectra of the spallation neutrons in the concrete. Figure 8 shows the source neutrons in concrete below 20 MeV, as well as the source neutrons above 20 MeV, which have been transported below this threshold energy. A few source neutrons are generated above 20 MeV and escape the system. It is clear from the figure that in the case of normal concrete or normal concrete plus boron, the spallation spectrum is composed of one

high-energy peak. In the case of barytes concrete, an additional peak centred at about 1.5 MeV is present. Thus, the additional source neutrons, introduced by using the barytes concrete, have on average a lower energy, so that they are easily moderated and absorbed by the shielding; the presence of barium helps in absorbing also a good fraction of the higher energy neutrons.

Figure 8. Spallation neutron spectra in the shielding for different concrete compositions
(As expected, the spectra are sensitive to the presence of barium. See explanation in the text.)



As shown below, the decrease of the dose rate is the same as for the flux, making the barytes concrete the most effective shielding for the reduction in the dose rate.

3) We considered different shielding options other than having a shielding made only of concrete. In particular, we considered the possibility of having an inner layer of a dense material like copper or iron, followed by barytes concrete. Iron and copper have high density and relatively low-Z, therefore they are excellent materials for rapidly slowing down fast neutrons, which then can be captured by the concrete.

Another option consisted of a buffer of borated polyethylene and a combination of iron and polyethylene. Having pure polyethylene should help in quickly moderate the neutrons.

The integral fluxes and the yields are reported in Table 3. We used a thickness of the Fe/Cu layer of 20 cm. It is clear that the shielding with a 20 cm layer of Fe or Cu results in a further reduction of the flux of escaping neutrons, with respect to the case with only barytes concrete. In fact, as shown in Figure 9, the effect of the iron layer is to decrease the fraction of fast neutrons coming

from the beam tube. The Fe/Cu layer has also the property that the spallation neutrons produced have on average a lower energy and are produced in the inner part of the beam line shielding, thus having a higher probability of being absorbed by the shielding. The overall improvement in the flux with respect to the barytes concrete shielding is of about a factor 4. However, this improvement goes at the expense of an increased weight and activation of the shielding. It should therefore be used only if absolutely necessary.

In the shielding configurations using polyethylene, there is a decrease in the efficiency of the shielding. This is due to the fact that spallation neutrons in polyethylene have on the average a higher energy, and require more shielding to be stopped.

Table 3. Main neutronic parameters for different shielding configurations (20 cm of the material indicated in the first column, plus 1.2 m thick barytes concrete) per 10 nA of beam losses

Inner layer	Flux of escaping neutrons (n/cm ² /s) <20 MeV	Flux of escaping neutrons (n/cm ² /s) >20 MeV	Total neutron yield	<20 MeV neutron yield	Yield in beam pipe	Yield in inner layer	Yield in concrete
20 cm Cu	1.0	0.5	0.230	0.195	0.105	0.085	0.005
20 cm Fe	1.0	0.6	0.219	0.184	0.104	0.073	0.007
20 cm borated polyethylene	4.9	1.2	0.166	0.142	0.100	0.015	0.027
5 cm Cu + 15 cm borated polyethylene	3.7	1.7	0.212	0.182	0.101	0.065	0.015

Variation of the beam pipe material and thickness

The concrete is obviously the most important element in the beam line shielding. However, an additional effect may come from the type and size of the material of the beam pipe. We investigated as possible materials aluminium and stainless steel, using both AISI304 and AISI316.

The test on the material was performed using an 8 mm thick beam pipe, and a barytes concrete shielding 1.4 m thick. With this configuration, an effect is indeed observed in the flux of escaping neutrons, as indicated in Table 4. It is interesting to observe the different features of the spallation neutron spectra with Al and stainless steel beam pipe (Figure 10). In fact, with an Al beam pipe most of the spallation neutrons are produced in the concrete, while the opposite situation happens with the AISI304 beam pipe. This will have an effect on the neutron flux and on the effective dose. However, this effect will be reduced if a thinner beam pipe is chosen. In fact, there is also an effect on the beam pipe thickness, and a thinner beam pipe is preferable, even though the effect is at the level of 10-20%.

Figure 9. Neutron flux spectra in the different components of the beam transfer line with the shielding option with a Fe layer, per 10 nA of beam loss

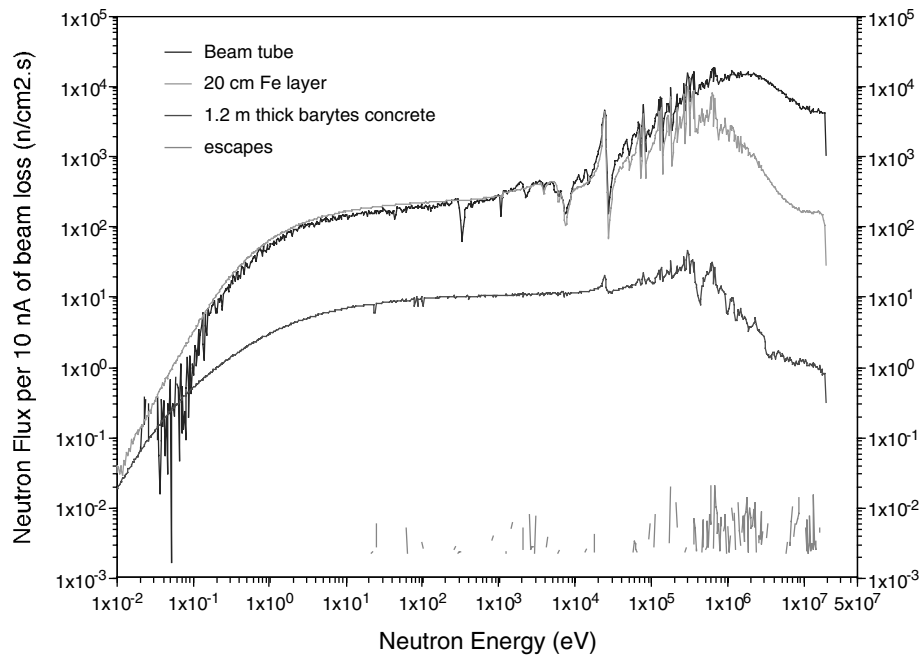


Figure 10. Energy spectra of source neutrons in the beam pipe (black) and concrete (red) with Al and AISI304 beam pipes

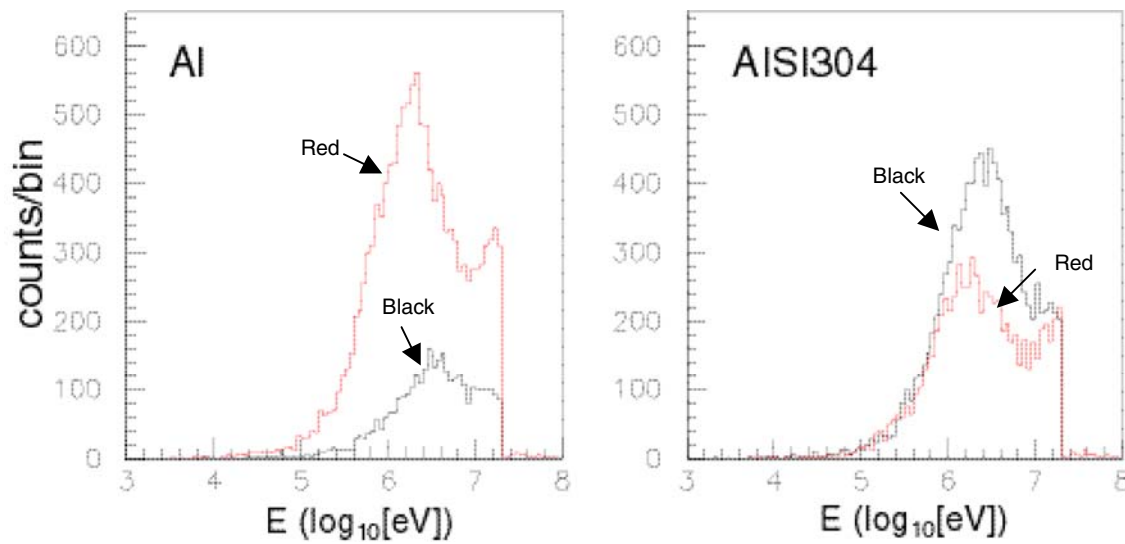


Table 4. Main neutronic parameters versus beam pipe material (of 8 mm thickness) for barytes concrete (1.4 m thick) per 10 nA of beam losses

Beam pipe material	Flux of escaping neutrons (n/cm ² /s) <20 MeV	Flux of escaping neutrons (n/cm ² /s) >20 MeV	Total neutron yield	<20 MeV neutron yield	Yield in beam pipe	Yield in concrete shield
Al	3.6	1.9	0.201	0.167	0.032	0.135
AISI304	3.2	1.3	0.203	0.172	0.104	0.073
AISI316	3.8	1.1	0.208	0.176	0.106	0.070

Effective doses

The results from the dose calculations using FLUKA for the different shielding configurations are summarised in Table 5. We neglected the contribution from activation in the calculations.

The shielding around the beam line must comply with the requirement that the personnel be allowed inside the reactor building and in the control room also during the accelerator running phases. These workers will be classified according to Italian legislation as *exposed workers of category A*, for which the reference annual dose limit is 20 mSv/y. In the control room (at about 7 m from the centre of the beam line) exposed workers will be allowed for a complete working shift (2 000 h/y) and a design limit 10 times lower than the reference one is assumed in this case as suggested by the Italian regulatory authority.

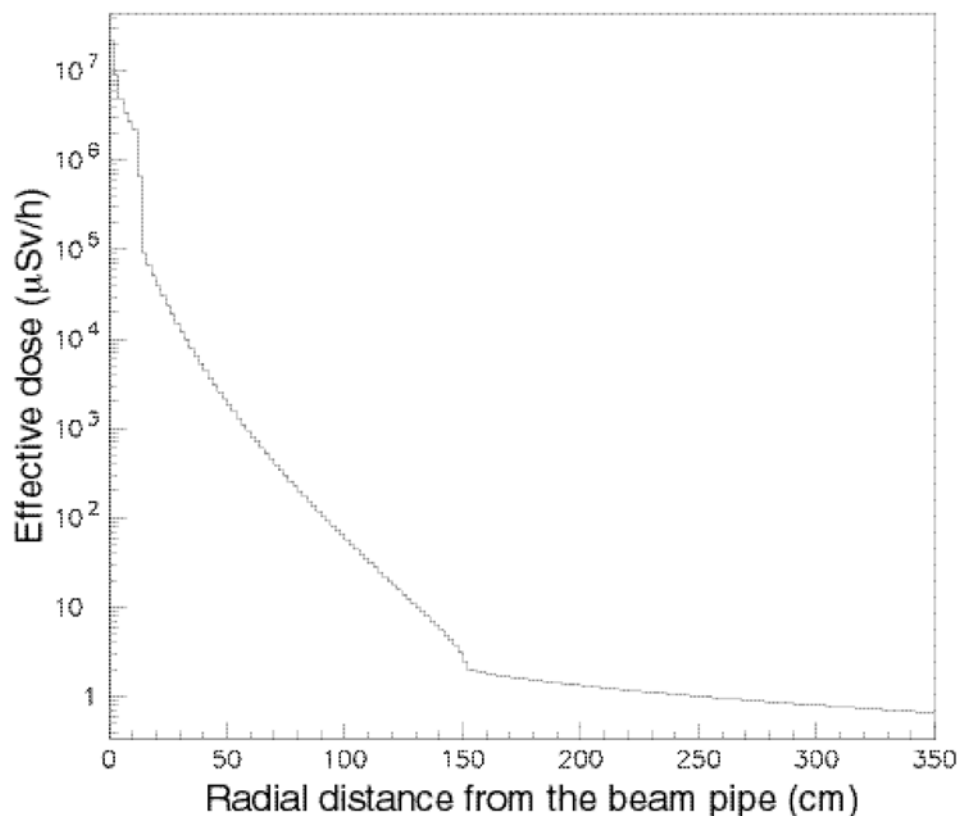
Table 5. Effective dose on the surface of the shielding and at 5 m from the same surface, for a beam loss of 1 nA/m along the 10 m of the beam line (straight section), for the different shielding configurations analysed

(The configurations are separated in three groups, having a total shielding thickness of 1 m, 1.4 m and 2 m, respectively. In bold the configuration chosen as reference is indicated.)

Beam pipe	Shielding configuration	Effective dose at the surface (μSv/h)	Effective dose 5 m from the surface (μSv/h)
8 mm Al	1 m normal concrete	350.00	64.00
8 mm Al	1 m barytes concrete	100.00	18.00
8 mm Al	1.4 m barytes concrete	9.50	2.40
8 mm AISI304	1.4 m barytes concrete	7.90	1.80
2 mm Al	1.4 m barytes concrete	8.30	1.90
2 mm AISI304	1.4 m barytes concrete	7.50	1.70
8 mm AISI304	20 cm Fe, 1.2 m barytes concrete	3.70	0.80
8 mm AISI304	20 cm Cu, 1.2 m barytes concrete	3.20	0.80
2 mm Al	20 cm Cu, 1.2 m barytes concrete	3.90	0.90
2 mm Al	5 cm Cu, 15 cm borated poly, 1.2 m barytes concrete	10.50	2.40
2 mm Al	20 cm borated poly, 1.2 m barytes concrete	10.80	2.50
2 mm AISI304	2 m barytes concrete	0.40	0.12
8 mm AISI304	20 cm Fe, 1.8 m barytes concrete	0.20	0.06
8 mm AISI304	20 cm Cu, 1.8 m barytes concrete	0.20	0.06

The dose rate at 6-7 m from the beam line must therefore not exceed 1 $\mu\text{Sv/h}$. This means that in contact with the surface, at about 2 m from the proton beam, a dose rate of about 10 $\mu\text{Sv/h}$ is acceptable.

Figure 11. Effective dose as a function of the radial distance to the beam pipe for a beam current of 0.25 mA and $10^{-6}/\text{m}$ beam losses for the reference shielding configuration



Another constraint to the dose rate is due to non-exposed workers walking outside of the reactor building at a minimum distance from the beam of about 20 m. An occupational factor of 1/6 is assumed in this case, and therefore 0.8 $\mu\text{Sv/h}$ is the design limit at 20 m distance, which is respected if the conditions for the exposed workers are respected.

This analysis has shown that it is possible to reduce the effective dose rate due to beam losses in normal operating conditions below the above mentioned limit of 10 $\mu\text{Sv/h}$. This reduction is achieved primarily by increasing the thickness of the concrete shielding. For instance, increasing the thickness by 1 m reduces the dose rate by more than two orders of magnitude. The presence of boron and barium in the concrete is also very important, giving a reduction of the dose rate by nearly a factor 4.

Inserting different Cu or Fe layers can further improve the dose rates emitted at the surface of the concrete shielding. For instance, with a 20 cm thick copper or iron layer surrounded by 1.8 m of barytes concrete, the effective dose at the surface is about 0.2 $\mu\text{Sv/h}$. However, the improvement in the

effective dose is achieved at the expense of an increase of activation, as well as in the overall weight of the beam line shielding.

Further reduction of the dose rate can be obtained by changing the composition and thickness of the beam tube. We find that the lowest dose rate is reached by using a thin beam tube made of AISI304.

Given these considerations, the layout consisting of 1.4 m of barytes concrete, with a 2 mm thick AISI304 beam pipe can be adopted as a reference configuration, resulting in an effective dose at the surface of the shielding of $7.5 \mu\text{Sv/h}$ for 1 nA/m beam losses at 1 mA proton current. However, the maximum beam current envisaged during the TRADE experiment will be about 0.25 mA in order not to exceed the limit of 50 kW of beam power imposed by the thermal hydraulic requirements of the spallation target. Consequently, an additional factor 4 should be applied to the doses reported in Table 5, resulting in an effective dose at the surface of about $2 \mu\text{Sv/h}$ for the reference case.

Figure 11 represents the effective dose as a function of the radial distance from the beam pipe for a beam current of 0.25 mA and 10^{-5} beam losses (0.25 nA/m of beam losses along 10 m of beam line) for the reference configuration.

In conclusion, the effective dose obtained for the reference configuration satisfies the safety requirements (at least for the straight section). Moreover, one should also consider that the calculational scheme adopted is a pessimistic one since we have used a user defined source routine which generates protons distributed along the length of the beam pipe and propagated outwards. In reality, the protons exiting the beam line will have a very small angle, and therefore will be attenuated even more. Indeed, we have checked that the reduction factor, assuming a divergence of 1° is of 2.5, reducing the effective dose at the surface of the shielding to about $0.8 \mu\text{Sv/h}$.

Different considerations should be made for the shielding around the M4 magnet. The design of the shielding around the magnet will have to face the fact that the beam losses in the magnet are two orders of magnitude higher than in the straight section. On the other hand, the loss will be localised in a relatively small spot, making it a point source of neutrons, as opposed to the extended source given by the straight section, which will constitute an advantage since the flux will be decreasing like $1/R^2$ instead of $1/R$.

Activation

The study of the activation of the different elements of the TRADE experiment is very important because of the presence of the accelerator and the spallation source. One should consider the activation induced by the beam-target interaction, the activation of the water due to beam losses and to neutrons streaming from the reactor core, the air activation and the activation of the beam line due to beam losses in normal conditions. Burnup calculations using the EA-MC code were carried out to study these cases.

Figure 12. Evolution of the radioactivity (Ci/mA·yr) of the tungsten spallation target as a function of time

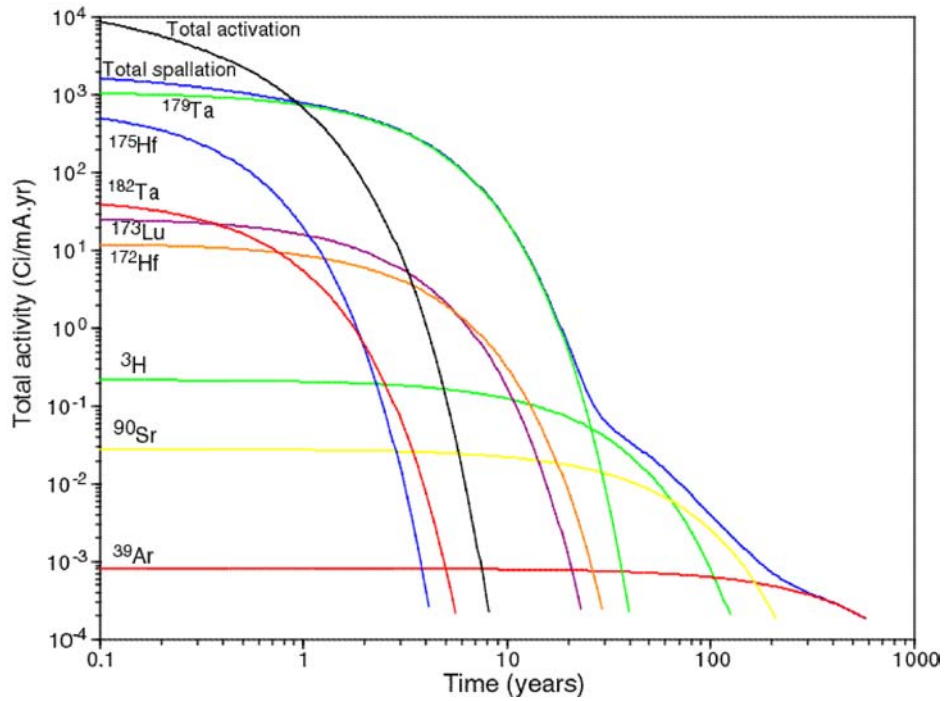


Figure 13. Left: Evolution of the radioactivity of water 10 cm from the beam line due to normal beam losses (1 nA/m of beam losses along 6 m of straight section).

Right: Evolution of the radioactivity of water coolant in different parts of the reactor core.

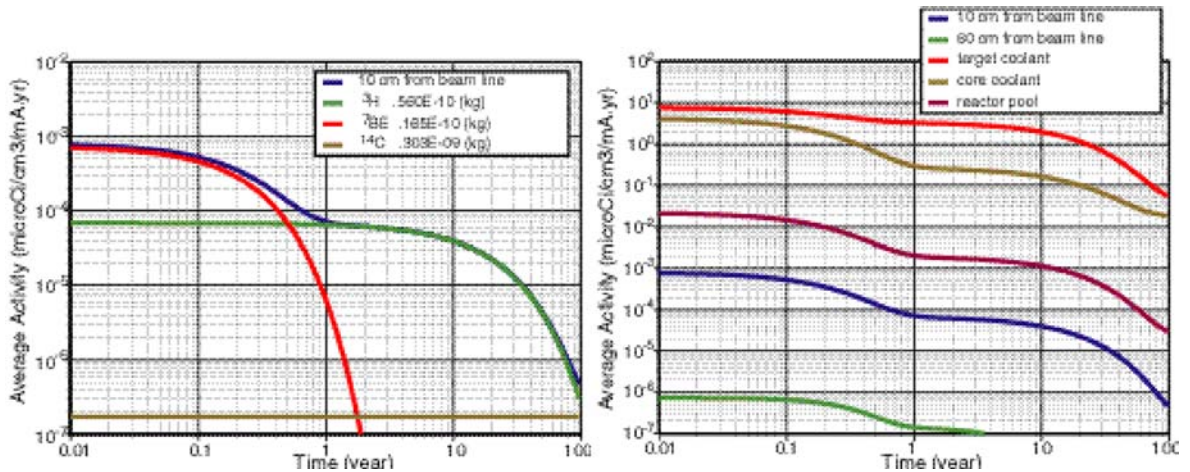
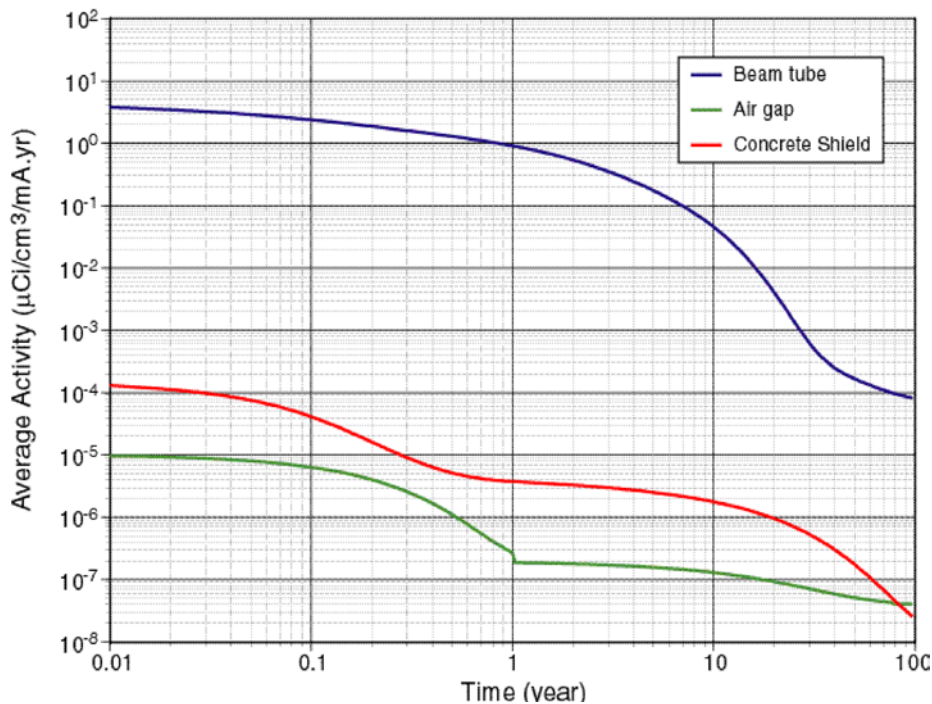


Figure 14. Evaluation of the radioactivity from the beam line due to normal beam losses (1 nA/m of beam losses along 10 m of straight section)



1) In the case of the beam-target interactions, we estimated the activation of the tungsten spallation target and its aluminium supports. Burnup calculations were performed up to 1 000 years from the experiment. The results are represented in Figure 12. The activity of the spallation target (expressed in Ci/mA/yr) is dominated by activation resulting from successive thermal neutron captures. After one year of cooling down the activity is dominated by the decay of the spallation products, mostly Ta, Lu and Hf isotopes. At longer times (>40 years) tritium and ⁹⁰Sr are the only isotopes of importance. Tritium is the only volatile isotope produced in the spallation target, which will however be continuously carried away by the vacuum system of the beam pipe.

These activation levels are comparable with those of the fuel elements. Therefore, the safety procedures for the fuel rods will also apply for the spallation target.

2) The activation of water contained around the beam tube during normal operation was also estimated (Figure 13). The activity of the water 10 cm from the beam line is dominated by the decay of the spallation products, mostly ⁷Be (8×10^{-4} µCi/cm³/mA/yr). After one year tritium and ¹⁴C are the only isotopes of importance. Similarly, the activity of the water surrounding the spallation target and that of core is entirely dominated by beryllium. The level of radioactivity is about 10⁴ the one induced in the water around the beam line. Air activation calculations were also performed, as well as ¹⁶N production from ¹⁶O(n,p)¹⁶N, indicating a negligible level of production [2]. These radioactivity levels are very low and do not constitute an issue.

3) Finally, we calculated the activity of the beam transfer line induced by the proton beam losses during normal operation. For these calculations we used a stainless steel tube, which activates more than aluminium. The spallation products generated in the beam tube mostly dominate the activity, shown in Figure 14. Again, the level of activation is very low.

Conclusions

This paper concentrated on the radiation protection aspects related to the beam losses in normal operating conditions. A shielding of barytes concrete of 1.4 m thickness is recommended to lower the dose rate below the acceptable limits for the exposed workers. The problem of the losses near the M4 magnet will have to be addressed next.

Another important aspect is beam-target interactions; in this case we have shown that there will be no additional radiation safety issues with respect to the situation related to a normal TRIGA reactor. The only new aspect consists in a slight irradiation of the lower bending magnet.

Calculations show that activation of water, air and beam line will be negligible with respect to the one of the core and of the spallation target. For the spallation target, the same safety procedures for the core elements will have to be applied.

REFERENCES

- [1] The European Technical Working Group on ADS, “A European Roadmap for Developing Accelerator-driven System (ADS) for Nuclear Waste Incineration”, April 2001.
- [2] “The Working Group on TRADE: TRiga Accelerator-driven Experiment”, *TRADE Final Feasibility Report*, March 2002.
- [3] Herrera-Martínez, A., *et al.*, “Radiological Impact of the TRiga Accelerator-driven Experiment (TRADE)”, CERN internal note SL/2002-007, and Proceedings of the 12th Biennial RPSD Topical Meeting, Santa Fe, USA, April 14-18, 2002.
- [4] Fassò, A., A. Ferrari, P.R. Sala, “Electron – photon transport in FLUKA status”, Proc. of the Monte Carlo 2000 Conference, Lisbon, October 23-26, 2000, A. Kling, F. Barão, M. Nakagawa, L. Távora, P. Vaz Eds., Springer-Verlag, Berlin, pp. 59-164 (2001).
Fassò, A., A. Ferrari, J. Ranft, P.R. Sala, *FLUKA*: “Status and Prospective for Hadronic Applications”, Proc. of the Monte Carlo 2000 Conference, Lisbon, 23-26 Oct. 2000, A. Kling, F. Barão, M. Nakagawa, L. Távora, P. Vaz Eds., Springer-Verlag Berlin, pp. 955-960 (2001).
- [5] Kadi, Y., *et al.*, “The EA-MC code package”, in Proc. of the Fifth International Meeting on Simulating Accelerator Radiation Environment – SARE 5: Models and Codes for spallation neutron sources; OECD Headquarters, Paris, France, 17-18 July 2000.
- [6] Ferrari, A., M. Pelliccioni, “Dose equivalents for mono-energetic electrons incident on the ICRU sphere”, *Radiation Protection Dosimetry*, 55 n. 3, 207-210 (1994) [also LNF-94/005 (P) (1994)].
“Dose equivalents for mono-energetic positrons incident on the ICRU sphere”, *Radiation Protection Dosimetry*, 55, n. 4, 309-312 (1994).

“Fluence to dose equivalent conversion data and effective quality factors for high energy neutrons”, *Radiation Protection Dosimetry* 76, n. 4, 215-224 (1998).

Ferrari, A., M. Pelliccioni, and M. Pillon, “Fluence to effective dose and effective dose equivalent conversion coefficients for photons from 50 keV to 10 GeV”, *Radiation Protection Dosimetry* 67, n. 4, 245-251 (1996).

“Fluence to effective dose and effective dose equivalent conversion coefficients for electrons from 5 MeV to 10 GeV”, *Radiation Protection Dosimetry* 69, n. 2, 97-104 (1997).

“Fluence to effective dose conversion coefficients for protons from 5 MeV to 10 TeV”, *Radiation Protection Dosimetry* 71, n. 2, 85-91 (1997).

**THERMAL RESPONSE OF THE MULTIPLIER OF
AN ACCELERATOR-DRIVEN SYSTEM TO BEAM INTERRUPTIONS**

Floyd E. Dunn

Argonne National Laboratory
9700 S. Cass Avenue, Argonne, IL 60439
Phone: (630) 252-4692
Fax: (630) 252-4500
fedunn@anl.gov

Abstract

Thermal response of the multiplier of an accelerator-driven system to beam trips has been calculated for sodium cooled and lead-bismuth cooled multipliers. The temperature transients caused by a beam trip lead to thermal fatigue in structural components, and restoring the beam causes an additional temperature transient that adds to thermal fatigue. Design lifetimes for various multiplier components are calculated, based on the frequency of beam interruptions and on the thermal fatigue per interruption. Mitigation strategies to increase design lifetimes are discussed.

Introduction

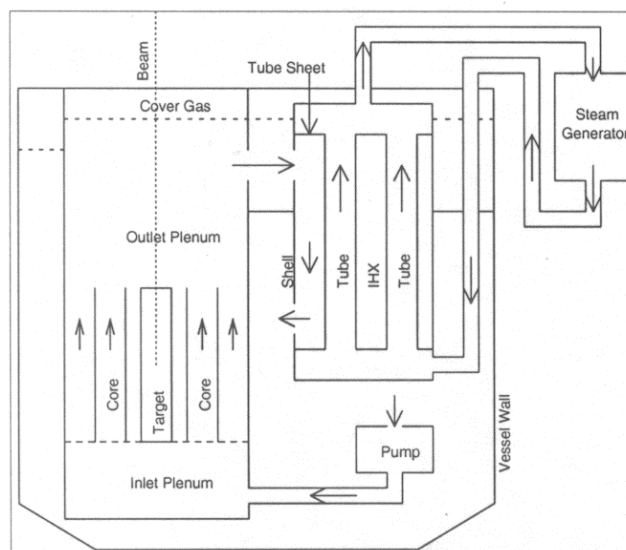
A beam trip in an accelerator-driven system leads to rapid temperature transients in the various parts of the multiplier. These temperature transients lead to thermal fatigue which limits the lifetimes of structural components. This paper discusses temperature transients in the multiplier, thermal fatigue and resulting limits on component lifetimes, and mitigation measures to improve component lifetimes.

Description of multiplier concepts

Three multiplier concepts are used in this paper. The first multiplier is based on the advanced liquid metal reactor (ALMR) concept [1]. This concept was used in the accelerator transmutation of waste (ATW) report to Congress [2]. This concept uses metal fuel and sodium coolant, and it has a nominal power level of 840 MWt. This concept is shown in Figure 1. The accelerator beam strikes a target in the middle of the multiplier core. The multiplier power is produced in the target and the core. Coolant flows upward through the core into the outlet plenum. From there the coolant goes to the shell side of a shell-and-tube intermediate heat exchanger (IHX) where it transfers its heat to the intermediate coolant loop. The primary coolant then goes to the cold pool. Coolant from the cold pool is sucked by the pump and pumped into the inlet plenum, from which it goes through the core. The intermediate coolant loop carries the heat to the steam generator.

The second multiplier concept is similar to the first, but lead-bismuth is used for the coolant instead of sodium. There is no intermediate loop in this concept. Instead, the steam generator is placed where the intermediate heat exchanger would be. In order to avoid excessive coolant pressure drop through the core, and to avoid corrosion of the steel by lead-bismuth, the coolant flow velocity through the core is limited by providing a larger flow area per pin in the core subassemblies. With lead-bismuth coolant one row of pins is removed from the subassembly, leaving 169 pins per subassembly instead of the 217 pins used with sodium. For both of the first two concepts the coolant temperature rise in the hottest core channel is 164 K, and the average coolant temperature rise is 139 K.

Figure 1. Schematic of multiplier coolant flow



The third multiplier concept is the subcritical multiplier (SCM-100) used with the accelerator-driven test facility (ADTF). This concept is based on the EBR-II reactor, scaled up to 100 MWt from 62.5 MWt. Thus, this concept is significantly smaller than the first two. The third multiplier concept also uses metal fuel and sodium coolant. In addition, in the third concept there is a cover on the outlet plenum and a pipe from the outlet plenum to the IHX. In this concept the average coolant temperature rise across the core is 100 K.

Analysis methods

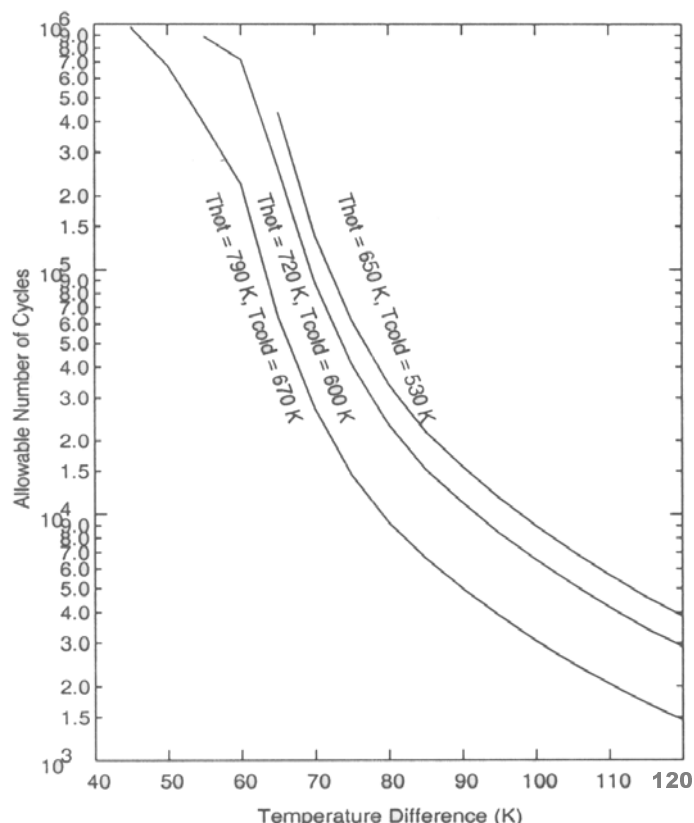
In order to analyse the consequences of a beam loss and return to power transient, the SASSYS-1 LMR systems analysis code [3] was used to obtain the time dependent temperatures of the coolant in contact with various structural components. Multi-node structural temperature calculations were then used to obtain minimum, maximum and average structure temperatures. The difference between the minimum or maximum temperature and the average structure temperature was multiplied by the thermal expansion coefficient to obtain the strain magnitude. The peak strain magnitude was used with the American Society of Engineers (ASME) Boiler and Pressure Vessel Code [4] to determine the allowable number of cycles the structural component can be subjected to. Beam reliability data [5] for the LANSCE accelerator were used to obtain the number of beam interruptions per year of a particular duration. The integral over interruption duration of the ratio of the interruptions per year for a particular interruption duration to the allowable number of cycles of that duration gave a damage function which determined the allowable lifetime for the structural component.

The SASSYS-1 LMR systems analysis code contains neutron kinetics coupled with a detailed thermal hydraulics treatment of the core, the primary and intermediate heat removal loops, and the steam generators. Both steady-state and transient calculations are done by the code. The neutron kinetics treatment contains point kinetics, with or without an external source. Also in the code is an optional 3-D time dependent neutron kinetics capability.

The method used for evaluation of low cycle fatigue at elevated temperatures is based on article T-1432 of Appendix T of subsection NH of the ASME Boiler and Pressure Vessel Code. This type of analysis is required when the temperatures exceed 700 or 800°F. The difference between the average structure temperature and the minimum or maximum temperature is multiplied by the thermal expansion coefficient to obtain the strain. The peak strain for a cycle is used to obtain the allowable number of cycles that the structure can be subjected to. Figure 2 shows results for 304 stainless steel. Note that an increase of only a few degrees in peak temperature difference can lead to a decrease of a factor of two in the allowable number of cycles.

Evaluation of low cycle fatigue in the HT-9 steel alloy used for cladding, subassembly duct walls, and shielding in the subassemblies is a special problem. Appendix T only includes data for four materials: 304 stainless steel, 316 stainless steel, Ni-Fe-Cr Alloy 800H, and 2¼ Cr 1 Mo steel. Furthermore, there appears to be no low cycle fatigue failure data anywhere for HT-9. What is done in this work is to evaluate HT-9 as if it were 316 stainless steel and then divide the allowable number of cycles by an uncertainty factor. In order to estimate the uncertainty factor, the ASME low cycle fatigue treatment in subsection NB of section III is used. This treatment is limited to temperatures below 700-800°F; but it is applicable to broad classes of steels, including one category for ferritic steels and another category for austenitic steels such as 316 stainless steel. Using this treatment the allowable number of cycles for the austenitic category tends to be about six times as great as the allowable number of cycles for the ferritic category with the same temperature difference. Therefore, a value of six is used for the uncertainty factor. Until fatigue data for HT-9 is available, there will be a significant uncertainty in the results for this material.

Figure 2. ASME thermal fatigue results



The data obtained by Eriksson for the frequency of beam interruptions of various durations in the LANSCE accelerator is shown in Table 1. This data is used as a reference point in calculating component lifetime. Compared to LANSCE, a new proton accelerator would probably be at least a factor of ten more reliable. One question to be addressed is whether a factor of ten improvement is sufficient.

Table 1. LANSCE data for the frequency of beam interruptions

Duration of interruption	Interruptions per day	Interruptions per year
10 seconds or more	39.00	14 200
1 minute or more	9.50	3 482
2 minutes or more	5.50	2 019
3 minutes or more	4.40	1 597
4 minutes or more	4.00	1 402
5 minutes or more	3.40	1 237
15 minutes or more	1.70	617
1 hour or more	.60	214
5 hours or more	.09	34

In order to evaluate the allowable component lifetime, a damage rate, d , is used to give the damage per year. The allowable lifetime is $1/d$ years. To evaluate the damage rate for a wide range of interruption durations, the interruption durations are grouped into intervals. Interval i includes interruptions with down times from t_{di} to t_{di+1} . Then the damage rate is given by

$$d = \sum I_i/A_i$$

where

A_i = allowable number of cycles for interruptions in interval i , and

I_i = interruptions per year in interval i .

Temperature transients

Analysis of the three multiplier concepts has shown where the critical structures are as far as thermal fatigue is concerned. For the sodium cooled ATW, the critical areas are the above core load pads on the subassembly duct walls and the outer rim of the upper tube sheet in the intermediate heat exchanger. For the lead cooled ATW the critical area is the upper tube sheet of the steam generator. For the sodium cooled ADTF the critical areas are the shielding inside the subassembly above the core and the outer rim of the upper tube sheet of the intermediate heat exchanger. Results for some of these critical areas are given in the sections below.

The normalised multiplier power after a beam trip is shown in Figure 3 for different values of the criticality, k_{eff} . The coolant pumps are assumed to continue operating after the beam trip, so the coolant flow continues at its initial value. The power drops almost instantaneously to 16% or 9%, depending on the criticality. Then the power drops gradually toward decay heat levels. Note that a lower criticality gives a more severe initial power transient. These results were calculated for the first multiplier concept, but similar results would be obtained for the other concepts.

Figure 3. Normalised multiplier power and coolant flow following a beam trip

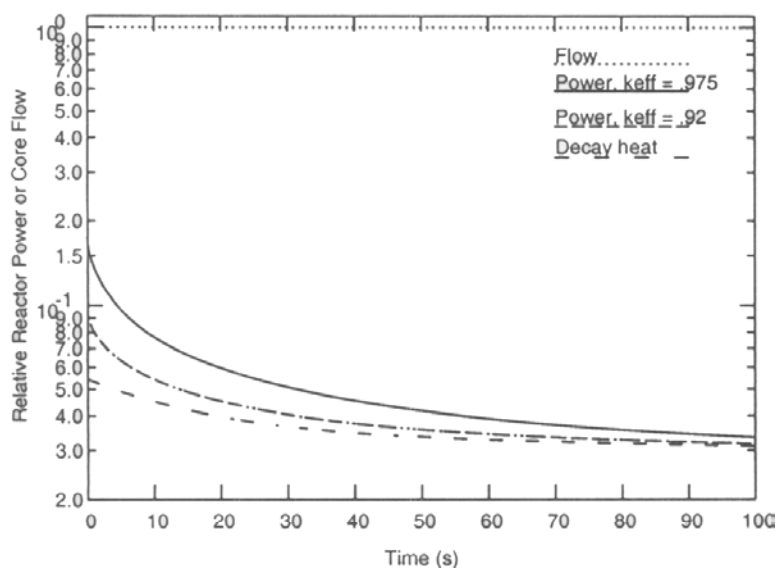
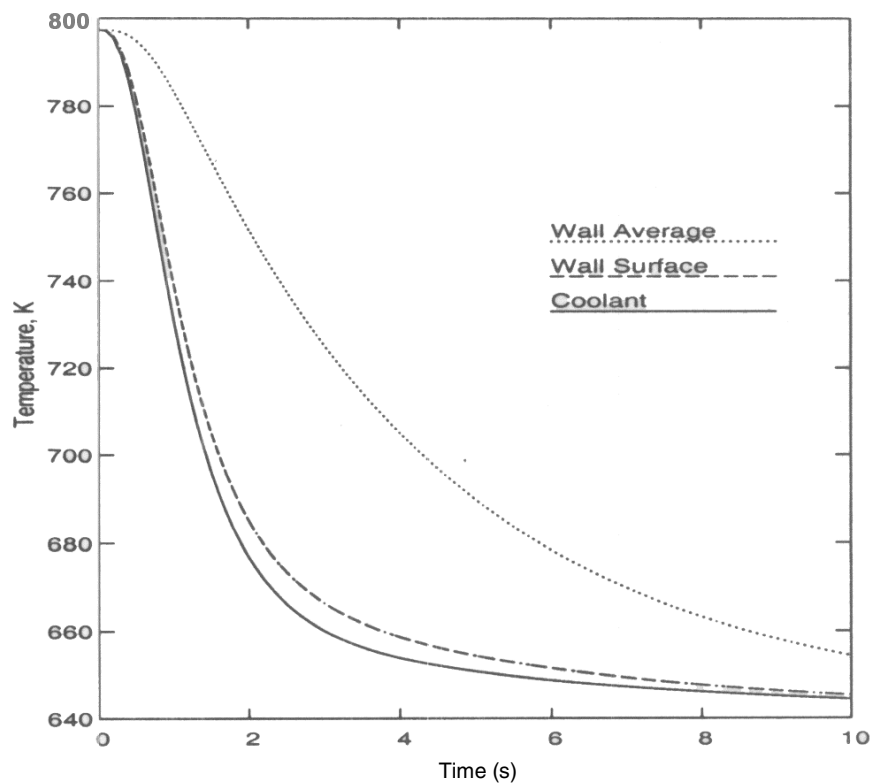


Figure 4 shows the subassembly wall temperatures and coolant temperatures following a beam interruption for the sodium cooled ATW concept. These temperatures are at the location of the above-core load pads. At this location the subassembly duct wall is thickened to provide spacing between subassemblies and to provide more strength at the point where the subassemblies are clamped together to limit lateral motion. In this case the wall surface temperature follows the coolant temperature closely, whereas the average wall temperature lags significantly. Figure 5 shows the difference between the average wall temperature and the wall surface temperature. This difference peaks at about 66 K two seconds after the beam interruption. Using the methods of the previous section, a 66 K temperature difference peak in HT-9 steel gives 7 500 as the allowable number of cycles for this transient, without accounting for additional thermal fatigue due to the return to power. The LANSCE data would give a duct wall lifetime of about .53 years for this case. Since it is desirable to operate subassemblies for three or four years before they are replaced, this is not an acceptable lifetime.

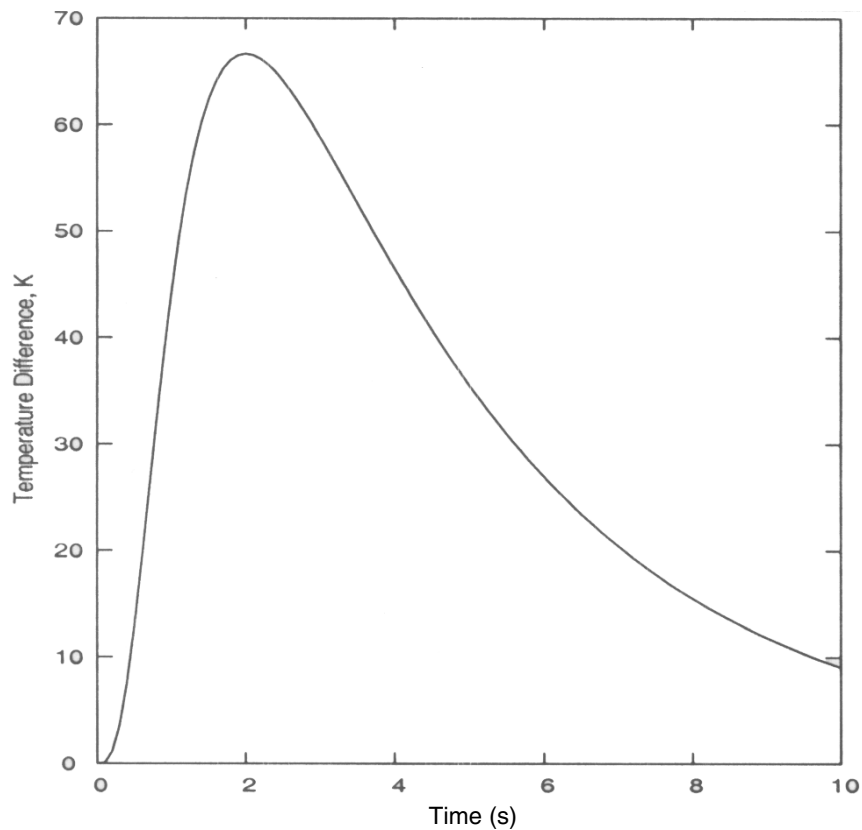
Figure 4. Coolant and structure temperatures at the above core load pads of a sodium cooled ATW following a beam interruption



The coolant and structure temperatures at the top of the core are shown in Figure 6 for the lead-bismuth cooled version of ATW. In this case the structure surface temperature does not follow the coolant temperature as closely as in the sodium coolant case, since the thermal conductivity of lead-bismuth is significantly lower than that of sodium.

The temperature differences across the structure are smaller. Without accounting for additional fatigue from return to power, the subassembly duct wall will last 4.8 years in the lead-bismuth case.

Figure 5. Difference between the structure average temperature and the structure surface temperature at the above core load pads of a sodium cooled ATW



The impact of a sudden return to power twenty seconds after a beam interruption is shown in Figure 7 for the above core load pads in the sodium cooled case. The structure surface temperature drops rapidly after the beam interruption and rises rapidly after the return to power. The average structure temperature lags behind the surface temperature. Figure 8 shows the difference between the structure average temperature and the structure surface temperature for this case. The return to power gives a curve that is a mirror image of the transient due to the interruption. In this case, the peak structure temperature difference that enters into the thermal fatigue calculation is twice as high as it would be with no return to power. This would reduce the component lifetime to 3 days.

Figure 6. ATW above core load pad temperatures after a beam interruption, Pb-Bi case

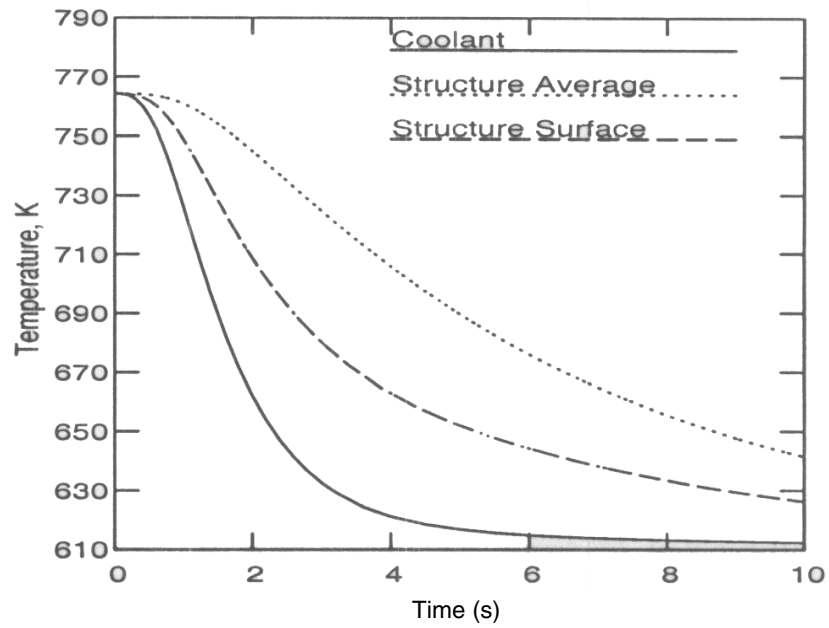
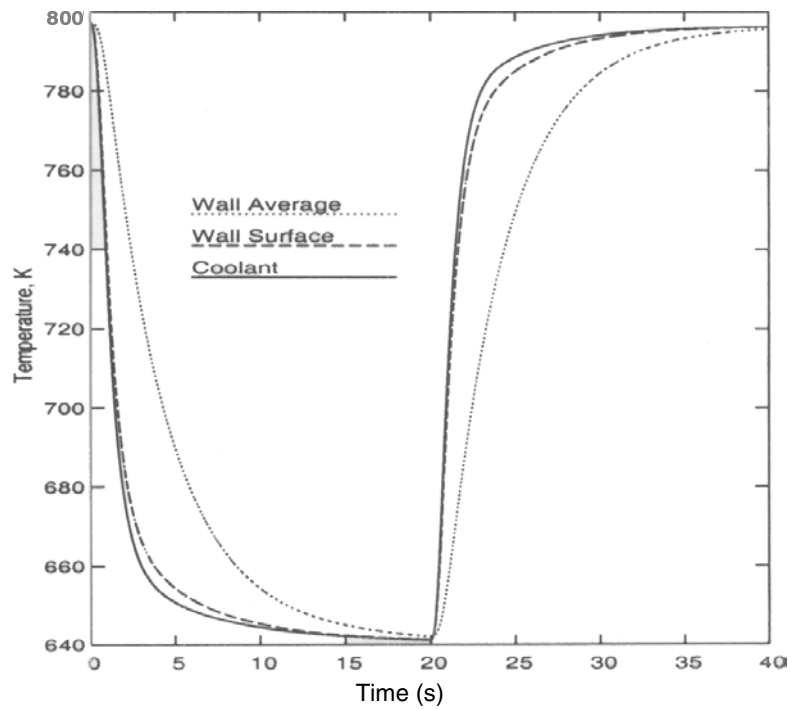


Figure 7. Coolant and structure temperatures at the above core load pad of a sodium cooled ATW due to a sudden return to power after a 20 second beam interruption



The results in Figure 8 demonstrate the need to return to power gradually rather than suddenly after a beam interruption. This topic has been investigated for the third multiplier concept, the sodium cooled ADTF. In this design there are no above core load pads on the subassembly walls. Instead there are dimples in the duct wall to provide spacing between subassemblies. The duct walls and dimples are thin enough that thermal fatigue is not an issue with them. Instead, what is an issue is the thick neutron shielding inside the subassemblies and above the core. Thermal fatigue cracks in this shielding may not matter if the material stays in place. On the other hand if cracked pieces move and block coolant channels then the cracks will matter a lot.

Figure 8. Average structure temperature minus structure surface temperature at the above core load pad of a sodium cooled ATW due to a sudden return to power after 20 seconds

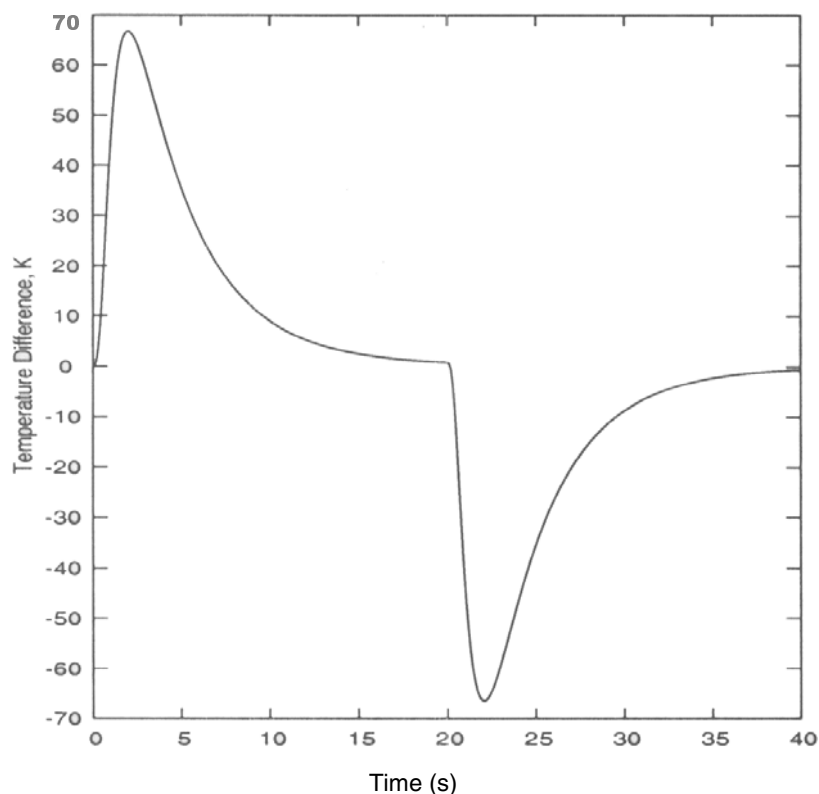


Figure 9 shows the structure temperature differences in the above core shielding for a beam interruption of 10 seconds followed by a ramp back to power with various ramp rates. An immediate return to power adds 40 K to the amplitude of the temperature transient. Even a 300 second ramp adds a few degrees to the amplitude.

The tubes going through the tube sheets of the IHX are spaced fairly close together, so when there is a temperature transient and the tube side coolant changes temperature the bulk of the interior of the tube sheet responds fairly rapidly and uniformly. On the other hand, at the outer edge of the tube sheet there is a fairly wide rim with no tube penetrations. The outer rim temperatures respond more slowly to temperature transients, leading to thermal strains in the outer rim. Figure 10 shows the difference between the outer rim temperature and the interior temperature for the upper tube sheet rim

for a beam interruption of 1 000 seconds followed by a ramp back to power. The time scales in this case are much longer than in previous cases. Even a 16 000 second ramp back to power adds more than 10 K to the amplitude of the transient.

Figure 9. Structure temperature differences in the above core shielding of the ADTF due to a beam interruption of 10 seconds, followed by a ramp back to power

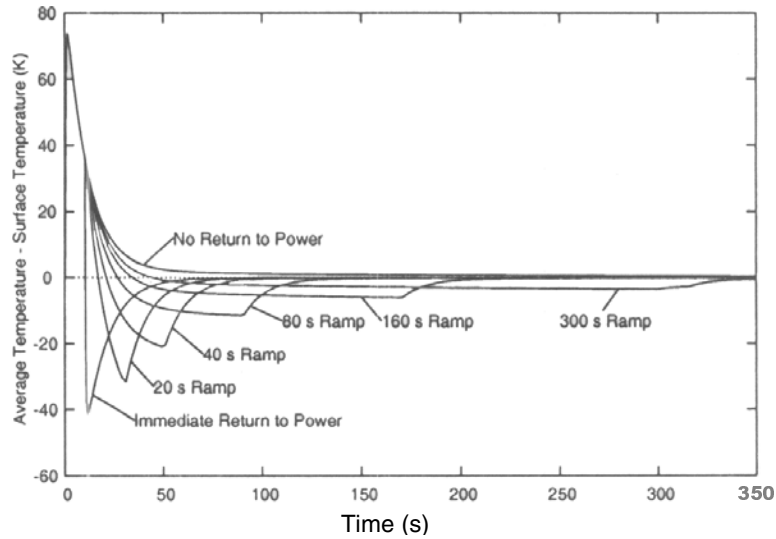


Figure 10. Structure temperature differences in the IHX tube sheet rim of ADTF due to a beam interruption of 1 000 seconds, followed by a ramp back to power

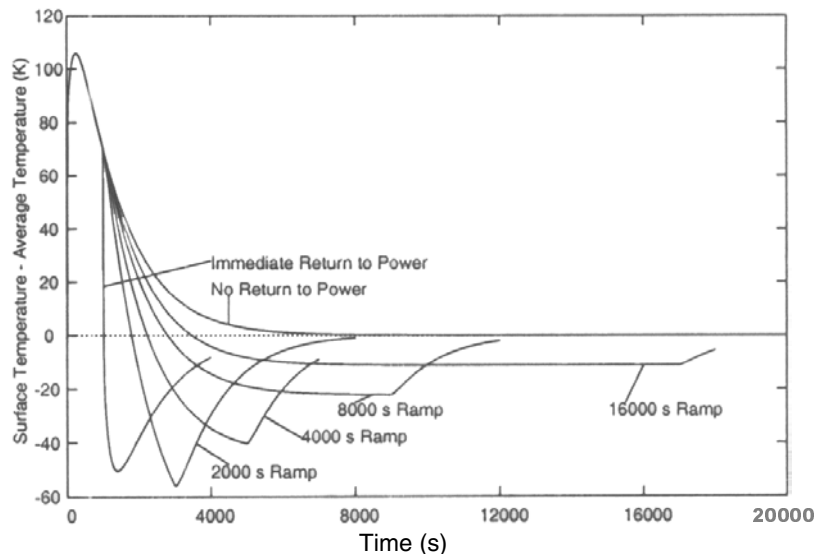


Figure 11. Structure temperature differences in the IHX tube sheet rim of ADTF due to a beam interruption of 20 seconds, followed by a ramp back to power

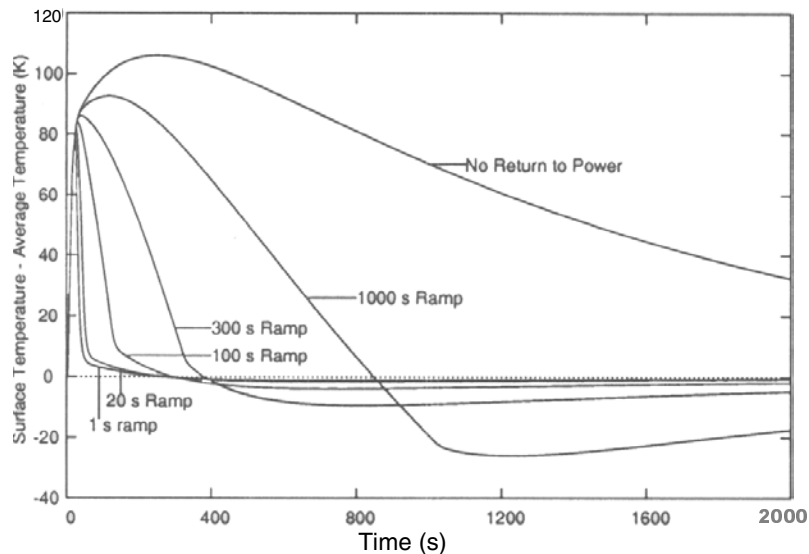


Figure 11 shows the structure temperature differences in the IHX upper tube sheet rim for a beam interruption of 20 seconds, followed by a ramp back to power. In this case the return to power starts before the temperature peak, and a rapid return to power is advantageous.

Return to power schemes

There is a conflict between specifying a return to power scheme to protect short time constant structures and specifying a scheme to protect long time constant structures. In the ADTF temperature differences in the above core shielding peak 1.4 seconds after an interruption, whereas temperature differences in the IHX tube sheet rim do not peak until 250 seconds after the interruption. For an interruption with a duration greater than 1.4 seconds but significantly less than 250 seconds, after the interruption one would want to return to power slowly to minimise the additional thermal fatigue in the above core shielding; but one would want to return to power quickly to minimise the peak temperature difference in the IHX tube sheet rim. Some compromise is necessary. Results obtained with two different return to power schemes are presented below to quantify the effects of this conflict.

Scheme A for return to power after a beam interruption

Interruption <1 s	return to power immediately, if possible
1 s ≤ interruption <50 s	ramp time =300 s for return to power
50 s ≤ interruption <400 s	double ramp, 0-.75 power in 300 s .75-1.0 power in 8 000 more s
interruption ≥400 s	ramp time =16 000 s

Scheme B for return to power after a beam interruption

Interruption <1 s	return to power immediately, if possible
1 s ≤ interruption <50 s	ramp time =100 s for return to power
50 s ≤ interruption <400 s	double ramp, 0-.75 power in 100 s .75-1.0 power in 8 000 more s
interruption ≥400 s	ramp time =16 000 s

Table 2. Component lifetimes, impact of return to power scheme

Component	Lifetime (years), ignoring temperature overshoot from return to power	Lifetime (years), scheme A	Lifetime (years), scheme B
IHX upper tube sheet rim	1.01	.48	.69
Above core shielding	.40	.26	.15

The difference between these two return to power schemes is that for short interruptions the ramp time in scheme B is 100 seconds instead of 300 seconds. Thus, scheme A provides more protection to the above core shielding, whereas scheme B provides more protection to the IHX upper tube sheet rim.

Mitigation measures

The component lifetimes in Table 2 are unacceptable. The subassemblies are left in the core for three or four years, so an above core shielding lifetime of at least three or four years is required. The lifetime of the IHX should be at least as long as the expected operational lifetime of the plant, although replacing the IHX once during the plant lifetime may be acceptable. Replacing the IHX would be expensive. Thus, some mitigation measures need to be taken to reduce accelerator beam interruptions and/or to increase the tolerance of the blanket to beam interruptions.

As mentioned above, a significant reduction in the frequency of beam interruptions should be possible. A new accelerator built with modern technology would be expected to be more reliable than LANSCE by a factor of ten or more. A factor of ten increase in component lifetime would be helpful but not sufficient. Additional improvement is necessary.

Increasing the tolerance of the blanket to beam interruptions requires design changes. Either the thicknesses of critical structural materials must be reduced or transient temperature changes must be reduced. An example of a SCM-100 design in which the transient temperature changes are reduced is given below.

A beam interruption tolerant design

The ADTF SCM-100 results presented here so far were for a design which is basically the EBR-II reactor scaled up from 62.5 MWt to 100 MWt by increasing the number of subassemblies in the core and increasing the number of tubes in the IHX. The average coolant flow per subassembly and the average power per subassembly were approximately the same in the scaled up version.

Also, the coolant temperature rise across the intermediate side of the IHX was similar. In the upper tube sheet rim of the IHX, the magnitude of the temperature perturbations caused by a beam interruption depends mainly on the IHX intermediate side coolant temperature rise. On the other hand, the magnitude of the temperature perturbations in the above core shielding depends mainly on the primary coolant temperature rise across the blanket subassemblies. Therefore, in the modified, more tolerant SCM-100 design both the primary and the intermediate coolant flow rates were increased to reduce coolant temperature rise.

Table 3 lists some of the relevant design and operating parameters of the modified SCM-100. Parameters for the original design and for EBR-II at the time of the SHRT-17 test are also listed for comparison. For the modified design, the total power and the number of driver subassemblies were held constant while the coolant flow per subassembly was increased about 25%. The same thermal fatigue result could have been achieved by holding the total power and the coolant flow rate per subassembly constant and increasing the number of driver subassemblies by about 25%.

In order to make use of the spare EBR-II IHX, two EBR-II IHXs were used in the modified design. The original design used one new IHX similar to but larger than the EBR-II IHX. It would probably be possible to achieve satisfactory thermal fatigue results with a single EBR-II IHX if the total primary and secondary coolant flows were the same as in this modified design, but the IHX pressure drops would be much higher. Thus, there may be a trade-off between paying more money for IHXs or paying more money for larger pumps. Also, note that the modified SCM-100 design is more expensive than the original design, especially in the requirement for larger pumps. In general, design modifications to increase tolerance of beam interruptions increase the cost of the multiplier.

Table 3. ADF SCM-100 and EBR-II design and operating parameters

	EBR-II	SCM-100 original	SCM-100 modified
Power (MWt)	62.5	100	100
Average coolant temperature rise in the core (K)	97	101	81
Peak coolant temperature rise in the hottest subassembly (K)	132	120	96
IHXs	1	1	2
Tubes per IHX	3 248	5197	3 248
Active length of IHX (m)	3.16	3.16	3.16
IHX intermediate flow/primary flow	.71	.68	1.00
Temperature rise across intermediate side of IHX (K)	139	148	81
Primary centrifugal pumps	2	2	2
Intermediate pumps	1	1	2
Pump head, primary (bar)	3.22	2.93	4.20
Pump flow, primary (Kg/s/pump)	242	409	511
Pump head, intermediate (bar)	3.64	4.68	7.93
Pump flow, intermediate (Kg/s/pump)	326	528	482

Table 4. Structural component lifetimes

Component	Lifetime (years) original design	Lifetime (years) modified design
IHX upper tube sheet rim	.48	13.1
Above core shielding	.26	4.9

Table 4 lists the component lifetimes for the modified SCM-100 design, using Eriksson's beam interruption frequency results and using return to power scheme A. Results for the original design are also listed for comparison. The above core shielding lifetime of 4.9 years should be adequate, since subassemblies are normally replaced after three or four years. The upper tube sheet rim lifetime will be adequate if there is any significant improvement (a factor of two or more) in beam reliability.

Conclusions

A beam trip in an accelerator-driven system leads to a rapid temperature transient that contributes to thermal fatigue in various structural components of the multiplier. Going back up to power contributes additional thermal fatigue. In an accelerator-driven system using an accelerator with the reliability of the LANSCE accelerator and using a multiplier not specifically designed to tolerate large numbers of beam interruptions the lifetimes of some structural components would be unacceptably small. A significant improvement in accelerator reliability would be expected with a modern accelerator. If the improvement in accelerator reliability is not enough, then the multiplier design can be modified to tolerate more beam interruptions. The multiplier modifications would add to the cost of the multiplier.

Acknowledgements

This work was supported by the United States Department of Energy under contract No. W-31-109-ENG-38.

REFERENCES

- [1] Magee, P.M., A.E. Dubberley, A.J. Lipps and T. Wu, "Safety Performance of the Advanced Liquid Metal Reactor", *Proceedings of ARS '94 International Topical Meeting on Advanced Reactors Safety*, Pittsburg, Pennsylvania, Vol. 2, pp. 826-833 (April 1994).
- [2] "A Roadmap for Developing Accelerator Transmutation of Waste (ATW) Technology", A Report to Congress, DOE/RW-0519 (October 1999).
- [3] Dunn, F.E., F.G. Prohammer, D.P. Weber and R.B. Vilim, "The SASSYS-1 LMFBR Systems Analysis Code", *ANS International Topical Meeting on Fast Reactor Safety*, Knoxville, TN, pp. 999-1006 (April 1985).
- [4] "The American Society of Mechanical Engineers", *1998 ASME Boiler & Pressure Vessel Code, an International Code*, Section III, Subsection NH, Appendix T, Article T-1432.
- [5] Eriksson, M. *et al.*, "Reliability Assessment of the LANSCE Accelerator System", *Proc. Workshop on the Utilization and Reliability of High Power Accelerators*, MITO, Japan (13-15 October 1998).

ACCELERATOR-DRIVEN TEST FACILITY: MODULAR TARGET AND MULTIPLIER SYSTEM CONCEPT DESIGN DESCRIPTION

M. Cappiello, K. Pasamehmetoglu, E. Pitcher, R. Guffee, W. Chaves, G. Willcutt
Los Alamos National Laboratory

Abstract

The accelerator-driven test facility (ADTF) modular design concept is a target/multiplier configuration that provides optimum flexibility in operation, and testing. The configuration proposed is based on demonstrated technologies and methods that are currently used in existing facilities. It consists of a centrally located target/multiplier experimental cell surrounded by shielding and three adjacent hot-cells. The experimental cell contains the neutron spallation source and two multiplier segments on either side. When assembled the system closely resembles a central spallation target with a surrounding multiplier in cylindrical geometry. At the completion of an irradiation cycle, target and multiplier components are moved into and out of the experimental cell horizontally from the adjoining hot-cells. All primary heat-removal equipment resides in the hot-cells providing for safe operation and maintenance. Scoping calculations show that reasonably high neutron flux levels are achievable over sufficient volume to meet the goals set for transmutation proof of performance tests. Using a safety by design strategy, a combination of active and passive safety features provide diverse and redundant beam shutdown and decay heat removal.

Facility arrangement

The concept is depicted in Figures 1-4, which show the facility isometric, plan view, primary shield isometric, and one possible arrangement for the experimental cell detail, respectively. The beam enters the experimental cell horizontally and impacts directly on the spallation neutron source, which is also inserted and removed horizontally in the opposite direction. The two multiplier segments are also inserted and removed horizontally, perpendicular to the beam-target axis (Figures 3 and 4). A steel-and-concrete shield surrounds the experimental cell, providing unrestricted access to surrounding support equipment. The inside surface of the cell is cooled to maintain the structure at a reasonable operating temperature. The hot-cells are designed such that remote operations may be performed while the beam is on. The physical interface between the target and multiplier segments allows for removal and insertion of a new target without moving the multiplier segments.

The three hot-cells adjacent and connected to the shield provide service to the target and the two multiplier segments, respectively (Figures 1 and 2). The hot-cells contain the primary heat-removal equipment, and all necessary remote handling equipment for replacement and movement of components. Piping that runs through the shield connects the heat-removal equipment to the target and multiplier segments. For the multiplier segments, the hot-cells contain sufficient space for storage of fresh and spent fuel, and space for disassembly and packaging of fuel and material test elements. Similarly for the target hot-cell, adequate space is provided for spent target materials, disposal containers, and material test coupon analysis.

Configurations of this type has been demonstrated successfully at the ISIS (UK), KENS (Japan), and IPNS (US) neutron-scattering facilities and is planned for use in the SNS (US) facility under construction at Oak Ridge, Tennessee. The layouts used in ISIS and SNS are shown in Figures 5 and 6 for comparison. These systems offer superior operational flexibility because it allows for quick replacement of the target, which is necessary to maintain overall facility availability. In the SNS facility, change-out of the liquid mercury target container is planned to take place in five days.

Figure 1. Target/multiplier building isometric

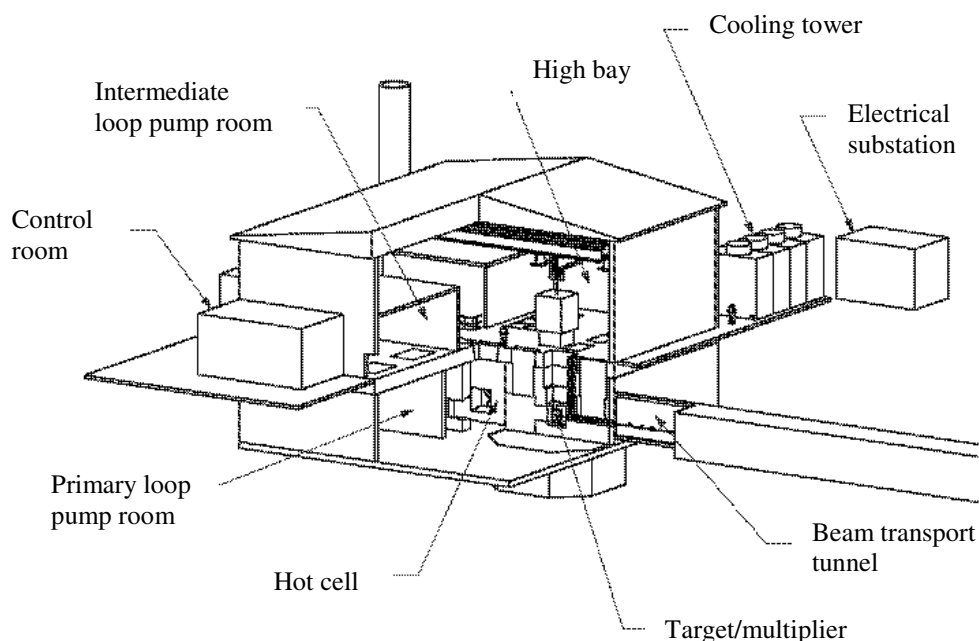


Figure 2. Target/multiplier building plan view

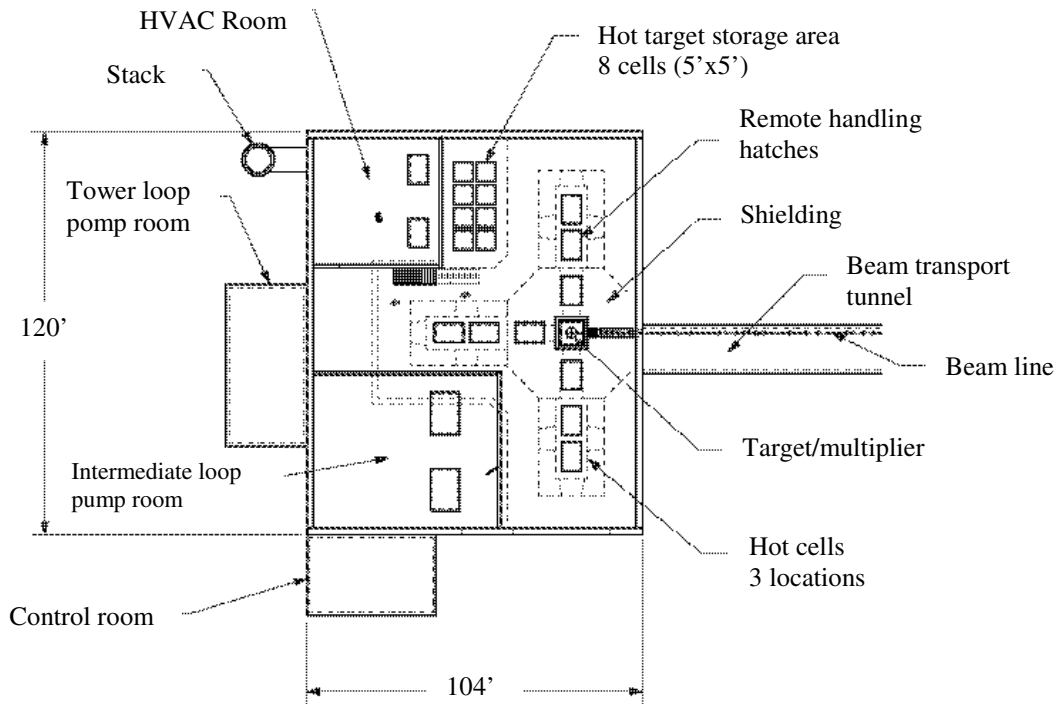


Figure 3. Shield isometric

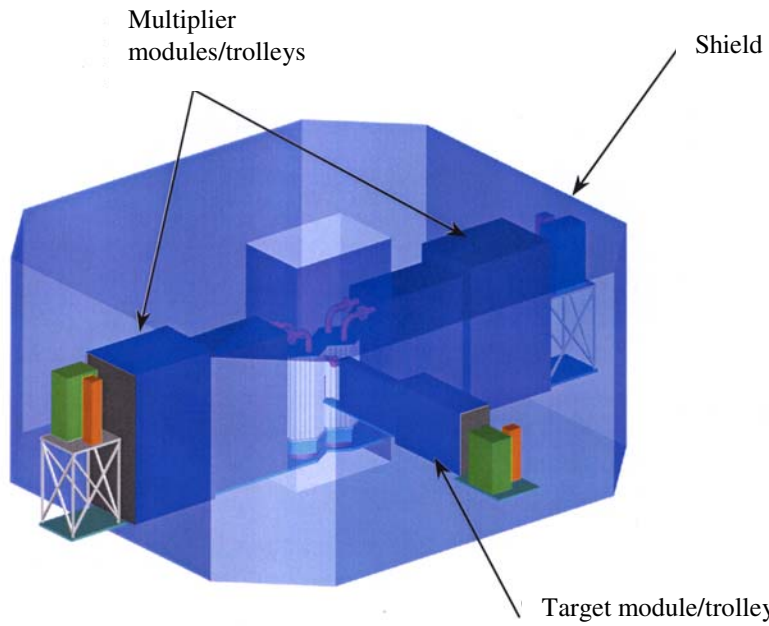


Figure 4. Experimental cell detail

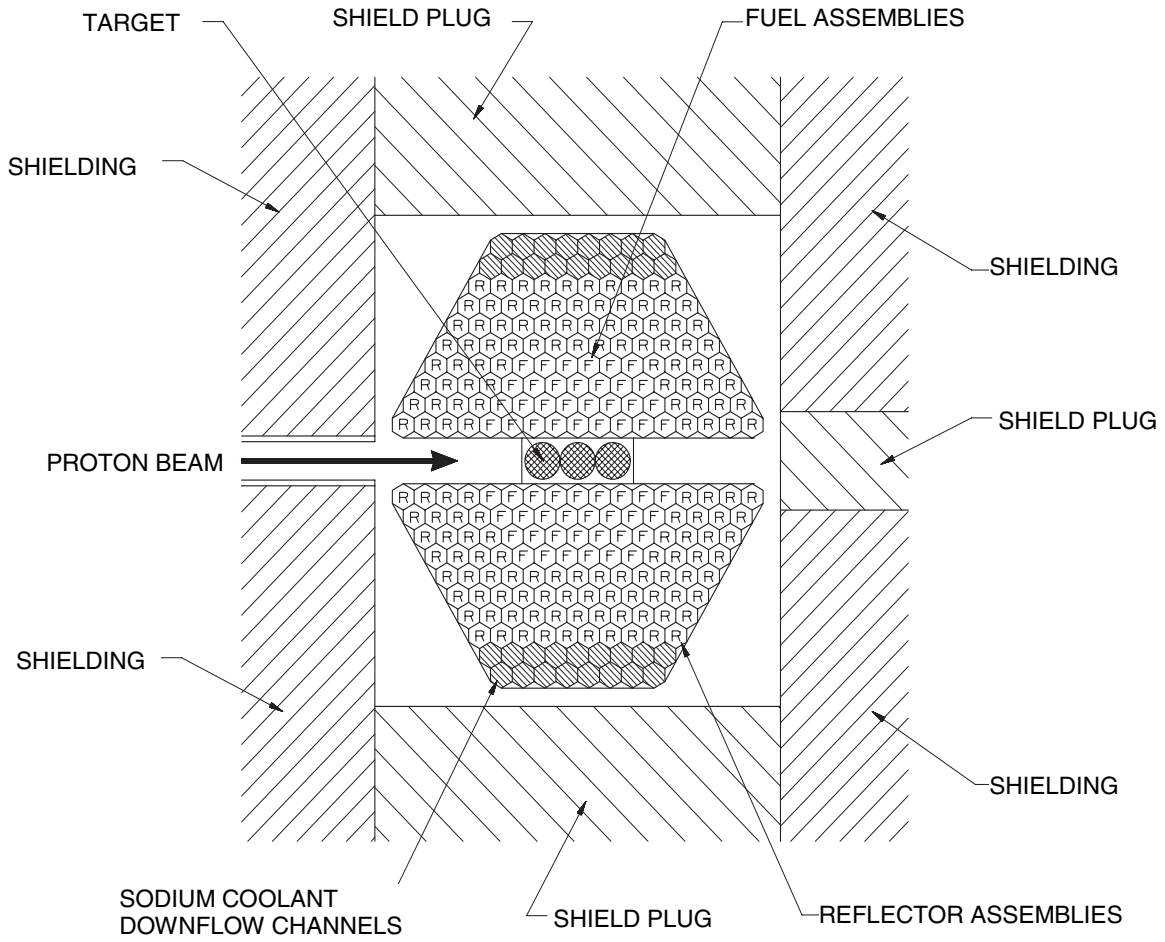


Figure 5. The ISIS facility at the Rutherford Appleton Laboratory

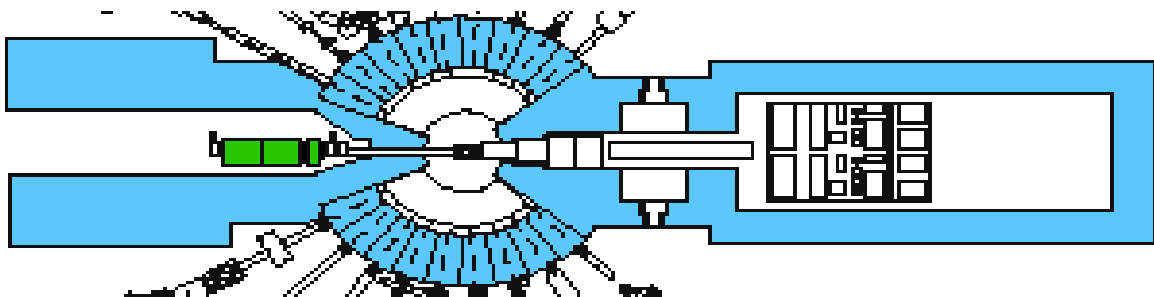
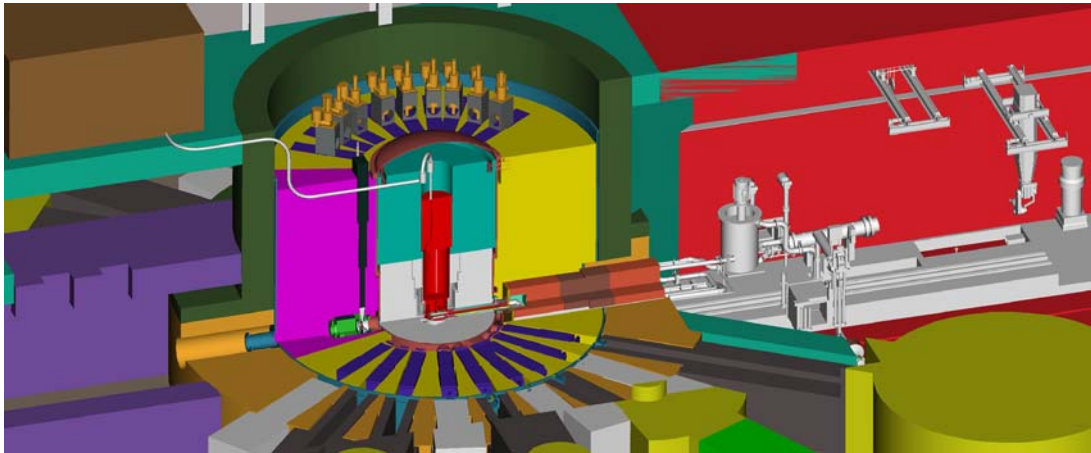


Figure 6. The spallation neutron source target/shield and hot-cell configuration



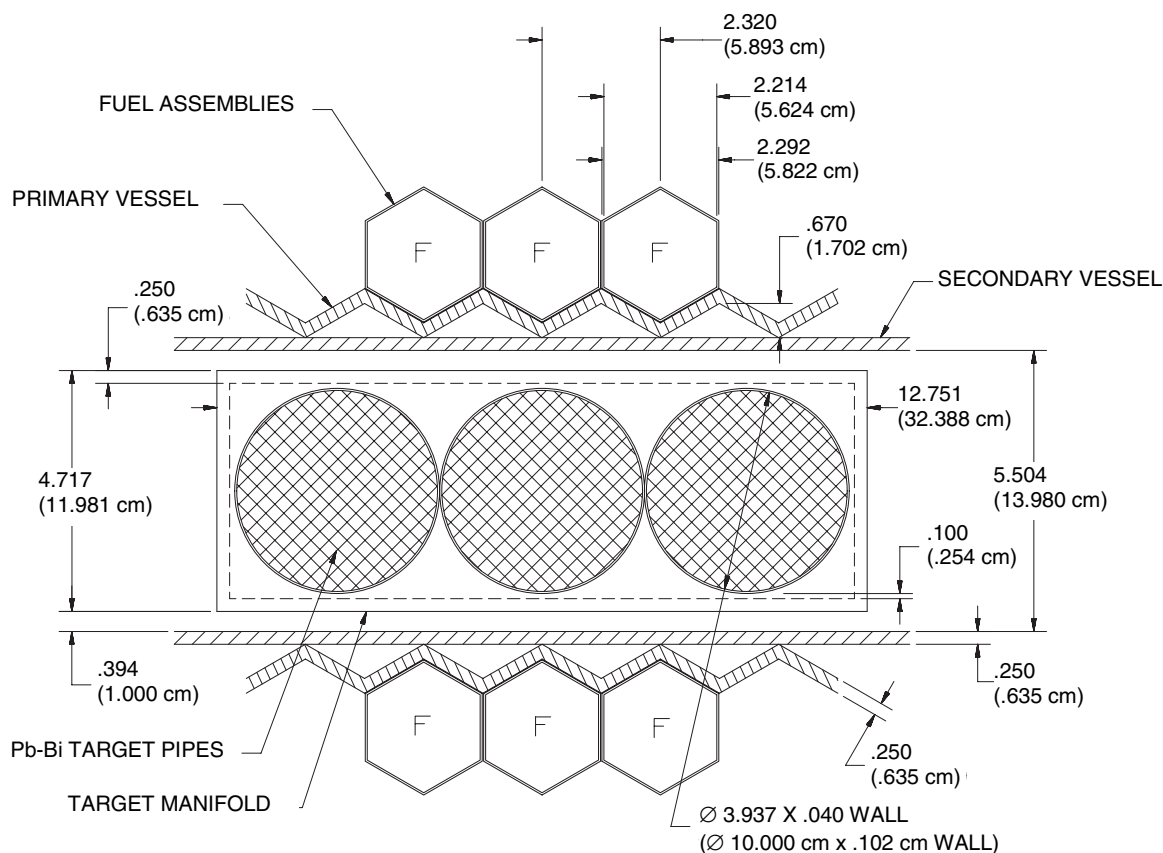
Target

The modular configuration can support the testing of either solid or liquid targets. A liquid target that provides good thermal and neutronic efficiency is the lead/bismuth eutectic (Figure 7). In this target, a row of three stainless steel pipes approximately 10 cm in diameter are positioned between the two multiplier segments. The pipes are positioned vertically, in line with the axis of the beam, and are connected at the top and bottom by inlet and outlet plena, respectively. The plena are connected to piping that runs through the removable shield and are connected to a heat exchanger and pump in the hot-cell. The lead/bismuth eutectic continually flows through the pipes, forming the neutron spallation target when impacted by the proton beam. Because the target material and coolant are the same, the amount of structural material and other low-atomic-number materials that the protons *see* are minimised. This, combined with the fact that lead/bismuth has very low neutron absorption, makes this spallation target very efficient neutronicly. The amount of lead/bismuth in the beam is sufficient to completely stop and *range out* all of the protons.

The proton beam that is delivered to the target will be at approximately 600 MeV, with up to 13 mA of current. The beam enters the experimental cell through a beam pipe in the shield and passes unobstructed to the front face of the first pipe of the target. The beam is expanded or rastered into a beam spot that is approximately 38 cm high by 6 cm wide. This beam-spot distribution and size can be changed, depending on the needs of the experimenter, as long as thermal, hydraulic, and structural limits are not exceeded in the target. Thermocouples on the front face of the target provide the necessary information for the operators to centre the beam. This is a common practice at existing spallation neutron sources. The 38×6 cm beam spot is chosen as a base case because it produces a reasonable power density in the lead/bismuth, and keeps the pipe wall at a reasonable temperature, even at 13 mA of current. If lower beam currents are used, then smaller beam spots are possible.

To provide for material coupon irradiation in the lead/bismuth environment, smaller-diameter pipes would be inserted in parallel with the three target pipes. These can be positioned in between, behind, or in front of the target pipes, depending on the needs of the experimenter.

Figure 7. Lead/bismuth target detail



The stainless steel pipes, which contain the lead/bismuth eutectic, are damaged by proton and neutron irradiation and must be replaced on a regular basis. Depending on the beam current and spot size that is utilized, replacement of the container may be required every 3 to 12 months, which is consistent with the expected multiplier irradiation cycle (e.g., both the fast flux test facility and experimental breeder reactor (EBR-II) operated on a 100-day cycle). To change out the container, the beam is shut down and the liquid is drained into a storage vessel that resides in the adjacent hot-cell. The target insert, which includes the target, piping, heat-removal equipment, and a section of shielding, is moved horizontally back into the hot-cell on rails. Remote manipulators are used to disconnect the target container at the piping-to-plena interface and replace it with the new one. The system is then leak-checked and refilled with the same fluid as before. Some clean-up may be needed (e.g., removal of spallation products) before the lead/bismuth is recycled. The entire assembly is then reinserted into the target cell.

Corrosion is an issue in a lead/bismuth target. An effective way of reducing the corrosion rate is to maintain a protective oxide layer on the pipe surface. For a short-lived target, it may be sufficient to control the initial oxygen content in the system. If necessary, an active oxygen control system can be easily implemented. In an active system, oxygen levels are continuously monitored. When needed, small amounts of oxygen are added to the lead/bismuth. Excess oxygen can be reduced by small additions of hydrogen.

If the use of an lead/bismuth target with a sodium-cooled multiplier is not desirable, an alternative target configuration would be a solid tungsten target with either sodium or helium coolant. This may be necessary for safety reasons because of a potentially exothermic chemical reaction between sodium and lead/bismuth when they are mixed together. Conceptually such a target would be similar to that shown in Figure 7, where tungsten tubes would be nested inside the vertical target pipes. Sodium or helium would flow upwards through the gaps between the tungsten tubes to provide cooling. A tremendous amount of fabrication experience was gained in the APT programme for the solid tungsten option, and would be directly applicable to this application.

To replace a solid target, the cooling fluid would remain flowing on the tungsten until decay heat was sufficiently low that the fluid could be safely drained (or, in the case of helium, removed). Then the target would be disconnected, removed, and replaced with the new one. To maintain adequate availability and provide flexibility in operation, adequate space exists in the hot-cell such that a spare target assembly can be readied for operation while the other assembly is in use. From a waste-generation standpoint, the liquid target offers a substantial advantage over the solid target because only the target container (stainless steel) needs to be replaced on a regular basis. Once radioactive, however, the lead/bismuth becomes a mixed waste and must be handled appropriately at the end of facility life.

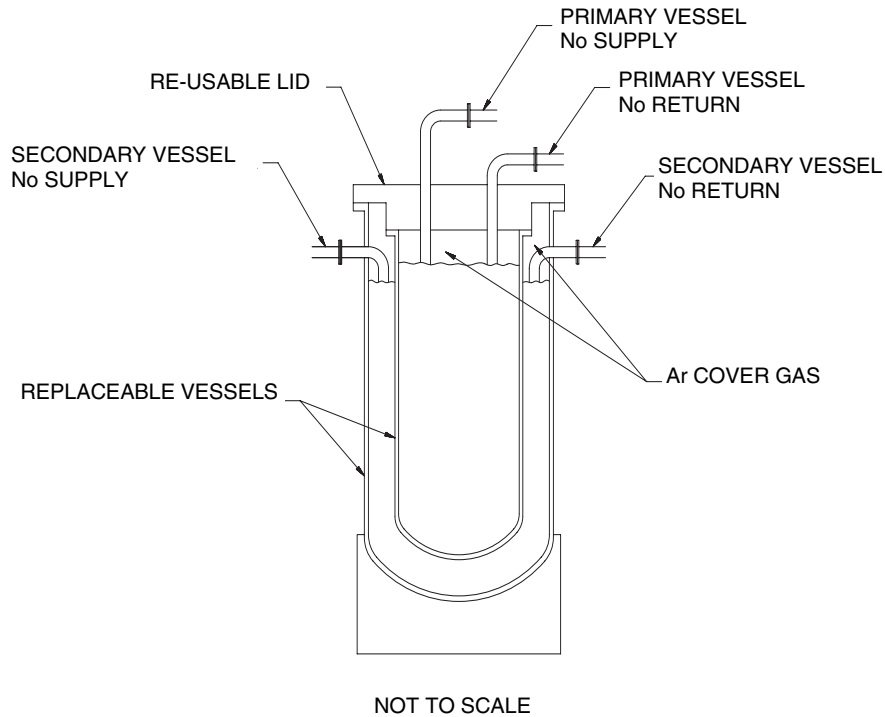
Multiplier

In the modular configuration the multiplier is separated into two segments that are brought in from the side (Figure 3). The segments can be identical or different, depending on the needs of the experimenter. Each segment has an attendant hot-cell similar to the target that allows for safe replacement of components. For the pre-conceptual design a fast-spectrum, sodium-cooled multiplier is being investigated as the base case, and as an option, a helium-cooled thermal-spectrum system that would be implemented using the same experimental cell but different multiplier components. This demonstrates the flexibility of the configuration for testing a wide range of nuclear systems and, therefore, supports both the transmutation and advanced nuclear technology missions. For instance, this concept provides an ideal setting if LBE is pursued as a nuclear coolant for ATW or advanced fast-reactor applications. For the current discussion, only the base-case fast-spectrum system is presented in detail.

For the fast-spectrum system, the fuel and reflector bundles are contained in a small vessel cooled with liquid sodium. As shown in Figure 8, this small primary vessel sits within an enclosed guard vessel that is also sodium-cooled but on a separate circuit. Note that this figure is not drawn to scale, and is used only to depict the principal concept. The heat-removal system for the primary vessel is configured to provide natural circulation decay-heat removal in the event of loss of forced flow. In addition, the flow of sodium in the guard vessel is sufficient to remove the decay heat, providing a redundant heat-removal mechanism. Diverse, redundant beam shutdown ensures that whenever cooling is degraded to the multiplier segments or the target, the beam is shut down with very high confidence through fail-safe connections to the accelerator injector.

Although not shown in Figure 3, the fuel or assemblies can easily be replaced with fuel test assemblies and material irradiation tests. Experimenters would position these assemblies and fuels to optimise the irradiation environment they seek. In the event that an experimenter desires a thermal flux over a small volume (for testing long-lived fission product targets), a reflector position could be replaced with an assembly containing yttrium hydride moderator to locally thermalise the neutron spectrum.

Figure 8. Multiplier vessel component



Depending on the flux level achieved, the small vessel components used in the multiplier will need to be replaced on a 1-3 year interval. In the conceptual design state, strategies to extend the vessel's lifetime will be pursued. For instance, designing an axisymmetric vessel capable of being rotated periodically will be considered. This will be performed in a manner similar to the target replacement. An inert atmosphere in the hot-cell will allow the safe removal of fuel elements out of the vessel and into storage or removal to a disassembly and packaging area. When fuel needs to be replaced or shuffled after an irradiation cycle or experiment bundles need to be removed, the vessel is moved into the hot-cell, and the operations are performed in the inert environment.

Heat removal

Because the primary coolants for both the target and multipliers will become highly radioactive, the heat exchangers and pumps are located in their respective hot-cells. Secondary coolants are pumped into the hot-cells to provide the necessary heat-removal capability. The heat from the secondary loop is dissipated to the environment through dump heat exchangers. The facility will not use the heat to run a steam cycle and produce electricity. The secondary system is modular such that increased heat-removal capability can be added in future facility upgrades. To support a helium-cooled primary system, the secondary system must have sufficient heat-removal capability with a compatible working fluid. Adequate space in the facility is provided to add this additional heat-removal equipment as well.

Although the accelerator will be designed to provide high reliability, a number of beam trips of both short and long duration are expected during the irradiation cycle. The structures and components that make up the primary heat-removal systems for both the target and the multipliers will be designed for the ensuing temperature transients in order to reduce transient stresses to allowable levels. Components that reach end-of-life due to fatigue will be engineered for easy replacement.

The inner lining of the target cell, which will be made of steel, is designed to last the life of the facility. Because of the intense radiation from the target and multipliers, the liner will need to be cooled to maintain a reasonable operating temperature, which is dictated by structural limits. The total heat load is expected to be in the kW range. The preferred heat removal will be performed with a passive system either using natural circulation or heat pipes.

On the secondary side, we are considering helium as the working fluid. This design will avoid the potential of sodium leaks and fire outside the hot-cell. In addition, because helium is compatible with all conceivable primary coolants, it provides additional flexibility for future multiplier test options (including water).

Beam transport

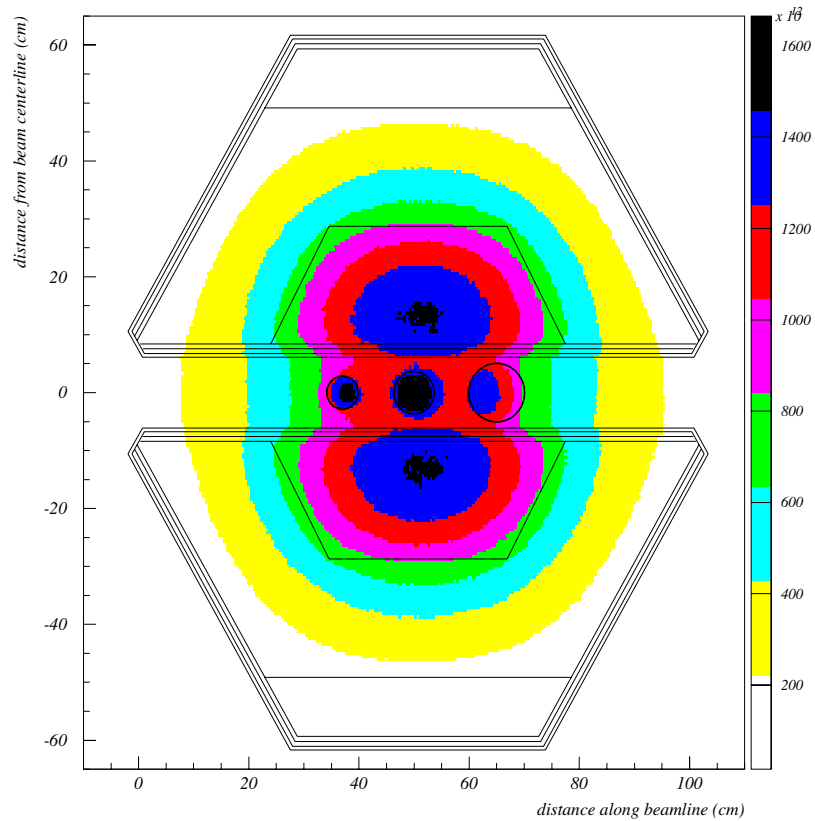
The proton beam is transported from the end of the accelerator to the target/multiplier building using the standard bending magnet and beam tube technology employed for the APT design. Vacuum pumps maintain the hard vacuum necessary for low-loss beam transport. Elevation of the beam is identical to that of the centroid of the target such that no vertical axis beam bending is required. Before entering the shielded experimental cell, a series of beam expansion and/or raster magnets are used to send the beam on a trajectory that provides the desired beam-spot distribution at the front face of the target. Assuming a raster system is acceptable (as was the case for APT), a beam distribution can be provided that is uniform with variations less than 10% over the desired area. Impact of a rastered beam on the neutronic fluctuations and cyclic thermal stresses will be assessed in deciding on the beam expansion strategy. For the beam to transport to the front face of the target with little or no loss, a relatively hard vacuum is required. To provide this vacuum level in the experimental cell without using a beam entrance window, vacuum pumping will be provided along the beamline, through the expansion chamber, and to the experimental cell. Vacuum seals for the target and multiplier inserts in the low-radiation zone on the outside of the shield provide the necessary pressure boundary. Redundant, fast-acting valves in the beamline outside the shield and upstream of the expansion magnets provide protection for the accelerator beamline in the event of the leak into the experimental cell. Any leak into the experimental cell, either from a seal failure or a container failure, automatically shuts down the accelerator, even if the active systems fail because the beam cannot be accelerated without sufficient vacuum. This provides a passive beam-shutdown mechanism in the event of either target container or multiplier guard vessel fails.

Irradiation environment

Initial scoping calculations have been performed on the fast-spectrum sodium-cooled multiplier system. For this analysis a total inventory of 339 kg of heavy metal was assumed in a core made up of 60 EBR-II type fuel assemblies. The fuel was assumed to be the standard EBR-II uranium/zirconium alloy metal with an enrichment of 67%. The resulting static k_{eff} of the system is 0.85. With the target operating at a power of 2.3 MW (beam current of 8.35 mA), the resulting power level in the two multipliers is approximately 20 MW, total. As shown in Figure 9, at this power level, the calculated peak neutron flux in the fuel is 2×10^{15} n/cm²/s, and the average neutron flux over the fuel volume is

1×10^{15} n/cm²/s. It is a significant advantage for the modular configuration that the spallation neutron-source distribution can be tailored to be uniform in the axial direction by control over the beam spot. This provides a uniform axial power distribution in the adjacent fuel over its full height, and therefore makes efficient use of the fuel.

Figure 9. Flux distribution in the target/multiplier



Fuel

For the two options being considered (fast-spectrum or thermal-spectrum), the fuel is vastly different. For the base-case fast-spectrum system EBR-II fuel is assumed, and for the thermal-system, unused Fort Saint Vrain fuel is assumed. Only the EBR-II fuel is discussed here.

The EBR-II fuel was made at the Argonne National Laboratory-West (ANL-West) outside Idaho Falls, Idaho. Approximately 32 subassemblies' worth of fuel slugs is in storage. The equipment used to fabricate the fuel and put it into the assemblies is in storage and can be reconstituted at a reasonable cost (few \$M). The facility used to fabricate the fuel is still in operation, performing other fuel-related tasks. Plans are to keep it operating for the future. To operate the ADTF, approximately 60 subassemblies will be required for a full load. However, it is expected that operation will start with a smaller amount of fuel and low multiplication constants, and then gradually work up to higher

power. Thus, 30 subassemblies may be sufficient for initial operation. Nevertheless, the fuel fabrication line at ANL-West should be set up starting approximately 3 years before beginning ADTF operation in order to provide the necessary fuel.

Because this fuel is fully qualified and demonstrated for a fast reactor operation, we assume we will use this exact fuel design for our *driver* fuel. The specifications and dimensions assumed are shown in Table 1. These dimensions are consistent with the sketches shown in Figures 4 and 7. As shown in the table, the uranium enrichment used in EBR-II was 67%. For our purposes, this is considered to be a maximum value. Lower enrichments are possible by blending in more natural uranium. This can be accommodated at the fuel fabrication facility. It is expected that varying the enrichment in the multiplier will be used to flatten the power distribution in the radial direction.

The environment in the current design is similar to but not identical to the EBR-II. In addition to the typical fast reactor spectrum, there is also some fraction of high-energy particles (scattered protons and spallation neutrons), especially in the row closest to the spallation target. Because of accelerator trips, the fuel and structures will experience a higher thermal cycling rate than in a critical reactor environment. Therefore in the early phase of operation, it is expected that the fuel-operating parameters (e.g., temperature, power density, maximum burn-up) will be limited to values more conservative than the limits used in the EBR-II.

Table 1. EBR-II Fuel and assembly specifications

Feature/dimension	Value
Fuel slug diameter	0.173 inch
Fuel slug length	13.5 inches
Fuel alloy	U10Zr
Uranium enrichment	67%
Clad diameter	0.230 inch
Clad thickness	0.015 inch
Slug to clad bond material	Sodium
Number of fuel rods per assembly	61
Pin to pin spacer	Wire wrap 0.042 inch diameter
Pin arrangement	Triangular pitch
Assembly duct	Hexagonal
Duct flat to flat distance inside	2.214 inches
Duct thickness	0.039 inch
Hex assembly pitch	2.320 inches

Safety features

The design strategy for the modular concept embraces the safety-by-design principal. During all phases of the design, safety features will be designed into the system initially rather than as an afterthought. For the modular design, the goal is to provide an overall level of safety that meets or exceeds that of advanced nuclear systems. Several features are used to meet that goal and are summarised below.

Beam shutdown

For subcritical systems, the beam acts as the power switch for the multiplier. With the beam off, the multiplier power quickly reaches decay-heat levels with a time transient behaviour similar to that of a critical reactor. In reactor terms, it can be thought of as an instantaneous control rod because it takes only microseconds to shut off once the trip signal is received.

There are several ways to shut down the beam, including turning off power to the accelerating cavities or the injector or losing vacuum in the beam tube. The easiest way is to turn off the beam at the injector. Several low-power switches must be simultaneously closed and the components operating correctly in order for the injector to provide the initial proton beam to the first accelerating structure. We will use these basic features to provide diverse and redundant beam shutdown. This system is fail-safe and will be implemented as a safety-class feature into the facility. For example, to protect against a loss-of-flow incident in the multiplier, a simple permanent magnet flow meter may be used in the primary sodium loop. The electric current created by the flowing sodium in the magnetic field acts as a flow switch and is connected directly to the injector. The current must be *on* for the injector to operate. The resulting fail-safe mechanism protects against any type of accident that causes flow to be reduced or to cease in the primary heat-removal system. Similar signals can be used in the guard vessel, target, and secondary coolant systems.

Another inherent safety feature of the modular configuration is derived from the fact that the experimental cell environment is connected directly to the accelerator vacuum. Active systems will shut the beam down in the event of loss of vacuum in the experimental cell or the beam pipe itself. Multiple, fast-acting valves in the beam transport line just upstream of the experimental cell shield will quickly close to protect the accelerator. In the extremely unlikely event that automatic shutdown does not occur, beam shutdown will occur naturally because it cannot be accelerated without sufficient vacuum. This provides a passive beam shutdown mechanism in the event the multiplier guard vessel, the target, or the vacuum seals leak.

Power and reactivity

To prevent over-power events, physical constraints are used in the injector to prevent the accelerator current from exceeding a pre-set value for the run cycle. The multiplier segments are designed so the multiplier is in its most reactive position during operation. Physical constraints on the vessels prevent the segments from moving closer together. Thus, the fuel cannot reach criticality unless reconfigured due to melting and pooling of the fuel

Decay-heat removal during postulated accidents

To preclude the possibility of accidental melt-driven criticality for all credible accidents, the fuel-assembly geometry is maintained by providing diverse and redundant decay-heat removal. The heat-removal system for the primary vessel is configured to provide natural circulation decay-heat removal in the event of loss of forced flow. In addition, the flow of sodium in the guard vessel is sufficient to remove the decay heat, providing a redundant heat-removal mechanism for both loss-of-flow and loss-of-coolant events in the primary system. A more detailed assessment of the decay-heat removal strategies for a variety of design basis accident initiators continues. Event trees are being developed to identify all the necessary mitigation systems and components.

Containment

The experimental cell and its shield form the containment boundary for the target/multiplier. Because a good vacuum level is required to operate the multiplier, the integrity of this system is being checked continuously during operation. The hot-cells offer excellent containment of upsets in the cooling loops. Because they operate in an inert argon atmosphere, coolant leaks can occur without the possibility of sodium fire. We are considering the use of helium in the secondary loop, as discussed previously. Thus, no liquid metal will exist outside the hot-cell.

Summary

The modular configuration for the ADTF offers a flexible system that can provide the test and irradiation environments necessary to demonstrate transmutation technologies and advanced nuclear systems. Horizontal beam insertion provides for a simple, straightforward beam transport system from the accelerator to the target/multiplier. Horizontal target and multiplier insertion configuration is a demonstrated technology based on existing and planned facilities such as the Spallation Neutron Source. A prototypic materials-irradiation environment is achieved for both the target and the multiplier regions with a flexible system for removal and retrieval. The base-case fast-spectrum design employs a driver-fuel design whose performance is predictable based on a previously established database. Upgrade to higher power levels (e.g., 100 MW) can be implemented using more fuel and an expandable heat-removal system.

Analyses show that using this design configuration, one can produce neutrons with a spectrum prototypical of the current base-case ATW system, which is envisioned to employ a sodium-cooled multiplier and a lead-bismuth target. The environment is achieved with a lead/bismuth target and sodium-cooled multiplier with a k_{eff} between 0.8 and 0.97. Calculations show a fast-spectrum flux level greater than 1×10^{15} n/cm²-s is achievable using metal fuel. The total multiplier power level is approximately 20 MW at this flux level. Because the beam is delivered to the target and multiplier horizontally, neutron source distribution can be tailored to provide a uniform flux over the length of the fuel.

The target/multiplier and beam shutdown systems are designed with the maximum reliance on passive safety features. Natural circulation of coolants for both the target and multiplier segments and diverse cooling mechanisms provide adequate protection in the event of accidents. In the event of a leak or break in either the target or multiplier pressure boundary inside the experimental cell, the loss of vacuum will passively shut down the beam.

Additional assessments in support of the pre-conceptual design continue. The on-going studies include neutronic and thermal-hydraulic sensitivity studies for different design options. Also, an initial assessment for the damage rates and the relevant structural design criteria is being developed. Decay heat removal strategies for a variety of design basis accidents and operational transients also are being assessed. In addition, different operational options are being identified for further considerations during the conceptual design phase. At the pre-conceptual design stage, some of the assessments will be qualitative in nature, especially for the support systems. These assessments will be used to guide the more quantitative design studies planned for the conceptual design phase.

LEAD-BISMUTH SPALLATION TARGET DESIGN OF THE ACCELERATOR-DRIVEN TEST FACILITY (ADTF)

**Yousry Gohar, Phillip Finck, Albert Hanson¹, Joe Hecceg, Maria Koploy², Lubomir Krajtl
Panto Mijatovic², W. David Pointer, James Saiveau, Tanju Sofu, Michael Todosow¹**

Argonne National Laboratory, Argonne, IL 60439, USA

¹Brookhaven National Laboratory, Upton, NY 11973, USA

²General Atomics, San Diego, Ca 92121, USA

Abstract

A design methodology for the lead-bismuth eutectic (LBE) spallation target has been developed and applied for the accelerator-driven test facility (ADTF) target. This methodology includes the target interface with the subcritical multiplier (SCM) of the ADTF and the different engineering aspects of the target design, physics, heat-transfer, hydraulics, structural, radiological, and safety analyses. Several design constraints were defined and utilised for the target design process to satisfy different engineering requirements and to minimise the time and the cost of the design development. Interface requirements with the subcritical multiplier were defined based on target performance parameters and material damage issues to enhance the lifetime of the target structure. Different structural materials were considered to define the most promising candidate based on the current database including radiation effects.

The developed target design has a coaxial geometrical configuration to minimise the target footprint and it is installed vertically along the SCM axis. LBE is the target material and the target coolant with ferritic steel (HT-9 Alloy) structural material. The proton beam has 8.33 mA current uniformly distributed and 8.14 cm beam radius resulting in a current density of $40 \mu\text{A}/\text{cm}^2$. The beam power is 5 MW and the proton energy is 600 MeV. The beam tube has 10 cm radius to accommodate the halo current. A hemi-spherical geometry is used for the target window, which is connected to the beam tube. The beam tube is enclosed inside two coaxial tubes to provide inlet and outlet manifolds for the LBE coolant. The inlet and the outlet coolant manifolds and the proton beam are entered from the top above the SCM. The paper describes the design criteria, engineering constraints, and the developed target design for the ADTF.

Introduction

Design methodology and spallation target design have been developed to generate the required neutron source for the subcritical multiplier (SCM) of the accelerator-driven test facility (ADTF). The ADTF is a major nuclear research facility that will provide multiple testing and production capabilities. The main ADTF mission includes the capability to assess technology options for the transmutation of spent nuclear fuel and nuclear waste through proof-of-performance demonstrations. The transmutation target station consists of a spallation target and a SCM with a power rating up to 100 MW. This SCM will provide the prototypic environment necessary to support the transmutation proof of performance. In addition, a target and material test station will be used to test a wide range of target designs, fuel assemblies, and coolants for developing components for the SCM. The work presented in this paper is intended to cover the design methodology and to introduce the SCM lead-bismuth target design.

A design methodology was developed to guide the target design process and to satisfy the target design requirements. Different engineering constraints were also developed to insure satisfactory target performance based on the current experience and the existing database. The physics analyses were performed using the Monte Carlo code MCNPX [1] to account for the geometrical details, the spallation process, and the production and the transport of the spallation particles and the generated photons. The thermal hydraulic analyses were performed to define the velocity distribution and the flow stability of the lead-bismuth eutectic and the temperature distribution in the target structure and the target coolant. The analyses utilised the commercially available computational fluid dynamics (CFD) software package STAR-CD [2] to account for the intrinsic feature of the target design. Structural analyses were performed in conjunction with the thermal hydraulics to check the design compliance with the stress and buckling design criteria developed for the accelerator production of tritium project [3] and the international thermonuclear experimental reactor [4] for irradiated structural materials. The results are used to select the shape and thickness of the beam window to maximise the engineering margins. Radiological analyses were performed to define the spallation products. These products define the radiological toxicity and the decay heat source from the lead-bismuth target material as function of the time after shutdown. The design analyses utilise the decay heat source to check the design performance during normal and abnormal conditions with respect to the maximum allowed temperature for the structural material. Also, the dose rate from the gamma rays of the LBE spallation products was calculated to define the required input for calculating the appropriate time and the shielding requirements for maintaining the target system. All these analyses were iterated to achieve a target design that satisfies the design constraints and the design requirements.

The spallation target design is based on a coaxial geometrical configuration to satisfy the SCM configuration requirements for minimising the space requirements and to maximise the SCM utilisation of the spallation neutrons. The target is installed vertically along the SCM axis. Lead-bismuth eutectic (LBE) is the target material and the target coolant. Ferritic steel (HT-9) Alloy is the selected structural material for the target based on the current database and the design analyses. Austenitic steel (Type 316 stainless steel) is the second choice. A uniform proton beam is employed to perform the spallation process. The beam power is 5 MW and the proton energy is 600 MeV. The inlet and the outlet coolant manifolds and the proton beam are entered from the top above the SCM. The LBE flow cross-section area is maintained at a constant value along the axial direction to maintain a constant average velocity, which improves the target hydraulic design. The geometrical configuration has been carefully designed to insure flow stability and adequate cooling for the beam window and the structure material. Target design objectives were defined for the design process. Several design constraints are defined and used in the target design process to satisfy different engineering

requirements, to minimise the design development time and cost, to insure a satisfactory operating performance, and to maximise the operating lifetime of the target structural material.

Design requirements, engineering constraints, and design criteria

The main objective of the target design is to generate the required neutron source to drive the SCM. The neutrons are generated from the spallation process driven by the 600 MeV proton beam. The beam has a total power of 5 MW and it has a uniform spatial distribution over the beam cross-section area. The SCM design requires a small target diameter to simplify the fuel and the target replacement procedures, to reduce the neutron losses in the beam direction, to decrease the shield volume, and to lower the required number of the SCM fuel assemblies for a specific power level. However, the structural material and the heat transfer considerations require a large beam diameter to reduce the energy deposition and the irradiation damage densities in the beam window. A $40 \mu\text{A}/\text{cm}^2$ current density was selected as a compromise to satisfy the engineering requirements for the window design and to extend its operating life without a significant impact on the SCM design. The other main objectives for the target design are to protect the SCM from the high-energy protons and neutrons, to contain the spallation products, to help achieving the availability goal of the facility, and to reduce the shut down time for target replacement during normal and abnormal conditions. Also, the target has to generate a uniform neutron source along the beam axis as much as possible to minimise the SCM axial power peaking.

Several design constraints are imposed on the target design process to satisfy different engineering requirements and to minimise the design development time and cost. Existing structural materials, HT-9 Alloy is the selected structural material for the target design. LBE is used as a target material and coolant to simplify the design. The surface temperature of the structural material in contact with the LBE is limited to less than 550°C to reduce erosion and corrosion concerns. This temperature limit assumes that the coolant chemistry is controlled to maintain an oxide layer on the structural material surface for corrosion protection. The stress analysis of the irradiated structural materials limits the maximum temperature to less than 550°C for HT-9. The average coolant velocity is limited to ~ 2 m/s based on the current database to avoid erosion and corrosion concerns. The coolant pressure is minimised to avoid high primary stresses in the structural material. The selected coolant inlet temperature is 200°C , which provides adequate design margin above the LBE melting point of 129°C . The outlet temperature is constrained by the maximum allowable temperature for the structural material. Heat conduction to the back shine shield in the beam tube, natural convection, and radiation to the sodium pool are used for decay heat removal. These objectives and constraints are utilised to develop the target design.

The ability of the target structure to withstand the mechanical and thermal loads is determined by comparing the induced stresses to allowable stresses based on the APT supplemental structural design requirements, the international thermonuclear experimental reactor, and the ASME Code. The allowable stresses take into consideration the change in the mechanical properties due to the radiation exposure. The ANSYS general-purpose finite element code [5] was used with a two-dimensional axisymmetric finite element model for the target. The LBE hydrostatic pressure load and the thermal stresses caused by the temperature gradient in the target structure were used in the ANSYS analysis. The buckling capabilities of the structure were initially evaluated using the ASME code. Then, a non-linear buckling analysis was performed using ANSYS code.

Design description and analyses

The proton beam has a total current of 8.33 mA distributed uniformly over a circular cross-section. The beam radius is 8.14 cm with a current density of $40 \mu\text{A}/\text{cm}^2$. The beam tube has 10 cm radius to accommodate the halo current. A hemi-spherical geometry is used for the target window, which is connected to the beam tube. The beam tube is enclosed inside two coaxial tubes to provide inlet and outlet manifolds for the LBE target coolant. The double function of the LBE as a target material and coolant does simplify the design. The radii of these tubes were adjusted to achieve the same average velocity in the inlet and the outlet manifolds. The outer manifold is used for the inlet flow for efficient beam window cooling. The edge of the inside tube between the inlet and the outlet flow is terminated with a rounded fairing to improve the flow stability. The fairing is tangent to the inlet side surface of the middle wall and extends into the outlet flow field. The geometrical details of the target design are shown in Figure 1. A guard tube is used to enclose the target. It provides a confined space to check and contain any LBE leakage. Also, this space provides a buffer between the SCM sodium pool and the LBE. Helium gas at low pressure is used to fill this space. HT-9 Alloy is the structural material. The LBE oxygen concentration is maintained in the range of 10^{-6} to 10^{-4} at.% to avoid corrosion concerns.

The beam tube enters the subcritical multiplier building horizontally above the subcritical multiplier. Then the beam is bended 90° to reach the subcritical multiplier. The vertical section of the beam tube is ~ 14.1 m after the last bending magnet. The coolant manifolds have a vertical length of about 10.1 m before changing direction to connect horizontally with the external section of the LBE loop. Pressurised helium gas is used to heat the target tubes before the target is filled with the LBE material. Also, helium is utilised to drain the LBE using a small vertical tube(s) of ~ 1 cm diameter, which reaches the target bottom section. In the target replacement procedure, the LBE is drained before the target tubes are disconnected for removal. The overhead crane is used to pull the empty target structure inside a target replacement cask.

Inside the guard tube, chemical and pressure sensors are used to check for Na or LBE leakage to shut down the target operation. This early warning avoids the possibility of mixing the two fluids, which reduces the maintenance down time and improves the safety performance. The beam tube vacuum is also monitored to detect any LBE leakage through the beam window.

The target design analyses were iterated using the design methodology shown in Figure 2. A sample of the results is discussed to highlight the performance parameters of the target design. MCNPX computer code was utilised to calculate spatial neutron distribution shown in Figure 3 and the energy spectrum of the spallation neutrons, the energy deposition in the target material displayed in Figure 4, and the nuclear responses in the beam window given in Table 1. In this target design, the proton beam generates a total of 10.3 neutrons per proton from which 7.8 neutrons are utilised for the SCM. In the beam window, the neutrons are responsible for 69% of the atomic displacement and the protons are generating more than 96% of the gas production rate. The neutron distribution peaks at ~ 12 cm from the upper surface of the lead-bismuth material while the high-energy neutrons (above 20 MeV) peak at ~ 14.5 cm. The peak to the average is 1.33 and the peak to the minimum is 4.11. The peak energy deposition value is $796 \text{ W}/\text{cm}^3$ at 1.75 cm from the LBE surface.

The thermal hydraulic characteristics of the evaluated target geometries were simulated using the commercially available CFD code STAR-CD and the temperature distribution of the target structure was transferred to the structural analyses. The simulation uses a uniform inlet velocity of 2 m/s and an inlet temperature of 220°C . Sufficient inlet and outlet manifold length is included to insure fully developed velocity and temperature profiles. Velocity and temperature profiles are shown

in Figure 5. The peak structural temperature is 501°C and the maximum LBE interface temperature is 340°C.

The ability of the target to withstand the mechanical and the thermal loads is determined by comparing the induced to allowable stresses. A stress analysis was performed to develop a beam window configuration, which would satisfy the stress and the buckling criteria. The ANSYS general-purpose finite element code was used with a two-dimensional axi-symmetric finite element model for the target. The LBE hydrostatic pressure load and the thermal stresses caused by the temperature gradient in the target structure were used. The buckling capabilities of the structure were initially evaluated using the ASME code. Then, a non-linear buckling analysis was performed using ANSYS code. Table 2 shows the calculated stresses during operation versus the allowable stresses for HT-9 with 72 dpa [6].

Radiological analyses were performed to define the spallation products. These products define the radiological toxicity and the decay heat source from LBE as function of the time after shutdown. The design analyses utilised the decay heat source to define the design performance during abnormal conditions with respect to the maximum allowed temperature for the structural material. Also, the dose rate from the gamma rays of the LBE spallation products was calculated to define the required input for calculating the appropriate time and the shielding requirements for maintaining the target system. The loss of flow analysis show that the management of the decay heat in the ADTF LBE target design does not require an active engineering system for the decay heat removal [6].

Conclusions

A target design methodology has been developed and successfully utilised for the LBE target of the subcritical multiplier station of the accelerator-driven test facility. In the design process, design objectives and engineering constraints were defined and satisfied. The target design has a coaxial geometrical configuration and HT-9 structural material, which achieves the ADTF design goals.

Acknowledgements

The submitted manuscript has been created by the University of Chicago as Operator of Argonne National Laboratory (“Argonne”) under contract No. W-31-109-ENG-38 with the US Department of Energy. The US Government retains for itself, and others acting on its behalf, a paid-up, nonexclusive, irrevocable world-wide license in said article to reproduce, prepare derivative works, distribute copies to the public, and perform publicly and display publicly, by or on behalf of the Government.

REFERENCES

- [1] Waters, L.S., Editor, MCNPX User's Manual – Version 2.1.5, TPO-E83-UG-X-00001, Revision 0, Los Alamos Report, November 14, 1999 and Version 2.4.j.
- [2] Star-CD Version 3.1B, CD-Adapco Group.
- [3] Supplemental Structural Design Requirements, PPO-P00-G-PRD-X-00006, Rev. A.
- [4] Majumdar, S. and P. Smith, Treatment of irradiation effects in structural design criteria for fusion reactors, Fusion Engineering and Design 41, 1998.
- [5] ANSYS Version 5.7, ANSYS, Inc., 2000.
- [6] Gohar, Yousry, Phillip Finck, Albert Hanson, Joe Herceg, Maria Koploy, Lubomir Krajtl, Panto Mijatovic, W. David Pointer, James Saiveau, Tanju Sofu, and Michael Todosow, "Lead-Bismuth Target Design for the Sub-critical Multiplier (SCM) of the Accelerator-driven Test Facility (ADTF)", Argonne National Laboratory Report, ANL/TD/02-01, 2002.

Table 1. Beam window nuclear responses

Energy deposition, W/cm ³	766.49
Atomic displacement, pa/y	
Neutrons	46.2
Protons	21.1
Total	67.3
Helium production, appm/fpy	
Low energy neutrons ≤ 20 MeV	5.7
High energy neutrons > 20 MeV	50.2
Protons	1 437.3
Total	1 493.2
Hydrogen production, appm/fpy	
Low energy neutrons ≤ 20 MeV	6.3
High energy neutrons > 20 MeV	1 010.1
Protons	26 753.1
Total	27 769.5

Table 2. Calculated stresses and HT-9 allowable stresses for the 3.5 mm spherical beam window

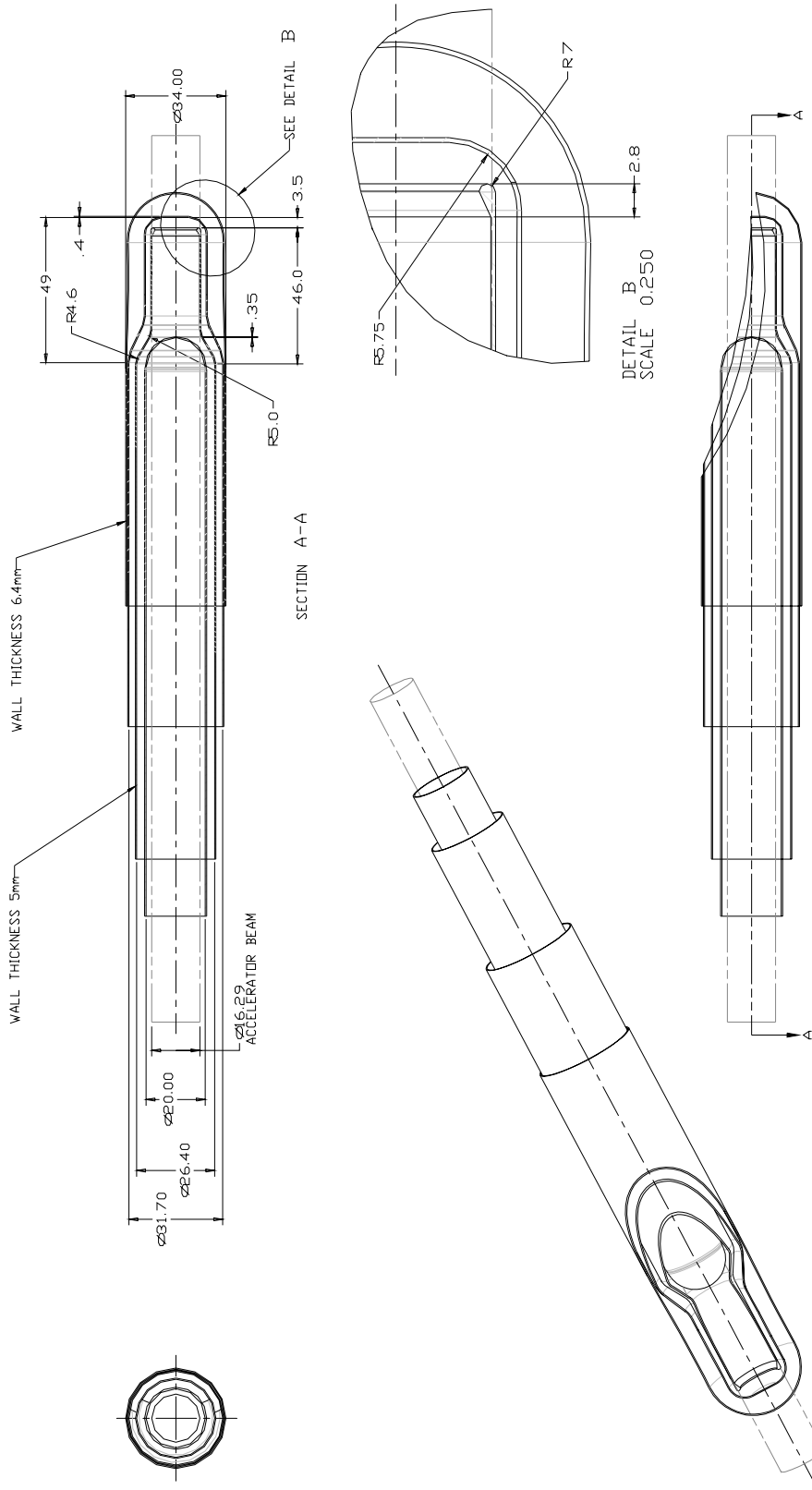
Stress component	Allowable stress	Calculated stress (MPa)	HT-9 allowable (MPa)	Temperature (°C)
P_M	S_m	23.6	181*	277
P_L+P_B	$K_{eff} S_m$	24.3	---**	277
P_L+Q_L	S_e	56.9	181	417
P_L+P_B+Q+F	S_{d1}	423.5	---***	500
P_L+P_B+Q	S_{d2}	374.2	386	500

* The allowable is calculated at the maximum temperature (417°C) to be on the conservative side since the S_m value is not available at 277°C.

** Larger or equal to S_m .

*** Larger than S_{d2} .

Figure 1. Lead-bismuth eutectic target design



Pb_Bi
 LEAD_BISMUTH_TARGET
 SCALE: .063in = 1cm
 REV. 05
 ADTF-0001
 09-25-01

Figure 2. Target design methodology

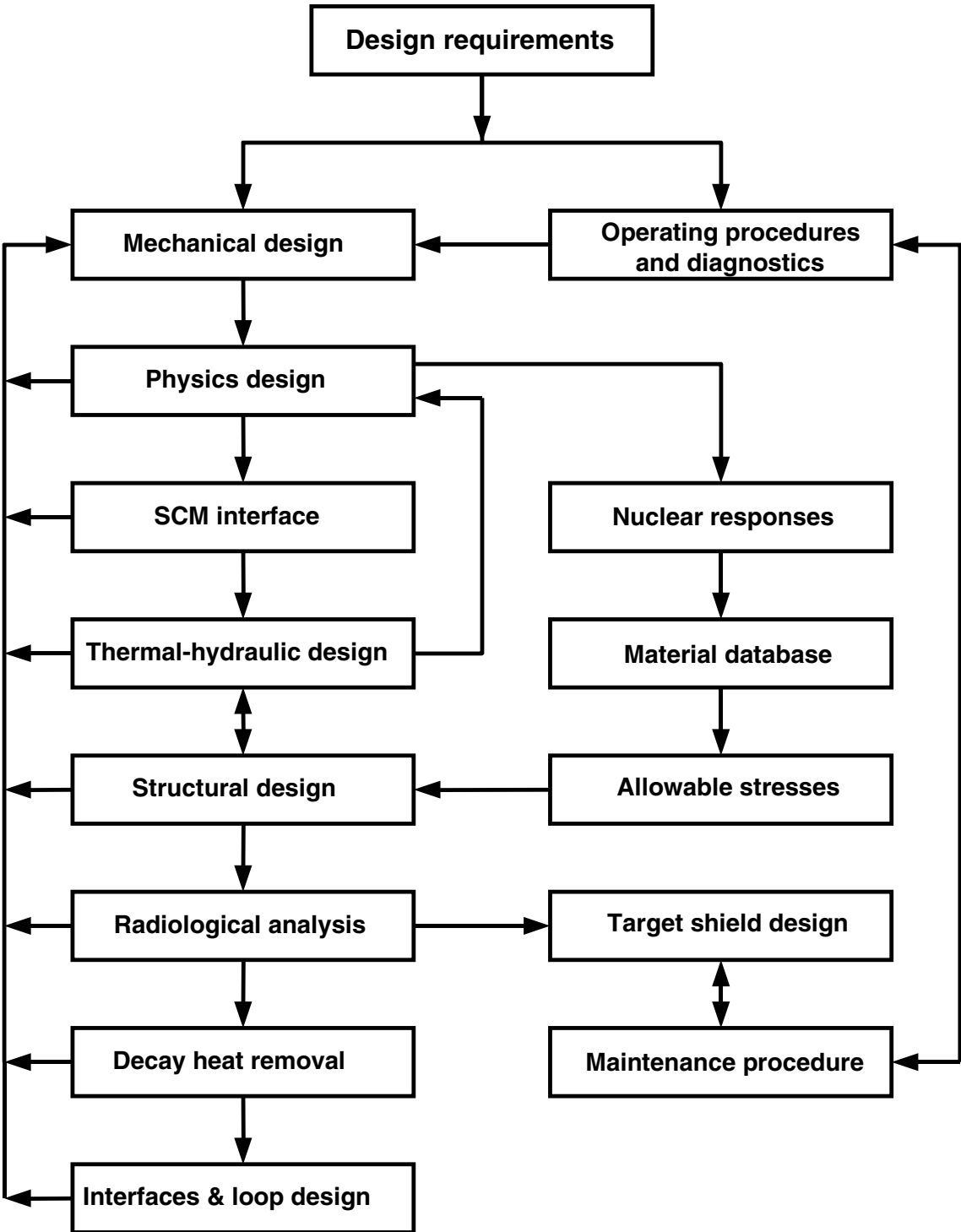


Figure 3. Spallation neutron distribution along the beam axis at the target boundary

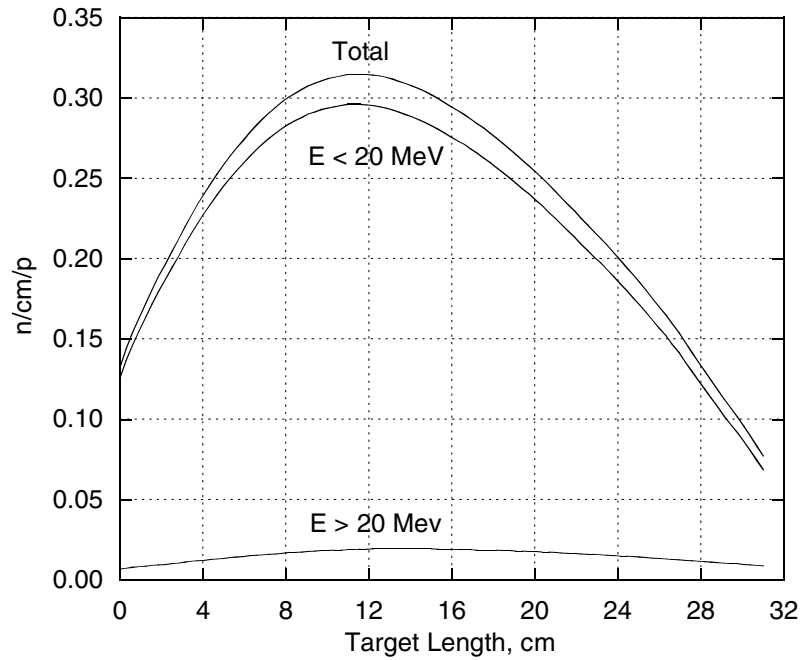


Figure 4. LBE axial energy deposition

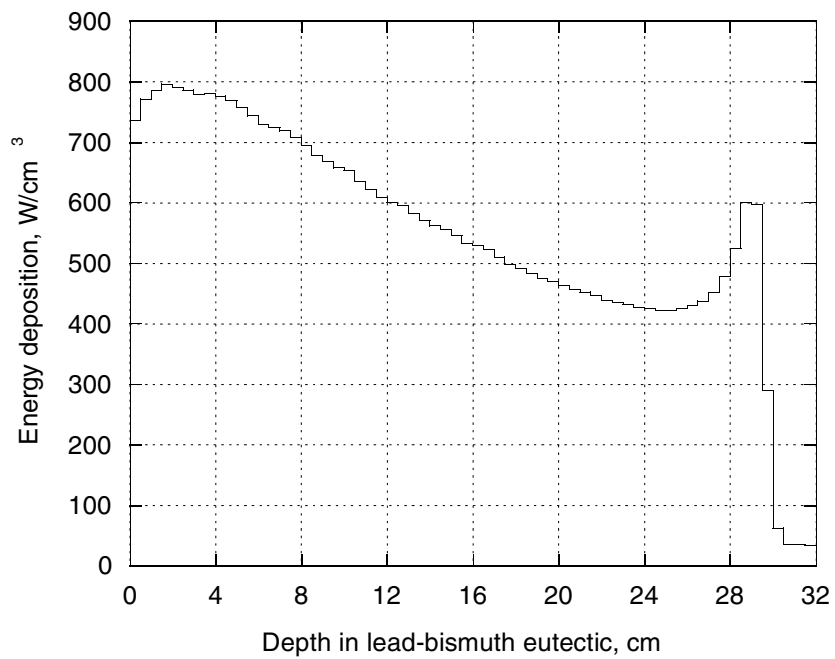
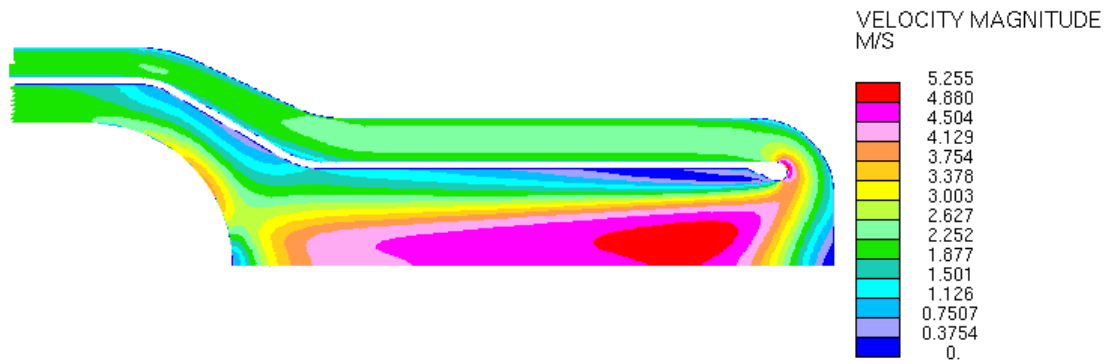
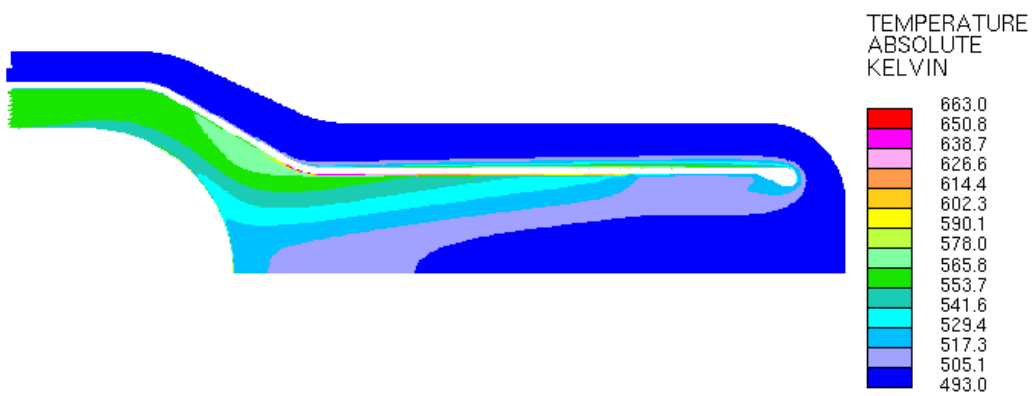


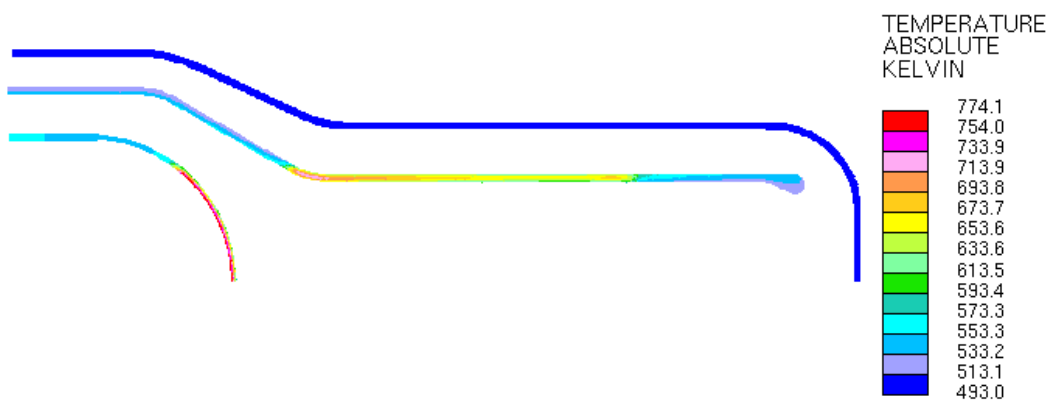
Figure 5. Lead-bismuth eutectic target contour plots showing:
(a) Fluid velocity, (b) Fluid temperature, and (c) Structural temperature profiles



(a)



(b)



(c)

RESULTS FROM THE INITIAL OPERATION OF THE LANL DELTA LOOP

Valentina Tcharnotskaia, Curtt Ammerman, Keith Woloshun

Los Alamos National Laboratory
P.O. Box 1663, Los Alamos, NM 87545, USA

Abstract

This paper summarises results from the initial operation and shakedown testing of the recently constructed DELTA (development of lead-bismuth target applications) loop at Los Alamos National Laboratory. The DELTA loop was designed to study the long-term corrosive effects of liquid lead-bismuth eutectic (LBE) on structural materials at temperatures up to 500°C. The DELTA loop can also be used to study thermal and hydraulic properties of LBE flow in future spallation target designs. The first run of DELTA loop took place on 5 December 2001. Since then, several hours of shakedown testing have been performed. These tests include calibration of the magnetic flow meter; pump operation with flow velocities up to 4 m/s in the test section, natural convection operation at velocities up to 0.5m/s in the test section, isothermal flow operation at temperatures up to 375°C, and heat exchanger operation at different capacities. The loop is scheduled to be ready for long-term, unattended operation early this summer followed directly by a planned, 1 000 hour material test.

Introduction

Liquid lead-bismuth eutectic (LBE) is being considered as a prototype target and coolant for the advanced accelerator applications (AAA) programme. LBE is a eutectic alloy of 44.5% lead and 55.5% bismuth with a melting temperature of 123.5°C and boiling temperature of 1 670°C. This liquid's relatively low melting point and high boiling point, in addition to good heat transfer properties, make it a very good candidate for a coolant. Relatively large neutron yield and low neutron capture cross-section make it an attractive target. Combining the target and coolant roles in one material allows for a simpler target design. In addition, a liquid spallation source eliminates some of the structural damage problems associated with solid targets.

One of the main problems in using LBE is its adverse effect on structural materials. This liquid metal dissolves stainless steel components promoting corrosion. A method to prevent corrosion in LBE systems was developed in Russia. This method is based on creating and maintaining a protective oxide film on the surface of stainless steel. Formation and longevity of this protective film depends on the oxygen concentration in the liquid metal.

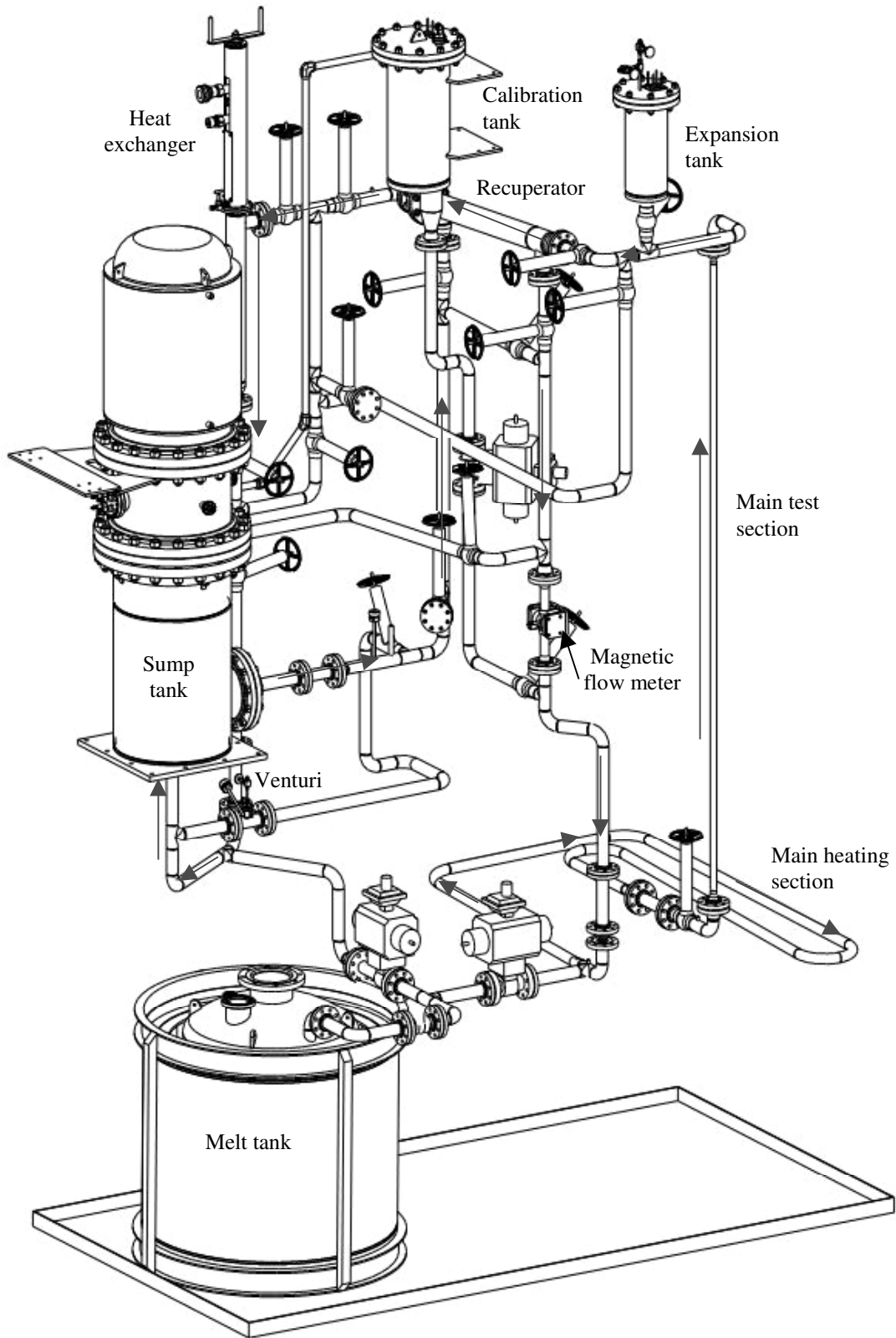
At Los Alamos, we have designed and constructed a test facility called development of lead-bismuth target applications (DELTA) loop to study the thermal-hydraulic and corrosive behaviour of LBE. The DELTA loop was designed in co-operation with Institute of Physics and Power Engineering (IPPE) of Obninsk, Russia. The main goals for the DELTA loop are:

- implementation of an oxygen measurement and control system in the LBE flow;
- investigation of the long-term corrosive effects of LBE on a variety of materials;
- implementation and investigation of natural convection flow in an LBE system; and
- investigation of the thermal-hydraulic properties of LBE in prototype target designs.

DELTA loop description

A drawing of the DELTA loop is shown in Figure 1. The loop is a closed system that is 6 meters high and is constructed primarily with 5.25 cm diameter, pipe. The loop components include an 18.6 kW, variable-speed, sump-type, centrifugal pump capable of delivering LBE at a rate of 13 m³/hr; a magnetic flow meter with an attached calibration tank; a 60 kW heat input section for raising the fluid temperature during material testing; a 3.3 m long test section where various material sample coupons will be placed for corrosion testing in the LBE flow; an expansion tank that provides a free surface during natural convection operation; a shell-and-tube recuperator capable of providing a 50°C fluid temperature change; a variable capacity, LBE-to-water heat exchanger; and a melt/drain tank that holds 3 500 kg of LBE and is equipped with a 45 kW, radiant heater. Approximately 80 kW of tape heaters are mounted on the external surfaces of the loop piping and vessels to provide trace heating. All vessels and piping are designed according to the ASME Boiler and Pressure Vessel Code [1] and ASME Piping Code [2] and are built from 316L stainless steel. The DELTA loop was designed to minimise the stresses due to gravity, internal pressure, thermal expansion and seismic loads. Some of the supports are flexible to allow for thermal expansion. The maximum design temperature of the loop is 550°C.

Figure 1. Drawing of the DELTA loop



The recuperator is an IPPE-designed shell-and-tube heat exchanger with 19, 1.43 cm diameter tubes enclosed in a 10.2 cm diameter shell. The heat exchanger is also designed by IPPE. It is an annular, counter-flow design using water at room temperature and atmospheric pressure as the cooling fluid. The water is separated from the LBE by a closed, intermediate annulus containing lead-bismuth. This intermediate fluid can be moved up and down inside the annulus by sliding the inside cylinder like a piston. When the piston is brought all the way up, it leaves the intermediate lead-bismuth at the bottom of the annulus, thus reducing the heat exchanging capacity to a minimum. When the piston is lowered to the very bottom, the intermediate fluid is pushed up into the annulus, thus increasing the heat exchanging area and increasing the heat exchanger capacity. Turning a screw handle at the top of the heat exchanger moves the piston.

Prior to operation, LBE is heated to 300°C in the melt tank, the piping and vessels are heated to 250°C using the trace heaters, and the loop is evacuated to a rough vacuum. The melt tank is then pressurised with helium to force the LBE up into the sump tank. Then the sump tank then is pressurised to force the LBE up into the rest of the piping. When the fill is complete, the pump can be started.

During operation, LBE leaves the sump tank and travels up to the recuperator's shell side where the fluid temperature is increased by 50°C. LBE then flows to the magnetic flow meter through a long vertical pipe leading from the recuperator's shell side to the heated section at the bottom of the loop. The tubing in the heated section is covered with band heaters that are used to raise the fluid temperature another 50°C. The heated fluid then enters the 2.65 cm diameter, vertical test section where material samples will be placed. Upon exiting the test section, the fluid then enters the tube side of the recuperator where the temperature is reduced by 50°C. After leaving the recuperator, the fluid flows to the heat exchanger where its temperature is again reduced by 50°C. The fluid leaves the heat exchanger and returns to the sump tank through the bottom inlet. Several pipes are built into the loop to allow bypasses of the recuperator, the heat exchanger or the sump tank. In addition, a bypass of the primary piping exists to enable flow rate and pressure adjustment of the main flow. A venturi is located in this primary bypass where oxygen and hydrogen clean-up gases are injected. The temperature changes shown in this paragraph are nominal for the design flow speed of 1 m/s in the test section or about 6 kg/s mass flow rate.

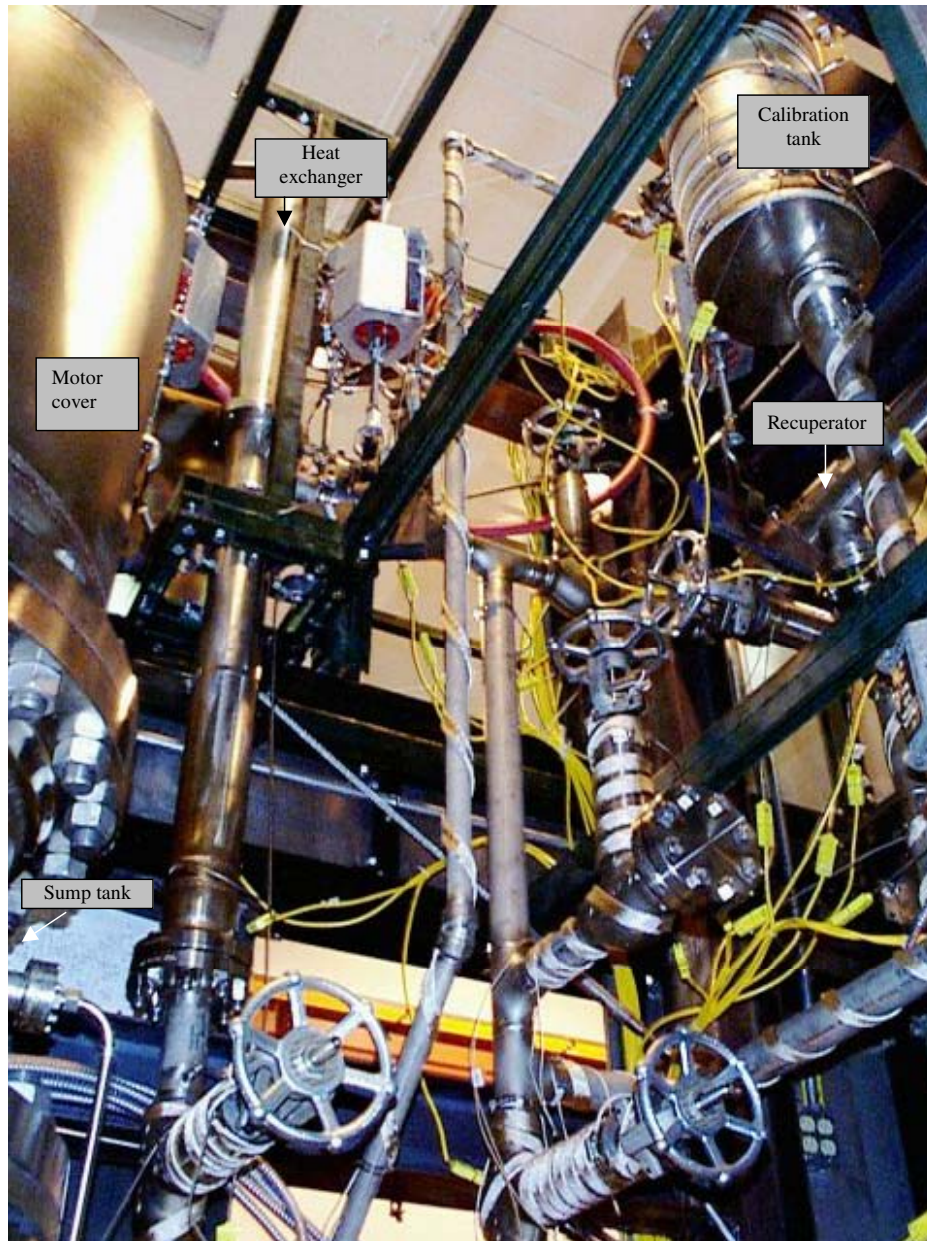
A photograph of the DELTA loop is shown on Figure 2. The loop is surrounded by a ventilated enclosure. At the time this photograph was taken, the top part of the enclosure was removed and the piping and vessels were uninsulated. One can see the trace heaters, thermocouples and the spring hangers that support the loop.

Instrumentation

Instruments and devices

The DELTA loop is equipped with pressure transducers, thermocouples, a magnetic flow meter, level sensors, water flow meters and oxygen sensors. Other equipment includes the pump, heaters and actuated valves.

Figure 2. DELTA loop. Sump tank is visible on the left, heat exchanger next to sump tank, calibration tank is at the right top corner, and recuperator is underneath calibration tank, in the shadow.



Standard thermocouples and pressure transducers are used. Pressure transducers in contact with the LBE are mounted on stand-offs to reduce the temperature at the transducer. Trace heaters are placed on the stand-offs to ensure they stay above the melt temperature of the LBE.

Level sensors are constructed of stainless steel rods welded to electrically insulated feed-throughs. The feed-throughs are mounted on the top of each tank with the rods protruding down into the tank. When liquid metal reaches a level sensor, the circuit is closed between the level sensor and the tank wall, providing a level indication to the data acquisition and control (DAC) system.

The LBE flow rate measurement is based on the magnetic induction principle. When a conducting fluid, such as a liquid metal, flows through a perpendicular magnetic field, it induces an electric current perpendicular both to the flow and to the magnetic field. The magnetic flow meter was constructed by IPPE and delivered to Los Alamos. It consists of a permanent magnet placed around a section of pipe with two electrodes welded to the pipe opposite each other and perpendicular to the magnetic field. The electrodes are exposed to the liquid metal. The flow meter was supplied with calibrations of flow rate vs. output voltage that were generated by IPPE.

The DELTA loop is equipped with an oxygen monitoring and control system that includes newly designed oxygen sensors and a venturi with a gas injector for clean-up gas control. The oxygen sensors were designed specifically for the DELTA loop by staff members at Los Alamos [3]. A section of this oxygen sensor design is shown in Figure 3. The main part of the oxygen sensor is a ceramic probe that is permeable to oxygen ions at temperatures above 350°C. The minimum temperature was determined in prior bench-top experiments with oxygen sensors of this design. The probe is immersed into the liquid lead-bismuth when the sensor is mounted on the pipe. Voltage is developed due to the difference between the oxygen concentrations on either side of the ceramic. A relationship between voltage and oxygen concentration was derived from formulas available in literature. Each of the oxygen sensors was calibrated before installation into the loop.

Oxygen concentration control is achieved using the clean-up gas injection system. Oxygen-helium or hydrogen-helium mixtures can be injected into the flow of LBE through small openings in a venturi located in a main bypass leg of the loop. In order to prevent liquid metal ingress into the gas injection lines when gas injection is not taking place, a freeze plug is formed in the gas line fitting on the venturi. Water flowing through a small water jacket around the fitting cools the LBE and solidifies it. The freeze plug is melted out for gas injection operations. Level sensors in the gas fitting allow DELTA loop operators to determine when the freeze plug is present.

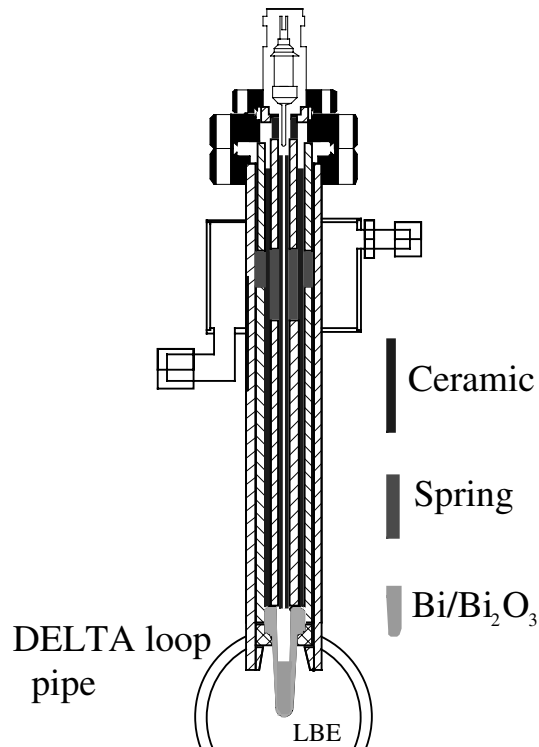
Data acquisition and control (DAC) system

A computer based DAC system displays and records the data collected by the various instruments. In addition, the DAC system allows the operator to control the pump, heaters and actuated valves. The DAC system also includes automatic pressure, temperature, and level control algorithms.

The DAC system programme is written in LabVIEW, a graphical programming language developed by national instruments. National instruments data acquisition hardware is used for data input/output. A picture of the DAC programme front panel is shown in Figure 4.

During long-term material testing, the DELTA loop will be operated in an unattended mode (without operators present) for extended periods of time. The DAC system, therefore, was programmed to handle many complex situations automatically. The system was designed to maintain specified operating conditions, to continuously monitor the status of the loop, and to safely drain the liquid metal into the melt tank in case of anomalous conditions. Examples of these anomalous conditions include temperatures or pressures outside of their normal operating ranges.

Figure 3. Cross-section of the LANL oxygen sensor



Current testing and preliminary results

The DELTA loop was operated for the first time on 5 December 2001. Since then, the loop has been operated for a total of over fifty pump-hours. During this time, we have examined a variety of flow conditions with flow speeds up to 4 m/s (8 m³/hr) in the 2.65 cm test section. Presently, the maximum LBE temperature achieved in the loop during this break-in period has been 375°C.

We have performed a calibration of the magnetic flow meter and compared it with the calibration provided by IPPE. The calibration was performed by diverting the main flow into the calibration tank after passing through the flow meter. The flow rate was determined by measuring the time intervals between subsequent level changes in the calibration tank. The resulting calibration curve is shown on Figure 5. The calibration curve supplied by IPPE is also shown. The calibration curve is linear as expected. The difference between the present calibration and the Russian calibration could be due to oxidation of the electrodes.

Figure 4. DAC programme front panel

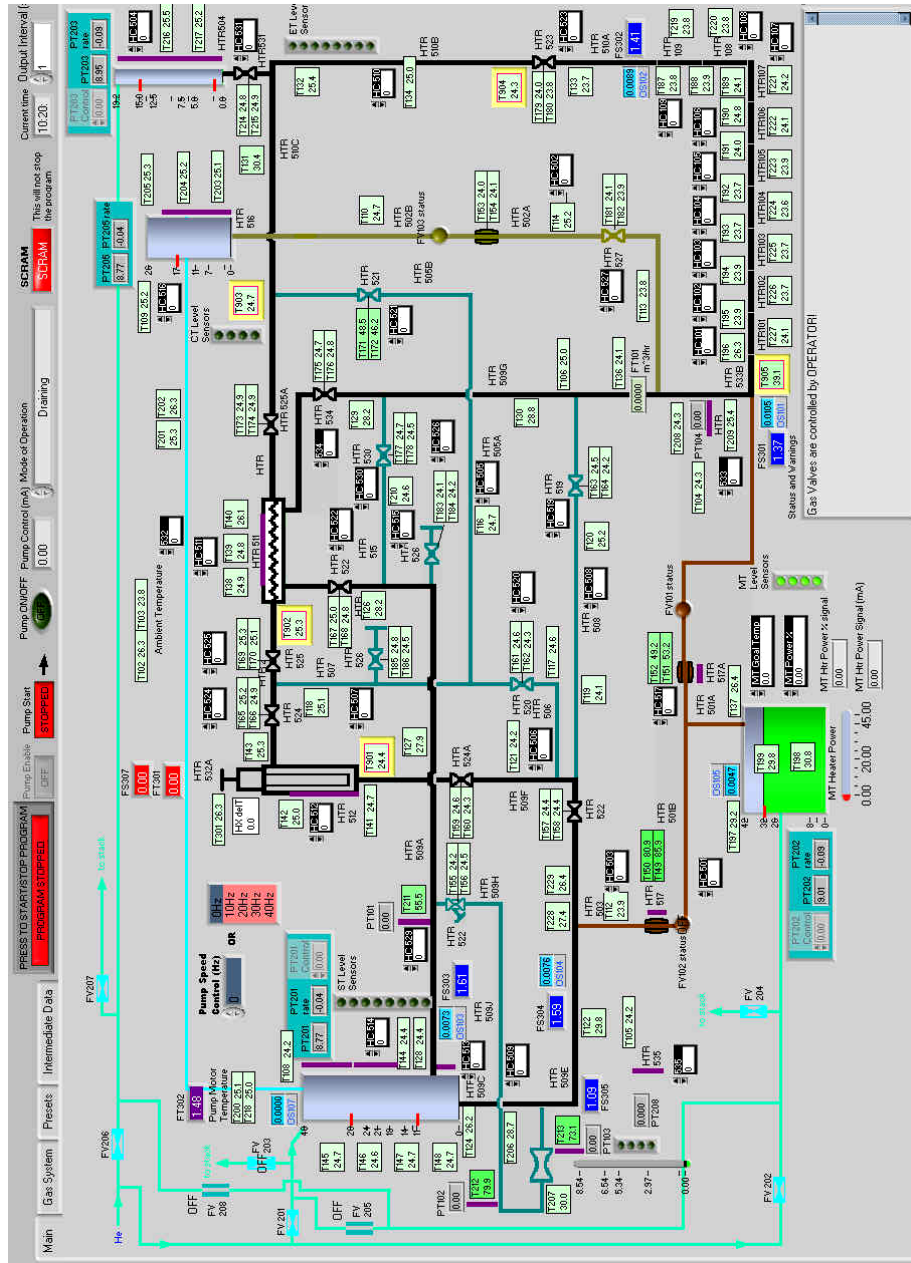
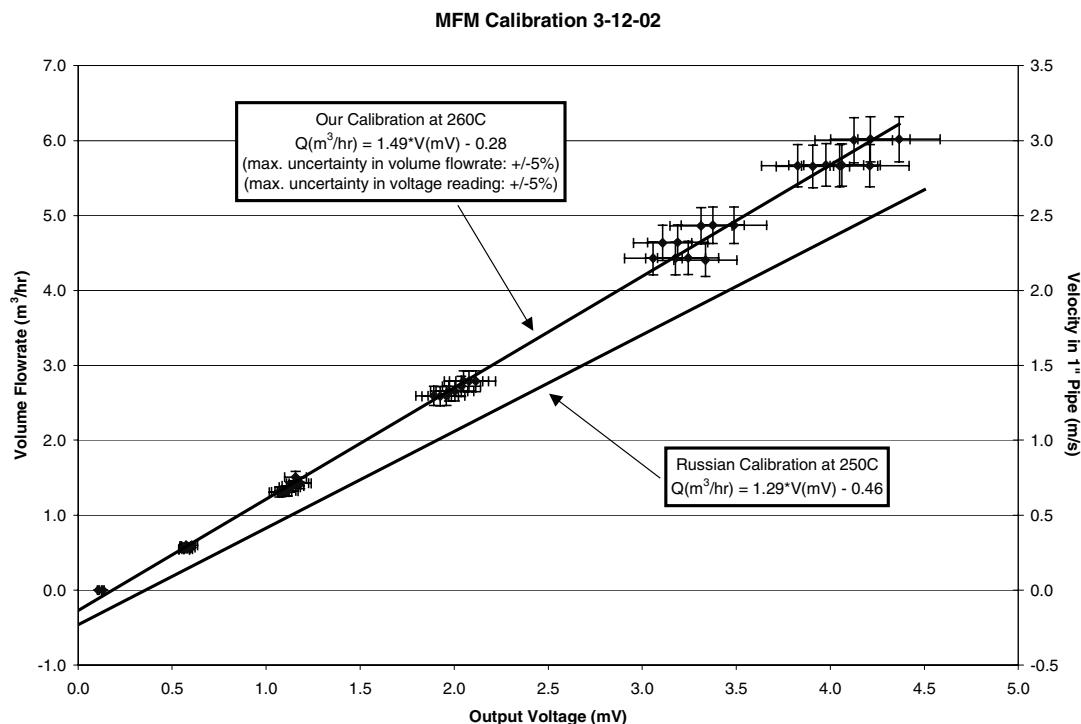


Figure 5. Magnetic flow meter calibration results



The heat exchanger has been successfully operated in concert with LBE heating. The capacity was varied to investigate the heat exchanger’s effect on temperature in the loop. The results for one such setting are shown in Table 1. For this case, the LBE flow rate was set to 2 m/s in the 2.65 cm test section. The main heating section was set to a power of 27 kW. The heat exchanger capacity was varied until a steady-state condition was achieved by adjusting the heat exchange area. Table 1 below shows the temperature changes in the heat exchanging sections.

Table 1. Temperature gradients during operation with the heat exchanger

ΔT in recuperator (cold side)	31°C
ΔT in main heater	14°C
ΔT in recuperator (hot side)	-31°C
ΔT in heat exchanger	-14°C

The DELTA loop was operated with fluid flow maintained by natural convection. In this configuration, the fluid is heated in the main heating section and flows up through the test section and through the tube side of the recuperator. The fluid then passes through the heat exchanger where the heat is removed. Upon exiting the heat exchanger, the LBE bypasses the sump tank and shell side of the recuperator and instead flows through the magnetic flow meter and then back to the main heating section. A flow speed of approximately 0.5 m/s in the test section was achieved at steady state

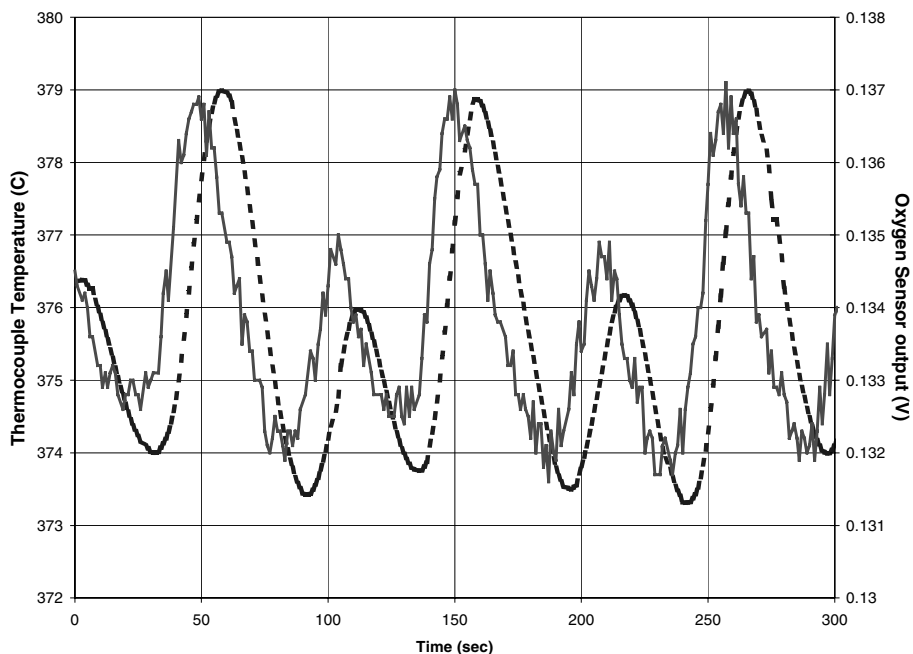
conditions using this technique. We want to be able to study natural convection flow of liquid lead-bismuth because it can be a useful, passive safety mechanism in accelerator-driven systems. Some of the slow flow tests can be accomplished without engaging the pump if natural convection provides reliable flow.

We have run preliminary experiments with the cleaning gas injection system and have examined the performance of the oxygen sensors. The sensors installed in the DELTA loop are operational and able to follow the oxygen concentration changes. The oxygen sensors showed readings consistent with predicted values. Figure 6 shows data from an oxygen sensor at the exit of the main heating section. The plot shows oxygen concentration near the saturated value with an imposed variation matching the temperature changes, as expected. The oxygen sensor is mounted upstream from the thermocouple mounted in a thermowell inside the LBE flow, thus the output from the thermocouple lags the output from the oxygen sensor.

The DAC system was tested for critical (SCRAM) conditions. SCRAM tests were part of preparation for unmanned operations. Conditions tested included temperature and pressure greater than maximum or lower than minimum. Also, the DAC programme checks water flow, vessels' levels, drain valves status, magnetic flow meter reading and enclosure pressure for critical conditions and it issues warnings or SCRAM commands accordingly. On SCRAM command the DAC system shuts down power to the loop causing it to shut down the pump and the heaters and to drain all LBE into the melt tank.

Presently, the DELTA loop has been commissioned to run in unattended mode and preparations are now underway for the first materials test, which will begin in June.

Figure 6. Oxygen concentration measurements



Conclusion

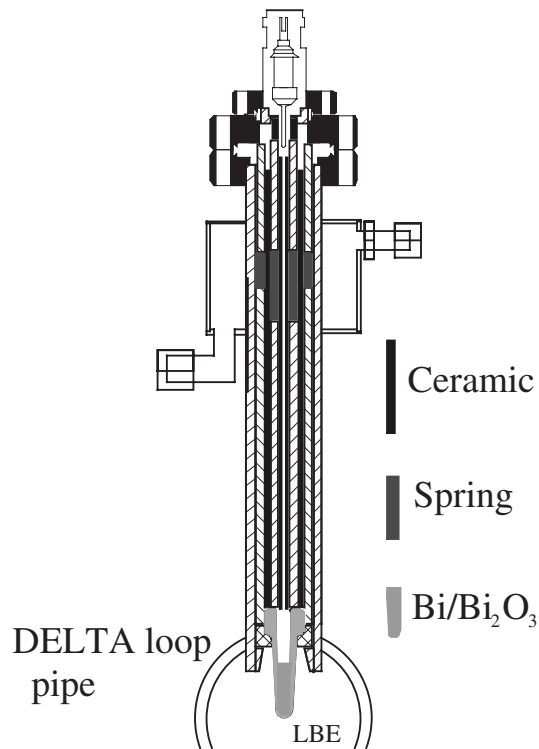
The design and construction of the DELTA loop is complete and initial operation has begun. The oxygen sensors have been installed in the loop and are operating successfully. The loop is ready for unattended operation and initial material testing will begin soon. Now that it is complete, the DELTA loop is a valuable tool for studying properties of liquid lead-bismuth. With the loop, we will be able to learn the corrosive effects of lead-bismuth on a variety of potential candidate materials for use in accelerator-driven systems. We will also learn how to control the corrosion and improve steel surface. Some of this liquid metal's cooling properties can be determined even during the initial testing, but even more valuable data will be derived from tests with specific geometries.

The DELTA loop was built to accommodate lead-bismuth eutectic, but the same design and testing principles can be utilised for other liquid metals. Since liquid metals are primary coolants considered for AAA applications the DELTA loop presents a useful facility for future work.

REFERENCES

- [1] ASME Boiler and Pressure Vessel Code, 2000.
- [2] ASME B31.1, Power Piping, 1998.
- [3] Darling, T., N. Li, "Oxygen Concentration Measurement in Liquid Pb-Bi Eutectic", AccAPP-ADTTA'01 meeting.

Figure 3. Cross-section of the LANL oxygen sensor



Current testing and preliminary results

The DELTA loop was operated for the first time on 5 December 2001. Since then, the loop has been operated for a total of over fifty pump-hours. During this time, we have examined a variety of flow conditions with flow speeds up to 4 m/s (8 m³/hr) in the 2.65 cm test section. Presently, the maximum LBE temperature achieved in the loop during this break-in period has been 375°C.

We have performed a calibration of the magnetic flow meter and compared it with the calibration provided by IPPE. The calibration was performed by diverting the main flow into the calibration tank after passing through the flow meter. The flow rate was determined by measuring the time intervals between subsequent level changes in the calibration tank. The resulting calibration curve is shown on Figure 5. The calibration curve supplied by IPPE is also shown. The calibration curve is linear as expected. The difference between the present calibration and the Russian calibration could be due to oxidation of the electrodes.

**SUMMARY
OF
DISCUSSION SESSIONS**

**SUMMARY OF
WORKING GROUP DISCUSSION ON
DESIGN CONSIDERATIONS, RELIABILITY PERFORMANCE
AND REQUIREMENTS FOR THE ACCELERATOR**

Chair: M. Cappiello

Topics

- Design considerations.
- Reliability performance.
- Requirements for the accelerator.

The accelerator reliability performance requirements are dictated by the design of the target/subcritical transmuter system. Reliability requirements provide the allowable number of beam trips per year for differing numbers of interrupt times. In this case the beamtrip is defined as the beam current being equal to zero for some period of time. It was also pointed out that another class of beam perturbations can also exist. That is some period of time where the beam current or energy may be below design level.

For determination of the allowable beam trips, fatigue (transient structural analyses) must be performed. For example, during an interrupt in the beam current, the structures (window, fuel, cladding, vessels, heat exchanges, etc.) will undergo a thermal transient that causes a fatigue stress. Fatigue analyses will then dictate the number of allowable trips or beam interrupts that can be accommodated by the components during their respective design lives. Obviously some designs will be more conducive to beam interrupts than others. For example, because of the differences in heat transfer coefficient between lead-bismuth and sodium, the thermal transient that a thick steel structure will endure is reduced in severity for lead-bismuth. Also, for fuel that is constructed with a helium gap between the pellet and cladding versus a molten metal, the thermal transient will be much less severe.

Analyses at the Belgian Nuclear Centre show that for oxide fuel with a helium gap, beam interrupts of 1 second or less do not cause excessive stress to the fuel and can be accommodated easily. The conclusion is that fatigue analyses must be performed for critical components of each design and the number of allowable beam interrupts and length of interrupts per year that the accelerator is required to deliver must be determined.

Various categories of beam interrupts exist. In general it was agreed that beam interrupts of less than 0.1 second are not of concern. Again, depending on design details, this may be as large as 1 second. Beam interrupts of ~10 seconds or larger will cause stress on loop components that will most likely require a slow ramp back to power. Allowable trips of this length are on the order of 100 per year, but again, they depend on the details of the design.

Some interrupts are beneficial. For example, regular interrupts of 1-2 milliseconds can be used to measure the level of subcriticality on a continual basis. This information is necessary for control and operation of the transmuter. This has been demonstrated at MASURCA/MUSE. Also, short interrupts of this length can increase reliability by allowing beam current measurement and control equipment to recalibrate.

Another discussion was held on the use of mercury as a target material. It has many advantages over lead-bismuth, but must be kept at less than ~350°C to avoid boiling.

**SUMMARY OF
WORKING GROUP DISCUSSION ON
ACCELERATORS**

Chairs: C. Pagani and P. Colestock

Following the general recommendations from the Workshop Chairman, the discussion was organised following three major topics:

- a) Technology options.
- b) Major issues.
- c) Proposed path forward.

Technology options

Two are the options for a high power proton driver: cyclotron and linac. The two options have both advantages and disadvantages, but they are quite different and the choice depends on the application. A general consensus was achieved on the following general considerations and statements.

Cyclotron

- For high power proton cyclotrons the only suitable reference machine is the PSI accelerator complex, delivering a 1.2 MW proton beam at 600 MeV. No remarkable R&D programs are under way to sensibly extend these limits, except for the new RF system for the PSI ring that would enhance the power to the 2 MW level. A preliminary design was proposed in the past for a more relativistic machine, however one disadvantage is the fact that its cost appears to scale nearly quadratically with the output energy.
- The reliability and availability obtained at PSI is very high, but its further improvement in the direction of the basic ADS requirements (very few unscheduled beam interruptions per year) looks very difficult. The machine concept does not allow the application of the concepts of redundancy and on-line spares, which are considered crucial for the demands of a full-scale demonstrator.

Linear accelerator

- For high power proton linacs a worldwide R&D effort has been in progress a few years already and the high potential value of these machines has been proven. Different programs have driven this effort: tritium production, spallation sources and ADS. Sources and RFQs up to 100 mA have been built and successfully operated, defining the technology up to ca. 7 MeV. The well-developed and highly efficient SRF technology is the technology of choice above 100 MeV. For intermediate energies, both solutions, normal or superconducting, are considered viable. The first of these options is already available and the second requires a significant R&D effort. In this type of accelerator the cost per MeV decreases with energy up to 1 GeV and above this value it stays nearly constant.
- Apart from the front end, which can be duplicated, the linac has an intrinsic high degree of modularity, which increases with energy. This machine can be designed on the basis of a properly apportioned redundancy in order to permit the use of the on-line-spares concept. Moreover, maintenance of components such as the power klystrons can be envisaged even during machine operation.

Final recommendations

- Cyclotrons of the PSI type should be considered as the natural and cost effective choice for preliminary low power experiments where availability and reliability requirements are less stringent.
- CW Linear accelerators must be chosen for demonstration facilities and full-scale plants, because of their high value potential regarding availability, reliability and power upgrade capability.

Major issues

On the basis of the discussion outlined above, it was decided to concentrate future work on the linac option, with the PSI cyclotron data as important background experience to be considered and used as needed.

Reliability and availability

- As a general rule, the machine must be designed with enough redundancy to guarantee just a small number of unscheduled failures per year. All failures that can be handled in less than a second are not counted.
- Over-design of critical components, redundancy and the on-line spares technique should be used as guiding design criteria.
- Because of the high degree of modularity of the outlined linac scheme, no major concerns were expressed regarding the potential of fulfilling this stringent demand implied by present knowledge and technology.
- Control electronics plays a critical role.

Beam trip handling

- Based on accelerator experience, sparks on high voltage components cause most of the beam trips. They can generally be handled in a small fraction of a millisecond and the beam can remain on. Because of their duration they are not counted.
- In principle a fast procedure to switch on the beam can be implemented to facilitate the use of redundancy and on-line-spares in a time of the order of one second.
- The required degree of over-design and redundancy is a direct function of the duration and frequency of the scheduled shutdown periods of reactor maintenance.
- The number of some redundant components, such as power supplies, could be reduced if they are located in a different building or tunnel. General cost analysis will define the relevant details.

Optimised design

- Because slightly different designs are being studied at present, they should be carefully analysed and compared in terms of their potential degree of modularity, reliability and cost.

- The final linac design has to be based on reliability and availability considerations, as defined for ADS application.

Control electronics

- Fast digital electronics must be implemented, based on the redundancy criteria already applied in other fields.
- Control of the beam power vs. time looks easy at the percent level. Better control can be achieved through a feedback from a reactor signal.
- As a general criterion, redundant fast electronics will be designed to avoid, in principle, the intervention of the last beam protection (robust beam shutdown), required for safety reasons.

Safety issues

- It is a general conviction of accelerator experts that the safety rules for the accelerator and the reactor have to remain separate entities. From the accelerator side, no major concerns have been expressed for the required safety issues, because of the low level of beam loss that is expected.
- As usual, the accelerator protection system will be based on redundant active systems.
- Beam handling, once in the reactor building, will follow appropriate reactor safety rules.

Proposed path forward

Due to limited time, this subject was not discussed separately but was included in the discussion outlined above. In summary, the effort should be focused on:

- Reliability analysis of components and subsystems.
- Design analysis of different linac schemes on the basis of reliability issues.
- Working prototypes of new major components to set reliability numbers.
- Development of redundant fast controls and fast beam-switching procedures.
- Development of fast beam-turn-off systems for the fail-safe reactor protection.

Concluding remarks

- The linac has to be considered as the only option for a high power demonstrator and for a full-scale ADS.
- The present technology is viable to permit a complete design of a linear accelerator fulfilling the ADS requirements in term of reliability and availability.
- An R&D effort of a few years, with adequate funding, is required both on accelerator components and accelerator system analysis before it is possible to build a linac fulfilling the ADS requirements.

**SUMMARY OF
WORKING GROUP DISCUSSION ON
MULTIPLIER**

Chairs: E. Pitcher and E. Gonzalez

The general consensus is that the multiplier will be a fast spectrum system cooled by liquid metal or gas. Six major issues related to the interface between the accelerator and the multiplier were identified.

Tolerance to beam trips

Beam trips will cause undesirable thermal cycling in components of the multiplier system. The multiplier can be designed to withstand beam trips of specified frequency and duration. The duration of the beam trips fall into three categories:

- Up to some beam interrupt duration on the order of 0.1 to 1 s, the beam trip is not detrimental because thermal transients in the multiplier are minimal.
- Tolerance of beam trips with durations beyond this lower limit depend on the particular multiplier design. The fuel will likely respond on the fastest time scale (on the order of seconds), fuel clad and thin structures on slightly longer time scales than the fuel (tens of seconds), and thick structures on still a longer time scale (minutes).
- If the ADS produces electricity, safe restart procedures will define tolerance to long-duration beam interrupts.

To date, very few analyses of current ADS concepts to beam interrupts have been performed. The working group feels it is important for multiplier designers to derive tolerance response functions (i.e. allowable frequency of beam trips as a function of beam trip duration) for current and future candidate multiplier concepts. These response functions will then set requirements for the accelerator design.

Accelerator maintenance schedule

To maximise overall plant availability, it is best if the accelerator maintenance schedule coincides closely with the periods for multiplier refuelling and fuel reshuffling. Current ADS concepts propose fuel cycles in the range of 0.3 to 3 years, with expected outage durations of approximately several weeks. Optimal operation would be achieved if the accelerator were designed to run for many months without shutting off for maintenance. This is recognised to be a radical departure from current modes of accelerator operation, and may not be practical in future accelerator designs. It is mentioned here as a goal in the design of accelerator with application to ADS.

Reactivity swing relative to initial reactivity

Multiplier designers recognise the need to minimise reactivity swing over an operating cycle in order to lessen the demand for increasing beam current throughout a cycle. However, optimal multiplier design may require the accelerator to increase beam current by a factor of perhaps two (or even more) in a slow and highly controlled manner. This is an important capability that the accelerator must be able to provide. The range of current required depends on the particular ADS concept, and should be specified by the multiplier designers.

Continuous versus pulsed beam operation

The consensus of the working group is that pulsed beam operation is probably acceptable if the repetition rate is greater than approximately 1 kHz since the thermal response frequency of any multiplier system will be less than this amount. The tolerance of a multiplier system to a beam pulse repetition rate below 1 kHz will depend on the particular multiplier design. Another requirement for pulsed beam operation is that the beam pulse width be sufficiently long (probably ~100 microseconds or longer) that excessive pressure pulses in the target material are avoided.

Momentary “drops” to zero beam current out of a continuous beam, with a frequency of approximately 1 Hz, are acceptable for multiplier operation if they have a duration on the order of 1 ms or less. In fact, such drops of the beam current may be used to monitor the k_{eff} of the multiplier system, and in this respect can be considered desirable.

Multiplier start-up and control

The start-up procedure should involve ramping the beam current to its desired value in a controlled manner, probably on the order of tens of seconds, in order to avoid inducing excessive thermal stresses in multiplier components. Alternatively, the controlled ramp to full multiplier power may be achieved by control rod withdrawal.

It is generally accepted that accelerator shutdown can be performed in a matter of microseconds once a determination is made that shutdown is desired. However, the response time for shutting off the beam in the case of thermal excursions in the multiplier will likely be dominated by the response time of the sensor detecting the thermal excursion, which may be several orders of magnitude larger than the several microseconds needed to shut off the beam.

Passive beam shutdown with multiplier temperature excursion

The requirement for one or more mechanisms to passively shut off the proton beam may be precluded by the implementation of redundant and diverse active shutdown systems. However, it is generally recognised that a passive shutdown mechanism is desirable from a safety standpoint. Credible passive safety mechanisms must be conceived and designed. This is an area that is ripe for development.

**SUMMARY OF
WORKING GROUP DISCUSSION ON
TARGET TECHNOLOGY**

Chairs: K. Pasemehmetoglu and G. Laffont

Constraints

The working group first evaluated the constraints imposed on the target as a result of ADS applications specific to spent fuel transmutation.

- The application requires a fast ADS spectrum, with a small hole to insert the spallation target and a high-temperature subcritical core.
- Because of availability and efficiency issues, a target replacement frequency of $\geq 1/\text{yr}$ is the ultimate objective.
- Again for the transmutation efficiency, the target availability must be greater than 75%.

Technology options

Currently, the leading technology option for the spallation target that is receiving universal attention is the lead-bismuth eutectic (LBE) or lead. The issues for lead or LBE are very similar. Thus, only LBE is further discussed with the team. The back-up option is a solid target (tungsten or tantalum) potentially cooled with sodium. However, there is not much on-going work in this area and the near-term international focus is on LBE.

The team also agreed that mercury could be a back-up liquid metal spallation target technology but it must be thermally decoupled from the subcritical core, which limits the design options.

In terms of materials, the ferritic-martensitic steels are the materials of choice for the target applications.

For liquid metal target, windowless target is a strong technology candidate that must be further pursued.

Major issues

The major issues (specific to lead or LBE target) are listed below. Some of these issues also apply to sodium-cooled tungsten (or tantalum) targets but solids targets are not discussed in detail during the working group meeting.

Below is a list of the major issues identified during the discussions:

- Liquid metal corrosion:
 - Oxygen control (effect of irradiation, low temperature sensors).
- Cavitation/pitting caused by beam pulses.
- Chemistry control (spallation products).
- Mechanical properties of structural materials (irradiation and temperature effects).

- Instrumentation (radiation effects).
- Flow stability/thermal-hydraulics:
 - window cooling;
 - windowless target interface design:
 - ◆ vacuum control;
 - ◆ flow pattern.
- Beam shutdown (active versus passive).
- High-energy particles: cross-section measurements and evaluations.
- Erosion with heavy metal flow.
- Coolant compatibility (if different coolants are used for the subcritical core and spallation target).
- Dose-conversion factors for spallation products.

Resolution strategy

It is agreed that adequate international infrastructure exist for addressing most of the issues associated with the LBE technology. An expert group (comprised of countries that have active LBE research programs) is proposed in terms of documenting the research results in the form of a handbook.

One area where experimental facilities are limited is in addressing the radiation effects. Paul-Scherrer Institute (PSI) in Switzerland within the framework of the MEGAPIE project is expected to provide some data in this area. If a test facility is built at LANSCE (LANL, USA) for materials testing the remaining data gaps can be filled. Other options include irradiation of capsules in thermal or fast test reactors, even though the spectral effects would not be prototypical.

**SUMMARY OF
WORKING GROUP DISCUSSION ON
CONTROL/SAFETY/SHUTDOWN**

Chair: M. Cappiello

Normal operation

- 1) There needs to be a procedure for safe start-up and shutdown. This can be accomplished by adjusting accelerator power and coolant flow to the transmuter in a safe, step-wise manner that eliminates the possibility of adverse power to flow ratio (i.e., $P/F \leq 1.0$).
- 2) During full-power operation, the accelerator and transmuter power are matched such that the $P/F=1.0$. Because of fuel burn-up, the multiplication constant of the transmuter will decrease. To maintain a constant power level, the accelerator power must be raised to compensate. Transmuter designs are possible to minimise the swing in transmuter k_{eff} from the beginning of cycle to end of cycle. Features that are possible include fuel design, burnable poison, movable poison, or shim rods. It was generally agreed that minimising the k_{eff} swing should be a transmuter design goal.

Safety and off-normal operation

Design basis accidents

Several design basis accidents (DBAs) will be analysed in support of obtaining allowance to operate from safety and licensing authorities. These include, but are not limited to, loss of flow, loss of heat sink, flow blockage, and loss of coolant. It was agreed that for all DBAs, beam shutdown will occur that will mitigate the potential for any adverse damage. It has been demonstrated, for example, in the APT project that active beam shutdown can be achieved with the probability of failure to trip the beam at less than 10^{-6} . This is achieved with 2 out of 4 sensor logic, and diverse and redundant sensors. Multiple methods exist to shut down the beam once the signal is received. This includes injector power, injector extraction voltage, RF power to the RFQ, RF power to other cavities, etc.

To protect against loss of flow, for example, sensors monitoring the pump rotation, fluid flow to the target and/or transmuter, and transmuter exit temperatures will all measure a value that is out of the normal range. The signal from the sensors passes through the logic circuitry and sends the signal to trip the beam to the accelerator control. Once received, the accelerator will be shut down reliably in a matter of microseconds. After this occurs, the removal of decay heat from the transmuter is performed in a way similar to critical reactor design. This usually is done in liquid metal systems with an active system and a passive, natural circulation system as backup.

Beyond design basis accidents

This class of accidents includes all of the DBAs (loss of flow, loss of heat sink, etc.) but with the added constraint that the active beam shutdown system fails. Although this is extremely unlikely (10^{-6} per year or less), it will be required by the licensing authority for analysis. In addition, it is strongly recommended by licensing authorities that, at least for critical reactors, passive means of mitigating accidents should be used.

Two main BDBAs were discussed: beam overpower and loss of flow with failure to trip the beam.

a) Beam overpower with failure to trip the beam.

By design, this scenario can be made an impossibility. For example, for the design case in which the transmuter design is such that the reactivity change (change in k_{eff}) is minimal during an operating cycle (100-300d), then the accelerator will always operate near or at maximum power. This means that it will be impossible to raise this power instantaneously. In the other example, where accelerator power changes during the cycle, beam overpower can be physically limited with the use of an aperture in the injector.

b) Loss of flow with failure to trip the beam.

This BDBA can be mitigated by use of passive beam shutdown mechanisms. Several examples were discussed: loss of accelerator vacuum by window breakages, movement of target neutron source outside the core, thermal fuse tied to the injector, injector extraction voltage tied to the transmuter, etc. All of these are in the concept stage and need to be developed and tested to make the case for the licensing authorities.

**SUMMARY OF
FINAL WORKING GROUP DISCUSSION**

Chair: K. Pasemehmetoglu

General

- **Safety vs. Performance:** k_{eff} for an ADS needs to be established (lower is safer, higher provides more performance); however, fuel must first be determined before a specific k_{eff} can be implemented in a design.
- **Reference design:** We need to establish a reference design to which we can assign a k_{eff} , define a fuel and a range of power. A lot of work has been done in the past 2 years, but there has been no progress on or application to a reference design.
- **Experimental validation:** We need experimental evidence of the concept. TRIGA/TRADE is a great experiment; the international community (IWURHPPA) should submit a proposal or define test plans for this experiment.
- **Safety:** We've designed many accelerators and many reactors, but we may need to make changes in the designs to couple them together. We need to define a new safety envelope. Although the reactor and accelerator are separate concerns, and the accelerator beam can be tripped very reliably, we must be able to shutter or stop the beam in the reactor itself. Also, the accelerator designers should try to develop a list of shutdown concepts (passive vs. active) in each safety class.
- **Licensing:** We must consider engaging the licensing authority early. We should implement a reference design or initiate a project with the involvement or under the scrutiny of a licensing authority. **IDEA:** Use existing reactor designs; follow MYRRHA as a test case on the design/licensing interactions; follow one in the US as well.

Accelerator

- **Reliability requirement:** Consensus is that we can have an accelerator that will fulfil the reactor (reliability) requirements within the next 4 years.
- **Experimental programme:** We need an experimental programme (like LEDA and IPHI) to gain the necessary confidence (in "beam continuity", new electronics, overdesign applications, etc.). This requires an R&D programme (\$30M–\$300M).
- **Focus:** We need to focus on one application (multi-purpose is difficult).

Target/window

- **Focus on LBE:** At the current pace of research worldwide, we can comfortably deliver the required LBE spallation target technology within ~5 years.
- **Window materials:** There are materials issues for the window, and there are no existing facilities to test the window at prototypic temperatures, fluence, etc.
- **Windowless technology:** R&D on windowless technology must continue to achieve this objective, and there are many benefits. A test facility with a beam is an issue.

Multiplier

- Fast spectrum is the correct choice.
- Liquid metal of 800-1 000 MWth is the desired system.
- LBE and a gas-cooled system is being pursued in Europe.
- Na is an option in the USA.
- Clad material choice is T-91 (9Cr-1Mo) as per MYRRHA X-ADS.
- Minimising reactivity swing is highly desirable.
- Pacing item is the fuel.
- Design improvements possible for thermal fatigue (focal issue for reference design studies).
- Design should consider long beam trips (e.g., 1 hour, 1 day).
- Consider maintenance and scheduled shutdown for different components.

LIST OF PARTICIPANTS

BELGIQUE

AÏT ABDERAHIM, Hamid
SCK•CEN
Boeretang 200
B-2400 MOL

Tel: +32 (14) 33 22 77
Fax: +32 (14) 32 15 29
Eml: haitabde@sckcen.be

ARIEN, Baudouin
SCK•CEN
Boeretang 200
B-2400 MOL

Tel: +32 (14) 33 22 56
Fax: +32 (14) 32 45 29
Eml: barien@sckcen.be

D'HONDT, Pierre
SCK•CEN
Boeretang 200
B-2400 MOL

Tel: +32 (14) 33 22 00
Fax: +32 (14) 32 15 29
Eml: pdhondt@sckcen.be

JONGEN, Yves
Ion Beam Applications
Chemin du Cyclotron, 3
B-1348 LOUVAIN-LA-NEUVE

Tel: +32 (10) 47 58 54
Fax: +32 (10) 47 59 52
Eml: jongen@iba.be

MESSAOUDI, Nadia
SCK•CEN
Boeretang 200
B-2400 MOL

Tel: +32 (14) 33 22 23
Fax: +32 (14) 32 15 29
Eml: nmessaou@sckcen.be

VAN TICHELEN, Katrien
SCK•CEN
Boeretang 200
B-2400 MOL

Tel: +32 (14) 33 21 96
Fax: +32 (14) 32 15 29
Eml: kvtichel@sckcen.be

FRANCE

CARLUEC, Bernard
Framatome ANP
10, rue Juliette-Récamier
F-69456 LYON CEDEX 06

Tel: +33 (4) 72 74 70 66
Fax: +33 (4) 72 74 73 30
Eml: bernard.carluec@framatome-anp.com

GOBIN, Raphael
Commissariat à l'énergie atomique, CEA–Saclay
DSM-DAPNIA
F-91191 GIF-SUR-YVETTE CEDEX

Tel: +33 (1) 69 08 27 64
Fax: +33 (1) 69 08 14 30
Eml: rjgobin@cea.fr

LAGNIEL, Jean-Michel
CEA-DAM, DPTA-SP2A
BP 12
F-91680 BRUYERES-LE-CHATEL

Tel: +33 (1) 69 26 52 49
Fax: +33 (1) 69 26 70 24
Eml: jean-michel.lagniel@cea.fr

MUELLER, Alex C.
CNRS/IN2P3, Institut de Physique Nucléaire
15, rue G. Clemenceau, Bâtiment 106
F-91406 ORSAY CEDEX

Tel: +33 (1) 69 15 62 40
Fax: +33 (1) 69 15 62 58
Eml: mueller@ipno.in2p3.fr

GERMANY

BAUER, Günter S.
ESS Projekt
Forschungszentrum Jülich
D-52425 JÜLICH

Tel: +49 (246) 16 18 670
Fax: +49 (246) 16 18 675
Eml: g.bauer@fz-juelich.de

CHENG, Xu
Forschungszentrum Karlsruhe
Postfach 3640
D-76021 KARLSRUHE

Tel: +49 (7247) 82 48 97
Fax: +49 (7247) 82 48 37
Eml: xu.cheng@iket.fzk.de

ITALY

BARNI, Danilo
INFN Milano
LASA, Via Fratelli 11i Cervi 201
I-20090 SEGRATE

Tel: +39 (02) 503 19 544
Fax: +39 (02) 503 19 543
Eml: daniло.barni@mi.infn.it

BURGAZZI, Luciano
ENEA
Via Martiri di Monte Sole, 4
I-40129 BOLOGNA

Tel: +39 (051) 60 98 556
Fax: +39 (051) 60 98 279
Eml: bugazzi@bologna.enea.it

CALABRETTA, Luciano
Laboratori Nazionali del Sud - INFN
Via S. Sofia n 44
I-96123 CATANIA

Tel: +39 (095) 54 22 59
Fax: +39 (095) 54 23 00
Eml: calabretta@lns.infn.it

CHINCARINI, Andrea
INFN Genova
Via Dodecaneso 33
I-16146 GENOVA

Tel: +39 (010) 35 36 326
Fax: +39 (010) 31 33 58
Eml: andrea.chincarini@ge.infn.it

CIAVOLA, Giovanni
INFN-LNS
Via S. Sofia, 44
I-95123 CATANIA

Tel: +39 (095) 54 22 62
Fax: +39 (095) 54 23 02
Eml: ciavola@lns.infn.it

COMUNIAN, Michele
INFN-LNL
Via Romea, 4
I-35100 LEGNARO, PADOVA

Tel: +39 (049) 80 68 501
Fax: +39 (049) 80 68 829
Eml: comunian@inl.infn.it

ESPOSITIO, Juan
INFN-LNL
Via Romea, 4
I-35100 LEGNARO, PADOVA

Tel: +39 (049) 80 68 423
Fax: +39 (049) 80 68 829
Eml: juan.esposito@int.infn.it

GEMME, Gianluca
INFN Genova
Via Dodecaneso, 33
I-16146 GENOVA

Tel: +39 (010) 35 36 326
Fax: +39 (010) 31 33 58
Eml: gianluca.gemme@ge.infn.it

MONTI, Stefano
ENEA-ADS Project
Via Martiri de Monte Sole, 4
I-40129 BOLOGNA

Tel: +39 (051) 60 98 462
Fax: +39 (051) 60 98 785
Eml: monti@bologna.enea.it

NAPOLITANO, Marco
University "Federico II" and INFI
Dipart. Di Scienze Fisiche, Via Cinthia
I-80126 NAPOLI

Tel: +39 (081) 67 61 29
Fax: +39 (081) 67 63 46
Eml: marco.napolitano@na.infn.it

NEGRINI, Alberto
Ansaldo Nucleare
Corso Perrone 25
I-16161 GENEVA

Tel: +39 (010) 65 58 516
Fax: +39 (010) 65 58 400
Eml: negrini@ansaldo.it

PAGANI, Carlo
University Milano and INFN
LASA, Via Fratelli Cervi 201
I-20090 SEGRATE

Tel: +39 (02) 503 19 561
Fax: +39 (02) 503 19 543
Eml: carlo.pagani@mi.infn.it

SERTORE, Daniel
INFN Milano
LASA, Via Fratelli Cervi 201
I-20090 SEGRATE

Tel: +39 (02) 503 19 563
Fax: +39 (02) 503 19 543
Eml: daniele.sertore@mi.infn.it

JAPAN

MATSUMOTO, Taka-aki
Hokkaido University
North 13, West 8
SAPPORO 060-0813

Tel: +81 (11) 706 6682
Fax: +81 (11) 706 7888
Eml: mtmt@qe.eng.hokudai.ac.jp

OUCHI, Nobuo
JAERI
TOKAI-MURA
Ibaraki-ken, 319-1195

Tel: +81 (29) 282 5481
Fax: +81 (29) 282 5663
Eml: ouchi@linac.tokai.jaeri.jo.jp

KOREA, REPUBLIC OF

PARK, Won Seok
Korea Atomic Energy Research Institute
P.O. Box 105, YUSONG
Daejeon

Tel: +82 (42) 868 8375
Fax: +82 (42) 868 2080
Eml: wonpark@kaeri.re.kr

RUSSIA

PONOMAREV, Leonid
Russian Research Center "Kurchator Institute"
and Research Coordinative Center MUCATEX
ul. Rogova dom 9. Korpus 2
MOSCOW, D-98 123098

Tel: +7 (095) 947 27 72
Fax: +7 (095) 947 27 87
Eml: mucates.leonid@g23.relcom.ru

SPAIN

GONZALEZ-ROMERO, Enrique
CIEMAT
Av. Complutense, 22
Depart. Fision Nuclear. Edifc. 17
S-28040 MADRID

Tel: +34 (91) 346 6118
Fax: +34 (91) 246 6576
Eml: enrique.gonzalez@ciemat.es

SWITZERLAND

STAMMBACH, Thomas
Accelerator Division, PSI
Abt. ABE
CH-5232 VILLIGEN

Tel: +41 (56) 310 3370
Fax: +41 (56) 310 3383
Eml: thomas.stammbach@psi.ch

UNITED STATES OF AMERICA

BELLER, Denis
Los Alamos National Laboratory
Harry Reid Center for Environmental Studies
4505 Maryland Parkway, Box 454009
LAS VEGAS, NV 89154-4009

Tel: +1 (702) 895 2023
Fax: +1 (702) 895 3094
Eml: beller@lanl.gov

BOORE, Brent
Westinghouse Savannah River Compagny
P.O. Box 616, 703-45A, Rm. 250
AIKEN, SC 29802

Tel: +1 (803) 725 2364
Fax: +1 (803) 725 0632
Eml: brent.boore@srs.gov

BOYACK, Brent
Los Alamos National Laboratory
P.O. Box 1663,
LOS ALAMOS, New Mexico 87545

Tel: +1 (505) 667 2023
Fax: +1 (515) 665 2897
Eml: bboyack@lanl.gov

BROWN, Peter
 Lawrence Livermore National Laboratory
 7000 East Avenue, L-561
 LIVERMORE, CA 94551
 Tel: +1 (925) 423 2098
 Fax: +1 (925) 423 2993
 Eml: pnbrown@llnl.gov

CAHALAN, James E.
 Argonne National Laboratory
 Reactor Analysis & Engineering Division
 9700 South Cass Ave.
 ARGONNE, IL 60439
 Tel: +1 (630) 252 4682
 Fax: +1 (630) 252 4500
 Eml: jecahalan@anl.gov

CALLAWAY, Tim
 Los Alamos National Laboratory
 P.O. Box 1663, MS H812
 LOS ALAMOS, New Mexico 87545
 Tel: +1 (505) 665 2393
 Fax: +1 (505) 667 7443
 Eml: ncallaway@lanl.gov

CAPPIELLO, Michael
 Los Alamos National Laboratory
 P.O. Box 1663, MS H816
 LOS ALAMOS, New Mexico 87545
 Tel: +1 (505) 665 6408
 Fax: +1 (505) 667 7443
 Eml: mcappiello@lanl.gov

CHANG, Britton
 Lawrence Livermore National Laboratory
 P.O. Box 808, L-561
 LIVERMORE, CA 94550
 Tel:
 Fax: +1 (925) 423 2993
 Eml: bchang@llnl.gov

CHIDESTER, Ken
 Los Alamos National Laboratory
 P.O. Box 1663, MS K551
 LOS ALAMOS, New Mexico 87545
 Tel: +1 (505) 667 2358
 Fax: +1 (505) 667 7443
 Eml: kchidester@lanl.gov

COHEN, Howard
 BREI
 2237 Trinity Dr.
 LOS ALAMOS, New Mexico 87544
 Tel: +1 (505) 661 4419
 Fax: +1 (505) 661 1350
 Eml: hcohen@roe.com

CULBRETH, William
 University of Nevada, Las Vegas
 4505 Maryland Parkway
 LAS VEGAS, NV 89154-4027
 Tel: +1 (702) 895 3426
 Fax: +1 (702) 895 3936
 Eml: culbreti@clark.nscee.edu

DEVLIN, Matthew
 Los Alamos National Laboratory
 P.O. Box 1663, MS H855
 LOS ALAMOS, New Mexico 87545
 Tel: +1 (505) 665 0421
 Fax: +1 (505) 665 3705
 Eml: devlin@lanl.gov

DUNN, Floyd
 Argonne National Laboratory
 9700 South Cass Ave., Bld. 208, Rm. C166
 ARGONNE, IL 60439
 Tel: +1 (630) 252 4692
 Fax: +1 (630) 252 4500
 Eml: fedunn@anl.gov

FINCK, Phillip J.
Argonne National Laboratory
9700 South Cass Avenue, Bldg. 207
ARGONNE, IL 60439

Tel: +1 (630) 252 1987
Fax: +1 (630) 252 4007
Eml: pfinck@anl.gov

GARNETT, Robert
Los Alamos National Laboratory
P.O. Box 1663, MS H855
LOS ALAMOS, New Mexico 87545

Tel: +1 (505) 665 2835
Fax: +1 (505) 665 2904
Eml: rgarnett@lanl.gov

GOHAR, Yousry
Argonne National Laboratory
9700 South Cass Avenue
ARGONNE, IL 60439

Tel: +1 (630) 252 4816
Fax: +1 (630) 252 4007
Eml: gohar@anl.gov

GOLDNER, Frank
US Department of Energy
1000 Independence Ave.
WASHINGTON, DC 20585

Tel: +1 (202) 586 1846
Fax: +1 (202) 586 3701
Eml: frank.goldner@hq.doe.gov

GUFFEE, Ray
Los Alamos National Laboratory
P.O. Box 1663, MS H821
LOS ALAMOS, New Mexico 87545

Tel: +1 (505) 667 1374
Fax: +1 (505) 667 3558
Eml: guffee@lanl.gov

HECHANOVA, Anthony
University of Nevada, Las Vegas
4505 Maryland Parkway, Box 454009
LAS VEGAS, NV 89154-4009

Tel: +1 (702) 895 1457
Fax: +1 (702) 895 3094
Eml: hechanova@univ.edu

HERCEG, Joseph
Argonne National Laboratory
9700 South Cass Avenue, Bldg 208, G123A
ARGONNE, IL 60439

Tel: +1 (630) 252 3333
Fax: +1 (630) 252 7577
Eml: jeherceg@anl.gov

HERRERA, LeeRoy
Los Alamos National Laboratory
P.O. Box 1663, MS P366
LOS ALAMOS, New Mexico 87545

Tel: +1 (505) 665 5593
Fax: +1 (505) 665 7530
Eml: ljherrera@lanl.gov

JAMES, Michael R.
Los Alamos National Laboratory
P.O. Box 1663, MS K575
LOS ALAMOS, New Mexico 87545

Tel: +1 (505) 665 6521
Fax: +1 (505) 665 2897
Eml: mrjames@lanl.gov

KRAKOWSKI, R
Los Alamos National Laboratory
P.O. Box 1663, F607
LOS ALAMOS, New Mexico 87545

Tel: +1 (505) 667 5863
Fax: +1 (505) 667 5283
Eml: krakowski@lanl.gov

LI, Ning Los Alamos National Laboratory P.O. Box 1663, MS H854 LOS ALAMOS, New Mexico 87545	Tel: +1 (505) 665 6677 Fax: +1 (505) 665 6927 Eml: ningli@lanl.gov
MALOY, Stuart Los Alamos National Laboratory P.O. Box 1663, MS H809 LOS ALAMOS, New Mexico 87545	Tel: +1 (505) 667 9784 Fax: +1 (505) 667 2787 Eml: maloy@lanl.gov
MCCONNELL, Steve Westinghouse Savannah River Compagny Savannah River Site, 705-A/102 AIKEN, SC 29808	Tel: +1 (803) 725 6025 Fax: +1 (803) 725 0888 Eml: steven.mcconnell@srs.gov
PACIOTTI, Michael Los Alamos National Laboratory P.O. Box 1663, MS H846 LOS ALAMOS, New Mexico 87545	Tel: +1 (505) 667 7127 Fax: Eml: paciotti@lanl.gov
PASAMEHMETOGLU, Kemal Los Alamos National Laboratory P.O. Box 1663, MS H816 LOS ALAMOS, New Mexico 87545	Tel: +1 (505) 667 8893 Fax: +1 (505) 667 7743 Eml: kop@lanl.gov
PEDERSEN, Dean Argonne National Laboratory 9700 South Cass Avenue ARGONNE, IL 60439	Tel: +1 (630) 252 3331 Tel: +1 (505) 665 6171 & (704) 799 1936 Eml: pederson@anl.gov
PITCHER, Eric Los Alamos National Laboratory P.O. Box 1663, MS H805 LOS ALAMOS, New Mexico 87545	Tel: +1 (505) 665 0651 Fax: +1 (505) 665 2676 Eml: pitcher@lanl.gov
ROGERS, Berylene Los Alamos National Laboratory P.O. Box 1663, MS H816 LOS ALAMOS, New Mexico 87545	Tel: +1 (505) 667 0414 Fax: +1 (505) 667 7443 Eml: brogers@lanl.gov
ROGLANS-RIBAS, Jordi Argonne National Laboratory 9700 South Cass Avenue, Bldg. 208 ARGONNE, IL 60439	Tel: +1 (630) 252 3283 Fax: +1 (630) 252 4620 Eml: roglans@anl.gov
RUSTHOI, Daniel Los Alamos National Laboratory P.O. Box 1663, MS H816 LOS ALAMOS, New Mexico 87545	Tel: +1 (505) 667 2796 Fax: +1 (505) 667 7443 Eml: rusthoi@lanl.gov

<p>RYDER, Richard Los Alamos National Laboratory P.O. Box 1663, MS H812 LOS ALAMOS, New Mexico 87545</p>	<p>Tel: +1 (505) 667 2936 Fax: +1 (505) 665 0046 Eml: ryder@lanl.gov</p>
<p>SALVATORES, Massino Argonne National Laboratory 9700 South Cass Avenue, Bldg. 208 ARGONNE, IL 60439</p>	<p>Tel: +1 630 252 4685 Fax: +1 630 252 4780 Eml: salvatores@anl.gov</p>
<p>SCHNEIDER, J. David Los Alamos National Laboratory P.O. Box 1663, MS A135 LOS ALAMOS, New Mexico 87545</p>	<p>Tel: +1 (505) 667 5454 Fax: +1 (505) 667 5739 Eml: jdschneider@lanl.gov</p>
<p>SHEETZ, Steve Westinghouse Savannah River Compagny P.O. Box 616, Bldg. 703-45A AIKEN, SC 29808</p>	<p>Tel: +1 (803) 725 2080 Fax: +1 (803) 725 0632 Eml: steve.sheetz@srs.gov</p>
<p>SHEFFIELD, Richard Los Alamos National Laboratory P.O. Box 1663, MS H851 LOS ALAMOS, New Mexico 87545</p>	<p>Tel: +1 (505) 667 1237 Fax: +1 (505) 667 8207 Eml: sheff@lanl.gov</p>
<p>TCHARNOTSKAIA, Valentina Los Alamos National Laboratory P.O. Box 1663, MS H855 LOS ALAMOS, New Mexico 87545</p>	<p>Tel: +1 (505) 665 9375 Fax: +1 (505) 665 3705 Eml: valentina@lanl.gov</p>
<p>VALDIVIEZ, Robert Los Alamos National Laboratory P.O. Box 1663, MS H817 LOS ALAMOS, New Mexico 87545</p>	<p>Tel: +1 (505) 667 2619 Fax: +1 (505) 665 2904 Eml: valdiviez@lanl.gov</p>
<p>WANGLER, Thomas Los Alamos National Laboratory P.O. Box 1663, MS H817 LOS ALAMOS, New Mexico 87545</p>	<p>Tel: +1 (505) 667 3200 Fax: +1 (505) 665 2904 Eml: twangler@lanl.gov</p>
<p>WARD, Thomas AAA University Programs NE-30 WASHINGTON, DC 20585</p>	<p>Tel: +1 (202) 586 7255 Fax: +1 (202) 586 1966 Eml: thomas.ward@nnsa.doe.gov</p>
<p>WILLCUTT, Gordon Los Alamos National Laboratory P.O. Box 1663, MS K575 LOS ALAMOS, New Mexico 87545</p>	<p>Tel: +1 (505) 667 5869 Fax: Eml: gwillcutt@lanl.gov</p>

INTERNATIONAL ORGANISATIONS

ZANINI, Luca
CERN
CH-1211 GENEVA 23

Tel: +41 (22) 767 5461
Fax: +41 (22) 767 7555
Eml: luca.zanini@cern.ch

NA, Byung Chan
OECD Nuclear Energy Agency, Data Bank
12 boulevard des Iles,
F-92130 ISSY-LES-MOULINEAUX

Tel: +33(0)1 4524 1091
Fax: +33(0)1 4524 1128
Eml: na@nea.fr

ALSO AVAILABLE

NEA Publications of General Interest

2001 Annual Report (2002)

Free: paper or Web.

NEA News

ISSN 1605-9581

Yearly subscription: € 40 US\$ 45 GBP 26 ¥ 4 800

Nuclear Science

Physics of Plutonium Recycling

Volume VII – BWR MOX Benchmark – Specification and Results (2003)

ISBN 92-64-19905-5

Price: € 45 US\$ 45 GBP 29 ¥ 5 500

Volume VI – Multiple Pu Recycling in Advanced PWRs (2002)

ISBN 92-64-19957-8

Price: € 45 US\$ 45 GBP 28 ¥ 5 250

Advanced Reactors with Innovative Fuels (2002)

ISBN 92-64-19847-4

Price: € 130 US\$ 113 GBP 79 ¥ 15 000

Basic Studies in the Field of High-temperature Engineering (2002)

ISBN 92-64-19796-6

Price: € 75 US\$ 66 GBP 46 ¥ 8 600

Fission Gas Behaviour in Water Reactor Fuels (2002)

ISBN 92-64-19715-X

Price: € 120 US\$ 107 GBP 74 ¥ 12 100

Shielding Aspects of Accelerators, Targets and Irradiation Facilities – SATIF 5 (2001)

ISBN 92-64-18691-3

Price: € 84 US\$ 75 GBP 52 ¥ 8 450

Nuclear Production of Hydrogen (2001)

ISBN 92-64-18696-4

Price: € 55 US\$ 49 GBP 34 ¥ 5 550

Utilisation and Reliability of High Power Proton Accelerators (2001)

(ISBN 92-64-18749-9

Price: € 130 US\$ 116 GBP 80 ¥ 13 100

Accelerator-driven Systems (ADS) and Fast Reactors (FR) in Advanced Nuclear Fuel Cycles (2002)

ISBN 92-64-18482-1

Free: paper or web.

Comparison Calculations for an Accelerator-driven Minor Actinide Burner (2002)

ISBN 92-64-18478-3

Free: paper or web.

Speciation, Techniques and Facilities for Radioactive Materials at Synchrotron Light Sources (2002)

Workshop Proceedings, Grenoble, France, 10-12 September 2000

ISBN 92-64-18485-5

Free: paper or web.

Pressurised Water Reactor Main Steam Line Break (MSLB) Benchmark (Volume III) (2002)

ISBN 92-64-18495-3

Free: paper or web.

A VVER-1000 LEU and MOX Assembly Computational Benchmark (2002)

Specification and Results

ISBN 92-64-18491-0

Free: paper or web.

Order form on reverse side.

ORDER FORM

OECD Nuclear Energy Agency, 12 boulevard des Iles, F-92130 Issy-les-Moulineaux, France
Tel. 33 (0)1 45 24 10 15, Fax 33 (0)1 45 24 11 10, E-mail: neapub@nea.fr, Internet: www.nea.fr

Qty	Title	ISBN	Price	Amount
Total*				

* Prices include postage fees.

Payment enclosed (cheque payable to OECD Publications).

Charge my credit card VISA Mastercard American Express

Card No.	Expiration date	Signature
Name		
Address		Country
Telephone	Fax	
E-mail		

OECD PUBLICATION, 2, rue André-Pascal, 75775 PARIS CEDEX 16
PRINTED IN FRANCE
(66 2003 09 1 P) – No. 53047 2003

OECD PUBLICATION, 2, rue André-Pascal, 75775 PARIS CEDEX 16
PRINTED IN FRANCE
(35 2003 01 3 P) – No. 52942 2003